Patching up the genome's guardian to fight cancer *p. 26*

Synthesizing the shine of mollusk shells *pp. 32 & 107*

Brain neurons still finding places after birth *pp. 38 & 81*

Science

$15
7 OCTOBER 2016
sciencemag.org

AAAS

SPECIAL ISSUE

GENES & ENVIRONMENT

CONTENTS

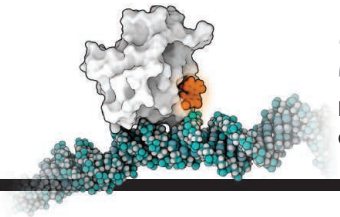

26
Fixing a broken cancer suppressor

7 OCTOBER 2016 • VOLUME 354 • ISSUE 6308

SPECIAL SECTION
GENES & ENVIRONMENT

ON THE COVER

A Sherpa porter at the base of the Khumbu Ice Fall, Mount Everest. Some human populations exhibit greater tolerance for high elevation, due to genetic variants that likely mitigate the deleterious effects of low oxygen concentrations at altitude. Genetic and epigenetic changes shape our response to the environment and may play a role in disease. For more on the interactions between genes and the environment, see page 52. *Photo: Max Lowe/National Geographic Creative*

NEWS

INSIGHTS

Published by AAAS

CONTENTS

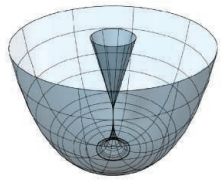

35 & 83
Cold atoms mimicking condensed matter

7 OCTOBER 2016 • VOLUME 354 • ISSUE 6308

SCIENCE (ISSN 0036-8075) is published weekly on Friday, except the last week in December, by the American Association for the Advancement of Science, 1200 New York Avenue, NW, Washington, DC 20005. Periodicals mail postage (publication No. 484460) paid at Washington, DC, and additional mailing offices. Domestic individual membership and subscription (51 issues): $165 ($74 allocated to subscription). Domestic institutional subscription (51 issues): $1522; Foreign postage extra: Mexico, Caribbean (surface mail) $55; other countries (air assist delivery) $89. First class, airmail, student, and emeritus rates on request. Canadian rates with GST available upon request, GST #1254 88122. Publications Mail Agreement Number 1069624. **Printed in the U.S.A.**
Change of address: Allow 4 weeks, giving old and new addresses and 8-digit account number. **Postmaster:** Send change of address to AAAS, P.O. Box 96178, Washington, DC 20090–6178. **Single-copy sales:** $15.00 current issue, $20.00 back issue prepaid includes surface postage; bulk rates on request. *Science* is indexed in the *Reader's Guide to Periodical Literature* and in several specialized indexes.

Published by AAAS

Science
AAAS
1200 New York Avenue, NW, Washington, DC 20005
Clarendon House, Clarendon Road, Cambridge, UK CB2 8FH

SUBSCRIPTION SERVICES For change of address, missing issues, new orders and renewals, and payment questions: 866-434-AAAS (2227) or 202-326-6417, FAX 202-842-1065. Mailing addresses: AAAS, P.O. Box 96178, Washington, DC 20090-6178 or AAAS Member Services, 1200 New York Avenue, NW, Washington, DC 20005

INSTITUTIONAL SITE LICENSES 202-326-6730 **REPRINTS:** Author Inquiries 800-635-7181 **COMMERCIAL INQUIRIES** 803-359-4578 **PERMISSIONS** 202-326-6765, permissions@aaas.org **AAAS Member Services** 202-326-6417 or http://membercentral.aaas.org/discounts

Science serves as a forum for discussion of important issues related to the advancement of science by publishing material on which a consensus has been reached as well as including the presentation of minority of conflicting points of view. Accordingly, all articles published in *Science*—including editorials, news and comment, and book reviews—are signed and reflect the individual views of the authors and not official points of view adopted by AAAS or the institutions with which the authors are affiliated.

INFORMATION FOR AUTHORS See pages 624 and 625 of the 5 February 2016 issue or access www.sciencemag.org/authors/science-information-authors

EDITORIAL

Gene–environment interplay

Editor-in-Chief,
Science *Journals*

The advent of increasingly powerful and inexpensive DNA sequencing methods is changing many aspects of genetics research. In particular, human genome sequencing is transforming our understanding of many aspects of human biology and medicine. However, we must be careful to remember that genes alone do not determine our futures—environmental factors and chance also play important roles.

I recall a discussion with Nobel laureate Michael Brown at a scientific meeting some years ago when he described his opening lecture for a medical school human genetics course. He asked the class, "How would you produce a new genetic disease in the state of Texas?" After listening to answers almost invariably based on inducing mutations, Dr. Brown described his preferred answer—he would change the building codes so that no doorway could be taller than 6 feet. This would produce a "bruised forehead syndrome" that would be sex-linked (more common in males) and would also have other predisposing genetic factors for which variations are associated with tall stature. His answer captures an essential aspect of the interplay between genes and environment. Genetic variants that have evolved in one set of circumstances to be beneficial or neutral can be quite detrimental in other conditions. For example, many aspects of our metabolism evolved under conditions where calories were hard to come by. Now, in the environments of rich nations where calories are all too easy to acquire, these genetic factors contribute to obesity and other detrimental health effects.

"...genes alone do not determine our futures..."

Among the oldest and most powerful methods for examining the genetic contributions to different traits is the study of twins. In these studies, populations of monozygotic ("identical") and fraternal twins are examined for the likelihood that twins share particular traits. For example, height is highly heritable, and most monozygotic twin pairs differ in height by less than an inch. Nonetheless, a small percentage of such twins show larger height differences, and these have been associated with the occurrence and timing of early childhood illnesses—chance events related to environmental factors. Other traits show much lower concordance in twin studies. For example, if one member of a monozygotic twin pair has developed the autoimmune disease rheumatoid arthritis, then the probability that the other member will develop it is estimated to be 15%. This is substantially higher than the risk in fraternal twin pairs, supporting the presence of important genetic risk factors; indeed, some important genes have been identified. Clearly, however, other, environmental and chance factors are also important, although these remain largely elusive at present.

Even if traits are largely determined by genetics, predicting these traits from genome sequence information can be extremely challenging. For example, in a recent large study, variations in more than 400 genes were associated with differences in adult stature that together account for less than half of the observed distribution in height. This result is humbling, but it should not be surprising considering all of the cell-cell interactions, growth factor expression cascades, and other events that occur between fertilization and maturity.

In addition to elucidating genetic makeup, powerful genetic analysis tools should enable progress in understanding environmental effects on health and other important traits. Investigators can stratify populations according to genetic makeup and inferred genetic risk as a prelude to examining environmental factors, just as has been done with monozygotic twins. Without tools for such stratification, the effects of genetic and environmental factors are entangled in ways that greatly obscure insight. This is particularly important because precise and accurate measurement of environmental exposures, including diet, materials in our surroundings, and stress, is a great challenge. New technologies such as wearable devices that monitor personal characteristics and, perhaps, environmental exposures may help in this regard, but only time will tell.

–Jeremy Berg

10.1126/science.aal0219

> “One of her favorite expressions is the four-paw pounce. Take her a weak idea and you’ll get the four-paw pounce.”
>
> **William Madia, vice president of the Stanford Linear Accelerator Center in Menlo Park, California**, on the high standards of Department of Energy Deputy Director for Science Programs Pat Dehmer, who steps down 10 November. **http://scim.ag/Dehmerretire**

IN BRIEF

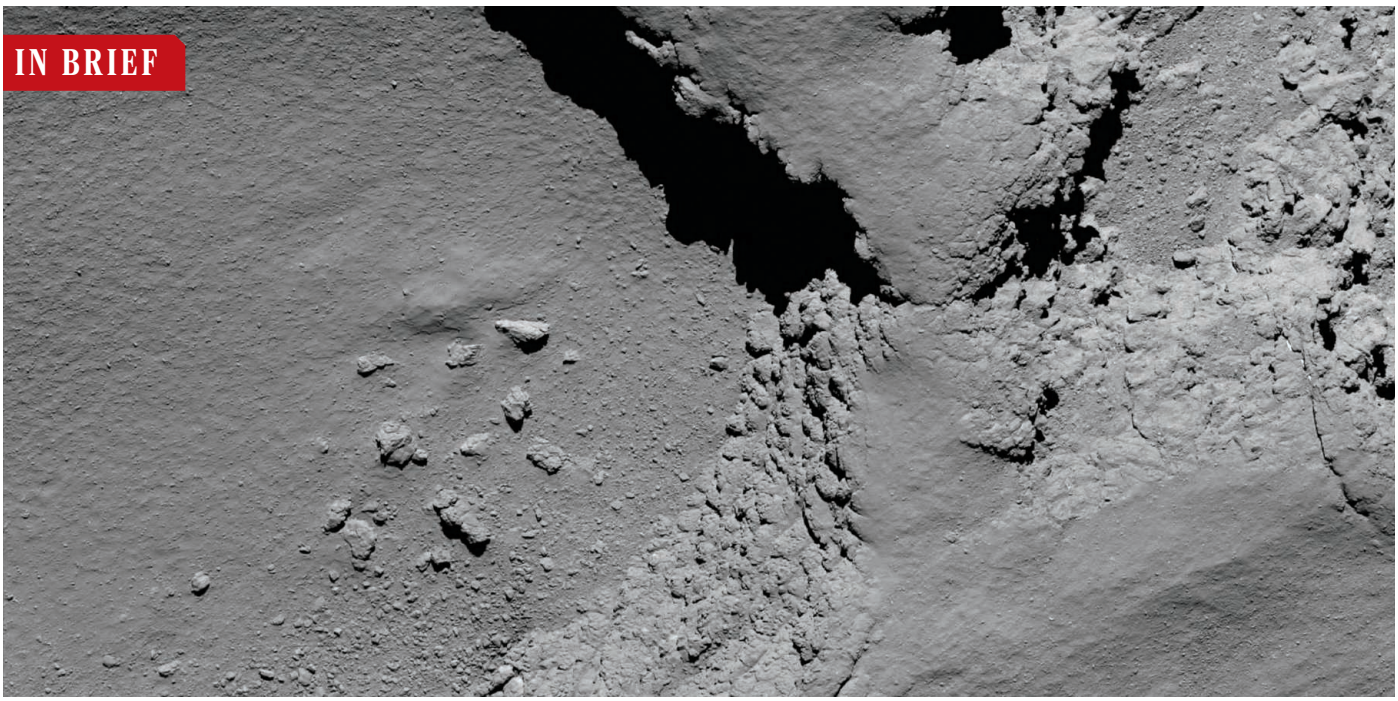

At 5.8 kilometers above the comet’s surface, Rosetta snapped an image of curious, 3-meter-wide “goosebumps” in deep pits on the comet; these may be its building blocks.

Rosetta’s last moments, in pictures

It was an unusual grand finale. The crowded European Space Agency operations center in Darmstadt, Germany, waited in silence. Then, the signal from the descending Rosetta mission simply stopped, at 1:19 p.m. local time—some 40 minutes after the spacecraft had, presumably, landed on comet 67P/Churyumov-Gerasimenko, because of the time the signal takes to reach Earth. Mission controllers hugged each other, and there was gentle applause from onlookers. Seven of Rosetta’s instruments kept gathering data until the end. Holger Sierks, principal investigator of the 12-year mission’s main camera, showed the gathered staff, officials, and journalists Rosetta’s final picture: the comet’s rough, gravelly surface, with a few larger rocks covering an area 10 meters across. “It’s very crude raw data … but this will keep us busy,” Sierks said. The mission achieved many firsts: orbiting a comet for the first time; landing on a comet, twice; finding organic molecules that could be the building blocks of life; and showing that the water on the comet is unlike that on Earth, confounding theories that comets supplied our planet with water. Said Patrick Martin, the mission manager: “Farewell Rosetta, you’ve done the job. That was space science at its best.”

AROUND THE WORLD

Acquittal ends L’Aquila saga

ROME | Seven years of legal and scientific wrangling ended last week when a judge cleared an Italian official of manslaughter charges in connection with the deadly 2009 earthquake in the city of L’Aquila. Guido Bertolaso, head of Italy’s Civil Protection department at the time, was accused of sending a panel of scientists to L’Aquila in the days before the disaster to falsely reassure citizens that hundreds of small tremors essentially ruled out a major quake. Judge Giuseppe Grieco acquitted Bertolaso on 30 September, and as a result of Italy’s “period of limitation,” time has already run out for prosecutors to appeal. The trial followed that of seven scientists found guilty of manslaughter in 2012 because they allegedly reassured L’Aquila residents. The convictions of six of them were later overturned (*Science*, 14 November 2014, p. 794), but one, Bertolaso’s deputy, Bernardo De Bernardinis, was confirmed with a lesser 2-year sentence, which will remain suspended. **http://scim.ag/BertolasoLAquila**

Kratom gets a reprieve

SPRINGFIELD, VIRGINIA | A Southeast Asian plant that has become a popular remedy for chronic pain remains legal—for now. The Drug Enforcement Administration (DEA), headquartered in Springfield, Virginia, on 30 August announced its plans to place the two active ingredients of *Mitragyna speciosa*, a tropical evergreen related to coffee, on its Schedule I listing of the most restricted drugs as early as 30 September. The news prompted a backlash, and as of 4 October, when *Science* went to press, the ingredients remained off the list. More than 140,000 people signed a petition urging the White House to block the listing; last week 51 members of the House of Representatives signed a letter asking DEA to allow more time for scientists and the public to weigh in on the potential benefits of kratom. The letter cites two research projects investigating its potential to help people suffering from opioid withdrawal. Kratom advocates hope for an indefinite postponement, but a DEA spokesperson told *U.S. News & World Report* last week: "It's not a matter of if, it's just a matter of when."

Ideology shapes views on climate

WASHINGTON, D.C. | Political ideology shapes what U.S. citizens think about climate researchers and their findings, suggest the results of a survey conducted in May by the Pew Research Center. Some 1534 adults answered questions about their trust in climate scientists and the role scientists should play in setting climate policy. The results, reported this week, revealed sharp divisions along party lines: Seventy percent of liberal Democrats said they trusted climate scientists "a lot," compared with only 15% of conservative Republicans; 45% of conservatives had "little or no trust" in scientists, compared with only 6% of liberals. Some 57% of conservative Republicans cited career advancement as a major driver of scientists' conclusions, compared with 16% of liberal Democrats. And 90% of respondents who care a lot about climate change said that scientists should play a major role, compared with 34% who don't care. As for trustworthiness: Thirty-nine percent of all respondents said scientists are trustworthy on climate issues—scoring well above the media, at 7%, and elected officials, at 4%.

U.S. shutdown averted

WASHINGTON, D.C. | The U.S. government remains open after Congress passed a 10-week budget extension on 28 September that freezes agency spending at current levels. The so-called "continuing resolution" provides $1.1 billion to combat Zika, but otherwise postpones a final decision on any proposed budget hikes for the 2017 fiscal year that began on 1 October until after the 8 November elections. Republican leaders say they hope to pass a new blueprint for federal investment in biomedical research after the elections, and bills to reauthorize programs at NASA and the National Science Foundation are also awaiting action.

PHOTO: DESIGN PICS INC/ALAMY STOCK PHOTO

Emissions from burning oil extracted from Alberta's oil sands face a tax under the carbon-pricing plan.

Trudeau says Canada will put a price on carbon

As federal, provincial, and territorial environment ministers met in Montreal, Canada, this week to hammer out a national carbon reduction plan, Prime Minister Justin Trudeau dropped a bombshell on their negotiations. He announced to the House of Commons on 3 October that in 2018, Ottawa will impose a pan-Canadian tax on carbon, at $7.62 per metric ton minimum. The tax will rise by $7.62 each year, up to $38.11 per metric ton in 2022. Some provinces and territories already have plans to help meet Canada's carbon emissions reduction goal: British Columbia and Alberta have introduced carbon taxes, and Ontario and Quebec began cap-and-trade systems to buy and sell emissions permits. But with Trudeau's announcement, the government will impose a tax on provinces and territories that don't pick an approach. Provincial reaction ranged from tacit approval to outrage: Three provincial environment ministers protested the announcement by walking out of the high-level meeting. Meanwhile, some critics say carbon pricing isn't enough, and that the country will also need strong regulations to meet its climate targets. Trudeau said he would meet with provincial and territorial ministers in December to finalize his plan. **http://scim.ag/Canadacarbon**

NEWSMAKERS

Three Qs

The new top scientist at NASA has spent the past 2 decades as a solar physicist at the University of Michigan, Ann Arbor. But **Thomas Zurbuchen**, who this week became associate administrator of NASA's science mission directorate, says he's well versed in all aspects of the agency's $5 billion portfolio, from earth and planetary science to astrophysics and heliophysics.

Q: What do you want to accomplish?
A: There's an amazing program going on right now, and I'll focus on executing that program to its success. [I also want] to build the future—to create success by working with the team that's there. I look forward to building consensus.

Q: How will your background inform your new role?
A: If you look carefully, you'll see that I've done more than heliophysics. I had an instrument on the MESSENGER mission [to Mercury], and I've written papers on intergalactic issues. I've worked in all phases of a mission; from the drawing board to an instrument crashing onto the planet Mercury after a successful mission and everything in between.

Q: Any particular missions or ideas you're excited about?
A: The knowledge in many fields is exploding. Look at the planetary side: The evidence for life and organics and other exciting processes is coming up in a variety of measurements, whether it's on Europa, or Mars, or elsewhere. That's really reformulating and redefining some of the questions we're asking.

PHOTO: HUGH AND CHRIS HEMPEL

BIOMEDICINE

Battle over rare disease drug ensnares NIH

Firms and parents of kids with fatal condition clash over drug delivery and role of agency

By **Meredith Wadman**

The National Institutes of Health's (NIH's) ambitious center devoted to speeding research from bench to bedside regularly touts an experimental drug for a rare metabolic disorder as one of its first big successes. But a bitter fight involving NIH, two companies, and opposing camps of researchers and parents of children with the fatal condition is marring the triumph. The flashpoints include how to administer the drug and whether the 5-year-old National Center for Advancing Translational Sciences (NCATS) in Bethesda, Maryland, has tilted the commercial playing field in favor of one company. A disgruntled, competing firm has even sent a letter to Francis Collins, the director of NIH, with copies to several members of Congress, complaining that the agency is "choosing winners and losers in the development programs of private enterprises."

The furor surrounds the use of cyclodextrins, a family of doughnut-shaped sugar molecules, to treat Niemann-Pick type C-1 (NPC), a lethal, inherited disease that prevents the body from metabolizing cholesterol and other lipids. The resulting accumulation of fats harms the brain, liver, and lungs. It is almost always the brain damage that kills, often by the time children reach their teens.

Over the past decade, researchers working with cat and mouse models of NPC have shown that cyclodextrins can alleviate symptoms and slow progression of the disease. Although their mechanism of action isn't fully understood, cyclodextrins readily bind cholesterol, depleting it from cells in culture. As word of the animal findings spread, a number of desperate parents obtained U.S. Food and Drug Administration approval for their physicians to administer the drug under "compassionate use" protocols. Their experiences produced anecdotal reports of improvements.

Meanwhile, to conduct lab studies of the compound and then formal human safety trials, NCATS was orchestrating a collaboration between several extramural investigators, six NIH institutes, and a handful of foundations launched by parents of children with NPC. In December 2014, the center entered a cooperative research and development agreement under which Vtesse, a Gaithersburg, Maryland, company, took over the therapy, speeding the drug into a pivotal, late-stage clinical trial in the space of 18 months. This is "a huge win for us, for patients: having gotten this compound through the so-called Valley of Death in this kind of collaborative team-based way in a remarkably short time and successfully handed it off to private industry," says NCATS Director Chris Austin.

But Vtesse has a rival, which is starting clinical trials of its own cyclodextrin. CTD Holdings, a small, Gainesville, Florida–based company that makes cyclodextrins for a broad variety of purposes, became aware of their potential as an NPC treatment after being contacted by Chris and Hugh Hempel, the parents of twin girls with the disease. Last month, it won regulatory approvals in the United States and the United Kingdom to launch trials studying the safety and pharmacological effects of Trappsol Cyclo, the cyclodextrin it has developed for NPC treatment. Whereas Vtesse's clinical trial delivers its drug, VTS-270, directly into the cerebrospinal fluid by lumbar puncture, CTD will test intravenous (IV) administration.

That difference is at the heart of the multifaceted dispute. To most effectively attack neurological symptoms, the drug must reach the brain, and cyclodextrin is a large molecule that does not cross the blood-brain barrier. That's why Vtesse, and before it the NCATS-convened team, chose the "intrathecal" route, into the cerebrospinal fluid. Vtesse says that unpublished results from an earlier trial when the drug was still being shepherded by NCATS showed that children with NPC who received the drug intrathecally had "significantly" less neurological progression after 12 and 18 months than a control group of untreated children. It is now running a late-stage, randomized, double blind, sham-controlled trial of its intrathecal cyclodextrin in children and teens with NPC in the

Hugh and Chris Hempel, whose daughters Addi (left) and Cassi have Niemann-Pick type C-1 and receive cyclodextrin intravenously and via spinal injections.

United States and Europe, with additional trial sites awaiting approval in Australia.

How the drug could aid the brain if instead given intravenously is unclear, but some data suggest it can. In mouse models of the disease, cyclodextrin administered peripherally delayed disease onset, reduced brain accumulation of fat, and lengthened life significantly, several published studies have found. In presentations this summer, CTD representatives reported anecdotal cases of neurological improvements—such as in motor skills and speech—in children treated intravenously with the company's cyclodextrin on a compassionate use basis, including the Hempels' daughters. The company further notes that the IV delivery method may protect other organs affected by NPC.

The suggestion that the IV form of the drug can cause meaningful neurological improvements in children enraged some parents, however. At a June meeting in Tuscon, Arizona, of the Ara Parseghian Medical Research Foundation "all hell broke loose," recalls biochemist Elizabeth Neufeld of the University of California, Los Angeles, an expert in lysosomal storage diseases including NPC. "I have never seen anything like that at a meeting." The tensions continued at an August meeting of the National Niemann-Pick Disease Foundation in Danvers, Massachusetts.

Some parents and scientists charge that CTD is promising brain improvements its drug cannot deliver and siphoning rare patients who might otherwise enroll in the Vtesse clinical trial. "If you are going to try to start selling parents on 'You don't need to do intrathecal,' you are putting children at risk in my opinion. I got very upset," says Philip Marella, who lost his daughter at 19 to the disease and whose 17-year-old son is receiving cyclodextrin intrathecally as part of Vtesse's trial. "If we could hold the neurological symptoms off some other way than giving my son a spinal tap every 2 weeks, believe me I would do it."

Some NPC researchers not connected to Vtesse echo such concern. "This is a neurological disease and to have the best hope of helping the kids, the drug has to get into the brain," says biochemist Suzanne Pfeffer of Stanford University in Palo Alto, California.

Yet some parents of children with NPC are supportive of CTD's proposed trial and equally adamant that the IV route should be an option. "Not all NPC patients present with neurological complications. To generalize about a condition that is highly heterogeneous misses the point entirely," Chris Hempel says. "Intrathecal therapy alone is not enough for him," adds Shannon Reedy, whose 7-year-old son Chase has NPC. "I can tell you with certainty that after beginning just intravenous [cyclodextrin] my son began rapidly adding vocabulary and had improved swallow studies. His fine motor improved markedly as well."

A European NPC expert, who has no ties to either company and wishes to remain anonymous, says that a clear case can be made for testing IV-only cyclodextrin treatment of the disease—for instance, in families that may not want to expose their children to the more invasive intrathecal procedures, and in adults who develop a later-onset form of the disease that progresses more slowly. This researcher says that the CTD trial, which is enrolling adults in the United States and children in Europe, should resolve whether IV therapy has no neurological benefit, as critics contend.

Andrew and Dana Marella, in 2012. Dana died in 2013. Now 17, Andrew receives cyclodextrin by spinal injection in a clinical trial. An estimated 43 babies are born with Niemann-Pick type C-1 in the United States each year.

In a new twist, two Vtesse-affiliated, NIH-funded scientists are proposing their own trials of IV delivery. The development has infuriated CTD, which is criticizing NIH and several of its intramural and extramural investigators who study NPC. In a 19 August letter to Collins, attorneys representing CTD warned that NIH will undermine the company if it supports the two proposed trials, which would test IV delivery of Vtesse's cyclodextrin in babies and children, in hopes of protecting their livers and other organs that intrathecal delivery cannot reach.

One of the proposals lambasted by CTD comes from Forbes Porter of NIH's Eunice Kennedy Shriver National Institute of Child Health and Human Development in Bethesda, who ran the NCATS-sponsored early human studies of the cyclodextrin that became VTS-270 and who now co-chairs Vtesse's Scientific Advisory Board. Porter would give the drug intravenously to affected children and monitor markers of chronic liver inflammation and liver lipid and cholesterol storage. In the other proposal, Daniel Ory, who studies NPC biomarkers at Washington University in St. Louis in Missouri and is a member of Vtesse's Preclinical Scientific Advisory Board, is seeking NIH funding to test VTS-270 intravenously in NPC newborns suffering from aggressive liver disease because of fat accumulation. The hope is that they might be spared liver transplants or downstream cancer or cirrhosis. In a second arm, Ory would add IV therapy to the regime of children receiving the drug intrathecally.

"Why would NIH launch an intravenous trial? That's a duplication of effort," charges developmental neuroscientist Sharon Hrynkow, CTD's senior vice president of medical affairs and former acting director of NIH's Fogarty International Center. "It's a waste of taxpayer dollars, because it is already being done by CTD."

CTD's complaints are "troubling" because the duplication of private sector work "is exactly what NCATS is not doing," Austin says. "We don't have any more control over what Vtesse is doing than I have over the Washington Nationals. … In fact, NCATS did exactly what the congressional legislation that established it said: to de-risk something just to the point where it can be licensed to the private sector."

N. Scott Fine, CTD's CEO, is not placated. "There is no line between Vtesse and NIH in this [VTS-270] development program. When NIH stands in public and speaks about cyclodextrin and Niemann-Pick type C, they speak from the mouth of Vtesse."

In the end, there is one thing that all sides agree on: that the conflict between parties who all share the goal of helping dying children is sad—and not what any of them would have chosen. Indeed, the whole controversy, says the European NPC expert, is muddying the water for parents challenged with deciding whether to enter a child in a clinical trial, and, if so, which one. "It makes it very difficult for them to make informed decisions about what they should do." ■

PHOTO: THE MARELLA FAMILY

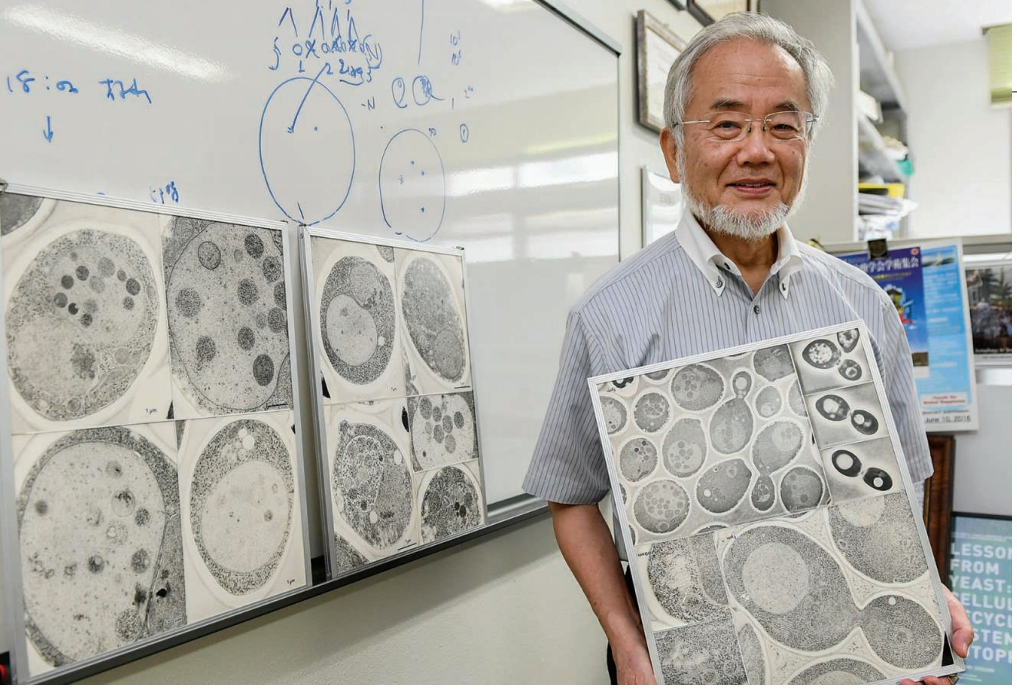

A key initial step in Yoshinori Ohsumi's Nobel-winning work was figuring out how to image recycling vesicles.

PHOTO: AKIKO MATSUSHITA/KYODO NEWS/AP

CELL BIOLOGY

Nobel honors discoveries in how cells eat themselves

Cellular sanitation helps keep diseases at bay

By **Martin Enserink** *and* **Elizabeth Pennisi**

As the stench of the streets during a garbage strike quickly drives home, sanitation workers are the unsung heroes of modern cities and towns. Similarly, the cell's garbage collectors are key to health. By performing "autophagy"—literally, self-eating—they degrade or recycle toxic protein aggregates and cell components, keeping neurodegeneration and infectious diseases at bay and perhaps even helping control cancer.

This week, the cell biologist who initially worked out much of the genetics and mechanics of this process received the 2016 Nobel Prize in Physiology or Medicine. When Yoshinori Ohsumi, now at the Tokyo Institute of Technology's Frontier Research Center, did his pioneering work in yeast in the early 1990s, his results drew little attention outside cell biology. But in the past 15 years, others have shown that cells' clean-up machinery is crucial to human health.

"This is an excellent decision," says biochemist Volker Haucke of the Leibniz Institute for Molecular Pharmacology in Berlin, who knows Ohsumi personally and calls him "a very modest man." He "is a prime example of someone who did basic research and discovered a process that otherwise might have stayed hidden for decades."

In the 1950s and 1960s, researchers recognized that some animal cells stuff proteins and other cellular machinery into sacs, or vesicles, to be recycled or disposed of. They knew that autophagy was especially active when the cell was under stress, for example when nutrients were in short supply or when the organism was fighting off an infection. But how the process worked—and even which cells it operated in—was unclear.

Ohsumi and his colleagues set out to explore these questions in yeast, a single-celled organism that nevertheless uses many of the same biochemical processes as animal cells. They developed yeast strains lacking key enzymes suspected of playing a role in autophagy, hoping to see what happened when the process didn't work as it should. When Ohsumi's team starved the yeast, the cells developed unusually large vacuoles, the cellular garbage dumps that collect materials to be recycled. Usually yeast vacuoles are too small to see under the light microscope, but in the mutant yeast, they were easy to observe, presumably because the mutant cells could not empty them of molecular garbage.

Ohsumi then used chemicals to induce still more mutations in the yeast strains, looking for cells that failed to form visible vacuoles even when they were starving. Such cells, he reasoned, lacked other key genes for autophagy. In a key 1993 paper, Ohsumi and his team identified 15 genes essential to the process. Further studies showed that very similar genes control autophagy in animal and human cells, and also helped piece together how the genes keep the cells' recycling running.

In a first step, damaged or excess proteins or organelles may be tagged with molecules that enable them to snare a piece of membrane, which expands and encircles the target. The resulting vesicle makes its way to another cellular component, the lysosome, fusing with it. Enzymes in the lysosome then break down the vesicle's contents.

Over the years, Ohsumi and others have shown that autophagy plays a crucial role in embryo development, cell differentiation, and the immune response. In animal models, a healthy autophagy system is correlated with longevity, whereas a faulty one can accelerate symptoms of aging and lead to a wide variety of diseases, including cancer, diabetes, and Huntington disease.

About half a dozen labs are studying existing drugs approved for other conditions but known to boost autophagy. They are testing them in animal models of Parkinson's, Alzheimer's, and Huntington diseases and in early clinical trials. Charbel Moussa at Georgetown University Medical Center in Washington, D.C., is planning trials of an autophagy-boosting drug normally used for leukemia in patients with neurodegenerative diseases. Beth Levine, an autophagy researcher at the University of Texas Southwestern Medical Center in Dallas, is part of a large effort funded by the National Institutes of Health to screen autophagy enhancers for the ability to combat infections. Thanks in part to Ohsumi's efforts, she says, "the field has evolved to the point where we can exploit the knowledge to begin to develop specific inducers to treat human diseases."

MEDICINE NOBEL

"… to a new paradigm in our understanding of how the cell recycles its content."

Yoshinori Ohsumi

Some of the work on mammalian autophagy was done by people trained in Ohsumi's lab, such as Tamotsu Yoshimori at Osaka University in Japan and Noboru Mizushima at the University of Tokyo. Both have "really been influential," says David Rubinsztein, a cell biologist at the University of Cambridge in the United Kingdom. "One thing that Ohsumi should get credit for is being a very good mentor."

"I couldn't be happier" seeing others build on his basic work, Ohsumi said after getting the Nobel news, adding, "I'm looking forward to seeing more and more light shed on this phenomenon." ■

With reporting by the Science *News staff.*

CONDENSED MATTER

Trio wins Nobel for effects of topology on exotic matter

Work presaged research revolution in topological insulators

By **Adrian Cho**

How is a doughnut like a coffee cup, but different from a coiled spring? The riddle is key to understanding this year's Nobel Prize in Physics, which honors theorists David Thouless of the University of Washington, Seattle, Michael Kosterlitz of Brown University, and Duncan Haldane of Princeton University.

The answer is that because each has one hole, the doughnut and the coffee cup have the same topology. An infinitely pliable cup could be molded into a doughnut without tearing it. The spring, on the other hand, can be unwound into a wire, flattened into a sheet, or squished into a ball. But it cannot be smoothly deformed to a make a doughnut. Thus, it has a different "topological charge"—essentially, the number of holes. Thouless, Kosterlitz, and Haldane showed that topology is more than a mathematical abstraction: It can show up in surprising ways and dramatically affect the properties of condensed matter, such as its ability to conduct electricity.

"These are three pioneers who are completely deserving of the honor," says Charles Kane, a condensed matter theorist at the University of Pennsylvania (UPenn). The prize is divided with one half going to Thouless, and the other half split between Haldane and Kosterlitz. "When I heard the names I had to look to see which of their many contributions they were cited for," says Eugene Mele, a theorist at UPenn.

In 1972, Kosterlitz and Thouless explained how topology can produce order where none is expected. The pair studied an abstract construct known as the XY model, which theorists had used to explain the onset of superfluidity in liquid helium—its ability to flow without resistance at temperatures below 2.17 K. That happens because all the atoms crowd into a single quantum wave that can be described by the XY model. However, in the 1960s theorists had argued that liquid helium in a 2D film could not become superfluid because thermal fluctuations would scramble the quantum wave.

Kosterlitz and Thouless showed otherwise. They realized that the lowest energy thermal fluctuations in the XY model would be tiny whirlpools called vortices and, at sufficiently low temperatures, they would appear only in countercirculating pairs with opposite topological charges. As a result, the effects of the paired vortices would largely cancel out, permitting a phase transition and superfluidity. In 1978, experimenters observed the predicted superfluidity in films of liquid helium.

In 1982, Thouless used topology to explain another odd phenomenon, the integer quantum Hall effect. It occurs when a thin semiconductor slab sits in a perpendicular magnetic field. As current runs along the slab, a voltage develops across it. The voltage increases with the strength of the magnetic field. But if the semiconductor is pure enough, the voltage goes up in specific jumps even as the magnetic field increases smoothly. Thouless showed that, at any given magnetic field, the complicated "bands" that describe the permitted energies and momenta of the electrons in a semiconductor have a specific topological charge. That charge can only change in jumps as the magnetic field increases, which explains the voltage steps.

PHYSICS NOBEL

"... for theoretical discoveries of topological phase transitions."

David Thouless

Duncan Haldane

Michael Kosterlitz

In 1983, Haldane analyzed a purely abstract model: quantum mechanical particles arranged like pearls on a string. Each particle could interact with its neighbors, and its behavior would depend on its spin. Physicists use spin to divide particles into two classes: bosons, such as photons, and fermions, such as electrons.

Defying expectations, Haldane showed that strings of fermions and bosons behave very differently. A chain of fermions can be excited by an infinitesimally small energy perturbation. Fiddle with the chain at all, and ripples of torqueing spins zip up and down the line. On the other hand, a chain of bosons needs a good jolt for an excitation. The difference depends on the topology of the quantum wave describing the particles, and the result persuaded researchers that they could engineer material properties by controlling such topology.

Since then, the tools that the new Nobel laureates developed have become bedrock for the study of so-called topological phases of matter—perhaps the hottest field in condensed matter physics. For example, insulators such as bismuth selenide are known to become conductive on their surface because their twisted band structures unwind at the material's edge. Other topological effects could lead to phenomena like unquenchable currents on the surfaces or edges of materials. Within materials, excitations that carry topological charges might even be braided with one another to perform quantum calculations. "A lot has been built on this foundation," Kane says.

At a press conference announcing the prize, Haldane said that in the 1980s his work seemed very abstract. "I wrote in my paper that [my model] seemed to be an interesting toy model," he said. Some toys are more interesting than others. ■

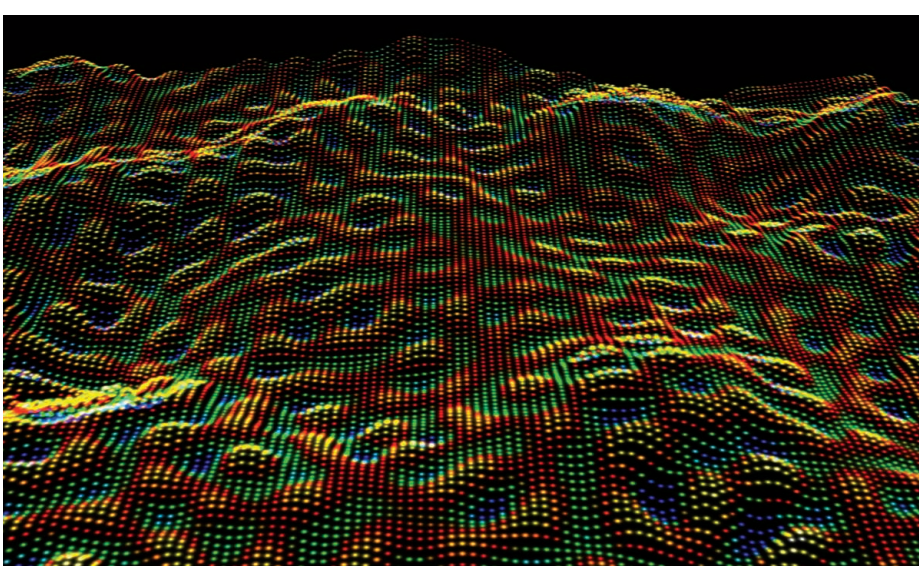

IMAGE: YAZDANI LAB, PRINCETON UNIVERSITY

A scanning tunneling microscope image shows quantum particles on the surface of a topological insulator.

The European XFEL's superconducting accelerator allows the machine to produce rapid-fire x-ray pulses.

FACILITIES

European XFEL to shine as brightest, fastest x-ray source

Free electron laser's rapid-fire pulses will probe free-floating molecules in their natural habitat

By **Edwin Cartlidge**

A 3.4-kilometer-long, fearsomely bright x-ray strobe is about to light up on the outskirts of Hamburg, Germany. On 6 October, scientists at the €1.4 billion European x-ray free electron laser (XFEL) will officially kick off a roughly 4-month-long process of cooling down and firing up the facility's superconducting electron accelerator, which powers the x-rays. By next June the machine should be delivering the world's brightest and fastest pulses of x-ray light to materials scientists and structural biologists probing the atomic structure of molecules in natural settings.

The new laser will help relieve the overwhelming demand for time on the world's handful of FELs, which includes the Linac Coherent Light Source (LCLS) at the SLAC National Accelerator Laboratory in Menlo Park, California, as well as an FEL in Japan and facilities due to open over the coming year in South Korea and Switzerland. There is a "tremendous shortage of FEL radiation worldwide," says Massimo Altarelli, European XFEL management board chair in Schenefeld, Germany.

The new light source will also stand out for its unique rapid-fire capability. With 27,000 flashes of light per second—more than 200 times the pulse rate of the LCLS—the European XFEL will allow scientists to get lucky, capturing free-floating molecules in dilute solutions where other FELs would fire and miss. "Researchers will be queuing around the block to use the machine," says admiring LCLS Director Mike Dunne.

For decades, ring-shaped accelerators called synchrotrons have been the workhorses of x-ray science. These machines tap the radiation that a beam of electrons emits as it is bent in a circular path. But synchrotron light is relatively dim and diffuse compared with FEL pulses. Scientists must package billions of identical molecules into large crystal lattices to generate x-ray diffraction patterns vivid enough to determine the molecular structure.

In 2009, the LCLS dazzled researchers when it opened as the world's first XFEL light source. Instead of sending electrons around a ring, FELs accelerate bunches of electrons to high energies in a linear accelerator and then send them through a gauntlet of magnets, which forces them through a series of slalom-like turns. At each wiggle the electrons emit x-rays that in turn exert a force on the electrons, causing them to bunch up and amplifying their emissions. The resulting laserlike flashes are up to a billion times brighter than synchrotron light.

With these bright and brief flashes, FELs can study short-lived phenomena like the making and breaking of chemical bonds. They can also determine the atomic structure of molecules arranged in crystals as small as a micrometer across. Christian Betzel, a biochemist at the University of Hamburg, says the capability is vital for studying biomolecules that cannot be grown into large crystals, such as certain cell membrane proteins that regulate molecular traffic.

The LCLS and other existing FELs can't produce these pulses in rapid succession, however. That's because the electrical power needed to achieve a higher pulse rate would destroy the bulbous metal cavities used to accelerate electrons, which are made from nonsuperconducting copper. In any case, the electricity would be prohibitively expensive. The lower pulse rate makes it challenging for investigators to go after individual molecules suspended in a fluid, rather than arrayed in a crystal, because the chance of any individual flash of x-ray light scoring a hit on a stray particle is low, Altarelli says.

The European XFEL's superconducting accelerator will change the calculus by vastly boosting the available pulse rate. Among

Going great guns

Three new free electron lasers (FELs) are set to open up in the next year. The European XFEL gets its high repetition rate from the superconducting cavities that drive its electron beam.

NAME/COUNTRY	LCLS/ UNITED STATES	LCLS-II/ UNITED STATES	SACLA*/ JAPAN	EUROPEAN XFEL/ GERMANY	SWISSFEL/ SWITZERLAND	PAL-XFEL*/ SOUTH KOREA
Date of first x-rays	2009	2020	2011	2017	2017	2016
Cost (in U.S. millions)	$415	$1000	$370	$1600	$280	$400
Number of instruments	7	9	8	6	3	4
Max. electron energy (GeV)	14.3	4.5	8.5	17.5	5.8	10
Min. pulse duration (femtoseconds)	15	15	10	5	2	30
Pulses per second	120	1,000,000	60	27,000	100	60

**SACLA is the Spring-8 Angstrom Compact free electron Laser and PAL-XFEL is the Pohang Accelerator Laboratory X-ray Free Electron Laser*

PHOTO: © HEINER MÜLLER-ELSNER/EUROPEAN XFEL

the molecules that could be scrutinized, says Dunne, are catalysts—substances that speed up chemical reactions—because studying them frozen in crystals reveals little about their behavior.

Going beyond the molecular scale, Andrea Cavalleri, a physicist at the Max Planck Institute for the Structure and Dynamics of Matter in Hamburg, is planning to use the European XFEL to track the real-time motion of electrons within high-temperature superconductors and other materials. Cavalleri will pump his test materials with precisely shaped laser pulses, and then use the FEL light to gauge the effect on the materials' electronic and magnetic properties.

Altarelli says that the superconducting accelerator should be fully operational by 2017 and that the first x-rays should arrive around mid-April. Two instruments are due to be available to users in June 2017, and the full suite of six should be up and running by the spring of 2018, he says. Not only will the higher pulse rate allow new types of experiments, but it also should make the science more efficient: Altarelli estimates that experiments will be carried out "two orders of magnitude faster" than on existing FELs.

Not to be outdone, physicists at SLAC are currently upgrading the LCLS to have a superconducting accelerator of its own. Expected to start up in 2020, the $1 billion LCLS-II will generate as many as a million x-ray pulses per second. Dunne thinks that this ultrahigh pulse rate could give the U.S. machine the edge when it comes to studying rapid processes, such as those in photosynthesis, in which certain proteins absorb four photons in quick succession. He also notes that the LCLS-II's pulses will be more uniformly spaced in time than those of the European device, which makes developing detectors easier.

Altarelli, in turn, points to what he calls the European XFEL's "real atomic resolution." The machine produces the highest energy light with the shortest wavelengths—as small as half the diameter of a hydrogen atom. That means it will do better resolving fine structure than the LCLS-II, which will produce light with wavelengths five times longer.

Still, the competition between facilities is "fair and very friendly," says Altarelli, and they organize "club of five" meetings once every year or so to compare notes. At the next meeting, late this month in South Korea, there will be plenty of discussion of the European facility's impending startup. But Altarelli says the transatlantic power shift hasn't happened, at least not quite yet. "Whether there will be one, we will see," he says. "It would be better to ask that question in a year or two." ■

SCIENTIFIC PUBLISHING

U.S. charges journal publisher with misleading authors

OMICS Group Inc. has drawn numerous complaints about allegedly shady editorial practices and meetings

By **John Bohannon**

In one of the first cases of its kind, the U.S. Federal Trade Commission (FTC) is taking action against a journal publisher accused of deceiving its authors. FTC is asking a federal judge to order OMICS Group Inc., the publisher of hundreds of open-access journals, to stop making false and misleading claims about its pricing, editorial staff, and peer-review practices. The agency is also asking the court to consider requiring the firm to refund authors and conference participants millions of dollars in fees.

The case, now before a federal judge in Las Vegas, Nevada, is sending shock waves through the traditionally self-regulated world of technical journals. "It's a shame it's the government that has to regulate the scholarly publishing industry," says Jeffrey Beall, a librarian at the University of Colorado, Denver, who has been an outspoken critic of what he calls "predatory" publishers. OMICS threatened Beall with a $1 billion lawsuit after he criticized its journal practices.

> ***"It is vital that we stop scammers who seek to take advantage of the changing landscape of academic publishing."***
>
> **Jessica Rich**, Federal Trade Commission

Since OMICS put its first journal online in 2008, the India-based firm has grown into a publishing empire that also sponsors conferences. The company, run by former biomedical researcher Srinubabu Gedela, publishes 653 of its own journals, on topics ranging from agrotechnology to zoology, according to its website. It publishes many more under an ever-changing array of subsidiaries. The articles are free to readers after authors pay fees of up to several thousand dollars to publish.

FTC, which enforces consumer protection laws, is suing Gedela, OMICS, and two related companies in the wake of numerous complaints from researchers who say OMICS journals charged for publishing their papers without delivering promised services, such as peer review, or that OMICS enticed them to poorly organized and attended meetings. FTC is also using as evidence the results of an investigation by *Science* that revealed that some OMICS journals accepted papers without peer review (*Science*, 4 October 2013, p. 60); this reporter was asked to submit a declaration about those findings to the court. "It is vital that we stop scammers who seek to take advantage of the changing landscape of academic publishing," said Jessica Rich, director of FTC's Bureau of Consumer Protection in Washington, D.C., in a statement.

Over the past year, FTC has been quietly building its case against OMICS by collecting statements from scholars including Pamela Regan, a psychologist at California State University, Los Angeles. "I was scammed," Regan claims. She says that in 2014 she received an unsolicited email from the *International Journal of Emergency Mental Health and Human Resilience* inviting her to submit a paper. She did not realize that the journal, once respected in her field, had been taken over by OMICS after the original publisher folded. She and a colleague submitted a review article they had worked on for months. There was no sign of any peer review. Instead, they received an invoice for $1819. Fearing that the journal had become illegitimate, says Regan, "I asked to withdraw the paper," and that's when things turned ugly. "They said I couldn't!"

After months of increasingly threatening email communications between OMICS and Regan, with help from the university's legal counsel, "things went quiet," she says. But just as she was about to submit the article to a different journal, OMICS notified her that it had published her paper. "I was horrified," she says. "It's so destructive to a scientist's reputation to have work published in a sham journal."

Seeking help, she contacted each of the 29 scholars named on the journal's masthead as editors. She discovered that "many of them had no idea their names were being used." Others had been trying to get OMICS to remove their names, to no avail. Finally, the journal withdrew her paper, but Regan was infuriated. She believes that OMICS takes advantage of inexperienced scientists who are eager to be published. "They are really targeting grad students and scholars in the developing world," she says. "It's shameful." OMICS did not respond to repeated emails from *Science*.

The Federal Trade Commission is "working towards favoring some subscription based journal publishers who are earning millions of dollars from scientists."
OMICS Group Inc.

At stake in the case is "the integrity of the marketplace of ideas," says Gregory Ashe, an FTC attorney in Washington, D.C. In its 25 August complaint, the agency lays out a long list of charges, among them that OMICS used researchers' names to promote journals and conferences without their permission; falsely claimed journals are indexed by PubMed, the citations database maintained by the National Library of Medicine in Bethesda, Maryland; and untruthfully stated that its journals were granted independently calculated impact factor scores (a measure of citation rates). The agency wants the judge to order OMICS to end such practices, and also to consider forcing the company to refund "ill-gotten monies." (Bank records obtained by the agency show OMICS earned revenues of $26 million between 2009 and 2015.)

In a 22 September response, OMICS claims that FTC has no jurisdiction over its activities and that the case is a conspiracy on the part of its competitors to shut down open-access publishing. The agency is "working towards favoring some subscription based journal publishers who are earning billions of dollars from scientists," OMICS alleges on its website.

As *Science* went to press, FTC was waiting for the court to decide whether it will grant a preliminary injunction against OMICS, ordering it to stop deceptive practices until a final resolution of the case. ■

The first Polynesians crossed thousands of kilometers of open ocean in outrigger canoes.

PHOTOS: STEPHEN ALVAREZ/NATIONAL GEOGRAPHIC CREATIVE

HUMAN EVOLUTION

First Polynesians launched from East Asia to settle Pacific

"Game-changing" study of ancient genomes traces Polynesian roots solely to East Asian farmers

By **Ann Gibbons**

It was only 3000 years ago that humans first set foot on Fiji and other isolated islands of the Pacific, having sailed across thousands of kilometers of ocean. Yet the identity of these intrepid seafarers has been lost to time. They left a trail of distinctive red pottery but few other clues, and scientists have confronted two different scenarios: The explorers were either farmers who sailed directly from mainland East Asia to the remote islands, or people who mixed with hunter-gatherers they met along the way in Melanesia, including those from Papua New Guinea.

The Lapita people left behind a trail of distinctive stamped red pots at about 100 archaeological sites in Oceania.

Now, the first genome-wide study of ancient DNA from prehistoric Polynesians has boosted the first idea: that these ancient mariners were East Asians who swept out into the Pacific. It wasn't until much later that Melanesians, probably men, ventured out into Oceania and mixed with the Polynesians, according to the new study.

"The paper is a game-changer," says Cristian Capelli, a population geneticist at the University of Oxford in the United Kingdom, noting that it settles a decades-long dispute. By showing that the East Asians hopscotched past islands already populated by Melanesians without picking up their genes, it is also a case study in how culture can initially bar mixing between groups. "Farmers move in and don't mix much with the hunter-gatherers," says evolutionary geneticist Mark Thomas of University College London. "We see this again and again and again" elsewhere in the world.

The first Polynesians left plenty of tantalizing artifacts, including their stamped red pottery, obsidian tools, and shell ornaments. Collectively known as the Lapita culture, this set of artifacts first appeared more than 3000

Peopling the Pacific

At least 3000 years ago, the first Polynesians sailed past New Guinea without mingling with the Melanesians already living there, and settled the distant islands of Vanuatu, Tonga, and beyond.

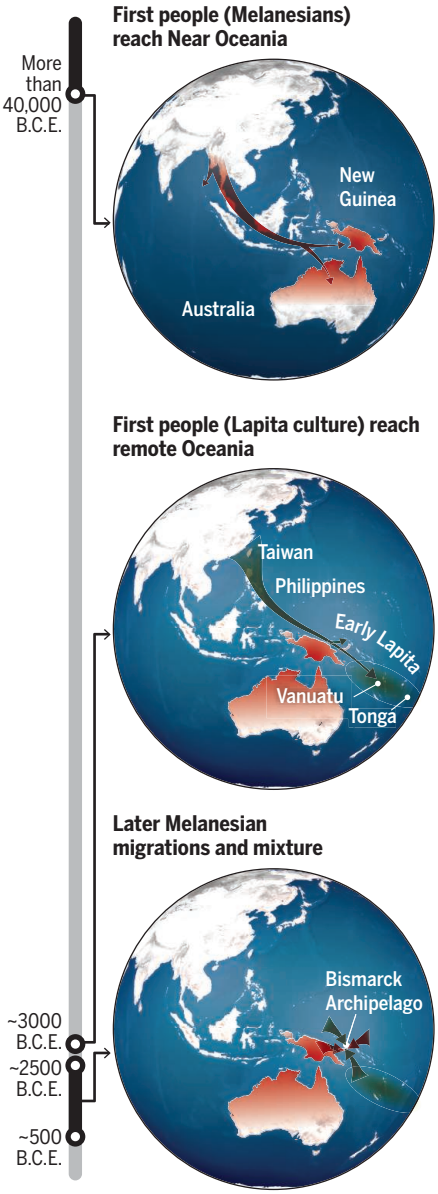

MAPS: V. ALTOUNIAN/*SCIENCE* ADAPTED FROM SKOGLUND *ET AL.*/*NATURE* (2016)

years ago in the Bismarck Archipelago east of New Guinea (see map, above). The Lapita grew taro, yams, and breadfruit, and brought pigs and chickens with them as they spread rapidly to the islands of Vanuatu and New Caledonia and eventually to Fiji, Tonga, Samoa, and beyond.

Back in 1985, archaeologist Peter Bellwood of the Australian National University in Canberra proposed that the Lapita had roots in farming cultures in East Asia. Based on dating of Lapita sites, he proposed that they moved rapidly from mainland China to Taiwan and the Philippines, then out across the open ocean from Vanuatu to Samoa, covering 2300 kilometers in about 300 years. This "express train" picture fit with linguists' models, in which Austronesian languages spread from East Asia into Oceania and were distinct from Papuan languages in Melanesia.

But other researchers argued that the DNA of living Polynesians showed evidence that their Lapita ancestors had lingered in Melanesia, mixing with the locals and slowly spreading eastward. This so-called "slow boat" model had prevailed in recent years (*Science*, 2 March 2001, p. 1735).

In the new study, an international team extracted ancient DNA from four skeletons, all female, from the islands of Vanuatu and Tonga and dated from 2300 to 3100 years ago; three skeletons were directly associated with the Lapita culture. The team sequenced the DNA at up to 231,000 positions across the genomes of each woman, and compared the sequences with those of nearly 800 present-day people from 83 populations in East Asia and Oceania.

The four women were from a distinct population that had no evidence of mixing with the ancestors of people living in Papua New Guinea today, as the team reports in *Nature* this week. Instead, the women shared all their ancestry with the indigenous Atayal people in Taiwan and the Kankanaey people in the Philippines. "The Lapita have no evidence for Papuan ancestry," says co-author Pontus Skoglund, a postdoc in David Reich's lab at Harvard Medical School in Boston. That suggests that their ancestors rode the fast train, sweeping all the way to Oceania without mixing with Melanesians on the way.

Polynesians today do carry a significant amount of Melanesian DNA. But that DNA is in relatively long, unbroken chunks, the analyses found, suggesting that it was incorporated into Polynesians' genomes recently, after the Lapita period, perhaps about 500 to 2500 years ago. The team also noted that the Polynesian X chromosome has less Melanesian DNA than other nuclear chromosomes. Because X chromosomes are more likely to be inherited from mothers (sons get only a Y from their fathers), that suggests that much of the Melanesian DNA came through the male line, as Melanesian men interbred with Polynesian women. "The female ancestors of modern-day Oceanians are mainly Lapita, whereas their male ancestors include Papuans," Skoglund says.

Bellwood is pleased. "All the evidence from different disciplines has come together," he says. By getting DNA from the ancient Polynesians themselves, "the genomics has clinched it." ■

RESCUING THE GUARDIAN OF THE GENOME

New drugs combat cancer by propping up a mutated tumor-fighting protein

By **Robert F. Service**

It has been nearly impossible to get a good look at Rommie Amaro's favorite protein in action. Called p53, the protein sounds the alarm to kill cells with DNA damage and prevent them from becoming cancerous—one reason why it has been called the "guardian of the genome." But it is big and floppy, a molecular shapeshifter that is hard to follow with standard imaging tools. So Amaro, a computational biologist at the University of California (UC), San Diego, turned to supercomputers. She plugged in new x-ray snapshots of p53 fragments and beefed up her program to make a movie of the quivering activity of each of the protein's 1.6 million atoms over a full microsecond, an eternity on the atomic scale that required about a month of supercomputer time. She watched as four copies of p53 linked up and wrapped themselves around a DNA strand, an essential dance the protein performs before it sends off messages for cellular self-destruction.

Amaro wasn't just interested in the behavior of healthy p53: She wanted to understand the effects of mutations that the gene for p53 is prone to. In dozens of simulations, she and her colleagues tracked how common p53 mutations further destabilize the already floppy protein, distorting it and preventing it from binding to DNA. Some simulations also revealed something else: a fingerhold for a potential drug. Once in a while, a small cleft forms in the mutated protein's core. When Amaro added virtual drug molecules into her models, the compounds lodged in that cleft, stabilizing p53 just enough to allow it to resume its normal functions.

For Amaro and a few other researchers, those computer simulations are an inspiration. "A long-standing dream of cancer biology is to find small molecule drug compounds to restore the activity of p53," Amaro says. "We're very excited about this."

Of the nearly 1.7 million people diagnosed with cancer each year in the United States alone, about half have mutated versions of p53—a sign of how important the normal protein is in preventing the disease. It is one of the most intensely studied proteins in science, and a highly sought-after target for drugmakers. But of the dozens of p53 drugs in development, the vast majority simply try to boost levels of healthy p53. And despite decades of effort, none has made it to market.

Amaro's work illustrates how a handful of academic labs and small companies are making progress with a fresh approach to targeting p53: rescuing it when it's sick. They're finding drugs that bind to and prop up copies of mutated p53, restoring its shape and ability to carry out its job. One such drug has already passed an early stage safety trial in humans, and a more advanced clinical trial is now underway in Europe. Other would-be medicines are nearing human tests. If any succeed in the clinic, they could dramatically change the landscape for cancer treatment—and for other diseases that involve misfolded proteins, perhaps even Alzheimer's.

It won't be easy. Restoring normal function to a mutated protein is more difficult than simply blocking a protein, the strategy used by most medical therapies, says Klas Wiman, a tumor cell biologist at the Karolinska Institute in Stockholm. As a result, large drug companies have shied away from the rescue approach and progress has been slow, he says. "It's a little out of the mainstream for big pharma."

The payoff could be big, however. Not only could the strategy treat many kinds of cancer, but just a handful of drugs might be enough, particularly when coupled with chemotherapy drugs that induce the tumor cell damage to which p53 responds. P53 mutations tend to be clustered in the core of the protein, where it binds to DNA, and they have similar effects on its shape. Cell assays and animal studies suggest that drugs that restore p53's activity work with not just one mutant form of the protein, but many, says Alan Fersht, a chemist at the University of Cambridge in the United Kingdom. "The beauty of these things is that they are broadly applicable."

> ***"A long-standing dream of cancer biology is to find small molecule drug compounds to restore the activity of p53."***
>
> **Rommie Amaro**, University of California, San Diego

AN UNDERSTANDING of p53's seemingly magical powers to suppress tumors didn't emerge until well after the protein's discovery in 1979. Early on it was thought to be an oncogene capable of turning a cell cancerous under some circumstances. Only a decade later was it confirmed to bind to DNA and turn on the expression of other genes aimed at healing cell damage. If that damage is deemed too extensive by other cellular actors that interact with p53, it triggers p53 to launch the call for the cell to commit suicide.

The protein is now known to interact with and control dozens of different genes and proteins, and it helps regulate the cycle of molecular events by which cells grow and reproduce. Because of its outsize importance, its presence in cells is tightly controlled. Another protein, MDM2, latches onto p53 molecules and destroys them, keeping their numbers in check.

But this control mechanism can fail in multiple ways. For starters, when p53 itself is mutated, MDM2 cannot attack it. As a result, the malfunctioning protein builds up in cells unchecked and keeps the remaining healthy p53 from doing its job. Without the genome's guardian on patrol, precancerous cells survive and reproduce. This gives them the opportunity to build up the additional mutations they need to become fully malignant.

Most attempts to target p53 in the cancer fight involve trying to boost its level. One popular approach has been to prevent MDM2, and a relative called MDMX, from reducing p53 levels. The hope has been that doing so might allow some nonmutated p53 to stick around longer and kill damaged cells. "Everyone is working on these [drugs] like crazy," says David Lane, a cancer biologist at the Agency for Science, Technology and Research in Singapore, and a co-discoverer of p53.

A host of cell culture and animal data suggests they should work. However, Lane adds, "the clinical trials have not been as successful as we hoped." For example, an MDM2-targeting drug shrank deep-tissue fat cell tumors in just one out of 20 patients in a phase I safety trial, published in 2012. Blocking MDM2 comes with other potential downsides, Fersht says—not least that the approach can only work if there is still healthy p53 left inside cells. Also, because p53 is involved in so many cellular processes, boosting its level too much can have side effects. In the 2012 trial, for example, eight people had serious side effects, such as a sharp decrease in immune cells called neutrophils, and 14 people had comparatively mild side effects like nausea. Yet many MDM2 blockers remain in human trials, and if they pass muster, they are likely to be the first p53 drugs on the market.

Still, Fersht, Lane, Amaro, and others want to target the heart of the problem: mutant p53. In the early 1990s, in vitro tests on cancer cells by Lane and his colleagues hinted that some compounds could restore mutant p53's normal function. But the drugs weren't always doing what investigators thought. It turned out that one compound, called CP-31398, was indeed triggering cell death—but not by restoring p53. It killed cells by gumming up their DNA.

Later candidates have done a better job. In 1998, for example, Wiman's team screened a library of 2000 compounds from the U.S. National Cancer Institute and found two that appeared to restore mutant p53's ability to kill cancer cells. One, known as MIRA-1, turned out to kill more than cancer cells: It was toxic in mice. But the other, called

ILLUSTRATION: DAVIDE BONAZZI

Cellular sentries

The protein p53 guards against genetic mutations that turn a cell cancerous. When mutations are detected, four copies of p53 join together and bind to DNA, sounding a cellular alarm that triggers repair or self-destruction.

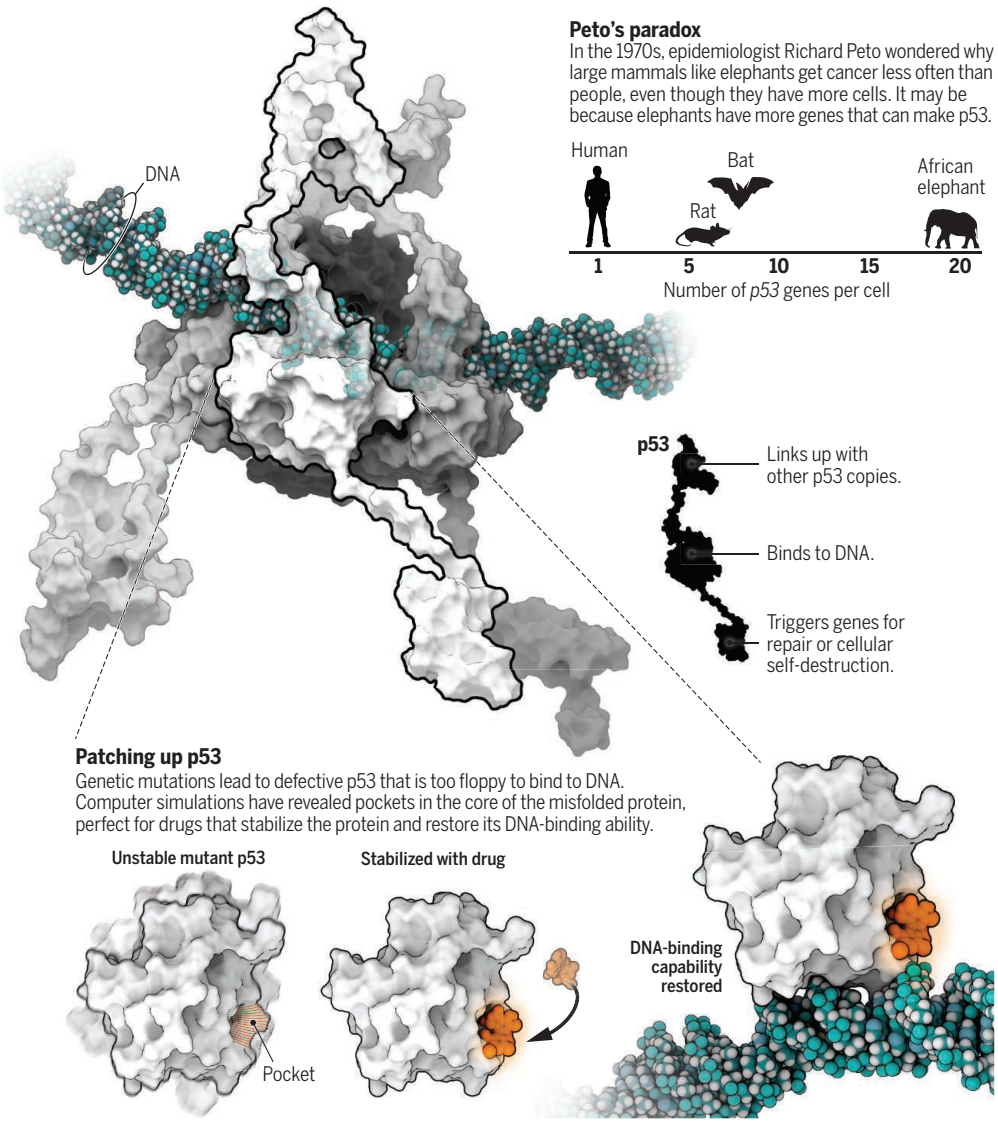

PRIMA-1, proved more promising. A later study showed that PRIMA-1 breaks down into another compound, abbreviated MQ, and 3 years ago Amaro and her colleagues reported computer modeling results that suggested MQ was binding to the inside of the pocket that forms within a mutated p53 core. Her results also showed that the compound props the protein back into shape, rescuing its function.

Wiman and his colleagues have since come up with a more active version of PRIMA-1, and the Karolinska Institute has spun out a biotech startup called Aprea AB to commercialize the drug. Now called APR-246, in 2012 it made it through the first round of safety trials on patients with a type of blood cancer that shows high rates of mutations in p53. It is now in a phase II clinical trial in women with ovarian cancer, which almost always has p53 mutations. The trial, at centers across Europe, will likely be completed within 2 years, says Lars Abrahmsen, Aprea AB's chief scientific officer in Stockholm.

Side effects are a concern because APR-246 binds to the amino acid cysteine and irrevocably changes it—and cysteines are abundant on numerous other proteins besides p53. But so far, Abrahmsen says, APR-246 has been tolerated well in clinical trials, even in relatively high doses. Wiman suspects that this is because the drug's shape makes it interact primarily with the cysteines in the core of mutated p53. But he and his colleagues are now working to confirm this.

Meanwhile, Fersht's group is making headway with other cysteine-binding compounds. And Amaro's computational studies suggest that the right molecule could lodge temporarily in the mutated p53's cleft, staying in place just long enough for the guardian protein to do its job. Yet unlike APR-246, it would eventually fall off and so would avoid making permanent changes to other proteins in the body, reducing the risk of side effects. In fact, a team led by Amaro, UC Irvine biochemist Peter Kaiser, and UC Irvine computer scientist Rick Lathrop recently used computer modeling to screen more than 1 million different compounds for binding in the cleft. The team found several hundred that might do so and restore the protein to its functional shape; more than 30 did the job when tested in cell culture, although they don't know whether they attached to p53 in the pocket. Several have now been licensed by a biotech startup in San Diego called Actavalon, founded in 2013 by Kaiser, Amaro, and others.

Another biotech startup, called Z53 Therapeutics, in Cleveland, Ohio, is taking aim not at the cleft in mutated p53, but at mutations that knock out a key site for binding zinc ions in p53's core. Without zinc, the protein loses the shape it needs to bind DNA. Drugs designed to shuttle zinc into cells can help restore the activity of the most common of these mutant p53s, lab studies suggest.

At this point, it's unclear which—if any—p53 stabilization strategy will pan out, Lane says. But success could leave a lasting mark on cancer care, by helping hundreds of thousands of patients every year, far more than other genetically targeted therapies. The protein-rescuing strategy could also pave the way for similar medications aimed at restoring other mutant proteins. The strategy is already helping fight cystic fibrosis, where a newly approved drug known as Orkambi helps stabilize the proper shape of proteins that balance the flow of ions in cells lining the lung's airways (*Science*, 16 September, p. 1194). And the same approach may eventually help treat patients with other misfolded protein disorders, such as Alzheimer's and Parkinson's.

But perhaps the most far-reaching goal of this approach would be to prevent tumors from ever arising in the first place. Wiman notes that current blood screening techniques can already reveal whether a person is shedding cancer-linked proteins into their blood stream, even before they show signs of having a full-blown tumor.

Someday it may be possible to give people with such warning signs drugs that rescue p53, getting their cellular guardians to snap to attention and wipe out the cancer before it ever gets started. "In the long run," Lane says, "it's a very attractive idea." ■

CREDITS: (DIAGRAM) V. ALTOUNIAN/*SCIENCE*; (DATA) THE AMARO LAB/UNIVERSITY OF CALIFORNIA, SAN DIEGO

INSIGHTS

A cold-atom quantum state simulator *p. 35* ▸

Apes understand false beliefs *p. 39*

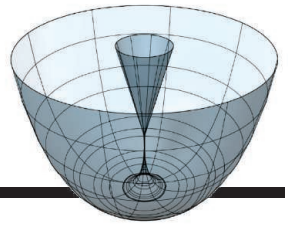

PERSPECTIVES

A layer of iridescent and resilient nacre constitutes the inner layer of mollusk shells.

PHOTO: JIRAWAT JERDJAMRAT/ALAMY STOCK PHOTO

BIOINSPIRED MATERIALS

Growing a synthetic mollusk shell

Three-dimensional organic templates control calcium carbonate precipitation

By **Francois Barthelat**

The deposition of dissolved minerals is usually harmful and can cause the failure of boilers or heat exchangers. Likewise, uncontrolled calcification in our bodies can cause kidney stones or failure of aortic valves. Yet mineralization is also critical in our bones and teeth to achieve stiffness, strength, and hardness. In these materials, biomineralization is controlled and harnessed through intricate organic templates that guide the growth and shape of crystals (*1*). As a result, bones, mollusk shells, diatoms, and corals have organic shapes that bear little resemblance to the angular crystals typical of geology. On page 107 of this issue, Mao *et al.* (*2*) report the biomimetic synthesis of nacre-like material fabricated by controlled mineralization of a multilayered organic template based on chitosan.

Nacre, also called mother-of-pearl, is the iridescent material found in the interior of mollusk shells. It features a "brick-and-mortar" microstructure, in which microscopic tablets of calcium carbonate (about 0.5 μm thick) are bonded by nanometers-thick layers of chitin and proteins.

Department of Mechanical Engineering, McGill University, 817 Sherbrooke Street West, Montreal, QC H3A 2K6, Canada. Email: francois.barthelat@mcgill.ca

Mollusks "grow" nacre through a complex sequence that starts with the secretion of a multilayer organic template (see the figure, top). Calcium carbonate slowly crystallizes at multiple locations simultaneously, filling the template and forming a highly regular, three-dimensional (3D) microscopic brick wall.

The final material is not only stiff and hard because of its high mineral content (>95% by volume) but is also surprisingly tough (it resists crack propagation and impacts). The micromechanisms of deformation and fracture in nacre are distinctive and involve crack deflection along the tablets, crack bridging, and "sliding" of the microscopic tablets over one another over large volumes (see the figure, bottom). These mechanisms make nacre three orders of magnitude tougher (on an energy basis) than the brittle mineral of which it is made, providing superb protection to mollusks (*3*). This level of toughness amplification has not been achieved to this day with any synthetic composite.

Can we make synthetic materials that duplicate the structure and mechanics of natural nacre? This question has been a focus of research for two decades. Conventional methods do not work well to make nacre-like composite materials (*4*), so creative approaches such as freeze-casting (*5*), magnetically assisted slip-casting (*6*), 3D printing (*7*), and laser engraving (*8*) were recently developed. These methods can produce composite materials with a large volume concentration of aligned inclusions at the microscale (*5*, *6*), but "perfect" brick wall–like structures can only be achieved at larger-length scales (*7*, *8*). Controlled mineralization is still of high interest because of the highly controlled structures it would enable at the microscale (*9*). Hydrogels have been successfully used as templates for mineralization (*10*) but only up to moderate levels of mineral content, in the form of isolated aggregates. Sequential layer-by-layer mineralization can produce highly mineralized nacre-like materials, but the method is relatively expensive and limited to thin films (*11*, *12*).

The mineralization method proposed by Mao *et al.* is a breakthrough because it successfully combines two critical steps: the fabrication of a large volume of a 3D multilayered template of chitosan with controlled microscopic spacing between the layers, and the complete mineralization of this template up to very high mineral contents (91% volume of calcium carbonate). The material is formed in only a couple of weeks (compared with years for natural nacre). A silk fibroin, infiltrated at the interfaces between the mineral layers, serves as the deformable mortar. The final material duplicates many of the features of nacre, including its brick-and-mortar microstructure and the nanostructure of the individual mineral tablets. In terms of mechanics, the weak interfaces in the material deflect cracks, which results in an increase in toughness (*13*). This synthetic nacre is about four to five times less "tough" than natural nacre (on an energy basis) but is 100 to 200 times tougher than the pure mineral.

This fabrication method could serve as a "sandbox" with which to study the fundamentals of biomineralization in highly controlled and tunable environments, by using different combinations of minerals and polymers as raw ingredients. This method could also be used to make large volumes of nacre-like bone grafts that would duplicate the mechanical and in vivo response of natural bone, an urgent challenge in orthopedics (*14*). Because the method works with various sets of organic and inorganic ingredients, it could also lead to many new "bioinspired" engineering materials. In particular, this method could lead to materials that are both very hard and tough, two properties that are mutually exclusive in traditional engineering materials (*15*). ■

A tough act to follow

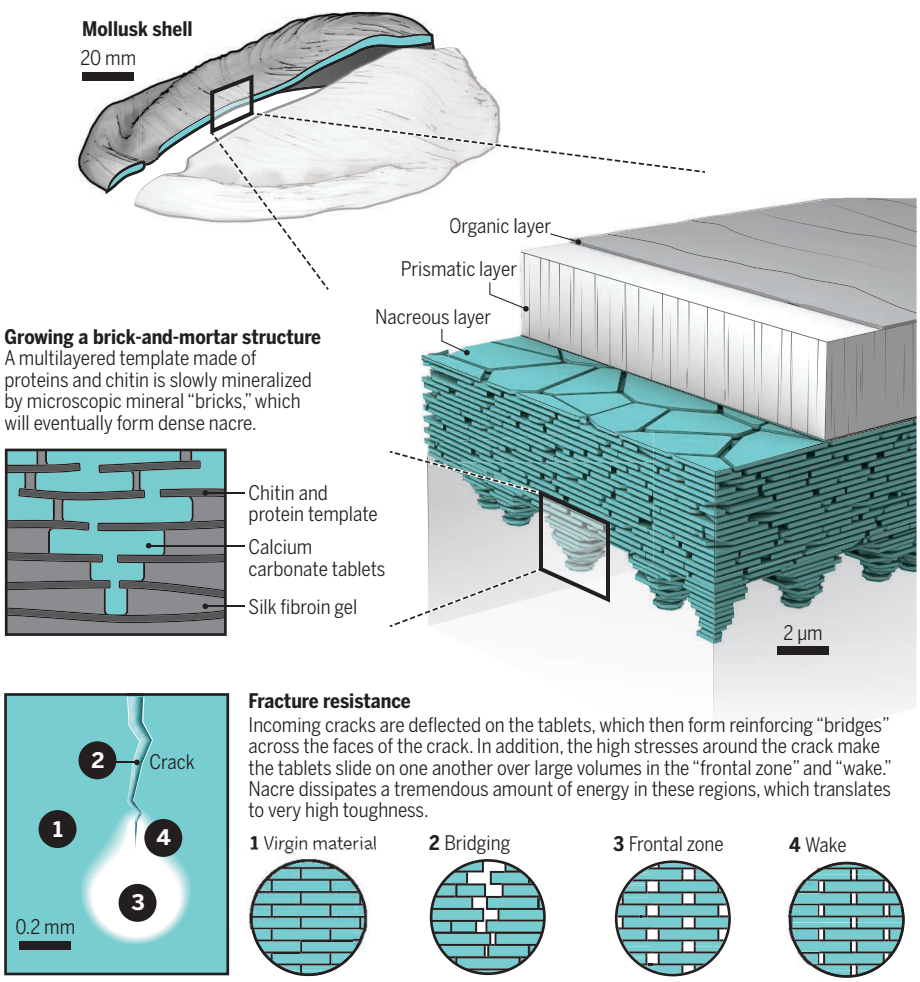

Growing a brick-and-mortar structure
A multilayered template made of proteins and chitin is slowly mineralized by microscopic mineral "bricks," which will eventually form dense nacre.

Fracture resistance
Incoming cracks are deflected on the tablets, which then form reinforcing "bridges" across the faces of the crack. In addition, the high stresses around the crack make the tablets slide on one another over large volumes in the "frontal zone" and "wake." Nacre dissipates a tremendous amount of energy in these regions, which translates to very high toughness.

GRAPHIC: V. ALTOUNIAN/*SCIENCE*

REFERENCES

1. F. C. Meldrum, H. Colfen, *Chem. Rev.* **108**, 4332 (2008).
2. L.-B. Mao *et al.*, *Science* **354**, 107 (2016).
3. F. Barthelat, *Philos. Trans. R. Soc. A Math. Phys. Eng. Sci.* **365**, 2907 (2007).
4. N. Almqvist *et al.*, *Mater. Sci. Eng. C Biomim. Supramol. Sys.* **7**, 37 (1999).
5. S. Deville, E. Saiz, R. K. Nalla, A. P. Tomsia, *Science* **311**, 515 (2006).
6. H. Le Ferrand, F. Bouville, T. P. Niebel, A. R. Studart, *Nat. Mater.* **14**, 1172 (2015).
7. H. D. Espinosa *et al.*, *Nat Commun.* **2**, 173 (2011).
8. S. M. M. Valashani, F. Barthelat, *Bioinspir. Biomim.* **10**, 026005 (2015).
9. A. M. Belcher, P. K. Hansma, G. D. Stucky, D. E. Morse, *Acta Mater.* **46**, 733 (1998).
10. E. Asenath-Smith, H. Y. Li, E. C. Keene, Z. W. She, L. A. Estroff, *Adv. Funct. Mater.* **22**, 2891 (2012).
11. H. Wei, N. Ma, F. Shi, Z. Q. Wang, X. Zhang, *Chem. Mater.* **19**, 1974 (2007).
12. A. Finnemore *et al.*, *Nat. Commun.* **3**, 966 (2012).
13. W. J. Clegg *et al.*, *Nature* **347**, 455 (1990).
14. M. Bohner, L. Galea, N. Doebelin, *J. Euro. Ceram. Soc.* **32**, 2663 (2012).
15. R. O. Ritchie, *Nat. Mater.* **10**, 817 (2011).

10.1126/science.aah6507

HEALTH CARE

A pragmatic way forward?

Training of informal providers may improve the quality of primary health care in rural India

By **Timothy Powell-Jackson**

Many health care providers in India have no formal medical training, despite regulations prohibiting informal practice. Although such informal providers typically offer poor-quality services, they are used by more than half of the population for outpatient care (*1*, *2*). A well-performing public sector might be expected to outcompete informal providers, putting them out of business (*3*), but the delivery of primary health care in India is generally considered to be weak (*4*). Some argue for accepting the reality on the ground and engaging with the informal sector, at least in the short term. On page 80 of this issue, Das *et al.* (*5*) show that a training intervention with 304 informal care providers in West Bengal, India, led to improved case management but had no effect on inappropriate drug prescriptions.

Conducting rigorous research on approaches to improving health care quality is challenging. What distinguishes the study by Das *et al.* is the randomized design that allows us to interpret the findings as causal. The study also uses "mystery clients" that provide excellent measures of clinical practice to evaluate the training program. To limit bias, providers were blinded to measurement, and trainers did not know what conditions the providers would be assessed on. The training program was atypically long (72 sessions over 9 months), used mixed training methods, focused on multiple diseases, and covered a diverse range of topics from human anatomy to clinical practice. Average attendance per session was 56%, impressively high given the duration. The training increased correct case management by 7.9 percentage points and improved adherence to disease-specific checklists by 4.1 percentage points but did not improve drug prescribing behavior.

The effect on correct case management is consistent with, albeit at the lower end of, other well-conducted studies of training included in a recent systematic literature review (*6*). The training in West Bengal raised correct treatment levels to that of qualified primary care providers in the public sector. But quality remained far below acceptable levels, with 40% of the intervention group continuing to manage cases incorrectly.

In India, health care providers without formal medical training are commonly referred to as informal providers. They are the first choice for many rural residents seeking care for common conditions, such as diarrhea and chest infections.

Caution must always be exercised when generalizing the findings from a single randomized trial (*7*). The most pertinent question is whether the training could be scaled up from a demonstration project to a state policy without diluting the effect. Ensuring a successful transition is likely to involve retaining the clinical focus, the use of mixed training methods, and the long duration of the training (*6*). The low cost of the training should make an expanded program affordable. But there are reasons to expect that the conditions under which the trial was conducted may differ once the training program is implemented at scale. The trial was conducted on a small scale by a well-run nongovernmental organization, and it is unclear whether such organizations have the capacity to implement the training program on a larger scale with the same degree of fidelity and high level of attendance. Future research should also explore whether the training remains effective when implemented by government, as has been done in studies on participatory women's groups in India (*8*).

To generalize the findings further, it will be important to better understand the pathways through which training improves quality of care. Training may improve clinical practice simply by increasing knowledge. Unfortunately, Das *et al.* do not report data on measures of knowledge to shed light on

London School of Hygiene and Tropical Medicine, London WC1E 7HT, UK. Email: timothy.powell-jackson@lshtm.ac.uk

PHOTO: MEENAKSHI GAUTHAM/LONDON SCHOOL OF HYGIENE AND TROPICAL MEDICINE

this channel. It is also possible that training increases health-worker effort, instills higher ethical standards, or gives health providers more confidence to trust their own judgment. Finally, understanding how training improves quality may help to explain why the program was unable to address the important problem of overprescribing antibiotics.

The government of India has endorsed the goal of providing "universal access to good quality health care services without anyone having to face financial hardship" (*9*). The informal health care sector has no role in this vision; that implies that directly funding the public sector to strengthen primary health care will crowd out unqualified providers from the market. Indeed, this has been the experience of countries such as Sri Lanka and Thailand (*10*). Government health expenditure in India is low by international standards (*11*), and it is plausible that this underlies the poor performance of the public sector. But most policy experts agree it is not just about resources (*12*). In many states of India, governance problems are pervasive, health workers are poorly motivated, and absenteeism is high. The informal sector is thus likely to persist, at least in the short term.

Better evidence on the effectiveness of approaches to improve health service delivery in India's public sector is needed before more money is poured into the system. The dearth of evidence in part reflects the inherent challenge of conducting this type of research, as well as the neglect of health systems research relative to clinical and epidemiological research (*13*). In the absence of such evidence, Das *et al.*'s findings provide a compelling case for training informal providers as a pragmatic way forward in the short term. Before scaling up this approach, however, it would be prudent to understand how high rates of attendance were achieved and why many providers did not improve clinical practices despite numerous hours of training. ■

REFERENCES

1. M. Sudhinaraset *et al.*, *PLOS ONE* **8**, e54978 (2013).
2. J. Das *et al.*, *Health Aff.* **31**, 2774 (2012).
3. B. McPake, K. Hanson, *Lancet* **388**, 622 (2016).
4. V. Patel *et al.*, *Lancet* **386**, 2422 (2015).
5. J. Das *et al.*, *Science* **354**, aaf7384 (2016).
6. A. Rowe *et al.*, in *Improving Quality of Care in Low- and Middle-Income Countries: Workshop Summary* (National Academies Press, Washington, DC, 2015), pp. 36–46.
7. A. Deaton, *J. Econ. Lit.* **48**, 424 (2010).
8. P. Tripathy *et al.*, *Lancet Glob. Health* **4**, e119 (2016).
9. Ministry of Health and Family Welfare, Government of India, *National Health Policy 2015 Draft* (December 2014); www.nhp.gov.in/sites/default/files/pdf/draft_national_health_policy_2015.pdf.
10. M. Mackintosh *et al.*, *Lancet* **388**, 596 (2016).
11. World Health Organization, WHO National Health Accounts, Global Health Expenditure Database (2016); www.who.int/health-accounts/ghed/en/.
12. P. Berman, *Lancet* **386**, e58 (2015).
13. D. Sanders, A. Haines, *PLOS Med.* **3**, e186 (2006).

10.1126/science.aai8652

GRAPHIC: N. CARY/*SCIENCE*

PHYSICS

Cold atoms twisting spin and momentum

Ultracold atoms can simulate complex quantum systems

By **Monika Aidelsburger**

Inspired by the intriguing topological phenomena recently observed in condensed-matter systems (*1*), a variety of different research areas, from optical to mechanical systems, have devoted their studies to topological physics. Owing to their high level of experimental controllability, cold atomic gases offer a promising platform to simulate condensed-matter models. Their charge neutrality, however, is an apparent limitation. To overcome these constraints, new experimental techniques are currently being developed that mimic the physics of charged particles. On page 83 of this issue, Wu *et al.* (*2*) report on such a new experimental technique to simulate two-dimensional (2D) spin-orbit coupling (SOC) for neutral atoms in an optical lattice—an important ingredient to explore topological quantum states.

SOC is a relativistic effect that links the spin degree of freedom of a particle to its momentum. Intuitively, this can be understood if we consider a moving particle in a static electric field. In the rest frame of the particle, the electric field gives rise to a magnetic field that interacts with the spin of the particle. This leads to a momentum-dependent Zeeman or spin-orbit interaction. A well-known example is the atomic fine-structure splitting that arises as a result of the motion of the electron in the electric field of the nucleus. In solids, the SO interaction emerges owing to the motion of the electrons in the intrinsic electric field of the material. It can occur in materials with broken interfacial or bulk inversion symmetry, known as Rashba (*3*) and Dresselhaus (*4*) contributions, respectively.

After the discovery of quantum Hall insulators, it was believed that topological quantum states can only exist in 2D and only if time-reversal (TR) symmetry is broken by applying a magnetic field. SOC was essential in understanding that there is a new class of topological materials that exists without TR symmetry breaking (*5*). The observation of 2D and even 3D topological insulators soon followed (*1*). More recently, there has been increasing interest in topological superconductors, in particu-

Laboratoire Kastler Brossel, CNRS, UPMC, ENS, Collège de France, 11 Place Marcellin Berthelot, 75005 Paris, France. Email: monika.aidelsburger@college-de-france.fr

Synthetic 1D-SOC with cold atoms

A pair of Raman beams couples two hyperfine levels labeled $|\uparrow\rangle$ and $|\downarrow\rangle$, using a two-photon transition (energy-level diagram). The resulting 1D-SOC leads to a band splitting and shifts the dispersion relation in a spin-dependent way, resulting in a twofold-degenerate ground state. (Right) Rotating the two parabolas around the vertical axis results in a ring of degenerate states at the bottom, the spin polarized with the opposite sign between the inner and outer surface.

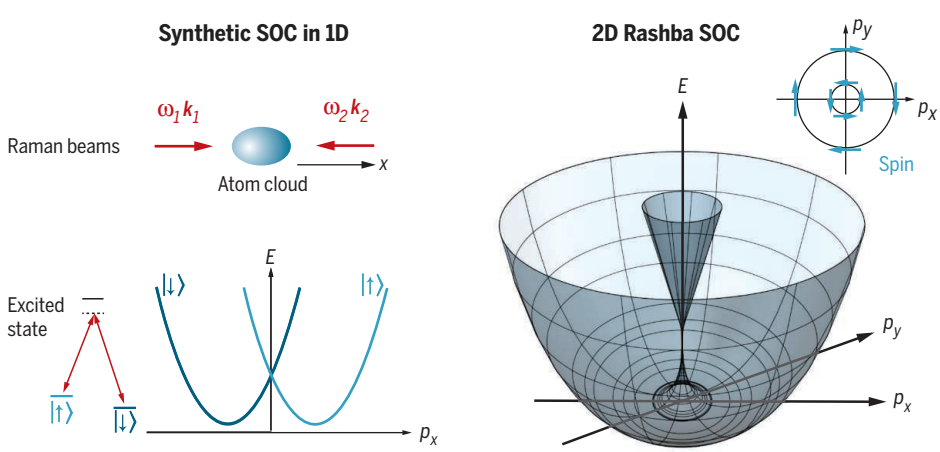

lar because they host exotic quasi-particle excitations known as Majorana fermions with fascinating properties. They are predicted to exhibit unusual exchange statistics that go beyond bosonic or fermionic ones and could find application in topological quantum computation (*6*). Again, the SO interaction was part of the breakthrough when it was realized that topological superconductivity could be induced in a material with strong SOC by making use of the proximity effect with a conventional superconductor.

Ultracold atoms provide a promising alternative to studying exotic quantum states that emerge as a result of SOC. But, because this type of interaction does not naturally arise in cold-atom experiments, it needs to be artificially synthesized by other means. Typically, the role of the spin is played by different internal states of the atom, and the coupling to its motional degrees of freedom is engineered with laser light (*7*). The technique of choice (*8*), now widely used in many laboratories, uses a pair of laser beams to couple two hyperfine levels via a Raman transition (see the figure, left panel). The atoms absorb a photon from one of the two laser beams and re-emit it into the second one. The atoms thereby experience a momentum kick given by the difference between the two photon recoil momenta. This couples spin and momentum and generates a 1D SOC. A first step toward higher-dimensional SOC was reported earlier this year (*9*), in which the authors demonstrated 2D-SOC with tunable anisotropy and magnitude. The experimental flexibility of cold atoms systems allows for the engineering of a variety of different forms of SOC even without solid-state analog, and combining them with optical lattice potentials may lead to even richer band structures (*10*).

Wu *et al.* demonstrate a new technique to simulate 2D-SOC in a square optical lattice using Raman transitions. The dimensionality is tunable between 1D and 2D, and the lowest-energy band can be made topologically nontrivial by changing the strength of an effective out-of-plane magnetic field. The setup is particularly appealing because it involves only a single laser source and does not require phase-locking between several optical beams. Instead, a single laser beam is split into two parts to produce a spin-independent optical lattice and a frequency-shifted Raman beam.

The latter, together with some of the optical lattice beams, creates a double Raman transition in the 2D plane to induce spin-flips. The engineered Hamiltonian has no analog in solid-state systems, but expanding it around zero quasimomentum reveals a term reminiscent of Rashba-type SOC (see the figure, right panel). In addition, there is a kinetic energy term that couples to the out-of-plane component of the spin that makes the system different from the normal Rashba Hamiltonian. It will be interesting to study in future theoretical and experimental works to what extent this Hamiltonian gives rise to Rashba-type physics or leads to novel exotic quantum states.

The study of SO-coupled quantum gases is a fascinating research area that is evolving rapidly and has a great potential for investigating exotic phenomena that go beyond traditional condensed-matter physics. As an example, the above ideas could be extended to 3D-SOC (*11*) or to exotic forms of SOC that involve larger spin states (*12*).

"...SO-coupled quantum gases...[have]... potential for investigating exotic phenomena...beyond traditional condensed-matter physics...[extending]...to exotic forms of SOC that involve larger spin states."

Currently, one limitation lies in heating of the quantum gas due to spontaneous emission of photons, and an important research direction consists of developing new schemes or identifying different atomic species, where such effects are mitigated. One of the major goals in the field is to study strongly interacting SO-coupled quantum gases, where many exciting questions remain to be addressed, both experimentally and theoretically. ■

REFERENCES

1. M. Z. Hasan, C. L. Kane, *Rev. Mod. Phys.* **82**, 3045 (2010).
2. Z. Wu *et al.*, *Science* **354**, 83 (2016).
3. Y. A. Bychkov, E. I. Rashba, *J. Phys. C Solid State Phys.* **17**, 6039 (1984).
4. G. Dresselhaus, *Phys. Rev. Lett.* **100**, 580 (1955).
5. C. L. Kane, E. J. Mele, *Phys. Rev. Lett.* **95**, 226801 (2005).
6. C. Nayak, S. H. Simon, A. Stern, M. Freedman, S. Das Sarma, *Rev. Mod. Phys.* **80**, 1083 (2008).
7. V. Galitski, I. B. Spielman, *Nature* **494**, 49 (2013).
8. Y. J. Lin, K. Jiménez-García, I. B. Spielman, *Nature* **471**, 83 (2011).
9. L. Huang *et al.*, *Nat. Phys.* **12**, 540 (2016).
10. N. Goldman, G. Juzeliūnas, P. Öhberg, I. B. Spielman, *Rep. Prog. Phys.* **77**, 126401 (2014).
11. B. M. Anderson, G. Juzeliūnas, V. M. Galitski, I. B. Spielman, *Phys. Rev. Lett.* **108**, 235301 (2012).
12. G. Juzeliūnas, J. Ruseckas, J. Dalibard, *Phys. Rev. A* **81**, 053403 (2010).

10.1126/science.aah7087

CELL DEATH

The MIFstep in parthanatos

Preventing cells from killing themselves may save tissues from damage during disease

By **Elizabeth Jonas**

If we knew how cells die, we might be able to prevent cell death, thereby saving vital tissues and organs in diseases as diverse as heart attack, stroke, diabetes, liver and kidney failure, and neurodegenerative diseases of the brain. Indeed, it has become clear from recent studies on anastasis, or reversal of apoptotic cell death (*1*), that cells can survive many severe insults and recover completely. On page 82 of this issue, Wang *et al.* (*2*) show that cell death can be prevented by blocking the breakdown of DNA that is a hallmark of a set of related cell death subtypes, grouped under the name of parthanatos (*3*).

Cells can die in several ways, such as loss of membrane integrity, loss of organelle function, loss of metabolites such as adenosine triphosphate (ATP), or damage and/or loss of genomic DNA. Investigators have focused on either preventing the cell from starting down the road toward death (e.g., opening a blocked artery in the brain during stroke) or finding the "commitment" step in the cell death pathway and thwarting death at that point, turning the cell back onto a road to recovery (*4*).

The phenomenon studied by Wang *et al.*, parthanatos, occurs when the prominent feature of injury is DNA damage, in the setting of imminent risk of cell death such as during stroke. When a cell's DNA repair pathways (*5*) are rendered ineffective or are simply missing, cells must decide either to live with damaged DNA or to die, as mutations may favor cancer or other disease states. Fragile mutant cells face difficulties surviving, and one decision point toward death occurs when DNA damage is too extensive for a given setting. Indeed, mutant cancer cells with defective DNA repair are vulnerable to treatments designed to disable the remaining DNA repair machinery (*6*). In injury, some repair enzymes become overwhelmed while others become overactivated, leading to the destruction of a cell's

Department of Medicine, Yale University, New Haven, CT, USA. Email: elizabeth.jonas@yale.edu

DNA. Parthanatos is associated with overactivation of the enzyme poly(ADP-ribose) polymerase (PARP), a member of a group of DNA repair proteins (*7*). PARP contains a DNA binding domain consisting of two zinc fingers, and a catalytic site containing a nicotinamide adenine dinucleotide (NAD) binding site and a poly(ADP-ribose) (PAR) synthesizing domain (*3*). The PARP enzyme makes use of oxidized NAD^+ to label broken DNA with PAR polymer, a signal that elicits the activation of a complex of proteins involved in cell stress management and DNA repair (see the figure). When DNA damage is extensive, lengthening and extensive branching of PAR occurs and the cell manifests further stress responses, including loss of mitochondrial membrane potential and release of the mitochondrial apoptosis-inducing factor (AIF). AIF translocates to the nucleus and activates an enzymatic system that causes large-scale DNA fragmentation, indicating that the cell has passed the point of no return. Wang *et al.* chose to look for the nuclease that carries out the final DNA destruction step during parthanatos by screening for AIF binding proteins. The screen identified macrophage migration inhibitory factor (MIF) as a new member of a large nuclease superfamily.

Given the known roles of MIF (*8*), it is perhaps not surprising that MIF would work with PARP-1 and AIF during parthanatos to accomplish large-scale DNA fragmentation, although a nuclease activity for MIF has not previously been described. MIF is a highly conserved 12.5-kDa protein with cytokine-like properties as well as endocrine and enzymatic functions. It works both outside the cell and intracellularly, where it regulates signaling pathways and presumably exerts tautomerase activity, although physiological substrates for this enzymatic activity have not yet been described (*9*). MIF was first discovered to have an innate immune function (*10*, *11*). In its canonical role, it participates in immune modulation during severe illnesses such as salmonella infection. In the setting of elevated secreted lipopolysaccharide (LPS) that forms part of the cell wall of Gram-negative bacteria, MIF up-regulates innate immunity to facilitate the response to LPS. MIF is then released by macrophages, other tissue cells, and lymphocytes and binds to receptors on T cells, promoting the production and release of cytokines. This leads to activation of intracellular signaling pathways and proliferation of immune cells.

MIF's contribution to proliferation, accompanied by its cytokine-releasing properties, can lead to an overstimulated immune response; overactivation of MIF is associated with a poor prognosis in septicemia, acute inflammatory lung diseases, cancer, diabetes, and rheumatological disorders. In these settings, MIF depletion or inhibition is protective (*12*). MIF is also present in the brain, where proinflammatory stimuli lead to an up-regulation of MIF. MIF has been suggested to play a physiological role in metabolism of neurotransmitters and a pathological role in the onset of inflammation contributing to neurodegenerative disease (*13*). It is now easy to see how the nuclease activity of MIF might contribute to protection from, or progression of, diverse brain diseases.

Wang *et al.* found that the overactivated version of MIF kills neurons in the brain during stroke. Inhibition of MIF's nuclease activity by mutation of its nuclease domain or by prevention of its translocation to the nucleus (by inhibiting its interaction with AIF) markedly attenuates acute brain injury during stroke in rodents and prevents the long-term sequelae of stroke. This may mean that neurons can step back from the brink of parthanatotic cell death to survive and repair their DNA, even after extensive DNA damage in cells that had already been marked for death. MIF may destroy not only severely damaged cells but also relatively healthy cells. This could occur even if MIF is not actually activated in the healthy cells but is instead secreted by unhealthy neurons and endocytosed (*14*) by relatively intact neurons whose DNA it might then be at liberty to "seek and destroy."

It is not difficult to imagine a positive role for MIF as a nuclease in long-lived postmitotic cells such as neurons, where DNA repair is crucial to cell health. It is also not surprising that a molecule that can so easily ramp up its activities is an important ally for PARP in the total destruction of neuronal DNA during parthanatos, when DNA damage has become too extensive for the cell to be salvageable.

When designing therapies for neuroprotection, it is crucial to take into account the dichotomy between beneficial and harmful actions of molecules such as MIF and PARP. Therapies to block DNA repair in the nervous system may not be advantageous over the long term because they will prevent DNA repair and immune modulation. Agents to specifically prevent the overactivation of these proteins will therefore need to be developed. Nevertheless, inhibition of MIF and PARP during acute stroke, as shown by Wang *et al.*, is clearly useful because these molecules are already in their destructive mode. The authors have demonstrated that neuroprotective strategies to halt the progression of parthanatos are well worth pursuing. ■

Thoroughly MIFfed

PARP requires the nuclease activity of MIF to execute the final steps of DNA destruction during parthanatos.

1 Loss of oxygen and abnormal release of neurotransmitter glutamate

2 Production of reactive oxygen species (ROS) and reactive nitrogen species ($ONOO^-$)

3 DNA damage, PARP activation, and DNA labeling with PAR at strand breaks

4 Depletion of NAD, depletion of ATP, loss of mitochondrial membrane potential, and release of AIF from mitochondria

5 Interaction of AIF with MIF, translocation to the nucleus of AIF-MIF, total DNA breakdown, and cell death

6 Translocation to nucleus of AIF–mutant MIF complex, DNA repair, and cell survival

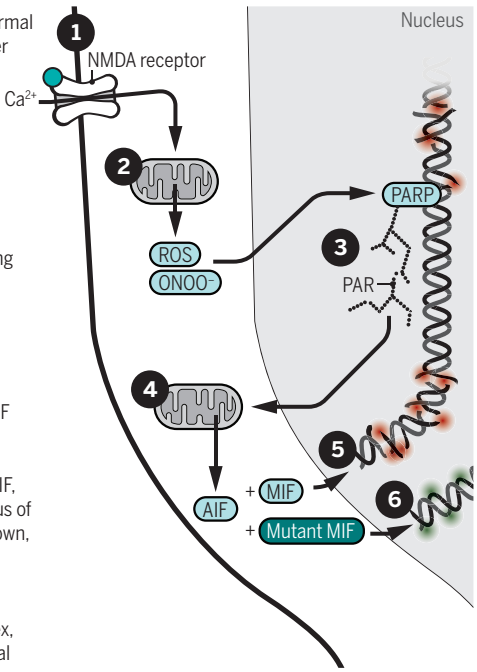

GRAPHIC: V. ALTOUNIAN/*SCIENCE*

REFERENCES

1. H. L. Tang, H. M. Tang, M. C. Fung, J. M. Hardwick, *Sci. Rep.* **5**, 9015 (2015).
2. Y. Wang *et al.*, *Science* **354**, aad6872 (2016).
3. A. A. Fatokun, V. L. Dawson, T. M. Dawson, *Br. J. Pharmacol.* **171**, 2000 (2014).
4. M. Adams, S. Cory, *Oncogene* **26**, 1324 (2007).
5. A. Sancar, *Angew. Chem. Int. Ed.* **55**, 8502 (2016).
6. M. J. O'Connor, N. M. Martin, G. C. Smith, *Oncogene* **26**, 7816 (2007).
7. P. Pacher, C. Szabo, *Am. J. Pathol.* **173**, 2 (2008).
8. T. Calandra, T. Roger, *Nat. Rev. Immunol.* **3**, 791 (2003).
9. P. D. Senter *et al.*, *Proc. Natl. Acad. Sci. U.S.A.* **99**, 144 (2002).
10. B. R. Bloom, B. Bennett, *Science* **153**, 80 (1966).
11. J. R. David, *Proc. Natl. Acad. Sci. U.S.A.* **56**, 72 (1966).
12. M. Bozza *et al.*, *J. Exp. Med.* **189**, 341 (1999).
13. M. Bacher *et al.*, *Mol. Med.* **16**, 116 (2010).
14. R. Kleemann *et al.*, *Nature* **408**, 211 (2000).

10.1126/science.aai8756

NEURODEVELOPMENT

Human brains teach us a surprising lesson

Young interneurons continue migrating to the frontal lobe during the first few months of life

By **Melissa McKenzie**[1] *and* **Gord Fishell**[2]

The unique cognitive abilities of humans have long captured the imagination of philosophers and neuroscientists alike. But which features of the human brain set us apart from other mammals? Most likely, our intellectual advantages result from a relative expansion of cortical regions responsible for associative and executive function (*1*). However, the question of how this cortical expansion is achieved during human development has remained unresolved. A major clue came from the elucidation of neurogenic events taking place during the later phases of embryonic human brain development. This began with the recognition that the human cortical subventricular zone is greatly expanded relative to that of lower mammals. This evolutionary innovation allowed for the marked expansion of associative cortex, especially the frontal lobes. Subsequently, a thorough investigation of the fetal human cortex revealed the existence of a number of distinct excitatory neuronal progenitor types (e.g., outer radial glia) that were identified as key to driving a remarkable burst of late neurogenesis (*2*). However, the cortex is able to function only when excitatory and inhibitory activities in the brain are balanced. On page 81 of this issue, Paredes *et al.* (*3*) identify a population of interneurons that migrate to the cortex during infancy to establish inhibitory circuits.

In rodents, inhibitory cortical interneurons are predominantly generated in the ventral telencephalon and then migrate into the cortex (*4*). There is also considerable postnatal neurogenesis of GABAergic interneurons that contributes to the olfactory bulb and, to a limited extent, the anterior forebrain (*5*). By contrast, previous human studies (*6*) hinted that inhibitory interneurons in humans could arise from within the cortical primordium itself. However, subsequent studies did not find evidence for cortically derived interneurons in humans (*7*, *8*). Furthermore, postnatal neurogenesis within humans appears to be considerably more modest than in rodents (*9*). Paredes *et al.* have now uncovered an alternative mechanism by which embryonically derived but uncommitted cortical interneurons integrate postnatally into the human cortex.

Paredes *et al.* examined postmortem human brain samples from infants between birth and 3 months of age. They discovered a periventricular complex of morphologically and biochemically identified young migrating neurons, which they named Arc cells for their characteristic trajectory from the ventricle. Arc cells appeared to form a four-tier assemblage that originated as a compact accumulation in the cortical subventricular zone (SVZ) and extended into chains of migrating neurons. The presence of these neurons in the SVZ is noteworthy, as the SVZ is the embryonic epicenter of pyramidal cell neurogenesis. During migration, Arc cells associated with blood vessels and formed finger-like chains connected by adherent junctions, reminiscent of migratory cells in the rodent cortex. Paredes *et al.* were able to label this population with adenovirus carrying green fluorescent protein, and then used video microscopy to capture them in the act of migration.

The authors found that migratory Arc cells primarily expressed markers associated with the inhibitory neurotransmitter γ-aminobutyric acid (GABA). However, unlike previous findings in rodents, actively proliferating cells were absent, which suggests that these migrating GABAergic neurons

PHOTO: SPLENDENS/ISTOCK PHOTO

[1]Department of Pathology and Cell Biology, Columbia University Medical Center, New York, NY 10032, USA. [2]Department of Neuroscience and Physiology, Neuroscience Institute, New York University Langone Medical Center, New York, NY 10016, USA, and NYU Abu Dhabi Center for Genomics and Systems Biology. Email: gordon.fishell@med.nyu.edu

are already generated before birth. Cortical interneurons are renowned for their diversity, which has been shown to relate to their region of origin (*10*). The Arc populations identified appear to run the gamut of different interneuron subtypes, which in rodents are known to arise from distinct ventral telencephalic progenitor zones. The source and precise timing of the origin of migrating Arc cells, and how they are assembled in the cortex, remain open questions.

Studies on human brain development are technically difficult and typically rely on piecemeal data. The heroic effort needed to histologically examine and track virally labeled Arc cells using the meager human samples available should not be underestimated. By overcoming the inherent difficulties involved in such studies, Paredes *et al.* have begun to scratch the surface of how this novel mode of circuit integration could influence human brain development. Despite the sparseness of their data, both indirect and direct lines of evidence support their conclusions. With striking symmetry, Arc cells migrate in a manner indistinguishable from their embryonic predecessors, making a strong but circumstantial case for their findings. More important, the authors were able to support their histologic evidence with T2 signal intensity in magnetic resonance images of developing and postnatal human brains, which allowed them to detect migratory streams of cells, providing an important in vivo correlate for their conclusions. The cross-correlation between high-resolution in vitro analysis and lower-resolution in vivo imaging is extremely promising. It suggests that with modest improvements, noninvasive clinical studies will allow us to explore the postnatal migration of cells within the human brain.

The dynamic integration of cells continues postnatally in the frontal lobe of humans.

What are the implications of these findings for our understanding of brain development? With a shift in focus from neurogenesis to maturation, the authors raise the question of what aspects of brain development we have missed. The loss of markers of young migrating neurons such as doublecortin by 6 months implies that shortly after birth the residual migration of interneurons is complete. Nonetheless, it remains possible that a postmigratory but immature interneuron population is retained within the young brain for months or perhaps years. If humans possess an "interneuron reserve," its potential to contribute to plasticity under normal or pathophysiological conditions may be considerable. Accumulated evidence indicates that specific interneuron populations control critical-period plasticity within the brain (*11*). Moreover, transplantation studies pioneered by this same group have indicated that the grafting of interneuron precursors can reopen critical-period plasticity (*12*). The present data suggest that these findings, rather than being epiphenomena, may reflect the underlying biology of how our brains are assembled. ■

REFERENCES AND NOTES

1. R. E. Passingham, J. B. Smaers, *Brain. Behav. Evol.* **84**, 156 (2014).
2. D. V. Hansen, J. H. Lui, P. R. L. Parker, A. R. Kriegstein, *Nature* **464**, 554 (2010).
3. M. F. Paredes *et al.*, *Science* **354**, aaf7073 (2016).
4. S. A. Anderson, D. D. Eisenstat, L. Shi, J. L. Rubenstein, *Science* **278**, 474 (1997).
5. C. Lois, J. M. García-Verdugo, A. Alvarez-Buylla, *Science* **271**, 978 (1996).
6. K. Letinic, R. Zoncu, P. Rakic, *Nature* **417**, 645 (2002).
7. D. V. Hansen *et al.*, *Nat. Neurosci.* **16**, 1576 (2013).
8. T. Ma *et al.*, *Nat. Neurosci.* **16**, 1588 (2013).
9. K. L. Spalding, R. D. Bhardwaj, B. A. Buchholz, H. Druid, J. Frisén, *Cell* **122**, 133 (2005).
10. A. Kepecs, G. Fishell, *Nature* **505**, 318 (2014).
11. T. K. Hensch, M. P. Stryker, *Science* **272**, 554 (1996).
12. D. G. Southwell *et al.*, *Science* **327**, 1145 (2010).

ACKNOWLEDGMENTS

We thank C. Mayer and R. Machold for critical reading and insightful comments on the manuscript. Supported by the Simons Foundation and NIH grants MH071679, MH111529, NS074972, and NS081297 (G.F.), and by NIH grant T32MH015174-39 (M.M.).

10.1126/science.aai9379

DEVELOPMENT

Apes know what others believe

Understanding false beliefs is not unique to humans

By **Frans B. M. de Waal**

Of all the human uniqueness claims proposed over the years, theory of mind enjoys perhaps the most prominent status. The term "theory of mind" refers to the ability to know what others know, that is, to attribute mental states such as intentions, goals, and knowledge to others. It is widely held to be unique to humans. Yet, given the results reported by Krupenye *et al.* on page 110 of this issue, this claim is starting to wobble (*1*). The authors show that apes can correctly anticipate where human actors will look for a hidden item, even if the apes know that the item is no longer there. Ironically, this finding brings us back to square one, because apes played a major role in the formulation of the theory of mind concept.

In the late 1960s, the primatologist Emil Menzel often took a young chimpanzee by the hand out into a large, grassy enclosure to show her hidden food or a scary object, such as a toy snake. After this, Menzel brought the ape back to a waiting group of juveniles and released them together. Would the others pick up on her knowledge? The other apes proved eager to follow an ape who knew a food location, but reluctant to stay with one who had seen a snake (*2*). Ever since, the hiding and finding of items has been the main way of investigating what individuals know about what others know. A more controlled ape experiment gave the phenomenon its name when Premack and Woodruff asked, "Does the chimpanzee have a theory of mind?" (*3*).

Theory of mind soon became a staple of developmental psychology. Many animal studies followed as well, including on monkeys and birds (*4*). During all of the debates about animal theory of mind, however, one assumption seemed unassailable: that nonhuman species have trouble with false beliefs. This means that they fail to grasp

Living Links Center of the Yerkes National Primate Research Center and Department of Psychology, Emory University, Atlanta, GA 30322, USA. Email: dewaal@emory.edu

Using eye-tracking technology, Krupenye *et al.* show that chimpanzees and other apes can grasp what others know, even when it differs from what they themselves know.

knowledge of others if it deviates from what they themselves know.

In children, the capacity for false beliefs is tested in a hiding-and-rehiding scenario. Children first see Sally, a doll, hide an item. Once Sally exits the room, another doll quickly rehides the item in a different place. The children are then asked where Sally will look upon return. Young children pick the place where they themselves know the item to be, but older children understand that Sally does not share their knowledge (*5*). In general, children pass this false-belief test only after the age of four.

In 2007, an innovative experiment challenged the conclusion that younger children fail to grasp false beliefs (*6*). Relying on eye-tracking technology, scientists measured where children look when the protagonist returns to the scene. Children as young as 24 months correctly anticipated the agent's searching pattern even if they knew it to be wrong. This experiment inspired Krupenye *et al.*'s ape study. The investigators had access to an unusually large number of apes of three species: 19 chimpanzees, 14 bonobos, and 7 orangutans. In the experiments, the apes watch videotapes in which a human actor interacts with another human actor in a King Kong (KK) suit.

In one scenario, an ape sees KK steal an object from a human actor and hide it under one of two boxes, say the one on the left. KK then chases off the human and secretly rehides the object under the box on the right. After this, KK takes the object away and leaves the scene. The human actor now returns to search for the object while an infrared eye-tracker measures precisely which parts of the video the ape subject pays attention to. Even though the ape knows that both boxes are empty, he should expect the human to go to the left-hand box, where he last saw the item being put. Eye-tracking shows that the apes correctly anticipate the human searching pattern, despite the discrepancy with their own knowledge.

This nonverbal paradigm is a genuine breakthrough, not only because it avoids an undue reliance on language skills required to understand narrative and questions in theory of mind testing in children but also because it highlights the mental continuity between great apes and humans. Given the importance attached to theory of mind in developmental psychology and its possible deficits in relation to autism spectrum disorder and schizophrenia, it is important to put this capacity in a biological context. It likely evolved in the complex societies that mark the Hominidae (humans and apes) to offer individuals the benefit of better anticipating the behavior of others.

The results contain a lesson for those who jump on negative outcomes regarding animal mental capacities as proof of human distinctiveness. As the old mantra goes, absence of evidence is not evidence of absence. We should always keep an open mind about the capacities of nonhuman species (*7*). Whether other animals possess theory of mind has been treated as an all-or-nothing question. It may be more fruitful, however, to break larger capacities into smaller elements, many of which may be shared across species (*8*).

Theory of mind is probably part of a much larger picture that includes empathy, social connectedness, and the way bodies relate to other bodies. It is no accident that the tests conducted here focus on the body, i.e., subjects' eyes following the physical movements of actors. As such, the study by Krupenye *et al.* may help us move away from the prevailing assumption that theory of mind relies on a cognitive simulation of what is going on in the heads of others. Reading others' minds is beyond anybody's capacity. All we can do—and what apes apparently do in similar ways—is read bodies. ■

REFERENCES

1. C. Krupenye, F. Kano, S. Hirata, J. Call, M. Tomasello, *Science* **354**, 110 (2016).
2. E. W. Menzel, in *Behavior of Nonhuman Primates*, vol. 5, A. M. Schrier, F. Stollnitz, Eds. (Academic Press, New York, 1974), pp. 83–153.
3. D. Premack, G. Woodruff, *Behav. Brain Sci.* **4**, 515 (1978).
4. J. M. Dally, N. J. Emery, N. S. Clayton, *Science* **312**, 1662 (2006).
5. H. Wimmer, J. Perner, *Cognition* **13**, 103 (1983).
6. V. Southgate, A. Senju, G. Csibra, *Psychol. Sci.* **18**, 587 (2007).
7. F. B. M. de Waal, *Are We Smart Enough to Know How Smart Animals Are?* (Norton, 2016).
8. F. B. M. de Waal, P. F. Ferrari, *Trends Cogn. Sci.* **14**, 201 (2010).

10.1126/science.aai8851

RETROSPECTIVE

Roger Y. Tsien (1952–2016)

An exceptionally creative scientist shed light (of many colors) on biological mysteries

By **Stephen J. Lippard**

The world of biological chemistry lost one of its most creative pioneers when Roger Y. Tsien died on 24 August 2016 at the age of 64 while biking on a challenging trail in Eugene, Oregon, where he and his wife Wendy had their home. Tsien, who shared the 2008 Nobel Prize in Chemistry, was a professor in the Departments of Pharmacology and of Chemistry and Biochemistry at the University of California, San Diego (UCSD). Born in New York City and raised in Livingston, New Jersey, Roger had special talents that were manifested early—he won the Westinghouse Science Talent Search at age 16 for his original research project, "Bridging in Transition Metal Thiocyanate Complexes." After graduating summa cum laude from Harvard College with a bachelor's degree in chemistry and physics, he studied at Cambridge University, receiving a Ph.D. in physiology in 1977 before joining the faculties of the University of California (UC), Berkeley, and, 7 years later, UCSD, where he spent most of his career. His thesis on the design and use of organic tools in cellular physiology set him on a course to investigate the chemistry of the brain.

I first met Roger in the late 1960s when he appeared at my office in the Chemistry Department of Columbia University as a high school senior trying to decide between Columbia and Harvard. It was immediately obvious that he was a very special person—bright, inquisitive, personable and, above all, determined. His choice of Harvard, I learned recently from Wendy, may have been influenced by his passion for combining science with music. Roger often walked wearing earbuds, deep in thought. He was also an avid photographer, a hobby that paralleled one of his principal scientific interests—using light to image biological function. Art and music were a huge part of his life. We reconnected in 1998, when I took a sabbatical in his lab at UCSD to steer my own research program toward "metalloneurochemistry." Roger's work on imaging calcium in biology provided powerful tools and tactics that I needed to learn. I was delighted that he found it "compelling" to host someone who had reached out to him when he was in high school to offer advice on how best to fulfill his own career ambition to use chemistry to reveal biology.

The Tsien lab at UCSD was a spectacular place. As a toolmaker, Roger was unparalleled, producing molecule after molecule that provided the means to unveil many mysterious intricacies of cellular processes. An early success was Fura-2, a fluorescent sensor for imaging Ca^{2+} in cells. Roger's seminal paper describing this and closely related Ca^{2+} sensors has been cited over 20,000 times. Additional Roger Tsien creations for probing calcium biology included chelators, like BAPTA, that bind to and prohibit the ion from performing its functions; acetoxymethyl esters that enable fluorescent sensors to enter cells in cases where a membrane is impenetrable; and so-called "caged" compounds, synthetic constructs that turn on illumination after photochemical cleavage of a bond to release the active species. This tool allows control of the timing, location, and signal intensity of a probe.

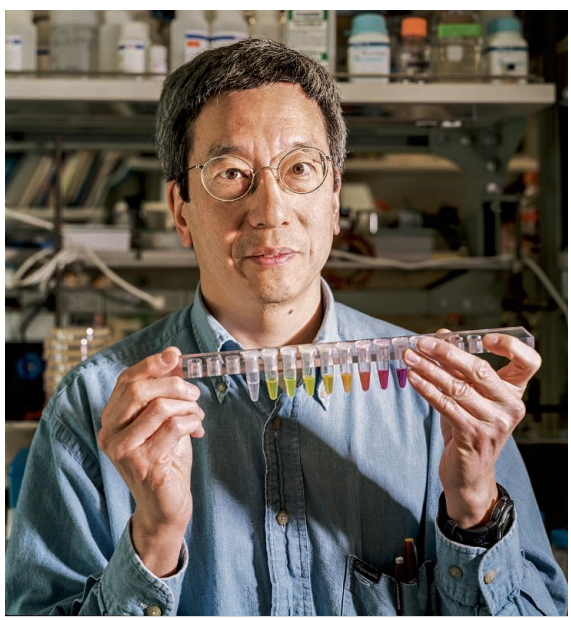

PHOTO: JOE TORENO/HOWARD HUGHES MEDICAL INSTITUTE

Roger had an encyclopedic knowledge of the literature, which enabled him to design synthetic routes to molecules with minimal sequential steps. After my sabbatical at UCSD, my lab at the Massachusetts Institute of Technology embarked on a program to image mobile zinc in the central nervous system. When our first construct (Zinpyr-2), prepared in a multistep synthesis, responded well to zinc in the test tube, I called Roger to enlist his assistance to image zinc in live cells. He was very excited to learn about this result (I could imagine him waving his hands in characteristic fashion as he spoke to me on the phone) because, for a very different reason, he had independently prepared a closely related compound that behaved similarly, in a single step! We published the results together and, needless to say, his Zinpyr-1 became the "go-to" molecule for imaging mobile zinc in the early days of our explorations.

Roger's work on calcium signaling was worthy of the Nobel Prize, and many were surprised when the announcement came from Stockholm that he received it for work on green fluorescent proteins (GFPs). These amazing proteins, discovered by Osamu Shimomura in the jellyfish *Aequorea victoria*, give off a green fluorescence upon irradiation with blue to ultraviolet light and could be genetically encoded into animals to explore biological phenomena, as demonstrated by Martin Chalfie. Roger, who referred to GFP as "dim, fickle, and spectrally impure" modified one of the amino acids at a key position in GFP to produce enhanced GFP, which shone more brightly, and then engaged in an extensive program to mutate amino acids across the 11-stranded β barrel of the protein to produce versions that fluoresced in colors across the rainbow. Shimomura, Chalfie, and Tsien shared the Nobel Prize for their work.

Toward the end of his all too short life, Roger became interested in contributing to medicine and devised a means to color-code nerve cells to enable surgeons to avoid cutting them during operations—fluorescence-guided surgery. He came up with ideas, and devised ways to test them, for investigating where long-term memories are stored in the brain. Early detection of cancer was also of interest, and he viewed cancer-illuminating probes (one is currently in clinical trials) as more important than nerve-highlighters.

One can only wonder what creative inventions were taken from us by the untimely loss of Roger Tsien, a true giant of chemistry and biology. He is survived by Wendy; two brothers, Richard and Louis; and stepson, Max Rink. We miss him greatly. ■

Department of Chemistry, Massachusetts Institute of Technology, Cambridge, MA 02139, USA. Email: lippard@mit.edu

10.1126/science.aak9585

COLLECTIVE ACTION

Social norms as solutions

Policies may influence large-scale behavioral tipping

By **Karine Nyborg, John M. Anderies, Astrid Dannenberg, Therese Lindahl, Caroline Schill, Maja Schlüter, W. Neil Adger, Kenneth J. Arrow, Scott Barrett, Stephen Carpenter, F. Stuart Chapin III, Anne-Sophie Crépin, Gretchen Daily, Paul Ehrlich, Carl Folke, Wander Jager, Nils Kautsky, Simon A. Levin, Ole Jacob Madsen, Stephen Polasky, Marten Scheffer, Brian Walker, Elke U. Weber, James Wilen, Anastasios Xepapadeas, Aart de Zeeuw**

Climate change, biodiversity loss, antibiotic resistance, and other global challenges pose major collective action problems: A group benefits from a certain action, but no individual has sufficient incentive to act alone. Formal institutions, e.g., laws and treaties, have helped address issues like ozone depletion, lead pollution, and acid rain. However, formal institutions are not always able to enforce collectively desirable outcomes. In such cases, informal institutions, such as social norms, can be important. If conditions are right, policy can support social norm changes, helping address even global problems. To judge when this is realistic, and what role policy can play, we discuss three crucial questions: Is a tipping point likely to exist, such that vicious cycles of socially damaging behavior can potentially be turned into virtuous ones? Can policy create tipping points where none exist? Can policy push the system past the tipping point?

In small groups, social norms can facilitate cooperation (*1*). Solutions can be specific to context (e.g., small-scale irrigated rice paddies in Nepal) and local in nature. Yet social norms can affect behavior on larger scales, e.g., cessation of smoking in public places (*2*, *3*), abandonment of foot-binding in China (*4*), and changed fertility norms (*4*)—all striking large-scale transformations of social (dis)approval and behavior.

The concept of social norms varies across disciplines [e.g., psychology (*5*) and economics (*4*)] and that creates an obstacle to interdisciplinary communication. We define a social norm as a predominant behavioral pattern within a group, supported by a shared understanding of acceptable actions and sustained through social interactions within that group (*1*). We focus on recurrent behavioral patterns that are widely conformed to but are also widely perceived as the right thing to do. Social feedback helps make norms self-reinforcing and thus stable.

When norms do change, however, that can happen abruptly. Ecologists have developed a thorough understanding of tipping points—and the role feedbacks play in crossing them—that is highly relevant to understanding social norm changes (*6*). Here, we try to integrate these views.

IS THERE A TIPPING POINT?

For vicious and virtuous behavioral cycles to arise, people must be more willing to choose a behavior the more widespread it is. The tipping point is where a vicious cycle turns into a virtuous one, or vice versa. Social, economic, and technical factors often invoke a need for people to coordinate their behavior. Striking cases are provided by network externalities, in which a good's value to the individual increases with the frequency of others consuming that same type of good. For example, if few own electric cars, charging stations are rare and few will buy electric cars; if most cars are electric, gas stations are rare, and few buy gas-fueled cars.

Similar coordination benefits occur in social life. Diet variation across countries cannot be fully explained by prices, incomes, and nutrition content (*7*); it appears that other forces, like norms, are involved. Differing diets make cooking shared meals cumbersome. If people tend to prefer the foods they are used to, sticking to the most common diet is convenient. The availability and quality of particular foods in stores and restaurants may increase with demand. Hence, if a less meat-intensive diet became the norm, individuals might conform partly owing to social pressure or a wish to be environmentally friendly; but a primary motive may simply be to enjoy pleasant and convenient joint meals.

When behavior is easily observable (e.g., smoking), social sanctioning can create tipping points. If norm followers sanction norm violators, the social sanctioning of violators increases as the share of followers grows (*2*). Other mechanisms inducing people to act like others include conditional cooperation—an often observed willingness to cooperate more when others cooperate more (*8*)—and social learning of personal moral responsibility through observing the behavior of others (*9*).

Social, economic, and other feedbacks can be intertwined and hard to disentangle. What matters for behavior is their combined effect. For example, recycling of household waste with curbside collection requires little cost and effort and is easily observable by neighbors. A modest social feedback, like conformity, may thus suffice to create a tipping point. In other cases, counteracting factors dominate: Misuse of antibiotics is not easily observed by peers, and perceived medical benefits can be substantial. Firms' and individuals' greenhouse gas emissions originate from a plethora of actions; many of which are

See supplementary materials for author affiliations. Email: karine.nyborg@econ.uio.no

barely observable and yield considerable material benefits. In such cases, there may be no tipping points.

In some cases, policy can make tipping points arise even where none were initially present (*10*). Policy can make individual choices more interrelated, e.g., by increasing visibility. Customers of a major electric utility were much more likely to participate in a program preventing blackouts when their neighbors could tell who signed up (*11*): Observability tripled participation, strongly outperforming a cash incentive of $25. If reinforcing social feedbacks are present but dominated by other incentives, policy can modify the latter through, e.g., taxes, subsidies, or infrastructure investments, like bicycle lanes. If new bicycle lanes are increasingly likely to be constructed when more people are cyclists, the policy itself adds reinforcing feedback.

PASSING TIPPING POINTS

Unlike ecological processes, human behavior is affected by expectations of others' behaviors and attitudes (*4*). When people prefer to act like most others, beliefs can be self-fulfilling—and changed expectations of what others will do can produce abrupt behavioral changes (*4*). Thus, a potentially powerful role of policy is to provide reasons for people to change their expectations (*4*). This is different from attempting to persuade people to change normative values.

Experiments confi rm that expectations are crucial for cooperative behavior and that they are affected by variables like framing, communication, moral suasion, and ability to be identified (*8*). Although formal enforcement of Norway's 1988 antismoking laws was limited, smokers began expecting stricter social sanctions, going outdoors to smoke even in unregulated areas like private homes. Nonsmokers became less accustomed to passive smoking, strengthening their negative reactions, until the new norm of not smoking indoors was nearly universal in regulated and unregulated areas (*2*). Even so, psychological phenomena like expectations are hard to steer: In Greece, antismoking laws did not seem to affect expected social sanctions sufficiently, and smoking prevailed (*3*).

Nevertheless, costly public investments, like bicycle lanes or charging points for electric cars, provide strong indications that a policy (and behaviors supported by the policy) will prevail. A policy that changes material incentives indicates to everyone that others' incentives are changed, not just their own, making expectations of behavioral changes reasonable. Making behaviors visible to peers can strengthen expected social reactions (*8*), but visibility can also create beliefs that others expect stricter social sanctions and thus will change their behavior. Simultaneous or well-sequenced introduction of several policy instruments may support the psychological perception of a major change. Norway has the world's highest per capita number of electric cars following multiple policy measures, such as bus lane access, exemption from road tolls, and reduced taxes (*12*).

Even temporary policies can be effective (*2*). If behaving like the crowd (e.g., not smoking) is easier or more convenient, substantial permanent external pressure (e.g., smoking ban or social sanctions) may no longer be needed once the tipping point has been passed.

DIFFUSION, FEASIBILITY, COLLABORATION

Theory on innovation diffusion (*13*) describes how a critical mass of connected people adopting a new behavior can spread a norm change through a social network. For example, encouraging a small set of randomly selected students in 56 U.S. schools to take a public stance against bullying reduced reported student conflicts by 30% in a year (*14*). Pioneers may invent a better (nonconformist) practice or perform new behavior just to deviate from the crowd (anticonformist). If others recognize an individual benefit of this behavior (*5*), a local cluster of adopters may emerge. The more socially infectious this group is and the more visible and easy to copy the new behavior, the faster and more widely the behavior spreads (*14*). Role models are critical in this process. The tipping point occurs when sufficient positive social feedback emerges, causing the new behavior to become cool and ultimately normal.

"...a potentially powerful role of policy is to provide reasons for people to change their expectations."

Information on what others do can affect behavior via direct messaging; metrics, such as fuel-efficiency labels; or other feedback (*5*, *15*). Before the tipping point is reached, however, awareness of others' nonadoption tends to work against change. For example, telling students that a majority of their peers drink more alcohol than they do may increase drinking (*15*). The potential impact of policy is also observed in negative examples. If not compatible with local social norms, legal and institutional measures may turn virtuous cycles into vicious ones (*1*).

Political feasibility may itself be part of a vicious or virtuous cycle that limits policy-makers' ability to act. If a high birth rate insures parents against poverty in old age, public pension systems can reduce preferred family size by providing alternative insurance. However, a high birth rate may itself limit political support for public pension schemes, because families with more children are less in need of pensions and less able to pay taxes. Without voter support, there may be little scope for policy change.

Judging whether patterns of socially or environmentally detrimental behaviors may be broken by changed social norms is not easy. When looking for tipping points, the following questions are useful: Is the behavior observable? Does it involve coordination benefits? Are tastes likely to be shaped by behaviors (e.g., preferring foods one is used to)? Is the alternative behavior low cost? If the answers are negative, policies may be used to change some of them. If answers are positive, the next step is to look for ways to break self-fulfilling expectations, by providing reasons for people to believe that others will take up less damaging behaviors.

The potentials and limits of social norm changes as a means to solve large-scale problems are not yet fully understood. Key issues we did not engage here but which require continued study include group norms, social identity, norm internalization, and the role of new technologies and social media. Active communication and collaboration between disciplines are key for success. ■

REFERENCES AND NOTES

1. E. Ostrom, *J. Econ. Perspect.* **14**, 137 (2000).
2. K. Nyborg, M. Rege, *J. Econ. Behav. Organ.* **52**, 323 (2003).
3. C. I. Vardavas *et al.*, *PLOS ONE* **8**, e72945 (2013).
4. H. P. Young, *Annu. Rev. Econ.* **7**, 359 (2015).
5. R. B. Cialdini, N. J. Goldstein, *Annu. Rev. Psychol.* **55**, 591 (2004).
6. M. Scheffer, *Critical Transitions in Nature and Society* (Princeton Univ. Press, Princeton, NJ, 2009).
7. P. Dubois, R. Griffith, A. Nevo, *Am. Econ. Rev.* **104**, 832 (2014).
8. A. Chaudhuri, *Exp. Econ.* **14**, 47 (2011).
9. K. A. Brekke, G. Kipperberg, K. Nyborg, *Land Econ.* **86**, 766 (2010).
10. S. Barrett, *Environment and Statecraft: The Strategy of Environmental Treaty-Making* (Oxford Univ. Press, Oxford, 2003).
11. E. Yoeli, M. Hoffman, D. G. Rand, M. A. Nowak, *Proc. Natl. Acad. Sci. U.S.A.* **110** (suppl. 2), 10424 (2013).
12. M. A. Aasness, J. Odeck, *Eur. Transp. Res. Rev.* **7**, 34 (2015).
13. E. M. Rogers, *Diffusion of Innovations* (Free Press, New York, ed. 5, 2003).
14. E. L. Paluck, H. Shepherd, P. M. Aronow, *Proc. Natl. Acad. Sci. U.S.A.* **113**, 566 (2016).
15. P. W. Schultz, J. M. Nolan, R. B. Cialdini, N. J. Goldstein, V. Griskevicius, *Psychol. Sci.* **18**, 429 (2007).

ACKNOWLEDGMENT

The Beijer Institute of Ecological Economics of the Royal Swedish Academy of Sciences supported the authors' collaboration.

SUPPLEMENTARY MATERIALS

www.sciencemag.org/content/354/6308/42/suppl/DC1

10.1126/science.aaf8317

The many-worlds interpretation of quantum mechanics is not, writes Roger Penrose, "a sensible viewpoint with regard to physical reality."

PHYSICS

The folly of fashionable thinking

A physicist casts a critical eye on popular ideas in cosmology, quantum mechanics, and string theory

By **Mario Livio**

Fashion, Faith, and Fantasy in the New Physics of the Universe
Roger Penrose
Princeton University Press, 2016. 519 pp.

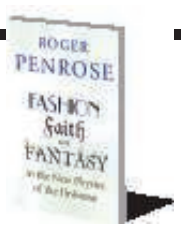

In the personal coda to *Fashion, Faith, and Fantasy in the New Physics of the Universe*, mathematical physicist Roger Penrose describes how, in response to a question by a Dutch journalist, he replied that he does not consider himself to be a "maverick." He interprets the term to mean someone who deliberately goes against conventional thinking for the sake of standing apart from the crowd. Under this definition, Penrose is indeed not a maverick. He does, however, stand out as an independent thinker, who for years has been critical of a few current trends in theoretical physics and cosmology.

You don't have to agree with all, or even a part, of Penrose's criticism to realize that his latest book represents an extremely original, rich, and thoughtful survey of today's most fashionable attempts to decipher the cosmos on its smallest and largest scales.

The "fashion" in the book's title refers mostly to the popularity of string theory and the so-called "M-theory"—the efforts to formulate a quantum theory of gravity. "Faith" refers to our persistent belief in the reality underlying quantum mechanics, even when it seems to clash with the reality we experience in the large-scale "classical" world. "Fantasy" targets mainly the inflationary model, which contends that our universe underwent a stupendous expansion when it was only a fraction of a second old. However, Penrose doesn't spare other theories that he regards as fantasies, such as eternal inflation and the multiverse, from harsh criticism either.

Penrose makes a strong case for the fact that once a physical theory becomes fashionable, students are mainly guided into that direction of research, sometimes at the expense of other, perhaps equally promising ideas. Using string theory as an example, he points out a number of potential difficulties with the theory's requirement for the existence of extra (unobserved) dimensions. As he has done in previous books, he also emphasizes the fact that string theories, despite their fashionable status, have failed so far to produce any directly testable predictions.

Penrose acknowledges the successes and predictive power of quantum mechanics. He argues, however, that there should be a limit to our quantum faith, such as when the theory's predictions are in clear conflict with macroscopic reality. (Schrödinger's proverbial cat could not pass simultaneously through two separate doors in the classical world, for example.) Penrose uses the example of a Geiger counter, which detects energetic particles resulting from radioactive decays, to construct an explanatory bridge between the subatomic and the classical worlds.

When it comes to cosmology, Penrose returns to a topic he has tackled before: the second law of thermodynamics (*1*, *2*). This impactful law states that the entropy in the universe constantly increases. One interpretation of this law argues that just as shaking a box containing a completed LEGO model will result in increased randomness, the universe started from an extraordinarily ordered state. Penrose uses this notion to argue that the inflationary model cannot provide the answer to a number of puzzling observations, such as the "smoothness" (the extreme cosmic uniformity) and "flatness" (the Euclidean geometrical structure) of the universe.

Penrose is not satisfied with merely criticizing fashionable theories. He concludes with a new theory that he calls "conformal cyclic cosmology," in which each cosmic eon is but one of an infinite succession of such eons. What is remarkable about this proposal is not necessarily its correctness—although he does offer a few potential observational tests—but rather the fact that Penrose has the imagination, creativity, and indeed "chutzpah" to suggest an original model that is entirely outside the mainstream.

As in his previous books, Penrose's concept of what constitutes a "popular" science book is somewhat different from that of most other science writers. Accordingly, even though much of the mathematics is pushed to appendices, uninitiated readers will probably find this book challenging. Those who put in the required effort, however, will be amply rewarded by the, dare I say, "fantastic" ideas of an original thinker with an unparalleled geometrical intuition.

The reviewer is an astrophysicist and the author of Brilliant Blunders *(Simon & Schuster, New York, 2013). Email: dr.mario.livio@gmail.com*

REFERENCES

1. R. Penrose, *The Emperor's New Mind: Concerning Computers, Minds, and the Laws of Physics* (Oxford Univ. Press, Oxford, 1989)
2. R. Penrose. *The Road to Reality: A Complete Guide to the Laws of the Universe* (Knopf, New York, 2004).

10.1126/science.aah4649

PHOTO: LEE DAVY/FLICKR

MATHEMATICS

Quantifying culture

A humanist's ode to mathematics reveals how numbers underlie literature, art, and music

Living by Numbers
In Defence of Quantity
Steven Connor
Reaktion Books, 2016. 296 pp.

By **Christopher J. Phillips**

Given the near-constant drumbeat promoting the promise of "Moneyball" methods, "data-mining" algorithms, and statistical models, one might argue that there is no need to defend mathematics in the early 21st century. Yet Steven Connor's *Living by Numbers: In Defence of Quantity* opens with the assertion that the "strength and prevalence" of an "anti-numerical animus" is "remarkable." His response, in this erudite and wide-ranging book, to those who lament the expansion of numerical methods into the humanities is that they fail to realize the degree to which math has been there all along.

Connor, a faculty member in English at the University of Cambridge, is mainly out to convince mathphobic humanists that literature, art, and music have long drawn explicitly on concepts of enumeration, cardinality, pattern, and quantity. Instead of blindly resisting mathematical tools, critics would do better to understand how number has already "entered into quality." (He reminds the reader that even expressing the fear that the qualitative might be reduced to the quantitative implies the measurability of both.)

Connor also seeks to convince those who would keep numbers locked away in some ideal Platonic realm or who imbue them with magical properties that they are missing mathematics' actual presence across many fields. Connor proposes the terms "quantality" and "quantical" for this tendency to express things in terms of quantity, which he argues was present long before formal statistical tests or electronic computers were invented.

Although written for those of a humanistic bent, the book is full of delights and insights for mathematicians and nonmathematicians alike, from the surprising etymology of "precision" (derived from the Latin for "cut off") and the humor inherent in numbers (many jokes, like mathematical proofs, take "effort to show that something is exactly what it was all along") to the significance of numerosity in poetry and music.

Connor is particularly focused on the 19th and 20th centuries, when mathematics took on pride of place in modernist expression: from James Joyce's novel *Ulysses* to Roman Opałka's serial painting 1965/1-∞. His analysis of the way literature became a mass phenomenon in the 19th century—a landslide of words alongside the avalanche of numbers provided by new statistical societies—is particularly evocative. *Living by Numbers* suggests that, even as literature was setting itself against mathematics, number concepts and word concepts were becoming ever more entangled.

Numbers in Color (1958-59), by Jasper Johns

At times, the book veers toward narrative chaos. A discussion about aggregation, for example, moves from the ancient Greek philosopher Eubulides through the Old Testament and Kantian philosophy to the 20th-century poet W. B. Yeats in less than four pages. As with any provocative book, there is much to quibble about (Is rereading *Middlemarch* really like the process of intuiting the Enigma machine?), but such claims help us see our own presumptions about literature and iteration afresh.

For those out of practice at reading philosophy, the prose will seem labored at times. "Number is that to which, and through which, time moves, for time is nothing without, and so nothing but, the movement of nothing into number," reads one, admittedly nonrandom, sentence.

Curiously, Connor mentions almost nothing about the ways we learn mathematics and consequently neglects how we come to experience and express so much about the world in mathematical idioms. He also doesn't explore the mundane ways (tip calculations, grocery store purchases) most people actually use mathematics.

Number concepts appear fully realized, ready to be deployed, rather than constantly negotiated and reimagined. It would have been nice for Connor to have engaged directly with the many thoughtful accounts provided by modern practitioners, rather than stopping with the early-20th-century work of English mathematician G. H. Hardy. I suspect that there will also be some mathematicians who recoil from Connor's occasionally glib portrayal of their discipline.

Living by Numbers turns the question of whether a problem might best be approached qualitatively or quantitatively on its head, suggesting that it misses the point. Instead of asking how the humanities and arts might respond to the expansion of statistics and data sciences, Connor asserts that the important questions about life—and the historical, philosophical, and artistic ways of addressing them—have always also been about numbers.

The reviewer is in the Department of History, Carnegie Mellon University, 240 Baker Hall, 5000 Forbes Avenue, Pittsburgh, PA 15213, USA. Email: cjp1@cmu.edu

10.1126/science.aai8110

LETTERS

NEXTGEN VOICES

Applied science

In July, we asked young scientists to **"describe one skill you've honed in your science career and one way you could apply that skill outside of academia."** We received more than 100 responses. We have printed some of the most interesting skills and applications below. –*Edited by* **Jennifer Sills**

Health

EVIDENCE-BASED CRITICAL THINKING has saved me a lot of trouble. Every day we are flooded with a stream of fad diets. When tempted to embark on a new nutritional regimen, I ask myself: "Is there solid evidence supporting this extravagant diet?" and "Has there been a large sample of individuals thriving on the advised or forbidden foods?" I often discover that the fad in question fails these logical tests, leading me to conclude that the best ingredient for a healthy life is a good dose of healthy skepticism.

Dario Del Giudice

Department of Global Ecology, Carnegie Institution for Science, Stanford, CA 94305, USA. Email: ddelgiudice@carnegiescience.edu

Sports

AS A BIOINFORMATICIAN and an amateur marathon runner, I have applied my data analysis skill to building a high-performance team. For each practice session, I keep track of the pace and the completed distance of each of my team members, run computer scripts to quantify improvements, identify abnormalities early on, and adjust our training schedule accordingly. My biomedical knowledge empowers me to interpret the nuanced changes in the data, which helps me and my teammates realize our full potential without getting sports injuries.

Kun-Hsing Yu

Biomedical Informatics Program, Stanford University, Stanford, CA 94305, USA. Email: khyu@stanford.edu

AS AN ECOLOGIST, I often create graphs to clarify my thinking. I have started applying this skill to paddling. As part of a canoe racing team, I am currently learning a new technique. To enforce learning, I have been visualizing a graph of body speed vs. time (similar to an electrocardiogram) as I paddle.

William King

Department of Biology, University of Washington, Seattle, WA 98195, USA. Email: wking2@uw.edu

Friendship

MY CAREER IN science has helped me limit my use of the term "maybe," and as a result I've become a much more reliable

ILLUSTRATION: GABY D'ALESSANDRO

colleague and friend. In industrial science, being decisive is critical—even if it means killing projects. I have found that in life, as in science, sometimes it's better to say "no" because it enables you to say "yes" and actually mean it.

Laura Kingsley

Genomics Institute of the Novartis Research Foundation, San Diego, CA 92121, USA. Email: lkingsle@gnf.org

IN THE SPIRIT of science, I have realized that my critics are often the solution to my problems. As a result, I've begun asking for criticism and opinions in all aspects of life. This constructive approach to critics has helped me foster stronger interpersonal relationships.

Raffaele Fiorenza

New York Genome Center, New York, NY 10075, USA. Email: ralphie.fiorenza@gmail.com

ONE SKILL THAT I have found particularly important for effective science communication is the ability to recognize when someone does not understand me. In order to maintain an engrossed audience, one must actively seek the social cues that signal confusion or inattentiveness. This skill can also be applied in the social arena when a story you think is entertaining misses the mark.

Joseph W. Meisel

Department of Chemistry and Biochemistry, University of Missouri, Saint Louis, Saint Louis, MO 63121, USA. Email: jwm5hd@umsl.edu

Business

ONE OF THE crucial skills I have learned as a scientist is the ability to work collaboratively with researchers from diverse backgrounds. I hope to apply this skill to the business world by helping to ensure that companies are using and coordinating their human capital in the most efficient and effective ways possible.

Noah Frey Greenwald

Allston, MA 02134, USA. Email: noahfgreenwald@gmail.com

I HAVE LEARNED to create visually gripping graphs and cover art for research papers. Industries love it when statistical graphs are presented on their websites.

Shrishti Singh

Department of Biomedical Engineering, University of Bridgeport, Bridgeport, CT 06604, USA. Email: shrsingh@my.bridgeport.edu

I BELIEVE THAT project management is the most important skill that I have picked up during my career. An excellent project manager must be able to abstract an entire project into orderly and discrete tasks; prioritize them by their logistical, time, and budgetary requirements; and ensure their efficient completion. I have used my experience managing academic projects to organize the operations of a residential construction company.

Julian Spagnuolo

Institute of Fundamental Sciences, Massey University, Palmerston North, 4442, New Zealand. Email: julianspagnuolo@gmail.com

Domestic Life

FAILURE! OH ALL the failures! In science, I've learned to live for the little wins (I didn't catch fire today!) as much as the big ones (I published a thing!). I appreciate completion and a sense of control over an outcome in my home life, whether it's the cake I managed not to burn or the novel I read in a single afternoon. If you concentrate only on the publications and big life milestones, you miss too much.

Matilda Skye Newton

Department of Biochemistry, Molecular Biology, and Biophysics, University of Minnesota, St. Paul, MN 55108, USA. Email: msnewton@umn.edu

MY SCIENTIFIC CAREER has taught me endurance: seeing that specific goal and being willing to work through lunch breaks or late nights for the best possible result. For me, the real-life equivalent of this is found during spring cleaning.

Maria Winberg Olsen

Department of Biology, Copenhagen University, Kongens, Lyngby, 2800, Denmark. Email: qks199@alumni.ku.dk

Politics

THE ABILITY TO quickly look over research and determine whether it met certain basic standards for quality, objectivity, and comprehensibility was incredibly useful for sorting out dueling studies on key issues when I worked for a state legislature.

Colin Murphy

NextGen Climate America, San Francisco, CA 94104, USA. Email: persuasivescience@gmail.com

Editor's Note: NextGen Climate America is unaffiliated with Science*'s NextGen VOICES survey.*

Baking

MY KITCHEN IS my laboratory. As it turns out, pharmaceutical compounding translates well to the art of baking. Rather than triturate tablets into dust for incorporation into dermatologic creams, the mortar and pestle in my kitchen is used to grind chocolate into a fine dust and pound almonds into coarse granules for use in my creations. Not every formulation is a success, but my mistakes and masterpieces are well-documented within a meticulous, laboratory-style notebook. Instead of USP-grade pharmaceuticals and prescriptions, grocery-grade goods are combined via amateur recipes—using geometric dilution and other techniques as required. After all, cooking is chemistry.

Joseph Michael Cusimano

Columbus, OH 43220, USA. Email: joecusi@hotmail.com

Art

IF THERE IS one transferable skill you acquire while pursuing a Ph.D., it is the confidence and intellectual rigor to teach yourself how to become an expert at just about anything. I've used this newfound ability to turn my interest in time-lapse photography into real expertise through seeking out professionals and conducting a number of failed experiments.

Tyler Hulett

Molecular Microbiology and Immunology, Oregon 97213, USA and Earle A. Chiles Research Institute, Providence Cancer Center, Portland, OR 97213, USA. Email: hulett@ohsu.edu

Parenthood

THE MOST VALUABLE skill I've honed in my science career has been learning how to put creative ideas into practice. As a science educator, it enables me to motivate and engage my students, which leads to better learning outcomes. As a mother, it provides me with joy in helping my young daughter construct crazy craft projects!

Rachel Pillar

Kangaroo Island Community Education, Kingscote, SA 5223, Australia. Email: rachel.pillar@kice.sa.edu.au

I LEARNED TO cope with exhaustion, both physical and mental. This better equipped me to become a mother. Spending hours in darkness staring at a computer trying to figure out what is wrong with your R code is not so different from spending the night trying to figure out why your little one won't stop crying.

Marie-Caroline Lefort

Unitec Institute of Technology and Bio-Protection Research Centre, Auckland, 1025, New Zealand. Email: mlefort@unitec.ac.nz

Cards

I've honed my ability to spot fraud. This ability will probably come in most handy at the poker table.

Richard I. Hilleary

Department of Botany, University of Wisconsin, Madison, Madison, WI 53706, USA. Email: hilleary@wisc.edu

GENES UNDER PRESSURE

By **Laura M. Zahn** *and* **Beverly A. Purnell**

Eons of selective pressure have shaped Earth's biological life, genetically optimizing organisms to survive varied environments and exposures. This selection may establish novel genetic variants in the genomes of a population or species, including humans. For example, genetic responses to diet and altitude helped humans adapt to new climes as they exited Africa and moved across the globe. Furthermore, the influence of environment can encompass the cellular level—for example, in shaping how cells in our immune system interact with both external and internal influences to maintain our health. Recent work shows that adaptation extends beyond changes in DNA sequences. The inheritance of environmentally influenced traits can also occur through epigenetic mechanisms. Although these mechanisms assist in adapting to new or shifting environments, some genetic and epigenetic changes may have resulted in modern pathology owing to recent and rapid changes in our diets, lifestyles, and exposures.

The challenge is to understand how we can mitigate harms caused by discordant responses to our surroundings. Understanding how human genetics and epigenetics respond to the multitude of external influences should help us prevent pathology and treat disease in ourselves and future generations.

PHOTO: LI QIAN/XINHUA/ALAMY STOCK PHOTO

A smoggy day in Qingdao, China. There is interest in the extent to which environmental pressures, such as pollution, may affect human genetic and epigenetic processes.

REVIEW

Going global by adapting local: A review of recent human adaptation

Shaohua Fan,[1]* Matthew E. B. Hansen,[1]* Yancy Lo,[1,2]* Sarah A. Tishkoff[1,3]†

The spread of modern humans across the globe has led to genetic adaptations to diverse local environments. Recent developments in genomic technologies, statistical analyses, and expanded sampled populations have led to improved identification and fine-mapping of genetic variants associated with adaptations to regional living conditions and dietary practices. Ongoing efforts in sequencing genomes of indigenous populations, accompanied by the growing availability of "-omics" and ancient DNA data, promises a new era in our understanding of recent human evolution and the origins of variable traits and disease risks.

Modern humans originated ~200,000 years ago in Africa. Over the past 100,000 years, humans spread across the globe into a variety of habitats, from tropical to arctic, from high altitudes to lowlands and even to toxic environments. After humans migrated out of Africa, they encountered and interbred with archaic populations such as Neandertals and Denisovans, resulting in introgression of archaic genomes into non-African modern human genomes (~1 to 6% of modern genomes) (*1*). Introgression within Africa also likely occurred (*2*) but is more challenging to quantify because ancient DNA (aDNA) does not preserve well in that region, and no archaic African genomes are currently available. Within the past 10,000 years, most human populations have transitioned from a hunting-gathering lifestyle to practicing agriculture and pastoralism, resulting in rapid population growth, increased population densities, and an increase in infectious diseases. The selection pressures for adapting to local environments and new diets have resulted in population- or region-specific genetic variants that influence variable phenotypes (such as height, innate immune response, lactose tolerance, fatty acid metabolic efficiency, and hemoglobin levels).

Establishing a complete picture of local human adaptation can be challenging because it involves identifying the genomic regions under selection, the phenotypes that selection is acting upon, and ideally, the external conditions driving the selection. Populations that have adapted to environments that severely challenge survival provide well-characterized cases for local adaptation. Here, we review several recent examples that illustrate the use of emerging data, such as aDNA and genome-wide association studies (GWAS), and the impact these adaptations have for disease risk (Fig. 1).

[1]Department of Genetics, University of Pennsylvania, Philadelphia, PA 19104, USA. [2]Institute for Biomedical Informatics, University of Pennsylvania, Philadelphia, PA 19104, USA. [3]Department of Biology, University of Pennsylvania, Philadelphia, PA 19104, USA.
*These authors contributed equally to this work. †Corresponding author. Email: tishkoff@mail.med.upenn.edu

Adaptation to dairy consumption

The advent of cattle domestication in the Middle East and North Africa, ~10,000 years ago, lead to strong selection pressure for the ability to drink milk as adults. Variants near the *LCT* locus—coding for the lactase enzyme that metabolizes lactose, the main carbohydrate in milk—show some of the strongest signals of selection in the human genome (*3*). In most mammals and in most humans, the level of the lactase enzyme decreases after weaning [lactase nonpersistence (LNP)]. However, many populations that have traditionally practiced dairying maintain high levels of lactase into adulthood [lactase persistence (LP)].

A genetic variant associated with LP in Europeans was mapped to intron 13 of *MCM6* upstream of *LCT* (*4*). Additional variants located within 100 base pairs (bp) of the European variant were identified in African populations (*5*). The *LCT* region was repeatedly reported as a target of a recent strong selective sweep (Fig. 2A) in Europeans and Africans, on the basis of numerous statistical tests including allele frequency comparisons between global populations [fixation index (F_{ST}) analyses] and extended haplotype homozygosity tests within [extended haplotype homozygosity (EHH) and integrated haplotype score (iHS)] and across [cross-population EHH (XP-EHH)] populations (Fig. 3) (*3*, *6*, *7*). Indeed, the homozygosity of African haplotypes containing the LP-associated variants extends on average nearly 2 Mb, but only ~2000 bp in ancestral haplotypes (*5*, *8*). In vitro studies showed that these derived alleles enhance the expression of *LCT* (*5*, *9*). The European LP-associated variant is estimated to be ~9000 years old, whereas the most common East African LP variant is ~5000 years old, which is consistent with archeological evidence for cattle domestication in the Middle East and east Africa (*5*). Sequencing of aDNA indicates that the European LP-associated allele was absent in early Neolithic Central Europeans and was at low frequency in late Neolithic Europeans (*10*), suggesting that LP spread recently (within the past ~4000 years) across Europe (*11*).

The genetic adaptations resulting in LP are examples of convergent evolution in modern humans (causative genetic variants arose independently in geographically diverse populations owing to strong selective pressure for an adaptive phenotype). However, the identified LP-associated variants do not entirely explain the LP phenotype, particularly in western Africans and some central and southern Asian pastoralist populations. For example, the Fulani populations from Nigeria and Cameroon have the European variant at moderate frequency but lack the eastern African LP-associated variants and have a distinct haplotype with extended homozygosity near *LCT*, suggesting the presence of additional unknown functional variants (*8*). Furthermore, an outstanding question is the role that the human gut microbiome plays in LP.

Adaptation to an arctic environment

The Inuit populations in Alaska, Canada, and Greenland have adapted to a cold and dark Arctic environment and a marine diet rich in omega-3 polyunsaturated fatty acids. A recent study compared genomic diversity in Greenlandic Inuits with Europeans and Chinese using the population branch statistic (PBS) (Fig. 3B, iii) (*12*) and found that the most differentiated region encompasses a gene cluster that codes for fatty acid desaturase enzymes (FADS), which are important modulators of fatty acid composition. Two variants in the FADS region were significantly associated with short stature in the Inuits, possibly because of the influence of fatty acid composition on growth hormone regulation (*12*). These variants were also associated with height in a larger study of Europeans, but the variants were present at low frequencies and would have been hard to discover without studying the Inuit population, demonstrating why studies of indigenous populations can be informative for identifying variants of functional importance across ethnic groups (*13*).

Adaptation to tropical rainforests

Tropical rainforests are some of the harshest environments in the world, characterized by high temperature and humidity as well as the prevalence of parasites and other pathogens. Individuals living in tropical environments often have very short life spans, which directly affects reproductive success and, hence, can act as a selective pressure.

Short stature

One distinctive phenotype thought to be adaptive to a tropical rainforest environment is short stature (commonly referred to as a "pygmy" phenotype), which is defined as an average height of <150 cm in adult males. The short stature trait is an example of convergent evolution in rainforest hunter-gatherer (RFHG) populations across Africa, Asia, and South America. Selection for small body size may be due to limited food resources, resistance to heat stress, immune response, and/or

a trade-off between early onset of reproduction and cessation of growth (*14*, *15*). Perturbations in the GH1-IGF1 pathway have been implicated to play a role in short stature in RFHG populations in central Africa and southeast Asia (*16*).

In central African RFHG populations where admixture with neighboring populations is common, short stature is significantly correlated with ancestry and is highly heritable (*14*). Central African RFHG–specific genomic adaptations were identified through comparisons with other African populations by using methods such as locus-specific branch length (LSBL) (*17*) and XP-EHH (*3*) tests, which have high power to detect population-specific positive selection (Fig. 3B). These tests identified a 15-Mb region on chromosome 3 that shows signatures of strong positive selection (*14*). Several genes in this region are associated with short stature in Pygmies, including *DOCK3*, which is associated with height variation in non-Africans, and *CISH*, which is important in immune response but also inhibits human growth hormone receptor activity, indicating that short stature could be a product of selection acting on pleiotropic loci (*14*). A subsequent study discovered a ~200-kb haplotype containing *HESX1* at high frequency in central African RFHGs but low frequency in other African populations; *HESX1* is involved in the development of the anterior pituitary, where growth hormone is produced (*18*). This haplotype was not tagged in previous genotyping arrays, demonstrating the importance of including ethnically diverse populations in whole-genome sequencing studies (*18*). However, RFHG and neighboring agriculturalist populations in Uganda exhibit a distinct set of loci associated with short stature, which raises the possibility of convergent evolution of this trait across the RFHGs in Africa (*15*).

The studies discussed above suggest that short stature in central African RFHG is mostly driven by strong selection affecting a relatively small number of loci of moderate to strong effect. In contrast, hundreds of loci are associated with European height variation (*19*, *20*). Detecting selection on a polygenic trait such as height is difficult because the causative variants can be ancient polymorphisms each of relatively small effect. Several recent methods use GWAS to identify trait-associated variants then test for allele frequency shifts between populations [either unweighted (*20*) or weighted by effect size (*21*)] greater than expected from neutral drift. Polygenic selection tests using GWAS data (Fig. 2C) have suggested weak selection influencing average height differences among European populations, with Northern Europeans generally being taller than Southern Europeans (*20*, *21*). A recent aDNA analysis of Neolithic European populations suggests that the North-South European height gradient may reflect selection for shorter height in Early Neolithic migrants into southern Europe and admixture of taller steppe populations with northern Europeans (*11*). Although analysis of aDNA holds great promise for revealing human phenotypic history, this approach faces challenges for studies of indigenous populations such as RFHG because DNA is not well-preserved in tropical climates, and large-scale GWAS are not available.

Adaptation to endemic pathogens

Pathogenic environments are an important driver of local adaptation in humans (*22*), and nowhere is the challenge of survival from pathogens greater than in tropical rainforests. In particular, malaria, a mosquito-borne protozoan parasitic infection, is a major cause of mortality in sub-Saharan Africa. The most lethal malarial species, *Plasmodium falciparum*, causes >1 million child deaths in Africa each year (*23*). Tropical populations have long been known to have genetic variants that confer resistance to malaria, including the sickle cell, α^+- and β^+-thalassemia–causing alleles at the hemoglobin loci, as well as variants at *ABO*, *GYPA*, *GYPB*, *GYPE*, and *G6PD* [reviewed in (*23*)]. These variants are likely adaptive, as initially evidenced by the strong correlation between allele frequency and prevalence of malaria infection. However,

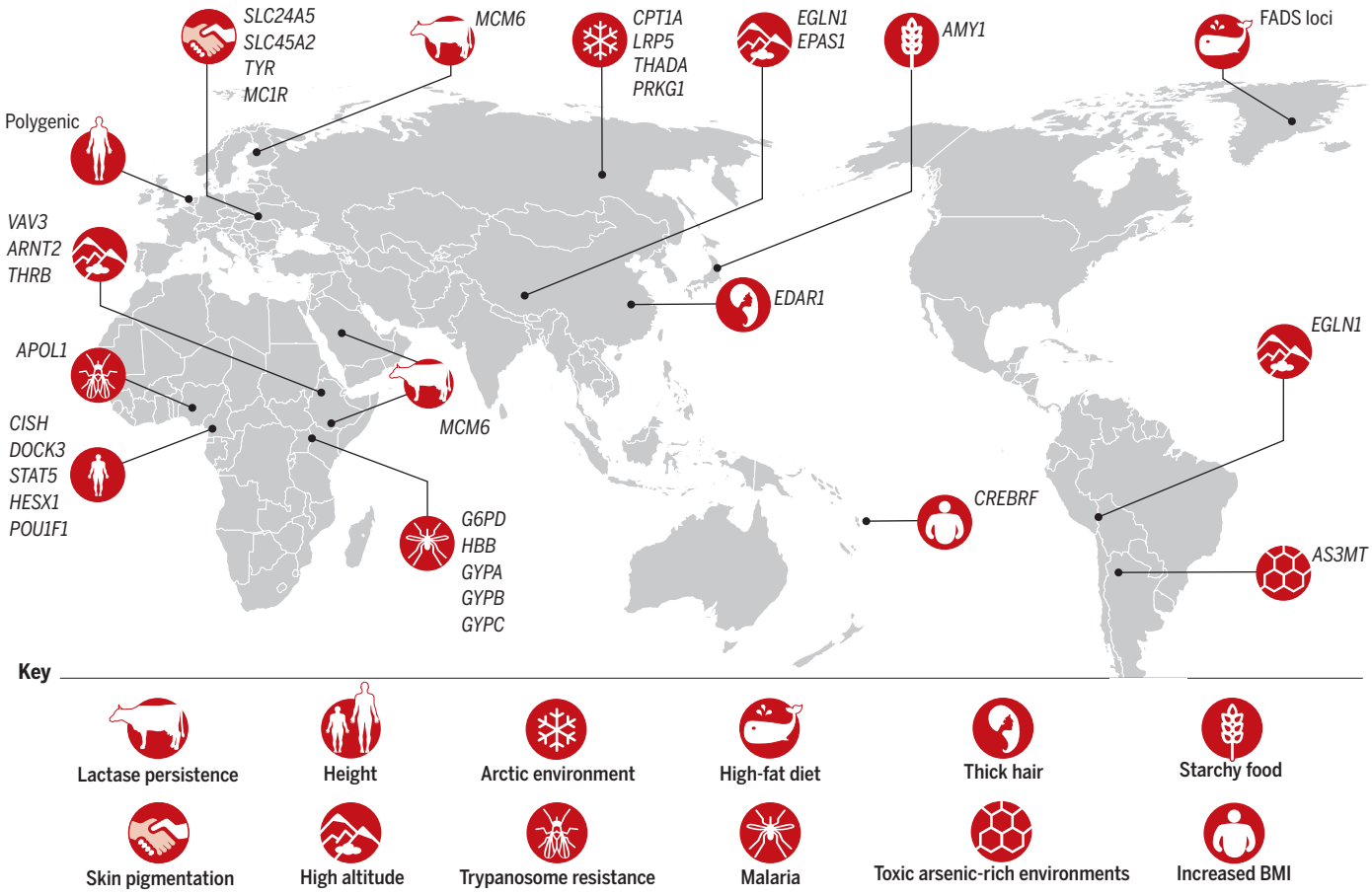

Fig. 1. Examples of human local adaptations, each labeled by the phenotype and/or selection pressure, and the genetic loci under selection. [Adapted from (*13*)]

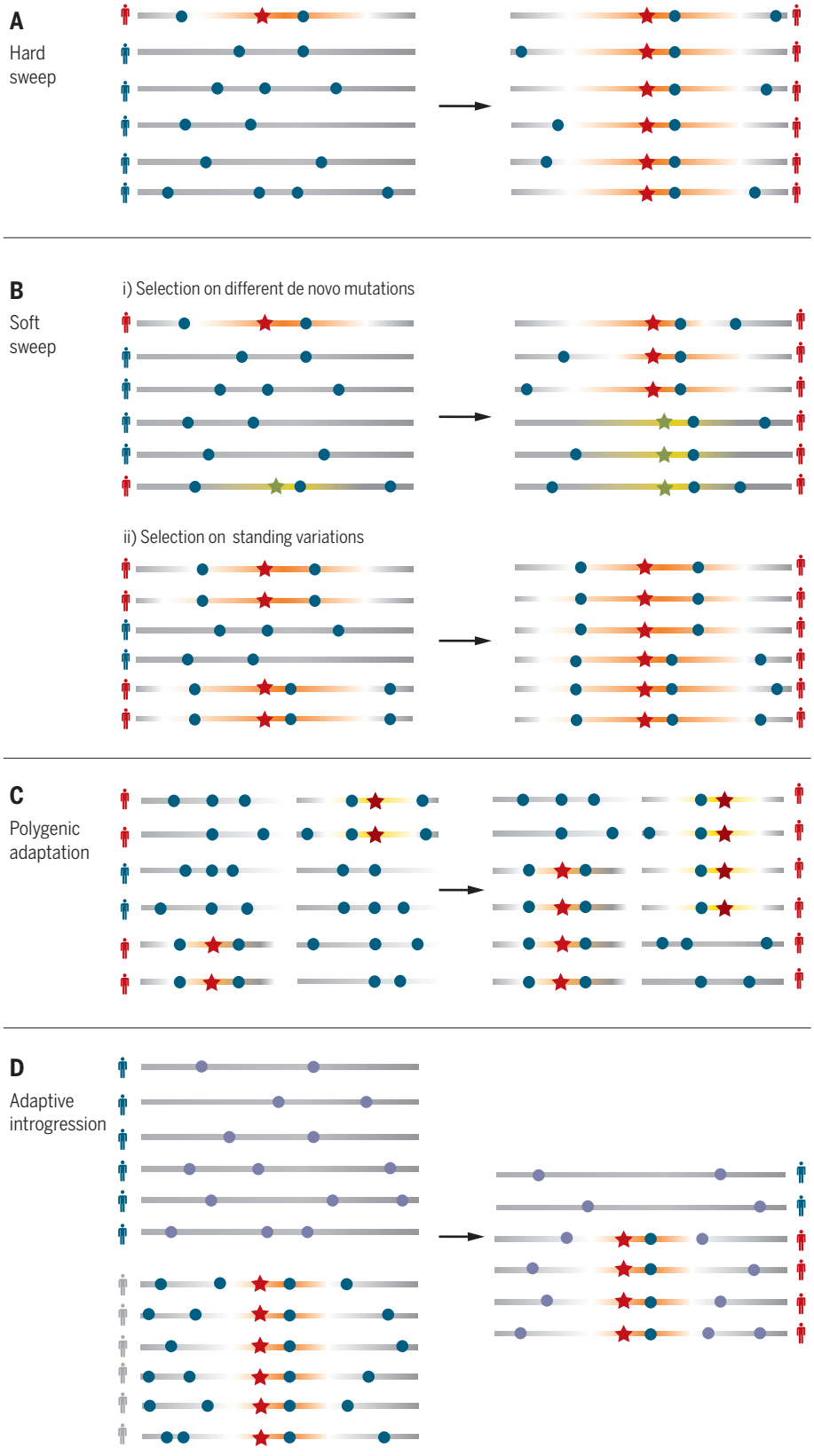

Fig. 2. Genomic signatures of local adaptation. (**A**) A hard sweep. (**B**) A soft sweep acting on (i) multiple de novo beneficial mutations and (ii) standing variation. (**C**) Polygenic adaptation. (**D**) Adaptive introgression. Each horizontal bar represents a haplotype (a sequence of genetic variants on the same chromosome). The orange segment is graded to indicate the strength of linkage disequilibrium between beneficial (stars) and neutral (dots) variants.

several malaria-protective variants also cause common Mendelian diseases in hemi- or homozygotes [such as sickle cell anemia, *G6PD* deficiency, and thalassemia (*23*)] and are maintained through balancing selection.

Another example of adaptation to pathogens resulting in high frequencies of genetic variants associated with disease is at the *APOL1* locus. The "G1" and "G2" genetic variants in the last exon of *APOL1* are associated with chronic kidney disease, which is disproportionately common among individuals of African descent (*24*). These variants also confer resistance to human African trypanosomes (causing "African sleeping sickness") by modifying the protein to lyse *Trypanosoma brucei rhodesiense*, a parasitic protozoa transmitted by the tsetse fly. The region flanking the G1 and G2 variants appear to be under recent positive selection, as indicated by extended haplotype homozygosity (*25*). G1 and G2 are common in some western African populations, but *T.b. rhodesiense* is currently common only in eastern and southern Africa, which raises questions about the evolutionary history of the *APOL1* locus and the pleiotropic effects of G1 and G2 (*25*).

Adaptation to high altitude

Living at high altitude (>2500 m above sea level) in regions such as the Tibetan Plateau, the Andean Altiplano, and the Semien plateau of Ethiopia can be deadly because of an insufficient supply of oxygen to vital organs (hypoxia). However, populations living in these high-altitude regions for thousands of years have adapted and thrived, with varying physiological adaptations to hypoxic environments [reviewed in (*26*)].

Recent genome-wide scans of selection (such as LSBL, PBS, iHS, and XP-EHH) (Fig. 3B) uncovered genetic adaptations to high altitude by comparing Andean, Ethiopian, and Tibetan genomes with lowland populations with similar genetic ancestry [reviewed in (*27*)]. Signatures of positive selection were found repeatedly at genes involved in the hypoxia-inducible factor (HIF) pathway [reviewed in (*28*)] but on different haplotype backgrounds (for example, *EGLN1* in Andean and Tibetan populations) owing to convergent evolution (*29*). One of the strongest signals of selection in the Tibetan populations is at *EPAS1*, a transcription factor influencing the HIF pathway. Sequence analysis suggests that the selected Tibetan haplotype may have originated from introgression of genomic DNA from Denisovans (Fig. 2D) (*30*).

Adaptation to toxic environments

Arsenic is acutely toxic to humans but is naturally present at high levels in groundwater across the globe (*31*). San Antonio de los Cobres (SAC), Argentina, is one such locale with high levels of arsenic yet has been settled by human populations for the past ~11,000 years. Arsenic metabolism involves methylating inorganic arsenic to monomethylarsonic acid (MMA) and subsequently to dimethylarsinic acid (DMA), which is less toxic. The fraction of arsenic metabolites (%DMA/%MMA) in urine indicates the efficiency of arsenic metabolism. Individuals in SAC show particularly

low urinary excretion of MMA, suggesting a local adaptation to arsenic. A recent association study in SAC identified potential protective regulatory variants upstream of *AS3MT*, a gene involved in the arsenic methylation pathway. The variants are likely under positive selection because they are embedded in long haplotypes in the SAC population and are at higher frequency than in neighboring low-arsenic groups with similar genetic ancestry (*31*).

Adaptation to ultraviolet exposure

Variation in human skin color is one of the most striking examples of human phenotypic diversity. Unlike other primates, human skin is not covered by dense body hair and is the primary interface between our body and the environment. Ultraviolet radiation (UVR) exposure is an important driver of pigmentation evolution in humans, with selection pressure for darker skin at low latitudes for UVR protection and for lighter skin at higher latitudes, possibly to maintain vitamin D photosynthesis (*32*).

The earliest studies of the genetics of human pigmentation were based on candidate genes identified in model organisms and highly penetrant genetic variants of Mendelian disorders [for example, *SLC24A5* in zebrafish color patterns, *MC1R* in mouse coat colors, and *OCA1-4* in human oculocutaneous albinism (*33*)]. GWAS in European populations have included additional candidate loci associated with light skin, a subset of which (such as *OCA2*, *TYRP1*, *TYR*, *SLC24A5*, and *SLC45A2*) are under strong selection, as evidenced by multiple genome-wide scans of selection [reviewed in (*33*)]. Furthermore, a recent analysis of 230 ancient Eurasian genomes found that the allele associated with light skin pigmentation has likely reached fixation in modern Europeans from very low frequency during the Neolithic period due to strong selection pressure over the past ~4000 years (*11*).

Although many genetic variants associated with European light skin color are identified, little is known about the genetic basis of skin color in Asia and Africa. Indeed, Africans exhibit high variability in skin color (ranging from dark-skinned Nilotic pastoralists to light-skinned San hunter-gatherers), and the genetic basis of pigmentation in these populations has just recently begun to be explored (*34*).

Impact of local adaptation on common complex diseases

Genetic variants that were adaptive in the past can be maladaptive in modern environments. For example, the high prevalence of type 2 diabetes was proposed to be due to common variants that were adaptive for the efficient conversion of food into energy in the past when resources were scarce, but are maladaptive in modern urban environments (the "thrifty gene hypothesis"). This hypothesis remains controversial; an alternative hypothesis is that the disease-associated variants were never beneficial but became common through genetic drift (the "drifty gene hypothesis") (*35*).

A recent study of Samoans provides functional evidence supporting the thrifty gene hypothesis. Over 80% of Samoans are overweight or obese [body mass index (BMI) > 26 kg/m^2], which is among the highest prevalence in the world (*36*). By genotyping ~3000 Samoans, a missense variant in *CREBRF* was found to be associated with BMI and fasting glucose levels. This variant is under strong recent positive selection, as evidenced by extended haplotype homozygosity and high allele frequency in the Samoan population but not other populations. Functional expression experiments in adipose cells showed that the Samoan variant decreases energy use and increases adipose fat storage, suggesting that this variant may have been adaptive in the past by increasing tolerance to periods of starvation but is associated with risk for obesity and type 2 diabetes in modern populations.

Future directions

Unearthing human adaptation with aDNA

aDNA sequencing provides a direct historical record of genomic variation and provides new possibilities for inferring recent human evolutionary history of modern phenotypes. Studies based on comparison of modern human with Neandertal and Denisovan genomes have found evidence of adaptive archaic haplotypes in genes related to innate immune response, metabolism, and skin phenotypes in ethnically diverse modern human populations [reviewed in (*1*)]. Future studies of aDNA will be informative for reconstructing the origin of functional variants and inferring the strength of selection based on direct observation of changes in allele frequencies over time (*37*). However, current understanding of ancient adaptation events is limited by sparse aDNA data over broad geographic and temporal scales. Moreover, methods for studying ancient genotype variation tend to focus on ascertained variants in specific populations, particularly Europeans (*1*).

Adaptive potential of structural variation

Structural variants (SVs)—including duplications, copy number variants, deletions, insertions, and inversions—encompass a much larger fraction of the genome than single-nucleotide polymorphisms (SNPs) [~4.1 million to 5.0 million base pairs for SNPs compared with ~20 million base pairs for SVs (*38*)] and may consequently have substantial contributions to human adaptive evolution (*39*). For example, Perry *et al.* (*40*) observed higher copy numbers of *AMY1*, an enzyme that breaks down starches, in populations with high-starch diets. Further, a common inversion polymorphism at chromosome 17q21.31 is hypothesized to be under positive selection in Europeans because of increased fecundity of women carrying the inverted haplotype (*41*). However, SVs are extremely challenging to detect by using short-read sequencing technologies. The development of cost-effective high-throughput methods for obtaining long-sequence reads and novel computational approaches will facilitate identification and characterization of SVs in the future (*42*).

Challenges to detecting selection

Although numerous methods for detecting selection have been developed, there is a known lack of concordance across methods (*43*), partly because of the different selection time scales each method is capable of detecting (*44*). Strong positive selection on a de novo (newly arising) mutation is the classic process that many methods have been devised to detect, in which the haplotype containing the beneficial variant rapidly rises in frequency in the population, resulting in long stretches of identical haplotypes around the selected variant within the population (Figs. 2 and 3). There is some debate over the fraction of the human genome affected by selective sweeps within the past ~250,000 years, in part owing to complexities in accounting for background selection that purges deleterious genetic variation (*45*, *46*) and the difficulty in detecting simultaneous selection on multiple beneficial haplotypes at a locus ("soft sweeps") (Fig. 2B) (*47*). Although recent methods have increased the power to scan for soft sweeps (*48*, *49*), their detection is still limited because of relatively weak genomic signals (*50*) and because regions flanking a hard sweep (the "shoulders") can mimic a soft sweep (*51*, *52*). Development of machine-learning methods, which can effectively "learn" the appropriate signals within complex data when given training examples, may be effective for detecting hard and soft selective sweeps (*53*).

Perhaps the largest challenge to detecting selection is the fact that most traits are polygenic. It is difficult to distinguish small frequency shifts over large numbers of independent loci (Fig. 2C) from neutral drift without knowing a priori which trait is under selection and the genetic variants that influence the trait. Incorporating the results of GWAS into selection tests (*20*, *21*) is one promising avenue to identify cases of polygenic adaptation, although such integration will have to overcome issues common to genetic association tests, including ascertainment bias in the set of genotyped variants, population stratification, and a lack of observed heritability ("missing heritability").

Integration of genetic, phenotypic, and functional data into adaptation studies

The best-characterized human adaptive variants are those related to Mendelian, or near Mendelian, traits for which the adaptive phenotype can be easily distinguished (for example, LP and skin pigmentation). Characterizing the functional variants that affect nonobvious or intermediate phenotypes—such as blood metabolite levels, gene expression across cell types, and epigenetic modifications—motivates the need for detailed phenotyping of global populations based on "-omics" profiling (such as transcriptomics, metabolomics, or epigenomics). Additionally, integration of genome-wide selection scans with GWAS helps improve the power of genotype-phenotype association analyses by localizing putative regions with a functional impact. This is particularly important in studies of indigenous populations, in which obtaining large sample sizes is challenging. Lastly, functional experiments in model organisms can directly establish the link between candidate adaptive variants and phenotypes. For example, a derived allele at the *EDAR* locus (EDAR370A) is significantly associated with hair thickness and dental morphology [reviewed in (*27*)] and is a target of

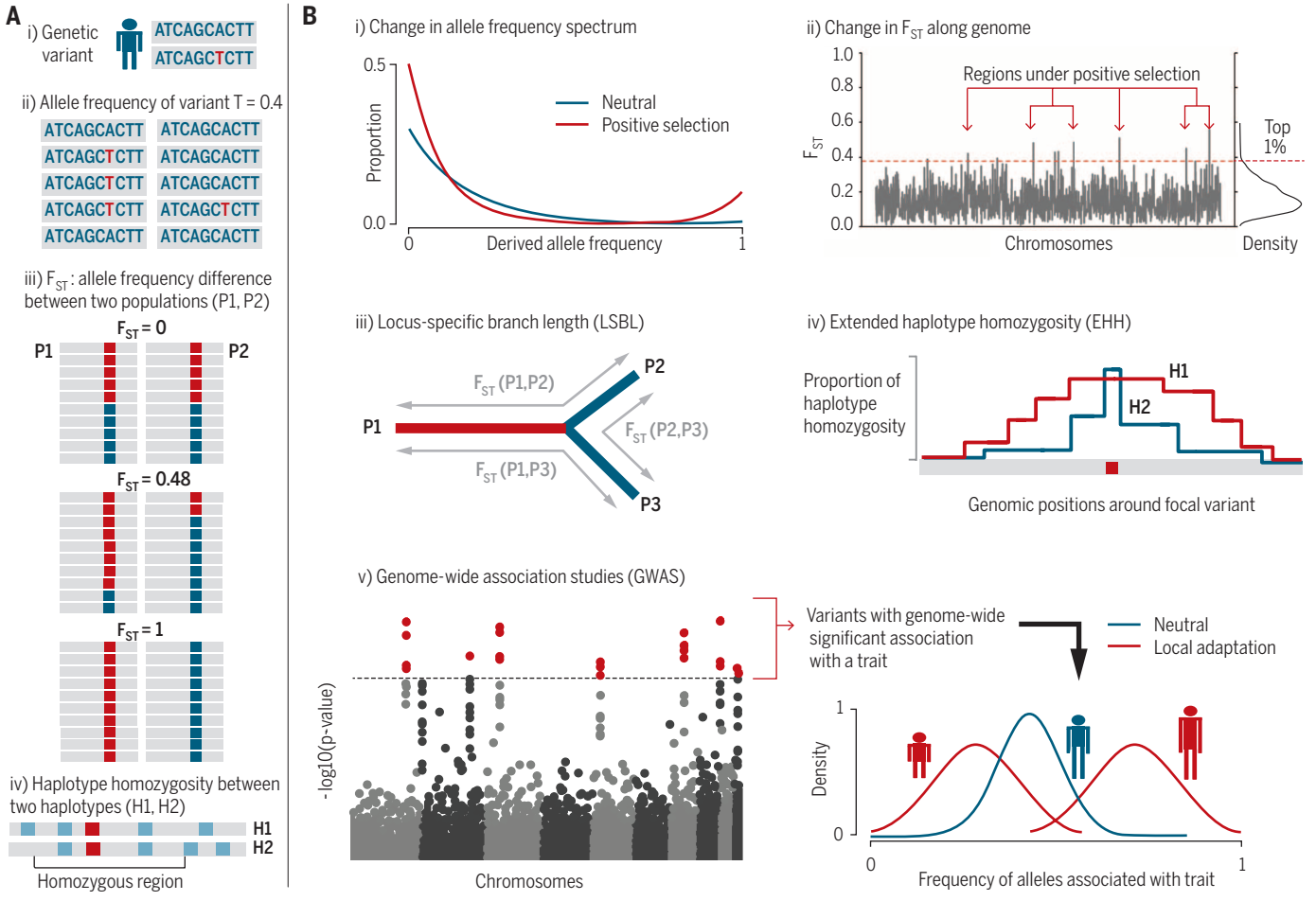

Fig. 3. Illustrations of basic concepts of population genetics and methods for detecting recent positive selection. (**A**) Population genetics terminology. (i) A genetic variant (A/T, red) on the diploid chromosomes of an individual. (ii) The allele frequency of a variant in a population is the fraction of chromosomes containing the variant. In this case, allele frequency of variant T (red) = 0.4. (iii) F_{ST} measures proportion of genetic differentiation between populations. F_{ST} = 0 means the two populations have equal allele frequencies. F_{ST} = 1 means the two populations are completely differentiated. (iv) Haplotype homozygosity is the shared stretches of variants between pairs of sampled haplotypes, typically measured around a focal variant (red square) and extending out to flanking variants (light blue). (**B**) Means of detecting positive selection. (i) Changes in the allele frequency spectrum. Positive selection (red) drives the alleles under selection and the hitchhiking alleles to high frequencies; at the same time, new mutations arise, creating an excess of rare alleles. (ii) F_{ST} along the genome. High F_{ST} values indicate loci enriched for targets of selection, with a cutoff (red dashed line) arbitrarily set to be the top 1%. (iii) LSBL, which quantifies branch lengths of a phylogenetic tree with three or more populations by using pairwise F_{ST} (*17*). At a locus, long branch length for one population (red) indicates a population-specific divergence. A similar statistic is the PBS. (iv) Haplotype homozygosity statistics [extended haplotype homozygosity (EHH) and integrated haplotype score (iHS)]. Overabundance of a long haplotype (H1, red) surrounding a focal variant indicates positive selection at the locus. The EHH statistic has also been extended to identify population-specific selective sweeps through cross-population comparisons (XP-EHH). (v) Results from GWAS, which identify genetic variants significantly associated with a specific trait (such as height), indicated by red dots on the Manhattan plot (left). Shifts in the frequency distribution of alleles associated with the trait (right) in specific populations (red) compared with the expectation under neutrality (blue) indicates that the trait is under selection. [Part of Fig. 3B is adapted from (*27*)]

recent strong positive selection in Asian populations (*3*, *54*). Development of humanized mice containing EDAR370A replicated the hair thickness phenotype and also identified previously unknown phenotypic impact on mammary and eccrine glands (*55*). With the development of in vitro and in vivo technologies, such as tissue-specific cell lines, genome/RNA-editing (such as CRISPR technology), and induced pluripotent stem cells, it is increasingly possible to validate the function of adaptive variants in humans.

Conclusions

Selection pressures in response to regional conditions have influenced global human genomic diversity, as evidenced by the reviewed local adaptations to diverse physical environments, pathogen exposure, and dietary practices. None of these insights would be possible without global genome-wide population genetic data collected over the past 15 years. New insights into local human adaptation will require high-coverage whole-genome sequencing of ethnically diverse populations and detailed phenotyping. Extending current GWAS-based methods to detect polygenic adaptation in order to include more accurate models of genetic architecture that take into account nonadditive, epistatic, and gene-environment effects is an important future direction. The integration of high-quality genomic data from ancient and modern populations, detailed phenotype data, and advances in computational approaches will illuminate the mode and tempo of local adaptation as humans settled the globe.

REFERENCES AND NOTES

1. F. Racimo, S. Sankararaman, R. Nielsen, E. Huerta-Sánchez, *Nat. Rev. Genet.* **16**, 359–371 (2015).
2. P. Hsieh *et al.*, *Genome Res.* **26**, 291–300 (2016).
3. P. C. Sabeti *et al.*, *Nature* **449**, 913–918 (2007).
4. N. S. Enattah *et al.*, *Nat. Genet.* **30**, 233–237 (2002).
5. S. A. Tishkoff *et al.*, *Nat. Genet.* **39**, 31–40 (2007).
6. B. F. Voight, S. Kudaravalli, X. Wen, J. K. Pritchard, *PLOS Biol.* **4**, e72 (2006).
7. S. H. Williamson *et al.*, *PLOS Genet.* **3**, e90 (2007).

8. A. Ranciaro *et al.*, *Am. J. Hum. Genet.* **94**, 496–510 (2014).
9. N. S. Enattah *et al.*, *Am. J. Hum. Genet.* **82**, 57–72 (2008).
10. T. S. Plantinga *et al.*, *Eur. J. Hum. Genet.* **20**, 778–782 (2012).
11. I. Mathieson *et al.*, *Nature* **528**, 499–503 (2015).
12. M. Fumagalli *et al.*, *Science* **349**, 1343–1347 (2015).
13. S. Tishkoff, *Science* **349**, 1282–1283 (2015).
14. J. P. Jarvis *et al.*, *PLOS Genet.* **8**, e1002641 (2012).
15. G. H. Perry *et al.*, *Proc. Natl. Acad. Sci. U.S.A.* **111**, E3596–E3603 (2014).
16. G. H. Perry, N. J. Dominy, *Trends Ecol. Evol.* **24**, 218–225 (2009).
17. M. D. Shriver *et al.*, *Hum. Genomics* **1**, 274–286 (2004).
18. J. Lachance *et al.*, *Cell* **150**, 457–469 (2012).
19. H. Lango Allen *et al.*, *Nature* **467**, 832–838 (2010).
20. M. C. Turchin *et al.*, *Nat. Genet.* **44**, 1015–1019 (2012).
21. J. J. Berg, G. Coop, *PLOS Genet.* **10**, e1004412 (2014).
22. M. Fumagalli *et al.*, *PLOS Genet.* **7**, e1002355 (2011).
23. D. P. Kwiatkowski, *Am. J. Hum. Genet.* **77**, 171–192 (2005).
24. G. Genovese *et al.*, *Science* **329**, 841–845 (2010).
25. W.-Y. Ko *et al.*, *Am. J. Hum. Genet.* **93**, 54–66 (2013).
26. C. M. Beall, *Integr. Comp. Biol.* **46**, 18–24 (2006).
27. J. Lachance, S. A. Tishkoff, *Annu. Rev. Ecol. Evol. Syst.* **44**, 123–143 (2013).
28. A. W. Bigham, F. S. Lee, *Genes Dev.* **28**, 2189–2204 (2014).
29. A. Bigham *et al.*, *PLOS Genet.* **6**, e1001116 (2010).
30. E. Huerta-Sánchez *et al.*, *Nature* **512**, 194–197 (2014).
31. C. M. Schlebusch *et al.*, *Mol. Biol. Evol.* **32**, 1544–1555 (2015).
32. N. G. Jablonski, G. Chaplin, *Proc. Natl. Acad. Sci. U.S.A.* **107** (suppl. 2), 8962–8968 (2010).
33. R. A. Sturm, D. L. Duffy, *Genome Biol.* **13**, 248 (2012).
34. S. Beleza *et al.*, *PLOS Genet.* **9**, e1003372 (2013).
35. J. R. Speakman, *Annu. Rev. Nutr.* **33**, 289–317 (2013).
36. R. L. Minster *et al.*, *Nat. Genet.* **48**, 1049–1054 (2016).
37. J. K. Pickrell, D. Reich, *Trends Genet.* **30**, 377–389 (2014).
38. A. Auton *et al.*, *Nature* **526**, 68–74 (2015).
39. D. W. Radke, C. Lee, *Brief. Funct. Genomics* **14**, 358–368 (2015).
40. G. H. Perry *et al.*, *Nat. Genet.* **39**, 1256–1260 (2007).
41. H. Stefansson *et al.*, *Nat. Genet.* **37**, 129–137 (2005).
42. M. Pendleton *et al.*, *Nat. Methods* **12**, 780–786 (2015).
43. J. M. Akey, *Genome Res.* **19**, 711–722 (2009).
44. P. C. Sabeti *et al.*, *Science* **312**, 1614–1620 (2006).
45. R. D. Hernandez *et al.*, *Science* **331**, 920–924 (2011).
46. D. Enard, P. W. Messer, D. A. Petrov, *Genome Res.* **24**, 885–895 (2014).
47. P. W. Messer, D. A. Petrov, *Trends Ecol. Evol.* **28**, 659–669 (2013).
48. J. J. Berg, G. Coop, *Genetics* **201**, 707–725 (2015).
49. B. A. Wilson, D. A. Petrov, P. W. Messer, *Genetics* **198**, 669–684 (2014).
50. J. K. Pritchard, J. K. Pickrell, G. Coop, *Curr. Biol.* **20**, R208–R215 (2010).
51. D. R. Schrider, F. K. Mendes, M. W. Hahn, A. D. Kern, *Genetics* **200**, 267–284 (2015).
52. J. D. Jensen, *Nat. Commun.* **5**, 5281 (2014).
53. D. R. Schrider, A. D. Kern, *PLOS Genet.* **12**, e1005928 (2016).
54. S. R. Grossman *et al.*, *Science* **327**, 883–886 (2010).
55. Y. G. Kamberov *et al.*, *Cell* **152**, 691–702 (2013).

ACKNOWLEDGMENTS

We thank M. Rubel for her assistance with creating Fig. 1 in this manuscript and members of the Tishkoff laboratory for helpful scientific discussions. This work is funded by NIH grants 1R01DK104339-01 and 1R01GM113657-01 and NSF grant BCS-1317217 to S.A.T., NIH grant T32ES019851-02 to M.E.B.H. through the Center of Excellence in Environmental Toxicology at the University of Pennsylvania, and NIH grants LM009012 and LM010098 to Y.L. through J. H. Moore.

10.1126/science.aaf5098

REVIEW

Transgenerational inheritance: Models and mechanisms of non–DNA sequence–based inheritance

Eric A. Miska[1,2] and Anne C. Ferguson-Smith[1]*

Heritability has traditionally been thought to be a characteristic feature of the genetic material of an organism—notably, its DNA. However, it is now clear that inheritance not based on DNA sequence exists in multiple organisms, with examples found in microbes, plants, and invertebrate and vertebrate animals. In mammals, the molecular mechanisms have been challenging to elucidate, in part due to difficulties in designing robust models and approaches. Here we review some of the evidence, concepts, and potential mechanisms of non–DNA sequence–based transgenerational inheritance. We highlight model systems and discuss whether phenotypes are replicated or reconstructed over successive generations, as well as whether mechanisms operate at transcriptional and/or posttranscriptional levels. Finally, we explore the short- and long-term implications of non–DNA sequence–based inheritance. Understanding the effects of non–DNA sequence–based mechanisms is key to a full appreciation of heritability in health and disease.

Advances in molecular biology in the second half of the 20th century firmly established DNA sequence as the molecular substrate of inheritance (*1*). DNA seems to satisfy the requirements of both Darwin and Wallace's evolutionary theory and Mendel's laws of inheritance, now unified in the "modern synthesis," as put forward by Huxley (*2*). DNA provides a substrate for random variation—for example, through mutation during replication. In the view of modern synthesis, biological forms or phenotypes interact with the environment and are the subject of natural selection, but the heritable substance or genotype is not. This strict separation of genotype from phenotype also led to the rejection of the inheritance of acquired traits. This was first formalized by Weismann in the germ-plasm theory (*3*) and is often also referred to as the "Weismann barrier." The idea of the Weismann barrier is that the information flow from genotype to phenotype is strictly irreversible. This places the germline on a pedestal, responsible for all inheritance devoid of influence from somatic cells. Today, genetics is usually and appropriately equated with DNA sequence–based mechanisms. Yet, it appears that biology is much richer: Many phenomena and mechanisms of nongenetic and/or non–DNA sequence–based inheritance have been described in a range of model organisms, challenging our perception of the well-established relationship between transmitted genotype and phenotype. How can we learn more about the mechanism and effects of this extended type of inheritance?

[1]Department of Genetics, University of Cambridge, Downing Street, Cambridge CB2 3EH, UK. [2]Gurdon Institute, University of Cambridge, Tennis Court Road, Cambridge CB2 1QN, UK.
***Corresponding author. Email: afsmith@mole.bio.cam.ac.uk**

What is the evidence for nongenetic or non–DNA sequence–based inheritance? Look beyond humans!

Given that DNA is the major substrate of inheritance, convincing evidence for inheritance that is not based on DNA sequence often emerges where genomic DNA can easily be experimentally controlled. This is the case for species that are parthenogenetic, self-fertilizing (hermaphroditic), or isogenic, as is the case for many laboratory model organisms. Even when genetics can be controlled, other caveats need to be considered: These include changes in the environment such as parental nurturing (*4*); microbiome; and, in mammals, milk (*5*) or even cultural influences. For example, in mice, maternal nurturing can have profound effects on phenotype (*6*). Finally, a useful distinction is often made between intergenerational and transgenerational inheritance. In the former, the environment of the parent can directly affect germ cells of the offspring. For the latter, in the case of mammals, a true transgenerational effect can be defined if transmitted to the F_3 and possibly future generations, arising

"...a complete understanding of non-DNA sequence-based heritable effects requires a number of components, and we do not currently have the complete picture for any natural example."

from a germline in the F_2 generation that has not been exposed (*7*, *8*). Examples of non–DNA sequence–based inheritance and/or the inheritance of acquired traits have recently been reviewed elsewhere (*7*–*11*) and span many diverse organisms. For instance, in plants, a naturally occurring mutant of *Linaria vulgaris* (toad flax) that was originally described by Linnaeus more than 250 years ago and dramatically alters the flower shape (Fig. 1) was found to be due to the methylation state of the *Lcyc* gene and did not involve alteration of the DNA sequence (*12*). In yeast, prions are a natural and common mechanism for the inheritance of traits independent of DNA (*13*). In the ciliate *Tetrahymena*, swimming behaviors in isogenic populations are dependent on the environment and are heritable (*14*). In animals, such as the nematode *Caenorhabditis elegans*, the RNA interference (RNAi) pathway results in non–DNA sequence–based heritable changes (*15*–*17*), genetic manipulation can result in multigenerational phenotypic variation that is independent of DNA sequence (*18*–*23*), and environmental perturbation can result in heritable phenotypic changes (*8*, *24*–*26*). In mice, a number of different types of nongenetic intergenerational or transgenerational inheritance have been observed, as reviewed in detail elsewhere (*8*, *9*, *11*, *27*, *28*). For example, genomic imprinting (as discovered in mice by Surani and Solter) results in the expression of genes being dependent on their parental origin, a process regulated by epigenetic mechanisms (*29*). In addition, specific loci show variable and heritable nongenetic changes in expression, such as at the Agouti viable yellow (*Avy*) locus affecting coat color and metabolic outcome, caused by the insertion of a transposable element, an endogenous retrovirus, providing a variably DNA methylated ectopic promoter for *agouti* (*30*). A number of such heritable effects, including at *Avy*, can be modulated by environmental influences. When considering environmentally induced effects, a particular emphasis has been put on nutrition and stress as inducers of nongenetic effects. For example, parental diet can affect the phenotype of the offspring (*27*, *31*–*34*), as shown in one recent study exploring metabolic outcomes in both male and female mice born to parents that consumed a high-fat diet (*33*). Early life stress is another example for which several rodent models have been reported (*35*–*37*). An emphasis on nutritional models in mice might be the consequence of evocative epidemiological studies in humans that suggest maternal and paternal inheritance of nutritional states (*38*, *39*). Although in most of the examples mentioned above the mechanisms of inheritance are unlikely to be DNA sequence–based, with varying strength of evidence, the mode(s) of transmission of nongenetic effects remain to be discovered.

"Many phenomena and mechanisms of nongenetic and/or non-DNA sequence-based inheritance have been described in a range of model organisms, challenging our perception of the well-established relationship between transmitted genotype and phenotype."

How to reconsider the concept of inheritance without the restriction of the DNA model—Replication or reconstruction?

The semiconservative mechanism of DNA replication (*40*) provides a clear paradigm of how genetic information is faithfully transmitted during each cell division in mitosis and meiosis. This paradigm is so powerful that great emphasis has been placed on replicative inheritance of other information. Due to the well-understood mechanisms associated with the propagation of epigenetic states such as DNA methylation, experiments analyzing epigenetic modifications to DNA and chromatin have proved popular in attempts to explain the heritable memory of environmental experience. In both cases, enzymes have been identified that can "read" a modification and replicate it locally on the newly synthesized strand (in the case of DNA) or can propagate it on newly assembled histones on chromatin (*41*). Both mechanisms fit an appropriately narrow mechanistic definition of "epigenetics" that is discussed in detail elsewhere (*42*).

Yet, as pointed out by Jablonka (*43*), information might not only be copied or replicated but may also be reconstructed in each generation (Fig. 2). Whether transgenerational mechanisms leading to adverse outcomes are replicated between generations or reconstructed in each generation (or a combination of both) has implications for our consideration

IMAGE: COURTESY OF ENRICO COEN ©

Fig. 1. Epialleles. Shown is an example of a natural non–DNA sequence–mediated multigenerational epigenetic inheritance in toad flax: breaking flower symmetry (*12*). The flower changes from bilateral symmetry (**left**) to radial symmetry (**right**) via a naturally occurring mutant. The molecular basis of this mutant is a metastable and heritable DNA methylation state of the *Lcyc* gene locus.

of the mechanisms themselves, as well as for the design of experiments to determine them. The prospect of reconstruction is possible at the *Avy* locus, where epigenetic reprogramming has been shown to occur in the preimplantation embryo despite the nongenetic transmission of the phenotype across generations. Metabolic or cell signaling loops or noncoding RNA expression are examples that might also fit a reconstructive model of inheritance. It is important to consider that epigenetic marks such as DNA methylation or histone modifications might be reconstructed with RNAs, transcription factors, or even metabolic loops acting as intermediate carriers of information. Heritable epigenetic information, including DNA methylation or histone marks, might therefore not be present in all cells of an organism but might be reconstructed in a specific tissue or tissues only. As a consequence, careful consideration of the underlying mechanisms of extended inheritance is relevant when considering specific paradigms and vice versa.

When one considers the basis for transgenerational inheritance of phenotypic traits, the first and most likely port of call will, and should, be a genetic one. DNA for the storage of heritable information is often thought to be exceptionally conservative. The replication error rate is small (~10^{-8} per base pair) and surprisingly similar across many organisms (*44*). However, the DNA mutation rate is not necessarily random throughout the genome (*45*), can depend on epigenetic state (*46*), and might be tunable in response to environmental stress, at least in some organisms (*47*). In particular, DNA methylation is a mutagen, with recent examples of its potential effect being observed in the increased incidence of C-to-T transitions found in cancer genomes (*46*). Once a genetic mechanism can be excluded and non–DNA sequence–based mechanisms inferred, such information might also reveal very distinct behaviors. Instead of being deterministic, this information might be metastable, stochastically switching between two (or more) states every few or many generations, or might exhibit parental-origin effects that differ based on whether it is transmitted via sperm or egg. A clear example of state-switching is found with metabolic loops in prokaryotes that have recently been characterized quantitatively (*48*). Any state-switching might be completely dependent, independent, or tunable through the environment. In the latter case, prolonged environmental exposure, perhaps even over several generations, might be required for state-switching. All of the above have been observed (*9*). When discussing the heritability of environmental information, or acquired traits, a controversy between Lamarckian and Darwinian models of heritability is often evoked, with the former having been largely dismissed. Alas, the history of the science of heredity is more complex; this has been discussed in detail elsewhere (*49*). For example, Darwin's theory of pangenesis suggested the presence of gemmules, nongenetic factors that could be transmitted via the germline to influence the inheritance of acquired characteristics (*50*).

What is the known mechanistic toolkit beyond DNA sequence?

A non–DNA sequence–based mechanism of heritability requires a substrate that transmits the information from one generation to the next. There must also exist a mechanism for the transmitted information to be "read" or interpreted in the offspring to alter the phenotype. Finally, when considering environmental cues, the transmitted information should also be tunable in the parent. Thus, a complete understanding of non–DNA sequence–based heritable effects requires a number of components, and we do not currently have the complete picture for any natural example. Nevertheless, diverse organisms provide clues and candidate mechanisms that we will examine here with regards to mammals, including humans (Fig. 3).

In plants, stable replicative inheritance of DNA methylation marks throughout many generations is a well-characterized mechanism (see above and Fig. 1). The simplicity of this mechanism and the fact that the DNA methylation machinery is conserved in mammals (*51*) makes

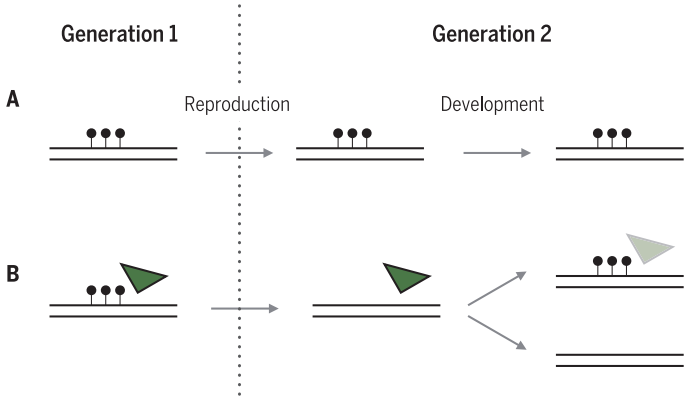

Fig. 2. Replication versus reconstruction as mechanisms of inheritance. As proposed by Jablonka and Raz (*9*, *43*), inheritance might be replicative in nature and involve direct copying of DNA and epigenetic marks (**A**) or, alternatively, inherited information might be reconstructed during development (**B**). In the latter case, the epigenetic marks are not present in all cells at all times. Instead, epigenetic information is reconstructed from another substrate (green cheese, RNA, etc.): "The laws of genetics had never depended upon knowing what the genes were chemically and would hold true even if they were made of green cheese" [Ed Lewis (*76*)].

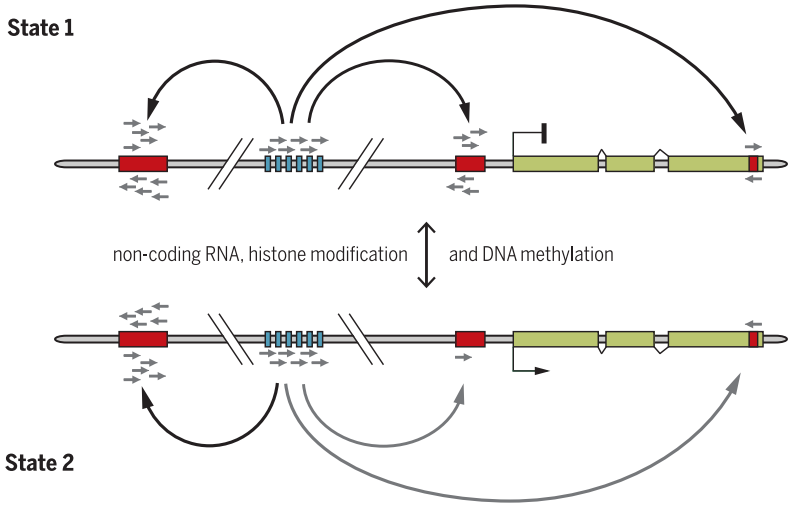

Fig. 3. Interaction between epigenetics and genetics. Genomes contain mobile elements (red) and genes (green). Cellular defense mechanisms such as piRNAs (blue) silence the expression of transcripts from mobile elements by modifying the epigenetic state (e.g., locus-specific histone modification, DNA methylation). Silencing of mobile elements that have inserted close to genes might affect gene expression locally (state 1). This polar effect on gene expression might be influenced through intrinsic and extrinsic factors (state 1 versus state 2).

this an attractive mechanistic model. The DNA methylation state of genomic DNA in somatic tissues can be modulated by the intrinsic developmental environment and age in mice and humans (*52*, *53*) and hence has the potential to be extrinsically and directly modulated. Still, germline and preimplantation reprogramming in mammals are formidable barriers to replicative inheritance: In both the female and male germlines, DNA methylation is largely eliminated from the genome and can be considered a molecular manifestation of the Weismann barrier (*54*). However, in mammals, germline DNA methylation erasure appears to be incomplete (*55*), with some nonrepetitive and particular classes of repeat sequences being reported as somewhat resistant to reprogramming. The idea of certain sequences that might be refractory to germline epigenetic reprogramming provides a compelling mechanism for the inheritance of modulated epigenetic states. A second wave of genome-wide reprogramming occurs in the mammalian preimplantation embryo. At this developmental stage, mechanisms exist to prevent the reprogramming of particular sequences, such as genomic imprints (*29*). Related mechanisms might also be operational at other sequences, including those targeting repressive epigenetic states to repetitive endogenous retroviral sequences during and after the reprogramming period. These epigenetic targeting approaches might provide a mechanism for reconstructing epigenetic states between one generation and another and may involve not only DNA methylation but also the targeting of repressive histone modifications (*56*).

Histones, which are closely associated with DNA in the histone octamer forming the nucleosome, are a suitable candidate substrate of information that can be propagated during DNA replication through local nucleosome retention. Analogous to DNA methylation, classes of "reader" and "writer" proteins that can maintain histone marks have been identified for a number of posttranslational modifications (*41*). Evidence from nematodes, flies, mice, and humans suggests that histone modifications might be involved in heritable effects (*19*, *20*, *57*–*59*). However, whether histone marks are heritable in a replicative manner across generations in mammals is questionable because they are subject to erasure during germline reprogramming, as is the case for DNA methylation (*54*). Furthermore, in the male germline, histones associated with genomic DNA are largely replaced with protamines in sperm. Immediately upon fertilization, the protamines are removed and the paternal chromatin rapidly remodeled using maternally deposited stores of histones. However, the few modified histones in sperm that are carried through to the egg upon fertilization have recently been linked to altered development in the offspring, indicating that their correct modification is important for offspring development (*60*, *61*). Hence, similar to DNA methylation, histone modifications might contribute a replicated mechanism of inheritance but might also be reconstructed upon remodeling of the parental genomes after fertilization. Therefore, environmental influences have the potential to compromise important normal developmental processes associated with the germline and early developmental dynamics of epigenetic states.

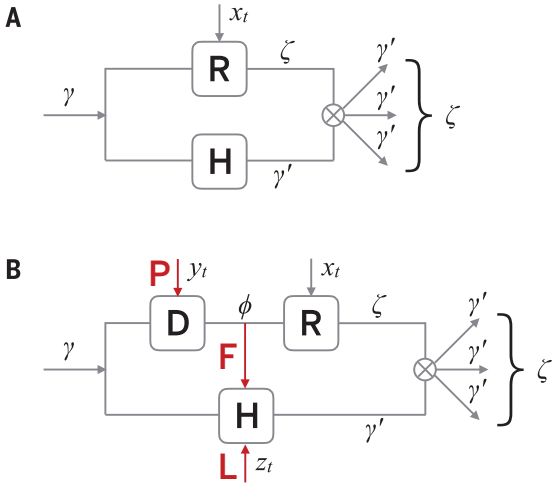

Fig. 4. A generalized model of inheritance: a role in adaptation and evolution? (**A**) The classic genetic model where a single attribute γ describes all heritable information that gives rise to γ′ in the offspring and that is operated on by two stochastic kernels that represent heritability (H) and reproduction (R), giving rise to ζ number of offspring. Reproduction is influenced by the environment x_t at the current time. (**B**) A generalized model where a third stochastic kernel represents development (D) that specifies a phenotype based on an inherited genotype γ. Development, reproduction, and heritability are all under the influence of external environmental factors (x_t, y_t, z_t). The three red arrows can be thought of as developmental plasticity (P), soma feedback to the germline (F), and Lamarckian effects (L). Certain environments might favor Lamarckian inheritance in the generalized model. [Adapted from figure 1 of (*70*)]

RNA-mediated mechanisms

Although DNA methylation and histone modification represent epigenetic mechanisms that are compelling heritable environmental mediators of nongenetic states, this is not necessarily the case for RNA. However, specific long and short noncoding RNAs are tightly linked to both mechanistic pathways and, hence, can contribute to a dialogue between environment and genome. This is particularly well understood for the small noncoding RNAs involved in RNAi–related pathways. Specifically, such small interfering RNAs and their relatives are known to direct histone modification and/or DNA methylation changes in a sequence-specific manner in yeasts, plants, nematodes, and insects (*7*). The current molecular models suggest that nascent gene transcripts are recognized by small RNAs through base-pairing, which brings about a local change in gene transcription through DNA methylation and histone modification.

An increasing literature implicates small RNA–mediated mechanisms in the nongenetic transmission of phenotypic traits in many organisms. In these instances, the models have small RNA amplification mechanisms that fit well with a reconstructive mode of inheritance. In some instances, specific patterns of DNA methylation and histone modification result in small RNA production that reconstructs the DNA methylation and histone state. The RNAi-related Piwi-interacting (piRNA) pathway in animals is a perfect candidate: It is conserved in mammals, including humans; is germline expressed; is known to direct histone modification and likely DNA methylation (*62*); and is amplified via the ping-pong pathway, among others. piRNAs themselves can be directly inherited by the offspring in invertebrates, fish, and possibly humans (*63*). In some paradigms of non–DNA-based inheritance in mice, sperm total RNA injection into oocytes was able to replicate paternal environmental exposure (*64*). However, although small RNA–based multigenerational inheritance in the nematode *C. elegans* has been directly demonstrated, such evidence is lacking in mammals. Other classes of RNA might be involved; for example, tRNA fragments are an abundant class of RNA in the sperm of mice and cows (*65*, *66*). Two recent studies of heritable effects of paternal diet in mice found that the sperm small RNA fraction (*67*, *68*) and even the tRNA fragments themselves (*67*) were able to phenocopy the effect of paternal diet when provided in the zygote. However, how parental diet might result in altered sperm tRNA fragment concentration or how these fragments might exert an effect in the egg remains entirely unknown.

The candidate mechanisms discussed above have the potential to share another biological function—namely, the control of the expression and mobility of transposable elements in the genome. The discovery of the first non–DNA-based alleles in plants, which are formed via a process known as paramutation (*69*), involved the interaction between transposable elements and genes. Many plant paramutation loci are now known to involve DNA methylation, histone modification, and repetitive genomic loci. In mice, the interindividual variation in expression at the *Avy* locus is modulated through variable methylation of an adjacent endogenous retroviral repetitive element (IAP), although a role for small RNAs in its control has not been shown. Finally, piRNAs and other small RNAs are important for transposable element control in many animal models, including mammals. Thus, transposable element insertions might sit at the interface between genetics and epigenetics and may generally be a source of metastable epigenetic alleles, some

of which (such as *Avy*) might be under environmental control. These examples emphasize the importance of the interaction between genetic and epigenetic factors in apparent nongenetic inheritance and provide an important framework through which to consider candidate mechanisms.

With a number of putative candidate mechanisms in mammals having been identified, it might be tempting to measure DNA methylation states, histone modification, RNAs, etc., in population studies to identify candidate loci. However, analogous studies in plants suggest that matching phenotypes to epialleles might be challenging. Instead, a focus on a few robust, highly penetrable phenotypes might be the key to demonstrating a molecular mechanism for non–DNA sequence–based inheritance in mammals.

Are non–DNA sequence–based mechanisms adaptive, and does this matter at a population and evolutionary level?

Assuming it will be possible to clearly demonstrate new inheritance mechanisms in mammals, what might be their effects? The concept of missing heritability is sometimes evoked in this context, referring to the fact that genome-wide association studies in humans often identify genomic loci whose effect sizes cannot explain the heritable component of the phenotype in question. However, contributions of additional rarer genetic loci that require large population sizes to pass significance thresholds might provide a more parsimonious explanation. A different and useful starting point might therefore be a theoretical consideration of non–DNA sequence–based mechanisms and the constraints that they themselves might be subject to, as outlined by Rivoire and Leibler (*70*) (Fig. 4). Linking quantitative genetics to stochastic control theory, the authors develop a mathematical model to compare the adaptive value of classic inheritance versus an extended model that allows for information flow from the soma to the germline. These considerations suggest that, given a changing environment, the inheritance of acquired traits can be adaptive. A clear demonstration of such adaptive behavior is currently lacking for most systems. However, hypotheses such as the "thrifty phenotype" idea, whereby a compromised in utero environment programs offspring for a similarly matched environment ex utero, compellingly explains the associations between poor fetal and infant growth and increased risk of metabolic syndrome in adults born into an unmatched ex utero environment (*38*). But these might be considered short-term adaptations. On even longer time scales, considerations of an evolutionary role for non–DNA sequence–based mechanisms have been met with severe criticism (*71*), yet a potential link might be found at the interface between epigenetics and genetics. For example, the increased mutation rate at 5-methylcytosine in DNA compared with unmethylated cytosine (*72*) provides a longer-term mechanistic link between DNA sequence and other mechanisms. Another complexity to consider at the interface between genetics and epigenetics is heterozygosity. Although it is important to exclude genetic variation when establishing epigenetic mechanisms, heterozygous individuals might enhance epigenetic effects. For example, a recent study of hybrid crosses in tomato revealed an extraordinary degree of epigenetic effects (*73*). In this context, it is also noteworthy that environmentally associated changes in epigenetic state that depend on underlying genetic variation have recently been described in both humans and mice (*74*, *75*).

"The idea of certain sequences that might be refractory to germline epigenetic reprogramming provides a compelling mechanism for the inheritance of modulated epigenetic states."

It really is the phenomenal success of molecular genetics and a deep understanding of DNA sequence–based variation and its inheritance that make non–DNA sequence–based heritable effects seem so exotic. However, nongenetic or non–DNA sequence–based forms of inheritance have major implications for human health. It will be particularly exciting to unravel the mechanisms and their effects on humans. The tractability of nonhuman paradigms with large intergenerational or transgenerational effects will be essential for elucidating the molecular mechanisms. The consequences of delineating the interactions between genetic and epigenetic factors, even in these established paradigms, is a challenge. However, it is worth considering that even minor effects of non–DNA sequence–based inheritance might play important roles at the level of human public health.

REFERENCES AND NOTES

1. J. D. Watson, F. H. Crick, *Nature* **171**, 964–967 (1953).
2. J. Huxley, *Evolution: The Modern Synthesis* (Allen and Unwin, 1942).
3. A. Weismann, *The Germ-Plasm. A Theory of Heredity* (Charles Scribner's Sons, 1893).
4. F. A. Champagne, J. P. Curley, *Neurosci. Biobehav. Rev.* **33**, 593–600 (2009).
5. D. S. Newburg, W. A. Walker, *Pediatr. Res.* **61**, 2–8 (2007).
6. M. J. Meaney, *Proc. Natl. Acad. Sci. U.S.A.* **113**, 6094–6096 (2016).
7. E. Heard, R. A. Martienssen, *Cell* **157**, 95–109 (2014).
8. A. C. Ferguson-Smith, M.-E. Patti, *Cell Metab.* **13**, 115–117 (2011).
9. E. Jablonka, G. Raz, *Q. Rev. Biol.* **84**, 131–176 (2009).
10. D. Weigel, V. Colot, *Genome Biol.* **13**, 249 (2012).
11. L. Daxinger, E. Whitelaw, *Nat. Rev. Genet.* **13**, 153–162 (2012).
12. P. Cubas, C. Vincent, E. Coen, *Nature* **401**, 157–161 (1999).
13. R. Halfmann *et al.*, *Nature* **482**, 363–368 (2012).
14. D. Jordan, S. Kuehn, E. Katifori, S. Leibler, *Proc. Natl. Acad. Sci. U.S.A.* **110**, 14018–14023 (2013).
15. A. Fire *et al.*, *Nature* **391**, 806–811 (1998).
16. N. L. Vastenhouw *et al.*, *Nature* **442**, 882 (2006).
17. R. M. Alcazar, R. Lin, A. Z. Fire, *Genetics* **180**, 1275–1288 (2008).
18. A. Ashe *et al.*, *Cell* **150**, 88–99 (2012).
19. M. Simon *et al.*, *Cell Reports* **7**, 762–773 (2014).
20. E. L. Greer *et al.*, *Nature* **479**, 365–371 (2011).
21. D. J. Katz, T. M. Edwards, V. Reinke, W. G. Kelly, *Cell* **137**, 308–320 (2009).
22. B. A. Buckley *et al.*, *Nature* **489**, 447–451 (2012).
23. M. J. Luteijn *et al.*, *EMBO J.* **31**, 3422–3430 (2012).
24. D. Schott, I. Yanai, C. P. Hunter, *Sci. Rep.* **4**, 7387 (2014).
25. M. A. Jobson *et al.*, *Genetics* **201**, 201–212 (2015).
26. O. Rechavi *et al.*, *Cell* **158**, 277–287 (2014).
27. O. J. Rando, *Cell* **151**, 702–708 (2012).
28. J. P. Lim, A. Brunet, *Trends Genet.* **29**, 176–186 (2013).
29. M. S. Bartolomei, A. C. Ferguson-Smith, *Cold Spring Harb. Perspect. Biol.* **3**, a002592 (2011).
30. H. D. Morgan, H. G. E. Sutherland, D. I. K. Martin, E. Whitelaw, *Nat. Genet.* **23**, 314–318 (1999).
31. B. R. Carone *et al.*, *Cell* **143**, 1084–1096 (2010).
32. E. J. Radford *et al.*, *Science* **345**, 1255903 (2014).
33. P. Huypens *et al.*, *Nat. Genet.* **48**, 497–499 (2016).
34. J. C. Jiménez-Chillarón *et al.*, *Diabetes* **58**, 460–468 (2009).
35. J. Bohacek, I. M. Mansuy, *Nat. Rev. Genet.* **16**, 641–652 (2015).
36. T. L. Roth, F. D. Lubin, A. J. Funk, J. D. Sweatt, *Biol. Psychiatry* **65**, 760–769 (2009).
37. T. B. Franklin *et al.*, *Biol. Psychiatry* **68**, 408–415 (2010).
38. C. N. Hales, D. J. Barker, *Br. Med. Bull.* **60**, 5–20 (2001).
39. M. E. Pembrey *et al.*, *Eur. J. Hum. Genet.* **14**, 159–166 (2006).
40. M. Meselson, F. W. Stahl, *Cold Spring Harb. Symp. Quant. Biol.* **23**, 9–12 (1958).
41. K. P. Nightingale, L. P. O'Neill, B. M. Turner, *Curr. Opin. Genet. Dev.* **16**, 125–136 (2006).
42. A. Bird, *Nature* **447**, 396–398 (2007).
43. E. Jablonka, *Prog. Biophys. Mol. Biol.* **111**, 99–107 (2013).
44. F. A. Kondrashov, A. S. Kondrashov, *Philos. Trans. R. Soc. London Ser. B* **365**, 1169–1176 (2010).
45. I. Martincorena, A. S. N. Seshasayee, N. M. Luscombe, *Nature* **485**, 95–98 (2012).
46. M. Tomkova, M. McClellan, S. Kriaucionis, B. Schuster-Boeckler, *eLife* **5**, e17082 (2016).
47. C. Saint-Ruf, I. Matic, *Environ. Microbiol.* **8**, 193–199 (2006).
48. E. M. Ozbudak, M. Thattai, H. N. Lim, B. I. Shraiman, A. Van Oudenaarden, *Nature* **427**, 737–740 (2004).
49. P. Corsi, *The Age of Lamarck: Evolutionary Theories in France, 1790–1830* (Univ. of California Press, 1988).
50. Y. Liu, *Biol. Rev. Camb. Philos. Soc.* **83**, 141–149 (2008).
51. I. Hernando-Herraez, R. Garcia-Perez, A. J. Sharp, T. Marques-Bonet, *PLOS Genet.* **11**, e1005661 (2015).
52. S. Bocklandt *et al.*, *PLOS ONE* **6**, e14821 (2011).
53. G. Hannum *et al.*, *Mol. Cell* **49**, 359–367 (2013).
54. J. A. Hackett, M. A. Surani, *Philos. Trans. R. Soc. London Ser. B* **368**, 20110328 (2013).
55. J. A. Hackett *et al.*, *Science* **339**, 448–452 (2013).
56. M. Friedli, D. Trono, *Annu. Rev. Cell Dev. Biol.* **31**, 429–451 (2015).
57. K.-H. Seong, D. Li, H. Shimizu, R. Nakamura, S. Ishii, *Cell* **145**, 1049–1061 (2011).
58. A. Öst *et al.*, *Cell* **159**, 1352–1364 (2014).
59. K. Dalgaard *et al.*, *Cell* **164**, 353–364 (2016).
60. K. Siklenka *et al.*, *Science* **350**, aab2006 (2015).
61. M. Teperek *et al.*, *Genome Res.* **26**, 1034–1046 (2016).
62. E.-M. Weick, E. A. Miska, *Development* **141**, 3458–3471 (2014).
63. E. F. Roovers *et al.*, *Cell Reports* **10**, 2069–2082 (2015).
64. K. Gapp *et al.*, *Nat. Neurosci.* **17**, 667–669 (2014).
65. H. Peng *et al.*, *Cell Res.* **22**, 1609–1612 (2012).
66. C. Belleannée, É. Calvo, J. Caballero, R. Sullivan, *Biol. Reprod.* **89**, 30 (2013).
67. U. Sharma *et al.*, *Science* **351**, 391–396 (2016).
68. Q. Chen *et al.*, *Science* **351**, 397–400 (2016).
69. R. A. Brink, *Cold Spring Harb. Symp. Quant. Biol.* **23**, 379–391 (1958).
70. O. Rivoire, S. Leibler, *Proc. Natl. Acad. Sci. U.S.A.* **111**, E1940–E1949 (2014).
71. K. Laland *et al.*, *Nature* **514**, 161–164 (2014).
72. D. N. Cooper, M. Mort, P. D. Stenson, E. V. Ball, N. A. Chuzhanova, *Hum. Genomics* **4**, 406–410 (2010).
73. P. V. Shivaprasad, R. M. Dunn, B. A. Santos, A. Bassett, D. C. Baulcombe, *EMBO J.* **31**, 257–266 (2012).
74. A. L. Teh *et al.*, *Genome Res.* **24**, 1064–1074 (2014).
75. M. L. Holland *et al.*, *Science* **353**, 495–498 (2016).
76. J. S. Dietrich, *Eng. Sci.* **59**, 2–7 (1996).

ACKNOWLEDGMENTS

This work was supported by grants from Cancer Research UK (C13474/A18583 and C6946/A14492) and the Wellcome Trust (104640/Z/14/Z and 092096/Z/10/Z) to E.A.M. and from the Medical Research Council (UK) (MR/J001597/1) and the Wellcome Trust (095606/Z/11/Z) to A.C.F.-S.

10.1126/science.aaf4945

REVIEW

Writ large: Genomic dissection of the effect of cellular environment on immune response

Nir Yosef[1,2]* and Aviv Regev[3,4]*

Cells of the immune system routinely respond to cues from their local environment and feed back to their surroundings through transient responses, choice of differentiation trajectories, plastic changes in cell state, and malleable adaptation to their tissue of residence. Genomic approaches have opened the way for comprehensive interrogation of such orchestrated responses. Focusing on genomic profiling of transcriptional and epigenetic cell states, we discuss how they are applied to investigate immune cells faced with various environmental cues. We highlight some of the emerging principles on the role of dense regulatory circuitry, epigenetic memory, cell type fluidity, and reuse of regulatory modules in achieving and maintaining appropriate responses to a changing environment. These provide a first step toward a systematic understanding of molecular circuits in complex tissues.

Homeostasis is a hallmark of biological systems that actively maintain a near-constant function in the face of a changing environment. In most animals, multiple systems, from the cellular to the organismal level—including the immune system, the nervous system, and fibroblasts in connective tissue—play crucial homeostatic roles as they sense, respond, and adapt to an ever-changing environment, both external and intraorganismal, in different tissues in the body. In particular, the immune system achieves tunability, plasticity, and adaptability to the environment at several levels (Fig. 1). First, immune cells have transient responses to diverse factors, such as microbes, vaccines, tissue damage, or cancer cells (*1*). Second, controlled differentiation from progenitor cells generates different cell type balances (*2*). Furthermore, cells exhibit plasticity, such that certain immune cells can change their identity in the context of new signals (*3*, *4*). Finally, cells can locate and relocate throughout the body, adapting their identity to their locale (*1*, *5*).

These abilities are controlled by a complex molecular circuitry, both intracellular (within immune cells) and through interaction among immune cells, or between immune cells and other cell types, including cells of the nervous system or fibroblasts. Malfunction in each of these mechanisms can contribute and give rise to disease. Manipulating them, in turn, provides important avenues for therapies, as has been the case in autoimmune disease and cancer. However, given the diversity of molecules, cell types, and tissues, as well as the inherent uncertainties and noise in both molecular systems and measurement techniques, systematic dissection of these intra- and intercellular circuitries is remarkably challenging.

Genomics approaches have opened unique opportunities to address this challenge (Fig. 2). Profiling of the genome, epigenome, transcriptome, proteome, and metabolome has been instrumental in defining cell types and states and characterizing the molecular changes that occur as cells respond to their surroundings. Recently, single-cell genomics can distinguish these with remarkable resolution, even when the types and states of immune cells are not necessarily known (*6*–*8*) and when they are embedded in complex tissues (*6*, *9*, *10*) with spatial resolution (*11*–*13*). Profiling assays, especially of molecular interactions with chromatin immunoprecipitation sequencing (ChIP-seq) (*14*) and interaction proteomics, help identify key aspects of the underlying molecular mechanisms, such as key transcription factors (TFs) and regulatory regions. To determine causality, large-scale perturbations, either engineered with RNA interference and clustered regularly interspaced short palindromic repeats (CRISPR)–based genome editing (*15*) or natural variation between individuals in a population (*16*–*19*), provide a systematic means to assess the causal role of different circuit components, including in the context of disease in vivo.

Although these assays can be applied in principle to many systems, analysis of immune cell responses has been at the forefront, providing a paradigm for other systems. First, the identity of many immune cell subtypes is known, and they can be isolated for analysis from both humans and mice; this has been critical, especially before the advent of single-cell genomics. Furthermore, many primary immune cells can be studied both ex vivo and in vivo, including adoptive transfer of cells, bone marrow transplants, and lineage tracing in animal models (*6*, *20*, *21*). Finally, immune cells are present throughout the body, differentiate

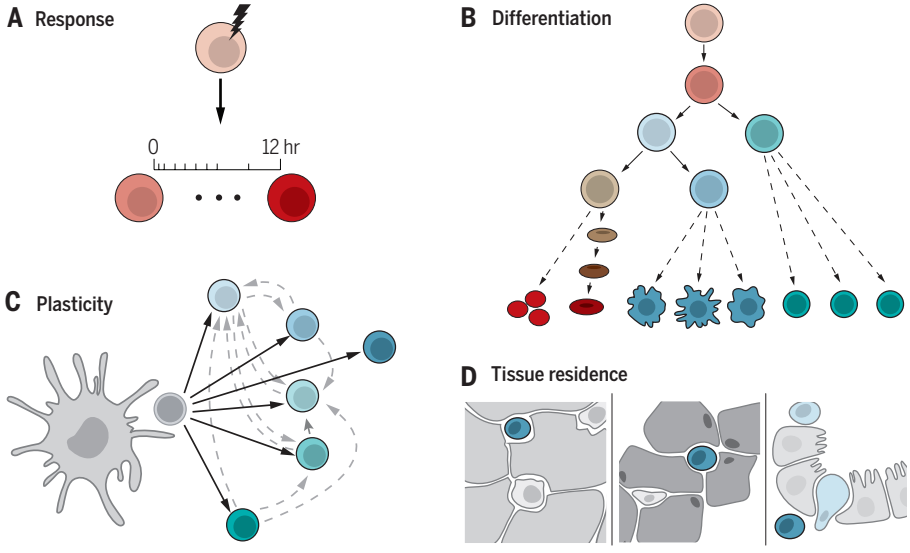

Fig. 1. Key modes of immune-environment interaction. (**A**) Transient responses to signals. A cell responds to an environmental signal (lightning bolt) with a short-term, transient response (marked time points). (**B**) Balanced differentiation along hematopoiesis. Shown is a schematic of a lineage tree. Solid arrows, individual (known) differentiation steps; dashed arrows, multistep process. (**C**) Stable yet plastic cell-type polarization. After polarization (solid black arrows) from a progenitor cell (e.g., naïve T_H cell; gray circular cell), cells with different differentiated states (colored cells) can plastically transition (dashed gray lines) to other states under appropriate signals—for example, from other immune cells (e.g, dendritic cell; large tentacle gray cell). (**D**) Malleable adaptation of tissue-resident cells. A cell of a single type (e.g., macrophage, gray; T cell, blue) can reside long term in different tissues (gray), assuming unique characteristics stereotypical to that tissue.

[1]Department of Electrical Engineering and Computer Science and Center for Computational Biology, University of California Berkeley, Berkeley, CA 94720, USA. [2]Ragon Institute of Massachusetts General Hospital, MIT, and Harvard, Cambridge, MA 02139, USA. [3]Broad Institute of MIT and Harvard, Cambridge, MA 02142, USA. [4]Howard Hughes Medical Institute and Koch Institute of Integrative Cancer Biology, Department of Biology, Massachusetts Institute of Technology, Cambridge, MA 02140, USA.
*Corresponding author. Email: niryosef@berkeley.edu (N.Y.); aregev@broadinstitute.org (A.R.)

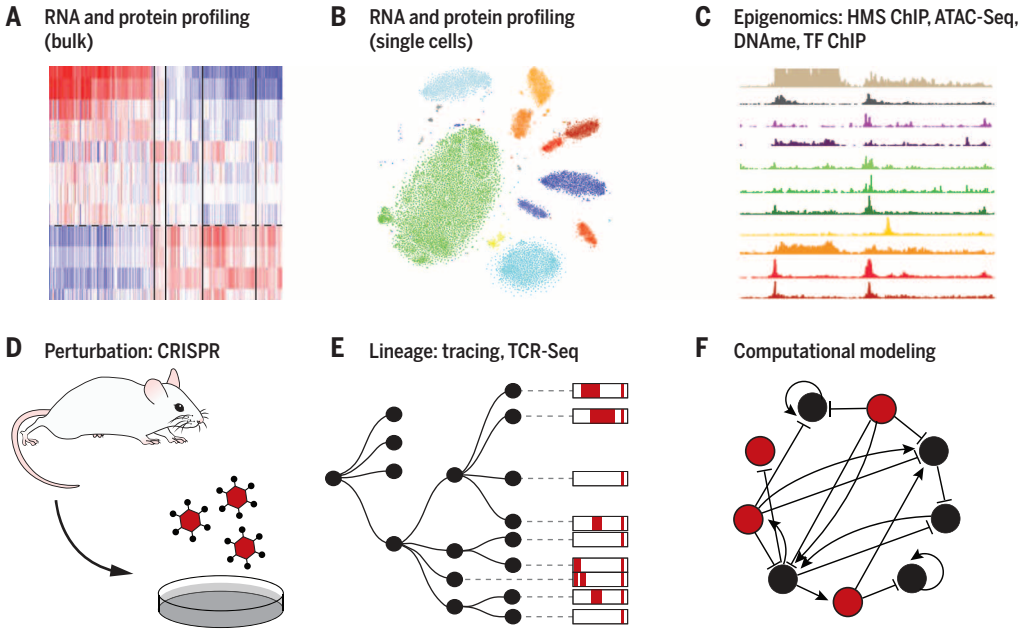

Fig. 2. Genomic tools for dissecting immune-environment interactions. Shown are key components of the current genomic tool box, including profiling of RNA, protein, and protein modification levels in bulk samples (**A**) and single cells (**B**); epigenomic measurements of TF binding, histone modification (HMS), DNA methylation, and chromatin accessibility (**C**); the ability to systematically perturb genes through genome engineering (**D**) or natural variation; tracing of cells and cell lineages with engineered molecular barcodes accruing throughout cell division or TcR and BcR clonality (**E**); and computational algorithms that use profiling and perturbation data to infer genetic causality and molecular mechanisms (**F**).

continuously, and are implicated in many diseases, thus providing a broad lens into organismal physiology.

Here, we highlight the power of genomics to dissect environmental responses in immune cells. We focus on assays related to the regulation of mRNA expression, especially transcriptional and epigenetic profiling. Using macrophages and T cells as case studies, we illustrate the types of features that are underscored with different genomic profiles, the resulting testable hypotheses that can be followed up in dedicated low-throughput experiments, and the emerging organizing principles and mechanisms (Fig. 3). Finally, we discuss how these lessons, learned in immune cells, can be extended to develop approaches to dissect the overall function of diverse cells in maintaining homeostasis.

Molecular responses of the immune system through transient intracellular circuits

Macrophages, innate immune cells of the myeloid lineage, serve key immune defense functions through phagocytosis and by communicating with adaptive immune cells through antigen presentation and secretion of and response to cytokines and chemokines (*22*–*24*). Mononuclear phagocyte subpopulations are located in the circulatory system and spleen and can differentiate into macrophages, but macrophages also reside in other tissues, where they acquire specific characteristics and contribute to local hemostasis (*1*, *22*, *23*).

In their role as immune sensors, macrophages express pattern-recognition molecules [e.g., Toll-like receptors (TLRs)], which detect conserved pathogen-associated or tissue damage–associated molecular patterns, and mount the appropriate response. Genomic analysis of macrophages provided key insights on how these transient responses (Fig. 1A) are carried out. For instance, transcriptional profiling along a time course after TLR4 activation with bacterial lipopolysaccharide (LPS), an inducer of inflammation, showed that genes are induced in several consecutive "waves" (*25*), a phenomenon observed in many other response systems (*26*) (Fig. 3). The response waves are regulated through successive activation of transcriptional regulators (*27*, *28*), whose identity can be predicted from DNA-binding motifs enriched in the 5′ regions of the responding genes. This approach helped identify activating TF 3 (ATF3) as an early regulator of the LPS response in macrophages (*25*). ATF3 was then shown to recruit histone deacetylase to repress its target genes, thus forming a negative feedback. This mechanism may be essential for controlling the extent and duration of TLR-induced inflammation during infection, avoiding rampant inflammation and tissue damage.

The importance of epigenetic regulation as a way of controlling macrophage activation was further demonstrated by investigating the formation of "memory" in antigen-exposed macrophages (Fig. 3), where macrophages repeatedly exposed to a specific component (e.g., LPS) become tolerant and selectively produce antimicrobial, but not proinflammatory, signals to avoid tissue damage (*27*, *28*). Profiling of gene expression and histone modifications (Fig. 3) during the macrophage response to repeated stimulation reveals that "tolerant" genes that are not reinduced in repeated exposure to LPS are enriched for proinflammatory functions and are transiently silenced by loss of activating histone marks. Conversely, nontolerant genes are enriched for antimicrobial functions and are associated with a faster and stronger transcriptional response upon LPS restimulation (compared with the primary stimulation) through persistence or rapid acquisition of activating histone marks (H3 trimethylation and H4 acetylation, respectively) and recruitment of RNA polymerase II (Pol II) and chromatin remodeling complexes. These distinct epigenetic mechanisms depend on the protein products generated during the first exposure to LPS, emphasizing the common role of negative feedback in controlling innate immune response (*26*, *29*) (Fig. 3).

Depending on their tissue of origin and stimulus, macrophages can acquire distinct functional states. Two well-studied states are proinflammatory *M1* cells, derived in the presence of interferon gamma, and immunosuppressive *M2* cells that can be induced with interleukin-4 (IL-4) or IL-13 (*30*). Profiling the transcriptional response of monocyte-derived macrophages to a more diverse set of stimuli suggests that macrophages can mount diverse transcriptional programs beyond these two states, depending on the metabolites, cytokines, or ligands to which they are exposed (*30*). Computational analyses of gene modules that are coregulated across programs suggested that diversity between programs is generated by different combinations of active transcriptional regulators (Fig. 3). Some of these regulators are "reused" across all programs (e.g., the lineage-specifying factor PU.1), whereas others are important only in certain contexts (e.g., STAT1 and STAT6, in the interferon gamma and IL-4 responses, respectively). Mapping the diverse activation programs also provided a way to decompose bulk samples into constituent responses—for instance, proposing that alveolar macrophages from chronic obstructive pulmonary disease patients are depleted in the inflammatory (M1) state, which may explain their poor response to anti-inflammatory therapeutics. Such analysis could further benefit from application of single-cell genomics (Fig. 3).

Systematic perturbations have helped establish the causality of circuits inferred from genomic profiles. Causal loci were discovered either by associating natural genetic variation with variation in the transcriptional response across human individuals (*16*, *18*, *19*) or mouse strains (*17*) or by perturbing genes and measuring the effect on the transcriptome (*15*, *29*).

Balanced differentiation from progenitor cells

The diverse cell types of the hematopoietic system are organized in a taxonomy of different lineages

and are produced daily from a small pool of stem cells (Fig. 1B). The composition of hematopoietic cell subsets is tightly controlled, ensuring both homeostatic control and responsiveness to environmental cues. As in studies of transient immune responses, genomic and epigenomic profiling have shed light on the transcriptional shifts during hematopoiesis and the regulatory programs that govern them (Fig. 3), primarily focusing on unperturbed, homeostatic conditions in humans (*2*, *31*) and mice (*14*, *32*). Transcriptional profiling revealed substantial expression changes between hematopoietic cell subtypes, comparable to those between different tissues (*2*). Computational analysis of these data, focused on "modules" of coregulated genes and the regulators associated with them, has identified global organizing principles in hematopoiesis that may also apply more generally (Fig. 3).

First, a large set of predicted transcriptional regulators (across all hematopoietic lineages) form a dense interconnected network of regulatory interactions in each cell type and with the same regulator used in multiple hematopoietic subsets. This organization may confer robustness but could also be liable to dysregulation and cancer (*2*). This model challenged and expanded an earlier hierarchal model of hematopoiesis controlled by a small number of TFs, expressed sequentially (*33*).

Furthermore, there is no simple partitioning of regulatory activity at different lineages. Instead, entire modules of coregulated genes, along with their upstream regulators, are reused across distinct lineages, either because of shared functional needs in otherwise different cells [e.g., mitochondrial and oxidative phosphorylation in erythroid progenitors, granulocytes, and monocytes (*2*)] or due to shared developmental descent. This latter pattern is often reflected in "transitional" cases (Fig. 3), with a gradual onset and offset of programs along the hematopoietic cell hierarchy (*2*). The transitional gene modules could be explained either by the presence of cells at different phases of development within seemingly pure populations of progenitor cells or because regulatory programs of a more differentiated state are foreshadowed by preexisting programs at earlier stages. Both models are plausible and nonexclusive, and the second model is strongly supported by profiling of TF binding in humans (*2*) and of chromatin organization in hematopoiesis in mice (*14*) and humans (*31*), where a large portion of the enhancers exhibited a "transitional" behavior—already established in the precursor cells, possibly in a poised (and transcriptionally inactive) state. Single-cell RNA-sequencing (RNA-seq) studies can help further address how transition to multiple lineages is concomitantly encoded in progenitor cells. To date, some studies suggested that there may be distinct subsets within myeloid progenitor cells that are partially skewed toward distinct functional fates by the expression of key sublineage regulators (*34*), whereas others emphasized evidence for obligatory mixed-lineage states within the same single progenitor cell (*35*).

While it is tempting to think of hematopoiesis as stereotypic, differentiation is affected and driven by the environment, including not only the stromal niche and other immune cells but also stress and pathogens (*27*, *36*). For example, stress signals can lead to production of more innate immune myeloid cells at the expense of other lineages, especially lymphoid cells (*36*). Furthermore, distinct subpopulations of stem and progenitor cells can be activated (*37*) to produce cytokines that affect core immune responses. Genomic analysis, including at the single-cell level, will shed more light on the regulation of hematopoiesis by such signals.

Plasticity of cell differentiation

As immune cells become more committed, differentiation and balancing between subtypes become even more intertwined with environmental responses. For example, naïve T helper (T_H) cells can differentiate into multiple specialized cell types, including conventional (T_{conv}) T_H cells (e.g., T_H1, T_H2, T_H17, and T_H9 cells) and regulatory T_H cells (e.g., T_{reg} and Tr1) (*4*). Given the diverse and partially opposing functions of different T_H cells (*4*), it is critical to maintain their correct blend in a manner sensitive to and controlled by environmental signals. First, the relative proportion of T_H subtypes that will develop from a limited pool of naïve T_H cells is regulated by the blend of cytokines to which a naïve cell is exposed, often produced by antigen-presenting cells (e.g., to T_{reg} cells in the presence of transforming growth factor–β but skewed to T_H17 cells if IL-6 is also present). Second, while differentiated T_H cell subtypes can be maintained stably over time, including in the memory pool (*38*), some can also transition into other, parallel subtypes (Fig. 1C), depending on extracellular signals, from cytokines, to oxygen or nutrients (*39*), to components of the microbiome (*3*). The process leading to these diverse types is often called polarization, rather than terminal differentiation, and the change between the types is referred to as plasticity (*1*, *4*) and can play critical physiological roles. For example, plastic polarization of tissue-resident macrophages helps fulfill changing functional demands from the tissue in which they reside (*1*, *40*); T_H cell plasticity could allow an organism to respond to a changing environment even if cells were originally committed to the memory pool in a different state (*20*).

The distinction between a permanent and plastic state can be defined in principle but is challenging to identify in practice (*41*) because it can be hard to determine whether a stable state is permanent and whether concomitant expression of markers of different cell type is not mere noise (*41*). Genomic profiling coupled with lineage tracing and functional studies were instrumental in addressing this question (Fig. 3).

Specifically, using the RNA profile of the cell as its functional identity and coupling it to lineage tracing has helped identify both how the state of TH cells is stably maintained and when it shifts plastically [(*20*, *38*, *42*), reviewed in (*4*)]. For example, T_H17 cells can begin to express both cytokines and seminal TFs of other T_H cells (*20*, *38*) but these could reflect either transition to another type or a transient functional deviation. Lineage tracing of T_H17 cells in the gut followed by RNA-seq showed that they can adopt a transcriptional signature of regulatory T cells and anti-inflammatory capacity (*20*). Conversely, tracing T_H17 cells in a melanoma mouse model showed that, although they can acquire transcriptional features of T_H1 cells, they remain distinct from similarly traced T_H1 cells, acquiring stem-cell–like signatures and longevity, with increased tumor eradication capacity (*38*).

Although these studies profiled cell populations defined by cell surface, cytokine, or TF expression, recent single-cell genomic studies (*6*, *43*) have increased the resolution at which we characterize cellular subtypes and their fluidity. For example, T_H17 cells were shown to span a continuum of states, from higher expression of a program associated with pathogenic effect to one characteristic of regulatory cells, with distinct regulators for each program (*6*). Single-cell RNA-seq also provides a way for lineage tracing by capturing the sequence of the T cell receptor transcript (*10*, *44*, *45*).

Profiling of chromatin organization, especially histone marks, across different T_H cell types highlighted how epigenetic memory maintains cell state stably, while remaining sufficiently malleable to allow for plasticity (Fig. 3). Although signature cytokines often have a chromatin pattern congruent with strict cell type definitions, chromatin at other key signature genes of one lineage is not always repressed in other T_H lineages, offering a possible basis for future plasticity. Indeed, chromatin marks and accessibility can change even for signature cytokines or TFs after stimulation (*46*). Conversely, DNA demethylation and stable chromatin organization, with contribution from chromatin regulators and long noncoding RNAs, play an important role in stability. For instance, demethylation of specific regulatory elements in a CpG island in the locus of Foxp3, a key regulator of T_{reg} cells, helps stabilize the cells' identity, further reinforced by a transcriptional positive feedback loop (*47*). The ability of chromatin organization to function as a malleable memory device is reflected by the preponderance of DNA variants associated with autoimmune disease that map to enhancer and other regulatory regions in T_H cells (*48*).

Finally, RNA and TF ChIP-seq profiles, combined with genetic perturbations, have helped shed light on the intricate intracellular circuits controlling these processes in T_{reg} (*49*) and inflammatory T_H17 cells (*50*, *51*). For example, in T_H17 cells, they revealed a "yin-yang" network of TFs, with two densely connected self-reinforcing, but mutually antagonistic, modules: A larger module promotes the T_H17 cell fate and suppresses alternative fates, and a smaller module has an opposite function (Fig. 3). The dense, interconnected positive module provides stability, as has also been proposed for other T_H lineages (*42*, *49*). The smaller negative module could promote alternative plastic fates.

Malleable cell states mirror tissue location

Immune cells sense, adapt, respond to, and affect their environment in the context of the tissue (Fig. 1D). Tissue-resident immune cells, sometimes lifelong sessile inhabitants, play critical

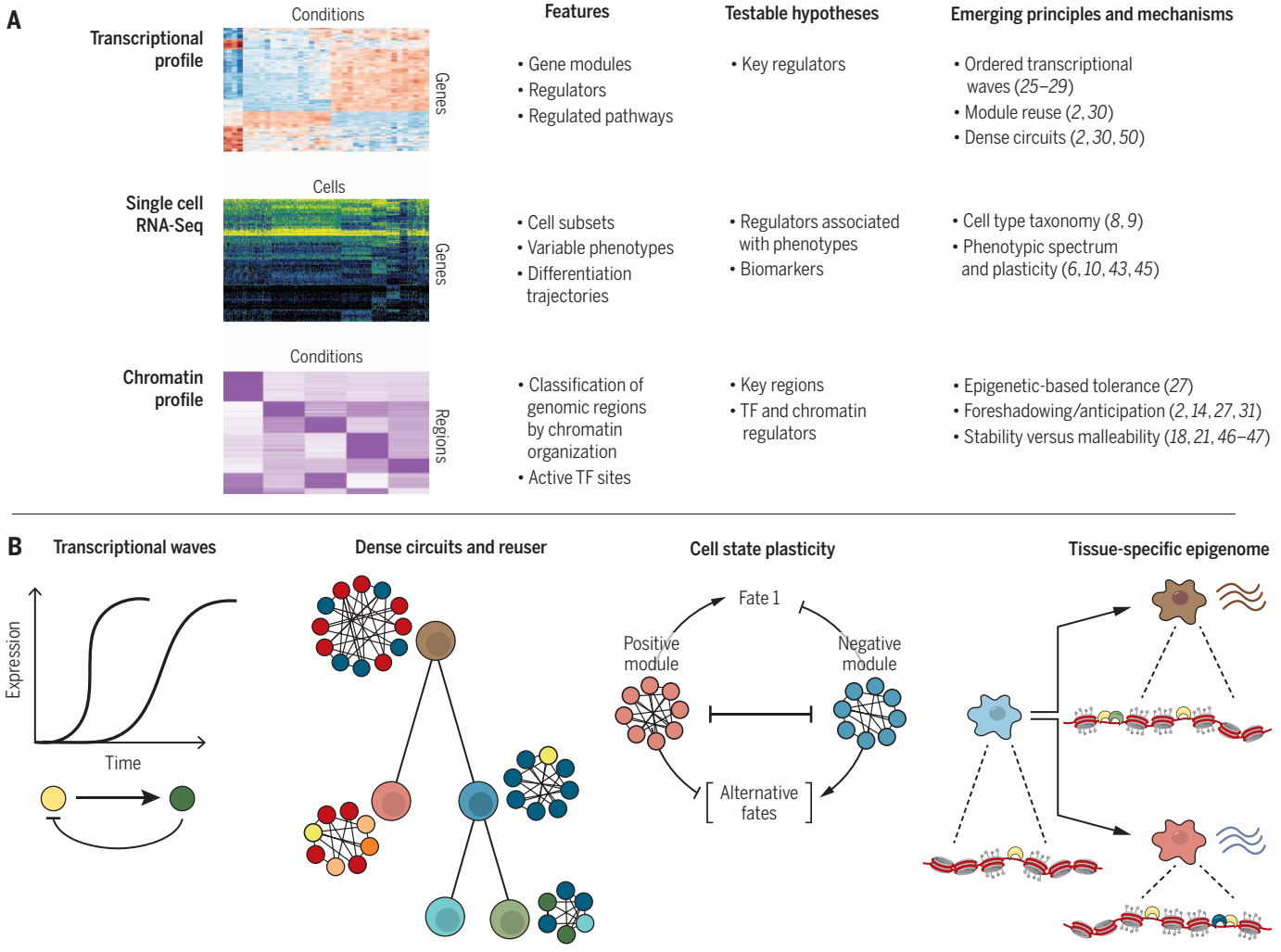

Fig. 3. Key features, hypotheses, and principles revealed by genomic studies of immune-environment interactions. (**A**) Three key genomic tools used to analyze transcription and epigenetic mechanisms that participate in immune cell responses. For each tool (left), shown are the main features it characterizes, testable hypotheses derived by computational analysis, and current emerging principles and mechanisms from such studies. (**B**) Example of key principles and mechanisms derived by genomic study of immune response to the environment. (Left) Consecutive transcriptional waves (top) are driven by sequential activation of regulators in a negative feedback loop (bottom) such that a regulator active at an earlier time point (yellow) activates (arrow) another regulator at a subsequent time point (green), which in turn represses (blunt arrow) the earlier regulator. (Second from left) Dense interconnected circuits and regulator reuse and foreshadowing in differentiation. Each transient and terminal cell state in differentiation is associated with a distinct dense interconnected circuit of regulators (circularly arranged nodes and arrows) with the same regulators (colored nodes) "reused" in multiple cell types and lineage, and regulators active at a later step in differentiation already affecting the cell (e.g., through chromatin structure) at earlier stages. (Third from left) Cell fate plasticity. Two densely interconnected modules of regulators (red and blue circularly arranged nodes, respectively) control a cell at a given fate 1 (top) (e.g., T_H17 cell), positively (arrow) and negatively (blunt arrow), respectively, with the inverse effect on alternative fates (bottom) and a mutually inhibitory effect (double blunt arrow in middle) on each other. (Right) Tissue-specific epigenomes. The epigenome (DNA, red; nucleosomes, gray; bound TFs, crescents) of tissue resident cells (right, e.g., macrophages) shares some common characteristics that are also present in their progenitors (left) (e.g., open chromatin region in center) but may also include features (e.g., enhancers and bound TFs) that are unique to the tissue of residence.

roles in homeostasis and pathology, well beyond responses to pathogens. Tissue-resident macrophages perform unique functions as "accessory cell types" (*1*) that serve "client" primary cells defining the respective tissue. For example (*1*, *23*), alveolar macrophages are critical for surfactant homeostasis in the lungs, microglia are essential for synaptic pruning in the brain, osteoclasts are critical for the dynamic balance of bone, and splenic red-pulp macrophages help manage heme and iron from aging red blood cells. Tissue-resident T_{regs} (*5*) have been identified in visceral adipose tissue (VAT) (*52*, *53*), the intestine (*54*), muscle (*55*), and lung (*56*), with roles from metabolic homeostasis to tissue repair and regeneration.

Genomic analysis has played a critical role in identifying tissue-resident immune cells, characterizing their unique features, determining their tissue-specific functions, and inferring the principles and mechanisms by which they adapt to the diversity of tissues in the body and their changing local conditions.

RNA profiling has identified the level at which immune cells of a single "type" vary given their tissue of residence (Fig. 3). In addition to a core set of macrophage-associated genes, tissue-resident macrophages (*18*, *21*, *40*, *57*) express distinct gene modules in each tissue type. For example, brain-resident microglia (which are deposited prenatally), develop in lockstep with the rest of the central nervous system during brain development and are susceptible to environmental signals prenatally (*58*). T_{regs} isolated from different tissues have shown similar distinctions (*52*–*55*). The profiles and derived gene signatures then become the fingerprint of the cell's identity, and—when coupled

to transfer, chimera, or lineage-tracing experiments—can establish whether a cell is stably resident in a tissue (*52*). It is possible that other immune lineages may also follow such principles; single-cell profiling of entire tissues (*9*, *10*) will help determine this.

Individual genes expressed in these tissue-specific modules—including TFs, cytokines, chemokines, and receptors—provide critical starting points to determine the cells' functions {e.g., lipid metabolism in T_{regs} in VAT (*53*), regulatory mechanisms [e.g., Gata6 in peritoneal macrophages (*57*)], and interaction with other tissue cells [e.g., T_{reg} -adipocyte interaction through IL-10 (*53*)]}. The exquisite tunability reflected by these programs led in turn to the exploration of how they are diversely yet stably imprinted on a cell type based on its local environment (*1*). Two distinct mechanisms (or a blend thereof) can in principle underlie this phenomenon: a preprogrammed set of states, both preceding and succeeding tissue residence, and/or an environmentally directed process, either permanent (tissue-resident differentiation) or signal-dependent (plasticity).

Epigenomic analysis of macrophages from different tissues strongly supports the environmentally directed, signal-dependent model. Tissue-resident macrophages have distinct enhancer landscapes (more so than promoters) in either poised or active state. These enhancers can be substantially, albeit not completely, reprogrammed by environment-specific signals in either bone-marrow transplant, tissue-transfer experiments, or ex vivo manipulations (*18*, *21*). As for T_H cell plasticity, such differential enhancer usage may underlie the preponderance of genetic variants associated with human immune disease in enhancer regions (*48*).

Combinatorial regulation by TFs helps in turn to establish transcriptional programs for tissue-resident macrophages. During differentiation, a set of lineage-determining "pioneer" factors delineates cell-type–specific enhancers through nucleosome repositioning and recruitment of histone-modifying enzymes. In macrophages (*18*, *21*), some enhancers are indeed shared across all tissues but are only poised. Signal-dependent TFs modulate the activity of this preexisting enhancer repertoire to achieve context-dependent gene expression. Other enhancers are formed "de novo" to create epigenetic memory of tissue residence. Thus, signal-dependent (*40*), tissue-specific TFs either can work cooperatively with the macrophage pioneer factor PU.1 to form new enhancers or can activate poised enhancers that have been formed and prebound by PU.1. This mechanism can also account for transient tissue-resident programs.

Tissue-specific T_{regs} also exhibit cooperation between tissue-specific and lineage-specific factors (*18*, *21*, *40*, *53*). For example, peroxisome proliferator–activated receptor γ (PPARγ), the master regulator of adipocyte differentiation, is the key regulator of the tissue-specific program in VAT T_{regs} (*53*). PPARγ in adipose tissue T_{regs} responds to the tissue's signal of insulin and orchestrates the relevant metabolic response, mediated through the same biochemical and molecular mechanisms as in adipocytes. It is tempting to speculate that this intracellular "molecular mirroring" between two different cell types in a single tissue could help synchronize not only their response to signal but also how this signal is precisely processed and affects the same output modules, beyond what could be achieved by intercellular communication alone. Such mirroring could exist between other cell types in tissue, immune and nonimmune.

Perspective: Toward a tissue circuit

The cellular environment is interwoven into a single integrated whole in tissues, bringing together diverse cell types—epithelial, immune, neural, stromal, and more—as they differentiate and respond to each other, microbes, nutrients, and other stimuli. These responses can be transient, permanent, or plastic and include migration. Every aspect of this "tissue circuit," including the proportion of cell types and their states, functions, and interactions, changes as the local environment varies.

Dissecting how cells interact to maintain tissue function requires knowing the census of cell types and states, their biological roles in the tissue, the signals received and emitted by each cell and their effects, and the cascade of events underlying dynamic tissue processes. Addressing these questions requires the ability to profile the individual cells that comprise the tissue, consider their spatial position and physical interactions in faithful biological samples, have computational means to reconstruct molecular-level quantitative models that combine intracellular with intercellular circuits, and have the functional means to test them. Recent technological breakthroughs in single-cell genomics (*59*), spatially resolved profiling (*12*, *13*), systematic genetic perturbations (*15*), and access to tissue biopsies and organoids provide promising steps in that direction.

Analysis at a whole-tissue level should provide an unprecedented view into the cellular and molecular composition of tissues and an understanding of the molecular and functional interactions by which cells cooperate to fulfill tissue function and maintain homeostasis. Ultimately, such an understanding will have the potential to be translated to exceptionally effective new therapies that can restore tissue function and human health.

REFERENCES AND NOTES

1. Y. Okabe, R. Medzhitov, *Nat. Immunol.* **17**, 9–17 (2016).
2. N. Novershtern *et al.*, *Cell* **144**, 296–309 (2011).
3. M. Bonelli *et al.*, *Curr. Top. Microbiol. Immunol.* **381**, 279–326 (2014).
4. M. DuPage, J. A. Bluestone, *Nat. Rev. Immunol.* **16**, 149–163 (2016).
5. M. Panduro, C. Benoist, D. Mathis, *Annu. Rev. Immunol.* **34**, 609–633 (2016).
6. J. T. Gaublomme *et al.*, *Cell* **163**, 1400–1412 (2015).
7. A. K. Shalek *et al.*, *Nature* **498**, 236–240 (2013).
8. A. K. Shalek *et al.*, *Nature* **510**, 363–369 (2014).
9. D. A. Jaitin *et al.*, *Science* **343**, 776–779 (2014).
10. I. Tirosh *et al.*, *Science* **352**, 189–196 (2016).
11. M. Angelo *et al.*, *Nat. Med.* **20**, 436–442 (2014).
12. K. H. Chen, A. N. Boettiger, J. R. Moffitt, S. Wang, X. Zhuang, *Science* **348**, aaa6090 (2015).
13. Z. Liu *et al.*, *Nature* **528**, 225–230 (2015).
14. D. Lara-Astiaso *et al.*, *Science* **345**, 943–949 (2014).
15. O. Parnas *et al.*, *Cell* **162**, 675–686 (2015).
16. B. P. Fairfax *et al.*, *Science* **343**, 1246949 (2014).
17. I. Gat-Viks *et al.*, *Nat. Biotechnol.* **31**, 342–349 (2013).
18. D. Gosselin *et al.*, *Cell* **159**, 1327–1340 (2014).
19. M. N. Lee *et al.*, *Science* **343**, 1246980 (2014).
20. N. Gagliani *et al.*, *Nature* **523**, 221–225 (2015).
21. Y. Lavin *et al.*, *Cell* **159**, 1312–1326 (2014).
22. I. Amit, D. R. Winter, S. Jung, *Nat. Immunol.* **17**, 18–25 (2016).
23. Y. Lavin, A. Mortha, A. Rahman, M. Merad, *Nat. Rev. Immunol.* **15**, 731–744 (2015).
24. T. A. Wynn, A. Chawla, J. W. Pollard, *Nature* **496**, 445–455 (2013).
25. M. Gilchrist *et al.*, *Nature* **441**, 173–178 (2006).
26. N. Yosef, A. Regev, *Cell* **144**, 886–896 (2011).
27. S. L. Foster, D. C. Hargreaves, R. Medzhitov, *Nature* **447**, 972–978 (2007).
28. D. C. Hargreaves, T. Horng, R. Medzhitov, *Cell* **138**, 129–145 (2009).
29. I. Amit *et al.*, *Science* **326**, 257–263 (2009).
30. J. Xue *et al.*, *Immunity* **40**, 274–288 (2014).
31. M. R. Corces *et al.*, *Nat. Genet.* (2016).
32. V. Jojic *et al.*, *Nat. Immunol.* **14**, 633–643 (2013).
33. H. Iwasaki, K. Akashi, *Immunity* **26**, 726–740 (2007).
34. F. Paul *et al.*, *Cell* **163**, 1663–1677 (2015).
35. A. Olsson *et al.*, *Nature* (2016).
36. J. L. Zhao *et al.*, *Cell Stem Cell* **14**, 445–459 (2014).
37. M. T. Baldridge, K. Y. King, M. A. Goodell, *Trends Immunol.* **32**, 57–65 (2011).
38. P. Muranski *et al.*, *Immunity* **35**, 972–985 (2011).
39. C. Wang, M. Collins, V. K. Kuchroo, *Curr. Opin. Immunol.* **37**, 6–10 (2015).
40. Y. Okabe, R. Medzhitov, *Cell* **157**, 832–844 (2014).
41. S. Sakaguchi, D. A. Vignali, A. Y. Rudensky, R. E. Niec, H. Waldmann, *Nat. Rev. Immunol.* **13**, 461–467 (2013).
42. W. Fu *et al.*, *Nat. Immunol.* **13**, 972–980 (2012).
43. V. Proserpio *et al.*, *Genome Biol.* **17**, 103 (2016).
44. M. J. Stubbington *et al.*, *Nat. Methods* **13**, 329–332 (2016).
45. S. Afik, K. B. Yates, K. Bi, S. Darko, J. Godec, U. Gerdemann, L. Swadling, D. C. Douek, P. Klenerman, E. J. Barnes, A. H. Sharpe, W. N. Haining, N. Yosef, Targeted reconstruction of T cell receptor sequence from single cell RNA-sequencing links CDR3 length to T cell differentiation state. *bioRxiv* 2016, 072744 (2016). http://biorxiv.org/content/early/2016/08/31/072744
46. R. Mukasa *et al.*, *Immunity* **32**, 616–627 (2010).
47. Y. Feng *et al.*, *Cell* **158**, 749–763 (2014).
48. K. K. Farh *et al.*, *Nature* **518**, 337–343 (2015).
49. D. Rudra *et al.*, *Nat. Immunol.* **13**, 1010–1019 (2012).
50. N. Yosef *et al.*, *Nature* **496**, 461–468 (2013).
51. M. Ciofani *et al.*, *Cell* **151**, 289–303 (2012).
52. D. Kolodin *et al.*, *Cell Metab.* **21**, 543–557 (2015).
53. D. Cipolletta *et al.*, *Nature* **486**, 549–553 (2012).
54. C. Schiering *et al.*, *Nature* **513**, 564–568 (2014).
55. D. Burzyn *et al.*, *Cell* **155**, 1282–1295 (2013).
56. N. Arpaia *et al.*, *Cell* **162**, 1078–1089 (2015).
57. E. L. Gautier *et al.*, *Nat. Immunol.* **13**, 1118–1128 (2012).
58. O. Matcovitch-Natan *et al.*, *Science* **353**, aad8670 (2016).
59. E. Z. Macosko *et al.*, *Cell* **161**, 1202–1214 (2015).

ACKNOWLEDGMENTS

A.R. was supported by the Howard Hughes Medical Institute. N.Y. was supported by NIH grants U01MH105979 and U01HG007910. A.R. is a member of the science advisory board of ThermoFisher Scientific and Syros Pharmaceuticals and a consultant for Driver Group.

10.1126/science.aaf5453

REVIEW

Exposing the exposures responsible for type 2 diabetes and obesity

Paul W. Franks[1,2,3] and Mark I. McCarthy[4,5]*

The rising prevalences of type 2 diabetes and obesity constitute major threats to human health globally. Powerful social and economic factors influence the distribution of these diseases among and within populations. These factors act on a substrate of individual predisposition derived from the composite effects of inherited DNA variation and a range of environmental exposures experienced throughout the life course. Although "Western" lifestyle represents a convenient catch-all culprit for such exposures, effective treatment and prevention will be informed by characterization of the most critical, causal environmental factors. In this Review, we examine how burgeoning understanding of the genetic basis of type 2 diabetes and obesity can highlight nongenetic exposures that drive development of these conditions.

About 10% of the global population already has type 2 diabetes (T2D) or is likely to develop it, and ~40% of adults are overweight or obese. Current strategies for prevention are limited in scope and effectiveness, and the persistently high prevalences of both conditions speak to the inadequacies of available therapeutic options.

Individual predisposition to these conditions has a strong genetic basis. Consensus estimates of heritability for obesity and T2D are ~70 and ~35%, respectively (*1*, *2*), and scores of genetic variants are now known to influence risk (*3*, *4*). T2D and obesity are, however, also "diseases of lifestyle." Rates of both have risen sharply over recent decades in tandem with widespread social changes, and these observations are supported by randomized lifestyle intervention trials that demonstrate convincing reductions in body weight and delayed progression to T2D in high-risk adults (*5*). The environmental exposures driving the development of these conditions must be both impactful, given the rapid shifts in disease prevalence that they have engendered, and pervasive, given that no contemporary industrialized population has been spared.

Epidemiological studies have highlighted many potential environmental "perpetrators" (Fig. 1), the combination of physical inactivity and caloric excess being the most prominent. There are, however, many other plausible environmental factors for which a role has been advanced, including sleep deprivation, endocrine disruptors, and smoking (*6*). The core limitations of observational studies—confounding, bias, and reverse causality—hinder efforts to determine which among these highly correlated exposures is truly causal (*7*). Yet clearer definition of these critical exposures is a prerequisite if more effective, targeted interventions are to be implemented at both the personal and the population levels.

The "nature versus nurture" framework for describing the contributions of genetic and environmental influences has been replaced by a more nuanced view that recognizes that the mechanisms through which environmental and genetic variation modify risk may be shared (Fig. 2). Environmental exposures that disturb cellular and physiological processes and influence individual predisposition to diseases such as T2D are likely to do so through active, or reactive, modulation of genome function (through changes in DNA methylation and transcription, for example).

Genetics of T2D and obesity

T2D is the consequence of reduced insulin secretion from pancreatic β cells, typically observed in the context of insensitivity to the peripheral actions of insulin. Such insulin insensitivity is usually compounded by excess lipid deposition, particularly in nonstandard sites such as the liver and muscle. Physiological and genetic data from humans and rodents support a model whereby multiple concurrent molecular, cellular, and physiological processes contribute to the development of disease (Fig. 3).

Rare variants of large effect are causal for extreme phenotypes such as neonatal diabetes and severe early-onset obesity, but these contribute little to the population burden of T2D and obesity. Genome-wide association studies (GWAS) have identified scores of loci containing common variants robustly associated with T2D and obesity (*3*, *4*), and elucidation of the mechanisms through which these operate provides novel pathophysiological insights. With notable exceptions (*8*), these common variant signals are of modest effect, collectively explaining only a minority of the overall genetic risk [~20% for T2D and <5% for body-mass index (BMI)] (*3*, *4*). Much of the remainder can be attributed to a large number of common variant signals with individual effects that are undetectable at stringent levels of statistical significance; for BMI, these underlie ~40% of overall variance (*9*). Sequence-based analyses are extending discoveries to variants of lower frequency, but the contribution that these make to population variation in the risk of T2D and obesity appears to be limited (*10*, *11*).

This Review focuses on the application of this improved understanding of genetically driven variation in disease risk to provide mechanistic insights into the causal impact of proposed environmental exposures and thereby to define more effective interventions. These applications may, for example, take genetic variants that mimic environmental exposures and use the principles of Mendelian randomization to determine whether those exposures are likely to be causal for disease (*7*). Alternatively, they may aim to detect gene-environment interaction effects, whereby the impact of a given genetic variant is modified by the environmental milieu (or the reverse). Data from rodent and cellular models can also provide clues as to mechanism and causation, but their value is crucially dependent on the extent to which these

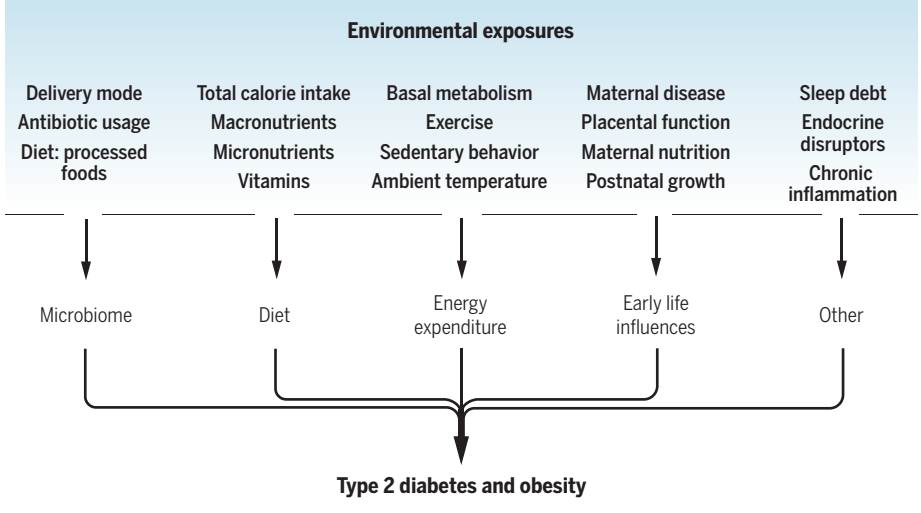

Fig. 1. Examples of environmental exposures and mechanisms implicated in the development of T2D and obesity. Inclusion in this figure does not indicate that a causal connection has been demonstrated.

[1]Department of Clinical Sciences, Genetic and Molecular Epidemiology Unit, Lund University, Malmö, Sweden. [2]Department of Public Health and Clinical Medicine, Umeå University, Umeå, Sweden. [3]Department of Nutrition, Harvard T.H. Chan School of Public Health, Boston, MA 02115, USA. [4]Oxford Centre for Diabetes, Endocrinology and Metabolism, University of Oxford, Oxford, UK. [5]Wellcome Trust Centre for Human Genetics, University of Oxford, Oxford, UK.
***Corresponding author. Email: mark.mccarthy@drl.ox.ac.uk**

GRAPHIC: K. SUTLIFF/*SCIENCE*

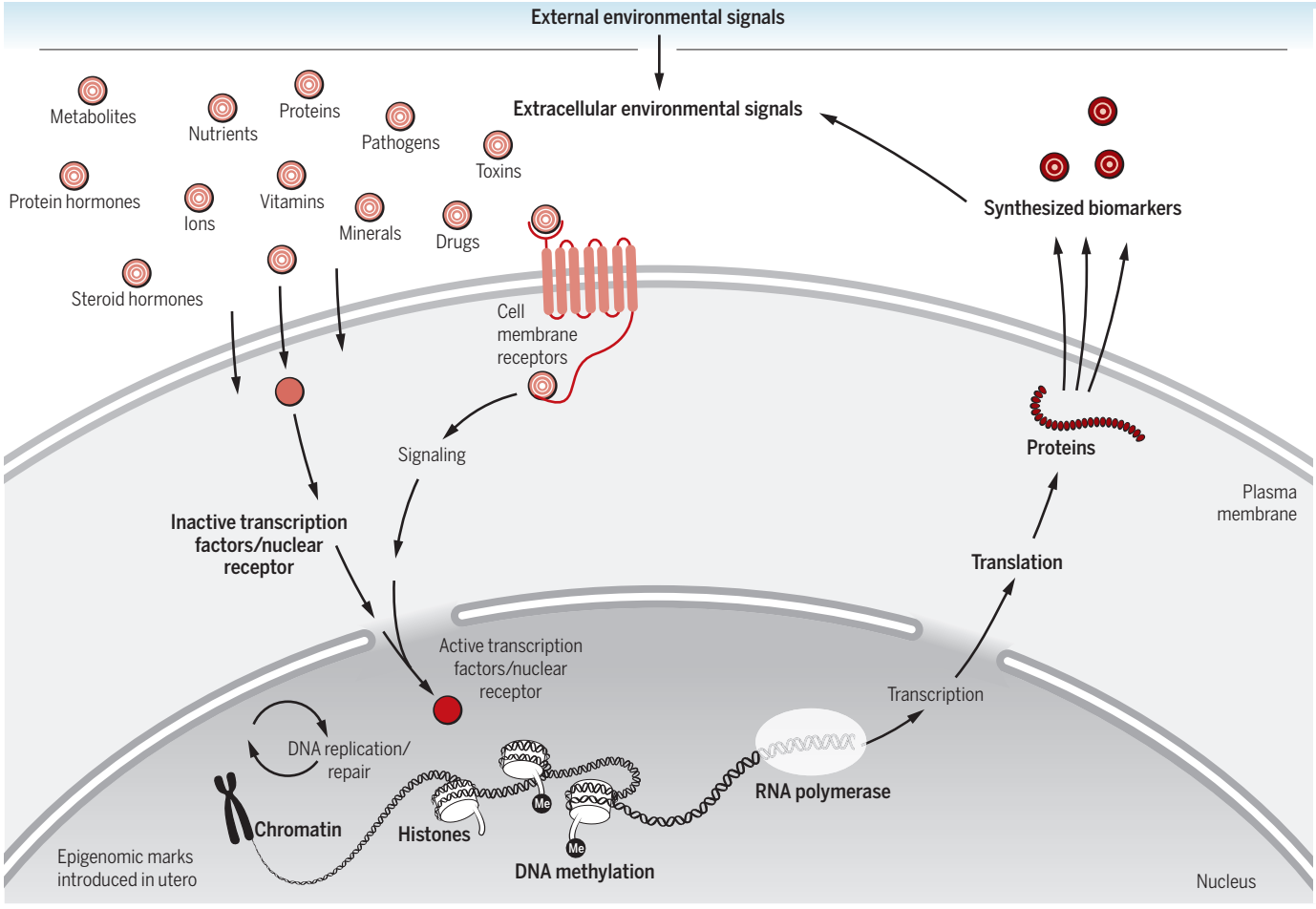

Fig. 2. Environmental exposures act in a range of ways to perturb genome function. The joint effects of genetic and environmental factors can, for example, drive variations in ligand binding efficiency, membrane channeling, DNA replication and repair, or methylation. Variations in the "intrinsic environment," reflected in metabolite, proteome, or microbiome profiles, for example, may also perturb genome function, thus generating complex feedback loops of gene-environment interactions.

models recapitulate exposures and processes that are relevant to humans.

Genetics and diet

Obesity is a major risk factor for the development of T2D. Most people with T2D are overweight or obese at the point of diagnosis, and interventions that reduce body weight lower diabetes risk (*5*). Those who develop T2D despite having a normal body weight tend to have more prominent defects in insulin secretion, which translate into a more rapid requirement for exogenous insulin treatment. In some individuals, this reflects patterns of genetic predisposition that have features of both T1D and T2D and concomitant loss of β-cell capacity caused by autoimmune insult; in others, T2D with a lean body composition simply reflects one end of the spectrum of T2D presentation.

The consensus is that increased energy intake, facilitated by widespread availability of energy-dense foods, has contributed, in concert with lower energy expenditure (e.g., reduced physical activity), to trends of positive energy balance (*12*). However, human diets are complex, and there are many specific dietary components that have, at various times, been implicated in T2D risk (Fig. 1). The details have been debated, most recently with respect to the relative dangers of diets rich in processed carbohydrates (especially sugars) and fats. Nevertheless, there is no compelling evidence from epidemiological or clinical trial data that any given dietary configuration is more effective at reducing long-term body weight (*13*), and it is becoming clear that although some types of dietary fat may be metabolically harmful, others may in fact be protective (*14*).

What insights can genetic data provide? Variants discovered by GWAS to influence overall adiposity are enriched for a role in hypothalamic control of energy balance, with overrepresentation of pathways involved in both food intake and physical activity (*3*). Common variation at the *FTO* locus (which accounts for ~1% of population variance in BMI) affects energy balance (*15*), and BMI-raising *FTO* alleles correlate with higher dietary protein intake in adults, but not children (*15*), and with higher total energy intake in children (*15*) and adults (*16*). More recently, BMI-associated alleles at this locus have been linked to increased expression of *IRX3* and *IRX5* during early adipocyte differentiation and a reduction in the potential to dissipate energy through adipocyte browning, raising the possibility that differences in food choice and energy intake associated with some BMI-risk variants are the consequence, rather than the direct cause, of primary alterations in adipose mass (*17*). Although taste, macronutrient preference, and food patterns are under some degree of genetic control (*18*), these variants have no evident impact on the risk of T2D or obesity. This highlights the complex ways in which adiposity loci such as *FTO* may act and illustrates the need for careful partitioning of causal from noncausal relationships.

Most of the ~100 loci known to influence T2D risk (*4*) do so through primary effects on insulin secretion, pointing to underlying defects in pancreatic islet development and/or function; only a minority act through reducing insulin action. Among these T2D loci, the most obvious mechanistic connection to diet involves coding variation within *PPARG*. This gene encodes a nuclear receptor implicated in insulin signaling, adipogenesis, and the matching of lipid storage provision to nutritional state. Modest interactions

GRAPHIC: K. SUTLIFF/*SCIENCE*

between *PPARG* variants and dietary fat type [mainly polyunsaturated fatty acids (PUFAs)] with respect to T2D risk have been reported, but these remain unconfirmed (*19*), and there is no evidence of positive clinical outcomes arising from individualized approaches to prevention or management of T2D predicated on *PPARG* variation.

Inherent challenges associated with the accurate assessment of nutritional intake complicate efforts to define the contribution of diet to the development of T2D and obesity. Genetic data can help to address some of these challenges, particularly with respect to the effects of micronutrients. Vitamin D [25(OH)D] deficiency, for example, has long been touted as a cause of T2D on the basis of abundant observational evidence (*20*) and experiments showing positive effects of vitamin D supplementation on insulin secretion (*21*). Genetic variants that influence vitamin D metabolism can be used to define population subgroups that will experience lifelong differences in 25(OH)D exposure. Because allocation to the high- and low-exposure groups reflects the chance segregation of alleles at fertilization (hence the term Mendelian randomization), such groups should be, subject to some critical assumptions, matched for environmental and other factors that might otherwise confound interpretation (*7*). Comparisons between such genotype-defined groups indicate that although BMI has a causal impact on 25(OH)D levels (*22*), there is little or no causal relationship between variation in 25(OH)D levels and T2D (*23*). This is consistent with recent randomized controlled trial data that indicate no clinically relevant effects of supplemental vitamin D on glycemic indices in people with or without T2D (*24*).

Increasing numbers of similar genetic "instruments" are being identified that serve as proxies for environmental exposures relevant to obesity and T2D. For example, failure to detect overlap between the sets of genetic variants influencing T2D and obesity and those influencing regulatory inflammatory and immune function argues strongly that the chronic inflammation characteristic of T2D and obesity is a reaction to, rather than a cause of, these conditions. More recently, identification of variants that influence sleep behavior has enabled dissection of causal relationships between sleep disturbance and metabolic disease (*25*).

A further opportunity for genetic insight is afforded by populations with distinct patterns of environmental exposure. Greenlandic Inuits, for example, have needed to survive in a cold climate on a marine diet rich in omega-3 PUFAs. This has driven genetic adaptation, with selection for variation at loci that influence fatty acid metabolism and brown fat differentiation (*26*). Some of these historically advantageous adaptations now seem to promote obesity and T2D (*8*). Homozygote carriers of the nonsense *p.Arg684Ter* allele in the *TBC1D4* gene, which is common among the Inuit but rare elsewhere, are at a severalfold increased risk of T2D. The underlying mechanism for this risk appears to involve muscle-selective loss of the long isoform of TBC1D4, leading to reduced insulin-stimulated GLUT4-mediated glucose uptake into muscle and marked postprandial (but not fasting) hyperglycemia.

In overfeeding studies in twins (*27*), phenotypic responses to dietary interventions demonstrate strong familial clustering in weight change; this may reflect the modifying effects of genetic variants on the response to dietary manipulation (that is, gene-environment interaction). Here we restrict the use of the term gene-environment interaction to situations of evident nonadditivity (that is, where the joint effects of a pair of specified genetic and nongenetic exposures are significantly greater or less than the sum of their individual effects). Identification of robust (independently replicated) gene-environment interaction effects could provide the basis for personalization of disease prevention and management. However, the detection of gene-environment interactions in humans is prone to multiple sources of bias and confounding (*28*), and power is constrained by imprecision in the measurement of exposures and outcomes (*29*).

Nevertheless, there is some evidence that "healthy" diets modify the impact of individual BMI-associated variants in observational studies (*30*) and clinical trials (*31*). Interactions have been reported between BMI-associated genetic risk scores and diverse exposures including sugar-sweetened beverages (*32*), fried foods (*33*), and television viewing (*34*), though replication data are sparse. The most comprehensive epidemiological study of gene-diet interactions in T2D, a prospective study involving ~4 million person-years of follow-up in 340,000 participants (*35*), provided no evidence that a Mediterranean diet influenced the individual or collective effects of known T2D variants.

Clinical trials are often thought to overcome the limitations of epidemiology that might lead to confounded results, but few trails account adequately for the effects that adherence and/or compensatory behaviors might have on metabolic traits. Lifestyle interventions typically occupy <5% of waking hours, and how participants behave during the rest of the day—the food they eat, the physical activities they pursue, and the quality of their sleep—is likely to contribute to heterogeneous responses (*36*). These limitations are hard to overcome, because lifestyle interventions, unlike drug interventions, cannot be easily masked, and the ubiquitous monitoring of behavior remains challenging. Nevertheless, the most comprehensive trial-based assessment of gene-lifestyle interactions in T2D incidence, which involved 2843 adults from the Diabetes Prevention Program, found no interaction between genetic measures of T2D risk and intervention with either metformin or lifestyle changes (*37*). Overall, on the evidence as it stands now, there is no compelling basis for using gene-diet interaction data to support clinically useful individualization of management for these conditions.

Genetics and energy expenditure

The processes that contribute to overall energy expenditure (including those related to basal metabolism, exercise, nonexercise activity thermogenesis, and food-related thermogenesis) are obvious candidates with respect to obesity risk. There is, however, little evidence to indicate that the T2D- and obesity-risk variants identified by GWAS directly influence these processes, and many of the candidate genes implicated by earlier studies (e.g., those encoding the uncoupling proteins) have not been substantiated in the much larger studies. Although intervention studies have demonstrated that phenotypic responses to exercise are familial (*38*), there has been little success

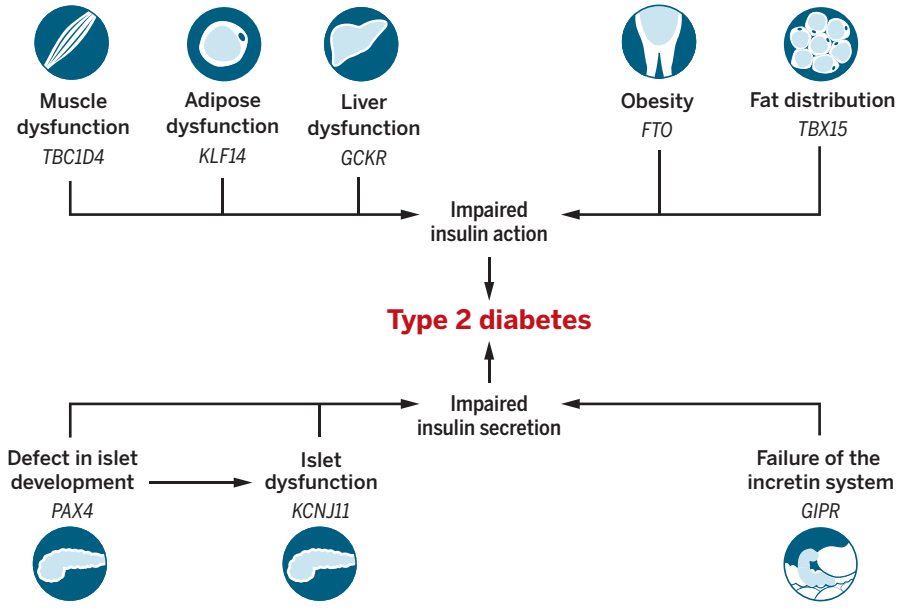

Fig. 3. Multiple processes contribute to the development of T2D. Examples are shown of T2D-associated loci for which the evidence points to specific mechanisms. At some of these loci, the specific effector gene has not yet been defined, so the gene labels are purely indicative.

GRAPHIC: K. SUTLIFF/*SCIENCE*

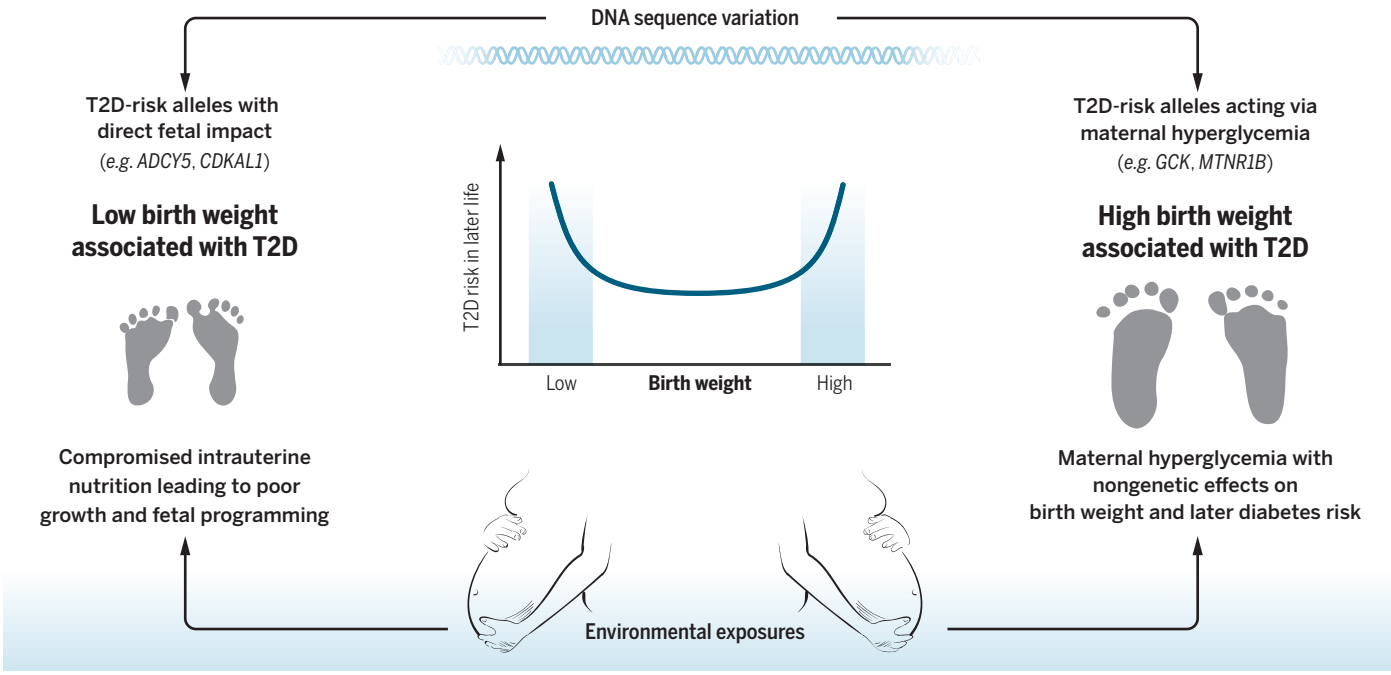

Fig. 4. Mechanisms underlying the observed relationships between extremes of fetal growth and subsequent risk of T2D. Distinct genetic and nongenetic processes are implicated in both arms of the U-shaped curve that describes the relationship between birth weight and future T2D risk.

in identifying specific variants that, at the population level, influence exercise tolerance or modulate how exercise influences weight gain or metabolism.

Interactions between BMI-associated variation and measures of physical activity that influence adult adiposity appear to be more robust than those involving dietary exposures or diabetes outcomes. The BMI effect associated with *FTO* variation has consistently been shown to be weaker in physically active than in inactive carriers (*39*), and there have been similar interactions found for sets of obesity-associated variants (*40*). However, such studies are challenging to perform and interpret (*41*) and need further replication. Despite promising epidemiological data, the largest clinical trial analysis found no evidence that *FTO* variation influences weight loss after lifestyle intervention (*31*).

Our assessment is that there is only meager evidence to date that common genetic variation modifies the effects of lifestyle exposures with respect to the development or management of obesity or T2D. This may be because the interaction effects are nonexistent or of small magnitude, or because our research methods and available data sets are insufficient to characterize the complexity of the interactions (Fig. 2).

Genetics and the microbiome

There has been an explosion of interest in the role of the gut microbiome in the development of T2D and obesity. Variation in the diversity and composition of gut microflora, in part reflecting personal histories of antibiotic exposure and dietary intake, has been tied to individual risk, as well as to the sharp rise in the prevalences of these conditions (*42*, *43*). In addition, the metabolic benefits of metformin and bariatric surgery have been ascribed to their impact on the microbiome (*44*, *45*). In rodents, manipulation of the microbiome (e.g., through fecal transplantation) can lead to weight loss and diabetes remission (*42*), though evidence that similar interventions are effective in humans remains limited (*46*). However, an algorithm that integrates personal clinical (biochemistry and anthropometry), behavioral (dietary preferences and physical activity), and microbiome data has been shown to predict an individual's metabolic response to food intake and to provide dietary recommendations that limit glycemic excursions after meals (*47*).

Several studies have detected marked shifts in microbiome content among those who are obese or diabetic, though the data are inconsistent (*48*, *49*). A variety of mechanisms for the metabolic effects of microbiome diversity have been proposed, including impacts on short-chain fatty acid production, bile acid metabolism, and inflammation. However, these studies tend not to distinguish between microbiome variation that is causal for T2D and/or obesity and that which is a function of the disease or its treatment or merely a consequence of correlated exposures. The range of environmental factors influencing gut microbiota is considerable (*50*), and, in the case of T2D, early reports of disease-associated variation in microbiome content proved to be confounded by metformin treatment, which has a marked impact on microbiome integrity (*44*). Characterization of the impact of host genome variation on microbiome diversity and content (*51*) will provide genetic instruments that will support efforts to define, much more precisely than has been hitherto possible, the extent to which genetic variants that influence individual risk of T2D and obesity do so through direct, or indirect, impacts on the gut microbiome.

Genetics and early life environment

Genetic and environmental exposures offer sharply contrasting explanations for the widely replicated associations between low birth weight (and early growth) and increased propensity to develop obesity, T2D, and cardiovascular disease in later life (*52*). The dominant explanation has been provided by the developmental origins (or "fetal programming") hypothesis, which attributes this relationship to the long-term effects of restricted intrauterine nutrient availability (reflecting maternal nutrition and placental function) on the risk of metabolic disease decades later. This hypothesis, which is consistent with observational studies in humans exposed to severe nutritional restriction during early life, is also supported by experimental studies in rodents. These studies have focused attention on the detection of methylation signatures that might convey the "memory" of early life events across the life course (*52*). However, most of the T2D- and obesity-associated methylation signals detected in blood-based epigenomic studies have either failed to be replicable or appear to be reactive or confounded, not causal (*53*). One exception may involve *TXNIP*, which encodes a thioredoxin-reducing protein implicated in diverse metabolic processes including nutrient sensing, islet function, and energy expenditure (*54*): Methylation in this region has been associated with both prevalent and incident T2D (*55*), though, as yet, not with early growth restriction.

In populations in which maternal obesity and gestational diabetes are frequent, the relationship

GRAPHIC: K. SUTLIFF/*SCIENCE*

between early growth and adult T2D is best described as U-shaped (*56*), in that both high and low birth weights are linked to T2D in later life. The elevated T2D risk in those with high birth weight likely reflects the impact of maternal hyperglycemia. Excessive placental transfer of glucose from hyperglycemic mothers not only promotes fetal growth (insulin is a major trophic factor in early life) but also drives a direct, nongenetic increase in offspring propensity to T2D (*57*), possibly because of the additional metabolic burden imposed on the developing endocrine pancreas.

Although the fetal programming hypothesis is alluring, the effects of shared genetic variants offer a complementary explanation for these observed relationships. Carriers of variant alleles that compromise insulin secretion or action and that therefore increase risk of T2D in later life, will also, given insulin's trophic effects, tend to exhibit reduced fetal growth (reproducing the low-birth-weight arm of the U). Those same risk alleles may, when present in the mother, contribute to maternal hyperglycemia, providing a potential mechanistic explanation for the high-birth-weight arm (*58*). Such genetically mediated links between early growth and subsequent metabolic dysfunction have been well documented in families segregating rare monogenic forms of diabetes, such as glucokinase MODY (maturity onset diabetes of the young) (*58*).

Common alleles implicated in T2D disproportionately influence variation in birth weight, though the directional relationships are complex (*59*). Children carrying the T2D-risk allele at some loci, such as *MTNR1B* and *GCK*, have higher birth weights, reflecting a predominant effect of those variants on maternal hyperglycemia. At other loci, such as *ADCY5* and *CDKAL1*, the T2D-risk allele lowers birth weight, a pattern consistent with direct fetal growth restriction. These explanations fit with the epidemiological data: In 236,000 UK Biobank participants, a paternal history of T2D was associated with reduced birth weight and a maternal history with elevated birth weight (*60*).

The model that emerges is one in which the relationship between early growth and later disease is influenced by an intimate weave of genetic and environmental mechanisms connecting both extremes of early growth and birth weight to subsequent T2D (Fig. 4). The direct effects of fetal genotype on both early growth and later T2D are modulated by the countervailing effects of the same genotypes in the mother (acting at least in part through the fetal environment) and by other nongenetic influences that affect fetal nutrition. This relationship may turn out to be even more mechanistically complex, subject to the contribution of transgenerational epigenetic influences (*61*) and/or environmentally triggered polyphenism (*62*).

Where next?

One-size-fits-all diet and exercise recommendations for weight loss and diabetes prevention elicit uneven and unpredictable responses, and the development of effective personalized approaches is a highly desirable goal that genetics might help us to achieve. However, at present, we lack definitive insight into the specific components of modern lifestyles that are most responsible for T2D and obesity risk, as well as the genetic variants that reliably predict individual metabolic or adiposity responses to common exposures, and that could justifiably be used to personalize lifestyle interventions.

Improved specification of the genetic basis of disease predisposition (through whole-genome sequencing) and more detailed temporal assessments of exposures and outcomes (combining near-continuous objective measurements of movement, sleep, and diet collected with biomarker technologies), conducted in ever larger biobanks and health care settings, will allow for the detection of mechanistic overlap and interaction and greater clarity regarding key causal exposures. An important opportunity exists in tying these data to robust, accessible, molecular signatures of individual disease trajectory, which are able to capture the summated, actual (rather than predicted) impact of genetic and environmental influences on a given individual at a given point in time. As well as quantifying risk, these signatures may provide a more nuanced classification of disease etiology and support more precise, personalized diagnostic assignment.

The discovery of such signatures will require investment in the analysis of longitudinal repeated-measures data from large population samples and trials. By enabling more accurate specification of individual disease risk and molecular pathology, such signatures have the potential to support more effective targeting of preventative and therapeutic strategies. By combining these approaches—definition of the key causal exposures and individualization of prognostic and diagnostic information—we can hope to move closer to the desired goals of effective prevention and treatment of T2D and obesity.

REFERENCES AND NOTES

1. G. Hemani *et al.*, *Am. J. Hum. Genet.* **93**, 865–875 (2013).
2. G. Willemsen *et al.*, *Twin Res. Hum. Genet.* **18**, 762–771 (2015).
3. A. E. Locke *et al.*, *Nature* **518**, 197–206 (2015).
4. DIAbetes Genetics Replication And Meta-analysis (DIAGRAM) Consortium, Asian Genetic Epidemiology Network Type 2 Diabetes (AGEN-T2D) Consortium, South Asian Type 2 Diabetes (SAT2D) Consortium, Mexican American Type 2 Diabetes (MAT2D) Consortium, Type 2 Diabetes Genetic Exploration by Next-generation sequencing in multi-Ethnic Samples (T2D-GENES) Consortium, A. Mahajan *et al.*, *Nat. Genet.* **46**, 234–244 (2014).
5. Diabetes Prevention Program Research Group, *Lancet* **374**, 1677–1686 (2009).
6. S. W. Keith *et al.*, *Int. J. Obesity* **30**, 1585–1594 (2006).
7. G. D. Smith, N. Timpson, S. Ebrahim, *Ann. Med.* **40**, 524–541 (2008).
8. I. Moltke *et al.*, *Nature* **512**, 190–193 (2014).
9. J. Yang *et al.*, *Nat. Genet.* **47**, 1114–1120 (2015).
10. V. Agarwala, J. Flannick, S. Sunyaev, D. Altshuler, *Nat. Genet.* **45**, 1418–1427 (2013).
11. C. Fuchsberger *et al.*, *Nature* **536**, 41–47 (2016).
12. L. J. Orozco *et al.*, *Cochrane Database Syst. Rev.*, CD003054 (2008).
13. F. M. Sacks *et al.*, *N. Engl. J. Med.* **360**, 859–873 (2009).
14. F. Qian, A. A. Korat, V. Malik, F. B. Hu, *Diabetes Care* **39**, 1448–1457 (2016).
15. T. Tanaka *et al.*, *Am. J. Clin. Nutr.* **97**, 1395–1402 (2013).
16. Q. Qi *et al.*, *Hum. Mol. Genet.* **23**, 6961–6972 (2014).
17. M. Claussnitzer *et al.*, *N. Engl. J. Med.* **373**, 895–907 (2015).
18. T. Pallister *et al.*, *Twin Res. Hum. Genet.* **18**, 793–805 (2015).
19. L. Palla, J. P. Higgins, N. J. Wareham, S. J. Sharp, *Am. J. Epidemiol.* **171**, 1225–1232 (2010).
20. L. Ceglia *et al.*, *Eur. J. Nutr.* 10.1007/s00394-015-1066-z (2015).
21. S. Inomata, S. Kadowaki, T. Yamatani, M. Fukase, T. Fujita, *Bone Miner.* **1**, 187–192 (1986).
22. K. S. Vimaleswaran *et al.*, *PLOS Med.* **10**, e1001383 (2013).
23. Z. Ye *et al.*, *Lancet Diabetes Endocrinol* **3**, 35–42 (2015).
24. Y. H. Krul-Poel *et al.*, *Diabetes Care* **38**, 1420–1426 (2015).
25. S. E. Jones *et al.*, *PLOS Genet.* **12**, e1006125 (2016).
26. M. Fumagalli *et al.*, *Science* **349**, 1343–1347 (2015).
27. C. Bouchard *et al.*, *N. Engl. J. Med.* **322**, 1477–1482 (1990).
28. P. W. Franks, G. Paré, *Curr. Diabetes Rep.* **16**, 57 (2016).
29. M. Y. Wong, N. E. Day, J. A. Luan, N. J. Wareham, *Stat. Med.* **23**, 987–998 (2004).
30. J. A. Nettleton *et al.*, *Hum. Mol. Genet.* **24**, 4728–4738 (2015).
31. G. D. Papandonatos *et al.*, *Diabetes* **64**, 4312–4321 (2015).
32. Q. Qi *et al.*, *N. Engl. J. Med.* **367**, 1387–1396 (2012).
33. Q. Qi *et al.*, *BMJ* **348**, g1610 (2014).
34. Q. Qi *et al.*, *Circulation* **126**, 1821–1827 (2012).
35. C. Langenberg *et al.*, *PLOS Med.* **11**, e1001647 (2014).
36. M. I. Goran, E. T. Poehlman, *Am. J. Physiol.* **263**, E950–E957 (1992).
37. M. F. Hivert *et al.*, Diabetes Prevention Program Research Group, *Diabetes* **60**, 1340–1348 (2011).
38. C. Bouchard, T. Rankinen, *Med. Sci. Sports Exercise* **33**, S446–S451, discussion S452–S453 (2001).
39. T. O. Kilpeläinen *et al.*, *PLOS Med.* **8**, e1001116 (2011).
40. S. Ahmad, T. V. Varga, P. W. Franks, *Hum. Hered.* **75**, 106–115 (2013).
41. S. Ahmad *et al.*, *PLOS Genet.* **9**, e1003607 (2013).
42. S. Ussar *et al.*, *Cell Metab.* **22**, 516–530 (2015).
43. L. M. Cox *et al.*, *Cell* **158**, 705–721 (2014).
44. K. Forslund *et al.*, *Nature* **528**, 262–266 (2015).
45. A. Palleja *et al.*, *Genome Med* **8**, 67 (2016).
46. A. Vrieze *et al.*, *Gastroenterology* **143**, 913–6.e7 (2012).
47. D. Zeevi *et al.*, *Cell* **163**, 1079–1094 (2015).
48. F. H. Karlsson *et al.*, *Nature* **498**, 99–103 (2013).
49. J. Qin *et al.*, *Nature* **490**, 55–60 (2012).
50. G. Falony *et al.*, *Science* **352**, 560–564 (2016).
51. J. K. Goodrich *et al.*, *Cell* **159**, 789–799 (2014).
52. K. M. Godfrey, P. D. Gluckman, M. A. Hanson, *Trends Endocrinol. Metab.* **21**, 199–205 (2010).
53. K. J. Dick *et al.*, *Lancet* **383**, 1990–1998 (2014).
54. H. Parikh *et al.*, *PLOS Med.* **4**, e158 (2007).
55. J. C. Chambers *et al.*, *Lancet Diabetes Endocrinol.* **3**, 526–534 (2015).
56. O. Naess *et al.*, *Eur. Heart J.* **34**, 3427–3436 (2013).
57. D. J. Pettitt *et al.*, *Diabetes Care* **31**, 2126–2130 (2008).
58. A. T. Hattersley, J. E. Tooke, *Lancet* **353**, 1789–1792 (1999).
59. M. Horikoshi *et al.*, *Nat. Genet.* **45**, 76–82 (2013);).
60. J. S. Tyrrell, H. Yaghootkar, R. M. Freathy, A. T. Hattersley, T. M. Frayling, *Int. J. Epidemiol.* **42**, 1714–1723 (2013).
61. G. E. Blake, E. D. Watson, *Curr. Opin. Chem. Biol.* **33**, 101–107 (2016).
62. K. Dalgaard *et al.*, *Cell* **164**, 353–364 (2016).

ACKNOWLEDGMENTS

M.I.M. is a Wellcome Trust Senior Investigator. He acknowledges funding from the Wellcome Trust (grant 098381), European Commission (grant HEALTH-F4-2007-201413), Medical Research Council (grants MR/L020149/1 and MR/M004422/1), and National Institutes of Health (grants DK098032 and DK105535) for research related to the contents of this review. P.W.F. holds a professorship from EXODIAB (Excellence in Diabetes Research in Sweden). He acknowledges funding from the European Commission (grants CoG-2015_681742_NASCENT, IMI_JU_2010_DIRECT, and IMI_JU_2016_RHAPSODY), Swedish Research Council (Distinguished Young Researchers Award in Medicine), Swedish Heart-Lung Foundation, Swedish Diabetes Association, European Foundation for the Study of Diabetes, and Novo Nordisk Foundation for research related to the contents of this review. M.I.M. is a member of advisory panels for Pfizer and Novo Nordisk and has received research support from Pfizer, Roche, Novo Nordisk, Eli Lilly, AstraZeneca, Sanofi Aventis, Johnson & Johnson, Roche, Servier, Takeda, and Boehringer Ingelheim. P.W.F. has been a member of advisory panels for Eli Lilly and Sanofi Aventis and has received research support from Novo Nordisk, Eli Lilly, Sanofi Aventis, Johnson & Johnson, Servier, and Boehringer Ingelheim.

10.1126/science.aaf5094

RESEARCH

MIF is a death effector assisting in DNA breakdown

Wang et al., *p. 82*

IN *SCIENCE* JOURNALS

Edited by **Caroline Ash**

Archaea make methane with a tungsten-containing enzyme.

CREDITS: (TOP TO BOTTOM) WANG *ET AL.*; KEVIN SCHAFER/ALAMY STOCK PHOTO

STRUCTURAL BIOLOGY

The long and winding road to methane

The process by which archaea make methane involves a series of reactions and enzymes. First, CO_2 and methanofuran (MFR) are reduced to formyl-MFR by an as yet unresolved mechanism. Wagner *et al*. solved the x-ray crystal structure of a tungsten-containing formyl-MFR dehydrogenase complex. Two active sites in the complex are separated by a 43-Å tunnel, which is responsible for transferring the formate made after CO_2 reduction. The complex also contains a chain of 46 iron-sulfur clusters. Although the exact function of this chain is unclear, it may electronically couple the four tungsten redox centers. —NW

Science, this issue p. 114

NEURODEVELOPMENT

Building the human brain

As the brain develops, neurons migrate from zones of proliferation to their final locations, where they begin to build circuits. Paredes *et al*. have discovered that shortly after birth, a group of neurons that proliferates near the ventricles migrates in chains alongside circulatory vessels into the frontal lobes (see the Perspective by McKenzie and Fishell). Young neurons that migrate postnatally into the anterior cingulate cortex then develop features of inhibitory interneurons. The number of migratory cells decreases over the first 7 months of life, and by 2 years of age, migratory cells are not evident. Any damage during migration, such as hypoxia, may affect the child's subsequent physical and behavioral development. —PJH

Science, this issue p. 81; see also p. 38

BIOCATALYSIS

Something like the real thing

Artificial metalloenzymes ideally combine the favorable properties of natural enzymes with the high efficiency of synthetic catalysts. Inserting new metal groups into existing native proteins, however, often leads to poorer overall catalytic efficiency. To break through this limitation, Dydio *et al*. replaced the iron in the heme group of cytochrome P450 with iridium and subjected it to directed evolution. The enzyme catalyzed a range of reactions with kinetics similar to those of the native enzyme. It was also able to functionalize fully unactivated C–H bonds, a reaction that previously has only been mediated by synthetic catalysts. Moreover, the artificial enzyme was stable across temperatures and scales that are used industrially. —NW

Science, this issue p. 102

COGNITION

Apes understand false beliefs

We humans tend to believe that our cognitive skills are unique, not only in degree, but also in kind. The more closely we look at other species, however, the clearer it becomes that the difference is one of degree. Krupenye *et al*. show that three different species of apes are able to anticipate that others may have mistaken beliefs about a situation (see the Perspective by de Waal). The apes appear to understand that individuals have different perceptions about the world, thus overturning the human-only paradigm of the theory of mind. —SNV

Science, this issue p. 110; see also p. 39

SOLAR CELLS

Maintaining a stable phase

For solar cell applications, all-inorganic perovskite phases could be more stable than those containing organic cations. But the band gaps of the former, which determine the electrical conductivity of these materials, are not well matched to the solar spectrum. The cubic structure

of $CsPbI_3$ is an exception, but it is stable in bulk only at high temperatures. Swarnkar *et al.* show that surfactant-coated α-$CsPbI_3$ quantum dots are stable at ambient conditions and have tunable band gaps in the visible range. Thin films of these materials can be made by spin coating with an antisolvent technique to minimize surfactant loss. When used in solar cells, these films have efficiencies exceeding 10%, making them promising for light harvesting or for LEDs. —PDS

Science, this issue p. 92

GEOPHYSICS

Earthquakes get a more flexible source

Earth's surface deforms in part as a result of ruptures along brittle crustal faults that generate earthquakes. Understanding rock deformation in the ductile lower crust and mantle is challenging. Using the densest seismic arrays in the world, Inbal *et al*. have found an unexpected localization of seismicity at these depths under the Newport-Inglewood fault in southern California. The seismicity points to a type of earthquake that may help us understand how ductile deformation operates in this region of Earth. —BG

Science, this issue p. 88

Deep ductile deformation in the lower crust causes localized seismicity.

WATER SUPPLY

Megadrought risk in the American Southwest

Prolonged droughts have long-term negative effects on water resources and agricultural productivity. Such events can be particularly devastating in regions such as the American Southwest, where fresh water is in short supply. Ault *et al.* are able to predict megadrought risk in that region based on how the moisture balance at Earth's surface responds to precipitation and temperature changes simulated by climate models. The findings are alarming, but the authors suggest that dramatic reductions in greenhouse gas emissions could cut megadrought risk by half. —KVH

Sci. Adv. 10.1126.sciadv.1600873 (2016).

CANCER

More than a FLT-ing success in leukemia

Acute myeloid leukemia is a difficult disease to treat under the best of circumstances, and the subtype containing internal tandem duplication of fms-like tyrosine kinase 3 (*FLT3*-ITD) is particularly challenging. In a high-throughput drug screen, Lam *et al*. identified homoharringtonine as a candidate treatment for this type of leukemia and confirmed its effectiveness in cancer cells, mouse models, and patients. Promising results were obtained from a phase II clinical trial that included elderly patients and patients for whom all previous treatments had failed. —YN

Sci. Transl. Med. **8**, 359ra129 (2016).

IN OTHER JOURNALS

Edited by **Sacha Vignieri** *and* **Jesse Smith**

PSYCHOLOGY

Learning physics through vectors

Long before they first learn about Newtonian mechanics, children develop an understanding of how objects interact. They learn that taller objects can hide shorter objects (visual occlusion) and that two objects cannot occupy the same space at the same time (collision). Wang *et al.* examined children's understanding of a third property (support) by investigating whether 7.5- and 8.5-month-old infants were surprised by the stable arrangement of a wide block resting on top of a small cube. When the center of the bottom of the wide block overhung the cube edge, only the older infants were surprised that it did not fall, which may signal the start of learning about the center of mass and gravity. —GJC

Cognition **157**, 100 (2016).

NEUROIMMUNOLOGY

Autoimmunity in narcolepsy

Narcolepsy is a neurological disorder characterized by sleep that can strike at any time, lasting from seconds to minutes. Most narcoleptics experience loss of muscle tone (cataplexy) and have low levels of orexin (hypocretin), a neurotransmitter that promotes wakefulness. Destruction of orexin-producing neurons in the brain is thought to cause narcolepsy. Bernard-Valnet *et al.* report that cytotoxic T cells infiltrate the brain, interact with orexin-producing neurons, and destroy them. The authors engineered a mouse model to express a specific self-antigen in hypothalamic neurons that produce orexin. Cytotoxic T cells that recognize this antigen infiltrated the brain and destroyed these neurons. Consequently, the animals had sleep attacks and cataplectic episodes. This potential autoimmune mechanism may provide targets for narcolepsy therapies. —LDC

Proc. Natl. Acad. Sci. U.S.A. 10.1073/pnas.1603325113 (2016).

NEURODEVELOPMENT

Modular brain construction

The mammalian cerebellum looks complex on the surface, with a stereotypical pattern of

PHOTOS: (LEFT TO RIGHT) PHOTO: ASHLEY COOPER PICS/ALAMY STOCK PHOTO; ZSV3207/ISTOCKPHOTO

ALSO IN *SCIENCE* JOURNALS

Edited by **Caroline Ash**

HEALTH ECONOMICS

Delivering health care to mystery patients

Many families in developing countries do not have access to medical doctors and instead receive health care from informal providers. Das *et al*. used "mystery" patients (trained actors) to test whether a 9-month training program improved the quality of care delivered by informal providers in West Bengal (see the Perspective by Powell-Jackson). The patients did not identify themselves to the providers and were not told which providers had participated in the training program. The results of this blinded assessment showed that medical doctors delivered better care than informal providers but that the training program closed much of the gap. —GJC

Science, this issue p. 80; see also p. 34

CELL DEATH

DNA damage–activated nuclease identified

Cells that experience stresses and accumulate excessive damage to DNA undergo cell death mediated by a nuclear enzyme known as PARP-1. During this process, apoptosis-inducing factor (AIF) translocates to the nucleus and activates one or more nucleases to cleave DNA. Wang *et al*. found that macrophage migration inhibitory factor (MIF) is an AIF-associated endonuclease that contributes to PARP-1–induced DNA fragmentation (see the Perspective by Jonas). In mouse neurons in culture, loss of MIF protected neurons from cell death caused by excessive stimulation. Targeting MIF could thus provide a therapeutic strategy against diseases in which PARP-1 activation is excessive. —LBR

Science, this issue p. 82; see also p. 36

QUANTUM SIMULATION

Spin-orbit coupling in an optical lattice

Studying topological matter in cold-atom systems may bring fresh insights, thanks to the intrinsic purity and controllability of this experimental setting. However, the necessary spin-orbit coupling can be tricky to engineer. Wu *et al*. conceived and experimentally demonstrated a simple scheme that involves only a single laser source and can be continuously tuned between one- and two-dimensional spin-orbit coupling (see the Perspective by Aidelsburger). Although this experiment used bosonic atoms, it is expected that the setup would also work for fermions. —JS

Science, this issue p. 83; see also p. 35

QUANTUM GASES

Sluggish turmoil in the Fermi sea

The nonequilibrium dynamics of many-body quantum systems are tricky to study experimentally or theoretically. As an experimental setting, dilute atomic gases offer an advantage over electrons in metals. In this environment, the heavier atoms make collective processes that involve the entire Fermi sea occur at the sluggish time scale of microseconds. Cetina *et al*. studied these dynamics by using a small cloud of ^{40}K atoms that was positioned at the center of a far larger ^{6}Li cloud. Controlling the interactions between K and Li atoms enabled a detailed look into the formation of quasiparticles associated with K "impurity" atoms. —JS

Science, this issue p. 96

DEVICE TECHNOLOGY

A flatter route to shorter channels

High-performance silicon transistors can have gate channel lengths as short as 5 nm before source-drain tunneling and loss of electrostatic control lead to unacceptable leakage current when the device is off. Desai *et al*. explored the use of MoS_2 as a gate material, given that its electronic properties as thin layers should limit such leakage. A transistor with a 1-nm physical gate was constructed with a MoS_2 bilayer gate and a single-walled carbon nanotube gate electrode. Excellent switching characteristics and an on-off state current ratio of ~10^6 were observed. —PDS

Science, this issue p. 99

BIOINSPIRED MATERIALS

Making nacre shine in the lab

Many of the materials that animals use to make shells and skeletons are built with brittle or soft molecules. They owe their amazing mechanical properties to their layered construction, which is a challenge for synthetic fabrication. Pearly nacre, for example, has proved challenging to make owing to its complex structure of aragonite crystals in an organic matrix. Using an assembly-and-mineralization approach, Mao *et al*. have managed to fabricate nacre in the laboratory (see the Perspective by Barthelat). First, a layered, three-dimensional chitosan matrix is made, within which aragonite nanocrystals are precipitated from a solution containing calcium bicarbonate. —NW

Science, this issue p. 107; see also p. 32

VIRAL INFECTION

Kinase inhibitors for viral encephalitis

Japanese encephalitis virus (JEV) is a mosquito-transmitted flavivirus related to dengue, West Nile, and Zika viruses. The neuroinflammation and severe neurological damage caused by JEV infection can be fatal. Ye *et al.* found that inhibiting kinase signaling pathways reduced inflammatory responses by infected glial cells in culture. Treating infected mice with a JNK kinase inhibitor improved survival and limited neuroinflammation and neuronal death. This strategy offers promise for treating JEV and other neurogenic viruses. —NRG

Sci. Signal. **9**, ra98 (2016).

Mammalian predators can make great pets, but as invasive species, they have big negative impacts on natives.

INVASIVE SPECIES

The problem with our predators

In our modern world, in which people move themselves and their goods across the entire globe, species invasions have become commonplace. Such invasions have varying degrees of impacts, with some species actually performing important functional replacements and others driving native species to extinction. Doherty *et al*. look at one of the most damaging groups, invasive mammalian predators. Just as predators in their own habitats have strong structuring effects, invading predators have large impacts on native species. Such effects are strongest and most damaging in island environments. Finding that islands should be the highest priority for action provides some hope for the potential to decrease predator impacts through removal, an option often frowned upon in continental areas, where invasive predators may be our own companions. —SNV

Proc. Natl. Acad. Sci. U.S.A. 10.1073/pnas.1602480113 (2016).

lobules and fissures. Although its subregions all seem to use similar types of cells, tracts coming from elsewhere in the brain target distinct portions of the cerebellum, suggesting that surface formations reflect functional zones. Legué *et al*., studying developing mouse brains, showed how the proliferation and differentiation of granule cells determines the size of a fully developed lobule. Each lobule gets a different proportion of granule cell progenitors; anchoring centers at the base of developing fissures prohibit sharing. The cerebellum thus develops as a modular construction, which may enable acquisition of new functions during evolution. —PJH

Neural Dev. 10.1186/s13064-016-0072-z (2016).

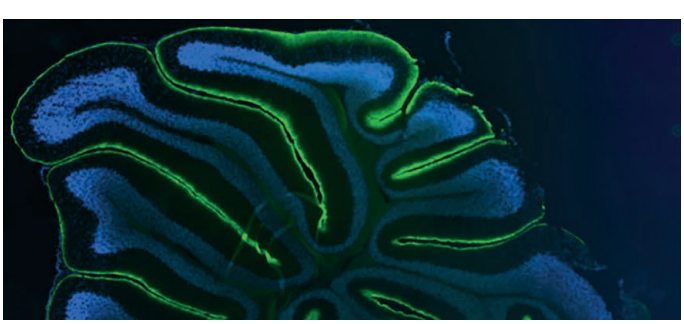

Compartmentalized granule cells feed cerebellar development.

PHOTO: E. LEGUÉ *ET AL*., *NEURAL DEVELOPMENT* **11**, 17 (8 SEPTEMBER 2016) © 2016 BIOMED CENTRAL LTD.

DIVERSITY

Instructor gender versus student ratings

Despite evidence suggesting that student evaluations of teaching are unreliable, they are often included in promotion and tenure criteria. How unreliable are student evaluations with respect to gender bias? Wagner *et al.* analyzed student evaluations of mixed-gender teaching teams at a multicultural European university. Covariates such as course leadership, teacher experience, and research quality were included in the analysis. Results showed a striking disadvantage for women, with women being 11 percentage points less likely to reach a promotion-level teaching score than men teaching the same course. Several policy implications are suggested by the authors, including the call for teacher evaluations to be adjusted for gender bias. —MM

Econ. Edu. Rev. 10.1016/j.econedurev.2016.06.004 (2016).

OCEAN CLIMATE

Clouds and Atlantic Ocean temperatures

The Atlantic Multidecadal Oscillation (AMO), which is characterized by quasi-periodic variations in sea surface temperature (SST) in the North Atlantic, has important effects on the weather and climate of the surrounding continents. Attention has been focused more on the details of the AMO in high and mid-latitudes and less on its tropical branch. Bellomo *et al.* present an analysis of long-term observational records for most of the past 70 years, finding evidence for a positive feedback between total cloud amount, SST, and atmospheric circulation that can strengthen the persistence and amplitude of the AMO at low latitudes. They estimate that cloud feedbacks can account for as much as nearly one-third of the observed AMO-related SST anomalies over the Atlantic tropics. —HJS

Geophys. Res. Lett. 10.1002/2016GL069961 (2016).

SUPERCONDUCTIVITY

Combining transport and photoemission

Angle-resolved photoemission spectroscopy (ARPES) is routinely used to map the electronic structure of complex materials. Most commonly when studying a phase transition, the spectra are recorded and analyzed as a function of temperature. Kaminski *et al.* expanded the use of ARPES in cuprate superconductors by taking measurements in a sample that was experiencing current flow. After taking into account the potentially confounding effects of Joule heating, the researchers found that the current destroyed single-particle coherence in an underdoped sample of $Bi_2Sr_2CaCu_2O_{8+\delta}$ before the normal state was reached. The technique may be useful in the study of other materials with complex phase diagrams. —JS

Phys. Rev. X **6**, 031040 (2016).

RESEARCH ARTICLE SUMMARY

HEALTH ECONOMICS

The impact of training informal health care providers in India: A randomized controlled trial

Jishnu Das, Abhijit Chowdhury, Reshmaan Hussam, Abhijit V. Banerjee*

INTRODUCTION: In rural India, health care providers without formal medical training and self-declared "doctors" are sought for up to 75% of primary care visits. The frequent use of such informal providers, despite legal prohibitions on their practices, in part reflects the absence of trained medical professionals in rural locations. For example, in the majority of villages in the Indian states of Rajasthan, Madhya Pradesh, and West Bengal, informal providers are the only proximate source of health care.

RATIONALE: The status of informal providers in the complex Indian health system is the subject of a highly charged debate among policy-makers and the medical establishment. The official view of the establishment is that fully trained providers are the only legitimate source of health care, and training informal providers legitimizes an illegal activity and worsens population health outcomes. In contrast, given the lack of availability of trained providers and the fact that informal providers are tightly linked with the communities that they serve, others believe that training can serve as a stopgap measure to improve health care in tandem with better regulation and reform of the public health care system. However, despite the policy interest and important ramifications for the country, there is little evidence regarding the benefits (or lack thereof) of training informal providers.

We report on the impact of a multitopic training program for informal providers in the Indian state of West Bengal that provided 72 sessions of training over 9 months. We used a randomized controlled trial design, together with visits by unannounced standardized patients ("mystery clients"), to measure the extent to which training could improve the clinical practice of informal providers over the range of conditions that they face. The conditions presented by standardized patients were blinded from program implementers. Therefore, we view the evaluation of this multitopic training program as a measure of impact on primary care in general. Standardized patient data are accompanied by data from day-long clinical observations, providing a comprehensive picture of provider practice. Our study also benchmarks the impact of training against the performance of doctors in public primary health centers serving the same region. Lastly, it explores whether the training affected patient demand for informal providers.

RESULTS: Mean attendance at each training session was 56% [95% confidence interval (CI): 51, 62%], with no contamination from the control group. Using standardized patient data, we find that providers allocated to the training group were 4.1 (1.7, 6.5) percentage points, or 15.2%, more likely to adhere to condition-specific checklists than those in the control group. The training increased rates of correct case management by 7.9 (0.4, 15.5) percentage points, or 14.2%, and patient caseload by 0.8 to 1.8 (0.13, 3.57) patients per day, or 7.6 to 17.0%. Data from clinical observations show similar patterns. Although correct case management among doctors in public clinics was 14.7 (−0.1, 30.4) percentage points, or 28.3%, higher than among untrained informal providers, the training program reduced this gap by half for providers with mean attendance and reduced the gap almost entirely for providers who completed the full course. However, the training had no effect on the use of unnecessary medicines and antibiotics, although both training- and control-group informal providers prescribed 18.8 (7.7, 28.9) percentage points, or 28.2%, fewer unnecessary antibiotics than public-sector providers.

CONCLUSION: Training informal providers increased correct case management rates but did not reduce the use of unnecessary medicines or antibiotics. At the same time, training did not lead informal providers to violate rules with greater frequency or worsen their clinical practice, both of which are concerns that have been raised by representatives of the Indian Medical Association. Our findings thus suggest that multitopic medical training may offer an effective short-run strategy to improved health care provision and complement critical investments in the quality of public care. ■

ON OUR WEBSITE

Read the full article at http://dx.doi.org/10.1126/science.aaf7384

Despite 56% mean attendance, trained informal providers correctly managed more cases, closing half the gap with the public sector.

Providers who completed the full training course correctly managed cases as often as public-sector doctors.

However, training had no impact on the avoidance of unnecessary antibiotics.

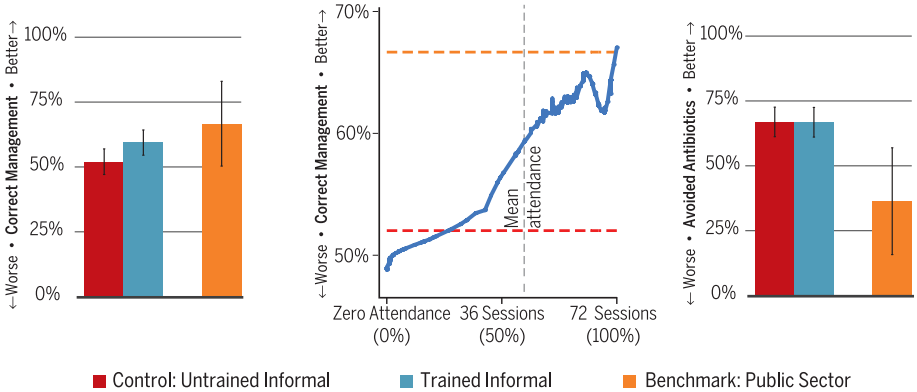

Informal health care providers are the backbone of India's primary health care system. In rural India, up to 75% of primary care visits are to informal providers. We evaluated a training program for these informal providers by using a randomized controlled design. In our sample of 200 villages in West Bengal, there are 30 informal providers for every public-sector doctor. Error bars show 95% CIs.

The list of author affiliations is available in the full article online.
*Corresponding author. Email: banerjee@mit.edu
Cite this article as J. Das *et al.*, *Science* **354**, aaf7384 (2016).
DOI: 10.1126/science.aaf7384

RESEARCH ARTICLE

HEALTH ECONOMICS

The impact of training informal health care providers in India: A randomized controlled trial

Jishnu Das,[1,2] Abhijit Chowdhury,[3] Reshmaan Hussam,[4] Abhijit V. Banerjee[5]*

Health care providers without formal medical qualifications provide more than 70% of all primary care in rural India. Training these informal providers may be one way to improve the quality of care where few alternatives exist. We report on a randomized controlled trial assessing a program that provided 72 sessions of training over 9 months to 152 informal providers (out of 304). Using standardized patients ("mystery clients"), we assessed clinical practice for three different conditions to which both providers and trainers were blinded during the intervention, representative of the range of conditions that these providers normally diagnose and treat. Training increased correct case management by 7.9 percentage points (14.2%) but did not affect the use of unnecessary medicines and antibiotics. At a program cost of $175 per trainee, our results suggest that multitopic medical training offers an effective short-run strategy to improve health care.

In countries such as Nigeria, India, Bangladesh, and Thailand, health care providers without formal medical training account for between one-third and three-quarters of primary care visits (*1*). In rural India, these estimates range from 54% in West Bengal to 75% in states such as Rajasthan, Madhya Pradesh, Andra Pradesh, and Uttarakhand (*2*–*5*). The frequent use of informal providers reflects, in part, their widespread availability in rural areas and the absence of trained medical professionals. Despite legal prohibitions on their ability to practice, a census of providers in rural Madhya Pradesh counted 12 times as many informal providers as trained doctors with M.B.B.S. degrees (the equivalent of the M.D. degree in the United States) (*3*), and a census in rural West Bengal identified over 107,000 rural informal providers in the state (*5*). Proportionally scaled up to all of India, this would imply a population of 1.6 million rural informal providers compared with just under 1 million M.B.B.S. doctors (*6*), a large proportion of whom are concentrated in urban areas. It is therefore no surprise that in the majority of villages in Rajasthan, Madhya Pradesh, and West Bengal, informal providers are the only proximate source of health care.

How to place these informal providers in the context of the health care system is now a highly charged debate among policy-makers and the medical establishment in India. Since the Bhore Committee Report in 1946, India specifically eschewed the model followed in several other low-income countries of allowing multiple cadres of medical professionals with varying degrees of training to diagnose and treat patients (*7*). In 25 of 47 countries in sub-Saharan Africa, for instance, officially recognized nonphysician clinicians play an active role in medical care, undertaking even specialty tasks such as Caesarean sections and anesthesia (*8*). The medical establishment in India has, however, relentlessly opposed any deviation from the standard degree requirement for practicing medicine. For example, attempts to introduce a 3-year diploma in the Indian state of Chhattisgarh for rural health care practitioners was attacked as a dilution of the standards of medical education and forced to stop (*9*).

The Indian medical establishment is equally opposed to the view that training informal providers is a useful stopgap response to the acute shortage of trained providers, especially given that informal providers are already tightly linked with the communities that they serve. The view that such training can act as a complement to better regulation and a ramping up of the public health care system clashes with the position of the medical establishment, which argues that such training will legitimize an illegal activity and worsen population health outcomes. For instance, a large-scale training program in the state of Andhra Pradesh in 2009 had to be terminated in 2012 because of increasing resistance from the Indian Medical Association. The chairman of the Andhra Pradesh Medical Council argued that it was unlikely that informal providers would alter their behavior after a matter of months of training (*10*): "They are already violating rules. [After the training] they will violate them even more." Similarly, in 2016, the president of the Indian Medical Association's Kolkata branch (Kolkata is the capital of West Bengal) equated training informal providers to "teaching burglars how to steal more effectively" (*11*).

One reason for the current impasse in this debate is the dearth of evidence on either side. Although recent research provides new insights into the availability and practice of informal providers, at present there is no comprehensive evaluation of the impact of training informal providers on their clinical practice. We cannot develop effective policy without understanding the nature of the demand for informal providers, the kind of health care that they provide, and whether the quality of care that they provide can be improved.

We report on a research project in the Indian state of West Bengal that attempts to bridge this evidence gap, building on a body of research in which some of us have been involved for over a decade. The study does three things: First, using a range of different approaches that we have developed in previous research, it provides detailed descriptive evidence on the clinical practice of informal providers and how that compares with the public M.B.B.S. doctors serving the same population. It then uses a randomized controlled trial (RCT) to measure the extent to which training can improve their clinical practice. Lastly, using the random variation brought about by the training, it asks whether potential patients react positively to improvements in quality by visiting trained informal providers more often.

To assess the training program, we used a new blinded methodology that differs from previous evaluations. Although there is a small amount of RCT literature on the impact of training informal providers, it focuses on the evaluation of only those specific conditions for which the informal providers were explicitly trained [for instance, see Adu-Sarkodie *et al.* (*12*) on the impact of training pharmacists for urethral discharge, Garcia *et al.* (*13*) on sexually transmitted illnesses (STI) in Peru, Shah *et al.* (*14*) on STI and HIV-focused training in Pakistan, and Abuya *et al.* (*15*) on treatment for malaria]. However, showing that informal providers can successfully execute the specific tasks in which they have been trained is far from dispositive from the point of view of the present policy debate. Because informal providers deal with a variety of conditions of unknown origins—a fever can indicate either malaria, a flu, or a large number of other illnesses—the relevant training program must be able to demonstrate improvement across the spectrum of clinical tasks that informal providers routinely need to perform. These can range from (i) immediate treatment for certain acute conditions to (ii) triage into higher-quality care for more serious conditions to (iii) diagnosis and maintenance care for chronic patients.

The training program and evaluation that we report here addresses this critical issue in two ways. First, the program offered a generalized curriculum, training providers on multiple topics such as basic physiology and anatomy, principles of harm reduction, and specific illnesses. Second, the program was evaluated using unannounced

[1]Development Research Group, The World Bank, 1818 H Street, NW, Washington, DC 20433, USA. [2]Centre for Policy Research, New Delhi, India. [3]Institute of Post Graduate Medical Education and Research, Seth Sukhlal Karnani Memorial Hospitals, 244 A.J.C. Bose Road, Kolkata, West Bengal, 700020 India. [4]Economic Growth Center, Yale University, 27 Hillhouse Avenue, New Haven, CT 06511, USA. [5]Department of Economics, Massachusetts Institute of Technology, 40 Ames Street, Cambridge, MA 02139, USA.
*Corresponding author. Email: banerjee@mit.edu

standardized patients, or trained actors playing the role of patients suffering from a particular condition. Our standardized patients, who were blinded to the group assignment of the providers that they visited, presented providers with a strategically chosen set of conditions that allowed us to assess provider ability across a broad range of the clinical tasks that they are expected to manage in their patient populations. Trainers and trainees in the program were both blinded to the conditions chosen for assessment, and the standardized patients were neither anticipated nor, ex post, recognized as actors. In addition to standardized patient data on clinical practice, we also implemented day-long clinical observations to verify clinical practice for a broader sample of patients, and we collected patient caseload and fees data to examine the effect of training on patient demand for informal providers' services.

The particular design of our evaluation therefore allows us to overcome the limitations of previous studies of this kind. This study provides the first reliable evidence on the impact of a multitopic training program on diagnostic and treatment quality for conditions unanticipated by both trainers and providers.

Intervention

The training program was designed and executed by the Liver Foundation, a public health organization based in West Bengal. The organization invited 360 providers across its district of operation to participate, out of whom 304 providers expressed interest and were randomized equally into training and control groups. Members of the training group were offered admission to the Liver Foundation Rural Health Care Practitioner Training Program, and those in the control group were told that they would be eligible for the program the next year. The control group was indeed offered the training program after the evaluation was complete. Sample selection is described in further detail in the Methods section.

Our sample was comparable to those of other studies of informal providers in India: 95% were male, with a mean age of 40 [95% confidence interval (CI): 39.16, 41.22] years and 13.1 (12.21, 14.07) years of experience; 62% had completed high school; and 75% reported zero formal training (table S1). The remaining providers were in possession of certificates of limited legal validity but of perceived credibility and value in the rural medical market.

The training consisted of 72 sessions and 150 teaching hours over a 9-month period. It included a wide variety of topics, with an emphasis on basic medical conditions, triage, and avoidance of harmful practices. The Methods section details the structure of the program, and the supplement materials provide the program curriculum.

From the beginning, the Liver Foundation stressed that informal providers would not receive any certificates on completion of the training and should not think of themselves as qualified doctors. The program was free to all students, each of whom was provided a transportation allowance of $1.30 and a meal at each training session. Throughout the training, providers continued to operate their clinics more or less as usual.

Measurement and data

To evaluate the program, we strategically chose three tracer conditions, targeting the multiple skills that need improvement, and used unannounced standardized patients as the primary means of assessment. Standardized patients are increasingly used to assess condition-specific quality of care in low-income countries (*16*–*21*) and regarded as being close to a gold-standard measure of clinical practice. The three tracer conditions that we chose—chest pain, respiratory distress, and child diarrhea—allowed us to assess the ability of the informal provider to triage a patient with a condition that is likely severe (chest pain); treat or refer a patient with a condition that requires management (respiratory distress); and assess and treat a patient with a condition that can potentially be managed at the primary level (child diarrhea). For each condition, we chose to teach the standardized patients the most obvious answers to history questions that should have led the provider, with proper questioning and examination, to conclude that the patient was suffering from angina (chest pain), asthma (respiratory distress), or dysentery (child diarrhea). Further details on standardized patient tracer conditions are included in the Methods section.

Throughout the intervention, the implementers and trainers in the program did not know the conditions for which the informal providers would ultimately be evaluated, limiting the possibility of teaching to the test. During the evaluation, the standardized patients were blind to the training status of their providers, limiting reporting bias from the patients. Given the standardization of patients across providers, this methodology also allowed us to address the possibility of confounders in terms of patient characteristics and illnesses. Lastly, the fact that the patients were unannounced trained actors also limited the possibility of Hawthorne effects, whereby providers would alter their behavior because they knew that they were being observed. Further information on the standardized patient recruitment and training process is detailed in the Methods section.

One limitation of the standardized patient approach is the small number of conditions (though wide in range) for which the providers can be evaluated. To extend our results to the typical patient who visits these informal providers, we therefore also assessed clinical practice by using trained observers who remained with the provider for 1 full day.

Lastly, we collected data on the prices and fees charged by the informal providers in the training and control groups. (Some informal providers charge fees, whereas others sell medicine to their patients at a premium in lieu of a fee. We report the sum of these two.) We also collected data on their caseload, or the number of patients that they see in a day. These data were collected through day-long clinical observations as well as weekly provider diaries, as detailed in the Methods section. We did this because one important aspect of the success of a training program is the effect of training on the demand for the services of the trainees. If improvements in clinical practice adversely affect the market share or earnings of informal providers, informal providers will either stop implementing what they have learned, or the decline in their caseload will affect their relevance and long-term sustainability. This is a legitimate concern, given that it has been documented that patients often make their health care choices on the basis of subjective theories that can be at odds with what science tells us (*22*, *23*). Conversely, if the quality of their treatment, earnings, and market share increased as a result of training, we would be reassured about the sustainability of the program and the welfare of the patients.

Baseline data were collected before the randomization and included information on provider backgrounds and practice characteristics. To allow for potential short-term decay in training skills, endline data collection commenced 3 to 6 months after the completion of training and 9 to 10 months after the completion of the illness-specific portion of the training. Standardized patients were sent to the entire study population, as well as to the total of 11 public primary health centers (PHCs) in the 203 villages. The quality of health care delivered in the PHCs was used to benchmark the performance of trained informal providers. After standardized patient data collection was complete, a day-long clinical observation was conducted with each provider, and the baseline measures were collected once again. Because the use of standardized patients and clinical observations could have primed providers to expect such cases in the future, both were restricted to the endline survey data collection only.

Our primary outcomes, pre-specified in our pre-analysis plan, are condition-specific metrics obtained from the standardized patient interactions. We assessed potential improvements in necessary care through condition-specific checklists of recommended care (supplementary materials) (*24*–*26*) and rates of correct case management. We present our results using three definitions of correct case management. The first is an inclusive binary definition, where the case is correctly managed as long as necessary care was provided, with or without additional components. In the second stricter binary definition, the case is correctly managed if only the necessary care was provided, without any unnecessary components. The third is a grade on a continuous scale, as evaluated by independent M.B.B.S. doctors blinded to providers' training status, which has the advantage that both necessary and unnecessary components are evaluated jointly, allowing for a more nuanced gradation of case management. All three are described in detail in the Methods section. We also assessed potential reductions in unnecessary or harmful care through the use of antibiotics, injections, and polypharmacy, the latter defined as the total number of medicines dispensed or prescribed. Antibiotic use was assessed for all three conditions, as well as for

Table 1. Impact of training on main standardized patient outcomes. History and exam checklist completion refers to the percent of items that were completed from the structured questionnaire. Correct case management is defined as an inhaler, corticosteroid, or referral for asthma; asking to see the child or recommending ORS for child diarrhea; and aspirin or referral for angina. Unnecessary or harmful medicines are any other medication treatment; a single case can be categorized as either or both correct and unnecessary or harmful treatment. "Correct management only" means correct case management without any unnecessary or harmful treatments. All regressions control for case presentation fixed effects and the age of the attending provider, with standard errors clustered at the level of the village. Ninety-five percent CIs are presented in parentheses below the means and estimated coefficients. Estimates that are significant at the 90% level of confidence are marked with an asterisk, at the 95% level of confidence with two asterisks, and at the 99% level of confidence with three asterisks. OR, odds ratios. Marginal effects (ME) are computed at the mean of dependent variables for the logistic specification and are the coefficients on training (ITT) or attendance (IV) in the linear specifications. The *F* statistic for the first stage in IV regressions is >300. Wilson intervals without continuity correction are used for dichotomous variables.

	Control group		Training group					
	n	Mean	*n*	Mean	ITT logistic OR	ITT logistic ME	Linear ME	IV Linear ME
Continuous outcome variables for desirable and nondesirable outcomes								
History and exam checklist completion (percent)	396	0.273 (0.259, 0.287)	388	0.314 (0.300, 0.328)			0.041*** (0.017, 0.065)	0.069*** (0.031, 0.107)
Consultation length (minutes)	396	3.252 (3.079, 3.425)	388	3.511 (3.326, 3.695)			0.247 (−0.046, 0.54)	0.416 (−0.064, 0.896)
Number of medicines	396	2.162 (2.033, 2.291)	388	2.222 (2.083, 2.36)			0.065 (−0.162, 0.291)	0.109 (−0.269, 0.487)
Dichotomous outcome variables for desirable outcomes								
Correct case management	396	0.520 (0.471, 0.569)	388	0.598 (0.549, 0.647)	1.402** (1.017, 1.931)	0.083** (0.004, 0.162)	0.079** (0.004, 0.155)	0.133** (0.009, 0.258)
Correct management only	396	0.109 (0.078, 0.139)	388	0.124 (0.091, 0.157)	1.124 (0.703, 1.798)	0.012 (−0.035, 0.058)	0.012 (−0.036, 0.060)	0.020 (−0.059, 0.100)
Average-quality case management or better	394	0.114 (0.083, 0.146)	384	0.174 (0.136, 0.213)	1.679*** (1.145, 2.462)	0.060*** (0.017, 0.104)	0.062*** (0.016, 0.107)	0.104*** (0.03, 0.178)
Referred case (asthma or angina)	263	0.285 (0.234, 0.343)	258	0.341 (0.283, 0.399)	1.306 (0.881, 1.937)	0.057 (−0.026, 0.14)	0.055 (−0.026, 0.137)	0.093 (−0.042, 0.228)
Dichotomous outcome variables for nondesirable outcomes								
Lowest-quality case management	394	0.142 (0.108, 0.177)	384	0.102 (0.071, 0.132)	0.664 (0.411, 1.073)	−0.042 (−0.091, 0.007)	−0.043 (−0.094, 0.008)	−0.072 (−0.156, 0.012)
Antibiotics (all)	396	0.477 (0.428, 0.527)	388	0.485 (0.435, 0.534)	1.059 (0.752, 1.49)	0.014 (−0.071, 0.099)	0.011 (−0.055, 0.077)	0.018 (−0.092, 0.129)
Antibiotics (asthma or angina)	263	0.331 (0.274, 0.388)	258	0.337 (0.279, 0.395)	1.047 (0.718, 1.526)	0.010 (−0.071, 0.091)	0.009 (−0.067, 0.086)	0.016 (−0.112, 0.143)
Offered injection (asthma or angina)	263	0.011 (0, 0.024)	258	0.019 (0.003, 0.036)	1.612 (0.337, 7.717)	0.004 (−0.012, 0.021)	0.007 (−0.017, 0.031)	0.012 (−0.028, 0.051)
Any unnecessary or harmful medicine	396	0.707 (0.662, 0.752)	388	0.701 (0.655, 0.747)	0.978 (0.673, 1.421)	−0.004 (−0.077, 0.068)	−0.004 (−0.07, 0.062)	−0.007 (−0.116, 0.102)

asthma and angina alone, because in these two instances, antibiotics are almost never required.

These condition-specific quality metrics were complemented with secondary outcomes that were not condition-specific but that have been shown to relate to higher-quality care (*16*). The general measures of care assessed, obtained from both the standardized patient interactions and clinical observations, included consultation length, history-taking, and examinations performed.

We present age-adjusted intention-to-treat (ITT) estimates, as well as age-adjusted instrumental variable (IV) estimates to deal with partial compliance. Standard errors have been adjusted for clustering at the village (standardized

Table 2. Clinical practice of control-group, training-group, and public providers, assessed using standardized patients. Shown (from left to right) are means for each group, estimated differences between informal providers in the control group and doctors in PHCs, and estimated differences between informal providers in the training group and doctors in PHCs. Definitions, asterisks, and the presentation of statistics are as in Table 1. All regressions include dummies for each condition, with standard errors clustered at the level of the village. Odds ratios could not be computed for lowest-quality case management because no interactions with PHCs fell into that category.

	Means			Control group − PHC		Training group − PHC	
	PHC (n = 33)	Control (n = 396)	Training (n = 394)	Linear regression ME	Logistic regression OR	Linear regression ME	Logistic regression OR
Continuous outcome variables for desirable and nondesirable outcomes							
History and exam checklist completion (percent)	0.202 (0.16, 0.244)	0.273 (0.259, 0.287)	0.313 (0.299, 0.327)	0.071** (0.017, 0.125)		0.111*** (0.055, 0.166)	
Consultation length (minutes)	1.735 (1.403, 2.067)	3.252 (3.079, 3.425)	3.495 (3.312, 3.677)	1.519*** (1.077, 1.961)		1.762*** (1.3, 2.223)	
Number of medicines	2.758 (2.296, 3.219)	2.162 (2.033, 2.291)	2.208 (2.07, 2.346)	−0.595** (−1.158, −0.031)		−0.548 (−1.123, 0.026)	
Dichotomous outcome variables for desirable outcomes							
Correct case management	0.667 (0.505, 0.828)	0.520 (0.471, 0.57)	0.594 (0.545, 0.643)	−0.147 (−0.304, 0.01)	0.519 (0.249, 1.082)	−0.073 (−0.23, 0.085)	0.724 (0.353, 1.482)
Correct management only	0.091 (0, 0.189)	0.109 (0.078, 0.139)	0.127 (0.094, 0.16)	0.018 (−0.077, 0.112)	1.219 (0.398, 3.737)	0.036 (−0.059, 0.131)	1.456 (0.484, 4.38)
Average-quality case management or better	0.182 (0.05, 0.314)	0.114 (0.083, 0.146)	0.174 (0.137, 0.212)	−0.068 (−0.177, 0.042)	0.580 (0.267, 1.26)	−0.007 (−0.118, 0.104)	0.954 (0.443, 2.054)
Referred case (asthma or angina)	0.182 (0.02, 0.343)	0.285 (0.23, 0.34)	0.344 (0.286, 0.401)	0.104 (−0.05, 0.258)	1.843 (0.665, 5.106)	0.162** (0.003, 0.32)	2.435* (0.87, 6.816)
Dichotomous outcome variables for nondesirable outcomes							
Lowest-quality case management	0 (0, −)	0.142 (0.108, 0.177)	0.103 (0.072, 0.133)	0.142*** (0.103, 0.181)	−	0.102*** (0.071, 0.134)	−
Antibiotics (all)	0.667 (0.505, 0.828)	0.477 (0.428, 0.527)	0.480 (0.43, 0.529)	−0.191** (−0.348, −0.034)	0.371** (0.156, 0.885)	−0.188** (−0.346, −0.029)	0.372** (0.156, 0.885)
Antibiotics (asthma or angina)	0.636 (0.435, 0.838)	0.331 (0.274, 0.388)	0.332 (0.275, 0.389)	−0.306*** (−0.502, −0.11)	0.244*** (0.095, 0.63)	−0.304*** (−0.503, −0.106)	0.242*** (0.094, 0.621)
Offered injection (asthma or angina)	0.045 (0, 0.133)	0.011 (0, 0.024)	0.019 (0.002, 0.036)	−0.034 (−0.123, 0.054)	0.233 (0.02, 2.674)	−0.026 (−0.116, 0.063)	0.403 (0.04, 4.06)
Any unnecessary or harmful medicine	0.879 (0.767, 0.99)	0.707 (0.662, 0.752)	0.695 (0.65, 0.741)	−0.171*** (−0.278, −0.063)	0.268** (0.095, 0.757)	−0.183*** (−0.289, −0.077)	0.276** (0.103, 0.738)

patient data) or provider (clinical observation data) level.

We show a CONSORT (Consolidated Standards of Reporting Trials) diagram of participant flow in fig. S1. Of the study population of 304 providers, standardized patients visited 267 (87.8%). There were no statistically significant differences in provider characteristics by training status between providers who were assessed at endline and those who were not (table S2). All baseline covariates were well balanced, except for provider age, which was slightly higher in the training group (table S1). We therefore controlled for age in our analysis.

Results

Attendance at training sessions

Mean attendance, or the average attendance of training-group providers at each session, was 56% (95% CI: 51, 62%). No control providers attended any session. Attendance in each session varied between 19 and 82% and was negatively correlated with distance to the training site and rainfall on the day of the training (fig. S2 and table S3).

Outcomes using standardized patients

Table 1 presents case management outcomes from standardized patient observations. Among providers in the control group, the mean standardized

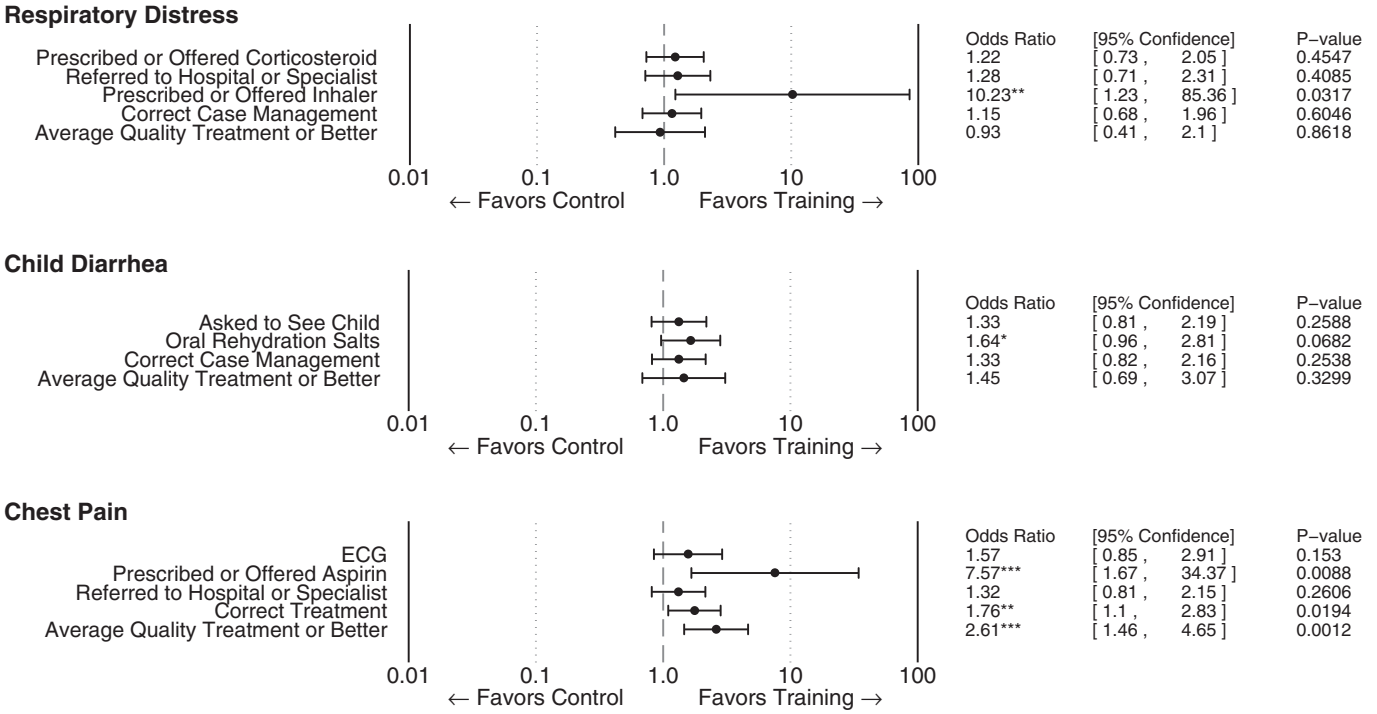

Fig. 1. Impact of training on condition-specific components of correct case management. The odds ratios of the ITT estimator are computed from a logistic regression model relating each outcome variable to group status (training versus control), with condition-specific dummies and age of the provider as additional controls. Every component of correct case management improved in the training group, although the small sample size limits the precision of the estimates. Estimates that are significant at the 90% level of confidence are marked with a single asterisk, at the 95% level of confidence with two asterisks, and at the 99% level of confidence with three asterisks.

patient interaction lasted 3.3 (95% CI: 3.08, 3.43) min, and mean adherence to the checklist of recommended questions and examinations was 27.3% (25.9, 28.7%). Correct case management was offered in 52% (47.1, 56.9%) of interactions, with independent raters grading (only) 11.4% (8.3, 14.6%) of all treatments in the control group as "average quality or higher." Polypharmacy and antibiotic use, the latter unnecessary in all cases, was high, with an average of 2.2 (2.03, 2.29) medicines dispensed per interaction. Unnecessary or harmful medicines were prescribed or dispensed in 70.7% (66.2, 75.2%) of standardized patient interactions, and antibiotics were prescribed or dispensed to 33.1% (27.4, 38.8%) of asthma and angina standardized patients, none of who should have been recommended such treatments. Control informal providers saw a mean of 8.4 (7.21, 9.53; clinical observations) to 10.6 (9.43, 11.72; provider diaries) patients per day and charged between 46.6 (40.07, 53.18; observations) and 73.1 (64.14, 81.98; diaries) rupees per visit. Caseloads are lower in the clinical observations data because they were conducted in a low-morbidity season, with less severe illnesses, relative to the provider diaries (table S5).

Correct case management was significantly higher among providers in the trained group [7.9 (0.4, 15.5) percentage points], as was the likelihood of providing "average-quality or higher" treatment [6.2 (1.6, 10.7) percentage points] (Table 1). Higher correct case management rates were also accompanied by greater adherence to condition-specific checklists (Table 1) among trained providers [4.1 (1.7, 6.5) percentage points].

Because the average provider attendance per session over the duration of the training course was 56%, we also used group assignment to estimate what would have happened if all the informal providers in the training group had attended every class. Only training-group providers were permitted to attend the training, so our setting is one of one-sided noncompliance—i.e., there are no noncompliers in the control group. Therefore, the local average effect of training in an IV analysis is equivalent to the "treatment on the treated," or in other words, the effect for an informal provider who attended every class (*27*). Identifying the impact of training on providers had they had 100% attendance is especially relevant because attendance rates were highly correlated with distance to the training center and might therefore be substantially improved by bringing the center closer to the program participants.

The IV results suggest that, with perfect attendance, correct case management rates would have been 13.3 (0.9, 25.8) percentage points higher in the training group than in the control group (Table 1). This is equivalent to a 25.6% increase in correct case management relative to the control group. However, neither the ITT nor the IV specifications show statistically significant differences in the use of antibiotics, injections, or polypharmacy or the likelihood of very low-quality case management, as assessed by the independent raters (Table 1).

With regard to specific process indicators across the three conditions presented by the standardized patients, providers assigned to the training group were more likely to prescribe inhalers and refer patients for symptoms of respiratory distress; recommend oral rehydration salts (ORS) for the child with diarrhea; and administer aspirin and refer patients for chest pain (Fig. 1). Encouragingly, out of 110 referrals for chest pain, 70 were to cardiologists or chest specialists, in line with recognition of a potentially serious heart condition. However, because the study was not powered to detect condition-specific differences, these results are imprecisely estimated and therefore generally not statistically significant, except in the use of inhalers for respiratory distress and correct case management for chest pain.

Outcomes calculated using clinical observations

Data from 2311 observations of clinical practice with real patients collected 3 months or more after the conclusion of training show similar improvements, with trained informal providers asking 0.65 (0.06, 1.24) or 13.0% more recommended history questions and conducting 0.42 (0.15, 0.68) or 18.3% more recommended examinations than their control counterparts. As in the case

of standardized patients, there is no evidence of a difference in the use of polypharmacy, injections, or antibiotics (table S4).

Benchmarking with public-sector performance among standardized patients

Table 2 presents results relative to the benchmark of the performance of the public-sector providers, all of whom have M.B.B.S. qualifications. Relative to public-sector providers in the same villages, untrained and trained informal providers were respectively 7.1 (1.7, 12.5) and 11.1 (5.5, 16.6) percentage points more likely to adhere to condition-specific checklists than public providers, who completed an average of 20.2% of checklist items (Table 2). Both trained and untrained informal providers also spent more time with their patients: Trained informal providers spent more than twice the amount of time as public providers, who averaged 1.74 min per patient. Polypharmacy, offers of injections, and antibiotic prescriptions were also substantially lower among informal providers, trained and untrained, relative to the public providers. For example, trained providers were 18.8 (7.7, 28.9) percentage points, or 28.2%, less likely than public providers to prescribe antibiotics to standardized patients.

However, public-sector doctors were 14.7 (−1.0, 30.4) percentage points more likely to correctly manage a case compared with untrained informal providers, with this difference halved for informal providers in the training group (neither difference is statistically significant because of the small total of 11 public-sector doctors). The likelihood of "correct case management only" as well as "average- or higher-quality case management" was equally high among public providers and informal providers in the training group, although the likelihood of "very low-quality case management" was lower for public doctors.

Heterogeneity in training impact

It is possible that these average effects mask heterogeneity linked to various provider characteristics. We explore the heterogeneity of training effects in five dimensions. Two of these proxy for prior learning (whether the provider had any formal training, which could include some months of distance education or training received through the government for community health work, and the provider's prior experience), one relates to the provider's connection to the community (whether the provider owned rather than rented his or her clinic), one proxies for local competition (whether there were other providers in the same village), and one measures provider caseload (table S6). Across all five dimensions, we find no evidence of heterogeneous effects in the training group. We do, however, find evidence suggestive of differential training effects related to case management rates predicted on the basis of providers' baseline characteristics. Providers who were predicted to perform poorly absent the training show larger training effects (table S7). For example, those providers in the middle tercile of correct case management had a response to the training that was four times as large [12.4 (−2.3, 27.1) percentage points] as those in the highest tercile [3.0 (−11.5, 17.5) percentage points], which is significant at the 10% level. This suggests that providers with lower quality of care improved the most through the program.

Furthermore, we find a strong dose response related to attendance among providers in the training group (fig. S3). Rates of correct case management remain roughly constant at the same level as the average of the control group until attendance reaches 40% and then rise continuously, peaking at nearly the level of PHCs by 90% attendance. Although attendance was not randomly allocated and more motivated providers likely had higher attendance, the dose response is consistent with training as the key channel for the impacts we observed.

Impact of training on demand and revenue

The number of patients counted on the day of clinical observation and in provider diaries suggests an increase in patient caseload. The IV estimate, which is the estimate relevant for assessing the provider's potential revenue gain from attending the training, is 1.30 (−1.33, 3.94) more patients per day based on our observations and 3.05 (0.24, 5.86) more patients per day based on the diaries (table S5). This implies an increase in patient demand of 15.5 to 28.9%. We do not find evidence of a change in the prices that providers charged, with positive but statistically insignificant estimates from standardized patients and negative but statistically insignificant estimates from clinical observations. The increased patient caseload is consistent with multiple channels of impact: Patients could be reacting to the improved treatment by returning to the same provider or recommending the provider to others; patients may have also heard that the provider received training and updated their expectations of the providers' ability. Although providers did not explicitly advertise their training (for example, by displaying a certificate—they received none), some providers reported informing their patients that their office was closed 2 days per week for the purpose of attending a training course in the district capital.

Program costs

On the cost side of the program, total costs included training center rent, staff salaries, materials, travel stipends, and meals for the providers. Assuming at least 50% attendance (comparable to the 56% actually attained), the per-student cost of the program was 10,528 rupees ($175 at 60 rupees to $1). A conservative estimate of a 10% increase in caseload (which is below our lowest estimate) with no change in prices charged (which is what we observed) suggests that the provider would earn 50.2 rupees ($0.84) extra per day, and 210 working days would be required to recoup the training costs, assuming no opportunity cost of training time and travel or the ability to shift additional patients to other times of the day. At the higher end of the caseload increase estimates, the cost of training would be fully recouped within 66 days. Although we did not experiment with providers' willingness to pay for the program, a priori, there appears to be a sufficient revenue gain for the program to be self-financing.

Limitations

Our study faces limitations inherent to the use of standardized patients to evaluate clinical practice. In addition, there is a question of generalizability, because the impact of training is estimated for those who expressed interest in the program, rather than all those who were approached. Lastly, in the absence of a household survey, we can only assess the change in caseload as an impact of the training; we cannot determine the quality of the provider that the marginal patient would have seen in the absence of training. We discuss each of these limitations in turn.

Extrapolation from standardized patients

The use of standardized patients restricts our primary outcomes to conditions for which (i) the lack of physical symptoms does not undermine the claim of an underlying condition, (ii) invasive examinations are not required, and (iii) a child need not be present at the clinic. Therefore, though our findings are considerably broader than those in the existing literature, we cannot extend them to all cases that informal providers may be required to manage.

The results from standardized patients also pertain to the specific characteristics of those individuals, which in our case could include a sense by the provider that the patient was more educated than the average villager and resided outside the village. Although this should not affect internal validity because both training- and control-group providers faced the same standardized patients, we cannot automatically extrapolate the findings to the entire patient population that informal providers treat in their clinics. However, it is worth pointing out that previous studies have found little influence of standardized patient characteristics on provider behavior (*19*). Moreover, the parallel evidence from our clinical observations, showing that more history-taking and physical examinations were performed for real patients by the trained providers, suggests that the findings from the standardized patients may hold for a wider set of illnesses and patients. It must be acknowledged, however, that to conclusively prove this, we would need to use a larger and more diverse population of standardized patients or obtain measures of population-level health outcomes. Lastly, the impact of training beyond the 9-month period is uncertain and depends on whether the effect of training decays over time (alternatively, it could be reinforced by the improved results) and, if so, the rate at which such decay (or reinforcement) occurs.

Extrapolations to training effects in the population

We are also limited in our ability to extrapolate training effects to the population of informal

providers, because this would have required a separate study design in which randomization occurred at the population level rather than among those informal providers who expressed an interest in the program. We can nevertheless make use of the fact that, out of the 360 informal providers who were approached, 304 consented to be part of the study. Assuming that the training effect would have been zero among the remaining 56, the estimated impact of training on correct case management in the population would have been 6.5 (95% CI: 3.9, 8.9) rather than 7.9 percentage points (fig. S4).

However, this may be too pessimistic. As we discussed previously, the distance to the training center was the single most important determinant of attendance (table S3 and fig. S2). It is not unreasonable to assume that, were the policy to be implemented on a larger scale, there would be more than one training center and they would be in different locations. If we make the (brave) assumption that the relation between distance and attendance that we estimate is causal, it implies that we could achieve around 80% attendance if a training center were within 5 km of each informal provider. If we additionally assume that the relation that we estimate between attendance and the training effect (fig. S5) is causal, we could conclude that those who attend 80% of the time have a training effect that is close to the IV estimate of 13.3 percentage points. Therefore, the IV estimate may well be the policy-relevant estimate. Alternately, if these providers were somehow different from those observed in the sample and continued to not attend the training despite greater proximity to the training center, their training effect would be zero. In this case, applying the IV estimate only to the 304 providers who chose to participate in the program and appropriately reweighting would suggest an IV estimate of 10.6 percentage points for the effect on correct case management.

Health care quality for patients who switched providers

The gap in correct case management rates between public and informal providers presents an additional concern to those explored above: Given that patient demand increased for trained informal providers, overall quality of care may have declined if patients switched away from the public sector toward trained informal providers. This is a concern in the 11 villages with a public PHC, because patients rarely seek primary care outside the surroundings of their own village (*16*). In fact, our data show that in the villages where both options exist, the training had no effect on the informal providers' caseloads; the caseloads of trained informal providers increased only in villages without a public-sector clinic. In addition, when we asked patients where they would seek care for a variety of conditions, including the conditions evaluated using standardized patients, 90% said they would use a local provider, with no difference between patients treated by providers in the training and control groups (table S8). This suggests that our increased caseload results for the trained providers must have come from an increased retention of existing patients or patients switching from other informal providers rather than from public M.B.B.S. doctors.

Discussion

Even with a relatively inclusive definition of correct case management that ignores the prescription of unnecessary medications, only 52% of control informal providers can be said to manage the cases of the standardized patients correctly, compared with 66% correct management for the 11 M.B.B.S. doctors. Both rates are very low, especially given that the cases were designed with no complications and the most obvious diagnosis, but broadly consistent with other studies from India and China that used standardized patients. In particular, using the same tracer conditions, Das *et al.* (*16*) reported correct case management rates of 42% among a representative sample and 50.7% among trained M.B.B.S. providers in rural Madhya Pradesh; Sylvia *et al.* (*17*) reported correct case management rates of 52 to 53% among village clinicians in rural China for chest pain and child diarrhea; and Mohanan *et al.* (*18*) reported that only 3.5% of providers recommended ORS for child diarrhea in Bihar. Low rates have also been reported for other tracer conditions; for tuberculosis, correct case management rates were 21% for a sample of providers from Delhi, India (*19*).

Against this worrying backdrop, our results offer some grounds for optimism. Despite an average of 13 years of experience, the clinical practice of informal providers appears to be highly malleable across multiple topics. Although proportions of correct case management are higher in PHCs than in informal provider clinics, this difference was cut in half through training, and our IV estimates suggest that it would have been nearly eliminated if attendance rates had been close to perfect.

Our estimates provide the first evidence that can inform an ongoing debate in India about the utility of multitopic training programs for informal providers. At the same time, any such debate also has to take into account important considerations regarding (i) the allocative efficiency of funding training programs for informal providers, rather than improving the public sector; (ii) the impact of training on health outcomes; and (iii) the absence of an effect of training on the use of unnecessary medicines or antibiotics. Our discussion brings in additional information and some speculation on each of these issues.

Training or investment in the public sector?

It is difficult at first to countenance the fact that, based on our IV estimates, 72 sessions of training can lead to equivalent or even better care than in the public sector ("better" because although the correct case management rates were similar among public-sector doctors and those informal providers who had high attendance rates, the use of unnecessary antibiotics and medicines was lower among all informal providers). This should not be interpreted to mean that the knowledge gained through this short training program is equivalent to the knowledge obtained from a professional medical degree granted by a reputed medical college. The equivalence that we document here points to two different explanations.

First, as has been previously documented, medical knowledge among doctors with a M.B.B.S. degree can vary dramatically, arguably because of differences in the quality of training among medical colleges (*28*). Second, low quality in the public sector is a reflection of poor governance that leads to very high levels of absence (*2*) and low effort (*29*). The mean consultation length in the public clinic was only 1.74 (95% CI: 1.40, 2.07) min, a result that has also been documented in samples from Delhi (the national capital) and the state of Madhya Pradesh (*16*, *30*). This is consistent with the fact that the quality of care from the same public-sector doctors is markedly higher when they practice in their private clinics rather than in their public role (*16*). Despite this lack of effort, the superior knowledge of the public-sector doctors allowed them to provide higher-quality care than our control-group informal providers; however, the training was sufficient to improve the clinical practice of the most regular attendees to the point where the performance of these informal providers matched that of better-trained, but presumably poorly motivated, public-sector doctors.

Given the greater knowledge of M.B.B.S. providers in the public sector, one could ask whether alternate (nontraining) investments that improved their effort and/or increased the use of the public system would yield higher dividends relative to training private-sector informal providers. In theory, this is an attractive option. In practice, it has turned out to be very hard to do. In terms of trying to directly influence provider effort, Banerjee *et al.* (*30*), in the state of Rajasthan and Dhaliwal and Hanna (*31*) in Karnataka worked closely with state governments to try to improve the simplest measure of governance—nurse and doctor attendance—but as their studies show, this has proven to be inordinately difficult owing to the combination of resistance from staff and the reluctance of the administration to enforce the programs. In terms of trying to manipulate the demand for care from the formal health care system, studies by Powell-Jackson, Mazumdar, and Mills (*32*) and Mohanan *et al.* (*33*) of large government programs that provided conditional cash transfers to households to encourage institutional births suggest that there was no impact on health outcomes.

We pair this literature with the reality that public health care infrastructure is exceedingly scarce in rural Indian villages relative to the ubiquity of informal providers (in our study's setting, the 203 villages had only 11 PHCs but at least 360 informal providers). This suggests that the magnitude of resources required to expand the care of public doctors to the full patient population would be considerable. A back-of-the-envelope calculation estimates that, at the average

yearly salary for a public M.B.B.S. doctor in West Bengal of $6000, the government could hire just 11 additional M.B.B.S. doctors for the same cost as training 360 informal providers yearly in training centers 5 km from their residences (*34*, *35*). We would expect this high-intensity repeated training to durably bring these informal providers to near-M.B.B.S. case management rates. In addition, this estimate ignores the costs of infrastructure for the PHCs and the various benefits (e.g., pensions and health care) that government doctors receive. Although speculative, the difficulty of improving the quality of public health care, combined with the scarcity and cost of such doctors, suggests that investing in the clinical practice of informal providers is at least an equally efficient allocation of resources.

Potential impact of training on health outcomes

Improved health care provision is only relevant if it generates improved patient health outcomes. This study was designed to assess the impact of training on the former rather than the latter, but now we explore two channels through which patient health may have been substantively affected. At the very least, training improved correct case management rates for the tracer conditions that we evaluated using standardized patients; in this case, the impact on health outcomes will depend on the prevalence of these conditions in the population and the health benefits accruing from the increase in correct case management. More optimistically, given that the conditions were blinded from the implementers and therefore did not receive special emphasis in the training, it is also plausible that the training generated improvements in correct case management for the broader range of conditions that informal providers see in their clinics, yielding a greater breadth of impact on the health of the patient population.

We focus first on the tracer conditions only. Diarrheal disease kills more than 200,000 children per year in India, and it is especially prevalent in low-lying areas with heavy rainfall, such as our study area (*36*, *37*). India has also seen a sharp increase in the prevalence of noncommunicable diseases (*38*). Although asthma prevalence is lower than the self-reported European Union (17-state) rate of 3.8% (*39*), the nationwide prevalence rate of 2.05% among adults in 2012 is consistent with a substantial burden in the population (*40*). With regard to angina, South Asians are particularly prone to the condition relative to Caucasians; for instance, the Whitehall-II study in the United Kingdom suggests a cumulative frequency of typical angina of 17.0% among South Asians versus 11.3% among Caucasians (*41*). Within India, the few existing epidemiological studies have all been conducted around the national capital of Delhi. In rural samples, two studies published 20 years apart suggest that the prevalence of probable chronic heart disease increased from 17 to 26 per 1000 (*42*).

Nevertheless, these statistics, given that they are drawn from very few epidemiological studies spread throughout the country, may not be relevant for our population. In interviews with providers (carried out after the standardized patient work), we therefore asked directly how often they saw patients with the symptoms that our standardized patients presented. Fifty-seven percent reported seeing a case of diarrhea or dysentery every day, 40% reported seeing a patient with symptoms consistent with asthma at least once every week, and 59% reported seeing a case of chest pain at least once every month (table S9). The relative frequencies are consistent with the underlying burden of disease from epidemiological studies. Equally, they suggest that the tracer conditions that we used are of more than marginal importance in this population.

It is difficult to benchmark the effect sizes that we observe on the treatment of these tracer conditions against health outcomes. This is because it is difficult to use clinical trials to compare the health outcomes of people with and without a correct diagnosis; typically, this would require the researcher to know the correct diagnosis but not inform the patient, which has obvious ethical implications. Nevertheless, systematic reviews conclude that the use of ORS and appropriate referral for diarrhea, the use of inhaled corticosteroids for asthma, and the use of aspirin and especially appropriate actions in the first day after a myocardial infarction can all have significant effects on subsequent health outcomes and mortality (*43*–*47*). In our data, ORS use increased by 9.5 percentage points, inhaled corticosteroids by 5.2 percentage points, referrals for angina [either for an electrocardiogram (ECG) or to higher care] by 8.0 percentage points, and aspirin prescription by 7.5 percentage points (table S10).

If we take the more optimistic view and look beyond the tracer conditions, we find some evidence that the training increased correct case management rates for the broader range of conditions that informal providers see in their daily practice. There was a significant increase among training-group providers in history-taking and examinations in clinical observation data with real patients. In our standardized patient data, greater history-taking and examinations measured through the checklist completion rate is consistently highly correlated with the rate of correct case management; correlational regression analysis suggests that a 100% increase in the checklist increases correct case management rates by 99.5 (72.7, 126.3) percentage points. Previously in the literature, an increase in checklist scores has been linked with improvements in health outcomes among children. Gertler and Vermeesch (*48*) showed that a 0.16-standard-deviation increase in the checklist score among Rwandan health care providers was associated with a 0.53-standard-deviation increase in the weight-for-age of children less than 1 year old and a 0.25-standard-deviation increase in the height-for-age of children between 2 and 4 years of age (*48*). In our data, the equivalent increase in the checklist score was 0.29 standard deviations. These facts taken together given us reason to believe that there was an improvement in correct case management for a broad range of conditions. It must be acknowledged, however, that without data on health outcomes, the potential impact on patient and population health remains speculative and open to multiple interpretations.

Why was there no effect on unnecessary medicines or antibiotics?

At the same time, the lack of any effect of training on the use of unnecessary medicines, injections, or antibiotics is worrying, particularly because it does not reflect a lack of adequate focus in the training program. In fact, one of the stated aims of the program was what the Liver Foundation calls "harm reduction," which specifically involved reducing the use of unnecessary medicines and antibiotics. We believe that these null results are directly tied to the revenue model of informal providers. In focus groups, informal providers clarified that their profits depended both on consultation fees and the medicines that they dispense in the clinic; patients pay a single price for the consultation and medicines. The medicines are either purchased directly from wholesale providers in big cities or from sales representatives of pharmaceutical companies. In our sample, 97% of the providers reported that they dispense at least some drugs. 75% reported purchasing from wholesale providers or sales representatives, with the bulk (70%) purchasing from the former only.

A standard result in economic models of health care is that in settings where providers can earn profits through medicine sales that are tied to their diagnoses, overtreatment is a natural outcome (*49*). This has led, for instance, to regulators in the West legislating a split between diagnosis and treatment; typically, primary care providers in the West are not allowed to profit from drug sales. Conversely, in our setting, an exit survey of 2318 patients collected on the same day as the clinical observation shows that 83% of all medicines were directly dispensed by the providers in our sample rather than prescribed. Therefore, it is likely that decreasing the use of unnecessary medicines and antibiotics would have a large effect on their revenues, and we find that training alone was insufficient to overcome this hurdle. In past studies, delinking drug purchases from the process of diagnosis has been shown to dramatically reduce the use of antibiotics (*50*).

We do not claim that this is the only reason for the lack of impact on unnecessary medicine use. Given that unnecessary or harmful practices are higher in the public sector, such behavior may also be driven by perceived (or active) patient demand for such drugs (*51*, *52*). Alternately, beliefs about the efficacy of antibiotics among providers may have been too rigid to change during this training; this remains an area of active research.

Conclusion

Our results provide the first evidence on the impact of non–disease-specific training for informal providers, an approach that is being considered by several Indian states as a complement to regulation (*53*). We do not find that training

informal providers leads them to violate rules with greater frequency or to worsen their clinical practice, which are both concerns that have been raised by representatives of the Indian Medical Association. In all dimensions, we either find significant improvements in clinical practice or no discernable change. It is noteworthy that the practices that do not change with training (for instance, the unnecessary use of antibiotics) are considerably worse among the fully trained public M.B.B.S. doctors in our sample, a result that has also been noted previously (*16*). Both the evidence of a potential beneficial effect of informal provider training as well as that of persistence in certain provider practices should be important inputs into the formulation of strategies regarding informal provider regulation and integration in low-income countries.

Methods

Training program sample selection

Between May and June 2012, the Liver Foundation invited 360 informal providers who had been practicing for at least three years in 203 villages across Birbhum district (one of 20 districts in the state) to participate in the training. This list of 360 providers was the outcome of a census conducted across three community development blocks (Illambazar, Labpur, and Sainthia) between 2011 and 2012. This census listed all untrained health workers who practiced modern (allopathic) medicine, and therefore did not include traditional healers, those who mostly practiced homeopathy or ayurveda, or veterinarians. It also excluded those providers who were not living in the villages in which they were working. Of these, 304 agreed to participate and were randomized into training and control groups with equal allocation to each. Providers randomized into the training group were offered admission to the Liver Foundation Rural Healthcare Practitioner Training Program, which commenced in January 2013. The providers randomized into the control group were informed that they would be eligible for the program at a later date. They were contacted again after the completion of the evaluation in June 2014 and offered enrollment into the next training program.

Structure of the training program

The objective of the training program was to improve the quality of curative care provision in rural areas, including primary, lifesaving, and referral services, by training the existing health care human resources of the informal sector within the community. Instruction focused on how to identify common ailments, provide early primary remedy, identify cases that required higher-level care, refer such cases to doctors and health facilities, and manage emergencies within a provider's locality before stabilizing the patient for transport to a facility. Emphasis was placed on the role of informal providers, not as "doctors," but as health workers who have the respect of the community as well as on "harm reduction" among informal providers.

The program covered a broad range of topics, ranging from anatomy and physiology to first aid in trauma and public health programs. All instruction was in the regional language (Bengali). Theoretical classes were supplemented with periodic patient simulations and clinical demonstrations of problems encountered in primary care.

The 9-month program was taught through two sessions a week, on two different days, with each session consisting of ~2 hours of interaction. Classes were taught at the district capital, which was 9 to 45 km from the providers' clinics. The program totaled 72 sessions and 150 hours of interaction. Trainees maintained their clinics as usual during the training period, though some had to close on the days of training given the long time commitment inclusive of travel. Teachers were all medical doctors with extensive work experience in rural areas.

Training on specific health conditions was conducted between the third and sixth months of the course, preceded by an introduction to medicine and followed by a focus on community medicine and humanity in medicine (table S11).

Standardized patient tracer conditions and correct case management

Three tracer conditions were used to assess the impact of the multitopic training for informal providers. These were: (i) Chest pain suggestive of unstable angina: The 40- to 45-year-old standardized patient begins his interaction with the provider with the opening statement: "Doctor, this morning I had pain in my chest." (ii) Respiratory distress suggestive of asthma: The 25- to 30-year-old standardized patient begins his interaction with the provider with the opening statement: "Doctor, last night I had a lot of difficulty with breathing." (iii) Diarrhea in a child sleeping at home: The father of the child begins his interaction with the provider with the opening statement: "My child has been having loose motion. Can you give me some medicines?"

Whether a standardized patient case was managed correctly was assessed in three ways. First, we defined correct case management for each standardized patient interaction (1 if correctly managed, 0 otherwise) on the basis of critical case-specific actions, even if paired with additional unnecessary treatments. Second, we defined "only correct case management" as 1 if correctly managed on the basis of critical case-specific actions without the prescription of additional unnecessary treatments, and 0 otherwise.

To account for the widespread use of unnecessary medicines and allow for finer assessments, our third definition employed three independent medical professionals (blinded to provider identity) at a leading teaching hospital in the state capital, Kolkata, who rated the quality of case management using a five-item Likert scale ranging from "Lowest quality case management" (1) to "Case management of choice" (5). Using these ratings, we construct two additional outcome variables: whether case management was "average quality or higher" and whether case management was the "lowest quality."

For the binary characterizations, we employed definitions of correct management appropriate for informal providers, which in practice implies that for conditions such as asthma, "referral" is coded as appropriate. Table S12 documents the condition-specific definitions used in the manuscript.

Alternatively, the treatment grading assigned by the raters allows for finer distinctions as well as the consideration of additional medicines that may have been unnecessary. The results in Table 1 therefore suggest that the findings are robust to alternate methods of assessing the quality of the treatment. Nevertheless, robustness to alternate definitions was also assessed. For instance, for diarrhea, the provision of ORS alone could be used as correct case management; for angina, referral or referral for an ECG could be used as the appropriate definition for correct case management. Depending on the specific definitions used, the most conservative estimate for the mean effects for the intention to treat estimator was 7.6 (95% CI: 0.4, 14.8) percentage points compared to 7.9 (0.4, 15.5) percentage points in the main text.

Standardized patient recruitment and training

An initial group of candidates was extensively screened, and a total of 16 standardized patients was recruited from this pool and trained for 150 hours by a multidisciplinary team. Protocols developed for a past deployment in rural India were followed in this study (*21*). There were no adverse events for standardized patients during the fieldwork, reflecting the standardized patients' ability to use evasion techniques developed during training to successfully avoid any such situations. During the interactions, standardized patients noted if the provider challenged the presentation, forcing them to disclose that the interaction was part of the standardized patient study; no such challenges were recorded so that detection rates were effectively zero.

Previous studies have documented low inter-rater differences in quality of clinical practice assessed using standardized patients (*19*). Nevertheless, in order to minimize potential bias from variation in care across different standardized patients, we ensured that each standardized patient visited multiple providers and each provider was visited by multiple standardized patients. The assignment allows us to use an additional full set of standardized patient indicators to control for potential inter-rater differences that may be correlated with the assignment to the training group. Including the full set of indicators does not alter any of the results, although there is a marginal decline in precision for some outcome variables (results available on request).

Clinical observation

The clinical observation tool assesses the behavior of health care providers with real patients using observers who remain in the providers' clinics for the entire duration of their practice for one day. Since providers saw patients at multiple times, and often at night, observer timings could vary, starting at 08:00 when the clinic

opened and finishing as late as 23:00 if the provider closed the clinic late. During the interaction with each patient, a structured questionnaire was completed by the observer with details such as the number and type of examinations completed, the number of questions asked, and the consultation time. Observers were not allowed to speak to the provider or patient at any time during the consultation. At the end of the consultation, the provider would list the medicines dispensed or prescribed for the patient, which would be noted in the structured observation form. The clinical observation tool was adapted for this study from previous use in a number of studies (*20*).

We recognize that clinical observations may be subject to Hawthorne effects as well as potential confounds—e.g. the patient population may be different for trained and untrained providers. It is also the case that the true underlying patient condition remains unknown to the observer. Nevertheless, clinical observations provide information on a broader sample of conditions that affect real patients and allow assessments of the impact of training on the actual use of injections and IVs, which were intentionally avoided by standardized patients.

Caseload and fees data collection

Caseload data was collected through clinical observations as well as provider diaries, in which informal providers recorded the number of patients seen one day of each week for three months between months 6 to 9 of the training program. Patient fees were assessed through clinical observations, standardized patient reports, and provider diaries.

Further methodological details are provided in the supplementary materials.

REFERENCES AND NOTES

1. M. Sudhinaraset, M. Ingram, H. K. Lofthouse, D. Montagu, What is the role of informal healthcare providers in developing countries? A systematic review. *PLOS ONE* **8**, e54978 (2013). doi: 10.1371/journal.pone.0054978; pmid: 23405101
2. A. Banerjee, A. Deaton, E. Duflo, Wealth, health, and health services in rural Rajasthan. *Am. Econ. Rev.* **94**, 326–330 (2004). doi: 10.1257/0002828041301902; pmid: 19305517
3. A. De Costa, V. Diwan, 'Where is the public health sector?' Public and private sector healthcare provision in Madhya Pradesh, India. *Health Policy* **84**, 269–276 (2007). doi: 10.1016/j.healthpol.2007.04.004; pmid: 17540472
4. M. Gautham *et al*., Informal rural healthcare providers in North and South India. *Health Policy Plan.* **29**, i20–i29 (2014). doi: 10.1093/heapol/czt050; pmid: 25012795
5. B. Kanjilal, S. Mondal, T. Samanta, A. Mondal, S. Singh, "A parallel health care market: Rural medical practitioners in West Bengal, India" (Future Health Systems Research Brief No. 2, Institute of Health Management Research, 2007).
6. "India has 9.36 lakh doctors of modern medicine," *India Medical Times*, 13 March 2015; www.indiamedicaltimes.com/2015/03/13/india-has-9-36-lakh-doctors-of-modern-medicine/.
7. Government of India, *Report of the Health Service and Development Committee* (Manager of Publications, Delhi, 1946).
8. F. Mullan, S. Frehywot, Non-physician clinicians in 47 sub-Saharan African countries. *Lancet* **370**, 2158–2163 (2007). doi: 10.1016/S0140-6736(07)60785-5; pmid: 17574662
9. S. Raha, T. Bossert, M. Vujicic, "The Chhattisgarh experience with a three-year course for rural health care practitioners" (Health, Nutrition and Population Discussion Paper, The World Bank, 2010).
10. P. Pulla, "Andhra Pradesh: The state that dared to train 'quacks' in medicine," *Mosaic: The Science of Life*, 5 November 2015; http://mosaicscience.com/extra/andhra-pradesh-quacks.
11. P. Pulla, "India is training 'quacks' to do real medicine. This is why," *Mosaic: The Science of Life*, 3 November 2015; http://mosaicscience.com/story/india-quacks.
12. Y. Adu-Sarkodie, M. J. Steiner, J. Attafuah, K. Tweedy, Syndromic management of urethral discharge in Ghanaian pharmacies. *Sex. Transm. Infect.* **76**, 439–442 (2000). doi: 10.1136/sti.76.6.439; pmid: 11221125
13. P. Garcia, J. Hughes, C. Carcamo, K. K. Holmes, Training pharmacy workers in recognition, management, and prevention of STDs: District-randomized controlled trial. *Bull. World Health Organ.* **81**, 806–814 (2003). pmid: 14758407
14. N. M. Shah, W. R. Brieger, D. H. Peters, Can interventions improve health services from informal private providers in low and middle-income countries? A comprehensive review of the literature. *Health Policy Plan.* **26**, 275–287 (2011). doi: 10.1093/heapol/czq074; pmid: 21097784
15. T. Abuya *et al*., Impact of Ministry of Health interventions on private medicine retailer knowledge and practices on anti-malarial treatment in Kenya. *Am. J. Trop. Med. Hyg.* **80**, 905–913 (2009). pmid: 19478247
16. J. Das, A. Holla, A. Mohpal, K. Muralidharan, *Am. Econ. Rev.* www.aeaweb.org/articles?id=10.1257/aer.20151138&&from=f (2015).
17. S. Sylvia *et al*., Survey using incognito standardized patients shows poor quality care in China's rural clinics. *Health Policy Plan.* **30**, 322–333 (2015). doi: 10.1093/heapol/czu014; pmid: 24653216
18. M. Mohanan *et al*., The know-do gap in quality of health care for childhood diarrhea and pneumonia in rural India. *JAMA Pediatr.* **169**, 349–357 (2015). pmid: 25686357
19. J. Das *et al*., Use of standardised patients to assess quality of tuberculosis care: A pilot, cross-sectional study. *Lancet Infect. Dis.* **15**, 1305–1313 (2015). doi: 10.1016/S1473-3099(15)00077-8; pmid: 26268690
20. J. Das, J. Hammer, Quality of primary care in low-income countries: Facts and economics. *Annu. Rev. Econ.* **6**, 525–553 (2014). doi: 10.1146/annurev-economics-080213-041350
21. J. Das *et al*., In urban and rural India, a standardized patient study showed low levels of provider training and huge quality gaps. *Health Aff.* **31**, 2774–2784 (2012). doi: 10.1377/hlthaff.2011.1356; pmid: 23213162
22. MAQARI Team, "Mapping medical providers in rural India: Four key trends" (Policy Brief, Center for Policy Research, New Delhi, India, 2011).
23. A. Banerjee, A. Deaton, E. Duflo, Health care delivery in rural Rajasthan. *Econ. Polit. Wkly.* **39**, 944–949 (2004).
24. S. K. Jindal, D. Gupta, A. N. Aggarwal, R. Agarwal; World Health Organization, Government of India, Guidelines for management of asthma at primary and secondary levels of health care in India (2005). *Indian J. Chest Dis. Allied Sci.* **47**, 309–343 (2005). pmid: 16255405
25. Ministry of Health and Family Welfare, Government of India, "Integrated management of neonatal and childhood illness: Physician chart booklet," 2009; www.medbox.org/integrated-management-of-neonatal-and-childhood-illness/download.pdf.
26. "Ischaemic heart disease: Acute myocardial infarction," http://cghealth.nic.in/ehealth/2013/QA_website/5StandardTreatmentGuidelines/AcuteMyocardialInfarction.pdf.
27. J. D. Angrist, J. S. Pischke, "IV with heterogeneous potential outcomes" in *Mostly Harmless Econometrics: An Empiricist's Companion* (Princeton Univ. Press, 2008), pp. 117–119.
28. J. Das, J. Hammer, Which doctor? Combining vignettes and item response to measure clinical competence. *J. Dev. Econ.* **78**, 348–383 (2005). doi: 10.1016/j.jdeveco.2004.11.004
29. J. Das, J. Hammer, Money for nothing: The dire straits of medical practice in Delhi, India. *J. Dev. Econ.* **83**, 1–36 (2007). doi: 10.1016/j.jdeveco.2006.05.004
30. A. V. Banerjee, E. Duflo, R. Glennerster, Putting a band-aid on a corpse: Incentives for nurses in the Indian public health care system. *J. Eur. Econ. Assoc.* **6**, 487–500 (2008). doi: 10.1162/JEEA.2008.6.2-3.487; pmid: 20182650
31. I. Dhaliwal, R. Hanna, "Deal with the devil: The successes and limitations of bureaucratic reform in India" (NBER Working Paper 20482, National Bureau of Economic Research, 2014).
32. T. Powell-Jackson, S. Mazumdar, A. Mills, Financial incentives in health: New evidence from India's *Janani Suraksha Yojana*. *J. Health Econ.* **43**, 154–169 (2015). doi: 10.1016/j.jhealeco.2015.07.001; pmid: 26302940
33. M. Mohanan *et al*., Effect of *Chiranjeevi Yojana* on institutional deliveries and neonatal and maternal outcomes in Gujarat, India: A difference-in-differences analysis. *Bull. World Health Organ.* **92**, 187–194 (2014). doi: 10.2471/BLT.13.124644; pmid: 24700978
34. West Bengal Recruitment Board, "Recruitment to the posts of Medical Officer (Specialist)," 2016; http://wbhrb.eadmissions.net/Images/WBHRB-MO-Specialist-March-4-2016.pdf.
35. The program costs ~$175 per provider ($2.3 per session), inclusive of all teacher salaries, training hall rentals, and transportation and meal fees. These costs are comparable to those of other published training programs, which range from $50 for 2 days of training to $200 for a longer-duration program designed to improve specific practices among pharmacists (cost calculations for the latter may not have included the time of government employees) (*15*, *54*).
36. R. E. Black *et al*., Global, regional, and national causes of child mortality in 2008: A systematic analysis. *Lancet* **375**, 1969–1987 (2010). doi: 10.1016/S0140-6736(10)60549-1; pmid: 20466419
37. Society for Health and Demographic Surveillance, *2015 Annual Report*, 2015; www.shds.in/pdfs/publication_2015_1.pdf
38. V. Patel *et al*., Chronic diseases and injuries in India. *Lancet* **377**, 413–428 (2011). doi: 10.1016/S0140-6736(10)61188-9; pmid: 21227486
39. OECD (Organization for Economic Co-operation and Development), "Asthma and COPD prevalence," in *Health at a Glance: Europe 2012* (OECD Publishing, 2012); www.oecd-ilibrary.org/social-issues-migration-health/health-at-a-glance-europe-2012/asthma-and-copd-prevalence_9789264183896-19-en.
40. S. K. Jindal *et al*., Indian study on epidemiology of asthma, respiratory symptoms and chronic bronchitis in adults (INSEARCH). *Int. J. Tuberc. Lung Dis.* **16**, 1270–1277 (2012). doi: 10.5588/ijtld.12.0005; pmid: 22871327
41. M. J. S. Zaman *et al*., Incidence and prognosis of angina pectoris in South Asians and Whites: 18 years of follow-up over seven phases in the Whitehall-II prospective cohort study. *J. Public Health (Oxf.)* **33**, 430–438 (2011). doi: 10.1093/pubmed/fdq093; pmid: 21045007
42. N. Ahmad, R. Bhopal, Is coronary heart disease rising in India? A systematic review based on ECG defined coronary heart disease. *Heart* **91**, 719–725 (2005). doi: 10.1136/hrt.2003.031047; pmid: 15894760
43. M. K. Munos, C. L. Walker, R. E. Black, The effect of oral rehydration solution and recommended home fluids on diarrhoea mortality. *Int. J. Epidemiol.* **39**, i75–i87 (2010). doi: 10.1093/ije/dyq025; pmid: 20348131
44. S. Suissa, P. Ernst, Inhaled corticosteroids: Impact on asthma morbidity and mortality. *J. Allergy Clin. Immunol.* **107**, 937–944 (2001). doi: 10.1067/mai.2001.115653; pmid: 11398069
45. P. Ernst *et al*., Risk of fatal and near-fatal asthma in relation to inhaled corticosteroid use. *JAMA* **268**, 3462–3464 (1992). doi: 10.1001/jama.1992.03490240070039; pmid: 1460737
46. D. M. Cutler, M. McClellan, J. P. Newhouse, What has increased medical-care spending bought? *Am. Econ. Rev.* **82**, 132–136 (1998).
47. M. McClellan, B. J. McNeil, J. P. Newhouse, Does more intensive treatment of acute myocardial infarction in the elderly reduce mortality? Analysis using instrumental variables. *JAMA* **272**, 859–866 (1994). doi: 10.1001/jama.1994.03520110039026; pmid: 8078163
48. P. Gertler, C. Vermeersch, "Using performance incentives to improve health outcomes" (Impact Evaluation Series No. 60, Policy Research Working Paper 6100, The World Bank, 2012).
49. U. Dulleck, R. Kerschbamer, On doctors, mechanics and computer specialists: The economics of credence goods. *J. Econ. Lit.* **44**, 5–42 (2006). doi: 10.1257/002205106776162717
50. J. Currie, W. Lin, W. Zhang, Patient knowledge and antibiotic abuse: Evidence from an audit study in China. *J. Health Econ.* **30**, 933–949 (2011). doi: 10.1016/j.jhealeco.2011.05.009; pmid: 21733587
51. X. Sun, S. Jackson, G. A. Carmichael, A. C. Sleigh, Prescribing behaviour of village doctors under China's New Cooperative Medical Scheme. *Soc. Sci. Med.* **68**, 1775–1779 (2009). doi: 10.1016/j.socscimed.2009.02.043; pmid: 19342138
52. D. Bennett, C. Hung, T. Lauderdale, Health care competition and antibiotic use in Taiwan. *J. Ind. Econ.* **63**, 371–393 (2015). doi: 10.1111/joie.12075
53. J. Varghese, The new rural doctor: Qualified quack or appropriate healthcare provider? *Indian J. Med. Ethics* **7**, 70–72 (2010). pmid: 20432877

54. J. Chalker, N. T. Chuc, T. Falkenberg, G. Tomson, Private pharmacies in Hanoi, Vietnam: A randomized trial of a 2-year multi-component intervention on knowledge and stated practice regarding ARI, STD and antibiotic/steroid requests. *Trop. Med. Int. Health* **7**, 803–810 (2002). doi: 10.1046/j.1365-3156.2002.00934.x; pmid: 12225513

ACKNOWLEDGMENTS

This study was funded through grants from the West Bengal National Rural Health Mission and The World Bank's Knowledge for Change Program, as well as a Bristol-Myers Squibb Foundation award under the Delivering Hope program to the Liver Foundation, West Bengal, India. At the Liver Foundation, the training program was implemented by S. Mazumdar and K. Chatterjee. R. Ghosh and P. Mukherjee were involved in the organization of the training. A. Barik, P. Goswami, and A. Dutta provided invaluable assistance in grading all the treatments received by standardized patients. We thank Purshottam, R. Singh, Devender, C. Nanda, S. Bajaj, Geeta, the standardized patients, and members of the Institute for Socioeconomic Research on Democracy and Development (ISERDD) in New Delhi for implementing the field work; V. Das and R. K. Das at ISERDD for their assistance in finalizing all field work material and overseeing the field work; D. D. Roy and S. Chakraborty of J-PAL (The Abdul Latif Jameel Poverty Action Lab) for project management; B. Daniels for excellent research assistance; and M. Pai, Z. Obermeyer, S. Satyanarayana, and A. Wagstaff for helpful comments. The findings, interpretations, and conclusions expressed in this paper are those of the authors and do not necessarily represent the views of The World Bank, its executive directors, or the governments that they represent. All data and replication materials are available on request. J.D., R.H., and A.V.B. declare no conflicts of interest. A.C. is a volunteer at the Liver Foundation and has no further conflicts to disclose.

SUPPLEMENTARY MATERIALS

www.sciencemag.org/content/354/6308/aaf7384/suppl/DC1
Materials and Methods
Supplementary Text
Figs. S1 to S5
Tables S1 to S10
Reference (*55*)

22 March 2016; accepted 25 August 2016
10.1126/science.aaf7384

RESEARCH ARTICLE SUMMARY

NEURODEVELOPMENT

Extensive migration of young neurons into the infant human frontal lobe

Mercedes F. Paredes, David James, Sara Gil-Perotin, Hosung Kim, Jennifer A. Cotter, Carissa Ng, Kadellyn Sandoval, David H. Rowitch, Duan Xu, Patrick S. McQuillen, Jose-Manuel Garcia-Verdugo, Eric J. Huang,* Arturo Alvarez-Buylla*

INTRODUCTION: Inhibitory interneurons balance the excitation and inhibition of neural networks and therefore are key to normal brain function. In the developing brain, young interneurons migrate from their sites of birth into distant locations, where they functionally integrate. Although this neuronal migration is largely complete before birth, some young inhibitory interneurons continue to travel and add to circuits in restricted regions of the juvenile and adult mammalian brain. For example, postnatally migrating inhibitory neurons travel from the walls of the lateral ventricle, along the rostral migratory stream (RMS) into the olfactory bulb. In humans, an additional ventral route branching off the RMS, the medial migratory stream (MMS), takes young neurons into the medial prefrontal cortex. It has been suggested that recruitment of neurons during postnatal life could help shape neural circuits according to experience. Specifically, inhibitory interneuron maturation during postnatal development is associated with critical periods of brain plasticity. We asked whether neuronal recruitment continues into early childhood in the frontal lobe, a region of the human brain that has greatly increased in size and complexity during evolution.

RATIONALE: Migrating young neurons persist for several months after birth in an extensive region of the subventricular zone (SVZ) around the anterior lateral ventricles in the human brain. Are all these young neurons migrating into the RMS and MMS, or do they have other destinations? Using high-resolution magnetic resonance imaging (MRI), histology, and time-lapse confocal microscopy, we observed the migration of many young inhibitory interneurons around the dorsal anterior walls of the lateral ventricle and into multiple cortical regions of the human frontal cortex. We determined the location and orientation of these young neurons, demonstrated their active translocation, and inferred their fates in the postnatal anterior forebrain.

RESULTS: A large collection of cells expressing doublecortin (DCX), a marker of young migrating neurons, traveled and integrated within the infant frontal lobe. This migratory stream, which was most prominent during the first 2 months after birth and persisted until at least 5 months, formed a caplike structure surrounding the anterior body of the lateral ventricle. We refer to this population of young neurons as the Arc. This structure could also be visualized by brain MRI. Young neurons in the Arc appeared to move long distances in distinct regions around the ventricular wall and the developing white matter. The orientation of elongated DCX^+ cells suggested that migratory neurons closer to the ventricular wall dispersed tangentially. In contrast, migratory neurons within the developing white matter tended to be orientated toward the overlying cortex. These cells expressed markers of interneurons, and their entry into the anterior cingulate cortex (a major target of the Arc used for quantification) was correlated with the emergence of specific subtypes of γ-aminobutyric acid (GABA)–expressing interneurons (neuropeptide Y, somatostatin, calretinin, and calbindin). Expression of transcription factors associated with specific sites of origin suggested that these neurons arise from ventral telencephalon progenitor domains.

ON OUR WEBSITE

Read the full article at http://dx.doi.org/10.1126/science.aaf7073

CONCLUSION: Widespread neuronal migration into the human frontal lobe continues for several months after birth. Young neurons express markers of cortical inhibitory interneurons and originate outside the cortex, likely in the ventral forebrain. The postnatal recruitment of large populations of inhibitory neurons may contribute to maturation and plasticity in the human frontal cortex. Defects in the migration of these neurons could result in circuit dysfunctions associated with neurodevelopmental disorders. ■

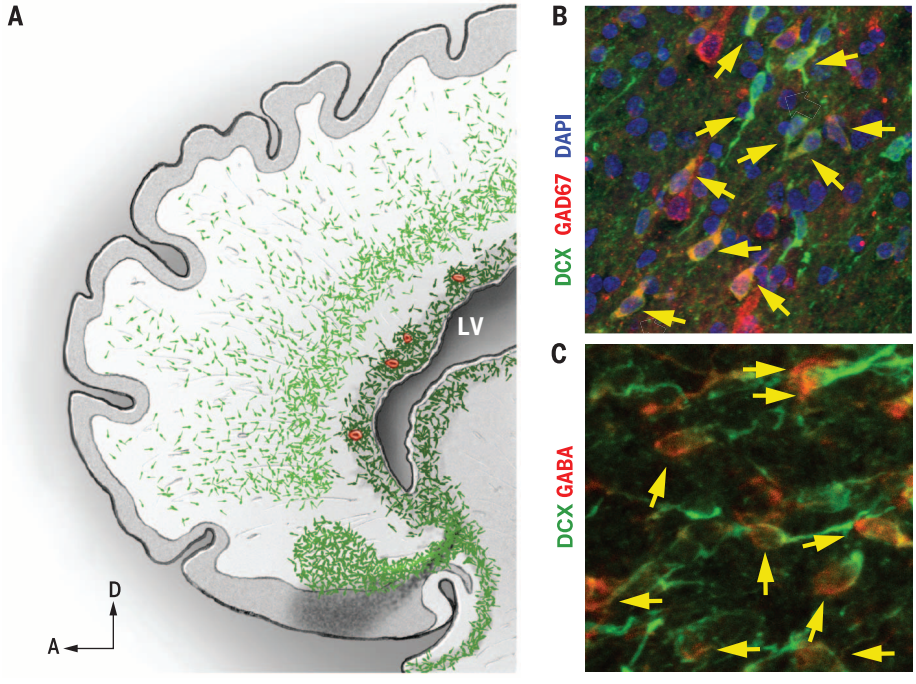

Widespread neuronal migration into the human frontal lobe continues during postnatal life. (**A**) Sagittal schematic of the newborn forebrain shows prominent collections of young migratory neurons (illustrated in green) adjacent to the lateral ventricle (LV) and in the overlying white matter. Directional axes: D, dorsal; A, anterior. (**B** and **C**) DCX^+ cells coexpress GABA and GAD67, markers of inhibitory interneurons (marked by arrows).

The list of author affiliations is available in the full article online.
*Corresponding author. Email: alvarezbuyllaa@ucsf.edu (A.A.-B.); eric.huang2@ucsf.edu (E.J.H.)
Cite this article as M. F. Paredes *et al.*, *Science* **354**, aaf7073 (2016). DOI: 10.1126/science.aaf7073

RESEARCH ARTICLE

NEURODEVELOPMENT

Extensive migration of young neurons into the infant human frontal lobe

Mercedes F. Paredes,[1,2] David James,[1,3] Sara Gil-Perotin,[4,5] Hosung Kim,[6] Jennifer A. Cotter,[7] Carissa Ng,[1,3] Kadellyn Sandoval,[1,2] David H. Rowitch,[1,8,9] Duan Xu,[6] Patrick S. McQuillen,[8] Jose-Manuel Garcia-Verdugo,[4] Eric J. Huang,[1,7]* Arturo Alvarez-Buylla[1,3]*

The first few months after birth, when a child begins to interact with the environment, are critical to human brain development. The human frontal lobe is important for social behavior and executive function; it has increased in size and complexity relative to other species, but the processes that have contributed to this expansion are unknown. Our studies of postmortem infant human brains revealed a collection of neurons that migrate and integrate widely into the frontal lobe during infancy. Chains of young neurons move tangentially close to the walls of the lateral ventricles and along blood vessels. These cells then individually disperse long distances to reach cortical tissue, where they differentiate and contribute to inhibitory circuits. Late-arriving interneurons could contribute to developmental plasticity, and the disruption of their postnatal migration or differentiation may underlie neurodevelopmental disorders.

Local inhibitory interneurons in the cerebral cortex play key roles in the final assembly of brain circuits, and their maturation is essential to critical-period plasticity and learning (*1*, *2*). Interneurons are born in ventral progenitor zones, primarily the medial and caudal ganglionic eminences (MGE and CGE), and then migrate dorsally to reach the cerebral cortex (*3*–*7*). Neuronal migration is largely completed during fetal development (*8*, *9*). However, in many species, migrating young neurons persist in the postnatal subventricular zone (SVZ) of the lateral ventricles (*10*, *11*). In rodents, SVZ-derived neurons migrate along the rostral migratory stream (RMS) into the olfactory bulb, where they replace neurons throughout life (*12*–*15*). A small number of these neurons, born perinatally, migrate into the anterior forebrain to become small axonless neurons (*16*, *17*) or into the ventral forebrain to become granule cells in the islands of Calleja (*18*). In the infant human brain, SVZ-derived young neurons migrate along the RMS (*19*, *20*) into the olfactory bulb, and a subpopulation of these cells migrates along a medial migratory stream (MMS) into the ventral medial prefrontal cortex (*20*). The postnatal human SVZ extends dorsally, but it is not known whether cells in this region also contribute to other areas of the human forebrain. Given the tremendous postnatal growth of the human frontal lobe and the prevalence of migrating young neurons in the adjacent SVZ, we investigated whether neurons also continue migrating into the frontal lobe of infants and young children.

Postnatal migratory pathways into the frontal lobes

In samples from the anterior forebrain of children younger than 3 months of age, regions of high cell densities were observed in the SVZ.

[1]Edythe Broad Institute for Stem Cell Research and Regeneration Medicine, University of California, San Francisco, CA 94143, USA. [2]Department of Neurology, University of California, San Francisco, CA 94143, USA. [3]Department of Neurological Surgery, University of California, San Francisco, CA 94143, USA. [4]Laboratory of Comparative Neurobiology, Instituto Cavanilles, Universidad de Valencia, CIBERNED, Valencia, Spain. [5]Multiple Sclerosis and Neural Regeneration Unit, Department of Neurology, Hospital Universitario y Politecnico La Fe, 46026 Valencia, Spain. [6]Department of Radiology and Biomedical Imaging, University of California, San Francisco, CA 94143, USA. [7]Department of Pathology, University of California, San Francisco, CA 94143, USA. [8]Department of Pediatrics, University of California, San Francisco, CA 94143, USA. [9]Department of Paediatrics, University of Cambridge, Cambridge CB2 0QQ, UK.
*Corresponding author. Email: alvarezbuyllaa@ucsf.edu (A.A.-B.); eric.huang2@ucsf.edu (E.J.H.)

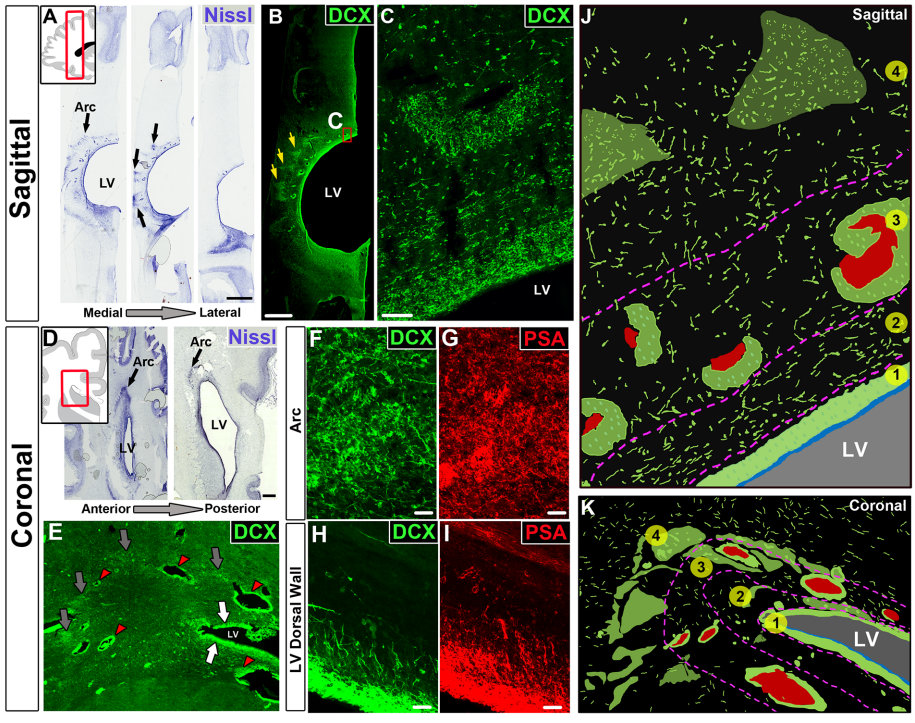

Fig. 1. Migrating young neurons in the infant frontal lobe are widely distributed in four tiers. (**A**) Serial Nissl-stained sections (taken at birth) reveal cell-dense collections around the anterior body of the lateral ventricle (black arrows, defined here as the Arc); LV, lateral ventricle. (**B** and **C**) The cells in these densities (yellow arrows) and next to the ventricular wall express DCX. (**D**) Coronal sections (38 GW) showing cell densities close to the ventricular wall (eyebrow-shaped, black arrows). (**E**) Dense aggregates of DCX$^+$ cells around the walls of the lateral ventricles (white arrows), around blood vessels (red arrowhead), and in the parenchyma within the Arc (gray arrows). (**F** to **I**) DCX$^+$ cells also express PSA-NCAM; (F) and (G) show cells within the Arc; (H) and (I) show cells next to the ventricular walls. (**J** and **K**) Schematic drawings of traced DCX$^+$ cells (in green) illustrating how cells within the Arc are organized into four tiers (see text). Blood vessels are shown in red; light green clusters correspond to DCX$^+$ cellular densities seen in (B) and (E). Scale bars, 2 mm [(A) and (B)], 50 μm (C), 1 mm (D), 25 μm [(F) to (I)].

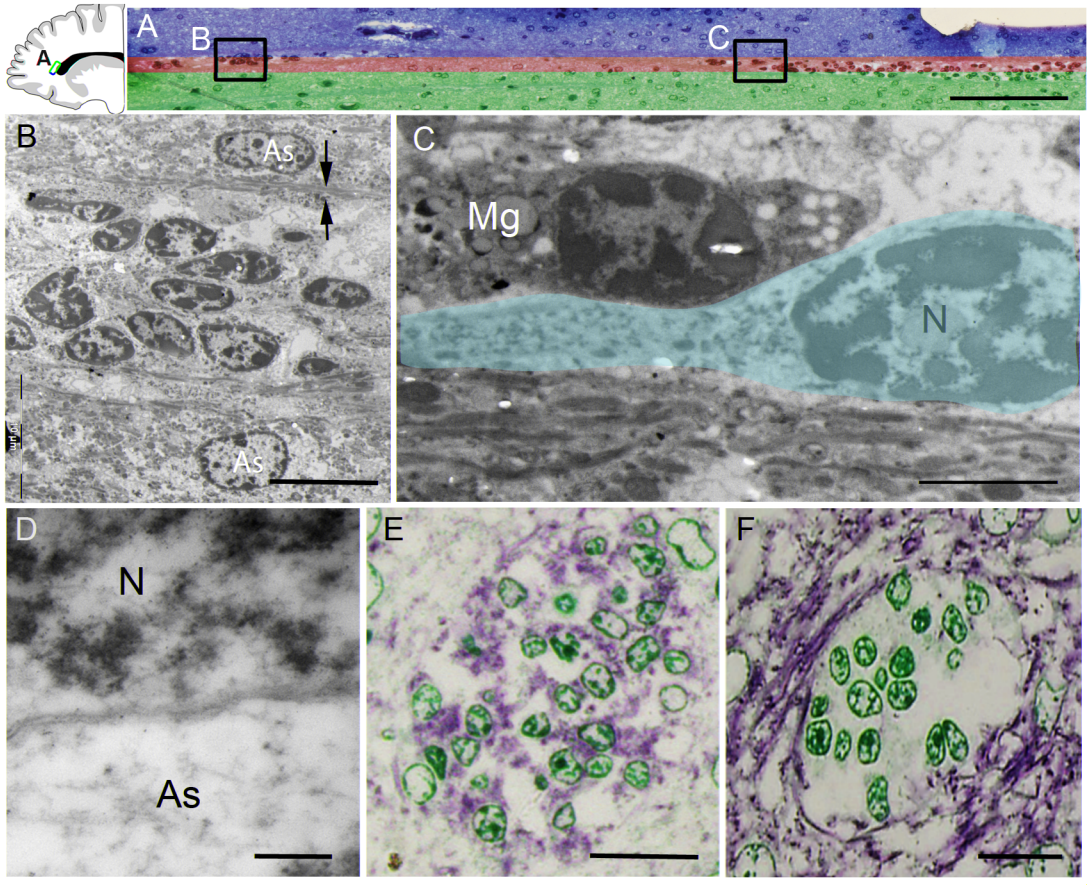

Fig. 2. Arc cells have ultrastructural features of migrating young neurons. (**A**) Toluidine blue staining of a semithin sagittal section from a 1-month-old brain showing a chain of cells around a blood vessel in tier 3 (see Fig. 1). Locations of images in (B) and (C) are shown. (**B**) Electron microscopy shows that this chain is made up of elongated cells with ultrastructural features of young migrating neurons; the chain is flanked by astrocytes (As) whose expansions (arrows) contain intermediate filaments. (**C**) An elongated migrating neuron (outlined in pink) next to a microglial cell (Mg). Migrating young neurons (N) frequently had an elongated morphology, a leading process, polyribosomes, and no intermediate filaments. (**D**) The cytoplasm of astrocytes is lighter and contains intermediate filaments. (**E** and **F**) 3,3′-Diaminobenzidine (DAB) staining of semithin coronal sections (adjacent to those used for electron microscopy) shows DCX expression within the chain and GFAP expression surrounding them; the counterstain is toluidine blue. Scale bars, 50 μm (A), 10 μm (B), 2 μm (C), 200 nm (D), 15 μm [(E) and (F)].

These densities were adjacent to the anterior body of the lateral ventricle and within the neighboring subcortical white matter, forming a distinct arching structure in sagittal sections or an eyebrow-shaped extension in coronal sections (Fig. 1, A and D, black arrows). The majority of cells within these regions coexpressed doublecortin (DCX) and polysialylated neural cell adhesion molecule (PSA-NCAM), markers of young migrating neurons (Fig. 1, B, C, and E, and fig. S1B) (*21*, *22*). Many of these cells displayed migratory morphology, with an elongated cell body and a leading process that was occasionally bifurcated (*23*–*25*). DCX^+ cells did not express Olig2 (see below), which marks oligodendrocytes and their precursor cells, nor the astrocytic markers glial fibrillary acidic protein (GFAP) and Aldh1L1 (fig. S1 and fig. S2, K and L).

In postmortem brains collected at birth and at 1 month, these putative migrating young neurons were organized into four layers, or tiers, around the anterior body of the lateral ventricles (Fig. 1, J and K, and fig. S1F). Tier 1 corresponded to a cell-dense SVZ band of DCX^+ cells next to the walls of the lateral ventricle; between 6 and 12 months, tier 1 is depleted of young neurons, becoming a hypocellular gap layer (*20*). Tier 2 contained a more dispersed collection of DCX^+ cells. Tier 3 was an intermediate region with many DCX^+ cells within clusters, frequently around blood vessels, and dispersed DCX^+ cells around these clusters (fig. S3). Tier 4 contained a group of DCX^+ cells dispersed within areas of the developing white matter. Many cells in tier 4 were organized around radial finger-like extensions of triangular shape (Fig. 1B, yellow arrows). We analyzed these tiered regions in 1-day-old and 28-day-old brains by electron microscopy. Cells with the ultrastructure of young migrating neurons were found throughout tiers 1 to 4. Migrating young neurons were organized as chains (*12*) or as individual cells (Fig. 2, A to D, and fig. S4, C and G). Those within chains had adherent junctions similar to those observed in the RMS (fig. S4, G and H). Confocal and electron microscopy showed that chains of migrating neurons were flanked by cells rich in intermediate filaments containing GFAP (Fig. 2F, fig. S1C, and movie S1).

To generate a multiplanar representation of migratory streams of cells, we used high-resolution magnetic resonance imaging (MRI) to image intact hemispheres from postmortem human brains between birth and 2 months of age, including a premature case born at 34 gestational weeks (GW) (table S1). MRI analysis revealed a T2 hyperintense signal adjacent to the anterior horn of the lateral ventricle (fig. S5, A and B, red shading). Three-dimensional rendering of the segmented areas of T2 signal in brains at 34 GW and at birth showed that this structure formed a cap around the anterior horn of the lateral ventricle (fig. S5D). In sagittal MRI planes, this cap structure had an arc shape (fig. S5, A and G), running parallel to the anterior cingulate cortex and extending caudally to approximately the level of the central sulcus. This arc was also observed in live MRI images of the developing human brain (fig. S5, H and I). The T2 hyperintense signal was localized to ventricular regions densely populated by DCX^+ cells (fig. S1, E to G). Given the organization we observed in both histological and radiographic images, we refer to these streams of cells as the "Arc."

Migratory features of young neurons in the human infant brain

To confirm that these cells were in fact actively migrating, we obtained human neonatal brain samples (table S1) with short postmortem intervals and infected them with adenovirus carrying green fluorescent protein (adenoGFP) for time-lapse confocal microscopy. Elongated GFP^+ cells (n = 18) with leading processes were identified, and we studied their behavior for 24 to 48 hours (Fig. 3C). As shown (movies S2 and S3), these cells actively migrated in coronal and sagittal slice cultures, displaying leading process extension, nucleokinesis, and retraction of trailing process. These features were indistinguishable from the migratory behavior of neurons in the

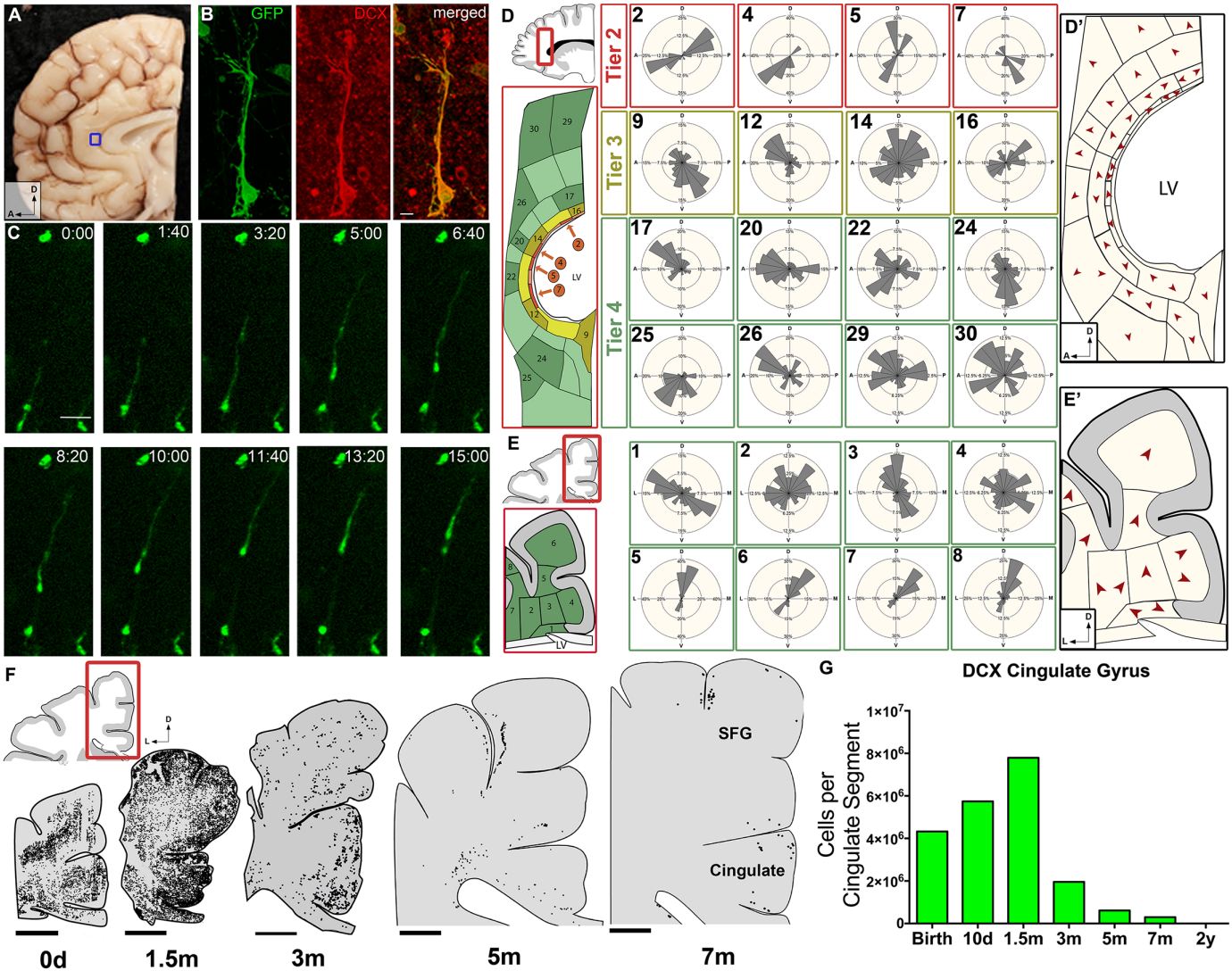

Fig. 3. Migration and directionality of young neurons in the infant brain. (**A**) Boxed region shows area of the neonatal brain that was imaged in (B) and (C) in the cingulate gyrus. (**B**) DCX$^+$ adenoGFP-labeled cell with migratory morphology. (**C**) Time-lapse sequence (15 hours) of adenoGFP-labeled cell revealing leading process extension, nucleokinesis, and trailing process retraction. This cell traveled ~100 μm, migrating anteriorly in the sagittal plane. (**D** and **E**) Vector mapping of orientation of DCX$^+$ cell leading processes, in sagittal and coronal sections; note how directionality changes in the different tiers. See figs. S6 and S7 for complete analysis. (**D´** and **E´**) Red arrowheads indicate the modal (most frequent) direction of DCX$^+$ cells' leading process. (**F**) Spatiotemporal mapping of DCX$^+$ cells in coronal cortical sections; between birth and 1.5 months, many DCX$^+$ cells have moved from the periventricular and parenchymal regions into the developing cortex of the cingulate and superior frontal gyrus. DCX$^+$ cells then rapidly decrease at 3 and 5 months, but a few DCX$^+$ cells with clear migratory morphology remain at 7 months. (**G**) Quantification of DCX$^+$ cells in the cingulate gyrus (white matter and gray matter). Scale bars, 10 μm (B), 50 μm (C), 5 mm (F). Directional axes: D, dorsal; L, lateral; A, anterior.

fetal brain (*24*, *26*, *27*). Active migration was also observed within clusters of cells (movies S3 and S4) at the dorsolateral ventricular edge, but because of their high cellular density, the behavior of individual cells was often not evident. In one of these clusters, we captured a labeled cell escaping the cluster to begin individual migration (movie S4). Immunostaining of these brain slices after time-lapse imaging confirmed that the migrating cells were DCX$^+$ (Fig. 3B). Thus, neurons in the newborn brain within the Arc and immediate surroundings are actively migrating.

Using fixed tissue, we inferred possible migratory trajectories from the orientation of the leading process of DCX$^+$ young neurons. We defined a vector from the center of the cell body in the direction of the leading process (see supplementary materials). We applied this analysis to DCX$^+$ cells in coronal and sagittal sections at birth and 1.5 months of age in periventricular and subcortical white matter regions in the frontal lobe (Fig. 3, D and E). We observed that the vector orientation of the cells changed depending on the region. The leading process of DCX$^+$ cells could not be discerned in tier 1 because of the high cellular density, but the majority of cells in tier 2 appeared to be migrating tangentially, parallel to the ventricle wall. In the sagittal plane, cells were oriented ventrally and dorsally. In tier 3, the orientation remained largely tangential, but cellular direction was more variable than in tier 2. Lastly, in tier 4 and at the gray matter–white matter junction, more cells were oriented toward the developing cortex (Fig. 3, D and E, and figs. S6 and S7). A similar pattern of vector orientation was also observed in the coronal plane of the frontal lobe at 1.5 months (fig. S8). These data suggest that young neurons in regions close to the ventricles primarily migrate in the tangential plane, whereas those in tiers 3 and 4, and in the developing white matter and cortex, are more widespread and cortically directed.

We next mapped the distribution of young migratory neurons adjacent to the ventricular wall and in the overlying cortices at birth and

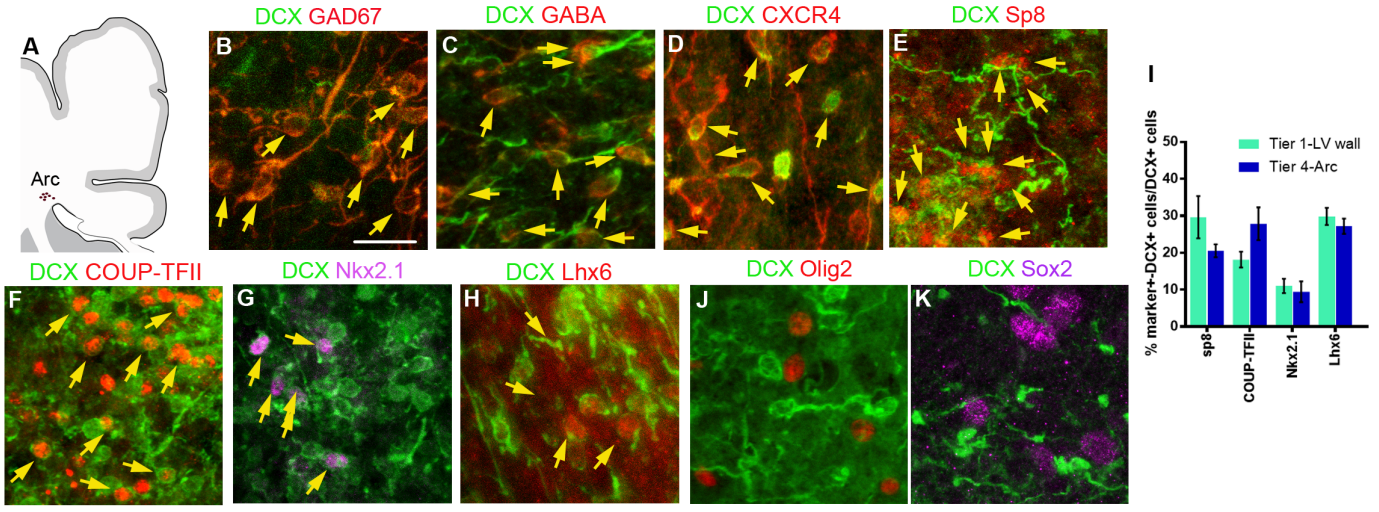

Fig. 4. Interneuron and subpallial marker expression in migrating DCX$^+$ cells in the infant brain. (**A**) Schematic of coronal section indicating the Arc area that was analyzed at the dorsolateral edge of the ventricle; see fig. S2 for marker expression next to the walls of the lateral ventricle. (**B** to **D**) DCX$^+$ cells express GAD67, GABA, and the cytokine receptor CXCR4 present in migrating interneurons. (**E** to **H**) Subpopulations of DCX$^+$ cells express different transcription factors associated with ventral telencephalic origin, including Sp8, COUP-TFII, Nkx2.1, or Lhx6 associated with the CGE or MGE. (**I**) Quantification of DCX$^+$ cells expressing Sp8, COUP-TFII, Nkx2.1, and Lhx6. Bars show means ± SEM of counts performed on three or four individual cases. (**J** and **K**) DCX$^+$ cells do not express Olig2 or Sox2. Scale bar, 20 μm.

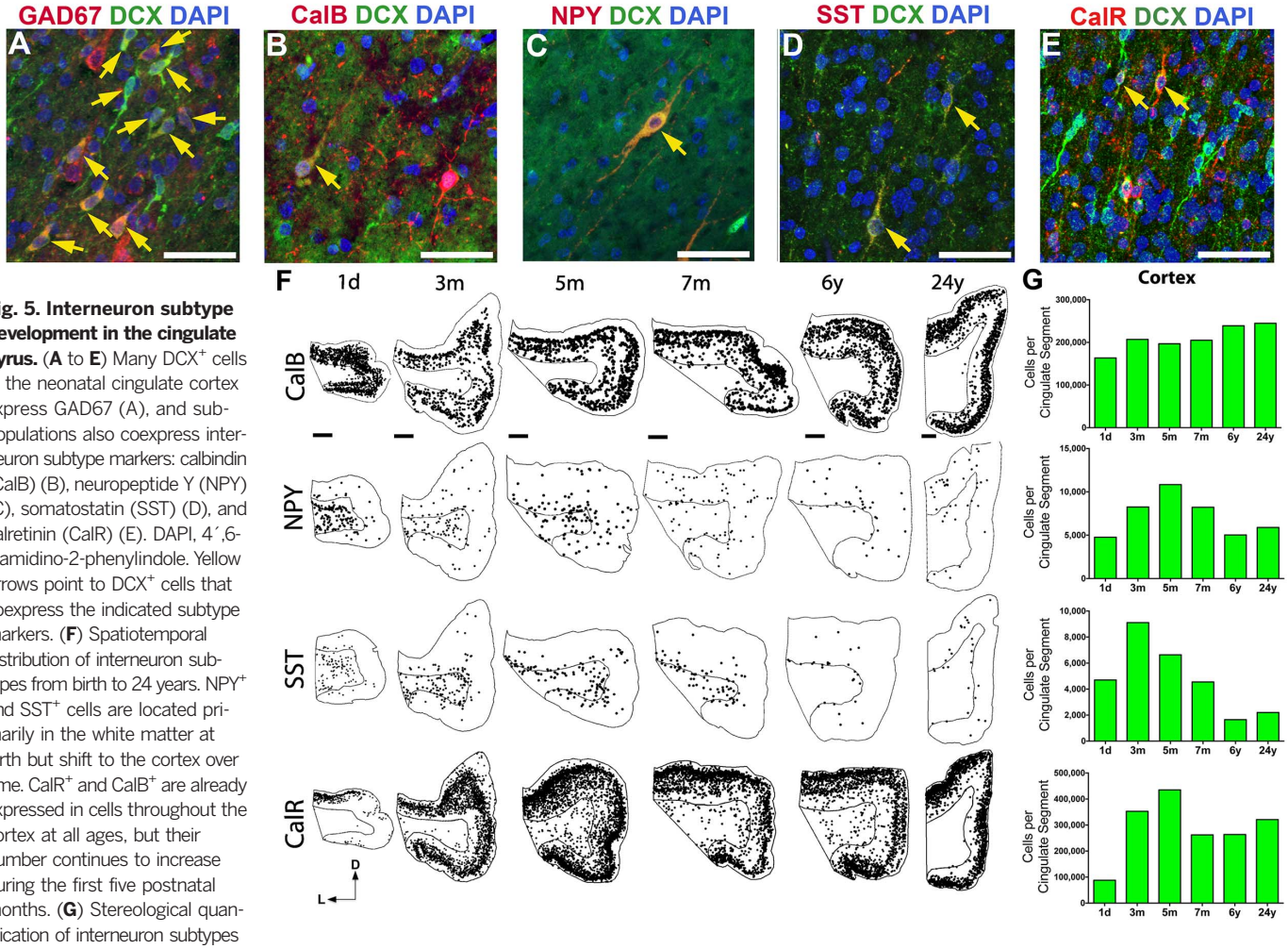

Fig. 5. Interneuron subtype development in the cingulate gyrus. (**A** to **E**) Many DCX$^+$ cells in the neonatal cingulate cortex express GAD67 (A), and subpopulations also coexpress interneuron subtype markers: calbindin (CalB) (B), neuropeptide Y (NPY) (C), somatostatin (SST) (D), and calretinin (CalR) (E). DAPI, 4′,6-diamidino-2-phenylindole. Yellow arrows point to DCX$^+$ cells that coexpress the indicated subtype markers. (**F**) Spatiotemporal distribution of interneuron subtypes from birth to 24 years. NPY$^+$ and SST$^+$ cells are located primarily in the white matter at birth but shift to the cortex over time. CalR$^+$ and CalB$^+$ are already expressed in cells throughout the cortex at all ages, but their number continues to increase during the first five postnatal months. (**G**) Stereological quantification of interneuron subtypes in the cingulate cortex from birth to 24 years. The number of NPY$^+$, SST$^+$, CalB$^+$, and CalR$^+$ cells increases between birth and 5 months, coinciding with the arrival of DCX$^+$ cells in the cingulate cortex (see Fig. 3G). Scale bars, 50 μm [(A) to (E)], 2 mm [(F), 1 day to 6 years], 1 mm [(F), 24 years]. Directional axes: D, dorsal; L, lateral.

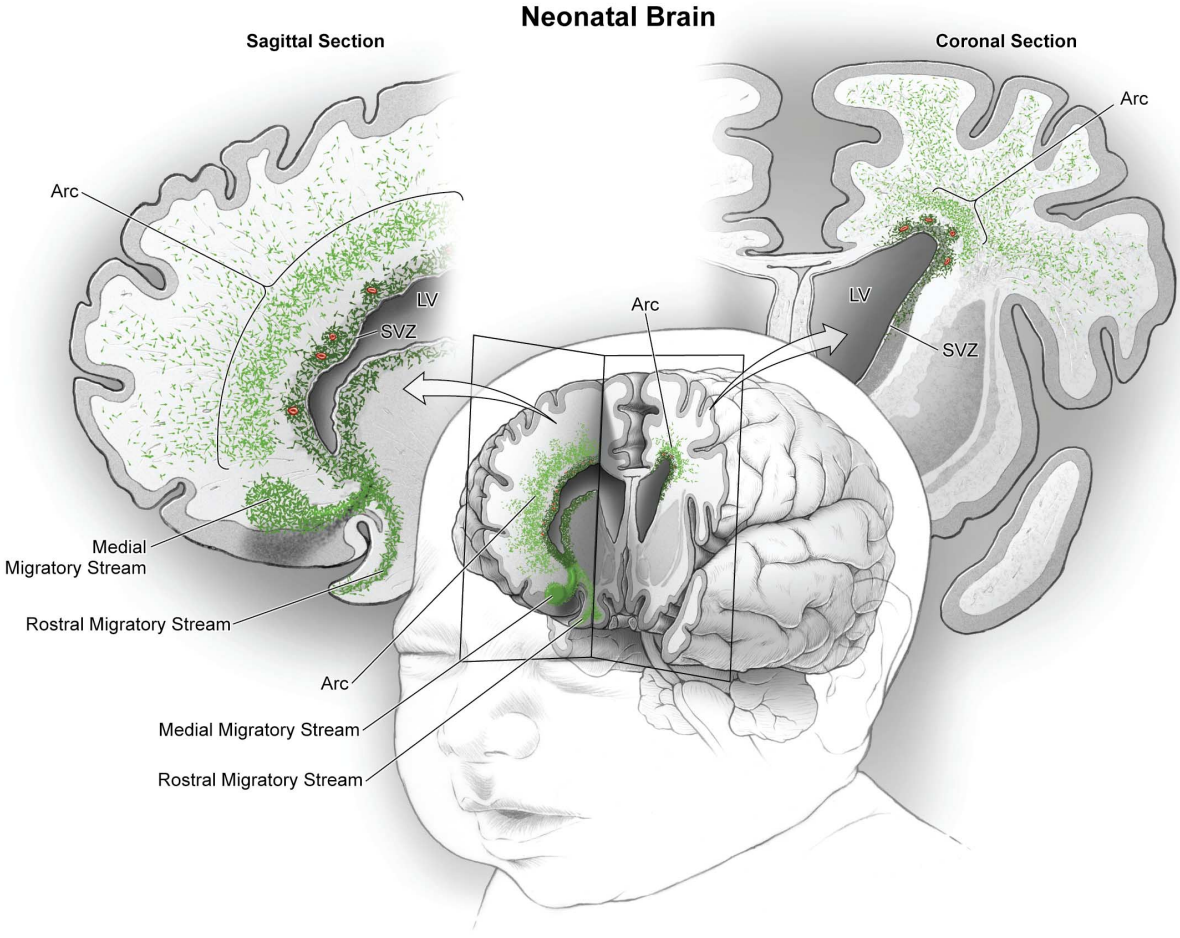

Fig. 6. Migratory streams of young neurons in the frontal lobe of the early postnatal human brain. In the frontal lobe of the neonatal human brain, cut in sagittal and coronal planes in this schematic, large numbers of young migrating neurons persist (shown in green) (see Figs. 1 to 3). Multiple concentric tiers of migrating cells are observed around the anterior pole of the lateral ventricle (see Fig. 1). Close to the ventricular wall, migrating young neurons are largely oriented tangentially; dense subpopulations are also clustered around blood vessels (red). Farther out, young neurons are more dispersed, many now oriented radially; they appear to migrate long distances through the developing white matter to reach the cortex. Ventrally, we also illustrate the RMS and the MMS, which target the olfactory bulb and medial prefrontal cortex, respectively (*20*).

at 1.5, 3, 5, and 7 months. At and immediately after birth, elongated DCX^+ cells were found at the dorsal ventricular wall and in the mantle region of the developing white matter (Fig. 3F). By 1.5 months, DCX^+ cells were mainly found in the dorsal cortex in the superior and middle frontal gyri and the cingulate cortex, but many remained in the developing white matter. The total number of DCX^+ cells with migratory morphology decreased between 1.5 and 7 months of age (Fig. 3, F and G; for representative DCX^+ cells at 5 and 7 months, see fig. S9). The entry of DCX^+ cells into the anterior cingulate gyrus was correlated with an increase in the number of cells expressing NeuN, a marker of mature neurons (fig. S10B). We also examined the cingulate cortex at 2, 6, and 15 years of age. Four to six DCX^+ cells were observed per section in the 2-year-old sample, but these cells did not have a clear migratory morphology. None were detected at 6 or 15 years. Sagittal sections mapped at birth also demonstrated migrating young neurons moving into the anterior pole of the developing human brain (fig. S11). These observations indicate that postnatal neuronal migration in the human frontal lobe, in the Arc and beyond, occurs primarily within the first 3 months after birth, with a few DCX^+ elongated cells persisting at 7 months.

Postnatally migrating neurons differentiate into interneurons

We sought to determine which types of neurons the DCX^+ cells in the Arc become. DCX^+ cells in all tiers at birth and at 1.5 months expressed γ-aminobutyric acid (GABA), the main inhibitory neurotransmitter in the adult brain; GAD67, an enzyme involved in the production of GABA; and the chemokine receptor CXCR4, seen in migrating interneurons (Fig. 4, B to D). Within tiers 1 and 2 (close to the ventricular wall), 92.5 ± 2.9% (SD) of DCX^+ cells were $GAD67^+$ and 96.1 ± 2.4% were $GABA^+$. Farther away, within tiers 3 and 4, 91.2 ± 4.4% of DCX^+ cells were $GAD67^+$ and 94.8 ± 5.8% were $GABA^+$. Because cortical interneurons primarily arise from the MGE and CGE (*3*, *5*, *19*, *22*), we asked whether DCX^+ cells in the Arc expressed Nkx2.1 or Lhx6 (transcription factors associated with the MGE), or Sp8 and COUP-TFII [associated with the CGE and possibly the lateral ganglionic eminence (LGE)]. At birth, about 10% of DCX^+ cells were $Nkx2.1^+$ and 28% were $Lhx6^+$ (Fig. 4, G to I, and fig. S2, F and G). Sp8 and COUP-TFII were expressed in 24% and 22% of DCX^+ cells, respectively (Fig. 4, E, F, and I, and fig. S2, D and E). DCX^+ cells did not express Sox2 or Tbr2, transcription factors associated with early and intermediate progenitor cells, respectively (Fig. 4K and fig. S2), nor did they express Emx1, CTIP2, or SATB2, transcription factors associated with excitatory neurons (fig. S2). In tiers 1 to 4 at birth, we found very few cells positive for Ki67, a marker of proliferating cells (fig. S12). Most of these $Ki67^+$ cells were also $Olig2^+$ and none were DCX^+. Thus, DCX^+ cells in the

postnatal frontal lobe correspond to postmitotic migrating young inhibitory interneurons, likely derived from the developing ganglionic eminences (CGE, MGE, and possibly LGE).

The interneuron subtype composition in the anterior cingulate cortex changes postnatally

To address how the Arc might contribute to developing cortical circuits, we mapped and quantified the total number of cells, neurons, and interneuron subtypes from birth until adulthood. We focused on the anterior cingulate cortex, which runs parallel to the Arc and had many DCX^+ cells during the first postnatal months. The cell number and volume of the cingulate cortex increased between birth and 5 months of age (fig. S10, A and C). The neuronal population in the cingulate cortex, as identified by NeuN expression, also increased during this time. These population changes followed the peak in the total number of DCX^+ cells, at ~1.5 months, suggesting that the cingulate cortex receives young migratory neurons up to 5 months after birth. Most DCX^+ cells found postnatally in the cingulate cortex white matter expressed GAD67, and a subpopulation expressed interneuron subtype markers [neuropeptide Y (NPY), somatostatin (SST), calretinin (CalR), or calbindin (CalB)] (Fig. 5, A to E). If these different subtypes of migrating young neurons enter the cingulate cortex, we hypothesized that its interneuron subtype composition would change over time. Indeed, by quantifying the abundance of different interneuron subtypes in this region, we found that the number of cells expressing NPY, SST, CalR, and CalB increased during the first 5 months after birth (Fig. 5, F and G). The number of parvalbumin-expressing cells also changed with age (from ~20,000 cells per cingulate segment at 3 months to >72,000 cells at 24 years), but we do not know whether this increase is due to cell addition or due to their late maturation (*28*, *29*). These data suggest that DCX^+ cells from the Arc contribute to interneuron subtype populations within the infant cingulate cortex.

Discussion

We have identified a large, heterogeneous population of late-migrating neurons in the infant human brain that targets an extensive region of the anterior forebrain, including the cingulate gyrus and prefrontal cortex. In the rodent cortex, a population of CGE-derived young migrating neurons continues to migrate into the cortex within the first few weeks of postnatal life (*16*, *17*, *30*). The population of young migrating neurons in the frontal lobe of postnatal humans appears to include this population but also others, including SST, NPY, and CalB. This assortment of subtypes, along with the expression of the regionally specific transcription factors Nkx2.1, Lhx6, COUP-TFII, and SP8, suggests that cells within the Arc derive from various progenitor zones in the ventral forebrain. The extensive tangential migration in the SVZ and perivascular region of the infant brain (Fig. 6 and movie S5) could allow for mixed populations of interneurons from distinct progenitor zones (*31*) to reach appropriate cortical regions. The precise time and birthplace of young migrating neurons within the postnatal human frontal lobe remains to be determined.

Because migrating neurons from the Arc reach cortical circuits during postnatal life, sensory experience could shape their recruitment and possibly their connectivity (*32*–*36*). Periods of plasticity are tightly linked to the time course of inhibitory interneuron maturation; thus, the late incorporation of inhibitory neurons into the frontal cortex could also be associated with the extension and delay in periods of plasticity during postnatal human development (*37*–*39*). Given the large numbers of young neurons that continue to migrate in the human brain at birth and during the first few months of life, injuries during this time (e.g., hypoxic ischemia) could affect neuronal recruitment from the Arc (*40*, *41*) and may contribute to sensorimotor handicaps and neurocognitive deficits, including those seen in epilepsy, cerebral palsy, and autism spectrum disorders (*42*, *43*).

REFERENCES AND NOTES

1. S. P. Gandhi, Y. Yanagawa, M. P. Stryker, Delayed plasticity of inhibitory neurons in developing visual cortex. *Proc. Natl. Acad. Sci. U.S.A.* **105**, 16797–16802 (2008). doi: 10.1073/pnas.0806159105; pmid: 18940923
2. T. Toyoizumi *et al.*, A theory of the transition to critical period plasticity: Inhibition selectively suppresses spontaneous activity. *Neuron* **80**, 51–63 (2013). doi: 10.1016/j.neuron.2013.07.022; pmid: 24094102
3. O. Marín, J. L. Rubenstein, A long, remarkable journey: Tangential migration in the telencephalon. *Nat. Rev. Neurosci.* **2**, 780–790 (2001). doi: 10.1038/35097509; pmid: 11715055
4. S. Nery, G. Fishell, J. G. Corbin, The caudal ganglionic eminence is a source of distinct cortical and subcortical cell populations. *Nat. Neurosci.* **5**, 1279–1287 (2002). doi: 10.1038/nn971; pmid: 12411960
5. T. Ma *et al.*, Subcortical origins of human and monkey neocortical interneurons. *Nat. Neurosci.* **16**, 1588–1597 (2013). doi: 10.1038/nn.3536; pmid: 24097041
6. D. V. Hansen *et al.*, Non-epithelial stem cells and cortical interneuron production in the human ganglionic eminences. *Nat. Neurosci.* **16**, 1576–1587 (2013). doi: 10.1038/nn.3541; pmid: 24097039
7. A. A. Lavdas, M. Grigoriou, V. Pachnis, J. G. Parnavelas, The medial ganglionic eminence gives rise to a population of early neurons in the developing cerebral cortex. *J. Neurosci.* **19**, 7881–7888 (1999). pmid: 10479690
8. H. Korr, C. Schmitz, Facts and fictions regarding post-natal neurogenesis in the developing human cerebral cortex. *J. Theor. Biol.* **200**, 291–297 (1999). doi: 10.1006/jtbi.1999.0992; pmid: 10527718
9. R. L. Sidman, P. Rakic, Neuronal migration, with special reference to developing human brain: A review. *Brain Res.* **62**, 1–35 (1973). doi: 10.1016/0006-8993(73)90617-3; pmid: 4203033
10. J. M. García-Verdugo *et al.*, The proliferative ventricular zone in adult vertebrates: A comparative study using reptiles, birds, and mammals. *Brain Res. Bull.* **57**, 765–775 (2002). doi: 10.1016/S0361-9230(01)00769-9; pmid: 12031273
11. M. F. Paredes, S. F. Sorrells, J. M. Garcia-Verdugo, A. Alvarez-Buylla, Brain size and limits to adult neurogenesis. *J. Comp. Neurol.* **524**, 646–664 (2016). doi: 10.1002/cne.23896; pmid: 26417888
12. C. Lois, J. M. García-Verdugo, A. Alvarez-Buylla, Chain migration of neuronal precursors. *Science* **271**, 978–981 (1996). doi: 10.1126/science.271.5251.978; pmid: 8584933
13. R. Betarbet, T. Zigova, R. A. Bakay, M. B. Luskin, Dopaminergic and GABAergic interneurons of the olfactory bulb are derived from the neonatal subventricular zone. *Int. J. Dev. Neurosci.* **14**, 921–930 (1996). doi: 10.1016/S0736-5748(96)00066-4; pmid: 9010735
14. P.-M. Lledo, A. Saghatelyan, M. Lemasson, Inhibitory interneurons in the olfactory bulb: From development to function. *Neuroscientist* **10**, 292–303 (2004). doi: 10.1177/1073858404263460; pmid: 15271257
15. S. O. Suzuki, J. E. Goldman, Multiple cell populations in the early postnatal subventricular zone take distinct migratory pathways: A dynamic study of glial and neuronal progenitor migration. *J. Neurosci.* **23**, 4240–4250 (2003). pmid: 12764112
16. D. Inta *et al.*, Neurogenesis and widespread forebrain migration of distinct GABAergic neurons from the postnatal subventricular zone. *Proc. Natl. Acad. Sci. U.S.A.* **105**, 20994–20999 (2008). doi: 10.1073/pnas.0807059105; pmid: 19095802
17. C. Le Magueresse *et al.*, "Small axonless neurons": Postnatally generated neocortical interneurons with delayed functional maturation. *J. Neurosci.* **31**, 16731–16747 (2011). doi: 10.1523/JNEUROSCI.4273-11.2011; pmid: 22090500
18. S. De Marchis, A. Fasolo, A. C. Puche, Subventricular zone-derived neuronal progenitors migrate into the subcortical forebrain of postnatal mice. *J. Comp. Neurol.* **476**, 290–300 (2004). doi: 10.1002/cne.20217; pmid: 15269971
19. C. Wang *et al.*, Identification and characterization of neuroblasts in the subventricular zone and rostral migratory stream of the adult human brain. *Cell Res.* **21**, 1534–1550 (2011). doi: 10.1038/cr.2011.83; pmid: 21577236
20. N. Sanai *et al.*, Corridors of migrating neurons in the human brain and their decline during infancy. *Nature* **478**, 382–386 (2011). doi: 10.1038/nature10487; pmid: 21964341
21. J. G. Gleeson, P. T. Lin, L. A. Flanagan, C. A. Walsh, Doublecortin is a microtubule-associated protein and is expressed widely by migrating neurons. *Neuron* **23**, 257–271 (1999). doi: 10.1016/S0896-6273(00)80778-3; pmid: 10399933
22. K. Ono, H. Tomasiewicz, T. Magnuson, U. Rutishauser, N-CAM mutation inhibits tangential neuronal migration and is phenocopied by enzymatic removal of polysialic acid. *Neuron* **13**, 595–609 (1994). doi: 10.1016/0896-6273(94)90028-0; pmid: 7917293
23. F. J. Martini *et al.*, Biased selection of leading process branches mediates chemotaxis during tangential neuronal migration. *Development* **136**, 41–50 (2009). doi: 10.1242/dev.025502; pmid: 19060332
24. H. Wichterle, J. M. Garcia-Verdugo, D. G. Herrera, A. Alvarez-Buylla, Young neurons from medial ganglionic eminence disperse in adult and embryonic brain. *Nat. Neurosci.* **2**, 461–466 (1999). doi: 10.1038/8131; pmid: 10321251
25. H. Wichterle, D. H. Turnbull, S. Nery, G. Fishell, A. Alvarez-Buylla, In utero fate mapping reveals distinct migratory pathways and fates of neurons born in the mammalian basal forebrain. *Development* **128**, 3759–3771 (2001). pmid: 11585802
26. B. Nadarajah, J. E. Brunstrom, J. Grutzendler, R. O. Wong, A. L. Pearlman, Two modes of radial migration in early development of the cerebral cortex. *Nat. Neurosci.* **4**, 143–150 (2001). doi: 10.1038/83967; pmid: 11175874
27. S. A. Anderson, O. Marín, C. Horn, K. Jennings, J. L. Rubenstein, Distinct cortical migrations from the medial and lateral ganglionic eminences. *Development* **128**, 353–363 (2001). pmid: 11152634
28. E. Soriano *et al.*, Late appearance of parvalbumin-immunoreactive neurons in the rodent cerebral cortex does not follow an 'inside-out' sequence. *Neurosci. Lett.* **142**, 147–150 (1992). doi: 10.1016/0304-3940(92)90360-J; pmid: 1454208
29. K. Letinic, I. Kostovic, Postnatal development of calcium-binding proteins calbindin and parvalbumin in human visual cortex. *Cereb. Cortex* **8**, 660–669 (1998). doi: 10.1093/cercor/8.7.660; pmid: 9823487
30. O. Riccio *et al.*, New pool of cortical interneuron precursors in the early postnatal dorsal white matter. *Cereb. Cortex* **22**, 86–98 (2012). doi: 10.1093/cercor/bhr086; pmid: 21616983
31. F. T. Merkle, Z. Mirzadeh, A. Alvarez-Buylla, Mosaic organization of neural stem cells in the adult brain. *Science* **317**, 381–384 (2007). doi: 10.1126/science.1144914; pmid: 17615304
32. M. Sakamoto *et al.*, Continuous postnatal neurogenesis contributes to formation of the olfactory bulb neural circuits and flexible olfactory associative learning. *J. Neurosci.* **34**, 5788–5799 (2014). doi: 10.1523/JNEUROSCI.0674-14.2014; pmid: 24760839
33. G. A. Cecchi, L. T. Petreanu, A. Alvarez-Buylla, M. O. Magnasco, Unsupervised learning and adaptation in a model of adult neurogenesis. *J. Comput. Neurosci.* **11**, 175–182 (2001). doi: 10.1023/A:1012849801892; pmid: 11717533

34. A. Barnea, F. Nottebohm, Seasonal recruitment of hippocampal neurons in adult free-ranging black-capped chickadees. *Proc. Natl. Acad. Sci. U.S.A.* **91**, 11217–11221 (1994). doi: 10.1073/pnas.91.23.11217; pmid: 7972037
35. L. Petreanu, A. Alvarez-Buylla, Maturation and death of adult-born olfactory bulb granule neurons: Role of olfaction. *J. Neurosci.* **22**, 6106–6113 (2002). pmid: 12122071
36. E. Gould, A. Beylin, P. Tanapat, A. Reeves, T. J. Shors, Learning enhances adult neurogenesis in the hippocampal formation. *Nat. Neurosci.* **2**, 260–265 (1999). doi: 10.1038/6365; pmid: 10195219
37. D. G. Southwell, R. C. Froemke, A. Alvarez-Buylla, M. P. Stryker, S. P. Gandhi, Cortical plasticity induced by inhibitory neuron transplantation. *Science* **327**, 1145–1148 (2010). doi: 10.1126/science.1183962; pmid: 20185728
38. T. K. Hensch, Critical period plasticity in local cortical circuits. *Nat. Rev. Neurosci.* **6**, 877–888 (2005). doi: 10.1038/nrn1787; pmid: 16261181
39. M. S. Lazarus, Z. J. Huang, Distinct maturation profiles of perisomatic and dendritic targeting GABAergic interneurons in the mouse primary visual cortex during the critical period of ocular dominance plasticity. *J. Neurophysiol.* **106**, 775–787 (2011). doi: 10.1152/jn.00729.2010; pmid: 21613595
40. S. Robinson, Q. Li, A. Dechant, M. L. Cohen, Neonatal loss of gamma-aminobutyric acid pathway expression after human perinatal brain injury. *J. Neurosurg.* **104** (suppl.), 396–408 (2006). pmid: 16776375
41. N. Salmaso, B. Jablonska, J. Scafidi, F. M. Vaccarino, V. Gallo, Neurobiology of premature brain injury. *Nat. Neurosci.* **17**, 341–346 (2014). doi: 10.1038/nn.3604; pmid: 24569830
42. V. S. Catts *et al.*, Rethinking schizophrenia in the context of normal neurodevelopment. *Front. Cell. Neurosci.* **7**, 60 (2013). doi: 10.3389/fncel.2013.00060; pmid: 23720610
43. O. Marín, Interneuron dysfunction in psychiatric disorders. *Nat. Rev. Neurosci.* **13**, 107–120 (2012). pmid: 22251963

ACKNOWLEDGMENTS

We thank the families who graciously donated the tissue samples used in this study; H.-H. Tsai, T. Nowakowski, K. Obernier, J. Barkovich, and L. Submaranian for experimental advice; J. Elsbernd and J. Che for technical support; and M. Kohn for statistical input. Supported by NIH grants RO1 HD032116-21 (A.A.-B.), PO1 NS083513-02 (A.A.-B., E.J.H., and D.H.R.), R01EB009756 and R01HD072074 (D.X.), MBRS-RISE R25-GM059298 (D.J.), K08NS091537-01A1 (M.F.P.), and 2R01 NS060896 (P.S.M.); California Institute of Regenerative Medicine grants TG-01153 (M.F.P.) and TB1-01194 (D.J.); Spanish Institute of Health Carlos III grant ISCIII2012-RD19-016 (J.-M.G.-V.); Rio Hortega fellowship CM12/00014 (S.G.-P.); Banting and FRS Canadian fellowships (H.K.); and Economics and Competitivity Ministry of Spain grant BFU2015-64207-P and Generalitat Valenciana grant Prometeoll 2014-075. Supplement contains additional data. A.A.-B. is on the scientific advisory board and is co-founder of Neurona Therapeutics.

SUPPLEMENTARY MATERIALS

www.sciencemag.org/content/354/6308/aaf7073/suppl/DC1
Materials and Methods
Figs. S1 to S12
Tables S1 to S4
Movies S1 to S5
References (*44*–*46*)

27 March 2016; accepted 4 August 2016
10.1126/science.aaf7073

RESEARCH ARTICLE SUMMARY

CELL DEATH

A nuclease that mediates cell death induced by DNA damage and poly(ADP-ribose) polymerase-1

Yingfei Wang,* Ran An, George K. Umanah, Hyejin Park, Kalyani Nambiar, Stephen M. Eacker, BongWoo Kim, Lei Bao, Maged M. Harraz, Calvin Chang, Rong Chen, Jennifer E. Wang, Tae-In Kam, Jun Seop Jeong, Zhi Xie, Stewart Neifert, Jiang Qian, Shaida A. Andrabi, Seth Blackshaw, Heng Zhu, Hongjun Song, Guo-li Ming, Valina L. Dawson,* Ted M. Dawson*

INTRODUCTION: Poly(ADP-ribose) (PAR) polymerase-1 (PARP-1) is a nuclear enzyme responding to oxidative stress and DNA damage. Excessive activation of PARP-1 causes an intrinsic caspase-independent cell death program designated parthanatos, which occurs in many organ systems because of toxic or stressful insults, including ischemia-reperfusion injury after stroke and myocardial infarction, inflammatory injury, reactive oxygen species–induced injury, glutamate excitotoxicity, and neurodegenerative diseases. Inhibition or genetic deletion of PARP-1 is profoundly protective against such cellular injury in models of human disease.

RATIONALE: The molecular mechanisms underlying parthanatos involve release of mitochondrial apoptosis-inducing factor (AIF) and its translocation to the nucleus, which results in chromatinolysis into 20- to 50-kb large DNA fragments—a commitment point for parthanatos. Because AIF itself has no obvious nuclease activity, we propose that AIF recruits a nuclease or a nuclease complex to the nucleus to trigger DNA cleavage and parthanatos. Although the endonuclease G (EndoG) homolog may promote DNA degradation in *Caenorhabditis elegans* through cooperating with the AIF homolog, our group and others showed that EndoG does not have an essential role in PARP-dependent chromatinolysis and cell death in mammals. Thus, the identity of the nuclease responsible for large DNA fragmentation following AIF entry to the nucleus during parthanatos has been a long-standing mystery.

RESULTS: Using two sequential unbiased screens, including a human protein array and a small interfering RNA screen, we discovered that macrophage migration inhibitory factor (MIF) binds AIF and is required for parthanatos. Three-dimensional modeling of MIF revealed that the MIF trimer has the same core topology structure as PD-D/E(X)K superfamily nucleases. In the presence of Mg^{2+} or Ca^{2+}, MIF has both 3′ exonuclease and endonuclease activity. It binds to 5′ unpaired bases of single-stranded DNA with stem loop structure and cleaves its 3′ unpaired bases. These nuclease activities allow MIF to cleave genomic DNA into large fragments. Depletion of MIF markedly reduced chromatinolysis and cell death induced by *N*-methyl-D-aspartate (NMDA) receptor–activated glutamate excitotoxicity in primary neuronal cultures, DNA damage caused by *N*-methyl-*N*′-nitro-*N*-nitrosoguanidine (MNNG) or focal stroke in mice. Mutating key amino acid residues in the PD-D/E(X)K nuclease domain of MIF eliminated its nuclease activity and prevented parthanatos. Disrupting the AIF and MIF interaction prevented the translocation of MIF from the cytosol to the nucleus and protected against parthanatos. Moreover, depletion of MIF, disruption of AIF and MIF interaction, and eliminating MIF's nuclease activity has long-lasting histological and behavioral rescue in the focal ischemia model of stroke.

CONCLUSION: We identified MIF as a PARP-1–dependent AIF-associated nuclease that is required for parthanatos. In response to oxidative stress or DNA damage, PARP-1 activation triggers AIF release from the mitochondria. AIF then recruits MIF to the nucleus where MIF cleaves genomic DNA into large fragments and causes cell death. Depletion of MIF, disruption of AIF and MIF interaction, or blocking MIF nuclease activity inhibited chromatinolysis and parthanatos. Targeting MIF nuclease activity may offer an important therapeutic opportunity for a variety of disorders with excessive PARP-1 activation. ■

ON OUR WEBSITE

Read the full article at http://dx.doi.org/10.1126/science.aad6872

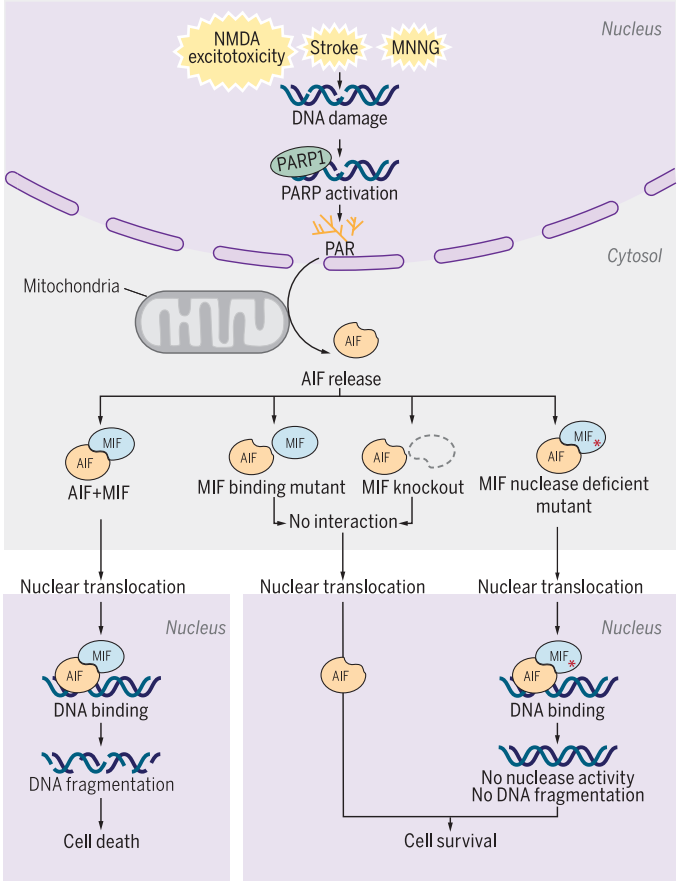

Stressors lead to DNA damage, PARP-1 activation, and PAR formation. PAR facilitates the release of AIF from mitochondria where it binds MIF. This complex translocates to the nucleus to bind DNA; the result is DNA fragmentation and cell death. Interference with this cascade by preventing the formation of the AIF-MIF complex or by a nuclease-deficient MIF prevents DNA fragmentation and promotes cell survival.

The list of author affiliations is available in the full article online.
*Corresponding author. Email: tdawson@jhmi.edu (T.M.D.); vdawson1@jhmi.edu (V.L.D.); yingfei.wang@utsouthwestern.edu (Y.W.)
Cite this article as Y. Wang *et al.*, *Science* 354, aad6872 (2016). DOI: 10.1126/science.aad6872

RESEARCH ARTICLE

CELL DEATH

A nuclease that mediates cell death induced by DNA damage and poly(ADP-ribose) polymerase-1

Yingfei Wang,[1,2,3,4]‡ Ran An,[1,2,5] George K. Umanah,[1,2] Hyejin Park,[1,2,6] Kalyani Nambiar,[1,2] Stephen M. Eacker,[1,2,6] BongWoo Kim,[3] Lei Bao,[3] Maged M. Harraz,[1,2,7] Calvin Chang,[1] Rong Chen,[1,2] Jennifer E. Wang,[3] Tae-In Kam,[1,2,6] Jun Seop Jeong,[8,9] Zhi Xie,[10]* Stewart Neifert,[1,2,6] Jiang Qian,[10] Shaida A. Andrabi,[1,2]† Seth Blackshaw,[7,9,10] Heng Zhu,[8,9] Hongjun Song,[1,2,7] Guo-li Ming,[1,2,7] Valina L. Dawson,[1,2,6,7,11]‡ Ted M. Dawson[1,2,6,7,8]‡

Inhibition or genetic deletion of poly(ADP-ribose) (PAR) polymerase-1 (PARP-1) is protective against toxic insults in many organ systems. The molecular mechanisms underlying PARP-1–dependent cell death involve release of mitochondrial apoptosis-inducing factor (AIF) and its translocation to the nucleus, which results in chromatinolysis. We identified macrophage migration inhibitory factor (MIF) as a PARP-1–dependent AIF-associated nuclease (PAAN). AIF was required for recruitment of MIF to the nucleus, where MIF cleaves genomic DNA into large fragments. Depletion of MIF, disruption of the AIF-MIF interaction, or mutation of glutamic acid at position 22 in the catalytic nuclease domain blocked MIF nuclease activity and inhibited chromatinolysis, cell death induced by glutamate excitotoxicity, and focal stroke. Inhibition of MIF's nuclease activity is a potential therapeutic target for diseases caused by excessive PARP-1 activation.

Poly(ADP-ribose) (PAR) polymerase-1 (PARP-1) is a nuclear enzyme that is activated by DNA damage and facilitates DNA repair (*1*). Excessive activation of PARP-1 causes an intrinsic caspase-independent cell death program designated parthanatos (*2*, *3*), which occurs after toxic insults in many organ systems (*4*, *5*), including ischemia-reperfusion injury after stroke and myocardial infarction; inflammatory injury; reactive oxygen species–induced injury; glutamate excitotoxicity; and neurodegenerative diseases, such as Parkinson's disease and Alzheimer's disease (*2*, *4*, *6*). Consistent with the idea that PARP-1 is a key cell-death mediator, PARP inhibitors or genetic deletion of PARP-1 protect against such cellular injury in models of human disease (*2*, *4*, *5*, *7*).

During parthanatos, PAR causes release of apoptosis-inducing factor (AIF) from the mitochondria and its translocation to the nucleus, resulting in fragmentation of DNA into 20- to 50-kb fragments (*2*, *8*–*11*). AIF itself has no obvious nuclease activity (*2*). Although it has been suggested that CED-3 protease suppressor (CPS)–6, an endonuclease G (EndoG) homolog in *Caenorhabditis elegans*, cooperates with the worm AIF homolog (WAH-1) to promote DNA degradation (*12*), mammalian EndoG does not seem to have an essential role in PARP-dependent chromatinolysis and cell death (*13*, *14*) and after transient focal cerebral ischemia in mammals (*15*). Thus, the nuclease responsible for the chromatinolysis during parthanatos is not known.

PARP-1–dependent cell death requires MIF

To confirm that the EndoG is dispensable for parthanatos, the CRISPR-Cas9 system was used to deplete (knockout) EndoG from human neuroblastoma cell line (SH-SY5Y) cells (fig. S1A). We found that knockout of EndoG failed to block *N*-methyl-*N*′-nitro-*N*-nitrosoguanidine (MNNG)–induced parthanatos (fig. S1B) and large DNA fragmentation (fig. S1C); thus, EndoG is unlikely to be the main contributor to PARP-1–dependent large DNA fragmentation and MNNG-induced cell death (fig. S1) (*13*, *15*).

To identify a PARP-1–dependent AIF-associated nuclease (PAAN), we probed protein chips containing more than 16,000 and 5000 human recombinant proteins in duplicate along with several control proteins (*16*) with recombinant mouse AIF. The 160 strongest interacting proteins were depleted with small interfering RNA (siRNA) in cultured human HeLa cells to screen for modifiers of parthanatos induced by MNNG (*2*, *9*, *11*) (Fig. 1, A and B). We further tested whether depletion of these potential AIF-interacting proteins provided protection equivalent to that of depletion of PARP-1 and whether the proteins exhibited sequence and structure similarity consistent with possible nuclease activity. Depletion of AIF interactor 18 was as protective as depletion of PARP-1 (Fig. 1B). AIF interactor 18 is previously known under various synonyms (glycosylation-inhibiting factor, phenylpyruvate tautomerase, L-dopachrome tautomerase, L-dopachrome isomerase), and it is collectively known as macrophage migration inhibitory factor (MIF or MMIF) (*17*, *18*). Effects of three different short hairpin RNA (shRNA) constructs against human and mouse MIF confirmed that depletion of MIF protected against parthanatos induced by MNNG toxicity in HeLa cells or *N*-methyl-D-aspartate (NMDA) excitotoxicity in mouse primary cortical neurons (fig. S2, A to F). To rule out off-target effects from the shRNA, we prepared MIF constructs that were resistant to shRNA 1 (RshRNA1) and 3 (RshRNA3). Cells expressing these constructs were impervious to effects of the shRNAs (fig. S2, G and H).

MIF contains three PD-D/E(X)K superfamily motifs that are found in many nucleases (*19*–*21*) (Fig. 1, C and D) and are highly conserved across mammalian species (fig. S3A). It also contains a CxxCxxHx(n)C zinc finger domain (Fig. 1C and fig. S3B), which is commonly found in DNA damage-response proteins (*20*). MIF exists as a trimer (*22*–*24*). The core PD-D/E(X)K topology structure in the MIF trimer consists of four β strands next to two α strands (Fig. 1E and fig. S3, C to G, and supplementary text), which is similar to those of well-characterized nucleases, including Eco RI, Eco RV, Exo III, and Pvu II (fig. S3, H to O, and supplementary text). These sequence analyses and three-dimensional (3D) modeling results indicated that MIF belongs to the PD-D/E(X)K nuclease-like superfamily (*25*, *26*).

MIF is a nuclease

To determine whether MIF has nuclease activity, we incubated a plasmid c–promoter DNA (pcDNA) vector with recombinant human MIF. Supercoiled pcDNA was cleaved by MIF—but not by its nuclease-deficient mutant MIF E22Q [in which glutamine (Q) replaces glutamic acid (E) at position 22] identified in the nuclease assays below—into an open circular form and, further,

[1]Neuroregeneration and Stem Cell Programs, Institute for Cell Engineering, Johns Hopkins University School of Medicine, Baltimore, MD 21205, USA. [2]Department of Neurology, Johns Hopkins University School of Medicine, Baltimore, MD 21205, USA. [3]Department of Pathology, University of Texas Southwestern Medical Center, Dallas, TX 75390, USA. [4]Department of Neurology and Neurotherapeutics, University of Texas Southwestern Medical Center, Dallas, TX 75390, USA. [5]Department of Neurology of Huashan Hospital, State Key Laboratory of Medical Neurobiology, Fudan University, Shanghai 200032, China. [6]Adrienne Helis Malvin Medical Research Foundation, New Orleans, LA 70130-2685, USA. [7]Solomon H. Snyder Department of Neuroscience, Johns Hopkins University School of Medicine, Baltimore, MD 21205, USA. [8]Department of Pharmacology and Molecular Sciences, Johns Hopkins University School of Medicine, Baltimore, MD 21205, USA. [9]Center for High-Throughput Biology, Johns Hopkins University School of Medicine, Baltimore, MD 21205, USA. [10]Department of Ophthalmology, Johns Hopkins University School of Medicine, Baltimore, MD 21205, USA. [11]Department of Physiology, Johns Hopkins University School of Medicine, Baltimore, MD 21205, USA.
*Present address: Zhongshan Ophthalmic Center, Sun Yat-sen University, Guangzhou, China. †Present address: Department of Pharmacology and Toxicology, University of Alabama at Birmingham, Birmingham, AL 35294, USA. ‡Corresponding author. Email: tdawson@jhmi.edu (T.M.D.); vdawson1@jhmi.edu (V.L.D.); yingfei.wang@utsouthwestern.edu (Y.W.)

to a linear form (Fig. 2A). Moreover, MIF cleaved human genomic DNA in a concentration- and time-dependent manner (fig. S4, A and B). Addition of 10 mM Mg^{2+}, 2 mM Ca^{2+}, or 1 mM Mn^{2+} was required for MIF nuclease activity (fig. S4C), consistent with the divalent cation concentrations required for in vitro activity of other similar nucleases (*27*). EDTA blocked MIF's nuclease activity against human genomic DNA (Fig. 2B). In the absence of the divalent cation or with the cation at 2 to 10 μM, MIF had no nuclease activity (fig. S4C). Addition of 200 μM Zn^{2+} precipitated genomic DNA in the presence of MIF, whereas 2 μM Zn^{2+} had no effect. Na^{+} had no effect on MIF's nuclease activity (fig. S4C). Pulsed-field gel electrophoresis indicated that MIF cleaves human genomic DNA into large fragments comparable to those of DNA purified from HeLa cells treated with MNNG (Fig. 2B, lane 8). Depletion of MIF with shRNA prevented MNNG-induced DNA cleavage, which was similar to the effect of PARP inhibition by 3,4-dihydro-5[4-(1-piperindinyl)butoxy]-1(2H)-isoquinoline (DPQ) (Fig. 2C). Because MIF has been reported to have tautomerase activity, we tested the effects of the MIF tautomerase inhibitor ISO-1 (*28*). ISO-1 failed to prevent MNNG-induced DNA damage (Fig. 2C). Moreover, the MIF P2G (also known as the P1G) tautomerase mutant, which lacks tautomerase activity (*29*), had no effect on MIF's nuclease

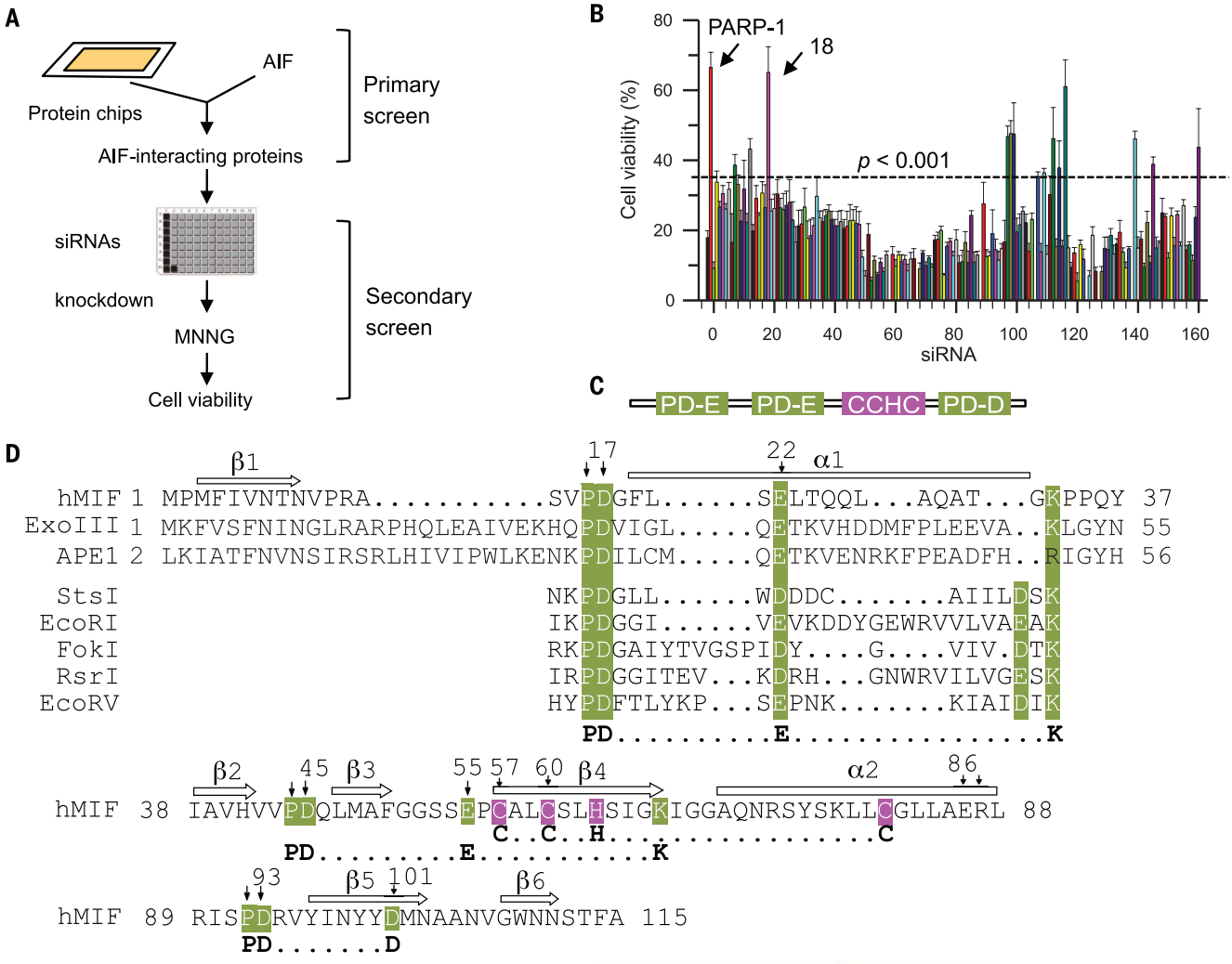

Fig. 1. Identification of MIF as a key cell-death effector mediating PARP-1–dependent cell death. (**A**) Strategy for identifying AIF-associated proteins involved in PARP-1–dependent cell death. (**B**) siRNA-based PARP-1–dependent cell viability high-throughput screening in HeLa cells 24 hours after MNNG treatment (50 μM, 15 min); $n = 8$. The experiments were repeated in four independent tests ***$P < 0.001$, one-way ANOVA. (**C**) Schematic representation of MIF's PD-D/E(X)K domains. Single-letter abbreviations for the amino acid residues are as follows: A, Ala; C, Cys; D, Asp; E, Glu; F, Phe; G, Gly; H, His; I, Ile; K, Lys; L, Leu; M, Met; N, Asn; P, Pro; Q, Gln; R, Arg; S, Ser; T, Thr; V, Val; W, Trp; Y, Tyr; and X, any amino acid. (**D**) Alignment of the nuclease domain of human MIF and other nucleases. Arrows above the sequence indicate β strands and rectangles represent α helices. Amino acid residues that were mutated are indicated with an arrow and number (see Results). Nuclease and CxxCxxHx(n)C domains are highlighted in green and pink, respectively. (**E**) Crystal structure of MIF trimer (pdb:1GD0) (left) and MIF PD-D/E(x)K motif in trimer (right).

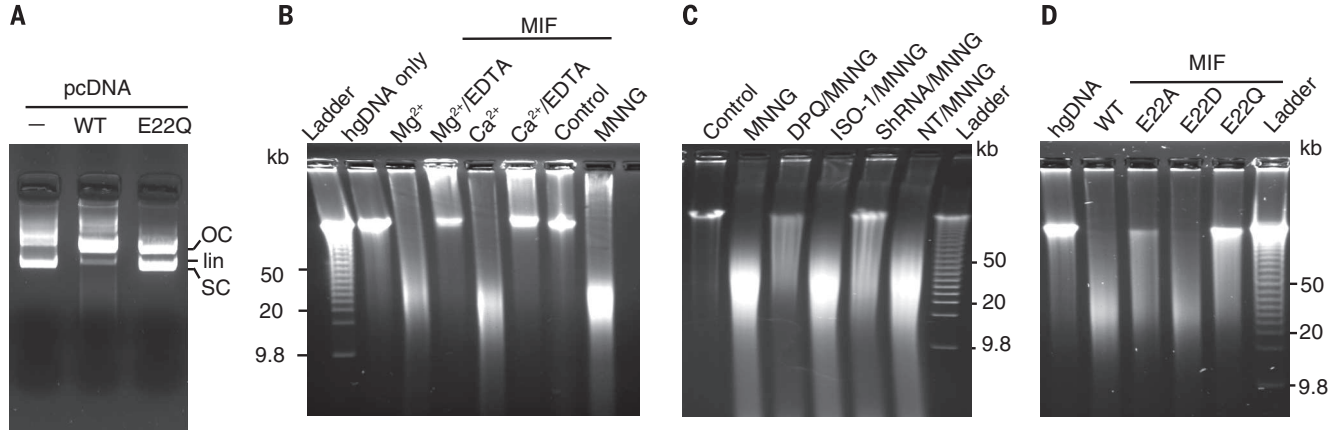

Fig. 2. MIF is a nuclease that cleaves genomic DNA. (**A**) In vitro MIF (2 μM) nuclease assay with pcDNA as substrate. (**B**) In vitro pulsed-field gel electrophoresis MIF (4 μM) nuclease assay with human genomic DNA (hgDNA) as a substrate in buffer containing Mg^{2+} (10 mM) with or without EDTA (50 mM) or Ca^{2+} (2 mM) with or without EDTA (25 mM). (**C**) Pulsed-field gel electrophoresis assay of MNNG-induced DNA damage in MIF-deficient HeLa cells and wild-type (WT) HeLa cells treated with or without DPQ (30 μM) or ISO-1 (100 μM). NT/MNNG (nontargeting shRNA/MNNG). (**D**) Nuclease assay of MIF WT and mutants (4 μM) using human genomic DNA as the substrate.

activity (fig. S4D). These data indicate that MIF is a nuclease that functions in PARP-1–dependent DNA fragmentation.

To identify amino acid residues critical for MIF's nuclease activity, we mutated key aspartate, glutamate, and proline residues within the PD-D/E(X)K domains of MIF. E22Q, but not Glu replaced by Asp (E22D), inhibited MIF's nuclease activity, whereas replacement with Ala (E22A) partially reduced MIF's nuclease activity (Fig. 2D; fig. S4, E to H; and supplementary text). Thus, this glutamic acid residue (E22) in the first α helix of MIF is critical for its nuclease activity, which is consistent with reports that this glutamic acid in the first α helix of many exonuclease-endonuclease-phosphatase (EEP) domain superfamily nucleases is highly conserved and that it is the active site for nuclease activity (*25*, *26*). MIF has both oxidoreductase and tautomerase activities (*28*, *30*, *31*). MIF active site mutants E22Q and E22A had no effect on MIF's oxidoreductase or tautomerase activities (fig. S5, A and B, and supplementary text). The lack of effect indicated that MIF nuclease activity is independent of its oxidoreductase and tautomerase activities. Moreover, MIF's protein conformation was unaffected by the E22Q and E22A mutations as determined by far-ultraviolet (UV) circular dichroism (CD) and near UV CD spectroscopy (fig. S5, C to M, and supplementary text). The purity of MIF proteins was confirmed by Coomassie blue staining, fast protein liquid chromatography (FPLC), and mass spectrometry (MS) assays (fig. S4G and fig. S5, C and D; Materials and methods; and supplementary text). No adventitious nuclease contamination was observed.

MIF preferentially binds to stem-loop single-stranded DNA

To determine the characteristics of DNA sequences bound by MIF in an unbiased manner, HeLa cells were treated with dimethyl sulfoxide (DMSO) or MNNG (50 μM, 15 min), followed by anti-MIF chromatin immunoprecipitation (ChIP) assays and deep sequencing (fig. S6 and supplementary text). We used the multiple Em for motif elicitation (MEME) program, which performs comprehensive motif analysis on large sets of nucleotide sequences (*32*), and we identified two classes of MIF-binding motifs (Fig. 3A). The first class (sequences 1 through 3) represents a highly related family of overlapping sequences (Fig. 3A and fig. S7A). The sequence features of this family are best captured in sequence 1 with 30 nucleotides and designated PS^{30}, the most statistically significant motif identified, as determined by the MEME program (E-value = 1.4e-051) (Fig. 3A and fig. S7A). The second class identified was a poly(A) sequence.

We performed 3D modeling to determine likely points of DNA interaction with MIF's PD-D/E(X)K motif. Within the PD-D/E(X)K motif, P16 and D17 on MIF are predicted to be positioned close to double-stranded DNA (dsDNA), whereas E22 is close to ssDNA, indicating MIF might bind single-stranded DNA (ssDNA), dsDNA, or both (fig. S7B). We examined both single-stranded and double-stranded forms of MIF DNA substrates for MIF binding and cleavage specificity. We synthesized the $ssPS^{30}$ sequence with a 5′ biotin label and subjected it to an electrophoretic mobility shift assay (EMSA) (fig. S7C). MIF bound to the biotin-labeled $ssPS^{30}$, forming one major complex in the presence of 10 mM Mg^{2+} (fig. S7C), which was completely disrupted by the addition of excess unlabeled DNA substrate (PS^{30}) or a polyclonal antibody to MIF (fig. S7C). MIF E22Q, E22A, P16A, P17A, and P17Q mutants still formed MIF/$ssPS^{30}$ complexes (fig. S7C).

Because $ssPS^{30}$ has the potential to form a stem-loop structure with unpaired bases at the 5′ and 3′ ends, we tested whether MIF binds to ssDNA with sequence or structure specificity. We used 5′ biotin-labeled $ssPS^{30}$ and sequence-related substrates with different structures created by removing unpaired bases at the 5′ end, 3′ end, or both 5′ and 3′ ends, or by eliminating the stem loop in the EMSA (Fig. 3B and fig. S8). Completely removing the 3′ unpaired bases (5′bLF) had no effect on the DNA-MIF complex formation (Fig. 3B). In contrast, removing the 5′ unpaired bases (5′bRF) reduced, but did not abolish DNA-MIF binding. Similar results are observed when both 5′ and 3′ unpaired bases were removed (5′bSL). Thus MIF appears to mainly bind to 5′ unpaired bases in ssDNA with stem-loop structures. We also used a poly(A) sequence that has no stem loop (5′bPA^{30}) and a short poly(A) sequence at the 5′ end of a stem-loop structure (5′b3F1) as the substrates. MIF failed to bind to 5′bPA^{30} but did bind to 5′b3F1. These results indicated that a stem loop is required for MIF-ssDNA binding (Fig. 3B and fig. S8). We also tested a substrate unrelated in sequence but that had a stem loop–like structure (5′bL3). MIF bound weakly to 5′bL3. But its binding efficiency was much lower than that of 5′bPS^{30}. These data indicate that MIF preferentially binds to ssDNA with a stem loop and that its specificity is not entirely determined by the sequence. We also tested whether MIF bound to dsDNA with PS^{30}; poly(A); substrates with sequence similarity to PS^{30} (5′bPS^{30}, 5′bSL, 5′bLF, 5′bRF, 5′bPA^{30}, and 5′bPA5E); and others with nonrelated sequences (PCS and 5′bL3) (Fig. 3B and fig. S8). MIF failed to bind to any of these double-stranded substrates (Fig. 3B).

MIF cleaves 3′ unpaired bases of stem-loop ssDNA

To determine whether MIF cleaves ssDNA or dsDNA, we added 35 random nucleotides to both the 5′ and 3′ ends of the PS^{30} DNA binding motif (designated PS^{100}) and, under identical conditions, measured cleavage of ssDNA ($ssPS^{100}$) or dsDNA ($dsPS^{100}$) . MIF cleaved $ssPS^{100}$ and its complementary strand $ssPS^{100R}$, but not $dsPS^{100}$ (fig. S9, A and B). The MIF DNA binding motif identified by ChIP sequencing (PS^{30}) appeared to be sufficient for MIF cleavage because MIF cleaved $ssPS^{30}$ in a concentration-dependent manner (fig. S9C). MIF cleavage of $ssPS^{30}$ required Mg^{2+}, and MIF E22Q and E22A mutations blocked the cleavage of $ssPS^{30}$ (fig. S9D). MIF cleaved $ssPS^{30}$ in a time-dependent manner with a $t_{1/2}$ of 12 min, and it cleaved $ssPS^{30}$ in a concentration-dependent

manner with an affinity for substrate (K_m) of 2 μM and a maximum initial velocity (V_{max}) of 41.7 nM/min (fig. S9, E to G). These kinetic properties are similar to those of other PD-D/E(X)K nucleases, such as Eco RI (*27*, *33*). MIF also cleaved dsPS^{30} (fig. S9H), but required at least 4 times as high MIF concentrations and a four-fifths reduction in substrate concentration (compare lane 2 of fig. S9C to lane 2 of fig. S9H). MIF failed to cleave its related sequence dsRF, or the nonrelated sequence dsL3 (fig. S9H). MIF's preference for ssDNA is consistent with the 3D model of ssDNA binding to MIF's active site (fig. S7B) and our MIF-DNA binding assays (Fig. 3B). In the presence of AIF, MIF more efficiently cleaved genomic DNA and dsPS^{30} (fig. S10, A to C), which might be because of the observation that AIF enhanced MIF binding to dsDNA (fig. S10D).

To determine whether MIF has sequence- or structure-specific endonuclease or exonuclease activity, we synthesized a series of variants labeled at the 5′ and 3′ ends with biotin, on the basis of the secondary structure of the DNA substrate ssPS^{30}, and measured their cleavage by MIF (Fig. 3C and fig. S8). MIF had 3′ exonuclease activity and preferentially recognized and degraded unpaired bases at the 3′ end of ssPS^{30}. This was blocked by biotin modification at the 3′ end (lanes 2 to 5 in Fig. 3C, fig. S8, and tables S1 and S2). MIF's 3′ exonuclease activity was also supported by cleavage assays in which the 5′bRF or 5′b3E substrates were used (Fig. 3C, fig. S8, and tables S1 and S2). Moreover, we used poly(A) (PA^{30}), which lacks secondary structure and cannot be stained by ethidium bromide (EtBr) (Fig. 3C, top). We found that MIF's 3′ exonuclease activity allowed it to cleave 5′ biotin–poly(A) (5′bPA^{30}), but not 3′ biotin–poly(A) (3′bPA^{30}), so that MIF's 3′ exonuclease activity can occur independently of secondary structure (Fig. 3C, bottom, and fig. S8). MIF endonuclease activity was also influenced by secondary structure, because it cleaved short unpaired bases of ssDNA at the 3′ end adjacent to the stem loop (5′bPS^{40}, 3′bPS^{40}, 5′b3F1, 3′b3F1, and 5′bL3), as well as 3′-OH or 3′-biotin adjacent to the stem loop (3′bSL and 3′bLF) (Fig. 3C and fig. S8). In contrast to its exonuclease activity, MIF's endonuclease activity was not blocked by biotin modification at the substrate's 3′ end (3′bSL, 3′bLF, 3′bPS^{40}, and 3′b3F1). However, 5′bL3, a sequence not related to PS^{30} but with a similar stem-loop structure, was cleaved by MIF, but with less efficiency (Fig. 3C and fig. S8). These results indicate that MIF has both 3′ exonuclease and endonuclease activities and cleaves unpaired bases of stem-loop ssDNA at the 3′ end. In the presence of AIF, AIF also increased the binding of MIF to ssDNAs, including 5′bPS^{30}, as well as 5′bSL, which has no 5′ unpaired bases (fig. S10D). Nevertheless, we found that AIF increased both exonuclease and endonuclease activities of MIF (0.5 μM) on 5′bPS^{30}, 3′bPS^{30}, and 3′bSL (fig. S10E). However, AIF has a rather weak effect, if any, on the nuclease activity of MIF at 4 μM (fig. S10F). At this higher concentration, MIF itself can efficiently bind and cleave ssDNAs. These data suggest that AIF may enhance MIF nuclease activity by increasing its binding to ssDNAs.

To further study where MIF cleaves DNA and to avoid the potential interference of biotin labeling, we used non-labeled PS^{30} and 3F1, which has only one unpaired base at the 3′ end of the stem-loop structure as substrates and customized two different DNA ladders based on PS^{30}. After incubation of these substrates with MIF (2 μM) for 2 hours, two major products of 20 and 22 nucleotides were detected (Fig. 3D). Faint bands of higher molecular mass were also observed. These bands

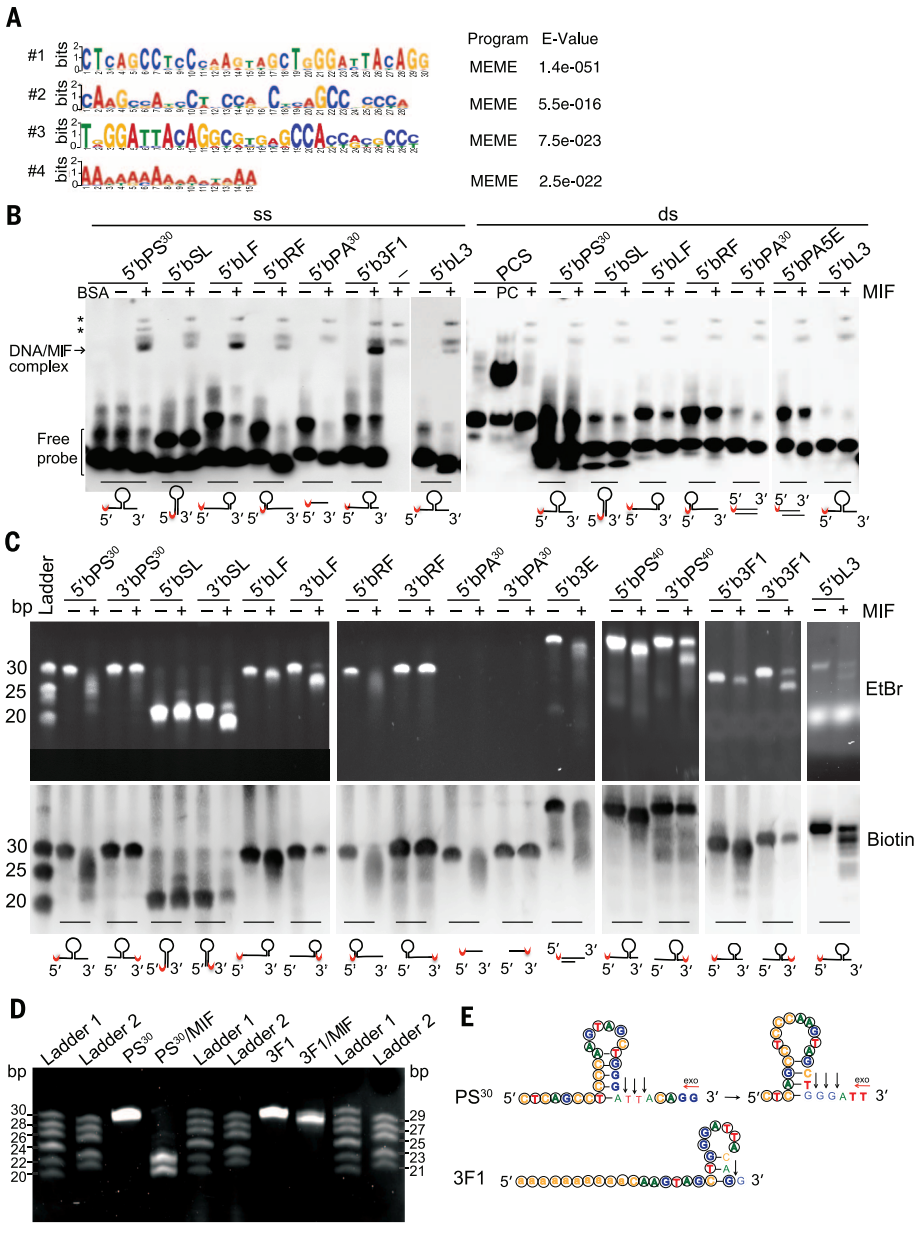

Fig. 3. MIF binds and cleaves ssDNA. (**A**) MIF DNA binding motif determined by ChIP-seq. (**B**) Binding of MIF to biotin-labeled small DNA substrates with different structures or different sequences in an EMSA assay (see fig. S8 for illustrations of substrates, and tables S1 and S2 for sequences). Arrow indicates the DNA-MIF complex. Asterisk indicates nonspecific bands. PCS, positive control substrate from the LightShift Chemiluminescent EMSA Kit (Thermo Scientific) containing 60 base pairs (bp) of 5′ biotin-labeled duplex. With or without BSA, bovine serum albumin; PC, Epstein-Barr nuclear antigen extract from the LightShift Chemiluminescent EMSA Kit or MIF. (**C**) MIF cleavage of unpaired bases at the 3′ end of the stem loop of 5′ or 3′ biotin-labeled small DNA substrates with various structures or sequences in a nuclease assay (see fig. S8 for illustrations of substrates, and tables S1 and S2 for sequences). Experiments were replicated four times with three independent preparations of MIF protein. (**D**) MIF cleavage of 3′ unpaired bases from nonlabeled PS^{30} and 3F1 substrates. DNA ladders 1 and 2 were customized with PS^{30} and its cleavage products by removing its 3′ nucleotides one by one. DNA ladder 1 was prepared using PS^{30}, PS^{28}, PS^{26}, PS^{24}, PS^{22}, and PS^{20}. DNA ladder 2 was prepared using PS^{29}, PS^{27}, PS^{25}, PS^{23}, and PS^{21}. (**E**) MIF cleavage sites on nonlabeled PS^{30} and 3F1 substrates.

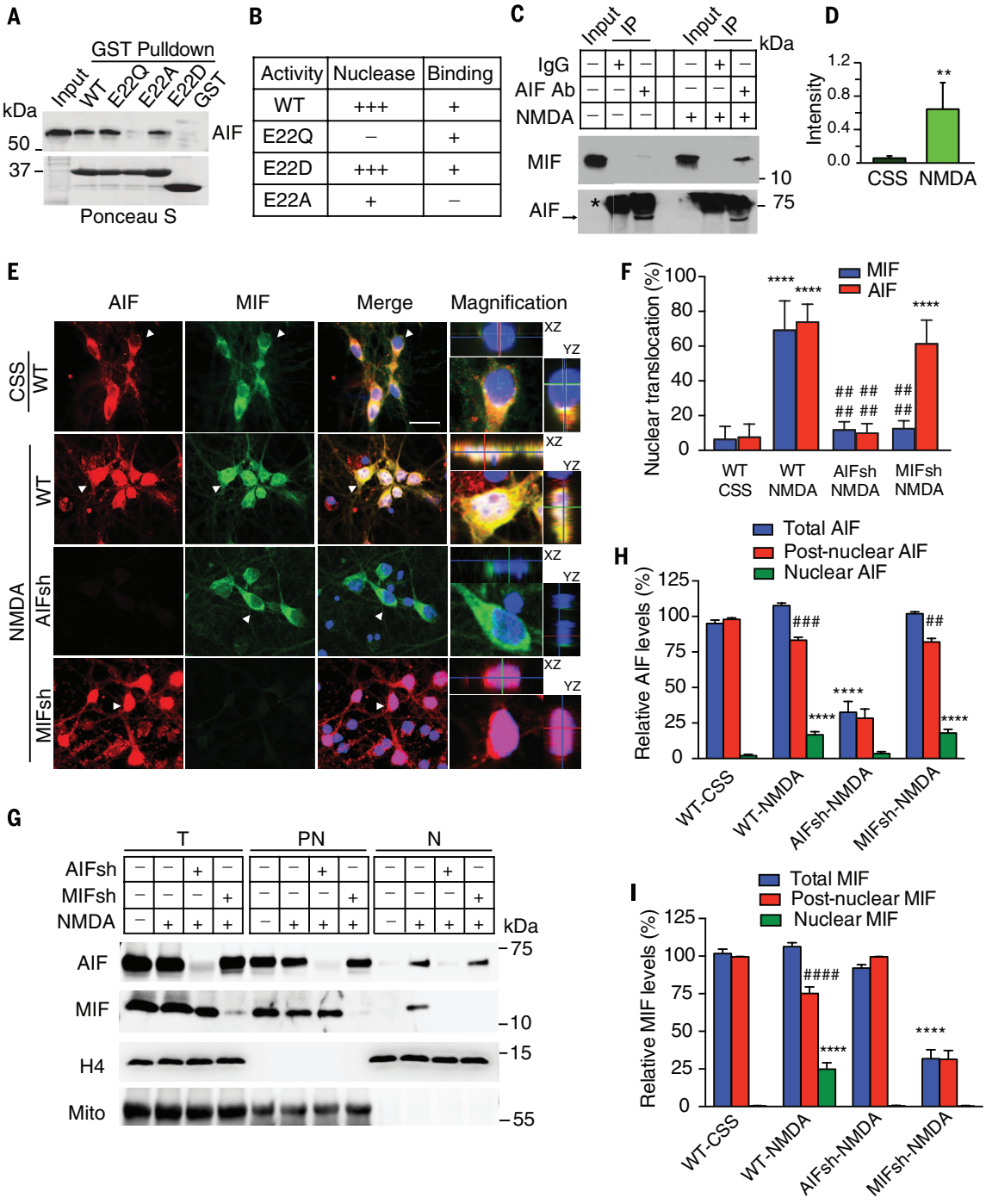

Fig. 4. Requirement of AIF for the recruitment of MIF to the nucleus in NMDA excitotoxicity. (**A**) Binding of immobilized GST-MIF WT and GST-MIF variants to AIF. (**B**) Nuclease activity and AIF-binding activity of MIF WT and MIF variants. (**C** and **D**) Coimmunoprecipitation (IP) of MIF and AIF in control (CSS) and NMDA-treated cortical neurons. Asterisk indicates IgG. Ab, antibody. (D) Intensity of treated versus untreated cultures. *$P < 0.05$, Student's t test. (**E**) Images of nuclear translocation of AIF and MIF after NMDA treatment in WT, AIF knockdown, and MIF knockdown cortical neurons. AIF shRNA (AIF sh) and MIF shRNA (MIF sh) caused a 71.3 ± 5.2% and 73.3 ± 6.1% protein reduction, respectively. White color indicates the overlay of AIF, MIF, and 4′,6′-diamidino-2-phenylindole (DAPI), showing the nuclear translocation of AIF and MIF. Purple color indicates the overlay of AIF and DAPI, showing the nuclear translocation of AIF. Z stacks illustrating the x,z and y,z axis are provided to demarcate the nucleus. Arrowheads indicate cells with the high magnification. (**F**) Quantification of the percentage of cells with nuclear translocation of MIF and AIF after NMDA treatment in WT, AIF knockdown, and MIF knockdown cortical neurons. CSS, control salt solution. ****$P < 0.0001$, versus its CSS control; $^{\#\#\#\#}P < 0.0001$, versus its WT treated with NMDA, one-way ANOVA. (**G**) Immunoblots of nuclear translocation of AIF and MIF after NMDA treatment in WT, AIF knockdown, and MIF knockdown cortical neurons. Compare total protein (T), post-nuclear fraction (PN), nuclear fraction (N), and Mito, mitochondrial antibody. (**H** and **I**) Relative levels of AIF and MIF in T, PN, and N. Means ± SEM. Experiments were replicated at least three times; ****$P < 0.0001$, versus its CSS control; $^{\#\#}P < 0.01$, $^{\#\#\#}P < 0.0001$, versus its total protein, one-way ANOVA.

were more obvious in the experiment in which PS^{30} was biotin labeled and the incubation time was 1 hour (Fig. 3D). MIF cleavage of the 3F1 substrate yielded only a 29-nucleotide (nt) band consistent with cleavage of one unpaired base at the 3′ end of the stem-loop structure (Fig. 3, D and E). These data indicate that PS^{30} is initially cleaved by MIF after "A23↓T24↓T25↓" (arrow indicates cleavage) by both 3′ exonuclease and endonuclease activity (Fig. 3E, left). Then the resulting product appears to form a new stem-loop structure, as predicted by the online RNA/DNA structure prediction software (http://rna.urmc.rochester.edu/RNAstructureWeb/Servers/Predict1/Predict1.html) (Fig. 3E, right). MIF then cleaves at the new unpaired bases at the 3′ end of this stem-loop structure after "G20↓G21↓G22↓". We conclude that MIF cleaves unpaired bases at the 3′ end adjacent to the stem loop at the +1 to ~+3 positions through both 3′ exonuclease and endonuclease activities.

AIF interacts with MIF and recruits MIF to the nucleus

Wild-type (WT) glutathione *S*-transferase–tagged AIF (GST-AIF) associated with MIF, and wild-type GST-MIF associated with AIF in GST pulldown analyses from cell lysates (Fig. 4A; fig. S11, A to D; and supplementary text). We mapped the MIF-AIF binding domain. MIF bound to AIF at amino acids 567 to 592 (fig. S11, A to C, and supplementary text). Conversely, the MIF E22A mutant showed reduced binding to GST-AIF, whereas the E22D and E22Q mutants still bound to GST-AIF (Fig. 4, A and B, and fig. S11D). The other PD-D/E(X)K and C57A;C60A mutations still bound GST-AIF (fig. S11D). Thus, MIF E22 appears to be critical for AIF binding. Endogenous AIF also coimmunoprecipitated with MIF from cortical neurons treated with NMDA (500 μM) but was barely detectable in untreated cultures (Fig. 4, C and D).

MIF was localized predominantly to the cytosol of both cortical neurons (Fig. 4E) and HeLa cells (fig. S12A). Both MIF and AIF translocated to the nucleus in cortical neurons treated with NMDA (Fig. 4, E and F) and HeLa cells stimulated with MNNG (fig. S12A). Depletion of AIF with shRNA led to a loss of MIF translocation to the nucleus, but depletion of MIF did not prevent translocation of AIF to the nucleus in cells exposed to NMDA (Fig. 4, E and F). Subcellular fractionation into nuclear and postnuclear fractions confirmed the translocation of MIF and AIF to the nucleus in cultured cortical neurons exposed to NMDA (Fig. 4, G to I). AIF was required for MIF translocation (Fig. 4, E to I). DPQ prevented accumulation of both MIF and AIF in the nucleus in HeLa cells treated with MNNG (fig. S12, A to C) and cortical neurons treated with NMDA (fig. S13, A to C). Consistent with the notion that NMDA excitotoxicity involves nitric oxide production, the nitric oxide synthase inhibitor nitro-arginine (N-Arg) prevented accumulation of both MIF and AIF in the nucleus (fig. S13, A to C).

We transduced primary cortical cultures from WT MIF knockout mice with lentivirus carrying Flag-tagged MIF (MIF-WT-Flag) or MIF mutants (MIF-E22Q-Flag and MIF-E22A-Flag) to confirm that AIF and MIF binding is required for MIF nuclear accumulation after NMDA administration (Fig. 5, A and B). Wild-type MIF and E22Q interacted with AIF, but MIF E22A did not bind to AIF (Fig. 5B). In nontransduced MIF knockout cultures and in MIF knockout cultures transduced with MIF-WT-Flag, MIF-E22Q-Flag, and MIF-E22A-Flag, AIF translocated to the nucleus when cells were exposed to NMDA (Fig. 5, C and D). Both MIF wild-type and MIF E22Q also translocated to the nucleus; however, the MIF E22A mutant, which is deficient in AIF binding, failed to do so (Fig. 5, C and D). Separation of nuclear and postnuclear fractions confirmed the observations made by immunofluorescence (Fig. 5, E to G). These results indicate that MIF's interaction with AIF is required for the nuclear translocation of MIF.

MIF nuclease activity is required for chromatinolysis and parthanatos

To determine whether MIF's nuclease activity and AIF-mediated recruitment are required for parthanatos, we transduced MIF knockout cultures with the nuclease-deficient MIF E22Q mutant and the AIF binding–deficient MIF E22A mutant. Consistent with the shRNA experiments, cortical cultures lacking MIF were resistant to NMDA excitotoxicity (Fig. 6, A and B). Transduction of cells with wild-type MIF or the tautomerase-deficient mutant MIF P2G fully restored NMDA excitotoxicity; conversely, neither MIF E22Q nor MIF E22A restored NMDA excitotoxicity (Fig. 6, A and B). By the comet assay, a method to measure DNA damage, we found that NMDA administration in wild-type cortical neurons resulted in substantial numbers of neurons with DNA damage, whereas no such damage was detected in MIF knockout neurons (Fig. 6, C to F). Transduction of knockout neurons with wild-type MIF, but not with MIF E22Q or MIF E22A, restored DNA damage in cells treated with NMDA (Fig. 6, C to F). Depletion of MIF with shRNA in HeLa cells with two different shRNAs resulted in a reduced number of cells showing damaged DNA after treatment with MNNG compared with DNA in cells treated with nontargeted shRNA (fig. S14, A to D). A pulsed-field gel electrophoresis assay of genomic DNA confirmed that NMDA administration caused large DNA fragments in wild-type cortical neurons but not in MIF knockout cortical neurons (Fig. 6G). No obvious large DNA fragments were observed in MIF knockout neurons transduced with MIF E22Q or MIF E22A (Fig. 6G). Transduction of knockout neurons with wild-type MIF or MIF P2G restored NMDA-induced formation of large DNA fragments (Fig. 6G). HeLa cells lacking MIF after we used CRISPR-Cas9 were resistant to MNNG toxicity (fig. S15, A to C). Transduction of knockout HeLa cells with wild-type MIF or MIF P2G restored MNNG-induced formation of large DNA fragments and toxicity (fig. S15). These results indicate that MIF is the major nuclease involved in large-scale DNA fragmentation during MNNG- or NMDA-induced parthanatos, which is independent from MIF's tautomerase activity.

To evaluate the requirement of MIF nuclease activity and MIF binding to AIF in cell death due to parthanatos in vivo, we transduced MIF knockout mice with adeno-associated virus serotype 2 virus (AAV2) containing wild-type MIF, or the nuclease-deficient MIF E22Q mutant or the AIF-binding-deficient MIF E22A mutant by injecting the different AAV2 MIFs into the intracerebroventricular zone of newborn mice. The effectiveness of transduction was confirmed by immunostaining for MIF-Flag in the cortex, striatum, and hippocampus in adult mice (fig. S16, A and B). Two-month old male mice were then subjected to 45-min transient occlusion of the middle cerebral artery (MCAO). Despite the similar intensity of the ischemic insult (fig. S16C), infarct volume as previously reported (*34*) was reduced in MIF knockout mice in the cortex, striatum, and hemisphere by about 75% compared to that in their wild-type counterparts (Fig. 7, A to D). Moreover, the neuroprotection in MIF knockout mice remained for at least 7 days (Fig. 7, C and D). Expression of wild-type MIF, but not MIF E22Q or MIF E22A, in the MIF knockout mice restored infarct volume to that observed in wild-type animals (Fig. 7, A to D). We assessed behavior by spontaneous activity in the open field task on days 1, 3, and 7 after MCAO. Consistent with the infarct data, MIF knockout mice had improved behavioral scores compared to those of wild-type mice. MIF knockout mice expressing wild-type MIF had behavioral scores equivalent to those of wild-type mice whereas expression of MIF E22Q or MIF E22A had no effect (Fig. 7, E and F). Over 3 and 7 days, the behavioral scores of MIF knockout mice remained higher than those of wild-type treated mice (Fig. 7, F and G). A corner test measuring sensorimotor function showed that all mice do not show a side preference before MCAO surgery. However, wild-type mice and MIF knockout mice expressing wild-type MIF had significantly ($P < 0.05$ to $P < 0.001$, one-way analysis of variance (ANOVA)] increased turning toward the non-impaired side at days 1, 3, and 7 after MCAO (Fig. 7G), indicating these mice have more severe sensory and motor deficits. No preference was observed in MIF knockout mice and MIF knockout mice with expression of MIF E22Q or MIF E22A (Fig. 7G).

Significant ($P < 0.0001$, one-way ANOVA) DNA damage as assessed by pulse field gel electrophoresis was observed at days 1, 3, and 7 after MCAO in wild-type mice or MIF knockout mice expressing wild-type MIF (Fig. 7, H and I). DNA damage was reduced in the MIF KO mice and MIF knockout mice expressing E22Q or E22A MIF (Fig. 7, H and I). We examined the localization of AIF and MIF by confocal microscopy in the penumbra region of the stroke (fig. S17, A and B). Consistent with the observation in cultured cortical neurons, AIF significantly ($P < 0.001$, one-way ANOVA) translocated to the nucleus at 1, 3, and 7 days after MCAO in wild-type animals. In MIF knockout animals as well as MIF knockout mice injected with MIF wild-type, E22Q, and E22A AIF significantly ($P < 0.001$, one-way ANOVA) translocated to the nucleus at 1 and 3 days after MCAO and there was reduced translocation of AIF at 7 days (fig. S17, A and B). Both MIF wild-type and MIF E22Q also significantly ($P < 0.001$, one-way ANOVA) translocated to the

nucleus at 1 and 3 days after MCAO and there was reduced translocation at 7 days; however, the AIF binding–deficient mutant MIF E22A failed to do so (fig. S17, A and B). These data indicate that MIF is required for AIF-mediated neurotoxicity and DNA cleavage and that AIF is required for MIF translocation in vivo.

Conclusion

We identified MIF as a PAAN. Prior crystallization studies of MIF allowed us to show via 3-D modeling that MIF is structurally similar to PD-D/E(x)K nucleases (*25*, *26*). The MIF monomer, which has pseudo 2-fold symmetry does not contain the core PD-D/E(X)K structure since the MIF monomer has four β strands next to the two α helices, and the orientations of the β-strands within an isolated monomer do not fit the requirement of the PD-D/E(x)K topology (*23*). However, our structure-activity analyses based on the MIF trimer, which has 3-fold symmetry, indicated that the interactions of the β strands of each monomer with the other monomers results in a MIF PD-D/E(x)K structure that consists of four β strands next to two α strands (*23*). Two of the β strands are parallel (β-4 and β-5), whereas the other two strands (β-6 and β-7) (from the adjacent monomer) are antiparallel. This topology exquisitely supports the idea that MIF's nuclease activity requires the trimer as the monomers do not support the required topology and is consistent with MIF existing as a trimer. The PD-D/E(X)K domains in MIF are highly conserved in vertebrates. The glutamic acid residue (E22) in

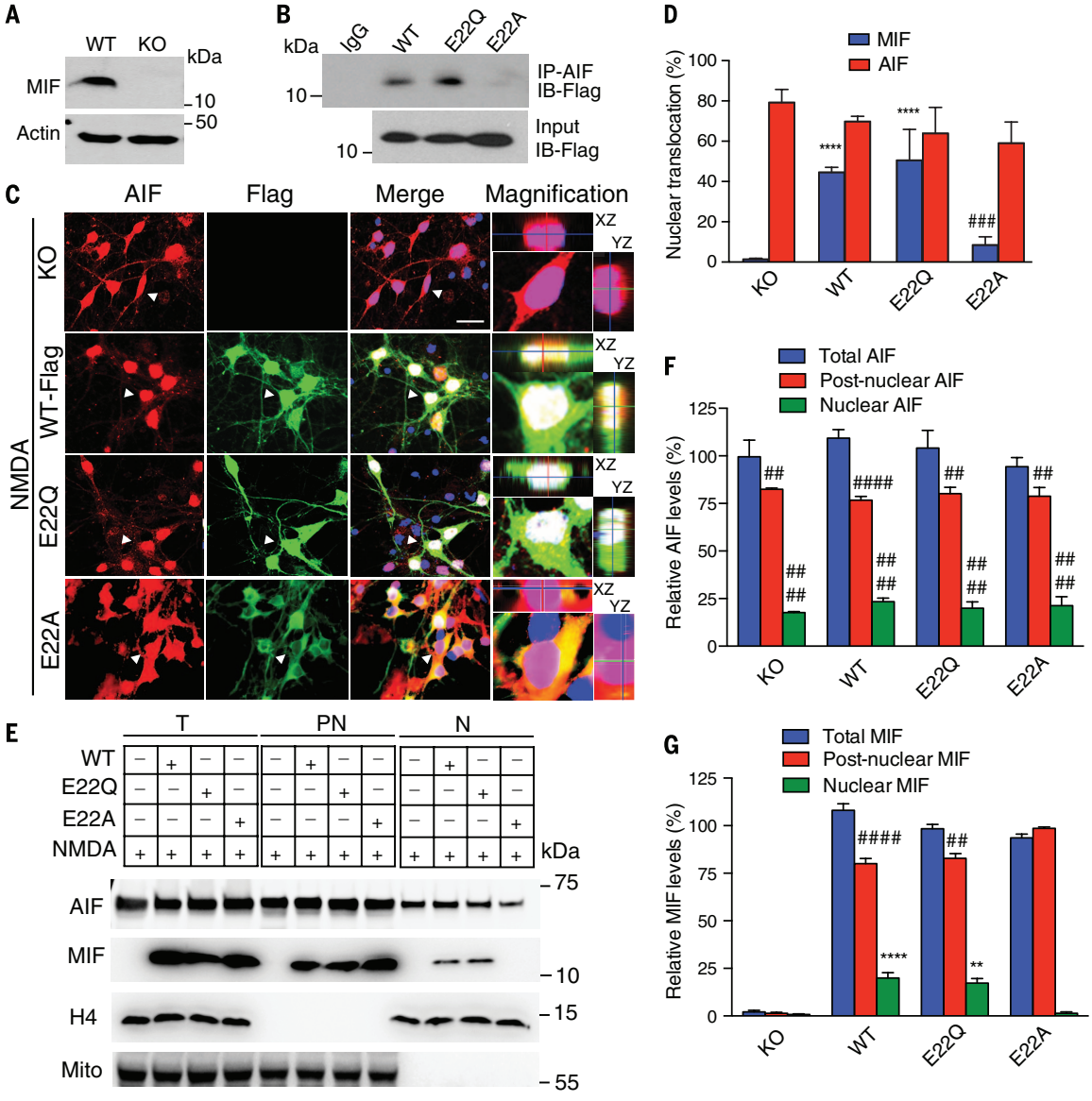

Fig. 5. MIF E22A mutant prevents AIF's recruitment of MIF to the nucleus in NMDA-excitotoxicity. (**A**) Expression of MIF in WT and knockout (KO) neurons. (**B**) Coimmunoprecipitation of Flag-tagged MIF variants and AIF in cortical neurons after NMDA treatment. (**C**) Images of nuclear translocation of AIF and exogenous MIF WT and MIF variants after NMDA treatment in MIF KO cortical neurons. Scale bar, 20 μm. White color indicates the overlay of AIF, MIF, and DAPI, showing the nuclear translocation of AIF and MIF. Purple color indicates the overlay of AIF and DAPI, showing the nuclear translocation of AIF. Z stacks illustrating the *x*,*z* and *y*,*z* axis are provided to demarcate the nucleus. (**D**) Quantification of the percentage of cells with nuclear translocation of AIF and exogenous MIF WT and MIF variants after NMDA treatment in MIF KO cortical neurons. $^{****}P < 0.0001$, versus KO group; $^{\#\#\#}P < 0.001$, versus KO-WT group, one-way ANOVA. (**E**) Immunoblots of nuclear translocation of AIF and exogenous MIF WT and MIF variants after NMDA treatment in MIF KO cortical neurons. H4, histone H4; mito, mitochondrial antibody. (**F** and **G**) Relative levels of AIF and MIF in total protein (T), postnuclear fraction (PN) and nuclear fraction (N). Means ± SEM. Experiments were replicated at least three times. $^{**}P < 0.01$, $^{****}P < 0.001$, versus KO control group; $^{\#\#}P < 0.01$, $^{\#\#\#\#}P < 0.0001$, versus its total protein, one-way ANOVA.

the first α helix of MIF is critical for its nuclease activity, which is consistent with prior reports that this glutamic acid in the first α helix of many exonuclease-endonuclease-phosphatase (EEP) domain superfamily nucleases is highly conserved, and it is the active site for nuclease activity (*25*, *26*).

MIF has both 3′ exonuclease and endonuclease activity. It preferentially binds to 5′ unpaired bases of ssDNA with the stem-loop structure and cleaves its 3′ unpaired bases. AIF interacts with MIF and recruits MIF to the nucleus where MIF binds and cleaves genomic DNA into large fragments similar to the size induced by stressors that activate parthanatos. MIF binding to AIF facilitates its cleavage of double-stranded genomic DNA, and, based on the chromatin immunoprecipitation sequencing ChiP-seq data, the average distance of MIF binding is about 15 to 60 kb, which is comparable to the size of large DNA fragments caused by MIF. MIF's cleavage of genomic DNA into 20- to 50-kb fragments is likely due to its rare binding on genomic DNA. Knockout of MIF reduces DNA fragmentation induced by stimuli that activate PARP-1–dependent cell death. Mutating a key amino acid residue, glutamic acid residue (E22), in the PD-D/E(X)K motif eliminates MIF's nuclease activity and protects cells from parthanatos both in vitro and in vivo. Disruption of the AIF and MIF protein-protein interaction prevents the translocation of MIF from the cytosol to the nucleus, which also protects against PARP-1–dependent cell death both in vitro and in vivo. Neither MIF's thiol-protein oxidoreductase activity nor tautomerase activity are involved in its actions as a nuclease. Knockout of MIF, a MIF nuclease–deficient mutant and a MIF AIF binding–deficient mutant all reduce infarct volume and have long-lasting behavioral rescue in the focal ischemia model of stroke in mice. Thus, MIF is a PAAN that is important in cell death because of activation of PARP-1 and the release of AIF (*2*). Future studies are required to further determine whether the stem-loop–ssDNA binding activity or the 3′ exonuclease and endonuclease activities of MIF, is important for its in vivo PAAN activity. In addition, our stroke data from MIF knockout mice indicate that other nucleases other than MIF might be involved in ischemic neuronal cell death. However, how these nucleases interact with MIF and contribute to PARP-1–induced cell death requires future studies.

MIF has a variety of pleiotropic actions. It is widely distributed throughout the brain (*35*, *36*). It functions as a nonclassically secreted cytokine and may play important roles in cancer biology, immune responses, and inflammation (*18*, *37*). MIF also has important roles in cellular stress and apoptosis (*34*, *38*, *39*). How MIF's nuclease activity relates to its role in the immune system and its other actions requires future studies.

Like PARP, inhibition of MIF nuclease activity is an attractive target for acute neurologic disorders. However, it may have advantages over PARP inhibition in chronic neurodegenerative diseases where long-term inhibition of PARP could impair detection and repair of DNA damage. Inhibition of MIF's nuclease activity could bypass

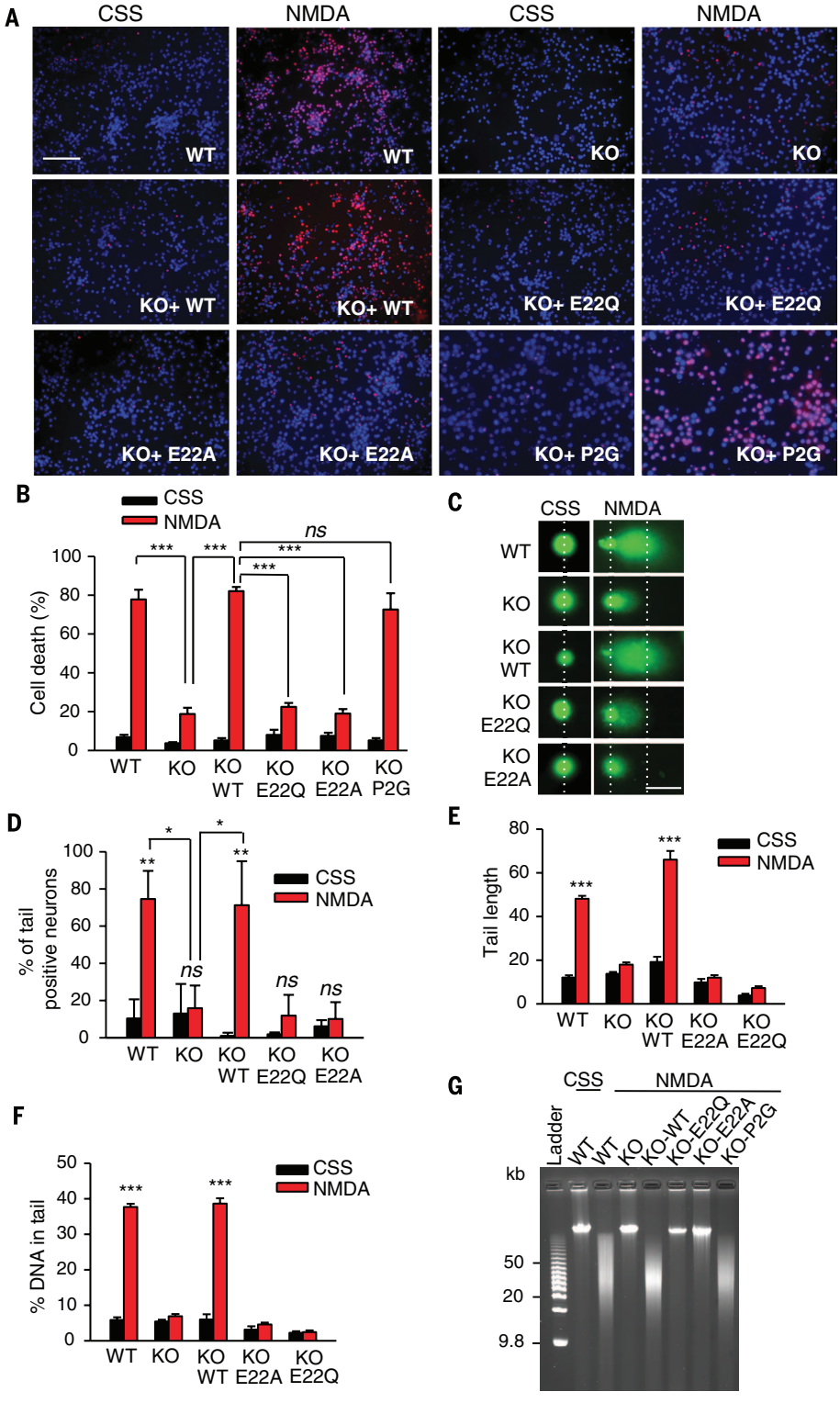

Fig. 6. MIF nuclease activity is critical for DNA damage and PARP-1–dependent cell death in cortical neurons. (**A**) Representative images and (**B**) quantification of NMDA-induced (500 μM for 5 min) excitotoxicity in MIF WT, KO, and KO cortical neurons expressing MIF WT, E22Q, E22A, or P2G. Scale bar, 200 μm. (**C**) Representative images and (**D** to **F**) quantification of NMDA-induced DNA damage 6 hours after treatment determined by the comet assay in MIF WT, KO, and KO neurons expressing MIF WT, E22Q, E22A, or P2G. Dashed lines indicate the center of the head and tail. Scale bar, 20 μm. (**G**) Pulsed-field gel electrophoresis assay of NMDA-induced DNA damage 6 hours after treatment in MIF WT and KO neurons and KO neurons expressing MIF WT, E22Q, E22A, or P2G. Means ± SEM are shown in (B), (D), (E), and (F). *P < 0.05, **P < 0.01, ***P < 0.001, one-way ANOVA; ns, nonsignificant.

this potential concern and offer a therapeutic opportunity for various disorders.

Materials and methods

Human protein chip high-throughput screening

Human protein chips (16K and 5K), which were prepared by spotting more than 16,000 or 5000 highly purified proteins onto special nitrocellulose-coated slides (*16*), were incubated in renaturation buffer containing 50 mM Tris-HCl, pH 8.0, 100 mM NaCl, 1 mM DTT, 0.3% Tween 20 for 1 hour at 4°C. After Blocking with 5% non-fat dry milk for 1 hour at room temperature, protein chips were incubated with purified mouse AIF protein (50 nM, NP_036149) in 1% milk for 1 hour. Protein interaction was then determined either by sequentially incubating with rabbit anti-AIF antibody (JH532, JHU) (*9*, *11*) and Alexa Fluor 647 donkey anti-rabbit IgG, or Alexa Fluor 647 donkey anti-rabbit IgG only as negative control. Protein microarrays were scanned with GenePix 4000B Microscanner (Tecan) using the Cy5 image and the median fluorescence of each spot was calculated. We used the same procedure described previously to identify interacting proteins (*16*).

Reverse transfection format siRNA-based screen for PARP-1–dependent cell viability

On-Target plus SMARTpool siRNAs targeting AIF-interacting proteins resulting from human protein chip high throughput screening were customized

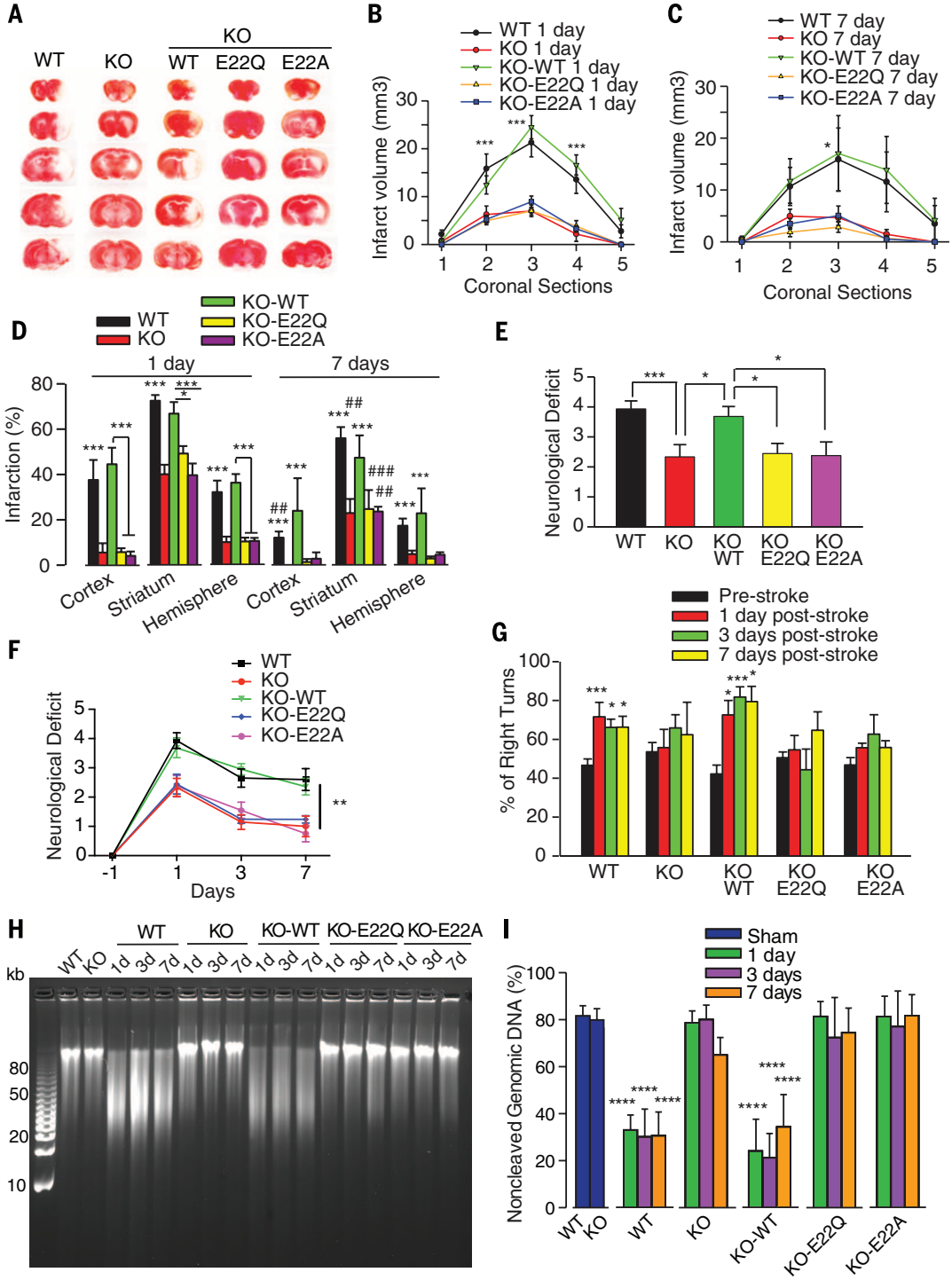

Fig. 7. MIF nuclease activity is critical for DNA damage and ischemic neuronal cell death in vivo. (**A**) Representative images of triphenyl tetrazolium chloride staining of MIF WT, KO, and KO mice that were injected with AAV2-MIF WT, E22Q, or E22A 24 hours after 45 min of middle cerebral artery occlusion (MCAO). (**B** to **D**) Quantification of infarction volume in cortex, striatum, and hemisphere 1 day or 7 days after 45-min MCAO. WT MCAO (n = 29); KO MCAO (n = 20); KO-WT MCAO (n = 23). KO-E22Q (n = 22) and KO-E22A MCAO (n = 19). $^{*}P < 0.05$, $^{***}P < 0.001$, versus KO group at the same time point; $^{\#\#}P < 0.01$, $^{\#\#\#}P < 0.001$, the same group at 7 days versus at 1 day after 45-min MCAO, one-way ANOVA. (**E** to **G**) Neurological deficit was evaluated by [(E) and (F)] open field on a scale of 0 to 5 and (G) corner test evaluated by percentage of right turns at 1 day, 3 days, or 7 days after MCAO surgery. WT MCAO (n = 16); KO MCAO (n = 12); and KO-WT MCAO (n = 16). KO-E22Q MCAO (n = 16) and KO-E22A MCAO (n = 16). Means ± SEM. $^{*}P < 0.05$, $^{***}P < 0.001$, one-way ANOVA in (E) and (G). $^{**}P < 0.01$, two-way ANOVA in (F), WT and KO-WT versus KO, KO-E22Q, and KO-E22A at different time points. (**H**) DNA fragmentation determined by pulsed-field gel electrophoresis in the penumbra 1 day, 3 days, or 7 days after 45-min MCAO surgery in MIF WT, KO, and KO mutant mice, which were injected with AAV2-MIF WT, E22Q, or E22A. WT MCAO (n = 15); KO MCAO (n = 15); and KO-WT MCAO (n = 15). KO-E22Q (n = 15) and KO-E22A MCAO (n = 15). (**I**) Quantification of noncleaved genomic DNA. Means ± SEM. $^{****}P < 0.0001$, versus its sham treatment group, one-way ANOVA.

in 96-well plates from Dharmacon. The plates were rehydrated using DharmaFECT 1 transfection reagent at room temperature for 30 min. HeLa cells were then seeded in the plates with the cell density at 1×10^4/well. 48 hours after transfection, cells were treated with MNNG (50 μM) or DMSO for 15 min and then incubated in normal complete medium for 24 hours. After adding Alamar Blue for 1-4 hours, cell viability was determined by fluorescence at excitation wavelength 570 nm and Emission wavelength 585 nm. PARP-1 siRNAs were used as the positive control and non-target siRNAs as the negative control.

Nuclease assays

Human genomic DNA (200 ng/reaction, Promega), pcDNA (200 ng/reaction) or PS[30] and its related and non-related substrates (1 μM) was incubated with wild-type MIF or its variants at a final concentration of 0.25-8 μM as indicated in 10 mM Tris-HCl buffer (pH 7.0) containing 10 mM $MgCl_2$ or specific buffer as indicated, for 1 hour (with pcDNA and small DNA substrates) or 4 hours (with human genomic DNA) at 37°C. The reaction was terminated with loading buffer containing 10 mM EDTA and incubation on ice. The human genomic DNA samples were immediately separated on a 1.2% pulse field certified agarose in 0.5 X TBE buffer with initial switch time of 1.5 s and a final switch time of 3.5 s for 12 hours at 6 V/cm. pcDNA samples were determined by 1% agarose gel. Small DNA substrates were separated on 15% or 25% TBE-urea polyacrylamide (PAGE) gel or 20% TBE PAGE gel. The gel was then stained with 0.5 μg/ml Ethidium Bromide (EtBr) followed by electrophoretic transfer to a nylon membrane. Biotin-labeled DNA was further detected by chemiluminescence using the Chemiluminescent Nucleic Acid Detection Module (Thermo Scientific).

Electrophoretic mobility shift assay (EMSA)

EMSA assays were performed using the LightShift Chemiluminescent EMSA kit (Thermo Scientific) following the manufactures instruction. Briefly, purified MIF protein (2 μM) was incubated with biotin-labeled DNA substrates (10 nM) in the binding buffer containing 10 mM $MgCl_2$ for 30 min on ice. Then samples were separated on 6% retardation polyacrylamide followed by electrophoretic transfer to a nylon membrane. Biotin-labeled DNA was further detected by chemiluminescence using the Chemiluminescent Nucleic Acid Detection Module (Thermo Scientific).

Comet assay

Comet assays were conducted following protocols provided by Trevigen (Gaithersburg, MD). Briefly, HeLa cells with or without MNNG treatment and cortical neurons with or without NMDA treatment were washed with ice-cold PBS 6 hours after the treatment, harvested by centrifugation at 720 *g* for 10 min and re-suspended in ice-cold PBS (Ca^{2+} and Mg^{2+} free) at 1×10^5 cells/ml. Cells were then combined with 1% low melting point agarose in PBS (42°C) in a ratio of 1:10 (v/v), and 50 μl of the cell–agarose mixture was immediately pipetted onto the Comet Slide and placed flatly at 4°C in the dark for 30 min to enhance the attachment. After being lysed in lysis buffer, slides were immersed with alkaline unwinding solution (200 mM NaOH, pH >13, 1 mM EDTA) for 1 hour at RT. The comet slides were transferred and electrophoresed with 1 L of alkaline unwinding solution at 21 Volts for 30 min in a horizontal electrophoresis apparatus. After draining the excess electrophoresis buffer, slides were rinsed twice with dH_2O and then fixed with 70% ethanol for 5 min and stained with SYBR Green for 5 min at 4°C. Cell images were captured using a Zeiss epifluorescent microscope (Axiovert 200M) and image analysis was performed with CASP software (version 1.2.2). The length of the "comet tail," which is termed as the length from the edge of the nucleus to the end of the comet tail, for each sample, was measured.

Protein expression and purification

Human EndoG (NM_004435), cyclophilin A (NM_021130), mouse AIF (NM_012019), human MIF (NM_002415) cDNA and their variants were subcloned into glutathione *S*-transferase (GST)-tagged pGex-6P-1 vector (GE Healthcare) by EcoRI and XhoI restriction sites and verified by sequencing. The protein was expressed and purified from *Escherichia coli* by glutathione sepharose. The GST tag was subsequently proteolytically removed for the nuclease assay. MIF point mutants were constructed by polymerase chain reaction (PCR) and verified by sequencing. The purity of MIF proteins that were used in the nuclease assays was further confirmed by mass spectrometry. MIF proteins purified by FPLC were also used in the nuclease assays and no obvious difference was observed between FPLC MIF and non-FPLC MIF proteins. GST protein was used as a negative control in the nuclease assay.

Middle cerebral artery occlusion (MCAO)

Cerebral ischemia was induced by 45 min of reversible MCAO as previously described (*40*). Adult male MIF knockout (KO) mice (2 to 4 months old, 20 to 28 g) were anesthetized with isoflurane and body temperature was maintained at 36.5 ± 0.5°C by a feedback-controlled heating system. A midline ventral neck incision was made, and unilateral MCAO was performed by inserting a 7.0 nylon monofilament into the right internal carotid artery 6-8 mm from the internal carotid/pterygopalatine artery bifurcation via an external carotid artery stump. Sham-operated animals were subjected to the same surgical procedure, but the suture was not advanced into the internal carotid artery. After 1 day, 3 days or 7 days of reperfusion, mice were perfused with PBS and stained with triphenyl tetrazolium chloride (TTC). The brains were further fixed with 4% PFA and sliced for immunohistochemistry (*9*, *11*, *41*).

ChIP-seq

We preformed ChIP-seq as previously described (*42*, *43*). Briefly, HeLa Cells were first treated with DMSO or MNNG (50 μM, 15 min). 5 hours after MNNG treatment, cells were cross-linked with 1% formaldehyde for 20 min at 37°C, and quenched in 0.125 M glycine. Chromatin extraction was performed before sonication. The anti-MIF antibody (ab36146, Abcam) was used and DNA was immunoprecipitated from the sonicated cell lysates. The libraries were prepared according to Illumina's instructions accompanying the DNA Sample kit and sequenced using an Illumina HiSEq. 2000 with generation of 50 bp single-end reads. Detailed procedures are as follows. HeLa cells were treated with DMSO or MNNG (50 μM) for 15 min and cultured in the fresh medium for an additional 5 hours. Cells were then cross-linked with 1% formaldehyde for 10 min at 37°C, and the reaction was quenched in 0.125 M glycine for 20 min at room temperature. Chromatin was extracted using SimpleChIP Enzymatic Chromatin IP kit from Cell Signaling Technology (Cat# 9003), and sonicated 30 s on and 30 s off for 15 cycles using a Bioruptor Twin (Diagenode). The quality and size of sheared chromatin DNA were examined on an agarose gel by DNA electrophoresis. 10% of chromatin was kept as input and the rest of the chromatin was diluted and pre-cleared using 10 μl Magnetic protein G agarose slurry for 30 min at 4°C to exclude non-specific binding to protein G agarose beads directly. The pre-cleared chromatin was incubated overnight with an anti-MIF antibody (3 μg/ml, ab36146, Abcam) or control IgG (3 μg/ml) in the presence of Magnetic protein G agarose slurry (30 μl) at 4°C. After washing the protein G agarose beads for 3 times, half of the protein G agarose/antibody complex was subjected to immunoblot assays to check the quality of the immunoprecipitation. Another half of the protein G agarose/antibody complex was eluted in 170 μl of elution buffer containing 1% SDS, 0.1 M $NaHCO_3$ at 65°C. The eluates as well as the chromatin input were treated with 1 mg/ml RNase A at 37°C for 30 min, and reverse-crosslinked by incubating at 65°C for 4 hours after adding 3 μl of 5 M NaCl and 1 μl of 10 mg/ml proteinase K. Finally the chromatin DNA was purified using phenol/chloroform/isoamyl alcohol and precipitated by ethanol. The ChIP and input DNA libraries were prepared using Illumina's Truseq DNA LT Sample Prep Kit according to the instructions. The final product was amplified for 15 cycles. The quality and the size of the insert was analyzed using a bioanalyzer. Sequencing was performed in the Next Generation Sequencing Center at Johns Hopkins using an Illumina HiSEq. 2000 with generation of 50 bp single-end reads. The ChIP-seq raw data have been deposited in the GEO database accession #: GSE65110.

ChIP-seq data analysis

Raw data from the HiSEq. 2000 was converted to FASTQ using CASAVA v1.8 and demultiplexed. Reads were mapped to the human genome (hg19) using Bowtie2 (v2.0.5) using the default parameters. Converted SAM files were passed to MACS (v1.4.1) for peak calling using the default parameters. Peaks from DMSO- and MNNG-treated libraries were reported in .bed format and are provided in GEO. Peaks differentially identified in the DMSO- and MNNG-treated groups were parsed by a custom R script. Sequence corresponding to

peaks identified in only MNNG-treated, but not DMSO-treated libraries were fed into SeSiMCMC_4_36, Chipmunk v4.3+, and MEMEchip v4.9.0 for motif discovery using default parameters.

Data transfer: The CASAVAv1.8 software was used to convert the raw files into FASTQ files as well demultiplex the lanes.

MIF-DNA docking methods

A DNA duplex structure (*44*) (PDB accession 1BNA) and a single-stranded DNA structure [PDB accession 2RPD (*45*)] were docked onto the surface of MIF [PDB accession 1FIM (*24*)] using *Hex-8.0.* protein-DNA docking program (*46*, *47*). The HEX program uses a surface complementarity algorithm to identify contact between protein and DNA. MIF surfaces were generated using Pymol. All images were viewed and labeled with pdb viewer, Pymol. The MIF-DNA docked models are shown as obtained from the HEX program.

Lentivirus, adeno-associated virus (AAV) construction and virus production

Mouse MIF-WT-Flag (NM_010798), MIF-E22Q-Flag and MIF-E22A-Flag were subcloned into a lentiviral cFugw vector by AgeI and EcoRI restriction sites, and its expression was driven by the human ubiquitin C (hUBC) promoter. Human MIF and mouse MIF shRNAs were designed using the website <http://katahdin.cshl.org/siRNA/RNAi.cgi?type=shRNA>. The program gave 97 nt oligo sequences for generating shRNAmirs. Using PacI SME2 forward primer 5' CAGAAGGTTAATTAAAAGGTATATTGCTGTTGACAGTGAGCG 3' and NheI SME2 reverse primer 5' CTAAAGTAGCCCCTTGCTAGCCGAGGCAGTAGGCA 3', we then PCR amplified them to generate the second strand and added PacI and NheI restriction sites to clone the products into pSME2, a construct that inserts an empty shRNAmir expression cassette in the pSM2 vector with modified restriction sites into the cFUGw backbone. This vector expresses GFP. The lentivirus was produced by transient transfection of the recombinant cFugw vector into 293FT cells together with three packaging vectors: pLP1, pLP2, and pVSV-G (1.3:1.5:1:1.5). The viral supernatants were collected at 48 and 72 hours after transfection and concentrated by ultracentrifugation for 2 hours at 50,000 g. MIF-WT-Flag, MIF-E22Q-Flag and MIF-E22A-Flag were subcloned into a AAV-WPRE-bGH (044 a.m./CBA-pI-WPRE-bGH) vector by BamHI and EcoRI restriction sites, and its expression was driven by chicken β-actin (CBA) promoter. All AAV2 viruses were produced by the Vector BioLabs.

Sequences of MIF substrates, templates, and primers

Sequences of MIF substrates, templates and primers used for shRNA constructs and point mutation constructs are provided in Table S1.

Cell culture, transfection, lentiviral transduction, and cytotoxicity

HeLa cells were cultured in Dulbecco's modified Eagle's medium (Invitrogen) supplemented with 10% fetal bovine serum (HyClone). V5-tagged MIF was transfected with Lipofectamine Plus (Invitrogen). Primary neuronal cultures from cortex were prepared as previously described (*9*). Briefly, the cortex was dissected and the cells were dissociated by trituration in modified Eagle's medium (MEM), 20% horse serum, 30 mM glucose, and 2 mM L-glutamine after a 10-min digestion in 0.027% trypsin/saline solution (Gibco-BRL). The neurons were plated on 15-mm multiwell plates coated with polyornithine or on coverslips coated with polyornithine. Neurons were maintained in MEM, 10% horse serum, 30 mM glucose, and 2 mM L-glutamine in a 7% CO2 humidified 37°C incubator. The growth medium was replaced twice per week. In mature cultures, neurons represent 70 to 90% of the total number of cells. Days in vitro (DIV) 7 to 9, neurons were infected by lentivirus carrying MIF-WT-Flag, MIF-E22Q-Flag, or MIF-E22A-Flag [1×10^9 units (TU)/ml] for 72 hours. Parthanatos was induced by either MNNG (Sigma) in HeLa cells or NMDA (Sigma) in neurons. HeLa cells were exposed to MNNG (50 μM) for 15 min, and neurons (DIV 10 to 14) were washed with control salt solution [CSS, containing 120 mM NaCl, 5.4 mM KCl, 1.8 mM $CaCl_2$, 25 mM tris-Cl, and 20 mM glucose (pH 7.4)], exposed to 500 μM NMDA plus 10 μM glycine in CSS for 5 min, and then exposed to MEM containing 10% horse serum, 30 mM glucose, and 2 mM L-glutamine for various times before fixation, immunocytochemical staining, and confocal laser scanning microscopy. Cell viability was determined the following day by unbiased objective computer-assisted cell counting after staining of all nuclei with 7 μM Hoechst 33342 (Invitrogen) and dead cell nuclei with 2 μM propidium iodide (Invitrogen). The numbers of total and dead cells were counted with the Axiovision 4.6 software (Carl Zeiss). At least three separate experiments using at least six separate wells were performed with a minimum of 15,000 to 20,000 neurons or cells counted per data point. For neuronal toxicity assessments, glial nuclei fluoresced at a different intensity than neuronal nuclei and were gated out. The percentage of cell death was determined as the ratio of live to dead cells compared with the percentage of cell death in control wells to account for cell death attributed to mechanical stimulation of the cultures.

Pull-down, coimmunoprecipitation, and immunoblotting

For the pull-down assay, GST-tagged MIF or AIF proteins immobilized glutathione Sepharose beads were incubated with 500 μg of HeLa cell lysates, washed in the lysis buffer, and eluted in the protein loading buffer. For coimmunoprecipitation, 1 mg whole-cell lysates were incubated overnight with AIF antibody (1 μg/ml) in the presence of protein A/G Sepharose (Santa Cruz Biotechnology), followed by immunoblot analysis with mouse anti-Flag antibody (Clone M1, Sigma), mouse anti-V5 (V8012, Sigma) or Goat anti-MIF (ab36146, Abcam). The proteins were separated on denaturing SDS-PAGE and transferred to a nitrocellulose membrane. The membrane was blocked and incubated overnight with primary antibody (50 ng/ml; mouse anti-Flag; rabbit anti-AIF; or goat anti-MIF) at 4°C, followed by horseradish peroxidase (HRP)–conjugated donkey anti-mouse, anti-rabbit or anti-goat for 1 hour at RT. After washing, the immune complexes were detected by the SuperSignalWest Pico Chemiluminescent Substrate (Pierce).

Subcellular fractionation

The nuclear extracts (N) and postnuclear cell extracts (PN), which is the fraction prepared from whole-cell lysates after removing nuclear proteins, were isolated in hypotonic buffer (*9*, *11*). The integrity of the nuclear and postnuclear subcellular fractions was determined by monitoring histone H3 or H4 and MnSOD or mitochondria antibody (MTC02) (Mito) immunoreactivity (*9*, *11*).

Immunocytochemistry, immunohistochemistry, and confocal microscopy

For immunocytochemistry, cells were fixed 4 hours after MNNG or NMDA treatment with 4% paraformaldehyde, permeabilized with 0.05% Triton X-100, and blocked with 3% BSA in PBS. AIF was visualized by Donkey anti-Rabbit Cy3 or donkey anti-rabbit 647. MIF was visualized by donkey anti-mouse cy2 (2 μg/ml), donkey anti-goat Cy2 or donkey anti-goat 647. Immunohistochemistry was performed with an antibody against Flag. Immunofluorescence analysis was carried out with an LSM710 confocal laser scanning microscope (Carl Zeiss) as described (*9*).

Quantification of relative percentage levels of AIF and MIF in subcellular fractions

The relative levels of AIF and MIF in different fractions were quantified and calculated as the percentage of their total proteins based on the intensity of protein signals relative to the protein amount prepared from the same number of cells (6 million). The detailed calculation is as follows: 1) The signal intensity of each interested band was measured and normalized to their mitochondrial and nuclear markers, with the total proteins of CSS in Fig. 4, G to I and knockout neurons treated with NMDA in Fig. 5 E to G. A volume factor was used to calculate the relative amount of total protein (T), post-nuclear protein (PN) and nuclear protein (N) prepared from the same number (6 million) of cells. As such, the relative ratio of different samples in the same fractions and the same sample in different fractions will be calculated as the relative intensity of total protein (T_i), post-nuclear fraction (PN_i) and nuclear fraction (N_i). 2) A Z factor for the adjusted total proteins for each sample was determined via $Z = (PN_i + N_i)/T_i$. 3) Relative protein levels in PN and N fractions were calculated as follows: $PN\% = (PN_i \times Z)/ T_i \times 100\%$; $N\% = (N_i \times Z)/ T_i \times 100\%$; $T\% = (T_i \times Z)/ T_i \times 100\%$.

FPLC

The native state and purity of the purified recombinant MIF were determined using standard calibration curve between elution volume and molecular mass (kD) of known molecular weight native marker proteins in Akta Basic FPLC

(Amersham-Pharmacia Limited) using Superdex 200 10/300GL column (GE Healthcare, Life Sciences). The gel filtration column was run in standard PBS buffer at a flow rate of 0.5 ml/min. The following molecular weight standards were used: Ferritin (440 kD), aldolase (158 kD), conalbumin (75 kD), ovalbumin (43 kD), carbonic anhydrase (29 kD), and ribonuclease (13.7 kD) respectively (GE Healthcare, Life Sciences). Eluted fractions containing MIF were resolved on 12% SDS-PAGE and stained with commassie blue to check the purity of the protein.

Mass spectrometry analysis for MIF protein purity

MIF proteins used for nuclease assays were also examined by mass spectrometry in order to exclude any possible contamination from other known nucleases. We performed analyses using different criteria at a 95% and lower confidence levels in order to capture any remote possibility of a nuclease. Analysis and search of the NCBI database using all species reveal that no known nuclease that can digest single or double-stranded DNA was detected in the MIF protein that was used in the nuclease assays.

Circular dichroism (CD) spectroscopy

CD spectroscopy was performed on a AVIV 420 CD spectrometer (Biomedical Inc., Lakewood, NJ, USA). Near-UV CD spectra were recorded between 240–320 nm using a quartz cuvette of 0.5 cm path length with protein samples at a concentration of 2 mg/ml at room temperature. Far UV CD spectra were also recorded at room temperature between 190–260 nm using quartz sandwich cuvettes of 0.1 cm path length with protein samples at a concentration of 0.2 mg/ml (*48*). The proteins were suspended in PBS buffer with or without magnesium chloride (5.0 mM) and/or zinc chloride (0.2 mM). The CD spectra were obtained from 0.5 nm data pitch, 1 nm/3 s scan speed and 0.5 s response time were selected for the recordings.

Oxido-reductase activity assay

The thiol-protein oxidoreductase activity of MIF was measured using insulin as the substrate as described previously (*30*). Briefly, the insulin assay is based on the reduction of insulin and subsequent insolubilization of the insulin β-chain. The time-dependent increase in turbidity is then measured spectrophotometrically at 650 nm. The reaction was started by adding 5 μM MIF to WT, E22A, E22Q, C57A;C60A or and P2G mutants dissolved in 20 mM sodium phosphate buffer (pH 7.2), and 200 mM reduced glutathione (GSH) to ice-cold reaction mixture containing 1 mg/ml insulin, 100 mM sodium phosphate buffer (pH 7.2) and 2 mM EDTA. MIF insulin reduction was measured against the control solution (containing GSH) in the same experiment.

Tautomerase activity assay

Tautomerase activity was measured using D-dopachrome tautomerase as the substrate as described previously (*49*). Briefly, a fresh solution of D-dopachrome methyl ester was prepared by mixing 2 mM L-3,4 dihydroxyphenylalanine methyl ester with 4 mM sodium peroxidate for 5 min at room temperature and then placed directly on ice before use. The enzymatic reaction was initiated at 25°C by adding 20 μl of the dopachrome methyl ester substrate to 200 μl of MIF WT, E22A, E22Q, C57A;C60A (final concentration 5 μM) or and P2G mutants prepared in tautomerase assay buffer (50 mM potassium phosphate, 1 mM EDTA, pH 6.0). The activity was determined by the semi-continuous reduction of OD 475 nm using a spectrophotometer.

Quantification of noncleaved genomic DNA

Noncleaved genomic DNA was quantified as percentage (%) of the total genomic DNA that included both noncleaved genomic DNA and cleaved genomic DNA in each individual group.

Quantification of cells with AIF and MIF nuclear translocation

Nuclear translocation of AIF and MIF was calculated as the percentage of total cells in each individual immunostained image. At least 5 to 12 images were quantified for each group. 500 or more neurons were counted for each condition. White indicates the overlay of AIF (red), MIF (green) and 4′,6′-diamidino-2-phenylindole (DAPI) (blue) suggesting the nuclear translocation of both AIF and MIF. Pink indicates the overlay of AIF (red) and DAPI (blue) suggesting the nuclear translocation of AIF only. Cyan indicates the overlay of MIF (green) and DAPI (blue) suggesting the nuclear translocation of MIF. Representative immunostaining images of MIF and AIF nuclear translocation were shown in Figs. 4E and 5C and fig. S17A.

Intracerebroventricular (ICV) injection

Three microliters of AAV2-MIF WT, E22Q and E22A (1×10^{13} GC/ml, Vector BioLabs) were injected into both sides of intracerebroventricular of the newborn MIF KO mice (*41*). The expression of MIF and its variants were checked by immunohistochemistry after MCAO surgery at 8–16 weeks of age.

Neurobehavioral activity

Spontaneous motor activity was evaluated 1 day, 3 days and 7 days after MCAO by placing the animals in a mouse cage for 5 min. A video camera was fitted on top of the cage to record the activity of a mouse in the cage. Neurological deficits were evaluated by an observer blinded to the treatment and genotype of the animals with a scale of 0-5 (0, no neurological deficit; 5, severe neurological deficit). The following criteria were used to score deficits: 0 = mice appeared normal, explored the cage environment and moved around in the cage freely; 1 = mice hesitantly moved in cage but could occasionally touch the walls of the cage, 2 = mice showed postural and movement abnormalities, and did not approach all sides of the cage, 3 = mice showed postural and movement abnormalities and made medium size circles in the center of cage, 4 = mice with postural abnormalities and made very small circles in place, 5 = mice were unable to move in the cage and stayed at the center. Recordings were evaluated by observers blinded to the treatment and genotype of the animals.

The corner test was performed 1 day, 3 days and 7 days after MCAO to assess sensory and motor deficits following both cortical and striatal injury. A video camera was fitted on top of the cage to record the activity of a mouse in the cage for 5 min. The mice were placed between two cardboards each with a dimension of 30 cm X 20 cm X 0.5 mm attached to each other from the edges with an angle of 30°. Once in the corner, the mice usually rear and then turn either left or right. Before stroke mice do not show a side preference. Mice with sensory and motor deficits following stroke will turn toward the non-impaired side (right). Percent of right turn = right turns/total turns × 100 was calculated and compared. Recordings were evaluated by observers blinded to the treatment and genotype of the animals.

Animals

The Johns Hopkins Medical Institutions are fully accredited by the American Association for the Accreditation of Laboratory Animal Care (AAALAC). All research procedures performed in this study were approved the Johns Hopkins Medical Institutions Institutional Animal Care and Use Committee (IACUC) in compliance with the Animal Welfare Act regulations and Public Health Service (PHS) Policy. All animal studies were performed in a blinded fashion. Mouse genotype was determined by K.N. Stroke surgery was performed by R.A. Mouse genotypes were decoded after the stroke surgery, mouse behavior tests and data analysis. Based on their genotype, mice were grouped as WT, KO, KO-WT, KO-E22Q and KO-E22A. Within each group, mice were randomly assigned to subgroups including sham, 1 day-post stroke, 3 days- or 7 days-post stroke.

Statistical analysis

Unless otherwise indicated, statistical evaluation was carried out by Student's *t* test between two groups and by one-way analysis of variance (ANOVA) followed by post hoc comparisons with the Bonferroni test using GraphPad Prism software within multiple groups. Data are shown as means ± SEM. $P < 0.05$ is considered significant. Experiments for quantification were performed in a blinded fashion. In order to ensure adequate power to detect the effect, at least 3 independent tests were performed for all molecular biochemistry studies and at least 5 mice from 3 different litters were used for animal studies.

REFERENCES AND NOTES

1. P. Bai, Biology of poly(ADP-ribose) polymerases: The factotums of cell maintenance. *Mol. Cell* **58**, 947–958 (2015). doi: 10.1016/j.molcel.2015.01.034; pmid: 26091343
2. A. A. Fatokun, V. L. Dawson, T. M. Dawson, Parthanatos: Mitochondrial-linked mechanisms and therapeutic opportunities. *Br. J. Pharmacol.* **171**, 2000–2016 (2014). doi: 10.1111/bph.12416; pmid: 24684389
3. Y. Wang, V. L. Dawson, T. M. Dawson, Poly(ADP-ribose) signals to mitochondrial AIF: A key event in parthanatos. *Exp. Neurol.*

218, 193–202 (2009). doi: 10.1016/j.expneurol.2009.03.020; pmid: 19332058
4. P. Pacher, C. Szabo, Role of the peroxynitrite-poly(ADP-ribose) polymerase pathway in human disease. *Am. J. Pathol.* **173**, 2–13 (2008). doi: 10.2353/ajpath.2008.080019; pmid: 18535182
5. C. Szabó, V. L. Dawson, Role of poly(ADP-ribose) synthetase in inflammation and ischaemia-reperfusion. *Trends Pharmacol. Sci.* **19**, 287–298 (1998). doi: 10.1016/S0165-6147(98)01193-6; pmid: 9703762
6. S. Martire, L. Mosca, M. d'Erme, PARP-1 involvement in neurodegeneration: A focus on Alzheimer's and Parkinson's diseases. *Mech. Ageing Dev.* **146–148**, 53–64 (2015). doi: 10.1016/j.mad.2015.04.001; pmid: 25881554
7. L. Virág, A. Robaszkiewicz, J. M. Rodriguez-Vargas, F. J. Oliver, Poly(ADP-ribose) signaling in cell death. *Mol. Aspects Med.* **34**, 1153–1167 (2013). doi: 10.1016/j.mam.2013.01.007; pmid: 23416893
8. H. Wang *et al*., Apoptosis-inducing factor substitutes for caspase executioners in NMDA-triggered excitotoxic neuronal death. *J. Neurosci.* **24**, 10963–10973 (2004). doi: 10.1523/JNEUROSCI.3461-04.2004; pmid: 15574746
9. Y. Wang *et al*., Poly(ADP-ribose) (PAR) binding to apoptosis-inducing factor is critical for PAR polymerase-1–dependent cell death (parthanatos). *Sci. Signal.* **4**, ra20 (2011). doi: 10.1126/scisignal.2000902; pmid: 21467298
10. S. W. Yu *et al*., Apoptosis-inducing factor mediates poly(ADP-ribose) (PAR) polymer-induced cell death. *Proc. Natl. Acad. Sci. U.S.A.* **103**, 18314–18319 (2006). doi: 10.1073/pnas.0606528103; pmid: 17116881
11. S. W. Yu *et al*., Mediation of poly(ADP-ribose) polymerase-1–dependent cell death by apoptosis-inducing factor. *Science* **297**, 259–263 (2002). doi: 10.1126/science.1072221; pmid: 12114629
12. X. Wang, C. Yang, J. Chai, Y. Shi, D. Xue, Mechanisms of AIF-mediated apoptotic DNA degradation in *Caenorhabditis elegans*. *Science* **298**, 1587–1592 (2002). doi: 10.1126/science.1076194; pmid: 12446902
13. K. K. David, M. Sasaki, S. W. Yu, T. M. Dawson, V. L. Dawson, EndoG is dispensable in embryogenesis and apoptosis. *Cell Death Differ.* **13**, 1147–1155 (2006). doi: 10.1038/sj.cdd.4401787; pmid: 16239930
14. R. A. Irvine *et al*., Generation and characterization of endonuclease G null mice. *Mol. Cell. Biol.* **25**, 294–302 (2005). doi: 10.1128/MCB.25.1.294-302.2005; pmid: 15601850
15. Z. Xu *et al*., Endonuclease G does not play an obligatory role in poly(ADP-ribose) polymerase-dependent cell death after transient focal cerebral ischemia. *Am. J. Physiol. Regul. Integr. Comp. Physiol.* **299**, R215–R221 (2010). doi: 10.1152/ajpregu.00747.2009; pmid: 20427721
16. S. Hu *et al*., Profiling the human protein-DNA interactome reveals ERK2 as a transcriptional repressor of interferon signaling. *Cell* **139**, 610–622 (2009). doi: 10.1016/j.cell.2009.08.037; pmid: 19879846
17. T. Calandra *et al*., Protection from septic shock by neutralization of macrophage migration inhibitory factor. *Nat. Med.* **6**, 164–170 (2000). doi: 10.1038/72262; pmid: 10655104
18. M. Merk, R. A. Mitchell, S. Endres, R. Bucala, D-Dopachrome tautomerase (D-DT or MIF-2): Doubling the MIF cytokine family. *Cytokine* **59**, 10–17 (2012). doi: 10.1016/j.cyto.2012.03.014; pmid: 22507380
19. J. Kosinski, M. Feder, J. M. Bujnicki, The PD-(D/E)XK superfamily revisited: Identification of new members among proteins involved in DNA metabolism and functional predictions for domains of (hitherto) unknown function. *BMC Bioinformatics* **6**, 172 (2005). doi: 10.1186/1471-2105-6-172; pmid: 16011798
20. K. Kratz *et al*., Deficiency of FANCD2-associated nuclease KIAA1018/FAN1 sensitizes cells to interstrand crosslinking agents. *Cell* **142**, 77–88 (2010). doi: 10.1016/j.cell.2010.06.022; pmid: 20603016
21. C. MacKay *et al*., Identification of KIAA1018/FAN1, a DNA repair nuclease recruited to DNA damage by monoubiquitinated FANCD2. *Cell* **142**, 65–76 (2010). doi: 10.1016/j.cell.2010.06.021; pmid: 20603015
22. H. Sugimoto, M. Suzuki, A. Nakagawa, I. Tanaka, J. Nishihira, Crystal structure of macrophage migration inhibitory factor from human lymphocyte at 2.1 A resolution. *FEBS Lett.* **389**, 145–148 (1996). doi: 10.1016/0014-5793(96)00553-4; pmid: 8766818
23. H. W. Sun, J. Bernhagen, R. Bucala, E. Lolis, Crystal structure at 2.6-A resolution of human macrophage migration inhibitory factor. *Proc. Natl. Acad. Sci. U.S.A.* **93**, 5191–5196 (1996). doi: 10.1073/pnas.93.11.5191; pmid: 8643551
24. M. Suzuki *et al*., Crystal structure of the macrophage migration inhibitory factor from rat liver. *Nat. Struct. Biol.* **3**, 259–266 (1996). doi: 10.1038/nsb0396-259; pmid: 8605628
25. M. Laganeckas, M. Margelevicius, C. Venclovas, Identification of new homologs of PD-(D/E)XK nucleases by support vector machines trained on data derived from profile-profile alignments. *Nucleic Acids Res.* **39**, 1187–1196 (2011). doi: 10.1093/nar/gkq958; pmid: 20961958
26. K. Steczkiewicz, A. Muszewska, L. Knizewski, L. Rychlewski, K. Ginalski, Sequence, structure and functional diversity of PD-(D/E)XK phosphodiesterase superfamily. *Nucleic Acids Res.* **40**, 7016–7045 (2012). doi: 10.1093/nar/gks382; pmid: 22638584
27. V. Pingoud *et al*., On the divalent metal ion dependence of DNA cleavage by restriction endonucleases of the EcoRI family. *J. Mol. Biol.* **393**, 140–160 (2009). doi: 10.1016/j.jmb.2009.08.011; pmid: 19682999
28. J. B. Lubetsky *et al*., The tautomerase active site of macrophage migration inhibitory factor is a potential target for discovery of novel anti-inflammatory agents. *J. Biol. Chem.* **277**, 24976–24982 (2002). doi: 10.1074/jbc.M203220200; pmid: 11997397
29. G. Fingerle-Rowson *et al*., A tautomerase-null macrophage migration-inhibitory factor (MIF) gene knock-in mouse model reveals that protein interactions and not enzymatic activity mediate MIF-dependent growth regulation. *Mol. Cell. Biol.* **29**, 1922–1932 (2009). doi: 10.1128/MCB.01907-08; pmid: 19188446
30. A. Kudrin *et al*., Human macrophage migration inhibitory factor: A proven immunomodulatory cytokine? *J. Biol. Chem.* **281**, 29641–29651 (2006). doi: 10.1074/jbc.M601103200; pmid: 16893895
31. E. Rosengren *et al*., The macrophage migration inhibitory factor MIF is a phenylpyruvate tautomerase. *FEBS Lett.* **417**, 85–88 (1997). doi: 10.1016/S0014-5793(97)01261-1; pmid: 9395080
32. P. Machanick, T. L. Bailey, MEME-ChIP: Motif analysis of large DNA datasets. *Bioinformatics* **27**, 1696–1697 (2011). doi: 10.1093/bioinformatics/btr189; pmid: 21486936
33. G. Zhao, B. Zhao, Z. Tong, R. Mu, Y. Guan, Effects of 2′-O-methyl nucleotide substitution on EcoRI endonuclease cleavage activities. *PLOS ONE* **8**, e77111 (2013). doi: 10.1371/journal.pone.0077111; pmid: 24194862
34. A. R. Inácio, K. Ruscher, L. Leng, R. Bucala, T. Deierborg, Macrophage migration inhibitory factor promotes cell death and aggravates neurologic deficits after experimental stroke. *J. Cereb. Blood Flow Metab.* **31**, 1093–1106 (2011). doi: 10.1038/jcbfm.2010.194; pmid: 21063426
35. M. Bacher *et al*., MIF expression in the rat brain: Implications for neuronal function. *Mol. Med.* **4**, 217–230 (1998). pmid: 9606175
36. W. Zhang *et al*., Expression of macrophage migration inhibitory factor in the mouse neocortex and posterior piriform cortices during postnatal development. *Cell. Mol. Neurobiol.* **34**, 1183–1197 (2014). doi: 10.1007/s10571-014-0094-1; pmid: 25118614
37. T. Calandra, T. Roger, Macrophage migration inhibitory factor: A regulator of innate immunity. *Nat. Rev. Immunol.* **3**, 791–800 (2003). doi: 10.1038/nri1200; pmid: 14502271
38. J. D. Hudson *et al*., A proinflammatory cytokine inhibits p53 tumor suppressor activity. *J. Exp. Med.* **190**, 1375–1382 (1999). doi: 10.1084/jem.190.10.1375; pmid: 10562313
39. R. Kleemann *et al*., Intracellular action of the cytokine MIF to modulate AP-1 activity and the cell cycle through Jab1. *Nature* **408**, 211–216 (2000). doi: 10.1038/35041591; pmid: 11089976
40. S. A. Andrabi *et al*., Iduna protects the brain from glutamate excitotoxicity and stroke by interfering with poly(ADP-ribose) polymer-induced cell death. *Nat. Med.* **17**, 692–699 (2011). doi: 10.1038/nm.2387; pmid: 21602803
41. J. J. Glascock *et al*., Delivery of therapeutic agents through intracerebroventricular (ICV) and intravenous (IV) injection in mice. *J. Vis. Exp.* **2001**, 2968 (2011). pmid: 21988897
42. Y. Chen *et al*., Systematic evaluation of factors influencing ChIP-seq fidelity. *Nat. Methods* **9**, 609–614 (2012). doi: 10.1038/nmeth.1985; pmid: 22522655
43. J. Feng, T. Liu, B. Qin, Y. Zhang, X. S. Liu, Identifying ChIP-seq enrichment using MACS. *Nat. Protoc.* **7**, 1728–1740 (2012). doi: 10.1038/nprot.2012.101; pmid: 22936215
44. H. R. Drew *et al*., Structure of a B-DNA dodecamer: Conformation and dynamics. *Proc. Natl. Acad. Sci. U.S.A.* **78**, 2179–2183 (1981). doi: 10.1073/pnas.78.4.2179; pmid: 6941276
45. T. Masuda, Y. Ito, T. Terada, T. Shibata, T. Mikawa, A non-canonical DNA structure enables homologous recombination in various genetic systems. *J. Biol. Chem.* **284**, 30230–30239 (2009). doi: 10.1074/jbc.M109.043810; pmid: 19729448
46. A. W. Ghoorah, M. D. Devignes, M. Smaïl-Tabbone, D. W. Ritchie, Protein docking using case-based reasoning. *Proteins* **81**, 2150–2158 (2013). doi: 10.1002/prot.24433; pmid: 24123156
47. G. Macindoe, L. Mavridis, V. Venkatraman, M. D. Devignes, D. W. Ritchie, HexServer: An FFT-based protein docking server powered by graphics processors. *Nucleic Acids Res.* **38** (Web Server), W445–W449 (2010). doi: 10.1093/nar/gkq311; pmid: 20444869
48. P. P. Reddy *et al*., Molecular dynamics of the neuronal EF-hand Ca2+-sensor Caldendrin. *PLOS ONE* **9**, e103186 (2014). doi: 10.1371/journal.pone.0103186; pmid: 25058677
49. K. Bendrat *et al*., Biochemical and mutational investigations of the enzymatic activity of macrophage migration inhibitory factor. *Biochemistry* **36**, 15356–15362 (1997). doi: 10.1021/bi971153a; pmid: 9398265

ACKNOWLEDGMENTS

This work was supported by NIH grant K99/R00 NS078049, American Heart Association (AHA) National Scientist Development Grant 12SDG11900071, and the University of Texas Southwestern Medical Center Department of Pathology Startup funds and UT Rising Stars to Y.W.; and grants from National Institute on Drug Abuse, NIH, DA000266; and National Institute of Neurological Disorders and Stroke, NIH, R01 NS067525, R37 NS067525, and NS38377 to T.M.D. and V.L.D. T.M.D. is the Leonard and Madlyn Abramson Professor in Neurodegenerative Diseases. The authors acknowledge the joint participation by the Adrienne Helis Malvin Medical Research Foundation through its direct engagement in the continuous active conduct of medical research in conjunction with the Johns Hopkins Hospital and the Johns Hopkins University School of Medicine and the foundation's Parkinson's Disease Program M-2016. ChIP-seq data are archived in National Center for Biotechnology Information, NIH, GEO, GSE65110. Y.W. contributed to all aspects of the project. R.A., G.K.U., K.N., H.P., B.K., L.B., M.M.H., C.C., R.C., S.M.E., M.M.H., T.-I.K., S.N., G.M., and H.S. helped with some experiments. J.S.J., S.B., and H.Z. provided protein chips. Z.X. and J.Q. helped with the bioinformatics analysis. Y.W., V.L.D., and T.M.D. designed experiments and wrote the paper. The study was conceived and scientifically directed by V.L.D. and T.M.D. Y.W., H.P., V.L.D., and T.M.D. are inventors on a patent application submitted by Johns Hopkins University that covers the use of inhibitors of MIF nuclease activity to treat stroke and other disorders. The supplementary materials contain additional data.

SUPPLEMENTARY MATERIALS

www.sciencemag.org/content/354/6308/aad6872/suppl/DC1
Supplementary Text
Figs. S1 to S17
Tables S1 and S2
References (*50*, *51*)

2 November 2015; accepted 22 August 2016
10.1126/science.aad6872

RESEARCH ARTICLE

QUANTUM SIMULATION

Realization of two-dimensional spin-orbit coupling for Bose-Einstein condensates

Zhan Wu,[1,2,3] Long Zhang,[1,4,5] Wei Sun,[1,2,3] Xiao-Tian Xu,[1,2,3] Bao-Zong Wang,[1,4,5] Si-Cong Ji,[1,2] Youjin Deng,[1,2,3] Shuai Chen,[1,2,3]* Xiong-Jun Liu,[4,5]* Jian-Wei Pan[1,2,3]*

Cold atoms with laser-induced spin-orbit (SO) interactions provide a platform to explore quantum physics beyond natural conditions of solids. Here we propose and experimentally realize two-dimensional (2D) SO coupling and topological bands for a rubidium-87 degenerate gas through an optical Raman lattice, without phase-locking or fine-tuning of optical potentials. A controllable crossover between 2D and 1D SO couplings is studied, and the SO effects and nontrivial band topology are observed by measuring the atomic cloud distribution and spin texture in momentum space. Our realization of 2D SO coupling with advantages of small heating and topological stability opens a broad avenue in cold atoms to study exotic quantum phases, including topological superfluids.

The spin-orbit (SO) interaction of an electron is a relativistic quantum mechanics effect that characterizes the coupling between the motion and spin of the electron when moving in an electric field. In the rest frame, the electron experiences a magnetic field proportional to the electron velocity and couples to its spin by the magnetic dipole interaction, rendering the SO coupling. The SO interaction plays an essential role in topological insulators, which have been predicted and experimentally discovered in two-dimensional (2D) and 3D materials (*1*, *2*), and topological superconductors (*3*, *4*), which host exotic zero-energy states called Majorana fermions (*5*) and still necessitate rigorous experimental verification. For topological insulators, the strong SO interaction leads to band inversion, which drives topological phase transitions in such systems. In superconductors, triplet p-wave pairing may occur when SO coupling is present and results in topologically nontrivial superconductivity under proper conditions (*6*).

Recently, there has been considerable interest in emulating SO effects and topological phases with cold atoms, driven by the fact that cold atoms can offer extremely clean platforms with full controllability to explore such exotic physics. In cold atoms, the synthetic SO interaction can be generated by Raman coupling schemes that flip atom spins and transfer momentum simultaneously (*7*, *8*); 1D SO interaction (*9*) has been successfully demonstrated in experiment for both cold boson (*10*, *11*) and fermion degenerate gases (*12*, *13*). With the 1D SO coupling, which corresponds to an Abelian gauge potential (*14*), one can study effects such as the magnetized or stripe ground states for bosons (*15*–*18*), spin dynamics (*19*, *20*), and 1D insulating topological states for fermions (*21*). Realizing higher dimensional SO couplings, which correspond to non-Abelian gauge potentials (*7*, *8*), can enable the study of a broader range of nontrivial quantum states such as topological insulators driven by 2D and 3D SO interactions (*1*, *2*). Furthermore, a 2D SO interaction is the minimal requirement to reach a gapped topological superfluid phase through a conventional s-wave superfluid state (*22*, *23*).

Several schemes have been proposed for generating 2D and 3D SO couplings (*7*, *8*, *24*–*26*). Notable progress was recently achieved when 2D SO couplings were demonstrated for pseudospins defined by two dark states in an empty tripod system (*27*). However, realizing 2D SO coupling for quantum degenerate atom gases remains challenging. Very recently, it was proposed that 2D SO coupling can be realized by a simple optical Raman lattice scheme that applies two pairs of light beams to create the lattice and Raman potentials simultaneously (*28*). However, this scheme requires the challenging realization of two Raman transitions with a locked relative phase. Here we propose a minimal scheme that overcomes these challenges and realizes 2D SO coupling with ^{87}Rb Bose-Einstein condensates (BECs).

[1]Shanghai Branch, National Laboratory for Physical Sciences at Microscale and Department of Modern Physics, University of Science and Technology of China, Shanghai 201315, China. [2]Chinese Academy of Sciences (CAS) Center for Excellence and Synergetic Innovation Center of Quantum Information and Quantum Physics, University of Science and Technology of China, Hefei, Anhui 230026, China. [3]CAS-Alibaba Quantum Computing Laboratory, Shanghai 201315, China. [4]International Center for Quantum Materials, School of Physics, Peking University, Beijing 100871, China. [5]Collaborative Innovation Center of Quantum Matter, Beijing 100871, China.
*Corresponding author. Email: shuai@ustc.edu.cn (S.C.); xiongjunliu@pku.edu.cn (X.-J.L.); pan@ustc.edu.cn (J.-W.P.)

Theoretical proposal

We aim to realize 2D SO coupling and topological band for ultracold atoms on a square lattice with the Hamiltonian

$$H = \left[\frac{\hbar^2\mathbf{k}^2}{2m} + V_{\text{latt}}(x,z)\right] \otimes \mathbf{1} + \mathcal{M}_x(x,z)\sigma_x + \mathcal{M}_y(x,z)\sigma_y + m_z\sigma_z \quad (1)$$

where ħ is Planck's constant h divided by 2π, $\mathbf{k}$ is the wave vector that represents the momentum of the atoms, $\mathbf{1}$ is the 2-by-2 unit matrix, $\sigma_{x,y,z}$ are Pauli matrices acting on the spins, m is the mass of an atom, V_{latt} denotes the lattice potential in the xz plane, $\mathcal{M}_{x,y}$ are periodic Raman coupling potentials, and m_z is a tunable Zeeman constant. The lattice potential V_{latt} is spin-independent and can induce nearest-neighbor hopping that conserves the atom spin, whereas $\mathcal{M}_{x,y}$ induce hopping that flips atom spin. This is different from the laser-assisted tunneling scheme without spin-flip (*29*–*31*). The overall effect of hopping along $\hat{x}$ and $\hat{z}$ directions results in 2D SO coupling, which can lead to nontrivial topological bands for the square lattice.

Here we propose to realize the Hamiltonian (Eq. 1) through a minimal scheme, which is generic and applicable to both boson and fermion atoms. Figure 1 illustrates the realization in a ^{87}Rb Bose gas, with $|\uparrow\rangle \equiv |1,-1\rangle$ and $|\downarrow\rangle \equiv |1,0\rangle$; the hyperfine state $|1,+1\rangle$ can be removed by a sufficiently large two-photon detuning. The minimal ingredients of the realization include a blue-detuned square lattice created with two light components denoted by the blue lines, and the periodic Raman potentials generated together with additional light components denoted by the red lines (Fig. 1A). Both ingredients can be achieved with a single in-plane (xz) linearly polarized laser source. The initial phases of the light beams have no effect on this optical Raman lattice scheme (*32*), and we neglect them in the following discussion. The optical lattice is generated by E_{1x} and E_{1z} (blue lines), which are incident from horizontal (x) and vertical (z) directions, respectively (Fig. 1A), and can be created from a single light of frequency ω_1 by a beam splitter. The beams are reflected by two mirrors (M_1 and M_2) and form standing waves in the intersecting area described by $\mathbf{E}_{1x} = \hat{z}\,\overline{E}_{1x}e^{i\varphi_L/2}\cos(k_0x - \varphi_L/2)$ and $\mathbf{E}_{1z} = \hat{x}\,\overline{E}_{1z}e^{i\varphi_L/2}\cos(k_0z - \varphi_L/2)$, where $\overline{E}_{1x/1z}$ are amplitudes and the phase $\varphi_L = k_0L$ is acquired through the optical path L from the intersecting point to mirror M_1, then to M_2, and back to the intersecting point, with $k_0 = \omega_1/c$. For alkali atoms, we can show that the optical potential generated by linearly polarized lights is spin-independent when the detuning Δ is much larger than the hyperfine structure splittings (*32*). The lattice potential then takes the form

$$V_{\text{latt}}(x,z) = V_{0x}\cos^2(k_0x - \varphi_L/2) + V_{0z}\cos^2(k_0z - \varphi_L/2) \quad (2)$$

where $V_{0x/0z} = \hbar|\Omega_{x/z}|^2/\Delta$. The Rabi frequency amplitudes of the standing waves $\Omega_{x/z} \equiv \mathbf{d}_{\text{eff}} \cdot \overline{\mathbf{E}}_{1x/1z}/\hbar$,

where $\overline{\mathbf{E}}_{1x/1z} = \overline{E}_{1x/1z}\hat{z}/\hat{x}$ and the effective dipole matrix $\mathbf{d}_{\text{eff}}$ takes into account the transitions from a ground state ($g_{\uparrow,\downarrow}$) to all relevant excited states in D_1 and D_2 lines (Fig. 1B). The lattice potential induces spin-conserved hopping, as illustrated in Fig. 1D.

The Raman couplings are induced when another beam E_{2z} of frequency ω_2 is incident from the z direction. The light components E_{1z} and E_{2z} can be generated from a single laser source via an acoustic-optic modulator (AOM), which controls their frequency difference $\delta\omega = \omega_1 - \omega_2$ and amplitude ratio $\overline{E}_{2z}/\overline{E}_{1z}$. The light E_{2z} generates plane-wave fields $\mathbf{E}_{2z} = \hat{x}\overline{E}_{2z}e^{ik_0z}$ and $\mathbf{E}_{2x} = \hat{E}_{2x}e^{i(-k_0x+\varphi_L-\delta\varphi_L)}$, where the irrelevant initial phase is neglected (*32*). The relative phase $\delta\varphi_L = L\delta\omega/c$, acquired by E_{2x}, is a crucial parameter, which can be precisely manipulated by changing the optical path L or $\delta\omega$, and it controls the dimensionality of the realized SO coupling. The standing-wave and plane-wave beams form a double-Λ type configuration (Fig. 1C), with E_{1x} and E_{2z} generating one Raman potential via $|F,0\rangle$ in the form $M_{0x}\cos(k_0x - \varphi_L/2)e^{i(k_0z-\varphi_L/2)}$, and E_{1z} and E_{2x} producing another one via $|F,-1\rangle$ as $M_{0y}\cos(k_0z - \varphi_L/2)e^{-i(k_0x-\varphi_L/2)-i\delta\varphi_L}$. Note that lattice sites of a blue-detuned lattice are located around zeros of optical fields. It follows that terms such as $\cos(k_0x - \varphi_L/2)\cos(k_0z-\varphi_L/2)$, which is antisymmetric with respect to each site in both x and z directions, have small contribution to low-band physics. Neglecting such terms yields

$$\mathcal{M}_x(x,z) = M_x - M_y\cos\delta\varphi_L \quad (3)$$

$$\mathcal{M}_y(x,z) = M_y\sin\delta\varphi_L \quad (4)$$

Here $M_{x/y} = M_{0x/y}\cos(k_0x/z - \varphi_L/2)\sin(k_0z/x - \varphi_L/2)$, with $M_{0x}/M_{0y} = \overline{E}_{1x}\overline{E}_{2z}/(\overline{E}_{1z}\overline{E}_{2x})$ (*32*). Together with an effective Zeeman term ($m_z = \hbar\delta/2$), which is controlled by tuning the two-photon detuning δ (Fig. 1C), we reach the effective Hamiltonian (Eq. 1). Note that M_x (M_y) is antisymmetric with respect to each lattice site along the $\hat{x}(\hat{z})$ direction (Fig. 1, E and F). This feature has an important consequence that M_x (M_y) leads to spin-flipped hopping only along x (z) direction. Moreover, the phase difference $\delta\varphi_L$ governs the relative strength of the σ_x and σ_y terms and thus determines the dimensionality of the SO coupling. For example, setting $\delta\omega$ = 50 MHz yields $\delta\varphi_L = \pi/2$ for L = 1.5 m, resulting in optimal 2D SO coupling. Further increasing the optical path to L = 3.0 m gives $\delta\varphi_L = \pi$, and the SO coupling becomes 1D. This enables a fully controllable study of the crossover between 2D and 1D SO couplings by tuning $\delta\varphi_L$ and provides a comparison measurement to confirm the realization of 2D SO interaction.

2D SO coupling and topological band

The Hamiltonian (Eq. 1) has an inversion symmetry defined by $(\sigma_z \otimes R_{2D})H(\sigma_z \otimes R_{2D})^{-1} = H$, where the 2D spatial operator R_{2D} transforms the Bravais lattice vector $\mathbf{R} \to -\mathbf{R}$. For the s-band, the Bloch Hamiltonian is given by $\mathcal{H}(\mathbf{q}) = [m_z - 2t_0(\cos q_x a + \cos q_z a)]\sigma_z + 2t_{so}\sigma_y \sin q_x a + 2t_{so}\,\sigma_x \sin q_z a$, which, around the Γ point, takes the form $\mathcal{H}(\mathbf{q}) = [m_z - 4t_0 + t_0a^2(q_x^2 + q_z^2)]\sigma_z + \lambda_{so}q_x\sigma_y + \lambda_{so}q_z\sigma_x$, with the SO coefficient $\lambda_{so} = 2at_{so}$ being tunable by varying Raman coupling strength (*32*), unlike in the previous schemes (*10*–*13*, *27*). Here, t_0 and t_{so} denote the spin-conserved and spin-flip hopping coefficients, respectively, and a is the lattice constant. This is a quantum anomalous Hall model driven by SO coupling (*28*), which cannot be exactly realized in solid-state materials. It was shown (*33*) that the topology of inversion symmetric Chern bands can be determined by the product of the spin-polarizations $P(\Lambda_j)$ at four highly symmetric momenta $\Theta = \Pi_{j=1}^{4}\text{sgn}[P(\Lambda_j)]$, with the momenta $\{\Lambda_j\} = \{\text{G}(0,0), X_1(0,\pi), X_2(\pi,0), M(\pi,\pi)\}$. The topological (or trivial) phase corresponds to $\Theta = -1$ (or +1). Two typical examples are shown in Fig. 2 by exactly diagonalizing H, with $V_{0x,z} = 5E_r$, $M_{0x,y} = 1.2E_r$, $\delta\varphi_L = \pi/2$, and $m_z = 0.1E_r$ (Fig. 2, A, B, E, and F) or $m_z = 0.4E_r$ (Fig. 2, C and D), where the recoil energy is $E_r = \hbar^2k_0^2/2m$. For the chosen parameters, the lowest two subbands are gapped (Fig. 2, A to D). When $m_z = 0.1E_r$, the spin polarizations at the Γ and M points are opposite (Fig. 2, B, E, and F), implying that the band is topologically nontrivial. In contrast, the polarizations are the same for $m_z = 0.4E_r$ (Fig. 2D), and the band is trivial.

The present scheme displays several essential advantages: (i) Fluctuations, such as those caused by the mirror oscillations, have a tiny effect on L and, thus, do not affect $\delta\varphi_L$ appreciably. The initial phases of light beams globally shift the optical Raman lattice but cannot affect the relative configuration between V_{latt} and the Raman

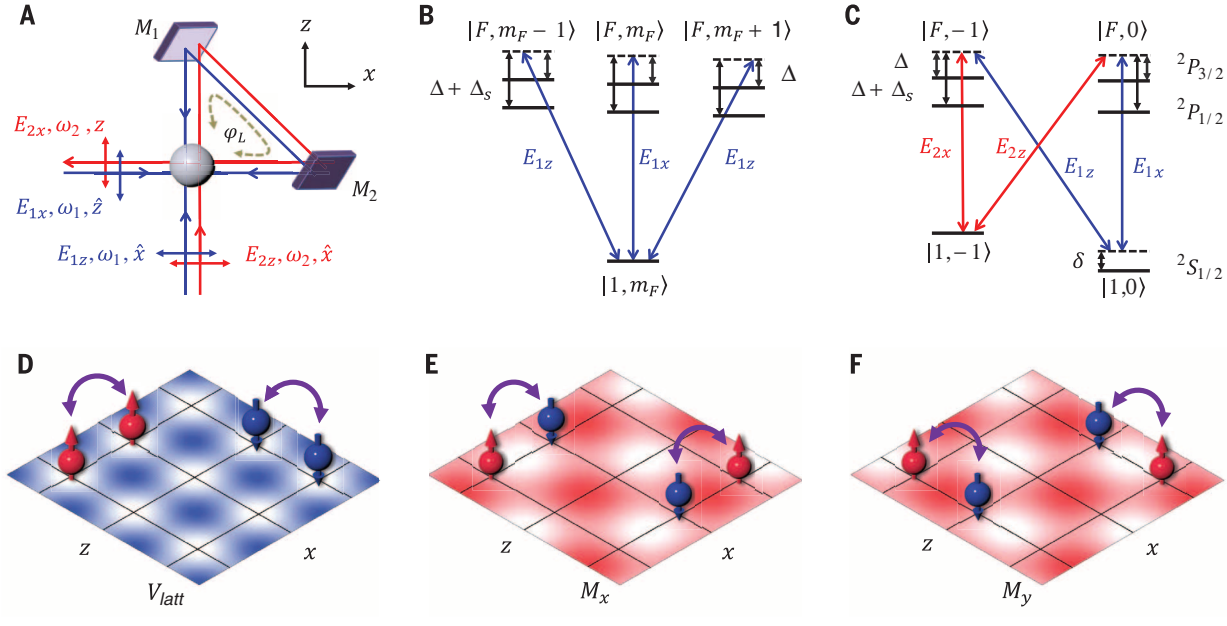

Fig. 1. Proposal of the optical Raman lattice scheme. (**A**) Sketch of the setup for realization. The light components $E_{1x,1z}$ (blue lines) form a spin-independent square optical lattice in the intersecting area and generate two periodic Raman potentials, together with the light components $E_{2x,2z}$ (red lines). (**B**) Optical transitions to generate lattice potentials by $E_{1x,1z}$ for the states $|1, m_F\rangle$ ($m_F = 0, -1$), with $|\uparrow\rangle = |1, -1\rangle$ and $|\downarrow\rangle = |1, 0\rangle$, including all relevant D_1 and D_2 transitions. Here, F is the quantum number of hyperfine states, m_F is the quantum number of magnetic substates, and Δ_s denotes the fine-structure splitting. (**C**) Two periodic Raman potentials are generated through a double-Λ type configuration by $E_{1x,2z}$ and $E_{1z,2x}$, respectively. (**D** to **F**) Profiles of lattice potential for $V_{0x} = V_{0z} = 5E_r$ (D) and Raman potentials M_x (E) and M_y (F) for $M_{0x} = M_{0y} = 1.2E_r$. The color intensity characterizes the relative height of the potentials. The Raman potentials M_x and M_y are antisymmetric (or symmetric) with respect to the lattice site along the x (or z) and z (or x) directions, respectively.

potentials (*32*). Thus, the present scheme is intrinsically immune to any phase fluctuations in the setting, which avoids the need for phase-locking, a challenging task in practical realizations. (ii) As long as $\overline{E}_{1x} = \overline{E}_{1z}$ and $\overline{E}_{2x} = \overline{E}_{2z}$, which are easily accomplished, the system becomes uniform in the x and z directions: $V_{0x} = V_{0z}$ and $M_{0x} = M_{0y}$. No fine-tuning of optical potentials is required. (iii) All of the coupling beams can be created from only a single laser source, simplifying the experimental layout. (iv) Compared with the generation of 1D SO coupling, the present double-Λ Raman configuration (Fig. 1C) does not suffer additional instability or heating in the realization. These advantages render the present scheme immediately feasible in ultracold atom experiments with the current technology.

Experimental setup

In our experiment, a BEC of about 1.5×10^5 ^{87}Rb atoms in the state $|1,-1\rangle$ is prepared in a crossed optical dipole trap with trapping frequencies of $\{\omega_x, \omega_y, \omega_z\} = 2\pi \times \{45, 45, 55\}$Hz, which can suppress the antitrapping effect of blue detuned lights. A bias magnetic field of 49.6 G is applied along the $\hat{z}$ direction to generate the Zeeman splitting and determine the quantization axis. As shown in Fig. 3A, three laser beams (wavelength = 767 nm) in the xz plane illuminate the atoms for the generation of the Hamiltonian (Eq. 1). Among these laser beams, a pair of counterpropagating lasers with the same frequency ω_1 (the blue lines in Fig. 3A labeled as "lattice lasers") produces the two-dimensional optical lattice. These two lasers are incident along the $\hat{x}$ and $\hat{z}$ directions, respectively, and are reflected by two mirrors (M_1 and M_2) to form the standing waves in both directions. The polarizations are set in the xz plane so that the interference between the $\hat{x}$and $\hat{z}$ directions is automatically avoided. The third laser with frequency ω_2 (the red line in Fig. 3A labeled as "Raman laser") is a running wave, which is incoming along the $\hat{z}$ direction with the same polarization as the lattice lasers. All three laser beams are generated from the same Ti: sapphire laser, and the frequencies and amplitudes of these beams are controlled by two phase-locked AOMs. Thus, the phase coherence is automatically kept, and no additional phase-locking is needed. The Raman and lattice lasers are also coupled into the same optical fiber and then lead to the science chamber, which helps to avoid the phase noise due to the imperfect overlap in propagation. The frequency difference $\omega_1 - \omega_2$ is set to 35 MHz to match the Zeeman splitting between the $|1,-1\rangle$ and $|1,0\rangle$ states. The $|1,1\rangle$ state is effectively suppressed because of a large quadratic Zeeman splitting, and the system can be treated as a two-level system. The detuning m_z can be adjusted by tuning the bias magnetic field. By controlling the intensities of the lattice and Raman lights, we set the lattice depth as $V_{0x} = V_{0z}$ and the Raman coupling strength as $M_{0x} = M_{0y}$.

In the experiment, the BEC is first prepared in the dipole trap with the bias magnetic field being switched on. Then, the intensities of the lattice and the Raman beams are simultaneously ramped up to the setting value in 40 ms. As a consequence, the BEC atoms are adiabatically loaded in the local minimum of the lowest band at the Γ point. The phase difference $\delta\varphi_L$ in the Hamiltonian can be achieved by setting the propagating length between the two mirrors M_1 and M_2. The detection is performed in the same way as described in (*11*, *18*, *34*). The spin-resolved time-of-flight (TOF) imaging is taken after all laser beams and the bias magnetic field are suddenly turned off and the gas has expanded freely for 24 ms within a gradient magnetic field to resolve both the momentum and spin.

Experimental results

To demonstrate the realization of 2D SO coupling, we study the crossover effect in the BEC regime by tuning $\delta\varphi_L$. At $m_z = 0$ and by preparing the atoms in the spin-up state, we can adiabatically load the ^{87}Rb condensate into the Γ point. Then, we perform the spin-resolved TOF expansion, which projects Bloch states onto free momentum states with fixed spin polarizations. Figure 3B shows the TOF images for various values of $\delta\varphi_L$. For the spin-up ($|\uparrow\rangle$) state, five atom clouds are observed: The major portion of the BEC cloud remains at momentum $(k_x, k_z) = (0, 0)$, whereas four small fractions are transferred to momenta $(\pm 2k_0, 0)$ and $(0, \pm 2k_0)$ by the first-order transitions due to the lattice potential V_{latt}. Depending on $\delta\varphi_L$, two or four small BEC clouds are formed in the $|\downarrow\rangle$ state at the diagonal corners with momenta $(\pm k_0, \pm k_0)$. This is a consequence of SO coupling; the atom clouds are generated by the Raman

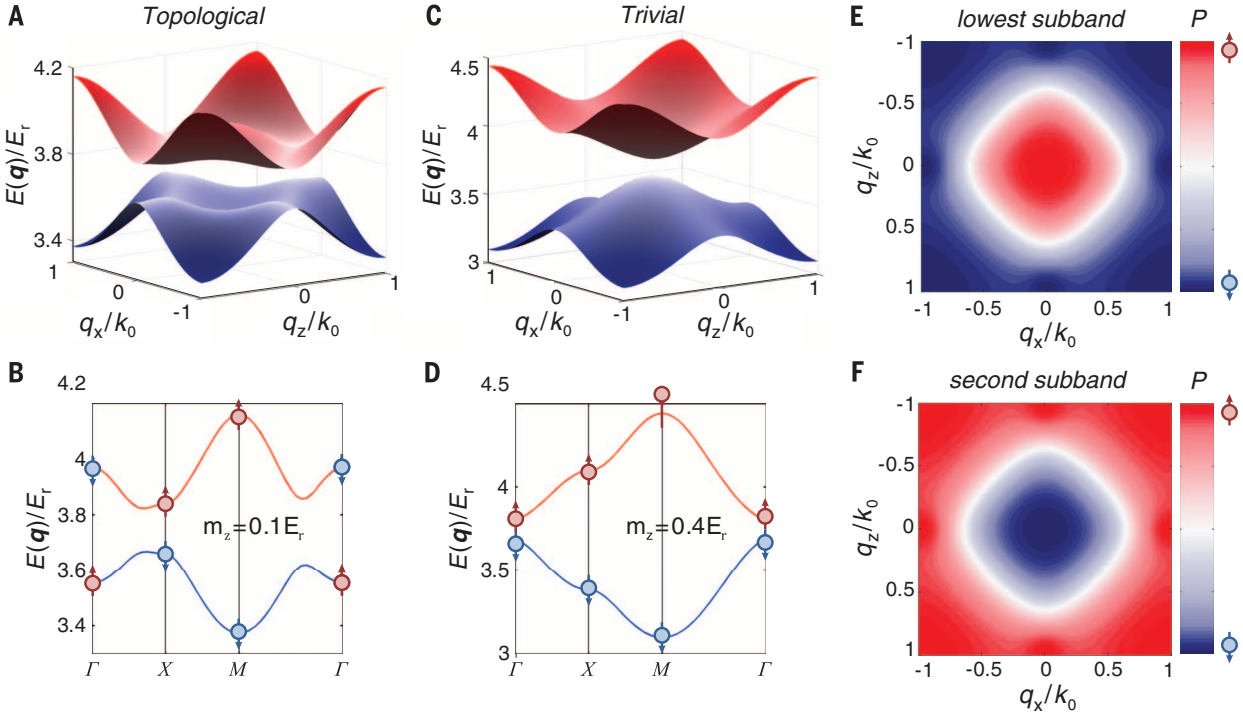

Fig. 2. Band structure and spin texture with 2D SO interaction. This figure shows an example of gapped band structure with nontrivial band topology (**A**), spin texture along the loop Γ-*X*-*M*-Γ (**B**), and spin polarization distributions $\langle\sigma_z\rangle$ of the lowest band (**E**) and the second band (**F**) for $m_z = 0.1E_r$. (**C** and **D**) Example of a trivial band with gapped band structure (C) and spin texture along the loop Γ-*X*-*M*-Γ (D) for $m_z = 0.4E_r$. For all panels, we take $V_{0x} = V_{0z} = 5E_r$, $M_{0x} = M_{0y} = 1.2E_r$, and $\delta\varphi_L = \pi/2$.

transitions, which flip spin and transfer momenta of magnitude $\sqrt{2}k_0$ along the diagonal directions. As given in Eqs. 3 and 4, the Raman terms $\mathcal{M}_x$ and $\mathcal{M}_y$ depend on $\delta\varphi_L$. For $\delta\varphi_L = \pi/2$, four small clouds in the $|\downarrow\rangle$ state with TOF momentum $\vec{k} = (\pm k_0, \pm k_0)$ are observed (Fig. 3B), reflecting the 2D SO coupling. On the other hand, by tuning the relative phase to $\delta\varphi_L = 3\pi/4$, the population of atom clouds in the two diagonal directions becomes imbalanced. Furthermore, the system reduces to 1D SO couplings when $\delta\varphi_L = \pi$ and 2π, with $\mathcal{M}_x = M_x \pm M_y$ and $\mathcal{M}_y = 0$. In this case, the Raman pumping generates only a single diagonal pair of BEC clouds, as shown in Fig. 3B for $\delta\varphi_L = \pi, 2\pi$. This is similar to the 1D SO coupling in the free space in (*11*), where the Raman coupling flips the atom spin and generates a pair of atom clouds with opposite momenta. Figure 3B also shows that there is a difference of distribution between the lower left and upper right BEC clouds at $|\downarrow\rangle$, which is due to non–tight-binding correction. A simple analysis reveals that although the fully antisymmetric Raman terms $\cos(k_0 x + \alpha)\cos(k_0 z + \beta)$ have negligible effects in the tight-binding limit of the lattice, they give finite contributions in the moderate lattice regime and are responsible for such difference of distribution (*32*). To quantify the crossover effect, we define $W = (\mathcal{N}_{\hat{x}-\hat{z}} - \mathcal{N}_{\hat{x}+\hat{z}})/(\mathcal{N}_{\hat{x}-\hat{z}} + \mathcal{N}_{\hat{x}+\hat{z}})$ to characterize the imbalance of the Raman coupling–induced atom clouds, with $\mathcal{N}_{\hat{x}\pm\hat{z}}$ denoting the atom number of the two BEC clouds along the diagonal $\hat{x}\pm\hat{z}$ direction. W can be fitted by a simple cosine curve $\cos\delta\varphi_L$ (Fig. 3C), reflecting the crossover between the 2D and 1D SO couplings realized in the present BEC regime.

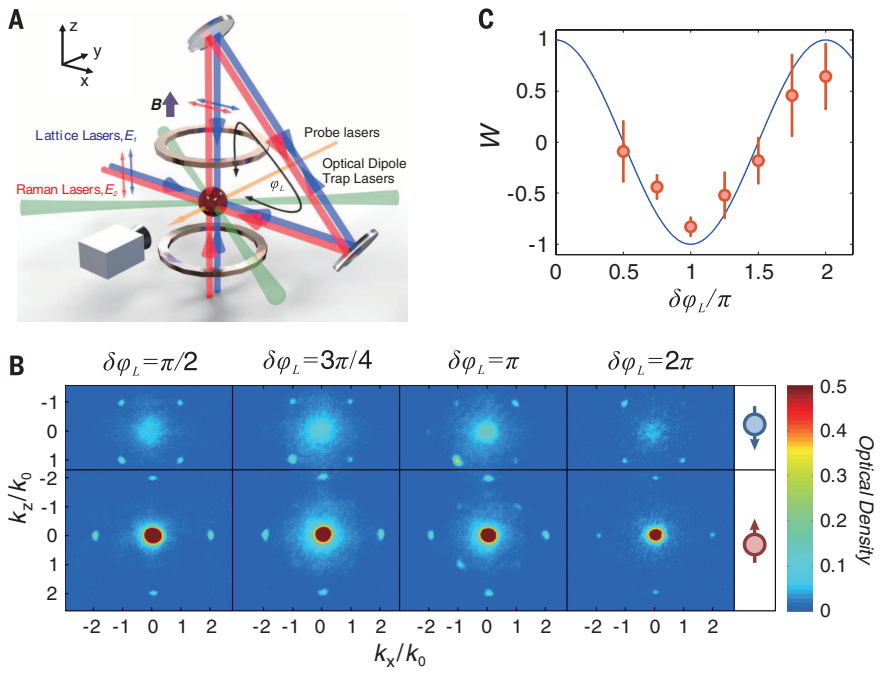

Fig. 3. Experimental realization of 2D SO interaction and 1D-2D crossover. (**A**) Experimental setup. ***B*** is the biased magnetic field, which generates the Zeeman splitting and gives the quantum axis of the atoms. (**B**) Spin-resolved TOF images of BEC atoms for $\delta\varphi_L = \pi/2$, $\delta\varphi_L = 3\pi/4$, $\delta\varphi_L = \pi$, and $\delta\varphi_L = 2\pi$. The other parameters are measured as $V_{0x} = V_{0z} = 4.16E_r$, $M_{0x} = M_{0y} = 1.32E_r$, and $m_z = 0$. (**C**) Measured imbalance W between the Raman coupling–induced atoms in the two diagonal directions as a function of the relative phase $\delta\varphi_L$, compared to a cosine curve $\cos\delta\varphi_L$. The results are averaged over ~30 TOF images.

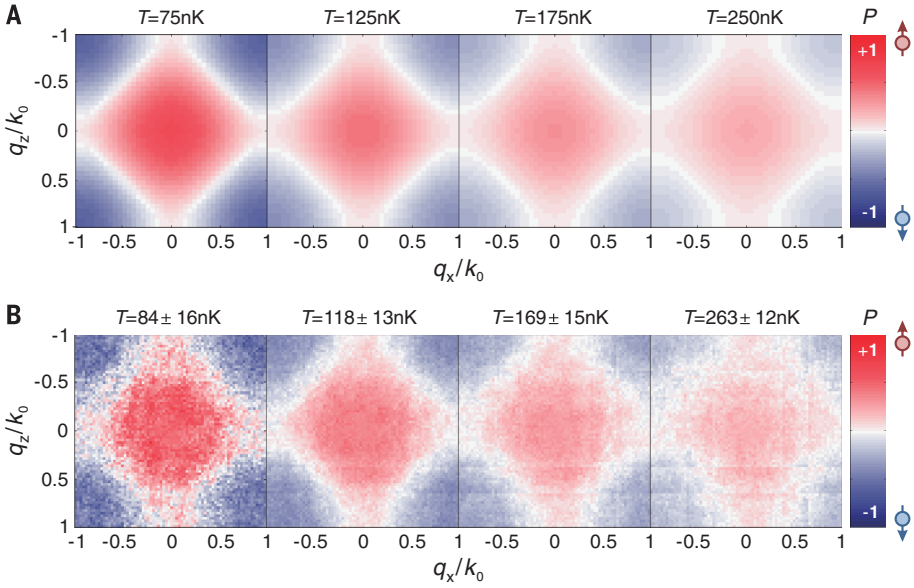

Fig. 4. Spin texture at different temperatures with $\delta\varphi_L = \pi/2$. (**A**) Numerical calculations for temperatures T = 250, 175, 125, and 75 nK. P is the polarization of the atomic spin, where +1 means spin up and –1 means spin down. (**B**) Experimental measurements of spin polarization at different measured temperatures. Parameters for the numerical calculation are the same as the experimental parameters: $V_{0x} = V_{0z} = 4.16E_r$, $M_{0x} = M_{0y} = 1.32E_r$, and $m_z = 0$.

Next, we focus on the 2D isotropic SO coupling with $\delta\varphi_L = \pi/2$, measure the spin distribution in the first Brillouin zone, and detect the topology of the bands by varying the bias magnetic field to tune δ, which governs m_z. For this purpose, we need a cloud of atoms with a temperature such that the lowest band is occupied by a sufficient number of atoms, whereas the population of atoms in the higher bands is small. A similar procedure used in the above BEC measurement is followed, except that the atoms are cooled to relatively higher temperatures, which are measured a posteriori using the momentum distribution of hot atoms. After a TOF expansion, we obtain the atom distributions of both spin-up and spin-down states in the momentum space and then map them back to the Bloch momentum space according to the plane-wave expansion of eigenfunctions. We define the spin polarization $P(\mathbf{q}) = [n_\uparrow(\mathbf{q}) - n_\downarrow(\mathbf{q})]/[n_\uparrow(\mathbf{q}) + n_\downarrow(\mathbf{q})]$, with $n_{\uparrow,\downarrow}(\mathbf{q})$ being the density of atoms of the corresponding spin state in the first Brillouin zone. Figure 4, A and B, shows the numerical results and experimentally measured spin polarizations at different temperatures, respectively, for $m_z = 0$, $V_{0x} = V_{0z} = 4.16E_r$, and $M_{0x} = M_{0y} = 1.32E_r$. In performing numerical simulation, the finite temperature effect is taken into account based on the Bose-Einstein statistics $f(E) = 1/[e^{(E_q - \mu)/k_B T} - 1]$, with k_B the Boltzmann constant and E_q given by band energies of the Hamiltonian (Eq. 1), plus the kinetic energy $\hbar^2 q_y^2/2m$ due to the motion in the out-of-lattice plane (y) direction. The average atom density is taken as $n = 3 \times 10^{19}$ m^{-3}, which determines the chemical potential μ. There is good agreement between the theoretical and experimental results, which demonstrates the feasibility and reliability of the spin polarization measurement. Furthermore, the results in Fig. 4 suggest that a temperature around T = 100 nK is optimal to extract

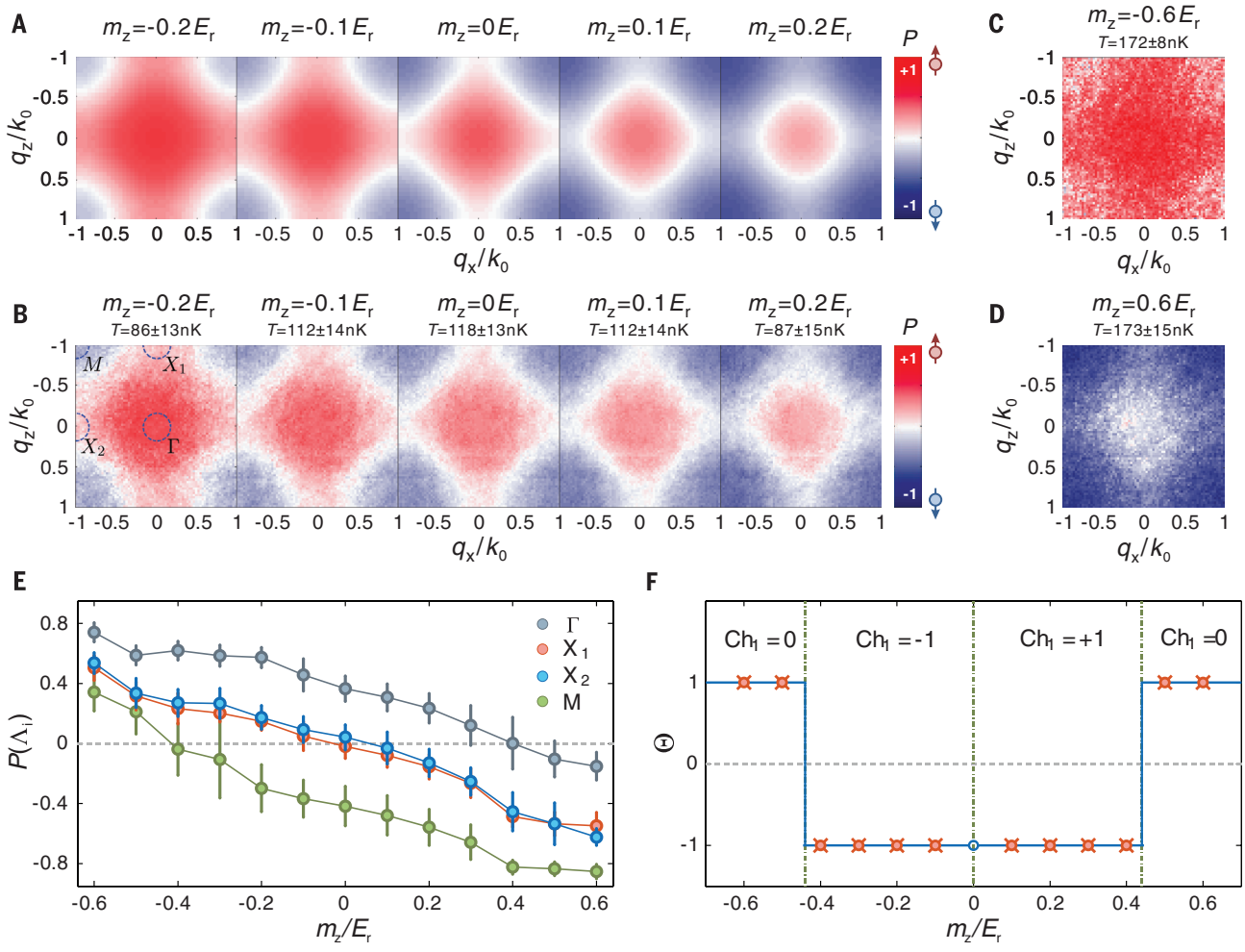

Fig. 5. Spin texture and band topology with $\delta\varphi_L = \pi/2$. (**A** and **B**) Spin texture at different m_z by tuning the two-photon detuning. Experimental measurements (B) are compared to numerical calculations at T = 100 nK (A). (**C** and **D**) Measured spin texture in topologically trivial bands at $m_z = -0.6E_r$ (C) and $m_z = 0.6E_r$ (D). (**E** and **F**) Measured spin polarization $P(\Lambda_j)$ at the four symmetric momenta $\{\Lambda_j\} = \{\Gamma, X_1, X_2, M\}$ as a function of m_z (E), and the product $\Theta = \Pi_{j=1}^{4}\mathrm{sgn}[P(\Lambda_j)]$ (F), which determines the Chern number Ch_1 and characterizes the topology of the band. In all the cases, we set $V_{0x} = V_{0z} = 4.16E_r$ and $M_{0x} = M_{0y} = 1.32E_r$.

the spin-texture information of the lowest band. In comparison, if the temperature is too high, atoms are distributed over several bands and the visibility of the spin polarization will be greatly reduced, whereas too low a temperature can also reduce the experimental resolution because the atoms will be mostly condensed at the band bottom.

We then measure the spin polarization as a function of detuning m_z to reveal the topology of the lowest-energy band, with $V_{0x} = V_{0z} = 4.16E_r$ and $M_{0x} = M_{0y} = 1.32E_r$. The numerical calculations and TOF-measured images of $P(\mathbf{q})$ are in agreement (Fig. 5A and Fig. 5, B to D, respectively). In Fig. 5E, we plot the values of polarization $P(\Lambda_j)$ for the four highly symmetric momenta Γ, X_1, M, and X_2. $P(X_1)$ and $P(X_2)$ always have the same sign, whereas the signs of $P(\mathrm{G})$ and $P(M)$ are opposite for small $|m_z|$ and the same for large $|m_z|$, with a transition occurring at the critical value of $|m_z^c|$ that is a bit larger than $0.4E_r$. At transition points, the spin polarization $P(X_1)$ or $P(X_2)$ vanishes due to the gap closing and thermal equilibrium. From the measured spin polarizations, the product Θ and the corresponding Chern number, given by $\mathrm{Ch}_1 = -\frac{1-\Theta}{4}\sum_{j=1}^{4}\mathrm{sgn}[P(\Lambda_j)]$ (*32*, *33*), can be read off (Fig. 5F). A numerical calculation using exact diagonalization (*32*) in the present experimental parameter regime can show two transitions between the topologically trivial and nontrivial bands near $m_z^c = \pm 0.44E_r$, according to the theory in (*33*), which agrees with the experimental observation. Note that around m_z = 0, the spin polarizations at $X_{1,2}$ change sign through zero, implying the gap closing at $X_{1,2}$ and a change of Chern number by 2. This confirms that for the 2D SO-coupled system realized in the present experiment, the energy band is topologically nontrivial when $0 < |m_z| < |m_z^c|$, whereas it is trivial for $|m_z| > |m_z^c|$.

Estimation of heating

The heating rate of the dipole trap is measured to be 18 nK/s, mainly owing to the photon scattering and the intensity noise. This results in a BEC lifetime of about 10 s. The heating rate of the lattice and the Raman lights caused by photon scattering is about four times that of the dipole trap, in the regime for $V_0 = 4.16E_r$ and $M_0 = 1.32E_r$ (*32*). Nevertheless, in the current experiment, residual heating is induced by the fluctuation of the bias magnetic field, which drives additional spin-flip dynamics in the presence of resonant Raman couplings. This contribution to the heating is about one order higher that of the dipole trap, reducing the lifetime of the SO-coupled BEC to just above 300 ms. This lifetime is sufficient to explore both single-particle and interacting physics for the ^{87}Rb BEC system. Moreover, stabilizing the bias magnetic field may result in an even longer lifetime of seconds in appropriate parameter regimes.

Discussion and outlook

The 2D SO coupling we realized here is for real spins (hyperfine eigenstates) of atoms, which can

be precisely measured and engineered experimentally. In comparison, a 2D SO coupling via a tripod system (*7*, *24*, *27*) or ring-coupling scheme (*25*) corresponds to pseudospins defined by superpositions of multiple hyperfine levels with superposition coefficients being spatially dependent. This conceptual difference manifests the advantages of the present realization for future broad studies of SO effects and interacting physics. Furthermore, owing to the realization in the optical lattice, the present 2D SO coupling can bring about much richer physics than a pure 2D Rashba correspondence. In the s-band regime, the present Bloch Hamiltonian describes a quantum anomalous Hall model driven by SO coupling, which cannot be exactly realized in solid-state materials. Thus, even in the single-particle regime, our realization leads to nontrivial topological bands, whereas a single-particle 2D Rashba system is topologically trivial. Moreover, even richer physics can be obtained if considering the higher-band (e.g., p-band) regimes.

Many experimental studies—including the measurement of topological Hall effects, Berry phase mechanism, and k-space monopole—can be performed on the basis of the present realization. On the other hand, with the high controllability of the present realization, the SO interaction can be readily switched on and off and can be adjusted between 1D and 2D limits. This may lead to rich quench spin dynamics in the optical lattice with nontrivial band topology. Moreover, with the present SO coupling in the optical lattice, one may explore states of matter [such as SO-coupled Mott insulators with interacting bosons (*35*, *36*)] that have no analog in solids.

Furthermore, the present optical Raman lattice scheme is generic and can be immediately applied to fermion systems (e.g., ^{40}K), in which case, the quantum anomalous Hall effect in the single-particle regime and topological superfluid (*28*) or novel magnetic phases (*37*) in the interacting regimes will be especially noteworthy. In particular, the topological superfluid phase is highly sought after because it hosts Majorana quasiparticles, which obey non-Abelian statistics (*38*) and have attracted attention in both condensed matter and cold atom physics (*5*). Finally, although the present study is focused on a 2D lattice system, generalizing our scheme to 3D optical lattices may lead to the realization of topological phases in 3D systems, including the Weyl topological semimetals (*39*, *40*).

REFERENCES AND NOTES

1. M. Z. Hasan, C. L. Kane, *Rev. Mod. Phys.* **82**, 3045–3067 (2010).
2. X.-L. Qi, S.-C. Zhang, *Rev. Mod. Phys.* **83**, 1057–1110 (2011).
3. N. Read, D. Green, *Phys. Rev. B* **61**, 10267–10297 (2000).
4. A. Y. Kitaev, *Phys. Uspekhi* **44**, 131–136 (2001).
5. F. Wilczek, *Nat. Phys.* **5**, 614–618 (2009).
6. J. Alicea, *Rep. Prog. Phys.* **75**, 076501 (2012).
7. J. Ruseckas, G. Juzeliūnas, P. Öhberg, M. Fleischhauer, *Phys. Rev. Lett.* **95**, 010404 (2005).
8. K. Osterloh, M. Baig, L. Santos, P. Zoller, M. Lewenstein, *Phys. Rev. Lett.* **95**, 010403 (2005).
9. X.-J. Liu, M. F. Borunda, X. Liu, J. Sinova, *Phys. Rev. Lett.* **102**, 046402 (2009).
10. Y.-J. Lin, K. Jiménez-García, I. B. Spielman, *Nature* **471**, 83–86 (2011).
11. J.-Y. Zhang *et al.*, *Phys. Rev. Lett.* **109**, 115301 (2012).
12. P. Wang *et al.*, *Phys. Rev. Lett.* **109**, 095301 (2012).
13. L. W. Cheuk *et al.*, *Phys. Rev. Lett.* **109**, 095302 (2012).
14. K. Jiménez-García *et al.*, *Phys. Rev. Lett.* **108**, 225303 (2012).
15. C. Wang, C. Gao, C.-M. Jian, H. Zhai, *Phys. Rev. Lett.* **105**, 160403 (2010).
16. C.-J. Wu, I. Mondragon-Shem, X.-F. Zhou, *Chin. Phys. Lett.* **28**, 097102 (2011).
17. T.-L. Ho, S. Zhang, *Phys. Rev. Lett.* **107**, 150403 (2011).
18. S.-C. Ji *et al.*, *Nat. Phys.* **10**, 314–320 (2014).
19. V. Galitski, I. B. Spielman, *Nature* **494**, 49–54 (2013).
20. T. F. J. Poon, X.-J. Liu, *Phys. Rev. A* **93**, 063420 (2016).
21. N. Goldman, G. Juzeliūnas, P. Öhberg, I. B. Spielman, *Rep. Prog. Phys.* **77**, 126401 (2014).
22. C. Zhang, S. Tewari, R. M. Lutchyn, S. Das Sarma, *Phys. Rev. Lett.* **101**, 160401 (2008).
23. M. Sato, Y. Takahashi, S. Fujimoto, *Phys. Rev. Lett.* **103**, 020401 (2009).
24. C. Zhang, *Phys. Rev. A* **82**, 021607(R) (2010).
25. D. L. Campbell, G. Juzeliūnas, I. B. Spielman, *Phys. Rev. A* **84**, 025602 (2011).
26. N. R. Cooper, *Phys. Rev. Lett.* **106**, 175301 (2011).
27. L. Huang *et al.*, *Nat. Phys.* **12**, 540–544 (2016).
28. X.-J. Liu, K. T. Law, T. K. Ng, *Phys. Rev. Lett.* **112**, 086401 (2014).
29. M. Aidelsburger *et al.*, *Phys. Rev. Lett.* **111**, 185301 (2013).
30. H. Miyake, G. A. Siviloglou, C. J. Kennedy, W. C. Burton, W. Ketterle, *Phys. Rev. Lett.* **111**, 185302 (2013).
31. M. Aidelsburger *et al.*, *Nat. Phys.* **11**, 162–166 (2015).
32. See supplementary materials for more details about model realization, SO coupling, nontrivial topological bands, band topological measurement, and estimation of heating.
33. X.-J. Liu, K. T. Law, T. K. Ng, P. A. Lee, *Phys. Rev. Lett.* **111**, 120402 (2013).
34. S.-C. Ji *et al.*, *Phys. Rev. Lett.* **114**, 105301 (2015).
35. Z. Cai, X. Zhou, C. Wu, *Phys. Rev. A* **85**, 061605(R) (2012).
36. W.-S. Cole, S. Zhang, A. Paramekanti, N. Trivedi, *Phys. Rev. Lett.* **109**, 085302 (2012).
37. J. Radić, A. Di Ciolo, K. Sun, V. Galitski, *Phys. Rev. Lett.* **109**, 085303 (2012).
38. D. A. Ivanov, *Phys. Rev. Lett.* **86**, 268–271 (2001).
39. S.-Y. Xu *et al.*, *Science* **349**, 613–617 (2015).
40. H. Weng, C. Fang, Z. Fang, B. A. Bernevig, X. Dai, *Phys. Rev. X* **5**, 011029 (2015).

ACKNOWLEDGMENTS

We thank J. Ho, T.-F. J. Poon, and G.-B. Jo for helpful discussions. This work has been supported by the Ministry of Science and Technology of China (under grants 2016YFA0301601 and 2016YFA0301604), National Natural Science Foundation of China, the CAS, the National Fundamental Research Program (under grant 2013CB922001), Fundamental Research Funds for the Central Universities (under grants 2030020028 and 2340000034), and Peking University Initiative Scientific Research Program. X.-J.L. acknowledges support from the National Natural Science Foundation of China (grant 11574008). X.-J.L. and L.Z. are also supported by the Thousand-Young-Talent Program of China.

SUPPLEMENTARY MATERIALS

www.sciencemag.org/content/354/6308/83/suppl/DC1
Supplementary Text
Figs. S1 to S6
References (*41*, *42*)

11 March 2016; accepted 12 September 2016
10.1126/science.aaf6689

REPORTS

GEOPHYSICS

Localized seismic deformation in the upper mantle revealed by dense seismic arrays

Asaf Inbal,* Jean Paul Ampuero, Robert W. Clayton

Seismicity along continental transform faults is usually confined to the upper half of the crust, but the Newport-Inglewood fault (NIF), a major fault traversing the Los Angeles basin, is seismically active down to the upper mantle. We use seismic array analysis to illuminate the seismogenic root of the NIF beneath Long Beach, California, and identify seismicity in an actively deforming localized zone penetrating the lithospheric mantle. Deep earthquakes, which are spatially correlated with geochemical evidence of a fluid pathway from the mantle, as well as with a sharp vertical offset in the lithosphere-asthenosphere boundary, exhibit narrow size distribution and weak temporal clustering. We attribute these characteristics to a transition from strong to weak interaction regimes in a system of seismic asperities embedded in a ductile fault zone matrix.

Earthquakes occurring along transform plate boundaries are generally confined to the upper portions of the crust, with upper mantle deformation being predominantly aseismic (*1*). Seismological investigations of active faulting at lower crustal depths are limited by highly attenuated signals whose level barely exceeds the noise at Earth's surface, and by the sparseness of regional seismic networks. Consequently, important physical parameters characterizing the transition from brittle fracture to ductile flow at the base of the seismogenic zone are generally very poorly determined (*2*).

Because seismic tomography usually cannot resolve features whose spatial extent is less than about 10 km in the mid-lower crust (*3*–*5*), the

Seismological Laboratory, California Institute of Technology, Pasadena, CA 91125, USA.
***Corresponding author. Email: ainbal@gps.caltech.edu**

occurrence of localized shear at those depths is largely inferred from geological observation of ancient shear zones, where tectonic deformation can be accommodated within a region whose thickness does not exceed 2 km (*6*). The presence of fault-generated melt in the form of pseudotachylytes injected into exposed mylonites, and the inferred subsequent ductile deformation of the two, indicate that seismic slip may occur within largely aseismic deep shear zones (*7*). This is often interpreted as resulting from ruptures that nucleate at shallow depth but penetrate into the deep ductile region enabled, for example, by thermal weakening mechanisms (*8*). Here, in contrast, we present evidence of deep seismicity that nucleates at lower crustal to upper mantle conditions.

The Newport-Inglewood fault (NIF), which hosts many deep earthquakes (*9*), is unusual in that it does not display the strong compression, relatively low heat flow, or strong topographical relief associated with deep faults in southern California (*10*–*12*). Moreover, given the local geothermal gradient [~32°C/km (*13*)], deep NIF seismicity nucleates at depths where typical continental crustal rocks are expected to deform in a ductile manner. To understand the long-term mode of seismic deformation along this fault, we examined a relocated earthquake catalog from the Southern California Seismic Network (SCSN) (*14*). We observed a systematic variation in the spatial pattern of microseismicity along the NIF strike, which we attribute to a transition in faulting style. Earthquake epicenters are tightly clustered on en echelon strike-slip faults northwest of Long Beach (LB) but do not follow the mapped trace of the NIF to the southeast of LB (Fig. 1A). From northwest to southeast, earthquake density decreases and maximum earthquake depth, which we define as the depth above which 95% of seismicity occurs, increases from 10 to 17 km. Along the same section, Mohorovičić discontinuity (Moho) depth decreases by about 5 km (Fig. 1C). The opposite trends of focal and Moho depths represent an unusual case in which the increase in seismogenic depth is anticorrelated with crustal thickness (*12*). Finding such deep events is surprising on a slow [0.5 to 1 mm/year (*15*)] tectonic fault such as the NIF. Ductile flow laws predict that the depth of the brittle-ductile transition increases with strain rate (*16*, *17*). This should result in a shallower transition along the NIF compared with that along the faster San Andreas fault [~2 cm/year (*18*)], assuming similar pressure and friction coefficient on these two faults. Moreover, if we make the common assumption that seismicity rate correlates with strain rate, then the observed 50-fold reduction in earthquake rate recorded by the SCSN from northwest of Rosecrans to LB (Fig. 1A) should have been accompanied by resolvably shallower seismicity. To improve our understanding of the spatial distribution of anomalous NIF seismicity, we examined earthquake properties in two NIF segments that host the deepest events reported in the regional catalog.

Our study is based on earthquake detection from continuous, simultaneous analysis of thousands of seismic channels from two dense arrays

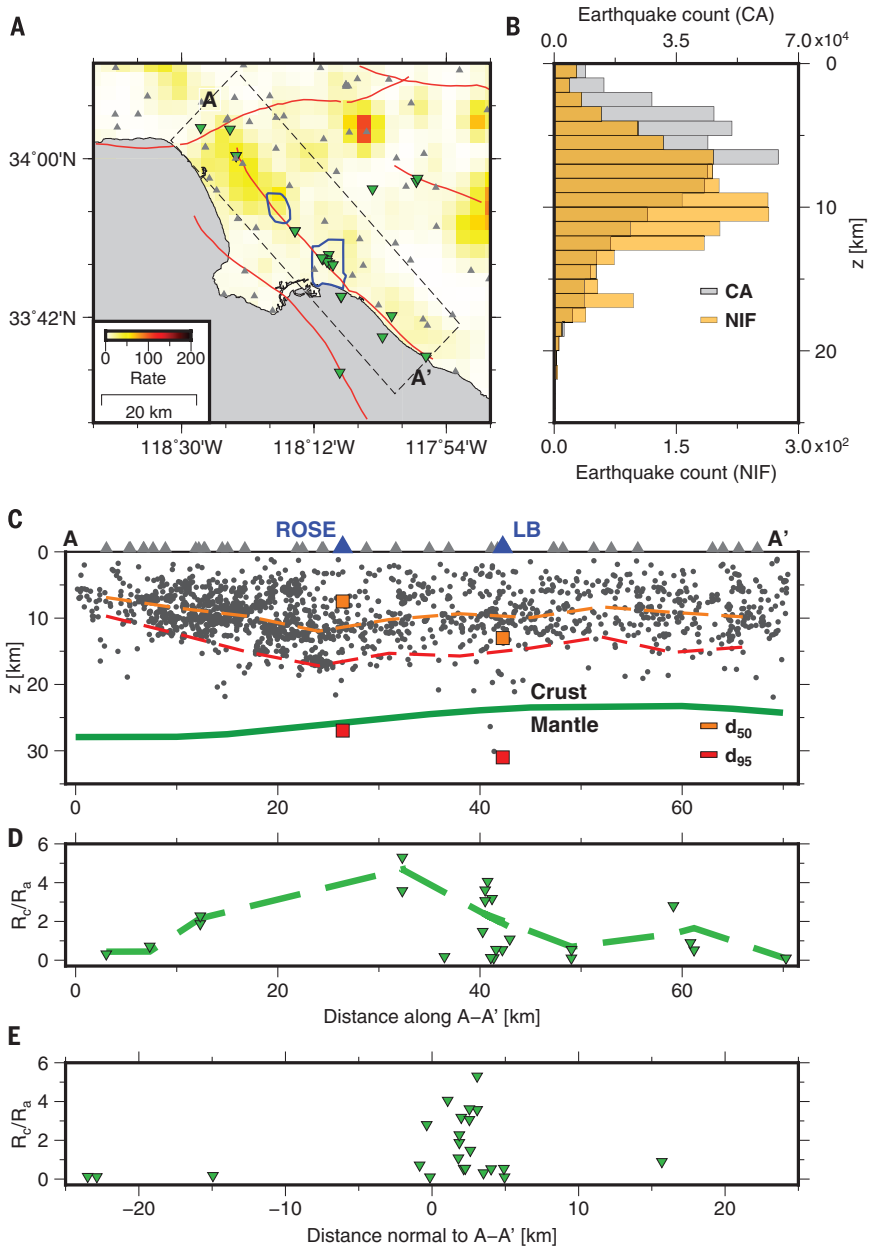

Fig. 1. Earthquake density, seismicity, and helium ratios. This figure shows the spatial distribution of seismicity that occurred between 1980 and 2011 and was recorded by the Southern California Seismic California (SCSN) (*14*), as well as helium ratios ($^3He/^4He$) in the LA basin, which were measured and corrected for air contamination by Boles *et al.* (*25*). (**A**) Earthquake density as a function of location. We used the color bar labeled "Rate" to indicate the spatially smoothed number of events over a 30-year period, binned in 9-km^2 squares. The locations of helium measurements, seismic stations, and dense seismic arrays are denoted by green inverted triangles, gray triangles, and blue polygons, respectively. The dashed rectangle indicates the region from which we extracted the earthquakes used to construct panels (B) and (C). Red curves denote the surface trace of active faults. (**B**) SCSN catalog seismicity depth distribution along the Newport-Inglewood fault (NIF) and in southern California (CA). *z* is the depth below sea level. (**C**) Depths of NIF seismicity and the Moho as function of location along line A-A′ in (A). The Moho (*45*, *46*) is indicated by the green curve. The depths (d) above which 50 and 95% of the earthquakes occur in the SCSN- and back-projection–derived catalogs are indicated by the orange and red dashed curves and squares, respectively. Gray triangles represent the projection of SCSN seismic stations onto the line A-A′; blue triangles denote the arrays. ROSE indicates the Rosecrans Array and LB denotes the Long Beach Array. (**D**) Helium ratios within the area enclosed by the dashed rectangle in (A), as a function of distance along A-A′. The dashed curve indicates the polynomial best fit to the observations. Green inverted triangles are the same as in (A). R_a is the $^3He/^4He$ ratio in air; R_c is the same for the crust. (**E**) Helium ratios as a function of distance normal to A-A′.

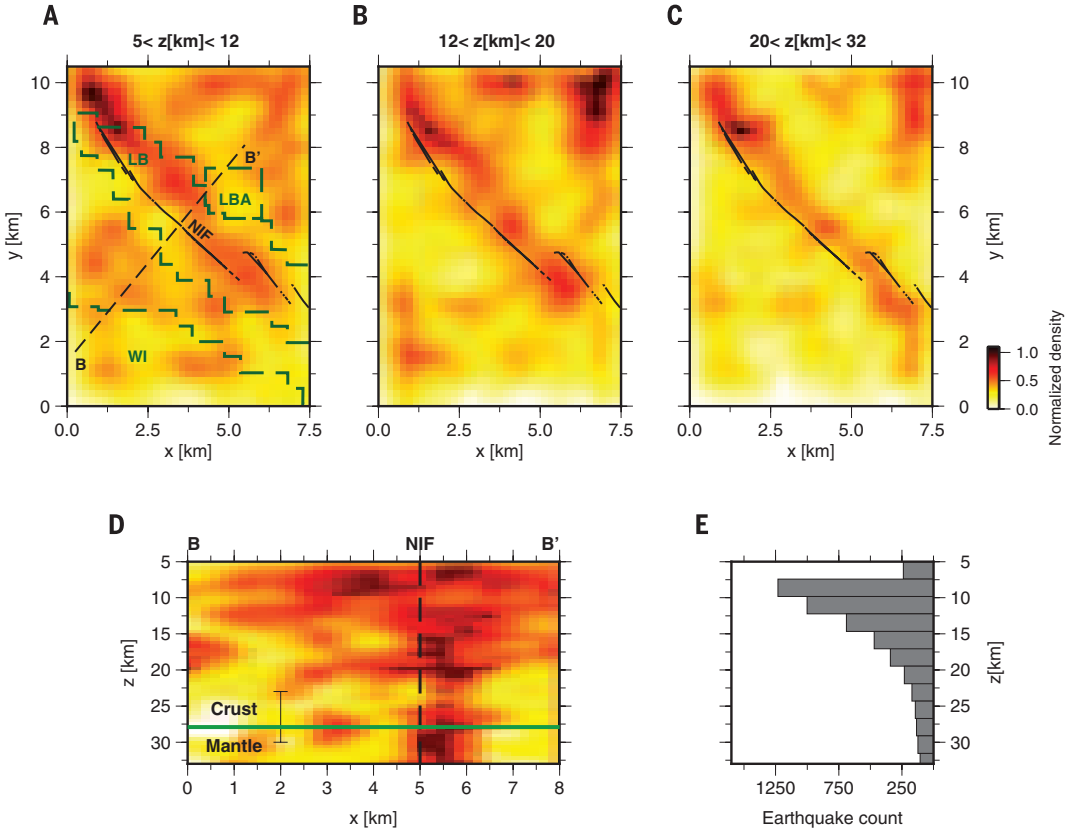

Fig. 2. Spatial distribution of earthquake density derived from a catalog spanning 93 nights of the LB Array data set. (**A** to **C**) Map view of event density in the following depth ranges: (A) 5 to 12 km, (B) 12 to 20 km, and (C) 20 to 32 km. Densities in each panel were normalized by their maximum value. Areas with intense seismicity are shown in orange and red; areas devoid of seismicity appear in yellow and white. The NIF surface trace and the local oilfields are denoted by black and green dashed lines, respectively. LB, Long Beach oilfield; LBA, Long Beach Airport oilfield; WI, Wilmington oilfield. (**D**) Vertical cross section showing event density along the B-B′ line in (A). We normalized the counts in each 2-km depth bin by their maxima. The Moho depth (*47*) is indicated by a green curve, and the uncertainty on this estimate was determined using previously published results (*26*, *38*, *48*). (**E**) Seismicity depth distribution in the LB Array data set.

(Fig. 1A and figs. S2 and S4 to S7) (*9*, *19*). We used the 5200-sensor 7-km–by–10-km LB Array and the 2600-sensor 5-km–by–5-km Rosecrans Array to compile catalogs with 6 and 1 month of data, respectively. The arrays contain 100-m-spaced, 10-Hz vertical geophones sampling at 500 Hz. We analyzed only nighttime data (6 p.m. to 5 a.m. Pacific time) to mitigate false detections. We used parallel computing on graphical processing units to process 80 terabytes, equivalent to about 80 years of waveform data from the Global Seismographic Network (*20*). The location uncertainties we estimated through synthetic tests (*21*) are 1 and 3 km in the horizontal and vertical directions, respectively, for events with moment magnitude (M_w) > 1.5 occurring below 27 km, but less than 1 km at shallower depths (fig. S1).

Our catalog illuminates a transition from diffuse seismic deformation in the upper crust to localized deformation in the lithospheric mantle. Shallow seismicity (<12 km) in LB is diffuse and uncorrelated with the mapped fault trace or with the nearby oilfield (Fig. 2A). To the southwest of the main NIF strand, we identify a northwest–north-northwest striking segment that is mostly active between 12 and 20 km but contains sparse seismicity outside this depth range. A second structure is located to the northeast. Below 20 km, this zone is very seismically active, but the location near the edge of the array prevents us from resolving its geometry in detail.

With increasing depth, seismicity progressively concentrates beneath the mapped trace of the NIF, and the width of the seismically active zone decreases (Fig. 2, A to C). Below ~20 km, seismicity localizes onto a 1-km-wide area that is located directly beneath the mapped trace of the NIF. The vertical cross section (Fig. 2D) clearly shows that the fault dip below 15 km is near vertical and that it retains this geometry in the upper mantle. In particular, our observations do not support a previous suggestion that the NIF is truncated at shallow depths by an active detachment fault (*22*). Accounting for location uncertainties in our catalog, the deformation zone illuminated by deep LB seismicity is no more than 2 km wide, consistent with several exhumed mylonite shear zones (*6*). We also find that deep seismicity (>20 km) accounts for, at most, 10 to 20% of the cumulative long-term moment rate accommodated by the fault, assuming a slip rate of 0.5 mm/year (*15*). On the basis of these results, we conclude that aseismic, viscous flow accommodates most of the deformation in the lower crust.

The spatial distribution of deep seismicity varies along the NIF strike. Seismicity in Rosecrans occurs along four or five strands that form a 5-km-wide fault zone, which is active down to about 15 km but contains few events below that depth. Unlike the LB segment, these strands appear to dip at up to 70° to the northeast (fig. S3). Multiple en echelon strike-slip faults are generally observed at shallower depths along that section (*23*), and our study confirms that these structures are active at larger depths. If the Rosecrans catalog is representative of the long-term deformation along that segment, then the scarcity of deep seismicity suggests that the zone of deep, localized seismic deformation extends no more than 15 km along the NIF strike to the northwest of LB.

Independent evidence compatible with deep faulting comes from recent measurements of the $^3He/^4He$ ratio, a primary indicator of mantle-derived phases within the crust (*24*), in deep boreholes in the Los Angeles (LA) basin (*25*) (Fig. 1, A, D, and E). In this basin, ^3He enrichment is more than twice as high as it is along the much more tectonically active San Andreas fault. The observed along-strike trend in the fraction of mantle-derived helium is well correlated with the seismicity depths in the regional catalog. They both first increase toward the southeast, then decrease somewhat and flatten southeast of LB (Fig. 1, C and D). Further evidence of the deep root of the NIF comes from the seismic imaging of a sharp vertical offset in the lithosphere-asthenosphere boundary (*26*), which extends to a depth of about 90 km beneath

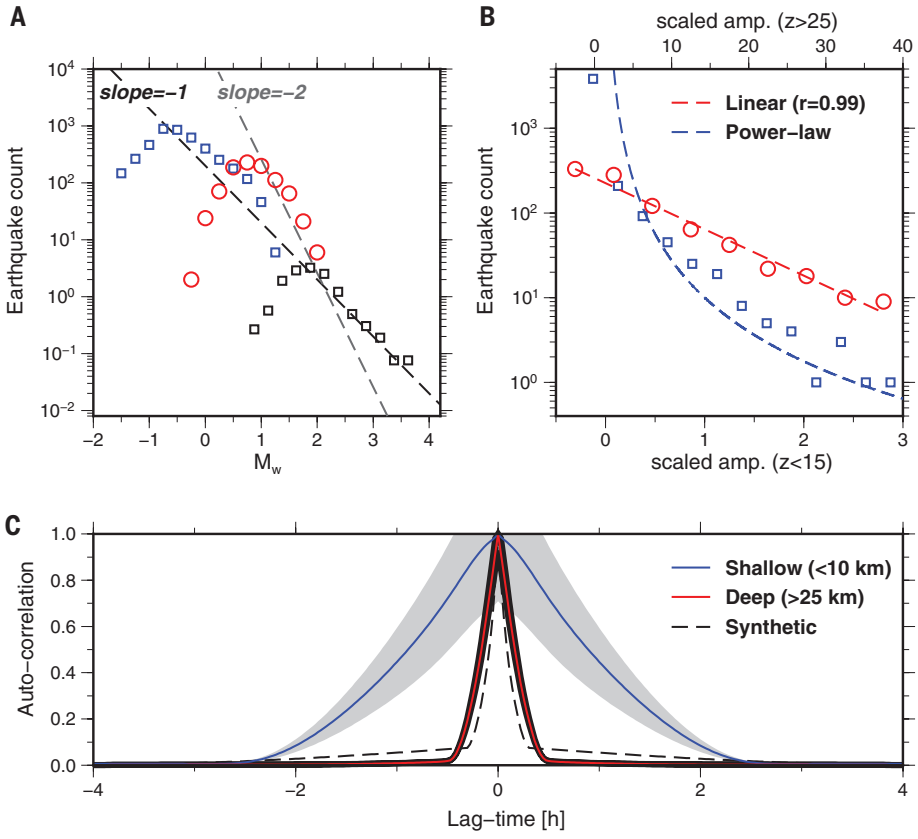

Fig. 3. Temporal analysis and earthquake size distribution in Long Beach. (**A**) Distribution of earthquake magnitudes. The blue squares and red circles denote shallow (<15 km) and deep (>25 km) events, respectively. The black squares are for the SCSN catalog and are normalized according to the LB Array spatiotemporal coverage. The slopes of black and gray dashed lines are equal to –1 and –2, respectively. (**B**) Distribution of earthquake signal amplitudes, which we define as the maximum of the downward-continued, migrated stack in a 5-s window containing the event, scaled by the maximum of the synthetic stack computed for a collocated source with M_w = 1. The best-fitting exponential model, which appears linear in this semi-logarithmic scale, is indicated by the red curve. The blue curve shows a power law. *r*, correlation coefficient. (**C**) Autocorrelation as a function of lag-time between earthquake rate time series for shallow (<10 km) and deep (>25 km) clusters. The blue and red curves indicate the average values for 112 shallow and 52 deep clusters, respectively. The gray shaded area denotes the 1σ uncertainties. The black dashed curve represent a synthetic earthquake catalog with a random, Poissonian distribution of earthquake occurrences.

the zone of deep seismicity and anomalous ^{3}He enrichment. We suggest that the narrow deformation zone hosting deep seismicity beneath LB acts as a major conduit for fluid transfer between the upper mantle and the crust. These fluids, in turn, could provide a source of high pressures that extend the depth of seismic deformation.

The along-depth variation in the spatial distribution of NIF seismicity is most likely due to a rheological transition, which we expected to manifest itself as a resolvable change in the statistics of the catalog. To test this hypothesis, we analyzed the temporal clustering of LB seismicity. Because our spatial resolution is limited by location uncertainties that are likely larger than the rupture dimensions of the earthquakes we imaged, we focused on aspects of the population's temporal and size distributions, which varied on scales of several hundred meters.

We can investigate the degree of earthquake interaction using the ratio between the number of small and large earthquakes, commonly characterized by the *b* value ($b = -d\log_{10}(N)/dM_w$, where *N* is the number of earthquakes of magnitude larger than M_w). In most tectonic environments, *b* values vary between 0.8 and 1.5 and decrease with increasing deviatoric stress (*27*). Larger *b* values are associated with an increase in ductility and a reduction of fault strength, both in the lab (*28*) and on natural faults (*29*). Recent observations of low-frequency earthquakes (LFEs), whose collective failure results in tectonic tremors, suggest that their numbers fall off rapidly with increasing size (estimated from tremor amplitudes). Those studies suggest that LFE numbers are better described by an exponential distribution (*30*–*32*) or a very steep power law (*33*). The rapid fall-off in LFE numbers with increasing size is similar to deep NIF seismicity (*9*). However, unlike other areas, the NIF catalog captures a depth-dependent transition in earthquake properties (Fig. 3, A and B). The distribution of shallow (<15 km) earthquakes in the 6-month period is consistent with that of the 30 years spanning SCSN catalog. Our analysis closes a gap between the LB and SCSN magnitude-frequency distributions between M_w = 1 and 2 in our 3-week catalog (*9*).

Spatiotemporal clustering is ubiquitous in earthquake catalogs and manifests most notably in the form of mainshock-aftershock sequences. We can model seismic activity as a random Poissonian process because it decorrelates at large distances or long time intervals. Our previous analysis of 3 weeks of LB seismicity (*9*) demonstrated Omori-type temporal clustering at interevent distances of up to 2 km. To determine whether this behavior is depth-dependent, we analyzed the temporal autocorrelation functions of the spatially smoothed earthquake rates at different depth ranges (*21*). We found that deep earthquake occurrence shows weak temporal correlation and resembles a random Poissonian process (Fig. 3C). This indicates diminished earthquake interactions at these depths.

Models of lithospheric strength may explain deep NIF seismicity while incorporating constrains on lower crustal rheology (*17*). However, relevant parameters such as temperature, grain size, lithology, and water content are generally poorly constrained. One possibility is that lateral as well as vertical compositional changes in the lower crust will promote brittleness within ductile, generally aseismic regions. A line of evidence supports the existence of considerable heterogeneity in material properties at lower crustal to upper mantle depth beneath the NIF. These include the observation of a sharp offset in the lithosphere-asthenosphere boundary extending to 90 km depth beneath the NIF (*26*); a 10-km jump in the Moho, 16 km to the west of the NIF (*34*); travel-time tomography showing a fast, possibly mafic body starting at ~18 km beneath the LA basin (*35*); magnetic profiles suggesting that the NIF is the southern boundary of an ultramafic body (*36*); and along-strike variations in the orientation of the principal stress axes (*37*), the distribution of mantle helium (*25*), and near-surface (*23*) and deep faulting styles. Structural factors may also assist slip localization. The fabric of foliated mica schists, which are thought to be distributed at lower crustal depths beneath California (*38*, *39*), possibly contains discrete surfaces accommodating seismic slip. Unstable frictional sliding of mafic rock has been observed in lab experiments (*40*, *41*) and in the field. (*42*, *43*). This behavior may be further encouraged in the presence of fluids, either by reducing the effective normal stress or by promoting strain localization in narrow shear bands (*44*), perhaps akin to the localized deformation zone we imaged beneath LB (Fig. 2C).

The rheological transition has profound implications on the degree of fault localization, relaxation mechanisms, and earthquake scaling properties. We can reconcile these observations with a conceptual framework in which deep deformation is predominately accommodated by ductile flow but interspersed by seismogenic asperities. Seismic rupture nucleated in a brittle asperity can penetrate into the surrounding region, up to a certain distance

that generally depends on the asperity size and stress drop and on the resistance of the matrix. This effective radius R_e controls the range of interaction between asperities. The ratio between R_e and the interasperity distance Δ determines the ability of asperities to break together in seismic events, despite the intervening creep, and thus influences the statistics of the earthquake catalog. When R_e/Δ is large, ruptures can involve multiple asperities. This strong interaction regime potentially leads to a scale-free, power-law earthquake size distribution (Fig. 3A) and temporal clustering (Fig. 3C), as observed at shallow depths. When R_e/Δ is small, asperities tend to break in isolation. In this weak interaction regime, seismicity is temporally uncorrelated and, if asperities have a characteristic size, the earthquake size distribution is scale-bound, as observed in the deep NIF beneath LB. A systematic decrease of R_e/Δ with increasing depth may result from several processes, which are not necessarily independent. One possibility is a rheological control: R_e may decrease with depth due to increasing velocity strengthening of the creeping matrix or decreasing stress drop within the asperities. Another possibility is a geometrical (or structural) control: At larger depths, the range of asperity sizes (and, hence, of R_e) may be narrower or Δ may be larger (e.g., due to lithological variations).

REFERENCES AND NOTES

1. A. Maggi, J. Jackson, D. McKenzie, K. Priestley, *Geology* **28**, 495–498 (2000).
2. R. Bürgmann, G. Dresen, *Annu. Rev. Earth Planet. Sci.* **36**, 531–567 (2008).
3. C. Thurber *et al.*, *Bull. Seismol. Soc. Am.* **96**, S38–S49 (2006).
4. M. Kahraman *et al.*, *Earth Planet. Sci. Lett.* **430**, 129–139 (2015).
5. J. H. Shaw *et al.*, *Earth Planet. Sci. Lett.* **415**, 1–15 (2015).
6. R. J. Norris, A. F. Cooper, *J. Struct. Geol.* **25**, 2141–2157 (2003).
7. J. C. White, *J. Struct. Geol.* **38**, 11–20 (2012).
8. J. R. Rice, *J. Geophys. Res.* **111**, B05311 (2006).
9. A. Inbal, R. Clayton, J.-P. Ampuero, *Geophys. Res. Lett.* **42**, 6314–6323 (2015).
10. A. S. Bryant, L. M. Jones, *J. Geophys. Res.* **97**, 437–447 (1992).
11. H. Magistrale, *Geophys. Res. Lett.* **29**, 87-1–87-4 (2002).
12. E. Hauksson, *Geophys. J. Int.* **186**, 82–98 (2011).
13. L. C. Price, M. J. Pawlewicz, T. A. Daws, "Organic metamorphism in the California petroleum basins: Chapter A, Rock-Eval and vitrinite reflectance" (U.S. Geological Survey Bulletin 2174-A, 1999).
14. E. Hauksson, W. Yang, P. M. Shearer, *Bull. Seismol. Soc. Am.* **102**, 2239–2244 (2012).
15. L. B. Grant, J. T. Waggoner, T. K. Rockwell, C. vonStein, *Bull. Seismol. Soc. Am.* **87**, 277–293 (1997).
16. D. L. Kohlstedt, B. Evans, S. J. Mackwell, *J. Geophys. Res.* **100**, 17587–17602 (1995).
17. G. Hirth, N. M. Beeler, *Geology* **43**, 223–226 (2015).
18. E. O. Lindsey, Y. Fialko, *J. Geophys. Res.* **118**, 689–697 (2013).
19. J. Gazdag, *Geophys.* **43**, 1342–1351 (1978).
20. IRIS, Incorporated Research Institutions for Seismology; www.iris.edu/hq.
21. Materials and methods are available as supplementary materials on *Science* Online.
22. J. Crouch, J. Suppe, *Geol. Soc. Am. Bull.* **105**, 1415–1434 (1993).
23. T. L. Wright, "Structural geology and tectonic evolution of the Los Angeles Basin, California," in American Association of Petroleum Geologists Memoir 52, K. T. Biddle, Ed. (1991), pp. 35–134.
24. B. M. Kennedy *et al.*, *Science* **278**, 1278–1281 (1997).
25. J. R. Boles, G. Garven, H. Camacho, J. E. Lupton, *Geochem. Geophys. Geosyst.* **16**, 2364–2381 (2015).
26. V. Lekic, S. W. French, K. M. Fischer, *Science* **334**, 783–787 (2011).
27. C. H. Scholz, *Geophys. Res. Lett.* **42**, 1399–1402 (2015).
28. C. H. Scholz, *Bull. Seismol. Soc. Am.* **58**, 399–415 (1968).
29. M. Spada, T. Tormann, S. Wiemer, B. Enescu, *Geophys. Res. Lett.* **40**, 709–714 (2013).
30. T. Watanabe, Y. Hiramatsu, K. Obara, *Geophys. Res. Lett.* **34**, L07305 (2007).
31. D. R. Shelly, J. L. Hardebeck, *Geophys. Res. Lett.* **37**, L14301 (2010).
32. J. R. Sweet, K. C. Creager, H. Houston, *Geochem. Geophys. Geosyst.* **15**, 3713–3721 (2014).
33. M. G. Bostock, A. M. Thomas, G. Savard, L. Chuang, A. M. Rubin, *J. Geophys. Res.* **120**, 6329–6350 (2015).
34. B. Schmandt, R. W. Clayton, *J. Geophys. Res.* **118**, 5320–5338 (2013).
35. E. Hauksson, *J. Geophys. Res.* **105**, 13875–13903 (2000).
36. T. Romanyuk, W. D. Mooney, S. Detweiler, *J. Geodyn.* **43**, 274–307 (2007).
37. E. Hauksson, *Bull. Seismol. Soc. Am.* **77**, 539–561 (1987).
38. R. Porter, G. Zandt, N. McQuarrie, *Lithosphere* **3**, 201–220 (2011).
39. P. Audet, *J. Geophys. Res.* **120**, 3527–3543 (2015).
40. D. S. H. King, C. Marone, *J. Geophys. Res.* **117**, B12203 (2012).
41. E. K. Mitchell, Y. Fialko, K. M. Brown, *Geochem. Geophys. Geosyst.* **16**, 4006–4020 (2015).
42. T. Ueda, M. Obata, G. Di Toro, K. Kanagawa, K. Ozawa, *Geology* **36**, 607–610 (2008).
43. A. K. Matysiak, C. A. Trepmann, *Tectonophys.* **530–531**, 111–127 (2012).
44. A. J. Getsinger, G. Hirth, H. Stunitz, E. T. Goergen, *Geochem. Geophys. Geosyst.* **14**, 2247–2264 (2013).
45. J. H. Shaw *et al.*, *Earth Planet. Sci. Lett.* **415**, 1–15 (2015).
46. C. Tape, A. Plesch, J. H. Shaw, H. Gilbert, *Seismol. Res. Lett.* **83**, 728–735 (2012).
47. Y. Ma, R. Clayton, *Geophys. J. Int.* **206**, 1645–1651 (2016).
48. Z. Yan, R. W. Clayton, *J. Geophys. Res.* **112**, B05311 (2007).

ACKNOWLEDGMENTS

We thank Signal Hill Petroleum and NodalSeismic for granting us permission to use the Long Beach Array data, and we thank Breitburn Energy and LA Seismic for permission to use the Rosecrans Array data. We acknowledge J. P. Avouac, R. Bürgmann, Y. Ma, and W. Frank for helpful discussions. This research was supported by NSF awards EAR-1214912 and EAR-1520081 and by the Terrestrial Hazard Observation and Reporting Center at Caltech. The seismic data are property of Signal Hill Petroleum and Breitburn Energy. Data are available for noncommercial use through a license agreement with the data owners that includes but is not limited to a nondistribution agreement. Please contact the authors for additional information.

SUPPLEMENTARY MATERIALS

www.sciencemag.org/content/354/6308/88/suppl/DC1
Materials and Methods
Figs. S1 to S7
References (*49*, *50*)

23 December 2015; accepted 31 August 2016
10.1126/science.aaf1370

SOLAR CELLS

Quantum dot–induced phase stabilization of α-$CsPbI_3$ perovskite for high-efficiency photovoltaics

Abhishek Swarnkar,[1,2] Ashley R. Marshall,[1,3] Erin M. Sanehira,[1,4] Boris D. Chernomordik,[1] David T. Moore,[1] Jeffrey A. Christians,[1] Tamoghna Chakrabarti,[5] Joseph M. Luther[1]*

We show nanoscale phase stabilization of $CsPbI_3$ quantum dots (QDs) to low temperatures that can be used as the active component of efficient optoelectronic devices. $CsPbI_3$ is an all-inorganic analog to the hybrid organic cation halide perovskites, but the cubic phase of bulk $CsPbI_3$ (α-$CsPbI_3$)—the variant with desirable band gap—is only stable at high temperatures. We describe the formation of α-$CsPbI_3$ QD films that are phase-stable for months in ambient air. The films exhibit long-range electronic transport and were used to fabricate colloidal perovskite QD photovoltaic cells with an open-circuit voltage of 1.23 volts and efficiency of 10.77%. These devices also function as light-emitting diodes with low turn-on voltage and tunable emission.

Hybrid organic-inorganic halide perovskites, with the common formulation ABX_3 (where A is an organic cation, B is commonly Pb^{2+}, and X is a halide), were first applied to photovoltaics (PVs) as methylammonium lead triiodide ($CH_3NH_3PbI_3$) in 2009 (*1*). Perovskite PV devices processed from solution inks now convert >22% of incident sunlight into electricity, which is on par with the best thin-film chalcogenide and silicon devices, but durability of the semiconductor presents a major technical hurdle to commercialization. Under environmental stress, $CH_3NH_3PbI_3$ dissociates into PbI_2 and CH_3NH_3I, the latter of which is volatile (*2*).

Thus, an all-inorganic structure without a volatile organic component is highly desired. The all-inorganic Pb-halide perovskite with the most appropriate band gap E_g for PV applications is cubic (α) $CsPbI_3$ (E_g = 1.73 eV) because geometrical constraints of the perovskite structure require a large +1 A-site cation, and Cs^+ is the most feasible. However, below 320°C, the orthorhombic (δ) phase (E_g = 2.82 eV) is thermodynamically

[1]Chemical and Materials Science, National Renewable Energy Laboratory (NREL), Golden, CO 80401, USA. [2]Department of Chemistry, Indian Institute of Science Education and Research (IISER), Pune 411008, India. [3]Department of Chemistry and Biochemistry, University of Colorado, Boulder, CO 80309, USA. [4]Department of Electrical Engineering, University of Washington, Seattle, WA 98195, USA. [5]Metallurgical and Materials Engineering, Colorado School of Mines, Golden, CO 80401, USA.
***Corresponding author. Email: joey.luther@nrel.gov**

preferred (*3*). Nevertheless, groups have explored $CsPbX_3$ compounds as PV materials, but films of α-$CsPbI_3$ undergo immediate transformation to the orthorhombic phase when exposed to ambient conditions (*4*). Attempts to stabilize the cubic phase through alloying with Br^- have been explored because $CsPbIBr_2$ shows a much reduced δ to α phase transition temperature of 100°C (*3*). However, the composition change leads to an undesired increase in the band gap. We show that nanocrystal surfaces can be used to stabilize α-$CsPbI_3$ at room temperature, far below the phase transition temperature for thin film or bulk materials. We further show that we can control the electronic coupling of quantum dots (QDs) to produce air-stable, efficient PV cells (initial efficiency above 10%) based on this all-inorganic material.

Many physical properties differ between nanometer-sized and bulk crystalline materials of the same chemical compound. One such example is the structural phase in which the constituent atoms are arranged. For example, the semiconductors CdS and CdSe embody a rock salt structure at high pressure. However, the solid-solid phase transition point between the rock salt phase and the hexagonal wurtzite phase can vary greatly in temperature and pressure as a function of crystal size (*5*, *6*). Manipulated size-dependent phase diagrams have been explored in a variety of material systems, with advantageous properties of the crystals emerging at reduced dimensions in oxides (such as TiO_2), lanthanides (such as $NaYF_4$) (*7*), metals (such as Ag) (*8*), and ferroelectrics (such as the perovskite $BaTiO_3$) (*9*).

Synthetic protocols of colloidal halide perovskite QDs have recently been reported (*10*–*17*). $CsPbX_3$ QDs exhibit improved room-temperature cubic-phase stability and attractive optical properties for a wide range of applications (*11*, *18*–*22*). Experiments on size- and shape-dependent optical properties (*11*, *23*–*25*), surface chemistry (*26*), and other photophysics (*27*) are being explored for $CsPbBr_3$ QDs. However, previous studies were unable to achieve α-$CsPbI_3$ QDs that were stable enough for extensive characterization or to be used in PV cells.

We present an improved synthetic route and purification approach of $CsPbI_3$ QDs. Once purified, the QDs retain the cubic phase for months in ambient air and even at cryogenic temperatures. A method for perovskite QD film assembly is described that allows for efficient dot-to-dot electronic transport while retaining the phase stability of the individual QDs. The PV cells produced from this approach have the highest power conversion efficiency (PCE) and stabilized power output (SPO) of any all-inorganic perovskite absorber, produce 1.23 V at open circuit (among the best of any perovskite PV cells), and also function as light-emitting diodes (LEDs), emitting visible red light with low turn-on voltage.

The tunability of the band gap via size control due to quantum confinement is shown in Fig. 1. The series of $CsPbI_3$ QDs, with varied size (band gap), were synthesized with the addition of Cs-oleate to a flask containing PbI_2 precursor, as first described by Protesescu *et al.* (*11*)—here, using

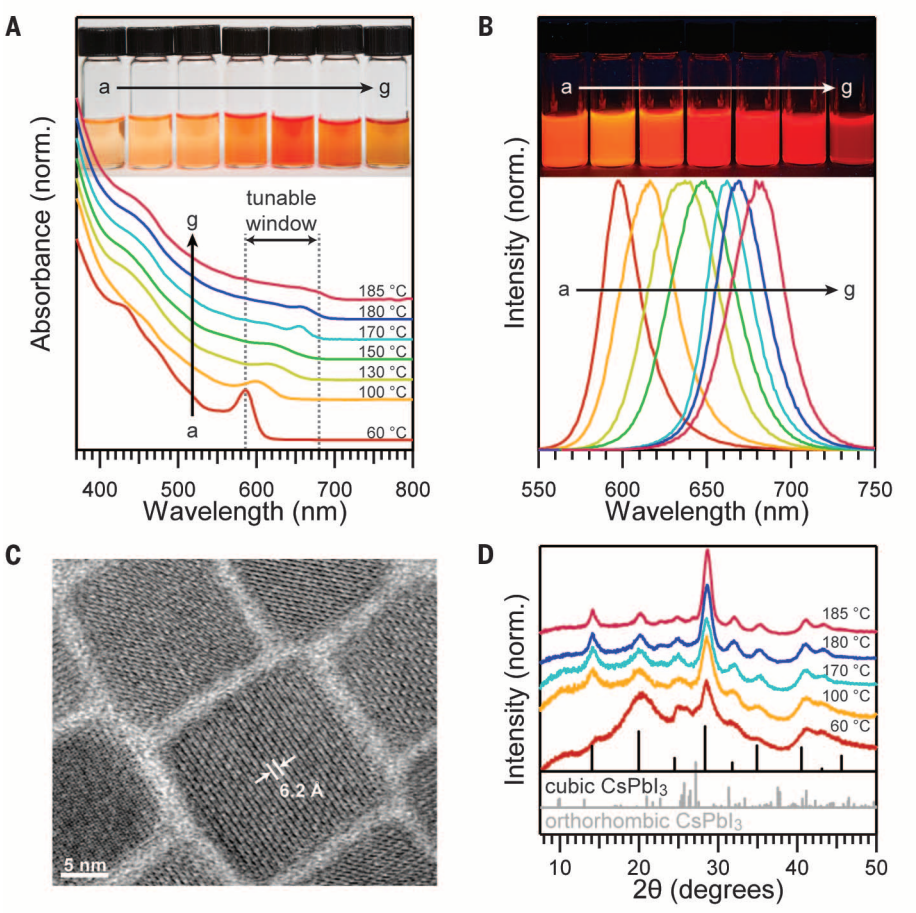

Fig. 1. Characterization of $CsPbI_3$ QDs. (**A**) Normalized UV-visible absorption spectra and photographs of $CsPbI_3$ QDs synthesized at (a) 60°C (3.4 nm), (b) 100°C (4.5 nm), (c) 130°C (5 nm), (d) 150°C (6.8 nm), (e) 170°C (8 nm), (f) 180°C (9 nm), and (g) 185°C (12.5 nm). The numbers in parentheses are the average size from TEM. (**B**) Normalized photoluminescence spectra and photographs under UV illumination of the QDs from (A). (**C**) High-resolution TEM of $CsPbI_3$ QDs synthesized at 180°C. (**D**) XRD patterns of QDs synthesized at (from bottom to top) 60°, 100°, 170°, 180°, and 185°C, confirming that they crystallize in the cubic phase of $CsPbI_3$.

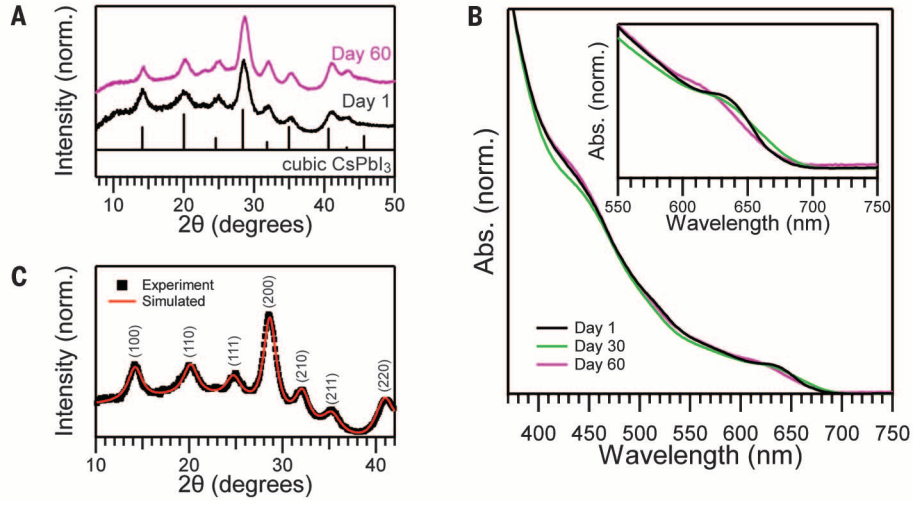

Fig. 2. Phase stability of $CsPbI_3$ QDs. (**A**) Powder XRD patterns and (**B**) UV-visible absorption spectra, normalized at 370 nm, of $CsPbI_3$ QDs synthesized at 170°C and stored in ambient conditions for a period of 60 days. (Inset) The slight blue shift that is seen in the excitonic peak with extended storage. (**C**) Rietveld refinement fitting of $CsPbI_3$ QD XRD pattern, revealing pure cubic-phase $CsPbI_3$.

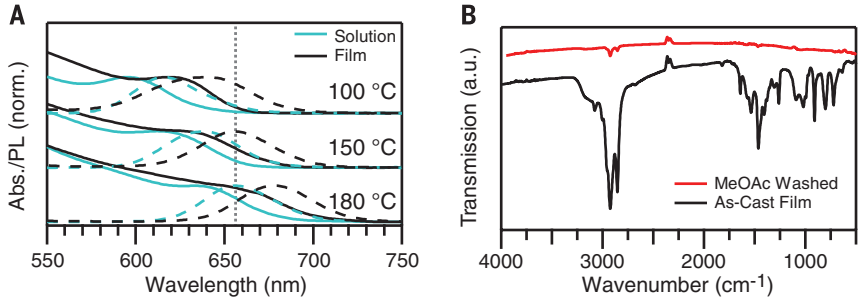

Fig. 3. $CsPbI_3$ QD films. (**A**) UV-visible absorption (solid lines) and PL spectra (dashed lines) of $CsPbI_3$ QDs in solution (blue) and as-cast films (black) for QDs synthesized at 100°, 150°, and 180°C. (**B**) FTIR spectra showing the IR transmission of a $CsPbI_3$ QD film as cast (black) and after treating with MeOAc (red).

injection temperatures between 60° and 185°C to control the size (*28*). This produces QDs solubilized by noncrystalline iodide and oleylammonium surface ligands (*26*). Unpurified QDs transform to the orthorhombic phase within several days (fig. S1) (*28*), as in previous reports (*29*, *30*). However, we developed a process to purify the QDs by using methyl acetate (MeOAc), an antisolvent that removes excess unreacted precursors without inducing agglomeration. Using this extraction procedure, we found that the QDs are stable in the cubic phase for months with ambient storage.

The excitonic peak of $CsPbI_3$ shifted between 585 and 670 nm, corresponding to QD sizes between 3 and 12.5 nm, respectively. The corresponding normalized photoluminescence (PL) spectra of the samples are shown in Fig. 1B, along with a photograph of the QDs in hexane. Upon ultraviolet (UV) excitation, emission was in the orange (600 nm) to red (680 nm) color range, corresponding to a band gap between 2.07 and 1.82 eV (photographs showing PL from dried QD powders are shown in fig. S2) (*28*). The full width at half-maximum of the PL for the smallest QDs was 83 meV and increased slightly for the larger sizes, whereas the PL quantum yield varied from 21 to 55% for different sizes (fig. S3) (*28*).

In contrast to the instability of the cubic phase of bulk $CsPbI_3$ at room temperature, QDs have been reported to retain the cubic phase because of the large contribution of surface energy (Fig. 1D) (*11*, *31*). The softer basic nature of I^- as compared with Br^- results in weaker acid-base interactions between the halide and the oleylammonium ligand (a hard acid) in the case of $CsPbI_3$, compared with that of $CsPbBr_3$ (*30*, *32*). Therefore, the isolation of $CsPbI_3$ QDs is more difficult than that of $CsPbBr_3$ QDs because of the loss of ligand during extraction, causing agglomeration and conversion to the orthorhombic phase. Thus, we found that MeOAc, which isolates the QDs without full removal of the surface species, is critical to the phase-stable devices described below.

The high-resolution transmission electron micrograph (TEM) of the sample synthesized at 180°C (Fig. 1C) shows an interplanar distance of 0.62 nm, which is consistent with the (100) plane of cubic phase $CsPbI_3$ (*24*, *31*, *33*). In Fig. 2, A and B, powder x-ray diffraction (XRD) patterns and UV-visible absorption spectra confirm the absence of diffraction peaks or the high-energy (~3 eV) sharp absorption characteristic of orthorhombic phase formation (*31*), even after 60 days of storage in ambient conditions. Additionally, the QDs remained in the cubic phase even after the solution was cooled to 77 K, further demonstrating the expanded temperature stability of the cubic phase.

Rietveld refinement of the XRD patterns (Fig. 2C) (*28*) allowed us to quantify the contribution from cubic and orthorhombic phases. No detectable orthorhombic phase was found. Additionally, lattice parameters of three different size $CsPbI_3$ QD samples were estimated (Table 1). The lattice parameter values showed a size dependence and were lower than the previously measured experimental value (6.2894 Å at 634 K) of bulk cubic $CsPbI_3$ (*33*). Our measurements were performed

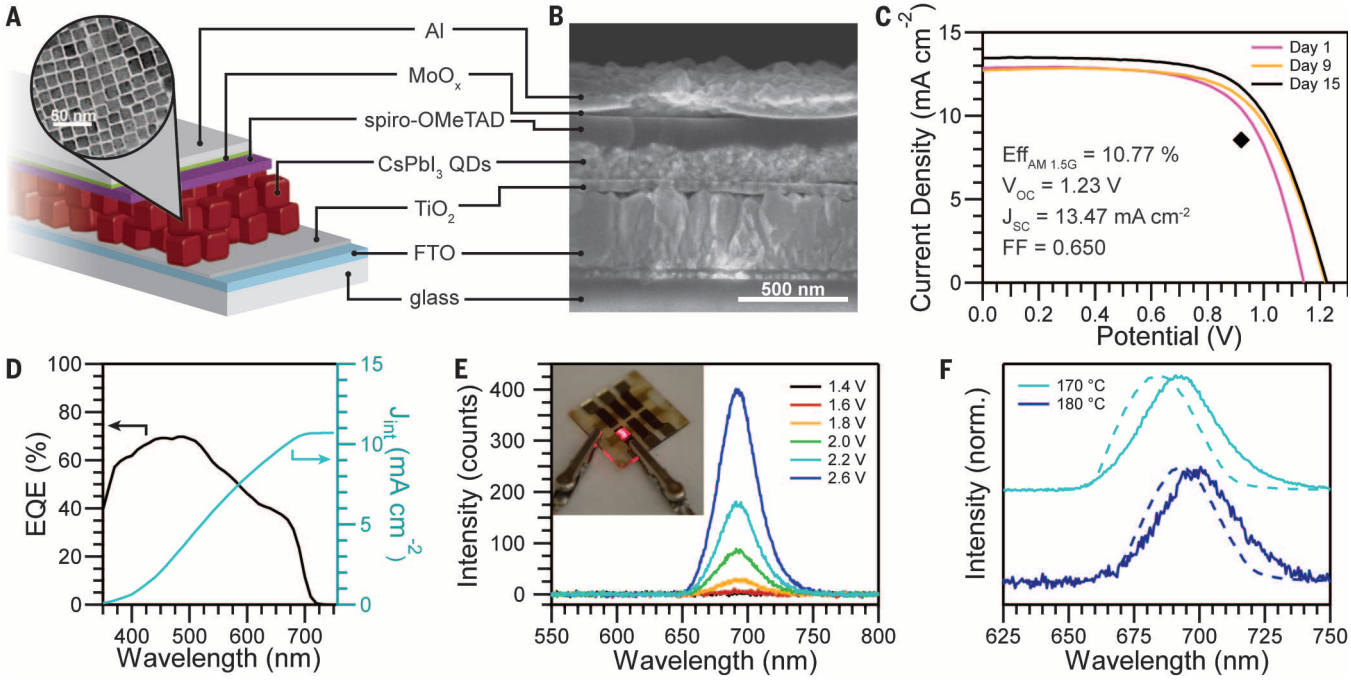

Fig. 4. $CsPbI_3$ optoelectronic devices. (**A**) Schematic (with TEM image of QDs) and (**B**) SEM cross-section of the $CsPbI_3$ PV cell. (**C**) Current density–voltage curves of a device measured in air over the course of 15 days. The black diamond represents the stabilized power output of the device at 0.92 V, as shown in fig. S9. (**D**) External quantum efficiency (black, left ordinate) and integrated current density (blue, right ordinate) of the device. (**E**) EL spectra of $CsPbI_3$ PV cell ($CsPbI_3$ QDs synthesized at 170°C) under forward bias. (Inset) A photograph of the luminescent device. (**F**) PL (dashed lines) and EL (solid lines) spectra of completed devices fabricated by using $CsPbI_3$ QDs synthesized at 170° and 180°C, demonstrating size quantization effects in the completed devices.

Table 1. Results of the Rietveld refinement. *a*, lattice parameter; R_{wp}, weighted-profile *R* factor.

QD size (TEM)	QD size (Rietveld)	*a* (Å)	R_{wp}
8 nm	9 ± 1 nm	6.231 ± 0.002	3.42
9 nm	10 ± 1 nm	6.220 ± 0.002	6.50
15.5 nm	17 ± 2 nm	6.189 ± 0.002	7.79

at 297 K, whereas high temperatures are required to characterize bulk cubic $CsPbI_3$. A similar increase in lattice parameter with decreasing particle size has been reported in other systems and attributed to electrostatic relaxation with decreasing crystal size (*34*).

In order to use these highly phase-stable α-$CsPbI_3$ QDs in optoelectronic devices, we developed a method to cast electronically conductive QD films. The QDs were first spin-cast from octane then dipped in a saturated MeOAc solution of either $Pb(OAc)_2$ or $Pb(NO_3)_2$ (neat MeOAc was used as a control). This process was repeated multiple times—typically, three to five—to produce QD films with thicknesses between 100 and 400 nm. The optical absorption and PL spectra (Fig. 3A, for three samples with indicated reaction temperature) show that in each case, the film absorbance and PL was red-shifted ~20 nm from that of the QDs in solution, whereas the tunable emission properties of the films indicate that quantum confinement is preserved. Fourier-transform infrared (FTIR) spectra show the removal of organic ligands from the film with exposure to neat MeOAc (Fig. 3B), given the near absence of C–H modes near 3000 cm^{-1} or below ~2000 cm^{-1} belonging to oleylammonium, oleate, or octadecene. We therefore attribute the preserved phase stability of the QDs in the films to the size of the crystals (given the quantum confined optical properties) independent of the surface species. However, we found that prolonged annealing at temperatures >200°C causes further grain growth and thus induces a phase transition to the orthorhombic phase (fig. S4 and table S1) (*28*). Additional strategies to preserve the phase in sintered QD films are being explored (*35*). We have observed cubic-phase $CsPbI_3$ with edge length up to 50 nm using the solution-phase synthesis described here.

We also probed the interaction of Pb^{2+} salts with QDs in solution and on films by monitoring the fluorescence (fig. S5) (*28*). Titration of a small amount of $Pb(OAc)_2$ dissolved in MeOAc to the QD solution showed an enhancement in PL, suggesting improved surface passivation. The surface treatments increase the PL lifetime over that of neat QD films, which highlights the importance of surface chemistry in this QD system (fig. S6 and table S2) (*28*). Titrations with only MeOAc caused fast PL quenching. Similarly, dip-coating of the QD film in a saturated solution of $Pb(OAc)_2$ in MeOAc resulted in a PL enhancement of ~350% compared with dip-coating in MeOAc alone.

We fabricated PV cells with $CsPbI_3$ QD films as the photoactive material. A schematic of the device architecture is shown in Fig. 4A, and a scanning electron micrograph (SEM) cross-section image of the reported device with 9 nm QDs is shown in Fig. 4B. The reverse-scan current density-voltage (*JV*) curves showed an open-circuit voltage (V_{OC}) of 1.23 V, and 10.77% PCE for a 0.10 cm^2 cell made and tested completely in ambient conditions (relative humidity ~15 to 25%) (Fig. 4C). The hysteresis along with SPO of a device scanned at various sweep rates is shown in fig. S7 (*28*). Furthermore, the PCE improved from its initial value over the course of 60 days storage in dry but ambient conditions (fig. S8) (*28*). In fig. S9 (*28*), we show the SPO of the cell by measuring the current density while the device is biased at 0.92 V. In Fig. 4D, the spectral response of the PV cell is shown, indicating a band gap of 1.75 eV for this film. We compare QD devices to thin-film $CsPbX_3$ perovskite solar cells following literature reports, which have thus far reported at 9.8% PCE and SPO as high as 6.5% (*4*, *31*, *36*). The QD devices show improved *JV*-scan efficiency, operational stability, and tolerance to higher relative humidity levels (figs. S10 and S11 and table S3) (*28*). The V_{OC} is remarkably higher than that of other QD solar cells (typically <0.7 V) and among the highest V_{OC} in all perovskite PV cells for band gap values below 2 eV (fig. S12, stabilized V_{OC}) (*28*). We have not optimized the device architecture or the QD film-treatment scheme. We found that dip-coating spin-cast films in neat MeOAc and MeOAc saturated with $Pb(OAc)_2$ or $Pb(NO_3)_2$ all work reasonably well (*JV*-scanned PCE > 9%) in PV devices. Large diffusion lengths and mobility values have been measured in $CsPbBr_3$ QDs by means of terahertz spectroscopy (*37*); however, a better understanding of the electronic coupling is critical to maximizing long-range transport in QD perovskite films.

Given the PL properties of these perovskite QDs, we explored their use as LEDs. The PV devices produced bright visible electroluminescence (EL) when biased above V_{OC} (Fig. 4E, inset). The EL had a low turn-on voltage near the band gap of the $CsPbI_3$, with increasing intensity at larger applied biases (Fig. 4E). These spectra provide direct evidence that quantum confinement is retained in the complete devices, which is critical to retaining the improved cubic-phase stability, as seen by the shift in both the EL and PL spectra of devices with different-size QDs (Fig. 4F). The synthesis of normally unstable material phases stabilized through colloidal QD synthesis provides another mechanism for material design for PVs, LEDs, and other applications.

REFERENCES AND NOTES

1. A. Kojima, K. Teshima, Y. Shirai, T. Miyasaka, *J. Am. Chem. Soc.* **131**, 6050–6051 (2009).
2. D. P. Nenon *et al.*, *Energy Environ. Sci.* **9**, 2072–2082 (2016).
3. S. Sharma, N. Weiden, A. Weiss, *Z. Phys. Chem.* **175**, 63–80 (1992).
4. R. E. Beal *et al.*, *J. Phys. Chem. Lett.* **7**, 746–751 (2016).
5. A. P. Alivisatos, *Science* **271**, 933–937 (1996).
6. S. H. Tolbert, A. P. Alivisatos, *Science* **265**, 373–376 (1994).
7. F. Wang *et al.*, *Nature* **463**, 1061–1065 (2010).
8. C. C. Yang, S. Li, *J. Phys. Chem. C* **112**, 16400–16404 (2008).
9. S. Schlag, H. F. Eicke, *Solid State Commun.* **91**, 883–887 (1994).
10. L. C. Schmidt *et al.*, *J. Am. Chem. Soc.* **136**, 850–853 (2014).
11. L. Protesescu *et al.*, *Nano Lett.* **15**, 3692–3696 (2015).
12. F. Zhang *et al.*, *ACS Nano* **9**, 4533–4542 (2015).
13. D. Zhang, S. W. Eaton, Y. Yu, L. Dou, P. Yang, *J. Am. Chem. Soc.* **137**, 9230–9233 (2015).
14. H. Huang *et al.*, *ACS Appl. Mater. Interfaces* **7**, 28128–28133 (2015).
15. Y. Hassan *et al.*, *Adv. Mater.* **28**, 566–573 (2016).
16. S. Sun, D. Yuan, Y. Xu, A. Wang, Z. Deng, *ACS Nano* **10**, 3648–3657 (2016).
17. T. C. Jellicoe *et al.*, *J. Am. Chem. Soc.* **138**, 2941–2944 (2016).
18. Y. Wang *et al.*, *Adv. Mater.* **27**, 7101–7108 (2015).
19. S. Yakunin *et al.*, *Nat. Commun.* **6**, 8056 (2015).
20. Y. Xu *et al.*, *J. Am. Chem. Soc.* **138**, 3761–3768 (2016).
21. A. Swarnkar *et al.*, *Angew. Chem. Int. Ed. Engl.* **54**, 15424–15428 (2015).
22. F. Hu *et al.*, *ACS Nano* **9**, 12410–12416 (2015).
23. Q. A. Akkerman *et al.*, *J. Am. Chem. Soc.* **138**, 1010–1016 (2016).
24. N. S. Makarov *et al.*, *Nano Lett.* **16**, 2349–2362 (2016).
25. Y. Bekenstein, B. A. Koscher, S. W. Eaton, P. Yang, A. P. Alivisatos, *J. Am. Chem. Soc.* **137**, 16008–16011 (2015).
26. J. De Roo *et al.*, *ACS Nano* **10**, 2071–2081 (2016).
27. Y. S. Park, S. Guo, N. S. Makarov, V. I. Klimov, *ACS Nano* **9**, 10386–10393 (2015).
28. Materials and methods are available as supplementary materials on *Science* Online.
29. C. C. Lin, A. Meijerink, R.-S. Liu, *J. Phys. Chem. Lett.* **7**, 495–503 (2016).
30. Q. A. Akkerman *et al.*, *J. Am. Chem. Soc.* **137**, 10276–10281 (2015).
31. G. E. Eperon *et al.*, *J. Mater. Chem. A* **3**, 19688–19695 (2015).
32. R. G. Pearson, *J. Am. Chem. Soc.* **85**, 3533–3539 (1963).
33. D. M. Trots, S. V. Myagkota, *J. Phys. Chem. Solids* **69**, 2520–2526 (2008).
34. S. Tsunekawa, K. Ishikawa, Z. Li, Y. Kawazoe, A. Kasuya, *Phys. Rev. Lett.* **85**, 3440–3443 (2000).
35. S. Dastidar *et al.*, *Nano Lett.* **16**, 3563–3570 (2016).
36. R. J. Sutton *et al.*, *Adv. Energy Mater.* **6**, 1502458 (2016).
37. G. R. Yettapu *et al.*, *Nano Lett.* **16**, 4838–4848 (2016).

ACKNOWLEDGMENTS

We thank J. van de Lagemaat, W. Tumas, H. Choi, M. Beard, and J. Berry for helpful discussions and B. To for SEM imaging. We acknowledge support from the Center for Advanced Solar Photophysics, an Energy Frontier Research Center funded by the U.S. Department of Energy, Office of Science, Office of Basic Energy Sciences for quantum dot coupling and solar cell structures. Device durability and structural phase characterization was performed within the hybrid perovskite solar cell program of the National Center for Photovoltaics funded by the U.S. Department of Energy, Office of Energy Efficiency and Renewable Energy, Solar Energy Technologies Office under contract DE-AC36-08GO28308DOE. The original conception and QD synthesis was performed under the Laboratory Directed Research and Development program at NREL. A.S. acknowledges the Bhaskara Advanced Solar Energy fellowship funded by the Department of Science and Technology, government of India, and Indo-U.S. Science and Technology Forum (IUSSTF). E.M.S. acknowledges a NASA Space Technology Research Fellowship. D.T.M. acknowledges the NREL Director's Fellowship. All data in the paper and supplementary materials are available. An application has been made for a provisional patent (U.S. patent application no. 62/343,251).

SUPPLEMENTARY MATERIALS

www.sciencemag.org/content/354/6308/92/suppl/DC1
Materials and Methods
Supplementary Text
Figs. S1 to S12
Tables S1 to S3
References (*38*, *39*)

1 June 2016; accepted 7 September 2016
10.1126/science.aag2700

QUANTUM GASES

Ultrafast many-body interferometry of impurities coupled to a Fermi sea

Marko Cetina,[1,2]* Michael Jag,[1,2] Rianne S. Lous,[1,2] Isabella Fritsche,[1,2] Jook T. M. Walraven,[1,3] Rudolf Grimm,[1,2]† Jesper Levinsen,[4] Meera M. Parish,[4] Richard Schmidt,[5,6] Michael Knap,[7] Eugene Demler[6]

The fastest possible collective response of a quantum many-body system is related to its excitations at the highest possible energy. In condensed matter systems, the time scale for such "ultrafast" processes is typically set by the Fermi energy. Taking advantage of fast and precise control of interactions between ultracold atoms, we observed nonequilibrium dynamics of impurities coupled to an atomic Fermi sea. Our interferometric measurements track the nonperturbative quantum evolution of a fermionic many-body system, revealing in real time the formation dynamics of quasi-particles and the quantum interference between attractive and repulsive states throughout the full depth of the Fermi sea. Ultrafast time-domain methods applied to strongly interacting quantum gases enable the study of the dynamics of quantum matter under extreme nonequilibrium conditions.

The nonequilibrium dynamics of fermionic systems is at the heart of many problems in science and technology. The wide range of energy scales, spanning the low energies of excitations near the Fermi surface up to high energies of excitations from deep within the Fermi sea, challenges our understanding of the quantum dynamics in such fundamental systems. The Fermi energy E_F sets the shortest response time for the collective response of a fermionic many-body system through the Fermi time $\tau_F = \hbar/E_F$, where $\hbar$ is the Planck constant divided by 2π. In a metal (i.e., a Fermi sea of electrons), E_F is in the range of a few electron volts, which corresponds to τ_F on the order of 100 attoseconds. Dynamics in condensed matter systems on this time scale can be recorded by attosecond streaking techniques (*1*), and the initial applications were demonstrated by probing photoelectron emission from a surface (*2*). However, despite these advances, the direct observation of the coherent evolution of a fermionic many-body system on the Fermi time scale has remained beyond reach.

In atomic quantum gases, the fermions are much heavier and the densities far lower, which brings τ_F into the experimentally accessible range of typically a few microseconds. Furthermore, the powerful techniques of atom interferometry (*3*) now offer an opportunity to probe and manipulate the real-time coherent evolution of a fermionic quantum many-body system. Such techniques have been successfully used to measure bosonic Hanbury-Brown-Twiss correlations (*4*), to demonstrate topological bands (*5*), to probe quantum and thermal fluctuations in low-dimensional condensates (*6*, *7*), and to measure demagnetization dynamics of a fermionic gas (*8*, *9*). Impurities coupled to a quantum gas provide a unique probe of the many-body state (*10*–*16*). Strikingly, they allow direct access to the system's wave function when the internal states of the impurities are manipulated using a Ramsey atom-interferometric technique (*17*, *18*).

We used dilute ^{40}K atoms in a ^{6}Li Fermi sea to measure the response of the sea to a suddenly introduced impurity. For near-resonant interactions, we observed coherent quantum many-body dynamics involving the entire ^{6}Li Fermi sea. We also observed in real time the formation dynamics of the repulsive and attractive impurity quasiparticles. In the limit of low impurity concentration, our experiments confirm that an elementary Ramsey sequence is equivalent to linear-response frequency-domain spectroscopy. We demonstrate that our time-domain approaches allow us to prepare, control, and measure many-body interacting states.

Our system consists of a small sample of typically 1.5×10^4 ^{40}K impurity atoms immersed in a Fermi sea of 3×10^5 ^{6}Li atoms (*19*, *20*). The mixture is held in an optical dipole trap (Fig. 1A) at a temperature of $T = 430$ nK after forced evaporative cooling. Because of the Li Fermi pressure, and because our optical potential for K has more than twice the strength of that for Li, the K impurities are concentrated in the central region of the large Li cloud. Here they experience a nearly homogeneous environment with an effective Fermi energy of $\varepsilon_F = k_B \times 2.6$ μK (*20*), where k_B is the Boltzmann constant. The corresponding Fermi time, $\tau_F = 2.9$ μs, sets the natural time scale for our experiments. The degeneracy of the Fermi sea is characterized by $k_B T/\varepsilon_F \approx 0.17$. The concentration of K in the Li sea remains low, with $\bar{n}_K/\bar{n}_{Li} \approx 0.2$, where $\bar{n}_{Li}$ is the average Li number density and $\bar{n}_K$ is the average K number density sampled by the K atoms (*20*).

The interaction between the impurity atoms in the internal state K|3⟩ (third-to-lowest Zeeman sublevel) and the Li atoms (always kept in the

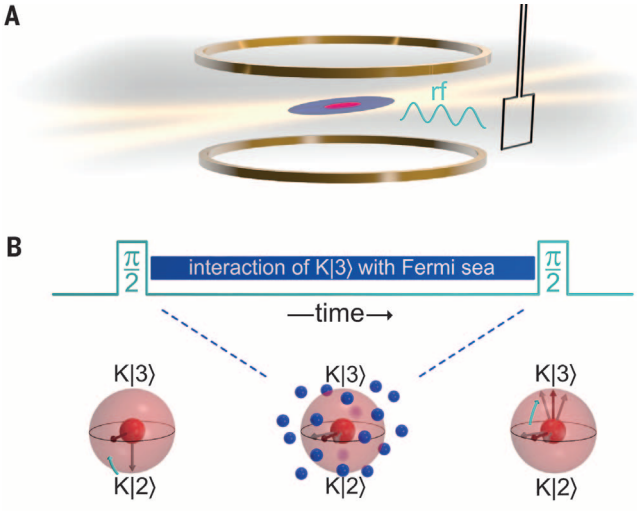

Fig. 1. Illustration of the experimental setup and procedure. (**A**) Li (blue) and K (red) atoms are held in a crossed-beam optical dipole trap, forming the Fermi sea and the sample of impurity atoms, respectively. The magnetic field coils (gold) are used to tune interactions via a Feshbach resonance, and the rf coil (black) allows the manipulation of the spin state of the impurity atoms. (**B**) The Ramsey sequence starts with a first rf $\pi/2$ pulse, which is applied in the presence of weak interactions between the impurity atoms and the Fermi sea. As illustrated on the Bloch sphere, this pulse drives an impurity atom (red dot) into a superposition of the spin states K|2⟩ and K|3⟩. By optical resonance shifting (see text), the interaction of the K|3⟩ component with the atoms of the Fermi sea (blue dots) is abruptly turned on while the K|2⟩ component remains noninteracting. The impurity state then evolves for a variable interaction time, at the end of which its state is probed by a second $\pi/2$ pulse and subsequent measurement of the spin-state populations.

[1]Institut für Quantenoptik und Quanteninformation, Österreichische Akademie der Wissenschaften, 6020 Innsbruck, Austria. [2]Institut für Experimentalphysik, Universität Innsbruck, 6020 Innsbruck, Austria. [3]Van der Waals–Zeeman Institute, Institute of Physics, University of Amsterdam, 1098 XH Amsterdam, Netherlands. [4]School of Physics and Astronomy, Monash University, Victoria 3800, Australia. [5]Institute for Theoretical Atomic, Molecular and Optical Physics (ITAMP), Harvard-Smithsonian Center for Astrophysics, Cambridge, MA 02138, USA. [6]Department of Physics, Harvard University, Cambridge, MA 02138, USA. [7]Department of Physics, Walter Schottky Institute and Institute for Advanced Study, Technical University of Munich, 85748 Garching, Germany.
*Present address: University of Maryland, College Park, MD 20740, USA. †Corresponding author. Email: rudolf.grimm@uibk.ac.at

lowest Zeeman sublevel) is controlled using a rather narrow (*20*) interspecies Feshbach resonance near a magnetic field of 154.7 G (*19*, *21*). We quantify the interaction with the Fermi sea by the dimensionless parameter $X \equiv -1/\kappa_F a$, where $\kappa_F = \hbar^{-1}\sqrt{2m_{Li}\varepsilon_F}$ is the Li Fermi wave number (with m_{Li} the Li mass) and a is the s-wave interspecies scattering length. Slow control of X is realized in a standard way by variations of the magnetic field, whereas fast control is achieved using an optical resonance shifting technique (*19*). The latter permits sudden changes of X by up to ±5 within $\tau_F/15 \approx 200$ ns.

Our interferometric probing method is based on a two-pulse Ramsey scheme (Fig. 1B), following the suggestions of (*17*, *18*). The sequence starts with the impurity atoms prepared in the spin state K|2⟩ (second-to-lowest Zeeman sublevel), for which the background interaction with the Fermi sea can be neglected. An initial radio-frequency (rf) $\pi/2$ pulse, of duration 10 μs, drives the K atoms into a coherent superposition between this noninteracting initial state and the state K|3⟩ under weakly interacting conditions (interaction parameter X_1 with $|X_1| \approx 5$). Using the optical resonance shifting technique (*19*), the system is then rapidly quenched into the strongly interacting regime ($|X| < 1$). After an evolution time t, the system is quenched back into the regime of weak interactions and a second $\pi/2$ pulse is applied. The population difference $N_3 - N_2$ in the two impurity states is measured as a function of the phase ϕ of the rf pulse. By fitting a sine curve to the resulting signal $(N_3 - N_2)/(N_3 + N_2)$, we obtain the contrast $|S(t)|$ and the phase $\varphi(t)$ (*20*), which yields the complex-valued Ramsey signal $S(t) = |S(t)| \exp[-i\varphi(t)]$. In the limit of low impurity concentration and rapid quenching, $S(t) = \langle \exp(i\hat{H}_0 t/\hbar)\exp(-i\hat{H}t/\hbar)\rangle$ describes the sensitivity of the time evolution to perturbations of the system. Here, the angle brackets denote the quantum statistical average, the Hamiltonian $\hat{H}_0$ describes the noninteracting Fermi gas, and the interacting Hamiltonian $\hat{H}$ differs from $\hat{H}_0$ by the additional scattering between the Fermi sea atoms and the impurity atoms. The function $S(t)$, which for pure initial states is often referred to as the Loschmidt amplitude (*22*), was introduced in the context of nuclear magnetic resonance experiments (*23*) and was also applied in the analysis of the orthogonality catastrophe (*24*) as well as in the study of quantum chaos (*25*).

We first consider the interaction conditions for which earlier experiments have demonstrated that the spectral response is dominated by polaronic quasi-particles (*15*). Figure 2, A to D, shows the evolution of the contrast and the phase measured in the repulsive and the attractive polaron regimes, where $X = -0.23 \pm 0.06$ and $X = 0.86 \pm 0.06$, respectively. For short evolution times up to ~4 τ_F, we observed that both contrast signals exhibit a similar initial parabolic transient, which is typical of a Loschmidt echo (*25*). For longer times, this connects to an exponential decay of the contrast and a linear evolution of the phase. In (*19*), we showed that the exponential decay of the contrast in this regime can be interpreted in terms of quasiparticle scattering. Here, the linear phase evolution corresponds to the energy shift of the quasiparticle state, for which we obtain $(+0.29 \pm 0.01)\ \varepsilon_F$ for the repulsive case in Fig. 2C and $(-0.27 \pm 0.01)\ \varepsilon_F$ for the attractive case in Fig. 2D. The longer-time behavior reflects the quasiparticle properties, whereas the observed initial parabolic transient reveals the ultrafast real-time dynamics of the quasiparticle formation.

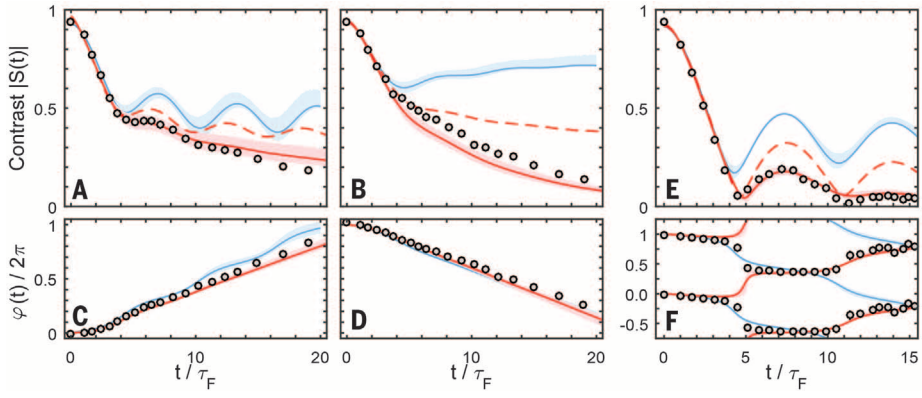

Fig. 2. Impurity dynamics in the Fermi sea. (**A** and **C**) Contrast $|S(t)|$ and phase $\varphi(t)$ of the interference signal depending on the interaction time t in the repulsive polaron regime for $X = -0.23 \pm 0.06$, with the rf pulse applied at $X_1 = -3.9$. (**B** and **D**) Same quantities in the attractive polaron regime for $X = 0.86 \pm 0.06$ and $X_1 = 5.8$. (**E** and **F**) Same quantities for resonant interactions ($X = 0.08 \pm 0.05$, $X_1 = 4.8$). The solid blue lines show the results of the TBM calculations. The solid red lines show the results of the FDA calculations at the measured temperature; the dashed red lines show the calculated results at zero temperature. The shaded regions indicate the uncertainty range resulting from the combined experimental errors in X, k_BT, and ε_F. The errors in the experimental data are typically smaller than the symbol size. The multiple representation of $\varphi(t)$ in (F) accounts for the ambiguity of a phase modulo 2π.

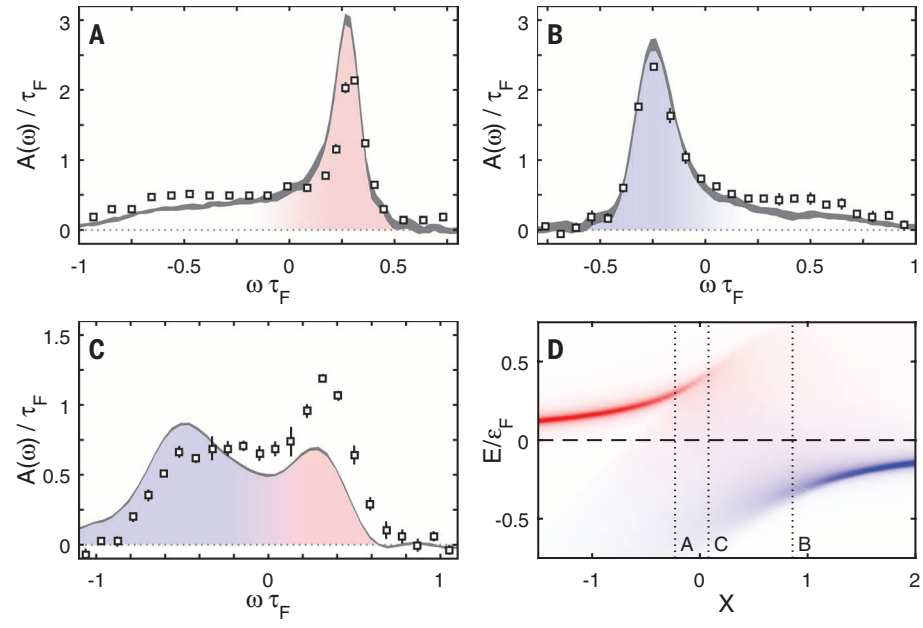

Fig. 3. Frequency-domain rf spectroscopy versus time-domain Ramsey spectroscopy. (**A** to **C**) The data points show the rf spectra for the repulsive ($X = -0.23 \pm 0.06$), attractive ($X = 0.86 \pm 0.06$), and resonant ($X = 0.08 \pm 0.05$) cases, all normalized to unit integral. Here, ω corresponds to the detuning of the rf frequency from the unperturbed transition frequency. The gray lines correspond to the Fourier transform of the $S(t)$ data from Fig. 2, with their widths indicating the standard error resulting from the combined experimental uncertainties in the $S(t)$ data. The red and blue shading indicates the repulsive and attractive parts of the excitation spectrum, respectively. (**D**) Diagram of the excitation energy versus the interaction parameter, showing the repulsive (red) and the attractive (blue) quasiparticle branches. For illustrative purposes, we model the spectrum by a calculation of the spectral function together with additional broadening simulating the effects of finite rf pulse duration and finite temperatures. The three vertical dotted lines indicate the interaction conditions of (A) to (C).

On resonance, for the strongest possible interactions, a description of the dynamics in terms of a single dominant quasiparticle excitation breaks down. In this regime, our measurements—displayed in Fig. 2, E and F, for $X = 0.08 \pm 0.05$—reveal the striking quantum dynamics of an interacting fermionic system forced into a state far out of equilibrium. The contrast $|S(t)|$ shows pronounced oscillations reaching almost zero, which indicates that the time-evolved state can become almost orthogonal to the initial state. Meanwhile, the phase $\varphi(t)$ exhibits plateaus with jumps of π near the contrast minima.

To further interpret our measurements, we used two different theoretical approaches: the truncated basis method (TBM) (*20*) and the functional determinant approach (FDA) (*18*). The TBM models our full experimental procedure assuming zero temperature and considering only single particle-hole excitations. This approximation, first introduced in (*26*) to model the attractive polaron, was later applied to predict repulsive quasi-particles in cold gases (*27*). The predictions of the TBM are represented by the blue lines in Fig. 2. This method accurately describes the initial transient as well as the period of the oscillations of $S(t)$ on resonance. Although the zero-temperature TBM calculation naturally overestimates the contrast in the thermally dominated regime ($t > 6\ \tau_F$), it accurately reproduces the observed linear phase evolution and thus the quasiparticle energy. The FDA is an exact solution for a fixed impurity at arbitrary temperatures, taking into account the nonperturbative creation of infinitely many particle-hole pairs. The FDA calculation is represented by the solid red lines in Fig. 2. We see excellent agreement with our experimental results, which indicates that the effects of impurity motion remain small in our system. This observation can be explained by the fact that our impurity is sufficiently heavy so that the effects of its recoil with energies of ~$0.25\ \varepsilon_F$ (*20*) are masked by thermal fluctuations. To identify the effect of temperature, we performed a corresponding FDA calculation for $T = 0$; the results are shown as dashed lines in Fig. 2. Here, we see a slower decay of $|S(t)|$, which follows a power law at long times (*20*) under the idealizing assumption of infinitely heavy impurities.

Time-domain and frequency-domain methods are closely related, as is well known in spectroscopy. In the limit of low impurity density, where the interactions between the impurities can be neglected, $S(t)$ is predicted to be proportional to the inverse Fourier transform of the linear excitation spectrum $A(\omega)$ of the impurity (*24*). To benchmark our interferometric method, we measured $A(\omega)$ using rf spectroscopy, similar to our earlier work (*12*) but with great care taken to ensure a linear response (*20*). The measured excitation spectra are shown in Fig. 3, A to C, together with a schematic energy diagram of the quasiparticle branches (Fig. 3D). In the repulsive and attractive polaron regimes, we observed the characteristic structure of a peak on top of a broad pedestal (*15*). The peak corresponds to the long-time evolution of the quasiparticle, whereas the pedestal is associated with the rapid dynamics related to the emergence of many-body correlations. For resonant interactions, the rf response is broad and nearly symmetric. The latter implies that the imaginary part of $S(t)$ remains small. Consequently, as seen in Fig. 2, E and F, the phase $\varphi(t)$ essentially takes values near 0 and π, and each phase jump is accompanied by a pronounced minimum of $|S(t)|$.

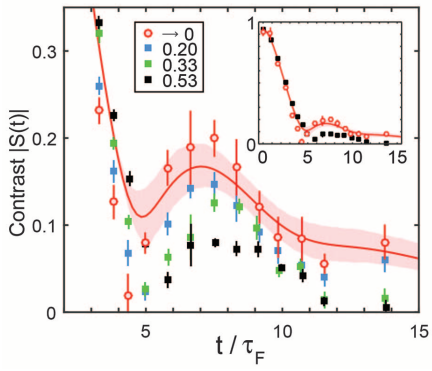

Fig. 4. Observation of induced impurity-impurity interactions. Resonant dynamics of the contrast is shown for $X = -0.01 \pm 0.05$, $X_1 = 5.2$, $\varepsilon_F = k_B \times (2.1 \pm 0.1)$ μK, $k_BT/\varepsilon_F = 0.24 \pm 0.02$, and different impurity concentrations $\overline{n}_K/\overline{n}_{Li}$. The black, green, and blue squares correspond to $\overline{n}_K/\overline{n}_{Li} = 0.53$, 0.33, and 0.20, respectively. The red circles correspond to the linear extrapolation of the complex $S(t)$ data to the limit of a single impurity, taking into account the errors in the data. The inset reproduces this extrapolation together with the highest-concentration data points. The red line shows the result of the FDA calculation, and the shaded region indicates the corresponding uncertainty range resulting from the combined experimental errors in X, k_BT, and ε_F.

The apparent double-hump structure of the spectral response in the resonance regime suggests an interpretation of the observed oscillations of $S(t)$ (Fig. 2E) in terms of a quantum beat between the repulsive and attractive branches of our many-body system. The two branches are strongly broadened and overlap (Fig. 3D), which results in a strong damping of the oscillations.

A detailed comparison of our time- and frequency-domain measurements reveals the potential of our approach to prepare and control many-body states. This is illustrated in Fig. 3, where we show the Fourier transform of the $S(t)$ data from Fig. 2 as gray curves. We observed that time-domain measurements where the rf pulses are applied in the presence of weakly repulsive interactions (Fig. 3A) emphasize the upper branch of the many-body system, whereas in the attractive case (Fig. 3, B and C), the lower branch is emphasized relative to the rf spectra. We interpret this as a consequence of the fact that the residual interactions during the rf pulse already bring the system into a weakly interacting polaron state before it is quenched to resonance (*20*). Relative to the noninteracting initial state used in frequency-domain spectroscopy, these polarons have an increased wave function overlap with the corresponding strongly interacting repulsive and attractive branches, leading to the observed shift in the spectral weight. Our measurements show that the control over the initial state of many particles can be used to manipulate quantum dynamics in the strongly interacting regime. This unique capability of time-domain techniques can potentially be exploited in a wide range of applications, including the study of the dynamical behavior near the phase transition from a polaronic to a molecular system (*15*) and the creation of specific excitations of a Fermi sea down to individual atoms (*28*).

Our interpretation of the results in Figs. 2 and 3 relies on the assumption that our fermionic impurities are sufficiently dilute so that any interactions between them can be neglected. By increasing the impurity concentration, we can extend our experiments into a complex many-body regime where the impurities interact both with the Fermi sea and with each other (*20*). Figure 4 shows the time-dependent contrast measured for $k_BT = 0.24 \pm 0.02\ \varepsilon_F$ and $\overline{n}_K/\overline{n}_{Li} = 0.20$, 0.33, and 0.53. An extrapolation of the $S(t)$ data to zero concentration (open red circles) lies close to the data points for $\overline{n}_K/\overline{n}_{Li} = 0.20$, which is the typical concentration in our measurements and agrees with the FDA calculation. This confirms that the physics that we access in the measurements with a small sample of fermionic impurities is close to that of a single impurity, which we posit to be a consequence of the fermionic nature of the impurities. When the impurity concentration is increased, we find that the contrast for $t > 5\ \tau_F$ is decreased and the period of the revivals of $|S(t)|$ is prolonged. We interpret this as arising from effective interactions between the impurities induced by the Fermi sea (*29*, *30*). Such interactions between fermionic impurities are predicted to lead to interesting quantum phases (*31*).

Our results demonstrate the power of many-body interferometry to study ultrafast processes in strongly interacting Fermi gases in real time, including the formation dynamics of quasi-particles and the nonequilibrium dynamics arising from quantum interference between different many-body branches. Of particular interest is the prospect of observing Anderson's orthogonality catastrophe (*18*, *20*) by further cooling the Li Fermi sea (*32*) while pinning the K atoms in a deep species-selective optical lattice (*33*).

REFERENCES AND NOTES

1. F. Krausz, M. Ivanov, *Rev. Mod. Phys.* **81**, 163–234 (2009).
2. R. Pazourek, S. Nagele, J. Burgdörfer, *Rev. Mod. Phys.* **87**, 765–802 (2015).
3. A. D. Cronin, J. Schmiedmayer, D. E. Pritchard, *Rev. Mod. Phys.* **81**, 1051–1129 (2009).
4. J. Simon *et al.*, *Nature* **472**, 307–312 (2011).
5. M. Atala *et al.*, *Nat. Phys.* **9**, 795–800 (2013).
6. M. Gring *et al.*, *Science* **337**, 1318–1322 (2012).
7. Z. Hadzibabic, P. Krüger, M. Cheneau, B. Battelier, J. Dalibard, *Nature* **441**, 1118–1121 (2006).
8. M. Koschorreck, D. Pertot, E. Vogt, M. Köhl, *Nat. Phys.* **9**, 405–409 (2013).
9. A. B. Bardon *et al.*, *Science* **344**, 722–724 (2014).

10. A. Schirotzek, C.-H. Wu, A. Sommer, M. W. Zwierlein, *Phys. Rev. Lett.* **102**, 230402 (2009).
11. S. Nascimbène *et al.*, *Phys. Rev. Lett.* **103**, 170402 (2009).
12. C. Kohstall *et al.*, *Nature* **485**, 615–618 (2012).
13. M. Koschorreck *et al.*, *Nature* **485**, 619–622 (2012).
14. Y. Zhang, W. Ong, I. Arakelyan, J. E. Thomas, *Phys. Rev. Lett.* **108**, 235302 (2012).
15. P. Massignan, M. Zaccanti, G. M. Bruun, *Rep. Prog. Phys.* **77**, 034401 (2014).
16. M. Sidler *et al.*, http://arXiv.org/abs/1603.09215 (2016).
17. J. Goold, T. Fogarty, N. Lo Gullo, M. Paternostro, T. Busch, *Phys. Rev. A* **84**, 063632 (2011).
18. M. Knap *et al.*, *Phys. Rev. X* **2**, 041020 (2012).
19. M. Cetina *et al.*, *Phys. Rev. Lett.* **115**, 135302 (2015).
20. See supplementary materials on *Science* Online.
21. D. Naik *et al.*, *Eur. Phys. J. D* **65**, 55–65 (2011).
22. J. Loschmidt, *Sitzungsber. Akad. Wissenschaften Wien* **73**, 128 (1876).
23. E. L. Hahn, *Phys. Rev.* **80**, 580–594 (1950).
24. P. Nozières, C. T. De Dominicis, *Phys. Rev.* **178**, 1097–1107 (1969).
25. R. A. Jalabert, H. M. Pastawski, *Adv. Solid State Phys.* **41**, 483–496 (2001).
26. F. Chevy, *Phys. Rev. A* **74**, 063628 (2006).
27. X. Cui, H. Zhai, *Phys. Rev. A* **81**, 041602 (2010).
28. J. Dubois *et al.*, *Nature* **502**, 659–663 (2013).
29. C. Mora, F. Chevy, *Phys. Rev. Lett.* **104**, 230402 (2010).
30. Z. Yu, S. Zöllner, C. J. Pethick, *Phys. Rev. Lett.* **105**, 188901 (2010).
31. W. Zwerger, Ed., *The BCS-BEC Crossover and the Unitary Fermi Gas* (Springer, 2012).
32. R. A. Hart *et al.*, *Nature* **519**, 211–214 (2015).
33. L. J. LeBlanc, J. H. Thywissen, *Phys. Rev. A* **75**, 053612 (2007).

ACKNOWLEDGMENTS

We thank M. Baranov, F. Schreck, G. Bruun, N. Davidson, and R. Folman for stimulating discussions. Supported by NSF through a grant for ITAMP at Harvard University and the Smithsonian Astrophysical Observatory (R.S.); the Technical University of Munich-Institute for Advanced Study, funded by the German Excellence Initiative and the European Union FP7 under grant agreement 291763 (M.K.); the Harvard-MIT Center for Ultracold Atoms, NSF grant DMR-1308435, the Air Force Office of Scientific Research Quantum Simulation Multidisciplinary University Research Initiative (MURI), the Army Research Office MURI on Atomtronics, M. Rössler, the Walter Haefner Foundation, the ETH Foundation, and the Simons Foundation (E.D.); and the Austrian Science Fund (FWF) within the SFB FoQuS (F4004-N23) and within the DK ALM (W1259-N27).

SUPPLEMENTARY MATERIALS

www.sciencemag.org/content/354/6308/96/suppl/DC1
Materials and Methods
Supplementary Text
Figs. S1 to S11
Table S1
References (*34*–*56*)

20 February 2016; accepted 6 September 2016
10.1126/science.aaf5134

DEVICE TECHNOLOGY

MoS_2 transistors with 1-nanometer gate lengths

Sujay B. Desai,[1,2,3] Surabhi R. Madhvapathy,[1,2] Angada B. Sachid,[1,2] Juan Pablo Llinas,[1,2] Qingxiao Wang,[4] Geun Ho Ahn,[1,2] Gregory Pitner,[5] Moon J. Kim,[4] Jeffrey Bokor,[1,2] Chenming Hu,[1] H.-S. Philip Wong,[5] Ali Javey[1,2,3]*

Scaling of silicon (Si) transistors is predicted to fail below 5-nanometer (nm) gate lengths because of severe short channel effects. As an alternative to Si, certain layered semiconductors are attractive for their atomically uniform thickness down to a monolayer, lower dielectric constants, larger band gaps, and heavier carrier effective mass. Here, we demonstrate molybdenum disulfide (MoS_2) transistors with a 1-nm physical gate length using a single-walled carbon nanotube as the gate electrode. These ultrashort devices exhibit excellent switching characteristics with near ideal subthreshold swing of ~65 millivolts per decade and an On/Off current ratio of ~10^6. Simulations show an effective channel length of ~3.9 nm in the Off state and ~1 nm in the On state.

As Si transistors rapidly approach their projected scaling limit of ~5-nm gate lengths, exploration of new channel materials and device architectures is of utmost interest (*1*–*3*). This scaling limit arises from short channel effects (*4*). Direct source-to-drain tunneling and the loss of gate electrostatic control on the channel severely degrade the Off state leakage currents, thus limiting the scaling of Si transistors (*5*, *6*). Certain semiconductor properties dictate the magnitude of these effects for a given gate length. Heavier carrier effective mass, larger band gap, and lower in-plane dielectric constant yield lower direct source-to-drain tunneling currents (*7*). Uniform and atomically thin semiconductors with low in-plane dielectric constants are desirable for enhanced electrostatic control of the gate. Thus, investigation and introduction of semiconductors that have more ideal properties than Si could lead to further scaling of transistor dimensions with lower Off state dissipation power.

Transition metal dichalcogenides (TMDs) are layered two-dimensional (2D) semiconductors that have been widely explored as a potential channel material replacement for Si (*8*–*11*), and each material exhibits different band structures and properties (*12*–*16*). The layered nature of TMDs allows uniform thickness control with atomic-level precision down to the monolayer limit. This thickness scaling feature of TMDs is highly desirable for well-controlled electrostatics in ultrashort transistors (*3*). For example, monolayer and few-layer MoS_2 have been shown theoretically to be superior to Si at the sub-5-nm scaling limit (*17*, *18*).

The scaling characteristics of MoS_2 and Si transistors as a function of channel thickness and gate length are summarized in Fig. 1. We calculated direct source-to-drain tunneling currents ($I_{SD\text{-}LEAK}$) in the Off state for different channel lengths and thicknesses using a dual-gate device structure (fig. S1) as a means to compare the two materials. MoS_2 shows more than two orders of magnitude reduction in $I_{SD\text{-}LEAK}$ relative to Si mainly because of its larger electron effective mass along the transport direction ($m_n^* \sim 0.55m_0$ for MoS_2 versus $m_n^* \sim 0.19m_0$ for Si [100]) (*19*), with a trade-off resulting in lower ballistic On current. Notably, $I_{SD\text{-}LEAK}$ does not limit the scaling of monolayer MoS_2 even down to the ~1-nm gate length, presenting a major advantage over Si [see more details about calculations in the supplementary materials (*20*)]. Finally, few-layer MoS_2 exhibits a lower in-plane dielectric constant (~4) compared with bulk Si (~11.7), Ge (~16.2), and GaAs (~12.9), resulting in a shorter electrostatic characteristic length (λ) as depicted in fig. S2 (*21*).

The above qualities collectively make MoS_2 a strong candidate for the channel material of future transistors at the sub-5-nm scaling limit. However, to date, TMD transistors at such small gate lengths have not been experimentally explored. Here, we demonstrate 1D gated, 2D semiconductor field-effect transistors (1D2D-FETs) with a single-walled carbon nanotube (SWCNT) gate, a MoS_2 channel, and physical gate lengths of ~1 nm. The 1D2D-FETs exhibit near ideal switching characteristics, including a subthreshold swing (SS) of ~65 mV per decade at room temperature and high On/Off current ratios. The SWCNT diameter $d \sim 1$ nm for the gate electrode (*22*) minimized parasitic gate to source-drain capacitance, which is characteristic of lithographically patterned tall gate structures. The ~1-nm gate length of the SWCNT also allowed for the experimental exploration of the device physics and properties of MoS_2 transistors as a function of semiconductor thickness (i.e., number of layers) at the ultimate gate-length scaling limit.

The experimental device structure of the 1D2D-FET (Fig. 2A) consists of a MoS_2 channel (number of layers vary), a ZrO_2 gate dielectric, and a SWCNT gate on a 50-nm SiO_2/Si substrate with a physical gate length ($L_G \sim d$) of ~1 nm. Long, aligned SWCNTs grown by chemical vapor deposition

[1]Electrical Engineering and Computer Sciences, University of California, Berkeley, CA 94720, USA. [2]Materials Sciences Division, Lawrence Berkeley National Laboratory, Berkeley, CA 94720, USA. [3]Berkeley Sensor and Actuator Center, University of California, Berkeley, CA 94720, USA. [4]Department of Materials Science and Engineering, University of Texas at Dallas, Richardson, TX 75080, USA. [5]Electrical Engineering, Stanford University, Stanford, CA 94305, USA.
*Corresponding author. Email: ajavey@eecs.berkeley.edu

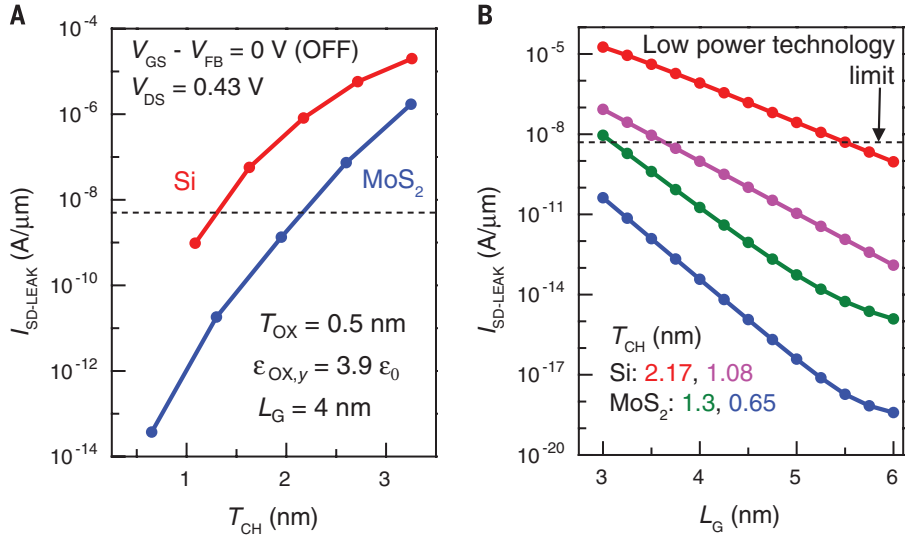

Fig. 1. Direct source-to-drain tunneling leakage current. (**A**) Normalized direct source-to-drain tunneling leakage current ($I_{SD-LEAK}$), calculated using the WKB (Wentzel-Kramers-Brillouin) approximation as a function of channel thickness T_{CH} for Si and MoS_2 in the Off state. $V_{DS} = V_{DD} = 0.43$ V from the International Technology Roadmap for Semiconductors (ITRS) 2026 technology node. (**B**) $I_{SD-LEAK}$ as a function of gate length L_G for different thicknesses of Si and MoS_2 for the same Off state conditions as Fig. 1A. The dotted line in Fig. 1, A and B represents the low operating power limit for the 2026 technology node as specified by the ITRS.

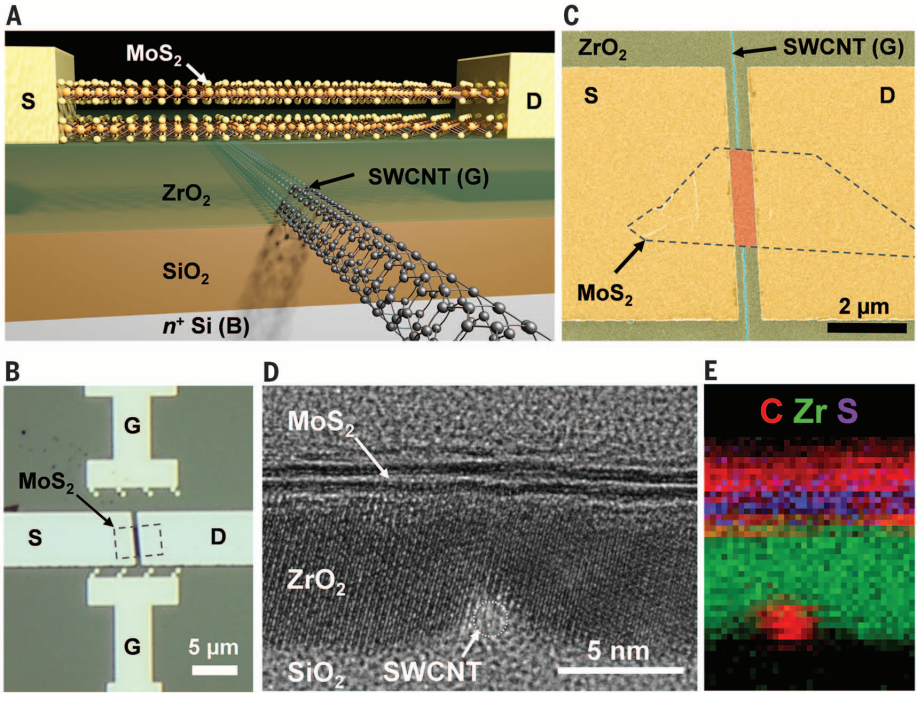

Fig. 2. 1D2D-FET device structure and characterization. (**A**) Schematic of 1D2D-FET with a MoS_2 channel and SWCNT gate. (**B**) Optical image of a representative device shows the MoS_2 flake, gate (G), source (S), and drain (D) electrodes. (**C**) False-colored SEM image of the device showing the SWCNT (blue), ZrO_2 gate dielectric (green), MoS_2 channel (orange), and the Ni source and drain electrodes (yellow). (**D**) Cross-sectional TEM image of a representative sample showing the SWCNT gate, ZrO_2 gate dielectric, and bilayer MoS_2 channel. (**E**) EELS map showing spatial distribution of carbon, zirconium, and sulfur in the device region, confirming the location of the SWCNT, MoS_2 flake, and ZrO_2 dielectric.

were transferred onto a n^+ Si/SiO_2 substrate (50-nm-thick SiO_2) (*23*), located with a scanning electron microscope (SEM), and contacted with palladium via lithography and metallization. These steps were followed by atomic layer deposition (ALD) of ZrO_2 and pick-and-place dry transfer of MoS_2 onto the SWCNT covered by ZrO_2 (*14*). Nickel source and drain contacts were made to MoS_2 to complete the device. The detailed process flow and discussion about device fabrication is provided in fig. S3.

Figure 2B shows the optical image of a representative 1D2D-FET capturing the MoS_2 flake, the source and drain contacts to MoS_2, and the gate contacts to the SWCNT. The SWCNT and the MoS_2 flake can be identified in the false-colored SEM image of a representative sample (Fig. 2C). The 1D2D-FET consists of four electrical terminals; source (S), drain (D), SWCNT gate (G), and the n^+ Si substrate back gate (B). The SWCNT gate underlaps the S/D contacts. These underlapped regions were electrostatically doped by the Si back gate during the electrical measurements, thereby serving as n^+ extension contact regions. The device effectively operated like a junctionless transistor (*24*), where the SWCNT gate locally depleted the n^+ MoS_2 channel after applying a negative voltage, thus turning Off the device.

A cross-sectional transmission electron microscope (TEM) image of a representative 1D2D-FET (Fig. 2D) shows the SWCNT gate, ZrO_2 gate dielectric (thickness T_{OX}~5.8 nm), and the bilayer MoS_2 channel. The topography of ZrO_2 surrounding the SWCNT and the MoS_2 flake on top of the gate oxide was flat, as seen in the TEM image. This geometry is consistent with ALD nucleation initiating on the SiO_2 substrate surrounding the SWCNT and eventually covering it completely as the thickness of deposited ZrO_2 exceeds the SWCNT diameter d (*25*). The spatial distribution of carbon, zirconium, and sulfur was observed in the electron energy-loss spectroscopy (EELS) map of the device region (Fig. 2E), thus confirming the location of the SWCNT, ZrO_2, and MoS_2 in the device (fig. S4) (*20*).

The electrical characteristics for a 1D2D-FET with a bilayer MoS_2 channel (Fig. 3) show that the MoS_2 extension regions (the underlapped regions between the SWCNT gate and S/D contacts) could be heavily inverted (i.e., n^+ state) by applying a positive back-gate voltage of $V_{BS} = 5$ V to the Si substrate. The I_D-V_{BS} characteristics (fig. S5) indicate that the MoS_2 flake was strongly inverted by the back gate at $V_{BS} = 5$ V. The I_D-V_{GS} characteristics for the device at $V_{BS} = 5$ V and $V_{DS} =$ 50 mV and 1 V (Fig. 3A) demonstrate the ability of the ~1-nm SWCNT gate to deplete the MoS_2 channel and turn Off the device. The 1D2D-FET exhibited excellent subthreshold characteristics with a near ideal SS of ~65 mV per decade at room temperature and On/Off current ratio of ~10^6. The drain-induced barrier lowering (DIBL) was ~290 mV/V. Leakage currents through the SWCNT gate (I_G) and the n^+ Si back gate (I_B) are at the measurement noise level (Fig. 3A). The interface trap density (D_{IT}) of the ZrO_2-MoS_2 interface estimated from SS was ~1.7 × 10^{12} cm^{-2} eV^{-1},

which is typical for transferred MoS_2 flakes (*26*) because of the absence of surface dangling bonds (*20*).

Figure 3B shows the I_D-V_{DS} characteristics at different V_{GS} values and fixed V_{BS} = 5 V. The I_D-V_{GS} characteristics depended strongly on the value of V_{BS}, which affects the extension region resistance. The inversion of the extension regions increased with increasing V_{BS}, thus reducing the series resistance and contact resistance and led to an increase in the On current and an improvement in the SS. At more positive values of V_{BS}, V_{GS} had to be more negative in order to deplete the MoS_2 channel, which in turn made the threshold voltage (V_T) more negative. Above V_{BS} = 1 V, the SS and I_{On} did not improve any further, and the extension regions were strongly inverted (Fig. 3C). Thus, the 1D2D-FET operated as a short-channel device.

We performed detailed simulations using Sentaurus TCAD to understand the electrostatics of the 1D2D-FET. The Off and On state conditions correspond to (V_{GS}-V_T) of −0.3 V and 1.5 V, respectively (which give an On/Off current ratio of ~10^6). The electric field contour plot (Fig. 3D) in the Off state has a region of low electric field in the MoS_2 channel near the SWCNT, indicating that it is depleted. The reduced electron density in the MoS_2 channel (Fig. 3E), and the presence of an energy barrier to electrons in the conduction band (fig. S6A) are also consistent with the Off state of the device. The extension regions are still under inversion because of the positive back-gate voltage. The electron density of the MoS_2 channel in the depletion region can be used to define the effective channel length (L_{EFF}) of the 1D2D-FET, which is the region of channel controlled by the SWCNT gate (*27*–*29*). The channel is considered to be depleted if the electron density falls below a defined threshold ($n_{threshold}$). The Off state L_{EFF}, defined as the region of MoS_2 with electron density $n < n_{threshold}$ ($n_{threshold}$ = 1.3 × 10^5 cm^{-2}), for this simulated 1D2D-FET is L_{EFF} ~ 3.9 nm (Fig. 3E). L_{EFF} is dependent on V_{GS} and the value of $n_{threshold}$ (fig. S7).

As the device is turned Off, the fringing electric fields from the SWCNT (Fig. 3D) deplete farther regions of the MoS_2 channel and thus increase L_{EFF}. The short height of the naturally defined SWCNT gate prevents large fringing fields from controlling the channel and hence achieves a smaller L_{EFF} compared with lithographically patterned gates (fig. S8). The electric field and electron density contours for the device in the On state confirm the strong inversion of the channel region near the SWCNT (Fig. 3, F and G) with L_{EFF} ~ L_G = 1 nm. The energy bands in this case are flat in the entire channel region (fig. S6B), with the On state current being limited by the resistance of the extension regions and mainly the contacts. Doped S/D contacts along with shorter extension regions will result in increased On current.

The effect of T_{OX} scaling on short-channel effects like DIBL was also studied using simulations (fig. S9). The electrostatics of the device improves, and the influence of the drain on the channel reduces, as T_{OX} is scaled down to values

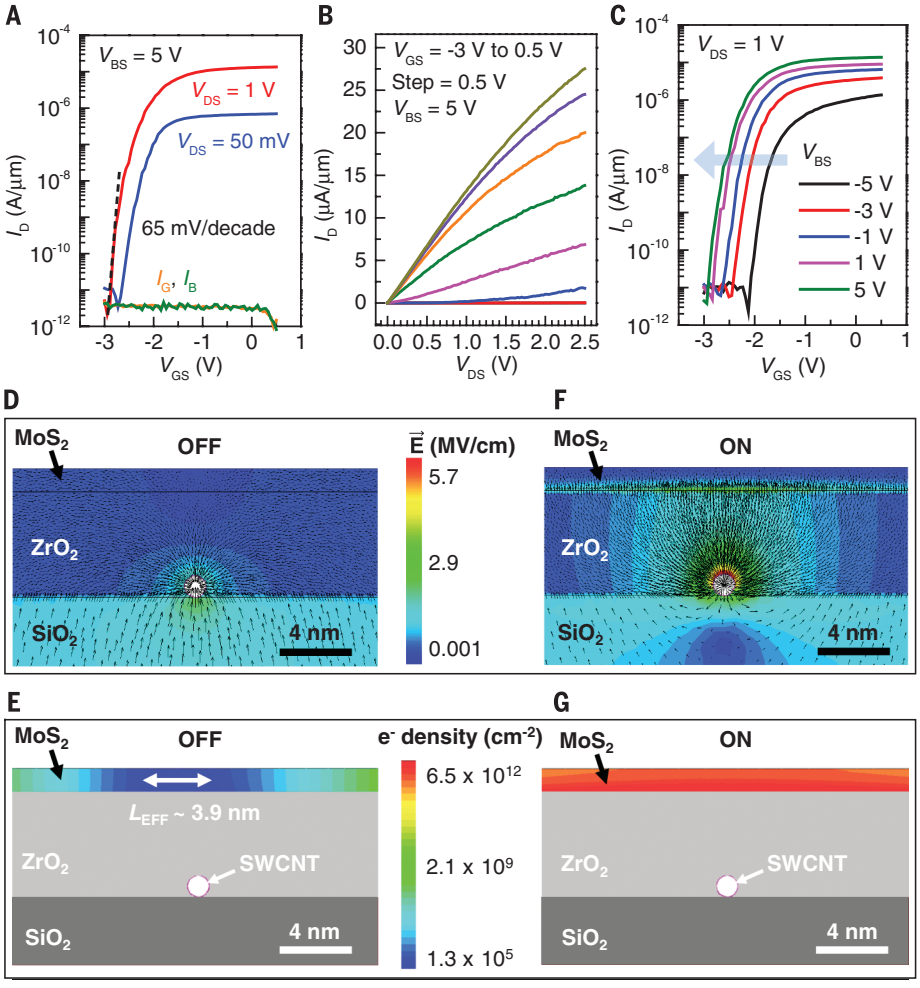

Fig. 3. Electrical characterization and TCAD simulations of 1D2D-FET. (**A**) I_D-V_{GS} characteristics of a bilayer MoS_2 channel SWCNT gated FET at V_{BS} = 5 V and V_{DS} = 50 mV and 1 V. The positive V_{BS} voltage electrostatically dopes the extension regions n^+. (**B**) I_D-V_{DS} characteristic for the device at V_{BS} = 5 V and varying V_{GS}. (**C**) I_D-V_{GS} characteristics at V_{DS} = 1 V and varying V_{BS} illustrating the effect of back-gate bias on the extension region resistance, SS, On current, and device characteristics. Electric field contour plots for a simulated bilayer MoS_2 device using TCAD in the (**D**) Off and (**F**) On state. Electron density plots for the simulated device using TCAD in the (**E**) Off and (**G**) On state. The electron density in the depletion region is used to define the L_{EFF}. L_{EFF} ~ d ~ L_G in the On state and L_{EFF} > L_G in the Off state because of the fringing electric fields from the SWCNT gate.

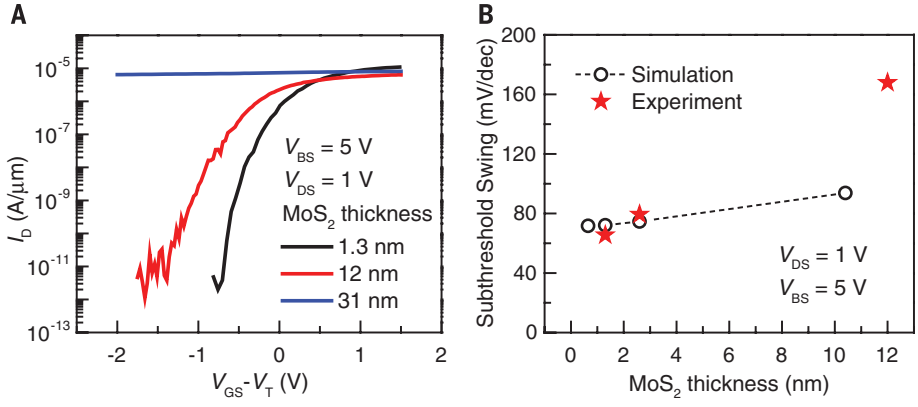

Fig. 4. MoS_2 thickness dependence. (**A**) Dependence of MoS_2 channel thickness on the performance of 1D2D-FET. SS increases with increasing MoS_2 channel thickness. (**B**) Extracted SS from experimental curves and TCAD simulations show increasing SS as channel thickness T_{CH} increases.

commensurate with L_G. This effect is seen by the strong dependence of DIBL on T_{OX}, thus demonstrating the need for T_{OX} scaling and high-κ (dielectric constant) 2D dielectrics to further enhance the device performance.

The effect of MoS_2 thickness on the device characteristics was systematically explored. At the scaling limit of the gate length, the semiconductor channel thickness must also be scaled down aggressively, as described earlier. The electrostatic control of the SWCNT gate on the MoS_2 channel decreased with increasing distance from the ZrO_2-MoS_2 interface. Thus, as the MoS_2 flake thickness was increased, the channel could not be completely depleted by applying a negative V_{GS}. Because of this effect, the SS for a 12-nm-thick MoS_2 device (~170 mV per decade) was much larger than that of bilayer MoS_2 (~65 mV per decade), and as the thickness of MoS_2 was increased to ~31 nm, the device could no longer be turned off (Fig. 4A). The experimental SS as a function of MoS_2 thickness was qualitatively consistent with the TCAD simulations (Fig. 4B and S10), showing an increasing trend with increasing channel thickness. The unwanted variations in device performance caused by channel thickness fluctuations (Fig. 4B and fig. S10), and the need for low Off state current at short channel lengths (Figs. 1 and 3), thus justify the need for layered semiconductors like TMDs at the scaling limit.

TMDs offer the ultimate scaling of thickness with atomic-level control, and the 1D2D-FET structure enables the study of their physics and electrostatics at short channel lengths by using the natural dimensions of a SWCNT, removing the need for any lithography or patterning processes that are challenging at these scale lengths. However, large-scale processing and manufacturing of TMD devices down to such small gate lengths are existing challenges requiring future innovations. For instance, research on developing process-stable, low-resistance ohmic contacts to TMDs, and scaling of the gate dielectric by using high-κ 2D insulators is essential to further enhance device performance. Wafer-scale growth of high-quality films (*30*) is another challenge toward achieving very-large-scale integration of TMDs in integrated circuits. Finally, fabrication of electrodes at such small scale lengths over large areas requires considerable advances in lithographic techniques. Nevertheless, the work here provides new insight into the ultimate scaling of gate lengths for a FET by surpassing the 5-nm limit (*3*–*7*) often associated with Si technology.

REFERENCES AND NOTES

1. T. N. Theis, P. M. Solomon, *Science* **327**, 1600–1601 (2010).
2. R. Chau, B. Doyle, S. Datta, J. Kavalieros, K. Zhang, *Nat. Mater.* **6**, 810–812 (2007).
3. A. D. Franklin, *Science* **349**, aab2750 (2015).
4. M. Lundstrom, *Science* **299**, 210–211 (2003).
5. M. Luisier, M. Lundstrom, D. A. Antoniadis, J. Bokor, in *Electron Devices Meeting (IEDM), 2011 IEEE International* (IEEE, 2011), pp. 11.12.11–1.12.14.
6. H. Kawaura, T. Sakamoto, T. Baba, *Appl. Phys. Lett.* **76**, 3810–3812 (2000).
7. W. S. Cho, K. Roy, *IEEE Electron Device Lett.* **36**, 427–429 (2015).
8. B. Radisavljevic, A. Radenovic, J. Brivio, V. Giacometti, A. Kis, *Nat. Nanotechnol.* **6**, 147–150 (2011).
9. D. Sarkar *et al.*, *Nature* **526**, 91–95 (2015).
10. H. Liu, A. T. Neal, P. D. Ye, *ACS Nano* **6**, 8563–8569 (2012).
11. H. Wang *et al.*, *Nano Lett.* **12**, 4674–4680 (2012).
12. K. F. Mak, K. L. McGill, J. Park, P. L. McEuen, *Science* **344**, 1489–1492 (2014).
13. D. Jariwala, V. K. Sangwan, L. J. Lauhon, T. J. Marks, M. C. Hersam, *ACS Nano* **8**, 1102–1120 (2014).
14. H. Fang *et al.*, *Proc. Natl. Acad. Sci. U.S.A.* **111**, 6198–6202 (2014).
15. K. S. Novoselov *et al.*, *Proc. Natl. Acad. Sci. U.S.A.* **102**, 10451–10453 (2005).
16. C.-H. Lee *et al.*, *Nat. Nanotechnol.* **9**, 676–681 (2014).
17. Y. Yoon, K. Ganapathi, S. Salahuddin, *Nano Lett.* **11**, 3768–3773 (2011).
18. L. Liu, Y. Lu, J. Guo, *IEEE Trans. Electron. Dev.* **60**, 4133–4139 (2013).
19. D. Wickramaratne, F. Zahid, R. K. Lake, *J. Chem. Phys.* **140**, 124710 (2014).
20. Supplementary materials are available on *Science* Online.
21. K. Suzuki, T. Tanaka, Y. Tosaka, H. Horie, Y. Arimoto, *IEEE Trans. Electron. Dev.* **40**, 2326–2329 (1993).
22. J. Svensson *et al.*, *Nanotechnology* **19**, 325201 (2008).
23. N. Patil *et al.*, *IEEE Trans. NanoTechnol.* **8**, 498–504 (2009).
24. J.-P. Colinge *et al.*, *Nat. Nanotechnol.* **5**, 225–229 (2010).
25. A. Javey *et al.*, *Nano Lett.* **4**, 1319–1322 (2004).
26. X. Zou *et al.*, *Adv. Mater.* **26**, 6255–6261 (2014).
27. Y. Taur, *IEEE Trans. Electron. Dev.* **47**, 160–170 (2000).
28. L. Barbut, F. Jazaeri, D. Bouvet, J.-M. Sallese, *Int. J. Microelectron. Comput. Sci.* **4**, 103–109 (2013).
29. S. Hong, K. Lee, *IEEE Trans. Electron. Dev.* **42**, 1461–1466 (1995).
30. K. Kang *et al.*, *Nature* **520**, 656–660 (2015).

ACKNOWLEDGMENTS

S.B.D. and A.J. were supported by the Electronics Materials program funded by the Director, Office of Science, Office of Basic Energy Sciences, Materials Sciences and Engineering Division of the U.S. Department of Energy under contract DE-AC02-05CH11231. A.B.S. was funded by Applied Materials, Inc., and Entegris, Inc., under the I-RiCE program. J.P.L. and J.B. were supported in part by the Office of Naval Research BRC program. J.P.L. acknowledges a Berkeley Fellowship for Graduate Studies and the NSF Graduate Fellowship Program. Q.W. and M.J.K. were supported by the NRI SWAN Center and Chinese Academy of Sciences President's International Fellowship Initiative (2015VTA031). G.P. and H.-S.P.W. were supported in part by the SONIC Research Center, one of six centers supported by the STARnet phase of the Focus Center Research Program (FCRP) a Semiconductor Research Corporation program sponsored by MARCO and DARPA. A.J., H.-S.P.W., and J.B. acknowledge the NSF Center for Energy Efficient Electronics Science (E^3S). A.J. acknowledges support from Samsung. The authors acknowledge the Molecular Foundry, Lawrence Berkeley National Laboratory for access to the scanning electron microscope. The authors acknowledge H. Fahad for useful discussions about the analytical modeling. All data are reported in the main text and supplementary materials.

SUPPLEMENTARY MATERIALS

www.sciencemag.org/content/354/6308/99/suppl/DC1
Materials and Methods
Supplementary Text
Figs. S1 to S10
Table S1
References (*31*–*44*)

30 June 2016; accepted 7 September 2016
10.1126/science.aah4698

BIOCATALYSIS

An artificial metalloenzyme with the kinetics of native enzymes

P. Dydio,[1,2]* H. M. Key,[1,2]* A. Nazarenko,[1] J. Y.-E. Rha,[1] V. Seyedkazemi,[1] D. S. Clark,[3,4] J. F. Hartwig[1,2]†

Natural enzymes contain highly evolved active sites that lead to fast rates and high selectivities. Although artificial metalloenzymes have been developed that catalyze abiological transformations with high stereoselectivity, the activities of these artificial enzymes are much lower than those of natural enzymes. Here, we report a reconstituted artificial metalloenzyme containing an iridium porphyrin that exhibits kinetic parameters similar to those of natural enzymes. In particular, variants of the P450 enzyme CYP119 containing iridium in place of iron catalyze insertions of carbenes into C–H bonds with up to 98% enantiomeric excess, 35,000 turnovers, and 2550 hours^{-1} turnover frequency. This activity leads to intramolecular carbene insertions into unactivated C–H bonds and intermolecular carbene insertions into C–H bonds. These results lift the restrictions on merging chemical catalysis and biocatalysis to create highly active, productive, and selective metalloenzymes for abiological reactions.

The catalytic activity of a metalloenzyme is determined by both the primary coordination sphere of the metal and the surrounding protein scaffold. In some cases, laboratory evolution has been used to develop variants of native metalloenzymes for selective reactions of unnatural substrates (*1*, *2*). Yet with few exceptions (*3*), the classes of reactions that such enzymes undergo are limited to those of biological transformations. To combine the favorable qualities of enzymes with the diverse reactivity of synthetic transition-metal catalysts, abiological transition-metal centers or cofactors have been incorporated into native proteins. The resulting artificial metalloenzymes catalyze classes of reactions for which there is no known enzyme (abiological transformations) (*3*, *4*).

Although the reactivity of these artificial systems is new for an enzyme, the rates of these reactions have been much slower and the

[1]Department of Chemistry, University of California, Berkeley, CA 94720, USA. [2]Chemical Sciences Division, Lawrence Berkeley National Laboratory, 1 Cyclotron Road, Berkeley, CA 94720, USA. [3]Department of Chemical and Biomolecular Engineering, University of California, Berkeley, CA 94720, USA. [4]Molecular Biophysics and Integrated Bioimaging Division, Lawrence Berkeley National Laboratory, 1 Cyclotron Road, Berkeley, CA 94720, USA.
*These authors contributed equally to this work. **†Corresponding author. Email: jhartwig@berkeley.edu**

turnover number (TON) much lower than those of reactions catalyzed by free metal complexes in organic solvents and lower than those typical of natural enzymes (*4*, *5*). In addition to lacking high activity, these enzymes lack practical characteristics of enzymes for synthetic applications, such as suitability for preparative-scale reactions and potential to be recovered and reused (*6*). One reason that artificial metalloenzymes react more slowly than native enzymes is the absence of a defined binding site for the substrate. Natural enzymes generally bind their substrates with high affinity and in a conformation that leads to extremely fast rates and high selectivity (*7*). If the artificial metalloenzyme is generated by incorporating a full metal-ligand complex into the substrate-binding site of a natural enzyme or protein, the space remaining to bind a reactant for a catalytic process is limited, and the interactions by which the protein binds the reactant are compromised (*4*, *8*). Recently, we reported artificial metalloenzymes generated by the formal replacement of an abiological metal for the natural iron in myoglobin that catalyzes abiological reactions (*9*), but the activity of the resulting enzymes was far from that needed for synthetic applications (*6*). Here, we show that artificial metalloenzymes created by substituting an iridium-methyl unit for the iron in cytochrome P450 enzymes (*10*) and modified by means of laboratory evolution catalyze abiological reactions with activities that are comparable with those of native enzymes (*5*).

P450 enzymes constitute a superfamily of heme-binding monooxygenases that are involved in various biosynthetic pathways, catalyzing reactions that encompass chemo-, regio-, stereo-, and site-selective C–H hydroxylations of complex natural products (*11*). We hypothesized that artificial metalloenzymes that are created with P450s from thermophiles, such as CYP119 (*12*) from *Sulfolobus solfataricus*, could improve the thermal stability of the resulting artificial metalloenzyme and create the potential to conduct reactions at elevated temperatures. Studies on stability revealed that the Ir(Me)-PIX protein formed from CYP119 did have a much higher melting temperature (T_m = 69°C) than those formed from the more commonly used P450-BM3 (45°C) or P450-CAM (40°C). Therefore, this protein was used for our studies on catalytic reactions.

By studying the model reaction to convert diazoester **1** into dihydrobenzofuran **2**, which does not occur in the presence of natural Fe-PIX enzymes, we found that the activity and selectivity of Ir(Me)-PIX CYP119 enzymes are readily evolved through molecular evolution of the natural substrate-binding site of the CYP119 scaffold (Figs. 1 and 2). The wild type (WT) Ir(Me)-CYP119 enzyme and its variant C317G [bearing a mutation that introduces space to accommodate the axial ligand of the Ir(Me)-PIX cofactor] (*13*) catalyze the intramolecular carbene insertion into a C–H bond to form **2**, although with low rates [turnover frequency (TOF) = 0.23 and 0.13 min^{-1}, respectively] and enantioselectivities (ee = 0 and 14%, respectively) for reactions conducted with 5 mM **1** and 0.1 mole % (mol %) catalyst. (Single-letter abbreviations for the amino acid residues are as follows: A, Ala; C, Cys; D, Asp; E, Glu; F, Phe; G, Gly; H, His; I, Ile; K, Lys; L, Leu; M, Met; N, Asn; P, Pro; Q, Gln; R, Arg; S, Ser; T, Thr; V, Val; W, Trp; and Y, Tyr. In the mutants, amino acids were substituted at specific locations; for example, C317G indicates that cysteine at position 317 was replaced by glycine.) To identify mutants that form **2** with higher rates and enantioselectivity, we used a directed evolution strategy targeting the residues close to the active site (L69, A209, T213, and V254) (Fig. 2). To retain the hydrophobicity of the active site, we introduced only hydrophobic and uncharged residues (V, A, G, F, Y, S, and T) through site-directed mutagenesis within a library of 24 double mutants of CYP119. The mutant C317G, T213G formed **2** with 68% ee and 80-fold higher activity (TOF = 9.3 min^{-1}) than did that of the single mutant C317G under the same reaction conditions, described previously. Two additional rounds of evolution, in which ~150 additional variants were analyzed, led to the quadruple mutant C317G, T213G, L69V, V254L (hereafter referred to as CYP119-Max), which formed **2** with 94% ee and with an initial TOF of 43 min^{-1}. This rate is more than 180 times faster than that of the WT variant.

Kinetic studies provided insight into the origin of the differences in the enzymatic activity between the various mutants of Ir(Me)-CYP119. In particular, we determined the standard Michaelis-Menten kinetic parameters (k_{cat} and K_M) for the mutants at each stage of the evolution. Using these parameters, we determined the catalytic efficiency of each enzyme, which is defined as k_{cat}/K_M (*14*) and considered to be one of the most relevant parameters for comparing engineered enzymes to natural enzymes (*5*). The affinity of substrate **1** for the WT enzyme is weak, as revealed by a high K_M (> 5 mM). The single mutant C317G, which lacks a sidechain at this position that could act as an axial ligand, exhibits higher substrate affinity (K_M = 3.1 mM), catalytic activity (k_{cat} = 0.22 min^{-1}), and therefore overall enzyme efficiency (k_{cat}/K_M = 0.071 min^{-1} mM^{-1}) than that of the WT enzyme. The double mutant T213G, C317G of Ir(Me)-CYP119 reacts with Michaelis-Menten parameters (k_{cat} = 4.8 min^{-1} and K_M = 0.40 mM, k_{cat}/K_M = 12 min^{-1} mM^{-1}) that are far more favorable than those of the single mutant C317G. The incorporation of two additional mutations (L69V, V254L) led to further improvements of both k_{cat} and K_M, creating an enzyme (CYP119-Max) with an efficiency that is greater than 4000 times (k_{cat} = 45.8 min^{-1}, K_M = 0.17 mM, and k_{cat}/K_M = 269 min^{-1} mM^{-1}) that of the WT system. These kinetic parameters mark a vast improvement over those of the variant of myoglobin Ir(Me)-PIX-mOCR-Myo H93A, H64V (k_{cat} = 0.73 min^{-1}, K_M = 1.1 mM, and k_{cat}/K_M = 0.66 $min^{-1}mM^{-1}$) (Fig. 2) (*15*). Furthermore, the rates of reactions catalyzed by CYP119-Max at concentrations below K_M are more than 20 times higher than those catalyzed by the free iridium-porphyrin in the presence of the same substrate concentration (TOF = 21 min^{-1} versus TOF = 0.93 min^{-1} at 0.15 mM **1**, respectively), even though the free cofactor lacks any steric encumbrance near the metal site necessary to enable selective catalysis. These results show the value of conducting this iridium-catalyzed reaction within the enzyme active site to control selectivity and increase the reaction rate simultaneously.

The kinetic parameters of reactions catalyzed by the Ir(Me)-PIX CYP119-Max enzyme are comparable with those of native reactions catalyzed by the natural enzymes involved in intermediate

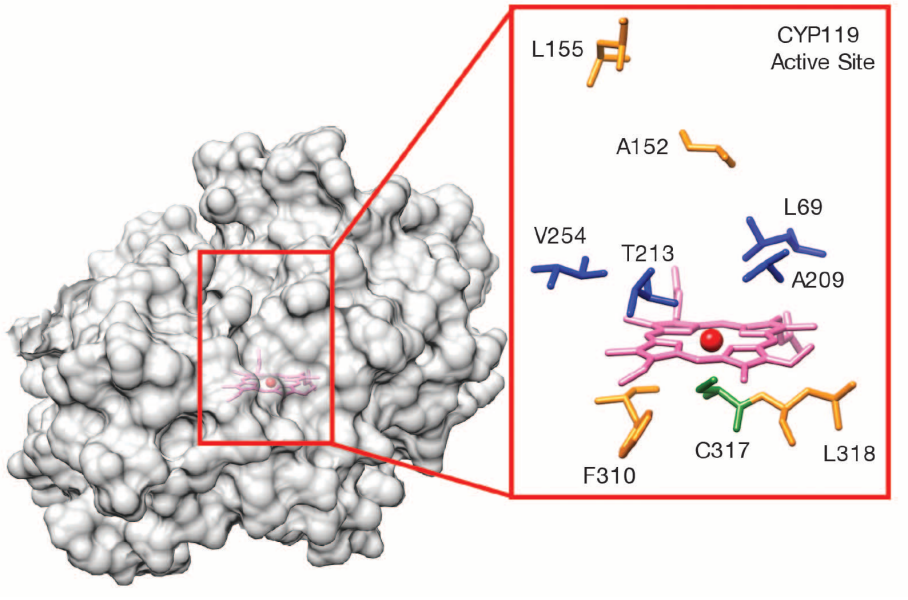

Fig. 1. Structure of WT Fe-CYP119. Image was prepared in Chimera from Protein Data Bank 1IO7. (**Left**) Complete structure of Fe-CYP119. (**Right**) Active-site residues modified during directed evolution of the protein scaffold to increase activity and selectivity for carbene insertions into C–H bonds.

and secondary metabolism (*5*), such as many cytochromes P450 (*16*). The binding affinity of Ir(Me)-CYP119-Max for the abiological substrate **1** is even higher than the affinity of P450s for their native substrates (compare K_M = 0.17 mM for CYP119-Max with K_M = 0.298 mM for P450-BM3 and its native substrate lauric acid) (*17*) and similar to the median K_M value for natural enzymes of this class (0.13 mM) (*5*). In addition, the k_{cat} of 45.8 min^{-1} for this enzyme is within an order of magnitude of the median k_{cat} of natural enzymes responsible for the production of biosynthetic intermediates (312 min^{-1}) and secondary metabolites (150 min^{-1}) (*5*).

The potential to evolve proteins having advantageous enzyme-substrate interactions should also create the possibility to catalyze the insertion of carbenes into the C–H bonds of diverse and less reactive substrates (Fig. 3). Directed evolution targeting high stereoselectivity led to mutants that form products **3** to **7** in up to ±98% ee, in reactions conducted with a fixed catalyst loading (0.17 mol %). The reactions to form products **3** to **5** show that the enzyme reacts as selectively with substrates containing substituents on the aryl ring as it does for unsubstituted **2**. Such reactivity is relevant to contemporary synthetic challenges. For example, compound (***S***)-**5** is an intermediate in the synthesis of BRL *37959*—a potent analgesic—and was prepared previously by means of kinetic resolution (*18*). This product was formed by variant 69Y-152W-213G in 94% ee. Product **6** results from carbene insertion into a secondary C–H bond, and product **7** results from carbene insertion into a sterically hindered, secondary C–H bond. Directed evolution furnished a mutant capable of forming **7** with high enantio- and diastereoselectivity (dr) favoring the cis isomer [90% ee, 12:1 dr (cis:trans)]. The previously reported Ir(Me)-PIX enzymes based on myoglobin produced this product in only trace amounts, and the free Ir(Me)-PIX cofactor formed predominantly the trans isomer (3:1 dr, trans:cis). This reversal of diastereoselectivity from that of the free Ir(Me)-PIX cofactor to that of the artificial metalloenzyme highlights the ability of strong substrate-enzyme interactions to override the inherent selectivity of a metal cofactor or substrate.

Ir(Me)-CYP119-Max also catalyzes the insertion of carbenes into fully unactivated C–H bonds. Although the structure of substrate **7** in Fig. 4 appears similar to that of substrate **1**, the primary C–H bonds in **7** are stronger and less reactive than those in **1**, which are located alpha to an oxygen atom (*19*).

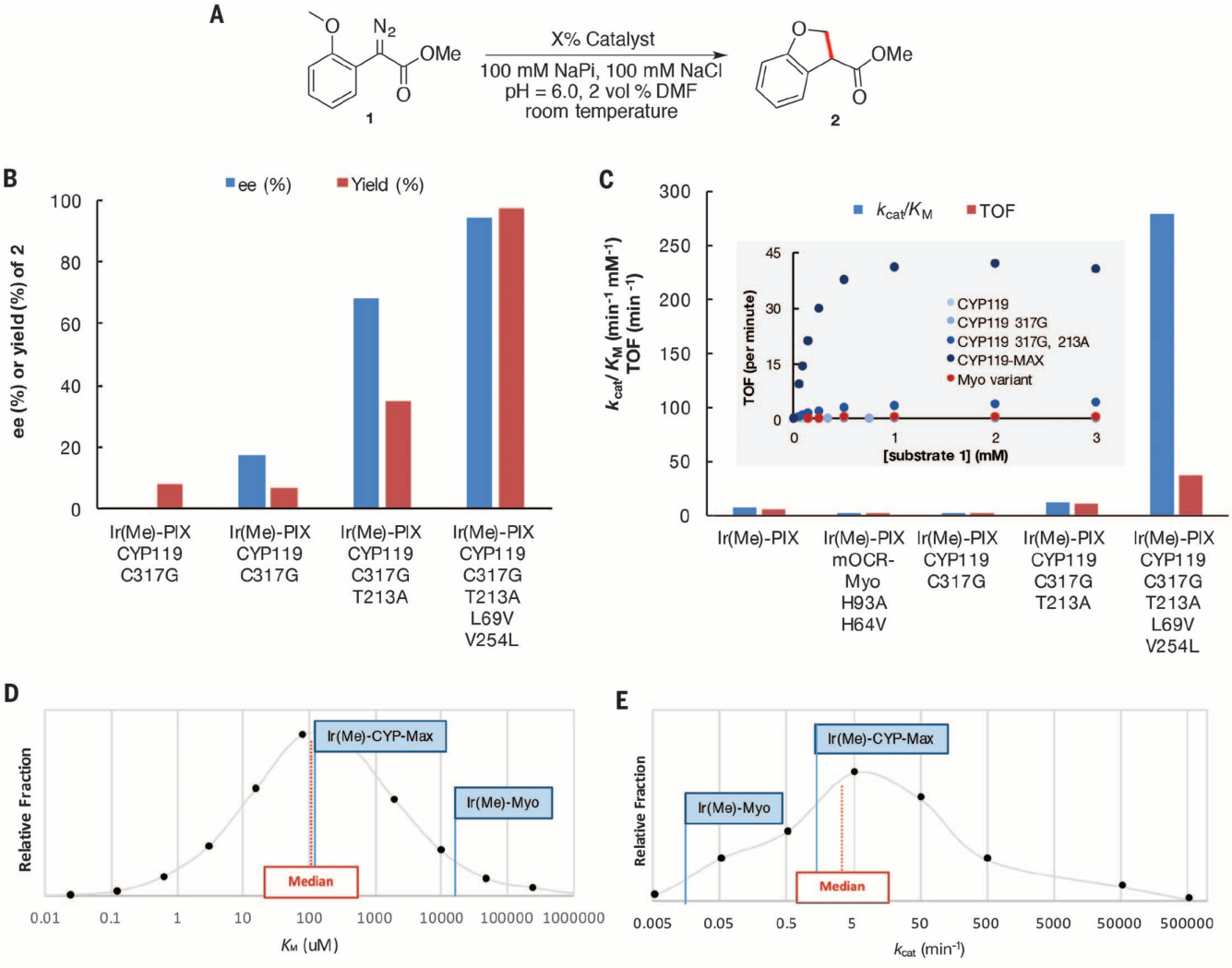

Fig. 2. Directed evolution of Ir(Me)-PIX CYP119 for enantioselective insertions of carbenes into C–H bonds. (**A**) Model reaction converting diazoester **1** to dihydrobenzofuran **2**. (**B**) Enantioselectivity and yields for the formation of **2** catalyzed by evolved variants of CYP119 (0.17% catalyst loading, 10 mM substrate). (**C**) Kinetic parameters describing the formation of **2** by variants of CYP119 (0.1 mol % catalyst loading, 5 mM substrate). For free Ir(Me)-PIX, k_1 (the first-order kinetic constant) is listed instead of k_{cat}/K_M (*16*). (Inset) Dependence of TOF on the initial concentration of **1** for reactions using 0.005 mM catalyst. (**D** and **E**) Comparison of K_M and k_{cat} values for CYP119-Max with those of natural enzymes involved in the metabolism of intermediate and secondary metabolites (*5*); for comparison, the kinetic parameters for Ir(Me)-PIX mOCR-myoglobin (H93A and H64V) catalyzing the same transformation are shown.

In fact, there are no metal catalysts of any type reported to form indanes via carbene insertion into an unactivated C–H bond with synthetically useful enantioselectivities. The synthesis of such chiral moieties was achieved only in a diastereoselective fashion, when a stoichiometric amount of a chiral auxiliary was built into the substrate (*20*). In contrast, Ir(Me)-CYP119-Max catalyzed the formation of **8** in 90% ee, with no need for the auxiliary. To observe substantial amounts of this product (TON = 31), the reaction was conducted at 40°C; the enantioselectivity of the product at this temperature was the same as that of the small quantity of product formed at room temperature.

In addition to catalyzing intramolecular reactions with unactivated C–H bonds, Ir(Me)-CYP119-Max catalyzes intermolecular carbene insertion into a C–H bond. This reaction is challenging because the metal-carbene intermediate can undergo competitive diazo coupling or insert the carbene unit into the O–H bond of water (*21*, *22*). In fact, the model reaction between phthalan (**10**) and ethyl diazoacetate (EDA) forms alkene and alcohol as the dominant products when catalyzed by the

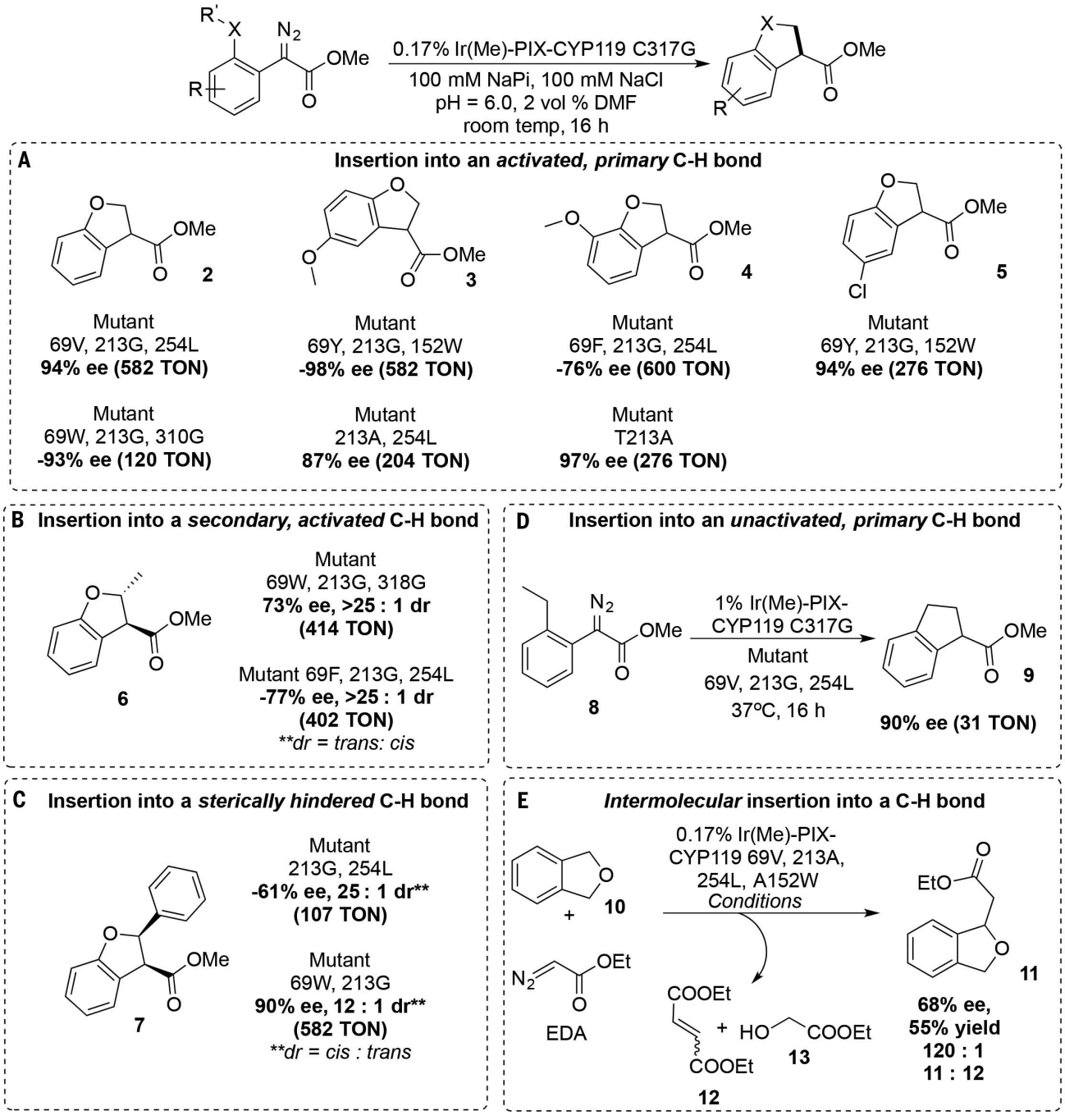

Fig. 3. Selective variants of Ir(Me)-PIX CYP119. These variants catalyze enantioselective intra- and intermolecular C–H carbene insertion reactions of activated and unactivated C–H bonds. (**A** to **D**) Intramolecular C–H carbene insertion reactions. Reactions were conducted at room temperature unless otherwise noted. (**E**) An intermolecular C–H carbene insertion reaction. Conditions: **10** (10 μmol) and EDA (100 μmol). EDA was added as a 50% solution in *N*,*N*′-dimethylformamide over 1 hour by use of a syringe pump.

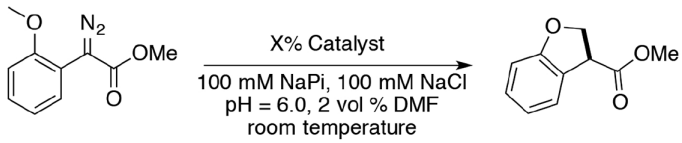

Reactions Conducted at a Range of Scales

mmol/ mg substrate	% catalyst	TON	Yield	ee (%)
0.0025 mmol, 0.5 mg	0.17%	330	56% yield (GC)	94%
0.2 mmol, 40 mg	0.25%	192	48% yield (Isolated)	92%
0.2 mmol, 40 mg	0.05%	1060	53% yield (Isolated)	92%
1.0 mmol, 206 mg	0.017%	3529	60% yield (Isolated)	93%
5.0 mmol, 1 gram	0.017%	3235	55% yield (Isolated)	93%

Reactions Conducted with a Range of Catalyst Loadings

[substrate], mg substrate	[catalyst]	TON	Yield	ee (%)
100 mM, 5 mg	0.025 mM	3800	95% yield	92%
100 mM, 5 mg	0.01 mM	8326	83% yield	92%
100 mM, 10 mg	0.0025 mM	30293	76% yield	92%
200 mM, 10 mg	0.0025 mM	35129	44% yield	91%

Fig. 4. Productivity of Ir(Me)-PIX CYP119. Intramolecular C–H carbene insertion reactions of substrate **1** catalyzed by Ir(Me)-PIX CYP119-Max under synthetically relevant reaction conditions.

free Ir(Me)-PIX cofactor; only trace amounts of carbene insertion product **11** were formed. In sharp contrast, the same reaction catalyzed by the mutant Ir(Me)-PIX CYP119-Max-A152F occurred to form **11** in 55% yield with 330 TON and 68% ee. Dimerization of the carbene when catalyzed by Ir(Me)-CYP119-Max is limited, presumably because of selective binding and preorganization of the substrate; the selectivity for formation of the product from C–H insertion **11** over the alkene side product **12** was 70-fold higher when catalyzed by Ir(Me)-PIX CYP119-Max-A152F than when catalyzed by the free cofactor.

For the ultimate goal of applying artificial metalloenzymes to the synthesis of organic molecules for fine chemicals, the reactions conducted by such catalytic systems should occur on preparative scales with high substrate concentrations, and the enzyme should react with high TONs and be amenable to attachment to a solid support for recycling. We found that a series of reactions containing between 40 mg and 1 g of substrate **1** catalyzed by Ir(Me)-CYP-Max occurred with yields and enantioselectivities that were similar to each other (91 to 94% ee), showing that the outcome of the reaction is independent of the scale (Fig. 4). Moreover, with 200 mM substrate, reactions catalyzed by Ir(Me)-CYP-Max (0.0025 mM) formed product **2** with up to 35,000 TON without loss of enantioselectivity (93% ee) (Fig. 4). Thus, this artificial metalloenzyme operates with high productivity under conditions suitable for preparative scales. Last, Ir(Me)-CYP-Max supported on CNBr-activated sepharose catalyzed the conversion of **1** to **2** via carbene insertion into a C–H bond in 52% yield and 83% ee. This supported catalyst was used, recovered, and recycled four times without loss of the enantioselectivity for formation of **2**, while retaining 64% of the activity (fig. S11).

Enzymes containing abiological transition-metal active sites that exhibit the kinetics, selectivity, and evolutionary potential of natural enzymes have been a major goal of catalyst design. Here, we show that artificial metalloenzymes catalyzing abiological processes can possess the fundamental characteristics of natural enzymes: fast kinetics, high productivity, and high selectivity under the same reaction conditions. Taken together, our results show that the kinetics of artificial metalloenzymes need not limit the merging of chemical and biocatalysis.

REFERENCES AND NOTES

1. M. W. Peters, P. Meinhold, A. Glieder, F. H. Arnold, *J. Am. Chem. Soc.* **125**, 13442–13450 (2003).
2. G.-D. Roiban, R. Agudo, M. T. Reetz, *Angew. Chem. Int. Ed. Engl.* **53**, 8659–8663 (2014).
3. T. K. Hyster, F. H. Arnold, *Isr. J. Chem.* **55**, 14–20 (2015).
4. J. C. Lewis, *ACS Catal.* **3**, 2954–2975 (2013).
5. A. Bar-Even *et al.*, *Biochemistry* **50**, 4402–4410 (2011).
6. K. M. Koeller, C.-H. Wong, *Nature* **409**, 232–240 (2001).
7. D. Ringe, G. A. Petsko, *Science* **320**, 1428–1429 (2008).
8. M. R. Ringenberg, T. R. Ward, *Chem. Commun. (Camb.)* **47**, 8470–8476 (2011).
9. H. M. Key, P. Dydio, D. S. Clark, J. F. Hartwig, *Nature* **534**, 534–537 (2016).
10. Materials and methods are available as supplementary materials on *Science* Online.
11. A. Sigel, H. Sigel, R. K. O. Sigel, Eds., *The Ubiquitous Roles of Cytochrome P450 Proteins* (John Wiley & Sons, 2007).
12. K. S. Rabe, K. Kiko, C. M. Niemeyer, *ChemBioChem* **9**, 420–425 (2008).
13. J. A. McIntosh, T. Heel, A. R. Buller, L. Chio, F. H. Arnold, *J. Am. Chem. Soc.* **137**, 13861–13865 (2015).
14. J. M. Berg, J. L. Tymoczko, L. Stryer, *Biochemistry* (W.H. Freeman, ed. 5, 2002).
15. This variant of myoglobin was used for comparison because this variant forms **2** with both high yield and high enantioselectivity [relative to other mutants of Ir(Me)-PIX Myo].
16. J. Romeo, Ed., *Secondary Metabolism in Model Systems* (Elsevier, 2004).
17. M. A. Noble *et al.*, *Biochem. J.* **339**, 371–379 (1999).
18. P. Bongen, J. Pietruszka, R. C. Simon, *Chemistry* **18**, 11063–11070 (2012).
19. S. M. Paradine, M. C. White, *J. Am. Chem. Soc.* **134**, 2036–2039 (2012).
20. B. Hong *et al.*, *J. Am. Chem. Soc.* **137**, 11946–11949 (2015).
21. P. Srivastava, H. Yang, K. Ellis-Guardiola, J. C. Lewis, *Nat. Commun.* **6**, 7789 (2015).
22. N. M. Weldy *et al.*, *Chem. Sci.* **7**, 3142–3146 (2016).

ACKNOWLEDGMENTS

This work was supported by the Director, Office of Science, of the U.S. Department of Energy under contract DE-AC02-05CH11231; by the NSF (graduate research fellowship to H.M.K.), and the Netherlands Organization for Scientific Research (the Rubicon postdoctoral fellowship 680-50-1306 to P.D.). We thank the QB3 MacroLab facility (competent cells), the University of California, Berkeley DNA Sequencing Facility (plasmid sequencing), and T. Iavarone and the QB3 Mass Spectrometry Facility [nano–electrospray ionization (NS-ESI) mass spectrometry data collection, supported by NIH grant 1S10OD020062-01] for native nanoESI-MS data and analysis. All data are provided in the supplementary materials. J.F.H., H.M.K., P.F.D., and D.S.C. are inventors on U.S. patent application numbers 62/241,487 and 62/384,011, submitted by the Lawrence Berkeley National Laboratory, that covers preparation and application of artificial metalloenzymes containing noble metal-porphyrins.

SUPPLEMENTARY MATERIALS

www.sciencemag.org/content/354/6308/102/suppl/DC1
Materials and Methods
Figs. S1 to S12
Tables S1 to S7
References (*23*–*28*)

28 June 2016; accepted 12 September 2016
10.1126/science.aah4427

BIOINSPIRED MATERIALS

Synthetic nacre by predesigned matrix-directed mineralization

Li-Bo Mao,[1,2] Huai-Ling Gao,[1,2] Hong-Bin Yao,[1,2] Lei Liu,[1,2,3] Helmut Cölfen,[3] Gang Liu,[4] Si-Ming Chen,[1,2] Shi-Kuo Li,[1,2] You-Xian Yan,[1,2] Yang-Yi Liu,[1,2] Shu-Hong Yu[1,2,4]*

Although biomimetic designs are expected to play a key role in exploring future structural materials, facile fabrication of bulk biomimetic materials under ambient conditions remains a major challenge. Here, we describe a mesoscale "assembly-and-mineralization" approach inspired by the natural process in mollusks to fabricate bulk synthetic nacre that highly resembles both the chemical composition and the hierarchical structure of natural nacre. The millimeter-thick synthetic nacre consists of alternating organic layers and aragonite platelet layers (91 weight percent) and exhibits good ultimate strength and fracture toughness. This predesigned matrix-directed mineralization method represents a rational strategy for the preparation of robust composite materials with hierarchically ordered structures, where various constituents are adaptable, including brittle and heat-labile materials.

Biological materials are built from limited components, but their mechanical performances, such as strength and toughness, are far beyond their artificial counterparts. The secret of success is their hierarchically ordered structure at multiscale levels (*1*–*4*). The most studied model among these biological materials is the nacreous part in some mollusk shells that consists of about 95 weight % (wt %) of brittle aragonitic $CaCO_3$ and 5 wt % of organic materials (*5*). Mollusks produce nacre by first generating several layers of insoluble β-chitin matrix filled with silk fibroin gel (*6*). Then aragonite cores form on the surface of the matrix at the nucleation sites (*7*), followed by lateral growth in the confined space of adjacent organic layers, which finally leads to a Voronoi pattern (*5*). These aragonite platelets, despite their single-crystal diffraction pattern, are not perfect single crystals but essentially consist of nanograins with the same crystallographic orientation (mesocrystals), whereby the platelets are not as fragile as perfect single crystals (*8*). The mature nacre has a "brick-and-mortar" microstructure where aragonite platelet layers are bound by an organic matrix (*3*). Through a number of such structural designs and toughening mechanisms at multiscale levels (*2*, *9*, *10*), nacre reconciles its toughness and strength, which are mutually exclusive in most artificial materials (*11*).

In contrast to biological materials, the evolution of synthetic structural materials has been achieved predominately by developing new synthetic compounds rather than optimizing the micro/nanostructures of existing materials. Therefore, bioinspired designs of multiscale structures are promising for developing surpassing structural materials (*5*, *12*). However, the fabrication of bulk biomimetic materials is by no means a low-hanging fruit (*12*), because it is hard to balance the well-organized hierarchical structure and the efficiency. For nacre, the strategies used for producing its artificial counterparts can be categorized into three groups: the layer-by-layer technique (*13*–*16*), the self-assembly technique (*17*–*20*), and the slurry-based freeze-casting/magnetic-field-assisted slip-casting and sintering technique (*21*–*25*). Although these artificial materials are to some extent similar to natural nacre, the state-of-the-art techniques focus on mimicking the layered structure by anisotropic assembly of building blocks but have not achieved the fabrication of bulk synthetic nacre via a mineralization strategy that is adopted by many living creatures to produce biomaterials, including nacre (*5*–*7*). Furthermore, the high-temperature heat treatment (*22*–*25*) excludes many heat-labile materials and thus substantially limits their applications.

Considering that mollusks build their nacre by the mineralization in a preformed laminated matrix (*5*), we developed a consecutive assembly-and-mineralization process (Fig. 1) to produce synthetic nacre by a mesoscale approach where the nanostructure and the microstructure are controlled simultaneously. Through a freezing-induced assembly process (Fig. 1, A and B, and fig. S1), a chitosan matrix with predesigned laminated structure is fabricated (fig. S2, A, B, D, and E). Then the matrix is acetylated (Fig. 1C) and transformed to β-chitin to avoid unwanted swelling or dissolution (fig. S2, C and E, and table S1). The acetylated matrix is mineralized in a peristaltic pump-driven circulatory system via the decomposition of $Ca(HCO_3)_2$ in the presence of polyacrylic acid (PAA) and Mg^{2+} (Fig. 1D). Then the final material is obtained by silk fibroin infiltration and hot-pressing of the mineralized matrix. The thickness of the bulk synthetic nacre is about 1 to 2 mm, based on the thickness of the original chitin matrix (Fig. 2B), which can be further increased by using thicker matrix (Fig. 1B). The $CaCO_3$ in the synthetic nacre is aragonite (fig. S3), which is attributed to the control of the additives (*26*).

Typically, as the size of the three-dimensional (3D) matrix increases, the mass transfer throughout

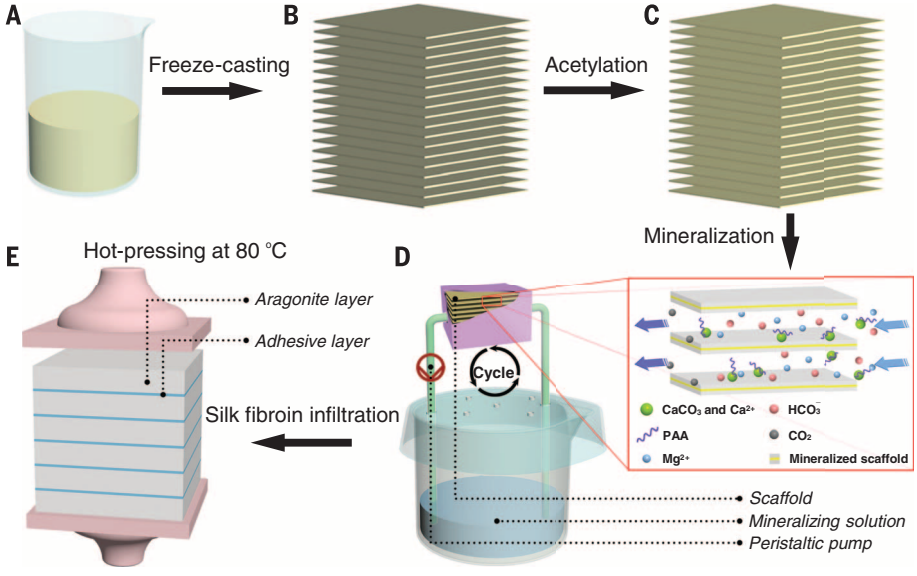

Fig. 1. Fabrication scheme of the synthetic nacre. (**A**) Starting solution, chitosan/acetic acid solution. (**B**) Freeze-casted laminated chitosan matrix. (**C**) Matrix after acetylation, where chitosan is converted to β-chitin. (**D**) Mineralization of the matrix. Fresh mineralizing solution is pumped to flow through the space between the layers in the matrix, bringing in Ca^{2+}, Mg^{2+}, HCO_3^-, and PAA for mineralization and taking out excess CO_2. $CaCO_3$ precipitates onto the layers and CO_2 diffuses into the air through the pin holes in the paraffin film. (**E**) Laminated synthetic nacre is obtained after silk fibroin infiltration and hot-pressing.

[1]Division of Nanomaterials and Chemistry, Hefei National Laboratory for Physical Sciences at the Microscale, University of Science and Technology of China, Hefei, 230026, China. [2]Chinese Academy of Sciences, Center for Excellence in Nanoscience, Collaborative Innovation Center of Suzhou Nano Science and Technology, Hefei Science Center, Department of Chemistry, University of Science and Technology of China, Hefei, 230026, China. [3]University of Konstanz, Physical Chemistry, Universitätsstraße 10, D-78457 Konstanz, Germany. [4]National Synchrotron Radiation Laboratory, University of Science and Technology of China, Hefei, 230029, China.
*Corresponding author. Email: shyu@ustc.edu.cn

the matrix will be more difficult, which means the mineralization of the whole matrix will be retarded. In our work, this problem is overcome through experimental designs. There is enough space between the chitin layers of the matrix, which is indispensable for the mass transfer across the whole laminated structure and thus facilitates the thorough mineralization of the matrix. Otherwise, a dense mineral shell will form on the surface and obstruct the mineralization process inside (fig. S4A). To promote the mass transfer in the matrix further, the precipitation of $CaCO_3$ is achieved by the decomposition of calcium bicarbonate rather than the gas-diffusion method because the spontaneous diffusion of CO_2 (fig. S4B) is much slower than the direct pump-driven injection of $Ca(HCO_3)_2$ (fig. S4, C and D). Consequently, the whole matrix mineralizes to the extent that the resulting synthetic nacre contains as much as 91 wt % of $CaCO_3$, which is quite comparable to natural nacre (*5*). Because of the high inorganic content, the synthetic nacre exhibits high stability in water without noticeable swelling (movie S1). More important, while the growth of natural nacre takes months or even years, only 2 weeks are needed for the preparation of the bulk synthetic nacre whose composition is almost the same as natural nacre (figs. S3 and S5) (*5*).

The synthetic nacre shares striking similarities with natural nacre from the shell of mollusk such as *Anodonta woodiana*. The fracture surface of the bulk synthetic nacre reveals a laminated nacre-like microstructure (Fig. 2, A to D; fig. S6, A and B; and movie S2). The thickness of the alternating aragonite and organic layers is 2 to 4 μm and 100 to 150 nm, respectively. Hence, it is supposed that the Bragg diffraction–induced structural coloration (*5*) of the synthetic nacre is not in the visible range (Fig. 2B). Each mineral layer is made up of tilelike aragonite platelets and exhibits a structure similar to Voronoi pattern, which is typically observed in natural nacre (Fig. 2, E and F) (*5*). However, as the mineralization conditions are complicated and the control of the process in our experiment is not as good as the biomineralization process in mollusks, the Voronoi patterns are not so perfect in the synthetic nacre (red circles in Fig. 2F). The formation of this pattern can be ascribed to the growth mechanism that $CaCO_3$ selectively precipitates at some nucleation sites (white arrowheads in Fig. 2F) that were identified to be rich in carboxyl groups (*7*), and then these initial crystals grow laterally on the chitin layers until they meet each other to form a boundary (fig. S6C and movie S3). As the matrix gradually mineralizes, the chitin layers are assimilated by the minerals, probably because of electrostatic attraction (figs. S7 and S8), whereas the infiltrated silk fibroin forms the organic layers between the aragonite layers (fig. S9). Both the average size and the aspect ratio of the aragonite platelets in the synthetic nacre are significantly larger than that in *A. woodiana* nacre (fig. S10), which greatly affect the properties of the as-fabricated nacre-like materials (*19*).

The aragonite platelets in the synthetic nacre consist of attached nanograins with diameters ranging from 10 to 100 nm (Figs. 2H and 3A), in accordance with those in natural nacre (Fig. 2G) (*8*). Further analysis of the nanograins reveals the crystallographic features of the platelets (Fig. 3, B to D). The single-crystal–like fast Fourier transform (FFT) patterns (Fig. 3, C and D) of the boundary areas (Fig. 3B) indicate the orientation continuity between adjacent nanograins in a single platelet, because the precipitation of $CaCO_3$ in our experiment should follow a nonclassical crystallization mechanism (*27*, *28*). Although the aragonite platelets are mesocrystals (*27*) due to the orientation continuity of individual nanoparticles, the aragonite platelets in a layer grow independently (fig. S6C and movie S3), and thus the crystal orientation degree of the whole synthetic nacre is as low as ~9%. Therefore, a single aragonite layer shows distinctive dark and bright mosaics under cross-polarized light where the brightness of these tiles depends on their orientations (Fig. 3E and fig. S10A). In addition, the adjacent layers do not contact each other during the mineralization process (fig. S4D), and thus the orientations of the adjacent layers are also self-reliant. Consequently, the x-ray diffraction pattern of the synthetic nacre is in line with *A. woodiana* nacre powder, where the aragonite platelets are randomly oriented, but not bulk *A. woodiana* nacre, where all the platelets have near-parallel (002) planes (fig. S3).

The microscopic mechanical properties of the synthetic nacre are comparatively studied by nanoindentation (NI). Long cracks are induced by the indents in both monolithic calcite and aragonite, and then they propagate easily along the cleavage planes (*8*). In comparison, no microscopic crack or crack propagation is observed in *A. woodiana* nacre or the synthetic nacre (Fig. 4A). The excellent antiflaw performance of both composites can

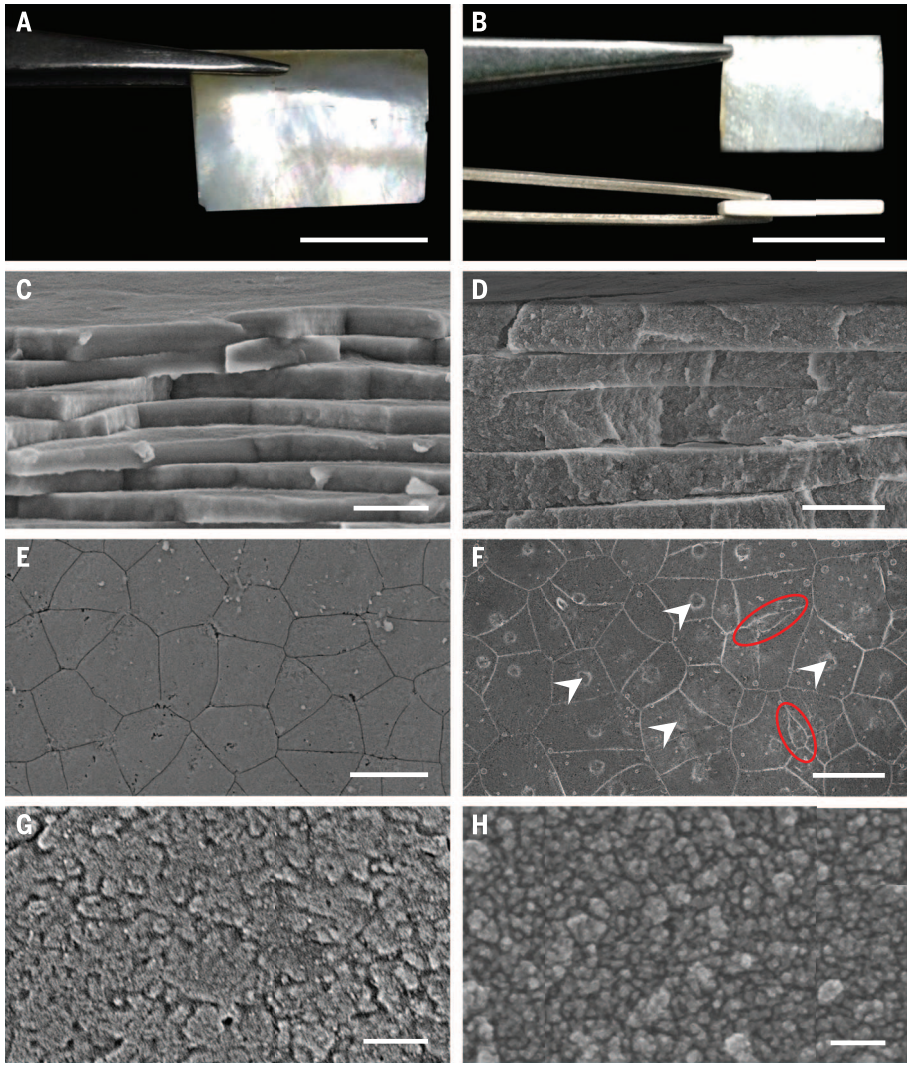

Fig. 2. The comparison of the appearance and multiscale structure between natural and synthetic nacre. (**A**) *A. woodiana* nacre. (**B**) Bulk synthetic nacre. (**C** and **D**) Fracture surface of (C) *A. woodiana* nacre and (D) synthetic nacre. (**E** and **F**) Voronoi pattern of the aragonite layer in (E) *A. woodiana* nacre and (F) synthetic nacre. (**G** and **H**) Enlarged micrographs of the aragonite platelet of (G) *A. woodiana* nacre and (H) synthetic nacre. Scale bars are 1 cm, 1 cm, 3 μm, 3 μm, 5 μm, 100 μm, 100 nm, and 100 nm for (A) to (H), respectively.

be attributed to their unique connected-nanograin structure (Fig. 2, G and H) (*29*). Like the nanograins in natural nacre that are bound by organics like proteins (*8*), it is suggested that the nanograins in the synthetic nacre (Fig. 3A) also contain or are connected by the added PAA molecules, which can strongly interact with $CaCO_3$ (*30*). Furthermore, the assimilated chitin shreds embedded in the aragonite layers (fig. S8, C and D) provide additional binding components and act as buffer zones for internal stress (*31*). Consequently, although there are weak cleavage planes in abiotic single crystals, there is no cleavage plane in these mesocrystals; the energy can be dissipated efficiently via breaking the bonding between nanograins, and the nanocracks in these mesocrystals can be localized (*8*, *32*). Using the Olive-Pharr model to analyze the data obtained from the NI tests, it can be found that the synthetic nacre undergoes losses in its elastic modulus and hardness (fig. S11), which is ascribed mainly to the thick grain boundaries between the aragonite nanograins (Fig. 3A, fig. S12, and the calculation in the supplementary materials). It is estimated that the volume fraction of organic components in the synthetic nacre is about 14%, whereas in *A. woodiana* nacre it is less than 8%. Accordingly, the macroscopic density of the synthetic nacre is significantly smaller than that of aragonite and *A. woodiana* nacre (fig. S13). Moreover, because the organic components in the grain boundaries are sensitive to water, the elastic modulus of the fully hydrated synthetic nacre decreases, whereas the ultimate strain increases remarkably (fig. S14).

As the composition and the hierarchical structure of the synthetic nacre bear a striking resemblance to natural nacre, the macroscopic mechanical properties of the synthetic nacre are also superior to pure aragonite and its related composites and comparable to that of natural nacre (Fig. 4B; see also fig. S13). The rising crack-extension resistance curves of both the synthetic and natural nacre indicate extrinsic toughening mechanisms in these materials (Fig. 4C). The reinforced performance of the synthetic nacre is attributed to the structural features at multiscale levels where the organic components play a key role (figs. S15 and S16). The assembled-nanograin architecture and the organic binders (e.g., PAA and chitin) by which energy can be dissipated and nanocracks can be localized are the structural basis of the macroscopic performance of the synthetic nacre. Moreover, the laminated nacre-like structure leads to crack branching, crack deflection, crack blunting, crack trapping in the organic layers, and platelet bridging (Fig. 4, D and E; see also fig. S17, E and F) (*33*). Some microscopic features, such as platelet waviness and dovetail structure that are responsible for the hardening and damage tolerance in natural nacre (*34*), have also been observed in the synthetic nacre (fig. S18). In addition, the delamination process is retarded by the infiltrated silk fibroin binding layers and thus further dissipates energy (Fig. 4F; see also fig. S9, A and B). However, because their microstructures (fig. S19) as well as the suggested micromechanical models are not exactly the same

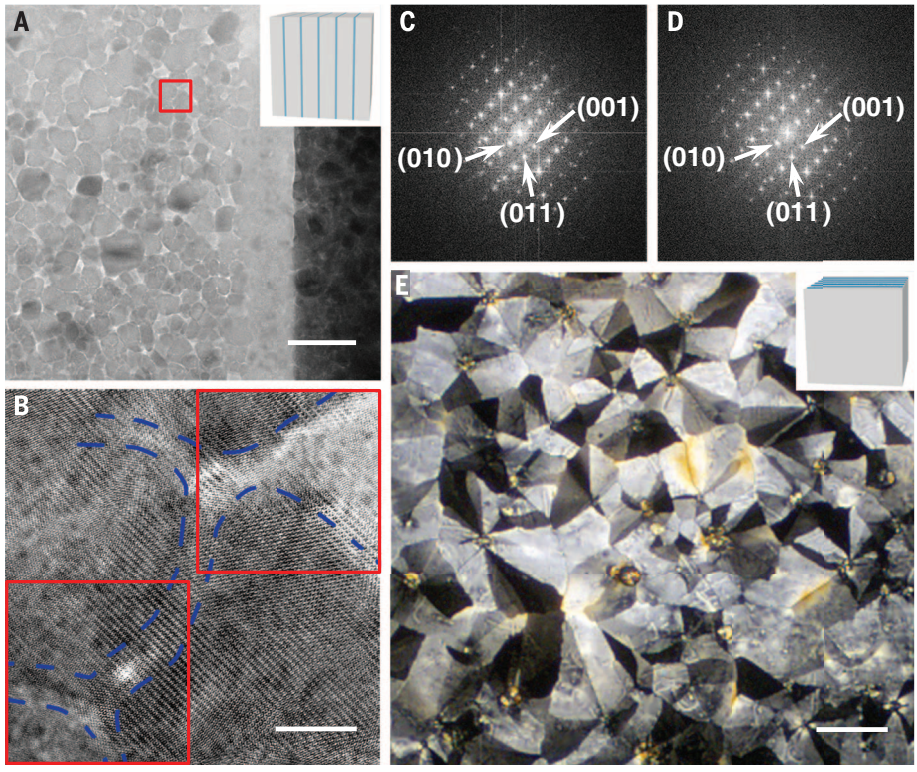

Fig. 3. Crystallographic structure of the synthetic nacre. (**A**) Cross-sectional transmission electron microscope (TEM) image of the synthetic nacre. The inset shows the view direction. (**B**) High-resolution TEM (HRTEM) image of the selected area in (A). The boundaries of the nanograins are marked with dashed blue lines. (**C** and **D**) FFT of the selected squares denoted by red lines in (B), where (C) corresponds to the top right square and (D) the bottom left. (**E**) Optical micrograph of the aragonite layer under cross-polarized light, where the inset shows the view direction. Scale bars are 100 nm, 10 nm, and 50 μm for (A), (B), and (E), respectively.

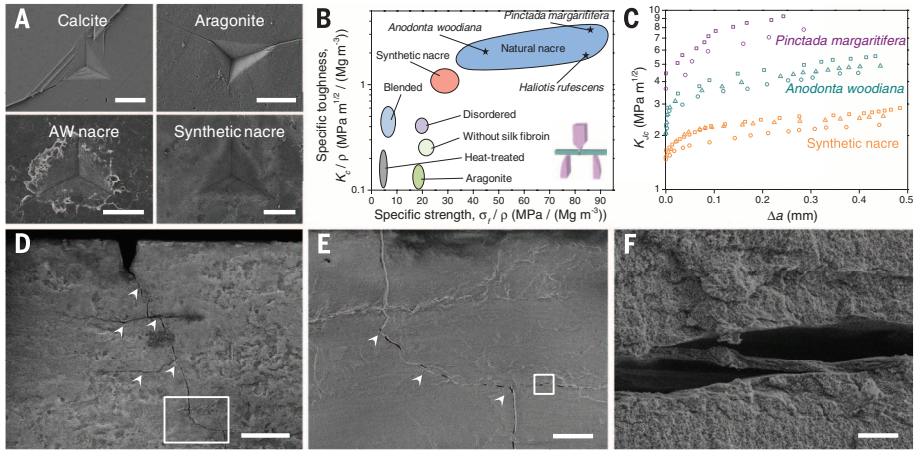

Fig. 4. Mechanical properties of the synthetic nacre. (**A**) Residual indents of the Berkovich diamond tip in abiotic minerals, *A. woodiana* (AW) nacre, and the synthetic nacre. (**B**) Specific fracture toughness versus specific ultimate flexural strength, illustrating the mechanical performance of the synthetic nacre, natural nacre, pure aragonite, and their related materials. (**C**) Rising crack-extension resistance curves (evaluated by the steady-state fracture toughness K_{JC}) of the synthetic nacre and some natural nacre. (**D**) Profile of the fractured synthetic nacre showing the multiple toughening mechanisms. (**E**) Crack deflection between layers and crack branching [enlarged micrograph of the marked area in (D)]. (**F**) Crack-induced interlamellar debonding in the synthetic nacre [enlargement of the marked area in (E)]. The data of *Pinctada margaritifera* and *Haliotis rufescens* are adapted from (*35*) and (*36*). Scale bars are 10, 200, 40, and 2 μm for (A), (D), (E), and (F), respectively.

(fig. S20), the mechanical properties of the synthetic nacre are still not as good as that of natural nacre (*35*, *36*) (Fig. 4, B and C). Due to the larger aspect ratio of the aragonite platelets in the synthetic nacre, the platelets exhibit a "partly pullout" behavior, which leads to lower crack-resistance capability.

Because the precipitation of the second phase onto the matrix relies on electrostatic force, $CaCO_3$ and chitin can be substituted by other precursors with opposite charges to make superior composites such as engineering ceramics (*21*–*24*) (figs. S21 and S22). Besides, as the dependence of properties of the composite materials on the characteristic length of their periodic microstructure (*37*), the mechanical performance of these materials can be optimized by adjusting the properties of the original matrix (*38*), which affect both the amount of electrostatically absorbed precipitates and the density of the nucleation sites. The fabrication of the laminated synthetic nacre is not a special case; there are other techniques, such as programmable 3D printing, for constructing predesigned macroscopic matrices that can be readily incorporated with our strategy to produce composite materials. Moreover, this strategy is also adaptable for fabricating robust bulk materials with brittle and heat-labile components (fig. S21B). Given the importance of nano- and microscopic structures for the materials performance, we thus anticipate that our method can be extended to produce various composite materials with unique properties.

REFERENCES AND NOTES

1. P. Fratzl, R. Weinkamer, *Prog. Mater. Sci.* **52**, 1263–1334 (2007).
2. B. Ji, H. Gao, *Annu. Rev. Mater. Res.* **40**, 77–100 (2010).
3. J. Wang, Q. Cheng, Z. Tang, *Chem. Soc. Rev.* **41**, 1111–1129 (2012).
4. M. A. Meyers, J. McKittrick, P.-Y. Chen, *Science* **339**, 773–779 (2013).
5. H.-B. Yao, J. Ge, L.-B. Mao, Y.-X. Yan, S.-H. Yu, *Adv. Mater.* **26**, 163–188 (2014).
6. A. G. Checa, J. H. E. Cartwright, M.-G. Willinger, *Proc. Natl. Acad. Sci. U.S.A.* **106**, 38–43 (2009).
7. L. Addadi, D. Joester, F. Nudelman, S. Weiner, *Chemistry* **12**, 980–987 (2006).
8. Z. Huang, X. Li, *Sci. Rep.* **3**, 1693 (2013).
9. P.-Y. Chen *et al.*, *J. Mech. Behav. Biomed.* **1**, 208–226 (2008).
10. I. Jäger, P. Fratzl, *Biophys. J.* **79**, 1737–1746 (2000).
11. R. O. Ritchie, *Nat. Mater.* **10**, 817–822 (2011).
12. U. G. K. Wegst, H. Bai, E. Saiz, A. P. Tomsia, R. O. Ritchie, *Nat. Mater.* **14**, 23–36 (2015).
13. Z. Tang, N. A. Kotov, S. Magonov, B. Ozturk, *Nat. Mater.* **2**, 413–418 (2003).
14. A. Finnemore *et al.*, *Nat. Commun.* **3**, 966 (2012).
15. Y. Kim *et al.*, *Nature* **500**, 59–63 (2013).
16. T. Kato, T. Suzuki, T. Irie, *Chem. Lett.* **29**, 186–187 (2000).
17. L. J. Bonderer, A. R. Studart, L. J. Gauckler, *Science* **319**, 1069–1073 (2008).
18. P. Laaksonen *et al.*, *Angew. Chem. Int. Ed.* **50**, 8688–8691 (2011).
19. P. Das *et al.*, *Nat. Commun.* **6**, 5967 (2015).
20. B. Zhu *et al.*, *Angew. Chem. Int. Ed.* **54**, 8653–8657 (2015).
21. H. Le Ferrand, F. Bouville, T. P. Niebel, A. R. Studart, *Nat. Mater.* **14**, 1172–1179 (2015).
22. S. Deville, E. Saiz, R. K. Nalla, A. P. Tomsia, *Science* **311**, 515–518 (2006).
23. E. Munch *et al.*, *Science* **322**, 1516–1520 (2008).
24. F. Bouville *et al.*, *Nat. Mater.* **13**, 508–514 (2014).
25. H. Bai, Y. Chen, B. Delattre, A. P. Tomsia, R. O. Ritchie, *Sci. Adv.* **1**, e1500849 (2015).
26. F. Zhu *et al.*, *Chem. Asian J.* **8**, 3002–3009 (2013).
27. M. Niederberger, H. Cölfen, *Phys. Chem. Chem. Phys.* **8**, 3271–3287 (2006).
28. H. Cölfen, M. Antonietti, *Mesocrystals and Nonclassical Crystallization* (Wiley, Chichester, UK, 2008).
29. J. Wang, L. L. Shaw, *Biomaterials* **30**, 6565–6572 (2009).
30. D. Gebauer, H. Cölfen, A. Verch, M. Antonietti, *Adv. Mater.* **21**, 435–439 (2009).
31. S. Weiner, L. Addadi, H. D. Wagner, *Mater. Sci. Eng. C* **11**, 1–8 (2000).
32. J. Seto *et al.*, *Proc. Natl. Acad. Sci. U.S.A.* **109**, 3699–3704 (2012).
33. Y. Shao, H. P. Zhao, X. Q. Feng, H. Gao, *J. Mech. Phys. Solids* **60**, 1400–1419 (2012).
34. F. Barthelat, H. Tang, P. Zavattieri, C. Li, H. Espinosa, *J. Mech. Phys. Solids* **55**, 306–337 (2007).
35. R. Z. Wang, Z. Suo, A. G. Evans, N. Yao, I. A. Aksay, *J. Mater. Res.* **16**, 2485–2493 (2001).
36. R. Rabiei, S. Bekah, F. Barthelat, *Acta Biomater.* **6**, 4081–4089 (2010).
37. P. Fratzl, O. Kolednik, F. D. Fischer, M. N. Dean, *Chem. Soc. Rev.* **45**, 252–267 (2016).
38. S. Deville, *Adv. Eng. Mater.* **10**, 155–169 (2008).

ACKNOWLEDGMENTS

The authors thank Y. Tian, L. Chen, and Y. Guan for computed tomography imaging, and L. Wang for sample preparation. The authors also thank Y. Ni and Z. Song for discussion about mechanical models. This work was supported by the National Natural Science Foundation of China (grant 21431006), the Foundation for Innovative Research Groups of the National Natural Science Foundation of China (grant 21521001), the National Basic Research Program of China (grants 2014CB931800 and 2013CB931800), the Users with Excellence and Scientific Research Grant of Hefei Science Center of CAS (2015HSC-UE007 and 2015SRG-HSC038), and Key Research Program of Frontier Sciences, CAS (Grant QYZDJ-SSW-SLH036). Data are available in the supplementary materials.

SUPPLEMENTARY MATERIALS

www.sciencemag.org/content/354/6308/107/suppl/DC1
Materials and Methods
Figs. S1 to S22
Table S1
Movies S1 to S3
References (*39*–*49*)

17 April 2016; accepted 4 August 2016
Published online 18 August 2016
10.1126/science.aaf8991

COGNITION

Great apes anticipate that other individuals will act according to false beliefs

Christopher Krupenye,[1]*† Fumihiro Kano,[2,3]*† Satoshi Hirata,[2] Josep Call,[4,5] Michael Tomasello[5,6]

Humans operate with a "theory of mind" with which they are able to understand that others' actions are driven not by reality but by beliefs about reality, even when those beliefs are false. Although great apes share with humans many social-cognitive skills, they have repeatedly failed experimental tests of such false-belief understanding. We use an anticipatory looking test (originally developed for human infants) to show that three species of great apes reliably look in anticipation of an agent acting on a location where he falsely believes an object to be, even though the apes themselves know that the object is no longer there. Our results suggest that great apes also operate, at least on an implicit level, with an understanding of false beliefs.

Central to everything that makes us human—including our distinctive modes of communication, cooperation, and culture—is our theory of mind (TOM). TOM is the ability to impute unobservable mental states, such as desires and beliefs, to others (*1*, *2*). For nearly four decades, a cardinal question in psychology has concerned whether nonhuman animals, such as great apes, also possess this cognitive skill (*1*, *3*). A variety of nonverbal behavioral experiments have provided converging evidence that apes can predict others' behavior, not simply based on external cues but rather on an understanding of others' goals, perception, and knowledge (*3*, *4*). However, it remains unclear whether apes can comprehend reality-incongruent mental states (e.g., false beliefs) (*3*), as apes have failed to make explicit behavioral choices that reflect false-belief understanding in several food-choice tasks (*4*–*6*). False-belief understanding is of particular interest because it requires recognizing that others' actions are driven not by reality but by beliefs about reality, even when those beliefs are false.

In human developmental studies, it is only after age 4 that children pass traditional false-belief tests, in which they must explicitly predict a mistaken agent's future actions (*7*). However, recent evidence has shown that even young infants can pass modified false-belief tests that involve the use of simplified task procedures and spontaneous-gaze responses as measures [e.g., violation of expectation (*8*), anticipatory looking (*9*, *10*)]. For example, anticipatory looking paradigms exploit

[1]Department of Evolutionary Anthropology, Duke University, Durham, NC 27708, USA. [2]Kumamoto Sanctuary, Wildlife Research Center, Kyoto University, Kumamoto, Japan. [3]Primate Research Institute, Kyoto University, Inuyama, Japan. [4]School of Psychology and Neuroscience, University of St Andrews, St Andrews, UK. [5]Department of Developmental and Comparative Psychology, Max Planck Institute for Evolutionary Anthropology, Leipzig, Germany. [6]Department of Psychology and Neuroscience, Duke University, Durham, NC 27708, USA.
*These authors contributed equally to this work. **†Corresponding author. Email: ckrupenye@gmail.com (C.K.); fkanou@gmail.com (F.K.)**

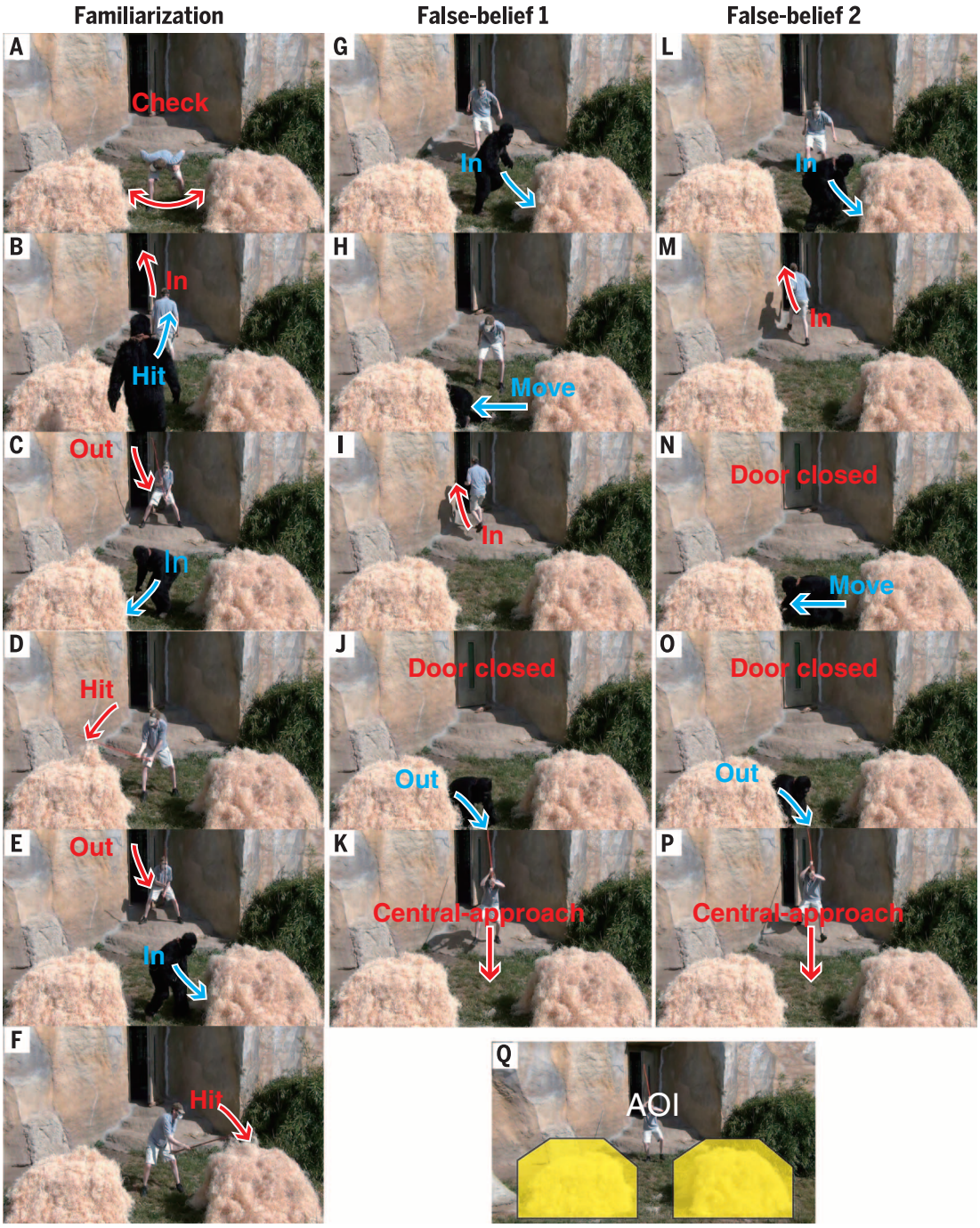

Fig. 1. Events shown in experiment one. (**A** to **F**) Familiarization. (**G** to **J**) Belief induction for the FB1 (false belief one) condition. (**K**) Central approach for FB1. (**L** to **O**) Belief induction for FB2. (**P**) Central approach for FB2. (**Q**) Areas of interest (AOIs) defined for the target and distractor haystacks. See movie S1.

individuals' tendency to look to a location in anticipation of an impending event and thus can measure a participant's predictions about what an agent is about to do, even when that agent holds a false belief about the situation. Only two studies have used spontaneous-gaze false-belief tasks with nonhuman primates. Both failed to replicate with monkeys the results with infants, despite monkeys' success in true-belief conditions (*11*, *12*).

In our study, we used an anticipatory looking measure (*10*) to test for false-belief understanding in three species of apes (chimpanzees, *Pan troglodytes*; bonobos, *Pan paniscus*; orangutans, *Pongo abelii*). Previous studies have established that apes reliably make anticipatory looks based on agents' goal-directed actions and subjects' event memories (*13*, *14*). In our experiments, apes watched short videos on a monitor while their gaze was noninvasively recorded using an infrared eye-tracker. Our design, controls, and general procedure replicated a seminal anticipatory looking false-belief study with human infants (*10*).

We conducted a pair of experiments using the same design but introduced distinct scenarios in each. The common design involved two familiarization trials followed by a single test trial [either the FB1 or FB2 (false belief one or two) condition; between-subjects design]. In our scenarios, a human agent pursued a goal object that was hidden in one of two locations. During the first familiarization, the agent witnessed the hiding of the object in one location before searching for it there. In the second, the object was hidden in the other location and the agent pursued it there. These trials served to demonstrate that the object could be hidden in either of the two locations and that, when knowledgeable, the agent would search for it in its true location. During the belief-induction phase, the agent witnessed the initial hiding of the object, but the object was then moved to a second location while the agent was either present

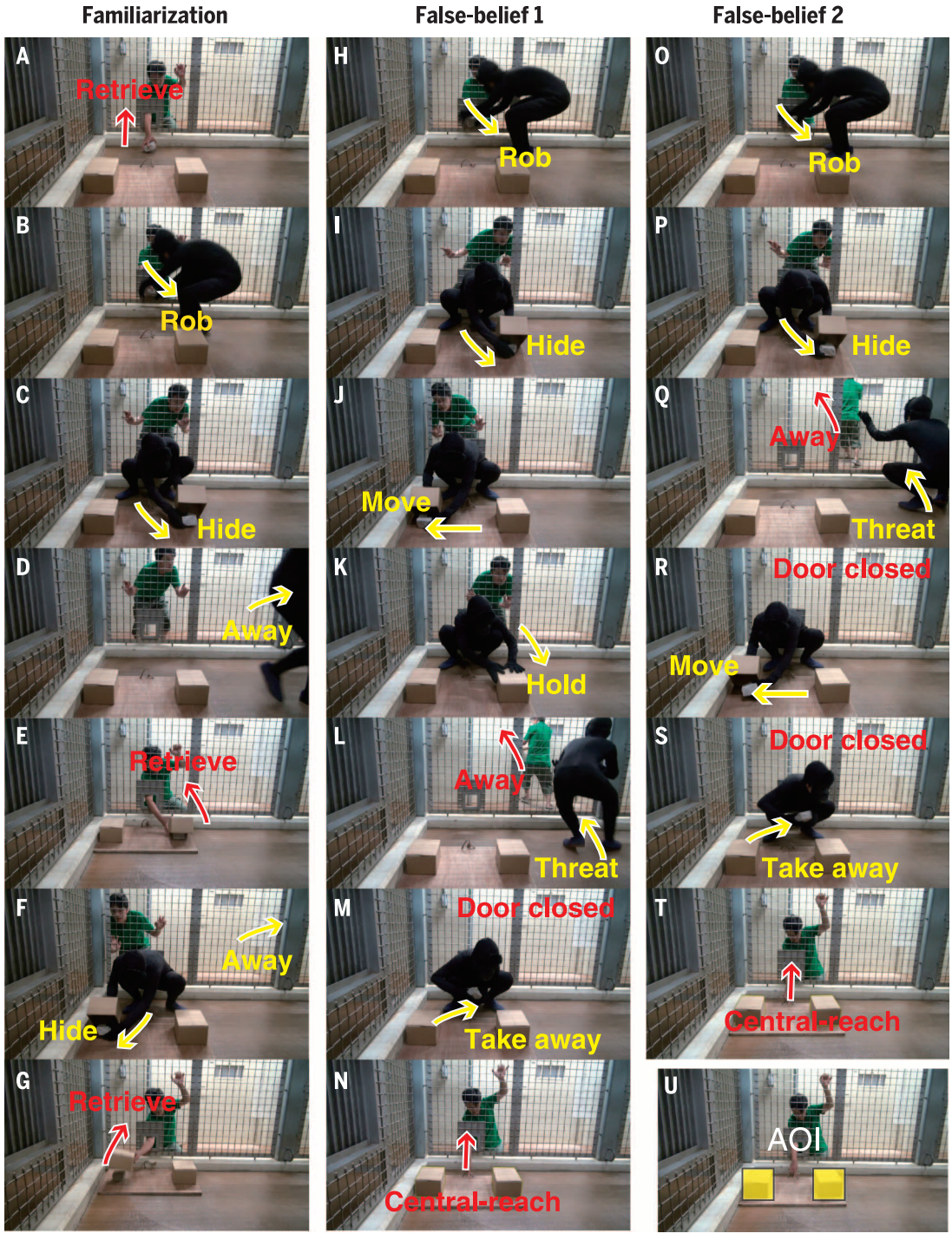

Fig. 2. Events shown in experiment two. (**A** to **G**) Familiarization. (**H** to **M**) Belief induction for the FB1 condition. (**N**) Central reach for FB1. (**O** to **S**) Belief induction for FB2. (**T**) Central reach for FB2. (**U**) AOIs defined for the target and distractor boxes. Following the infant study (*10*), we included an additional action in FB1 [KK touched the distractor box (K)] to control for subjects looking to the last place that the actor attended. See movie S2.

(FB1) or absent (FB2). In both conditions, the object was then completely removed before the agent returned to search for it. The actions presented during the induction phase controlled for several low-level cues—namely, that participants could not solve the task by simply expecting the agent to search in the first or last location where the object was hidden or the last location where the agent attended (*10*). Whether the object was hidden first in the left or right location during familiarization trials and whether the target of the agent's false belief was the left or right location during test trials were counterbalanced across subjects.

Experiments one and two presented scenarios that were specifically intended to evoke apes' spontaneous action anticipation in different contexts. To encourage subjects' engagement, we presented simulated agonistic encounters between a human (actor) and King Kong (KK), an unreal apelike character unfamiliar to the subjects (*14*). To minimize the possibility that apes could solve the task by responding to learned behavioral cues, our scenarios involved events that were novel to our participants. In experiment one, the actor attempted to search for KK, who had hidden himself in one of two large haystacks (Fig. 1 and movie S1). In experiment two, the actor attempted to retrieve a stone that KK had stolen and hidden in one of two boxes (Fig. 2 and movie S2). We confirmed that apes unambiguously attended to the depicted actions during the belief-induction phases of both experiments (figs. S3 and S4) (*15*).

Apes' anticipatory looks were assessed on the basis of their first looks to the target (the location where the actor falsely believed the object to be)

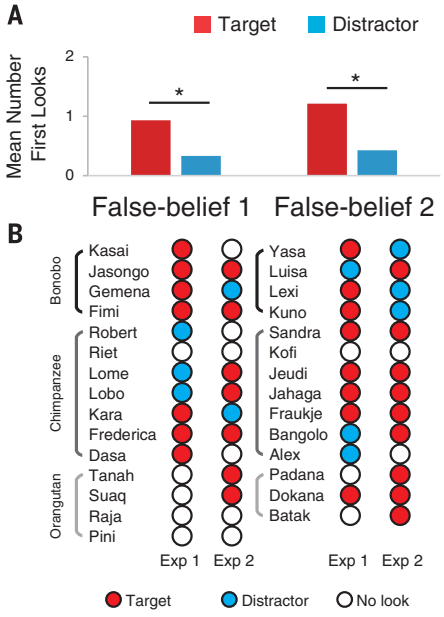

Fig. 3. Apes' performance across the two experiments. (**A**) Mean number of first looks to the target and the distractor for the 29 subjects who participated in both experiments. Asterisks indicate $P < 0.05$, Wilcoxon signed rank test. (**B**) Individual scores in each experiment.

Table 1. Number of participants who made first looks to either the target or the distractor during the agent's approach in experiments one ($N = 40$) and two ($N = 30$). Values in parentheses indicate the number of participants who did not look at either.

Condition	Target	Distractor	Total
Experiment one			
FB1	10	4	14 (6)
FB2	10	6	16 (4)
Total	20	10	30 (10)
Experiment two			
FB1	8	2	10 (6)
FB2	9	3	12 (2)
Total	17	5	22 (8)

or the distractor (the other location) as the actor ambiguously approached the two locations—from the start to the end of the actor's walk toward the haystacks [central approach; experiment one (Fig. 1, K and P)] and reach toward the boxes [central reach; experiment two (Fig. 2, N and T)] (both 4.5 s). Software scored looks automatically on the basis of areas of interest (*15*) (Figs. 1Q and 2U). The actor's gaze and gait during the central approach and central reach provided no directional cues (figs. S1 and S2) (*15*), and the videos ended without the actor hitting or grabbing the target. We used two different scenarios to gauge the robustness of apes' responses under different conditions.

Table 1 summarizes the results for each experiment. In experiment one, we tested 40 apes [19 chimpanzees, 14 bonobos, and 7 orangutans (table S1) (*15*)]. Thirty subjects looked to either the target or the distractor during the central-approach period. Of these 30, 20 looked first at the target ($P = 0.098$, two-tailed binomial test). There was no difference between the FB1 and FB2 conditions ($P = 0.70$, Fisher's exact test). In experiment two, we tested 30 subjects (29 from experiment one, plus one additional bonobo). Twenty-two apes made explicit looks to the target or the distractor during this period. Of these 22, 17 looked first at the target ($P = 0.016$, two-tailed binomial test), and there was no difference between the FB1 and FB2 conditions ($P = 1.0$, Fisher's exact test).

We then conducted a combined analysis with the 29 apes that participated in both experiments. We compared the number of first looks (maximum of two looks; i.e., one per experiment) each subject made to the target versus to the distractor during the central-approach and central-reach periods (Fig. 3). Apes made significantly more first looks to the target than to the distractor, both overall (Wilcoxon signed rank test: $Z = 3.25$, $N = 29$, $P = 0.001$, $r = 0.42$) and in each condition (FB1: $Z = 1.98$, $N = 15$, $P = 0.046$, $r = 0.36$; FB2: $Z = 2.15$, $N = 14$, $P = 0.031$, $r = 0.40$) (Fig. 3A). No significant difference was detected across species. To test this, we first calculated difference scores for each ape (number of first looks to target minus to distractor) and then subjected these scores to the Kruskal-Wallis H test [$\chi^2(2) = 0.46$, $P = 0.79$] (Fig. 3B).

Our findings show that apes accurately anticipated the goal-directed behavior of an agent who held a false belief. Our design and results controlled for several explanations. First, apes could not solve the task by simply expecting the actor to search in the first or last location where the object was hidden, the last location the actor attended, or the last location KK acted on. Second, apes could not merely respond to violations of three-way associations between the actor, the target object, and the object's location, formed during familiarization or belief-induction phases (*16*). Instead, the apes actively predicted the actor's behavior. Heyes (*17*) argued that a low-level account could explain Southgate *et al.*'s (*10*) results if subjects overlooked the object's movement while the agent was not attending and imagined the object in its previous location. We confirmed that apes closely tracked all such movements (figs. S3 and S4) (*15*). Third, our results cannot be explained as attribution of ignorance rather than false belief. Apes did not simply expect the actor's ignorance to lead to error or uncertainty (*18*); they specifically anticipated that the actor would search for the object where he falsely believed it to be.

Apes were never shown the actor's search behavior when he held a false belief, precluding reliance on external behavioral cues learned during the task. By requiring subjects to make predictions in situations that involved a constellation of novel features (e.g., a human attacking an apelike character hiding in a haystack), we also minimized the possibility that subjects could apply behavior rules acquired through extensive learning during past experiences. Nevertheless, we acknowledge that all change-of-location false-belief tasks are, in principle, open to an abstract behavior rule–based explanation—namely, that apes could solve the task by relying on a rule that agents search for things where they last saw them (*16*). However, this explanatory framework cannot easily accommodate the diversity of existing evidence for ape TOM (*3*) nor can it account for recent evidence that human infants and apes appear to infer whether others can see through objects that look opaque, based on their own experience with the occlusive properties (i.e., see-through or opaque) of those objects (*19*, *20*).

Thus, our results, in concert with existing data, suggest that apes solved the task by ascribing a false belief to the actor, challenging the view that the ability to attribute reality-incongruent mental states is specific to humans. Given that apes have not yet succeeded on tasks that measure false-belief understanding based on explicit behavioral choices (*4*–*6*), the present evidence may constitute an implicit understanding of belief (*9*). Differential performance between tasks may reflect differences in task demands or context, or less flexible abilities in apes compared with humans. At minimum, apes can anticipate that an actor will pursue a goal object where he last saw it, even though the apes themselves know that it is no longer there. That great apes operate, at least on an implicit level, with an understanding of false beliefs suggests that this essential TOM skill is likely at least as old as humans' last common ancestor with the other apes.

REFERENCES AND NOTES

1. D. Premack, G. Woodruff, *Behav. Brain Sci.* **1**, 515–526 (1978).
2. R. W. Byrne, A. W. Whiten, *Machiavellian Intelligence: Social Expertise and the Evolution of Intellect in Monkeys, Apes, and Humans* (Clarendon Press, 1988).
3. J. Call, M. Tomasello, *Trends Cogn. Sci.* **12**, 187–192 (2008).
4. B. Hare, J. Call, M. Tomasello, *Anim. Behav.* **61**, 139–151 (2001).
5. J. Kaminski, J. Call, M. Tomasello, *Cognition* **109**, 224–234 (2008).
6. C. Krachun, M. Carpenter, J. Call, M. Tomasello, *Dev. Sci.* **12**, 521–535 (2009).
7. H. M. Wellman, D. Cross, J. Watson, *Child Dev.* **72**, 655–684 (2001).
8. K.H. Onishi, R. Baillargeon, *Science* **308**, 255–258 (2005).
9. W. A. Clements, J. Perner, *Cogn. Dev.* **9**, 377–395 (1994).

10. V. Southgate, A. Senju, G. Csibra, *Psychol. Sci.* **18**, 587–592 (2007).
11. D. C. Marticorena, A. M. Ruiz, C. Mukerji, A. Goddu, L. R. Santos, *Dev. Sci.* **14**, 1406–1416 (2011).
12. A. Martin, L. R. Santos, *Cognition* **130**, 300–308 (2014).
13. F. Kano, J. Call, *Psychol. Sci.* **25**, 1691–1698 (2014).
14. F. Kano, S. Hirata, *Curr. Biol.* **25**, 2513–2517 (2015).
15. Materials and methods are available as supplementary materials on *Science* Online.
16. J. Perner, T. Ruffman, *Science* **308**, 214–216 (2005).
17. C. Heyes, *Dev. Sci.* **17**, 647–659 (2014).
18. R. Baillargeon, R. M. Scott, Z. He, *Trends Cogn. Sci.* **14**, 110–118 (2010).
19. A. Senju, V. Southgate, C. Snape, M. Leonard, G. Csibra, *Psychol. Sci.* **22**, 878–880 (2011).
20. K. Karg, M. Schmelz, J. Call, M. Tomasello, *Anim. Behav.* **105**, 211–221 (2015).

ACKNOWLEDGMENTS

We thank the staff at the Wolfgang Kohler Primate Research Center and Kumamoto Sanctuary for assistance. Financial support was provided by the NSF Graduate Research Fellowship Program (grant DGE-1106401 to C.K.), the Ministry of Education, Culture, Sports, Science and Technology of Japan (grant K-CONNEX to F.K.), the Japan Society for the Promotion of Science (grants KAKENHI 26885040 and 16K21108 to F.K. and grants KAKENHI 26245069 and 24000001 to S.H.), and the European Research Council (Synergy grant 609819 SOMICS to J.C.). Data are available in the main text and supplementary materials.

SUPPLEMENTARY MATERIALS

www.sciencemag.org/content/354/6308/110/suppl/DC1
Materials and Methods
Supplementary Text
Figs. S1 to S5
Tables S1 to S5
Movies S1 and S2

27 April 2016; accepted 26 August 2016
10.1126/science.aaf8110

STRUCTURAL BIOLOGY

The methanogenic CO_2 reducing-and-fixing enzyme is bifunctional and contains 46 [4Fe-4S] clusters

Tristan Wagner,[1] Ulrich Ermler,[2] Seigo Shima[1,3]*

Biological methane formation starts with a challenging adenosine triphosphate (ATP)–independent carbon dioxide (CO_2) fixation process. We explored this enzymatic process by solving the x-ray crystal structure of formyl-methanofuran dehydrogenase, determined here as Fwd(ABCDFG)$_2$ and Fwd(ABCDFG)$_4$ complexes, from *Methanothermobacter wolfeii*. The latter 800-kilodalton apparatus consists of four peripheral catalytic sections and an electron-supplying core with 46 electronically coupled [4Fe-4S] clusters. Catalysis is separately performed by subunits FwdBD (FwdB and FwdD), which are related to tungsten-containing formate dehydrogenase, and subunit FwdA, a binuclear metal center carrying amidohydrolase. CO_2 is first reduced to formate in FwdBD, which then diffuses through a 43-angstrom-long tunnel to FwdA, where it condenses with methanofuran to formyl-methanofuran. The arrangement of [4Fe-4S] clusters functions as an electron relay but potentially also couples the four tungstopterin active sites over 206 angstroms.

Methanogenic archaea produce ~1 billion tons of methane per year and thus play an important ecological role in the global carbon cycle (*1*). Biological methane is produced mainly from acetate and CO_2-H_2 (*1*). For methanogenesis from CO_2, the metabolic pathway starts with the reduction of CO_2 to form formyl-methanofuran (formyl-MFR) (E_0' = −530 mV, where E_0' is the standard redox potential at pH 7) (*2*), using reduced ferredoxin (E' = ~−500 mV, where E' is a physiological redox potential at pH 7) (*1*) as the electron donor (Fig. 1A). The reaction is catalyzed by formyl-MFR dehydrogenase. There are two isoenzymes in most methanogens, a tungsten iron-sulfur protein (Fwd) and a molybdenum iron-sulfur protein (Fmd) (*3*–*9*).

Formyl-MFR dehydrogenase uses CO_2 rather than bicarbonate as a substrate (*10*, *11*). CO_2 spontaneously reacts with MFR to form carboxy-MFR at a rate that is compatible with carboxy-MFR being an intermediate in CO_2 reduction to formyl-MFR (*10*, *11*). Therefore, it was assumed that carboxy-MFR is reduced to formyl-MFR in a subsequent step at the tungsten or molybdenum active site of formyl-MFR dehydrogenases. This reaction sequence is in line with all other CO_2-fixing enzymatic processes, except for that of acetogenesis, where CO_2 is first reduced to formate and then conjugated with N-10 of tetrahydrofolate using adenosine triphosphate (ATP) (*12*).

To elucidate the catalytic mechanism of this sequence, we purified and crystallized the tungstopterin-containing formyl-MFR dehydrogenase (FwdABCDFG) complex from the thermophilic methanogenic archaeon *Methanothermobacter wolfeii* (fig. S1) under strict anoxic conditions in four crystal forms (table S1) (*13*). The x-ray analysis of individual subunit structures and, subsequently, of the whole protein complex is primarily based on orthorhombic and triclinic crystals diffracting to 1.9 and 2.6 Å resolution, in which the enzyme is present as a dimer of the FwdABCDFG heterohexamer [12-subunit oligomer (12-mer)] (Fig. 1B and fig. S2A) and a tetramer of the heterohexamer (24-mer) (fig. S2B), respectively. Notably, FwdF and FwdG were absent in gel electrophoresis but are integral components of the enzyme complex.

Subunit FwdA (63 kDa) is structurally classified as a member of the amidohydrolase superfamily, which includes urease, phosphotriesterase, dihydroorotase, and dihydropyrimidinases (fig. S3) (*7*–*9*). These enzymes are characterized by a binuclear metal center positioned inside a deep solvent-accessible cavity at the entry of an $(\alpha/\beta)_8$ TIM barrel. The metal center is predicted to be composed of two zinc atoms that are analogous to the most structurally related enzyme, dihydroorotase (*14*). FwdA also contains zinc ligands, N6-carboxylysine, and a catalytically crucial aspartate, all of which are strictly conserved in the amidohydrolase superfamily (Fig. 2D and figs. S3A and S4). The x-ray structure of the triclinic 24-mer crystals soaked with MFR revealed the bulky C1 carrier in the cavity between the dinuclear metal center and the bulk solvent (Fig. 2D and fig. S4).

Subunit FwdB (48 kDa) harbors the tungstopterin active site and a [4Fe-4S] cluster. This subunit is structurally related to domains I, II, and III of molybdenum- and tungsten-containing formate dehydrogenase (*7*–*9*); FwdD (14 kDa) is structurally related to domain IV (*7*–*9*). A solution nuclear magnetic resonance structure of FwdD from *Archaeoglobus fulgidus* has been reported (Protein Data Bank ID: 2KI8). The redox-active tungsten of FwdBD (FwdB and FwdD) is coordinated by four dithiolene thiolates of two tungstopterin guanine dinucleotide molecules (Fig. 2, A to C), by the thiolate of Cys^{118}, and by an inorganic sulfido ligand (fig. S5). The residues involved in the [4Fe-4S] cluster, pterin-binding, tungsten-ligation, and active sites are essentially conserved between FwdBD and the molybdenum- or tungsten-containing formate dehydrogenases (*15*–*18*). FwdC (29 kDa) is a subunit with low sequence similarity to the C-terminal domain of glutamate synthase (*19*), flanking the tunnel that channels ammonia between the two active sites.

FwdF (39 kDa) is a polyferredoxin composed of four similar ferredoxin domains (*7*–*9*) that are arranged in a T-shaped conformation (Fig. 1C and figs. S6 and S7). The fusion of the ferredoxin domains, each carrying two [4Fe-4S] clusters, does not occur consecutively; the third ferredoxin domain (amino acids 143 to 221) is inserted into the second ferredoxin domain (amino acids 106 to 137 and 228 to 257) (fig. S7A). FwdG (8.6 kDa) adopts a classical ferredoxin fold that hosts two [4Fe-4S] clusters.

The 12-mer has an electron-supplying core (two FwdFG subunits) and two flanking catalytic sections, each formed by FwdA and FwdBD.

[1]Max Planck Institute for Terrestrial Microbiology, Karl-von-Frisch-Straße 10, 35043 Marburg, Germany. [2]Max Planck Institute of Biophysics, Max-von-Laue-Straße 3, 60438 Frankfurt am Main, Germany. [3]Precursory Research for Embryonic Science and Technology (PRESTO), Japan Science and Technology Agency (JST), 332-0012 Saitama, Japan.
*Corresponding author. Email: shima@mpi-marburg.mpg.de

Likewise, the 24-mer core (four FwdFG subunits) is flanked by four catalytic sections. The FwdA and FwdBD subunits harbor one active site each, such that both reactions proceed spatially separated from each other (Fig. 2, A and B). In contrast to previous proposals, the structural data strongly suggest that in the first step, CO_2 is reduced to formate (E_0' = −430 mV) by ferredoxin (E' = ~−500 mV) at the tungstopterin active site in FwdBD; the protons required for the reaction could be supplied by a hydrophilic cavity filled with plenty of water molecules (figs. S8 and S9). This revision is in accordance with the high structural similarity between FwdBD and tungsten- or molybdenum-containing formate dehydrogenases and the direct connection with the adjacent electron-supplying system (see below) (Fig. 2C). The molybdenum-containing formyl-MFR dehydrogenase isoenzymes (Fmd) from *M. wolfeii* and *Methanosarcina barkeri* are known to exhibit weak formate oxidation activity (*3*, *4*), which supports our proposal. The deeply buried redox-active tungsten center is only connected with the bulk solvent via a narrow hydrophobic tunnel that is 40 Å long (fig. S10). Therefore, the active site is accessible to CO_2 but not to formate, the formate transition state analog azide (*20*), and the bulky MFR.

In a subsequent step, the produced formate is covalently bound to the amino group of MFR to generate formyl-MFR at the second active site localized in FwdA. This reaction was deduced from the high similarity of the active sites between FwdA and other enzymes of the amidohydrolase superfamily (*14*). In particular, the production of formate from formyl-MFR catalyzed by an FwdABC homolog (FhcABC from methylotrophic bacteria that is devoid of the pterin cofactor) underlines our conclusion (*21*). Moreover, the determined structure of the FwdA-MFR complex revealed a mechanistically relevant active-site geometry (Fig. 2D and fig. S4); the catalytically active amino group of MFR directly interacts with the binuclear metal site and Asp^{385} (Fig. 2D and fig. S4). On the basis of this finding and detailed information of a related amidohydrolase catalyzing the analogous formation of dihydroorotate from carbamoyl aspartate (*14*), we postulated a plausible catalytic mechanism for the reaction between formate and MFR to generate formyl-MFR (fig. S11).

The proposed two-step scenario of CO_2 reduction and fixation is further corroborated by an internal hydrophilic tunnel (43 Å long) between the active sites of FwdBD and FwdA, which is ideally suited for the transport of formate and formic acid [pK_a = 3.75 (K_a, acid dissociation constant)] (Fig. 2B and fig. S12). The tunnel consists of a wide solvent-filled cavity with a narrow passage in front of each active site (Figs. 2B and 3). Arg^{288} of FwdB and Lys^{64} of FwdA are positioned at these bottlenecks and might control gate opening and closing, with the aim of arresting formate until MFR binding. Supplemented formate is not used as a substrate by FwdABCDFG from *M. wolfeii* (*3*, *4*), which is consistent with a completely tight tunnel between the active sites inside the FwdABCDFG protein complex. Release or uptake of formate into or from the solution is then impossible. The weak formate oxidation activity of the aforementioned molybdenum-containing isoenzymes (*3*, *4*) suggests a leaky tunnel. Tunneling of intermediates has been reported for several bifunctional enzymes, such as glutamate synthase (fig. S13) and the carbon monoxide dehydrogenase–acetyl-CoA synthase complex (*22*, *23*), to allow for the migration of small molecules in a facilitated one-directional diffusion process, thus optimizing catalysis (*24*).

Considering that under standard conditions at pH 7.0 the formation of formyl-MFR from formate and MFR is an endergonic reaction (Gibbs free energy change $\Delta G^{\circ\prime}$ = +12 to 19 kJ/mol) (*2*), energy coupling with the exergonic reduction of CO_2 to formate with reduced ferredoxin might be accomplished by pumping formate into the encapsulated tunnel to increase its local concentration. The only sequentially related CO_2 reduction-and-fixation

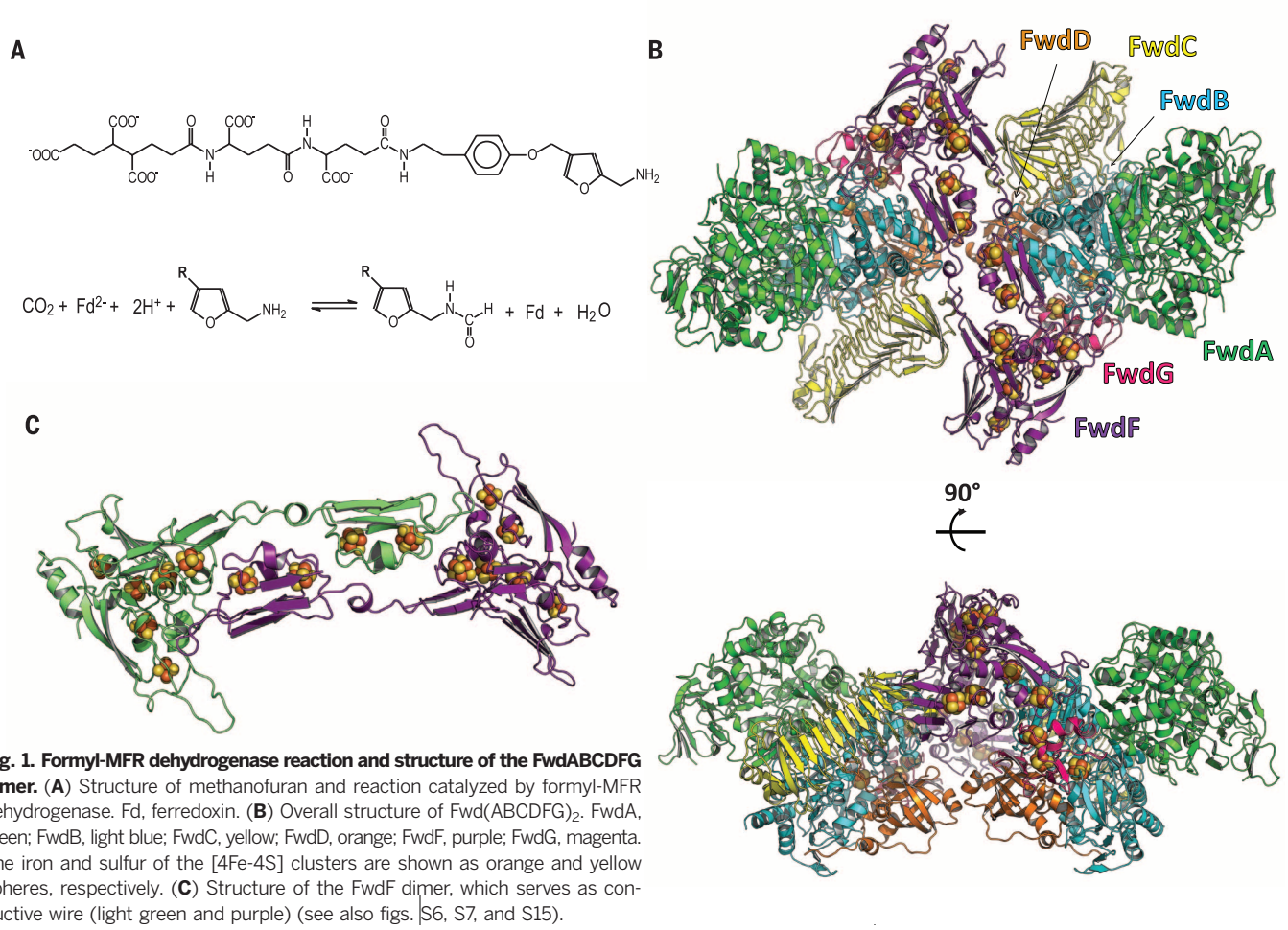

Fig. 1. Formyl-MFR dehydrogenase reaction and structure of the FwdABCDFG dimer. (**A**) Structure of methanofuran and reaction catalyzed by formyl-MFR dehydrogenase. Fd, ferredoxin. (**B**) Overall structure of Fwd(ABCDFG)$_2$. FwdA, green; FwdB, light blue; FwdC, yellow; FwdD, orange; FwdF, purple; FwdG, magenta. The iron and sulfur of the [4Fe-4S] clusters are shown as orange and yellow spheres, respectively. (**C**) Structure of the FwdF dimer, which serves as conductive wire (light green and purple) (see also figs. S6, S7, and S15).

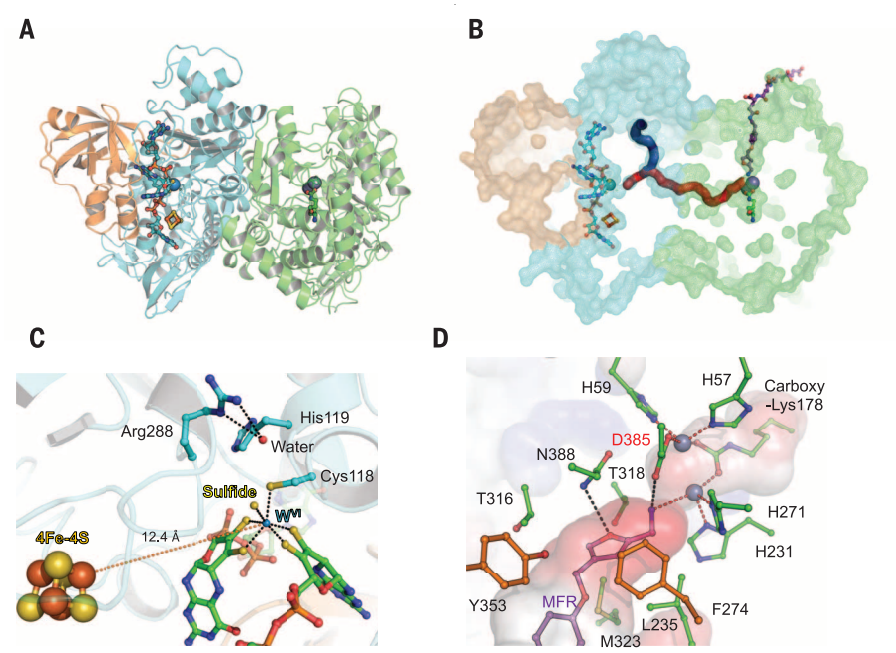

Fig. 2. Structures of the FwdABD subcomplex. (**A**) Catalytic subunits. The amidohydrolase FwdA (green) and the formate dehydrogenase FwdBD (light blue, orange) are shown. Tungstopterin (carbon in blue), the [4Fe-4S] cluster (orange and yellow), and the carboxylysine (carbon in green) at the binuclear zinc center are depicted as ball-and-stick models. (**B**) Surface model of FwdABD with cofactors and MFR (purple). The proposed formate tunnel (in red, solid surface) connects the active sites of FwdB and FwdA, and the narrow CO_2 tunnel (dark blue, solid surface) exclusively allows CO_2 to reach the tungsten center from the bulk solvent. (**C**) Active site of FwdB. The tungsten (light blue) of tungstopterin (green) is coordinated by six sulfurs (yellow) in a distorted octahedral arrangement. The space between Cys^{118}, the inorganic sulfur tungsten ligand, His^{119}, and Arg^{228} is occupied by solvent but appears to be well suited for CO_2 binding (*17*). (**D**) Active site of FwdA bound to MFR. The two zinc ions are coordinated to four histidines and an N6-carboxylysine protruding from the cavity bottom. One zinc ion is ligated to the catalytically essential Asp^{385}. Aromatic (orange) and hydrophobic side chains flank the *p*-(β-aminoethyl)phenoxymethyl group. The 2-aminomethylfuran moiety is anchored to the polypeptide by two hydrogen bond donors and one π-stacking interaction with Phe^{274}. Coordination of the binuclear center and the hydrogen bonds of the MFR to the protein are indicated by red and black dashed lines, respectively. The electrostatic surface of the protein is shown in the gradient from red (acidic) to blue (basic). H, His; N, Asn; D, Asp; T, Thr; Y, Tyr; F, Phe; L, Leu; M, Met.

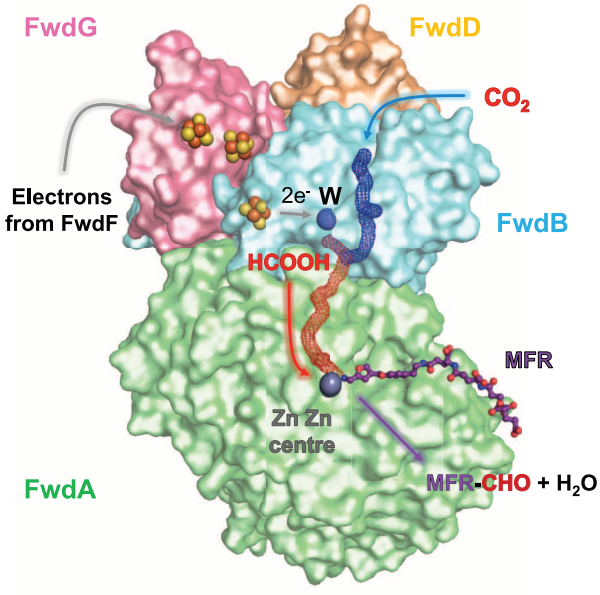

Fig. 3. Proposed mechanism of CO_2 reduction to formyl-MFR catalyzed by the FwdABCDFG complex. Electrons (e^-) are funneled through the [4Fe-4S] cluster chain to the tungsten center. CO_2 enters the catalytic chamber through a hydrophobic tunnel (blue mesh) of FwdBD and is reduced to formate; W^{IV} is oxidized to W^{VI}. Formic acid (or formate) diffuses via a hydrophilic tunnel (red mesh) to the active site of FwdA, where it is condensed with MFR at the binuclear zinc center (gray sphere).

process found in acetogenesis is catalyzed by two separate enzymes, formate dehydrogenase and formyl-tetrahydrofolate synthetase, the latter of which requires ATP for formate activation.

In the 24-mer, two 12-mers are associated in an hourglass-like arrangement (Fig. 4), thereby furnished with an additional [4Fe-4S] cluster per each 12-mer that covalently links the two FwdF subunits (fig. S6). The two extra [4Fe-4S] clusters in the 24-mer are 7.7 Å apart from each other and 10.3 Å away from the next [4Fe-4S] cluster (figs. S2B and S14), which allows interdodecameric electron shuttling (Fig. 4 and fig. S15). The cysteine ligands of the two additional [4Fe-4S] clusters originating from both FwdF subunits are fully conserved in methanogens without cytochromes, except for those belonging to Methanomicrobiales. The residues of the surrounding loop, which are involved in interdodecameric interactions, are also conserved to a great extent (fig. S14). In addition, the 24-mer was observed in another crystal form [$P3_221$ (fig. S2B and table S1], which grew in a different crystallization solution (see supplementary materials). Finally, formyl-MFR dehydrogenase appears to make a huge complex with heterodisulfide reductase and other catabolic enzymes (*25*, *26*), which may stabilize the 24-mer FwdABCDFG structure. Therefore, the 24-meric supercomplex is assumed to be a physiologically active state and not a crystallographic artifact.

The 46 [4Fe-4S] clusters in the 24-mer are arranged in a stringlike distribution (Fig. 4). The edge-to-edge distances of 8.6 to 12.4 Å are characteristic of electrically connected redox centers (fig. S15) (*27*, *28*). Because polar and charged residues are known to affect the redox potential of iron-sulfur clusters (*29*), their similar surroundings concerning structure and electrostatics suggest that electrons are conducted almost isopotentially, without obvious thermodynamic barriers. The formed electron wire extends over distances of 188 Å between the redox-active tungsten centers of the 12-mer. The 24-mer uses the interdodecamer bridge between the two wires of the 12-mers to extend over 206 Å between active sites. The outer cluster of the two [4Fe-4S] clusters in the branched peripheral arm of the T-shaped FwdF subunits might serve as the entry point for electrons (Fig. 4) from where the electrons flow to the tungsten center via a chain of optimally spaced [4Fe-4S] clusters. Association between the formyl-MFR dehydrogenase complex and the electron-bifurcating [NiFe]-hydrogenase–heterodisulfide reductase complex (MvhABD-HdrABC) (*25*) implicates a long, direct electron transfer route from the site of electron bifurcation (HdrA) to the site of CO_2 reduction (FwdBD), perhaps via the FwdF entry point.

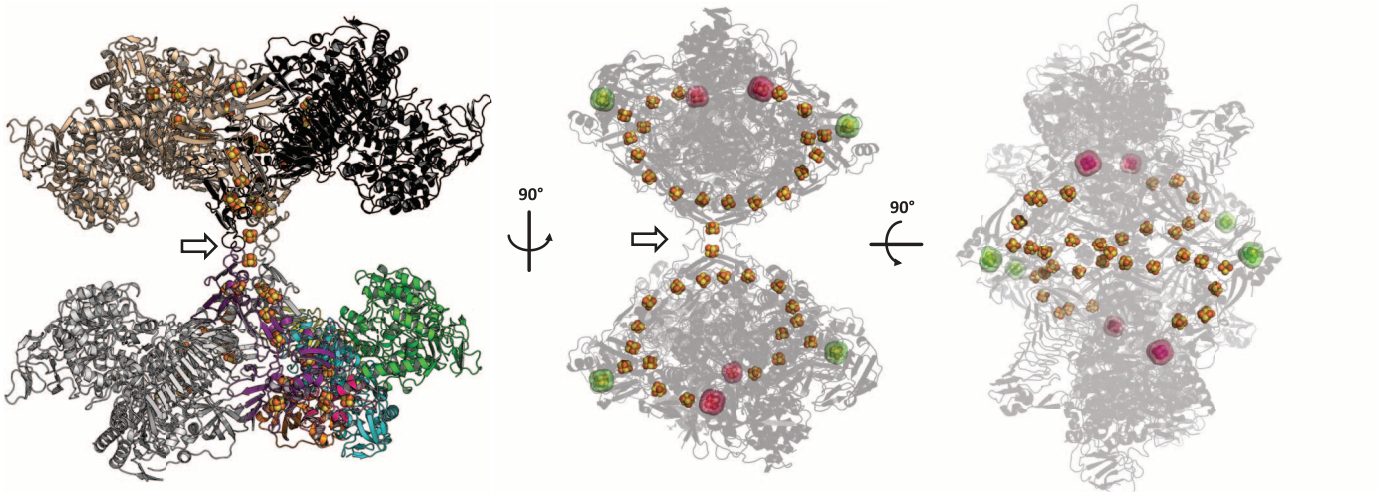

Fig. 4. Structure of the tetrameric FwdABCDFG supercomplex. (**Left**) Hourglass-shaped arrangement of the two Fwd(ABCDFG)$_2$ complexes (24-mer). The four heterohexamers are shown in black, gray, beige, and multicolor (the color code is the same as in Fig. 1B). The iron and sulfur of the [4Fe-4S] clusters are shown as orange and yellow spheres, respectively. (**Middle** and **Right**) Transparent side views. The four green [4Fe-4S] clusters mark the postulated entry point for the electrons; the four pink [4Fe-4S] clusters are the clusters next to tungsten. The two 12-mers interact via the two FwdF dimers, each with an extra [4Fe-4S] cluster (arrows).

It is unlikely that such a sophisticated apparatus of 46 electronically coupled [4Fe-4S] clusters evolved simply for supplying low-potential electrons for CO_2 reduction. Therefore, we assume an additional function regarding the 24-mer Fwd complex and, more broadly, methanogenic energy metabolism. For example, the four tungstopterin redox centers may couple each other over 206 Å and may also couple to the preceding enzymatic process reducing the [4Fe-4S] clusters for synchronizing the redox reactions. Alternatively, these clusters may function to store reducing equivalents in a manner similar to multicytochromes (*30*) and multiheme enzymes (*31*). A low-potential electron pool would allow for reaction flexibility with temporally varying amounts of CO_2.

REFERENCES AND NOTES

1. R. K. Thauer, A. K. Kaster, H. Seedorf, W. Buckel, R. Hedderich, *Nat. Rev. Microbiol.* **6**, 579–591 (2008).
2. P. A. Bertram, R. K. Thauer, *Eur. J. Biochem.* **226**, 811–818 (1994).
3. P. A. Bertram *et al.*, *Eur. J. Biochem.* **220**, 477–484 (1994).
4. R. A. Schmitz, S. P. J. Albracht, R. K. Thauer, *Eur. J. Biochem.* **209**, 1013–1018 (1992).
5. R. A. Schmitz, S. P. J. Albracht, R. K. Thauer, *FEBS Lett.* **309**, 78–81 (1992).
6. R. A. Schmitz, M. Richter, D. Linder, R. K. Thauer, *Eur. J. Biochem.* **207**, 559–565 (1992).
7. A. Hochheimer, R. A. Schmitz, R. K. Thauer, R. Hedderich, *Eur. J. Biochem.* **234**, 910–920 (1995).
8. A. Hochheimer, R. Hedderich, R. K. Thauer, *Arch. Microbiol.* **170**, 389–393 (1998).
9. A. Hochheimer, D. Linder, R. K. Thauer, R. Hedderich, *Eur. J. Biochem.* **242**, 156–162 (1996).
10. S. Bartoschek, J. A. Vorholt, R. K. Thauer, B. H. Geierstanger, C. Griesinger, *Eur. J. Biochem.* **267**, 3130–3138 (2000).
11. J. A. Vorholt, R. K. Thauer, *Eur. J. Biochem.* **248**, 919–924 (1997).
12. L. R. Celeste *et al.*, *Protein Sci.* **21**, 219–228 (2012).
13. Materials and methods are available as supplementary materials on *Science* Online.
14. J. B. Thoden, G. N. Phillips Jr., T. M. Neal, F. M. Raushel, H. M. Holden, *Biochemistry* **40**, 6989–6997 (2001).
15. J. C. Boyington, V. N. Gladyshev, S. V. Khangulov, T. C. Stadtman, P. D. Sun, *Science* **275**, 1305–1308 (1997).
16. H. Raaijmakers *et al.*, *Structure* **10**, 1261–1272 (2002).
17. L. B. Maia, J. J. G. Moura, I. Moura, *J. Biol. Inorg. Chem.* **20**, 287–309 (2015).
18. M. Jormakka, S. Törnroth, B. Byrne, S. Iwata, *Science* **295**, 1863–1868 (2002).
19. C. Binda *et al.*, *Structure* **8**, 1299–1308 (2000).
20. J. S. Blanchard, W. W. Cleland, *Biochemistry* **19**, 3543–3550 (1980).
21. B. K. Pomper, O. Saurel, A. Milon, J. A. Vorholt, *FEBS Lett.* **523**, 133–137 (2002).
22. H. Dobbek, V. Svetlitchnyi, L. Gremer, R. Huber, O. Meyer, *Science* **293**, 1281–1285 (2001).
23. T. I. Doukov, T. M. Iverson, J. Seravalli, S. W. Ragsdale, C. L. Drennan, *Science* **298**, 567–572 (2002).
24. X. Huang, H. M. Holden, F. M. Raushel, *Annu. Rev. Biochem.* **70**, 149–180 (2001).
25. K. C. Costa *et al.*, *Proc. Natl. Acad. Sci. U.S.A.* **107**, 11050–11055 (2010).
26. K. C. Costa, T. J. Lie, Q. Xia, J. A. Leigh, *J. Bacteriol.* **195**, 5160–5165 (2013).
27. A. Volbeda *et al.*, *Nature* **373**, 580–587 (1995).
28. J. W. Peters, W. N. Lanzilotta, B. J. Lemon, L. C. Seefeldt, *Science* **282**, 1853–1858 (1998).
29. S. Santabarbara, P. Heathcote, M. C. W. Evans, *Biochim. Biophys. Acta* **1708**, 283–310 (2005).
30. A. Esteve-Núñez, J. Sosnik, P. Visconti, D. R. Lovley, *Environ. Microbiol.* **10**, 497–505 (2008).
31. K. D. Bewley, K. E. Ellis, M. A. Firer-Sherwood, S. J. Elliott, *Biochim. Biophys. Acta* **1827**, 938–948 (2013).

ACKNOWLEDGMENTS

We thank R. Thauer for discussions and helpful suggestions, H. Michel for support, J. Koch for laboratory maintenance, the staff of the Swiss Light Source (Villigen, Switzerland) for help with data collection, and A. Poehlein for genome sequencing at the Institute of Microbiology and Genetics of the Georg August University Göttingen. This work was supported by grants from the Max Planck Society (to R. Thauer, S.S., and U.E.) and the PRESTO program from the JST (to S.S.). Structure factors and models have been deposited in the Protein Data Bank under identification numbers 5T5I (12-mer, $P2_12_12_1$), 5T61 (24-mer bound MFR, $P1$), and 5T5M (12-mer, $P3_221$).

SUPPLEMENTARY MATERIALS

www.sciencemag.org/content/354/6308/114/suppl/DC1
Materials and Methods
Figs. S1 to S15
Table S1
References (*32*–*43*)

18 May 2016; accepted 2 September 2016
10.1126/science.aaf9284


Genomics has
met its match
MEET METABOLON, GENOMICS' PERFECT COMPLEMENT
Explore the relationship between genotype and phenotype with Metabolon's revolutionary solutions.
Our team of experts takes metabolomics to the next level with a unique approach to bioinformatics.
We turn data into actionable insight so you can unlock the full potential of the genome.
See why genomics and metabolomics are better together at **metabolon.com/ebook**
METABOLON®
Where **knowing** comes to **life**™

HUMAN HEALTH

ENVIRONMENTAL HEALTH

FROM EXTRACTION TO ANALYSIS GENOMICS SOLUTIONS THAT GO WHERE THE SCIENCE LEADS

Generating accurate, reproducible results efficiently is top of mind in *everyone's* genomic lab. And the answer is applications expertise, up and down the workflow – from extraction to analysis. With our chemagic™ extraction technology, fully integrated automated library prep, robust sequencing chemistries, sample quality quantitation, visualization and analysis of complex sequencing data, and much more, we help you deliver top-quality samples for your world-class research. PerkinElmer genomics solutions: Wherever your science leads, we'll be there.

For Research Only. Not for use in diagnostic procedures.

For more information, please visit us at ASHG booths #1201, 1202 and 1124 or www.perkinelmer.com/ASHG

PerkinElmer®
For the Better

Overview of Shunde's Investment Environment

Shunde, a city filled with investments and business opportunities, possesses advantageous locations as well as abundant carrier space. By virtue of solid manufacturing foundation, Shunde will be built up as the core area of advanced equipment manufacturing and major development zone of modern services industry in West Bank of the Pearl River.

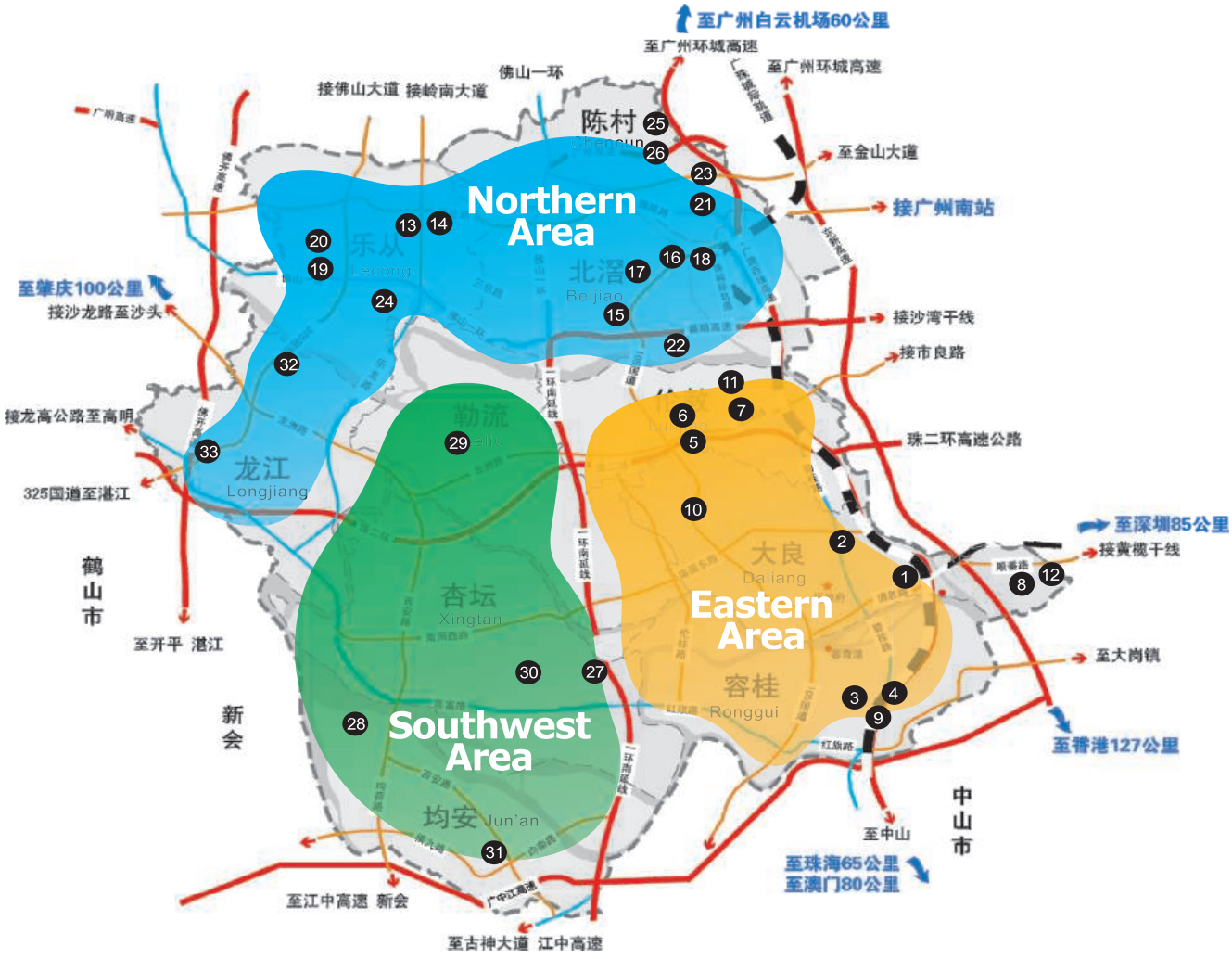

Eastern Area

1. South China Wisdom Valley
2. Shunde Innovation Park
3. Shunde Innovation and Technology Center
4. Dymatic New Material Innovation Park
5. Guangjin Commercial Center
6. Hebao Center
7. Shunde Jewelry Public Services
8. The European Industrial Park
9. Tian Fu Lai Industrial Park
10. Chuanghui • Smart Manufacturing Park
11. South Machinery Center
12. ProLogis

Northern Area

13. Foshan Sino-German Industrial Services Zone
14. Sino-European Services Center
15. Guangdong Industrial Design City
16. E-world center
17. Huicong Jia Dian City
18. Beijiao International Fortune Center
19. WIOT Industrial Park
20. Guangdong Bio-industrial Park
21. Pacific Plaza Dingwang Center
22. Jia Li Yuan International Industrial City
23. Sunlink International Machinery City
24. Lecong Steel World
25. Guotong Logistics City
26. Guangdong Xiong Ying Logistics

Southwest Area

27. Shunde Hi-Tech Industrial Development Zone
28. The New Industrial Base
29. Hong Yu (Leliu) Industrial Park
30. Wisdom and Wealth Garden of Shunde
31. Shi You Industrial City
32. Longjiang Gelunbao S&T Park
33. Longjiang Furniture E-commerce Center

Convenient Transportation

As the vital transportation junction in the West Bank of the Pearl River Delta, Shunde is a significant component in the Pan PRD economic circle , which is close to major consumer cities in Pearl River Delta, such as Guangzhou, Shenzhen, Hong Kong and Macau.

At present, 8 highways traverse Shunde. The road density of Shunde is 223km/100km², higher than the provincial level of 109.6km/100km²; Highway density in Shunde is 11.7km/100km², higher than the provincial level of 3.1km/100km². A 30:15 network is formed, that is, 30 minutes to each town, and 15 minutes to highway entrance.

Moreover, there is an urban railway in the service, 8 metros will be served in succession.Convenient traffic network has criss-crossed the city into the 2-hour traffic circle of the PRD and Hong Kong and Macau.

Shunde Railways and Ports

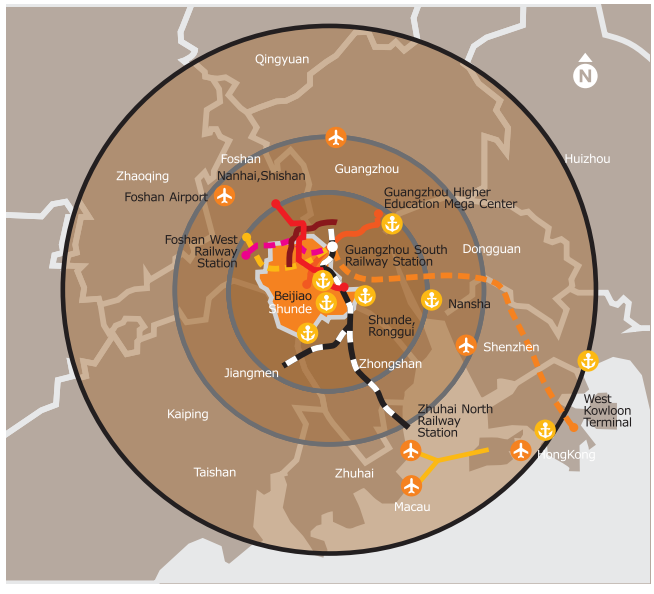

Abundant carrier space

A number of specialized parks were built in Shunde, the reasonable planning helps attract clusters, providing beneficiary support for talents and facilities.

Apart from Sino-German Industrial Services Zone, which gives priority to cooperate with Germany and build high-end industrial platform, the major carriers also include Lecong Beiwei, Huayin Industrial Park, Jialiyuan International Industr City, SShunde Hi-Tech Industrial Development Zone, Shunde Wisdom and Wealth Garden, , the European Industrial Park, Keying Industrial Park, Junan New Industrial Base etc., which give priority to developing machinery equipment industry.Shunde is willing to work together with investors, create top-ranking business environment, deepen international communication and cooperation, and grow together with enterprises and entrepreneurs, and work together to promote the sound development of Shunde economy.

NEW ENGLAND BioLabs® Inc.

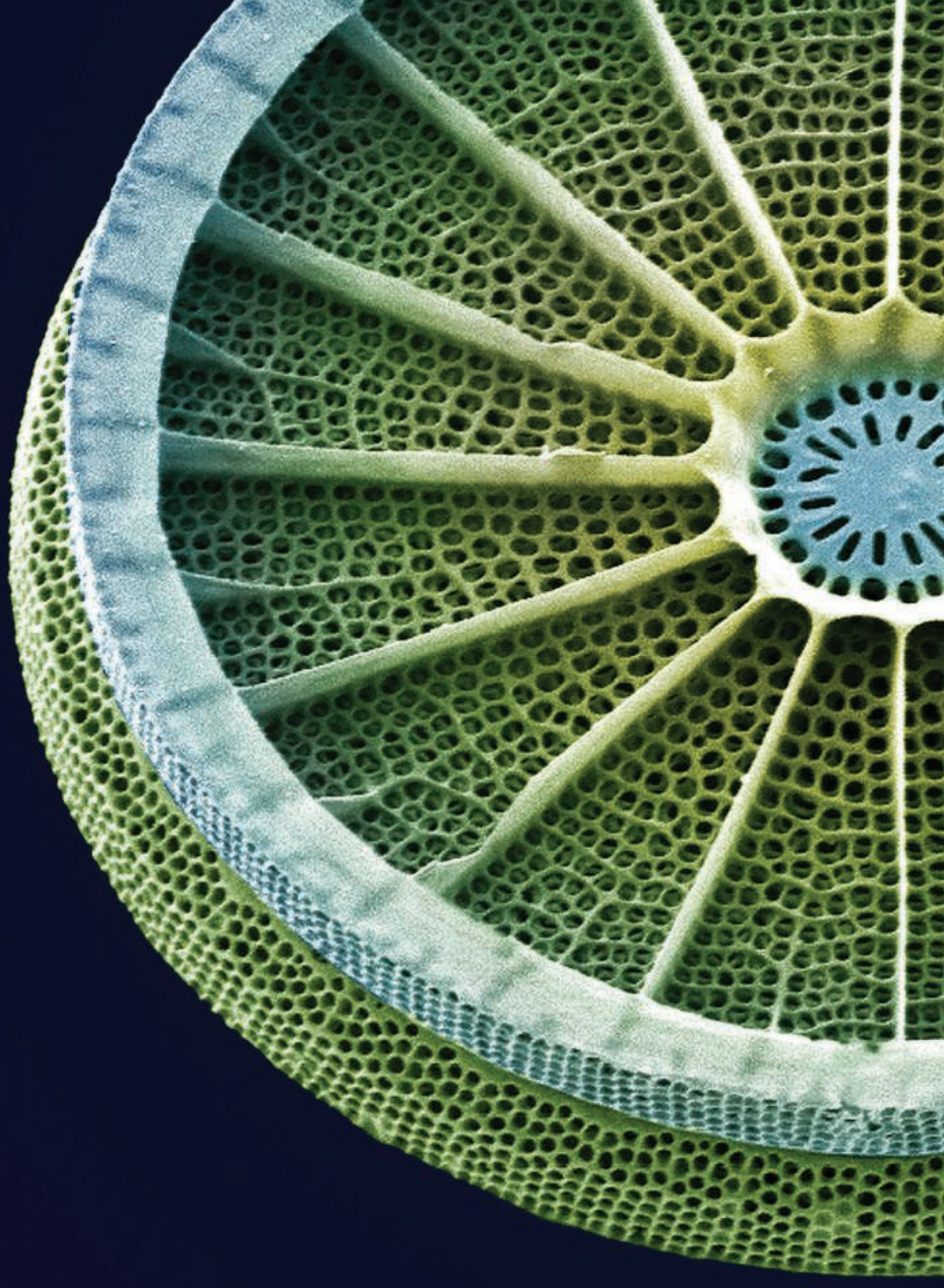

Target with precision.

Introducing the NEBNext Direct™ Cancer HotSpot Panel

Using a unique approach, the NEBNext Direct Cancer HotSpot Panel enriches for 190 common cancer targets from 50 genes prior to next generation sequencing. Combining a novel method for hybridization-based target enrichment with library preparation, the NEBNext Direct technology reduces processing time and minimizes sample loss. Ideal for automation, NEBNext Direct enables highly-specific deep sequencing of genomic regions of interest for the discovery and identification of low frequency variants from challenging sample types.

Visit **NEBNextDirect.com** to learn more and to inquire about sampling this product.

TARGETS INCLUDE REGIONS FROM THE FOLLOWING CANCER-RELATED GENES, INCLUDING >18,000 COSMIC FEATURES:

ABL1	EGFR	GNAQ	KRAS	PTPN11
AKT1	ERBB2	GNAS	MET	RB1
ALK	ERBB4	HNF1A	MLH1	RET
APC	EZH2	HRAS	MPL	SMAD4
ATM	FBXW7	IDH1	NOTCH1	SMARCB1
BRAF	FGFR1	IDH2	NPM1	SMO
CDH1	FGFR2	JAK2	NRAS	SRC
CDKN2A	FGFR3	JAK3	PDGFRA	STK11
CSF1R	FLT3	KDR	PIK3CA	TP53
CTNNB1	GNA11	KIT	PTEN	VHL

For research use only; not intended for diagnostic use.

89 NORTH®

PhotoFluor® LM-75

The world's first direct-mounted metal halide light source.

89 North's PhotoFluor LM-75 is designed for extended use with minimal down time and maximum benefits.

Direct mounting eliminates need for unreliable liquid light guides

As much or more **stable power** at the sample than a 200W metal halide light source

Broad spectrum with strong UV is **compatible with any filter set**

Pre-aligned, **user-exchangeable lamp** with a long lifetime

Extremely quiet operation with **minimal heat** production in rooms with multiple microscopes

Built-in DC ballast eliminates need for external control box, **reducing needed bench space**

Low up-front cost and lower overall cost of ownership than other fluorescence light sources

Contact 89 North for your ideal light source for *fluorescence in situ hybridization.*

PHONE +1-802-881-0302 1-877-417-8313 **WEB** sales@89north.com 89north.com

CHROMA®

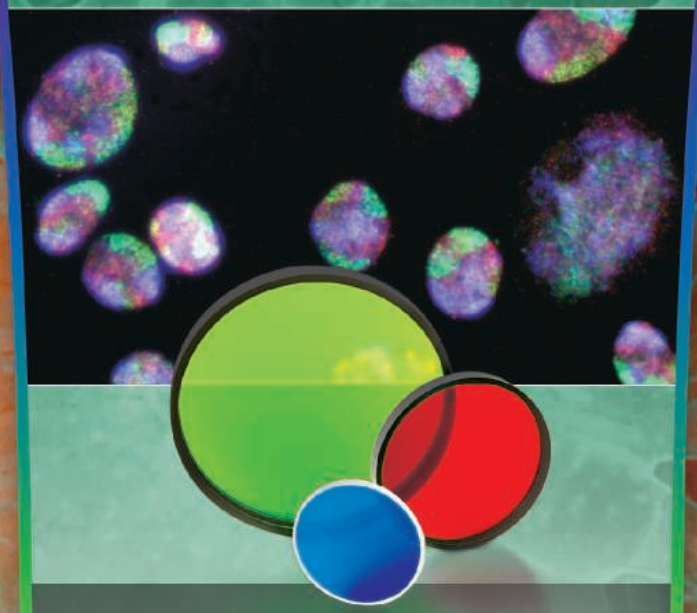

ET FISH Filter Sets

High-performance filter sets for fluorescence in situ hybridization.

Chroma's ET FISH filter sets provide brighter signals and excellent color separation for accurate scoring.

Eliminate bleedthrough of Gold and Aqua from Green signals to reliably discriminate between Aqua/Green/Gold/Red

Dual Band Sets with **balanced Green/Orange and Green/Red** signals for different light sources

Zero-pixel-shift sets for **perfect image registration**

Special Red and Orange filter sets to **separate Orange from Red signals** (advanced expertise required)

Less eye fatigue thanks to brighter fluorescent signals

No need for filter replacement – **lifetime warranty**

Contact Chroma for assistance in choosing filters for your fluorescent genetic testing application.

PHONE +1-802-428-2500 1-800-824-7662 **WEB** sales@chroma.com chroma.com

Genomic workflows

Empowered.

Genomic workflows are fraught with challenges, from inconsistency of yields to scalability and costs. Tecan has been helping its customers to address these challenges and advance their laboratory goals for over 35 years.

Talk to a Tecan expert
and turn our know-how into your advantage.

More information:
www.tecan.com/genomicworkflows

TECAN.

appliedbiosystems

For when every move needs to be precise

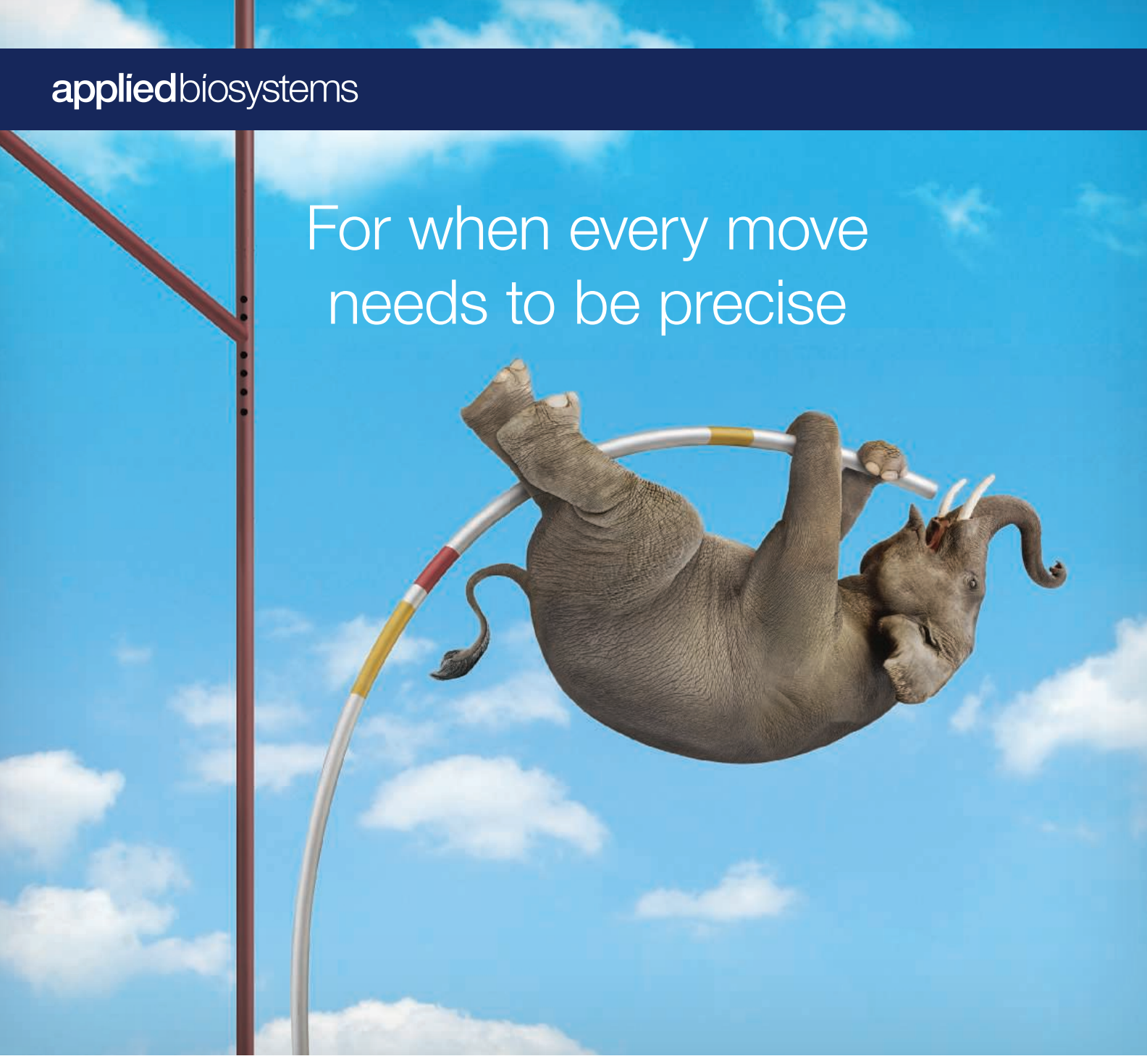

Applied Biosystems™ thermal cyclers enable consistent, precise results no matter the challenge

- Engineered with your highest standards in mind
- Designed to consistently deliver the highest performance
- Accuracy you need to advance your research

Request an in-lab demo at **thermofisher.com/consistent**

ThermoFisher SCIENTIFIC

eppendorf

Visit us at the ASHG Meeting 2016, Booth 719

What`s Next?

NGS Sample Preparation and Library Construction

As a workflow oriented provider of lab equipment, Eppendorf offers instruments, consumables, and accessories that perfectly fit the NGS sample preparation and library construction workflow. Especially cumbersome steps are simplified or even fully automated.

> Reproducible nucleic acid purification and library preparation with the Liquid Handling workstation ep*Motion*® 5075
> Reliable DNA/RNA quantification with the Eppendorf BioSpectrometer® fluorescence
> Mastercycler® pro with excellent block homogeneity and evaporation protection

www.eppendorf.com/NGS

WANTED:

Splice variants

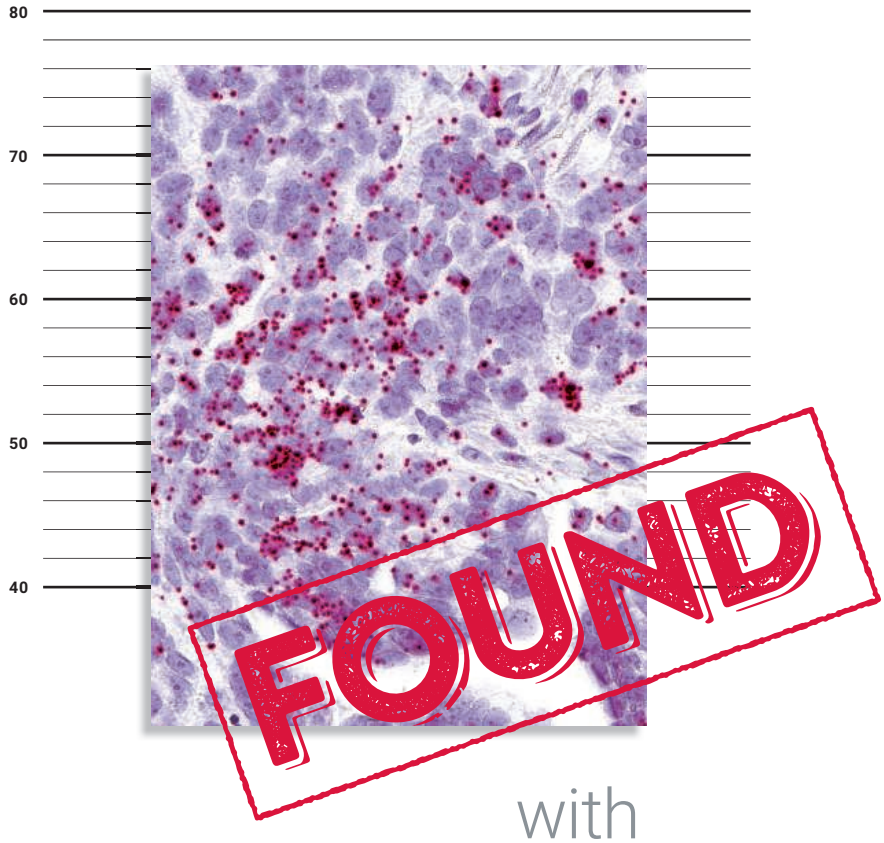

with BaseScope™ Assays

Detect and visualize even the most elusive mRNA targets with BaseScope™ ISH assays

Built on RNAscope® ISH technology, BaseScope™ ISH assays enable highly sensitive and specific detection of RNA targets. Now you can visualize splice variants, homologous sequences, CAR-T cell clones, genes edited with CrispR/Cas9 and more, all within cellular morphological context.

ACD
a bio-techne brand

Enabling Research, Drug Development & Diagnostics

Find more at
acdbio.com/basescope

AAAS 2017 ANNUAL MEETING

FEBRUARY 16-20 • BOSTON

SERVING SOCIETY THROUGH

SCIENCE POLICY

Online Program Now Available

The 2017 meeting focuses on how to inform policies with the best available scientific evidence.

The AAAS Annual Meeting is the largest and most widely recognized global science gathering with exciting scientific sessions, renowned speakers, and valuable networking opportunities.

Advance registration is now open.
Register now for lower rates.

aaas.org/meetings

affymetrix
part of Thermo Fisher Scientific

Genotype your precision medicine cohorts NOW

$18–$29 USD per sample. No minimum commitment.

New Axiom® Precision Medicine Research Array

Multi-year precision medicine cohort studies demand high-density genotyping arrays that deliver reproducible results and no loss of SNP markers from lot to lot. Axiom Precision Medicine Research Array was specifically designed to do just that—and more.

To provide valuable insights into human disease and translate them into effective clinical use, this new Axiom® array contains 25% more GWAS markers and 100% more clinically relevant pathogenic variants from ClinVAR, ACMG, CPIC, and biobanks worldwide.

See the SNP list at www.affymetrix.com/PMRA

P/N GGNO07664 Rev. 1

Go FISHing

Label Your Own FISH Probes

Ensure Peak Labeling Performance for FISH Probe Synthesis

Fluorescent dye-dUTPs are well recognized as superior to analogous methods using cumbersome indirect two-step labeling methods. When coupled with the Nick Translation DNA Labeling System, this direct approach provides a simple and efficient method to label FISH probes which are suitable for a wide range of molecular biology and cytogenetics applications.

Fluorescent dye-dUTPs

- Eight distinct colors to choose from, spanning the visible light spectrum
- High signal intensity and good photostability
- Available in aqueous format or lyophilized sizes

Nick Translation DNA Labeling System

- Simple and efficient method for generating labeled DNA
- Flexible format enables optimization of dye incorporation and product size
- Compatible with both biotin-labeled and fluorophore-labeled nucleotides

Visit Us at ASHG Booth #1513

Total FISH Solution:
Fluorescent dye-dUTPs + Nick Translation Kit

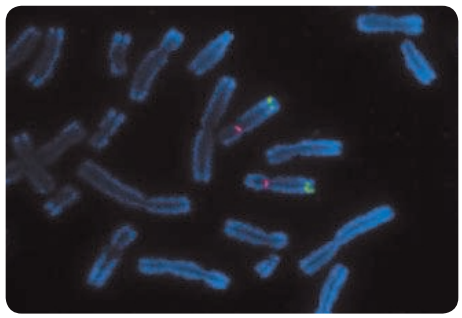

Composite fluorescent image using the Nick Translation DNA Labeling System and BAC Target DNA labeled with Enzo's Green 496 dUTP (ENZ-42831) and Centromere BAC Probe labeled with Enzo's Orange 552 dUTP (ENZ-42842). Metaphase chromosome spreads were counterstained with DAPI.

scientists ***enabling*** scientists.™

www.enzolifesciences.com/fish

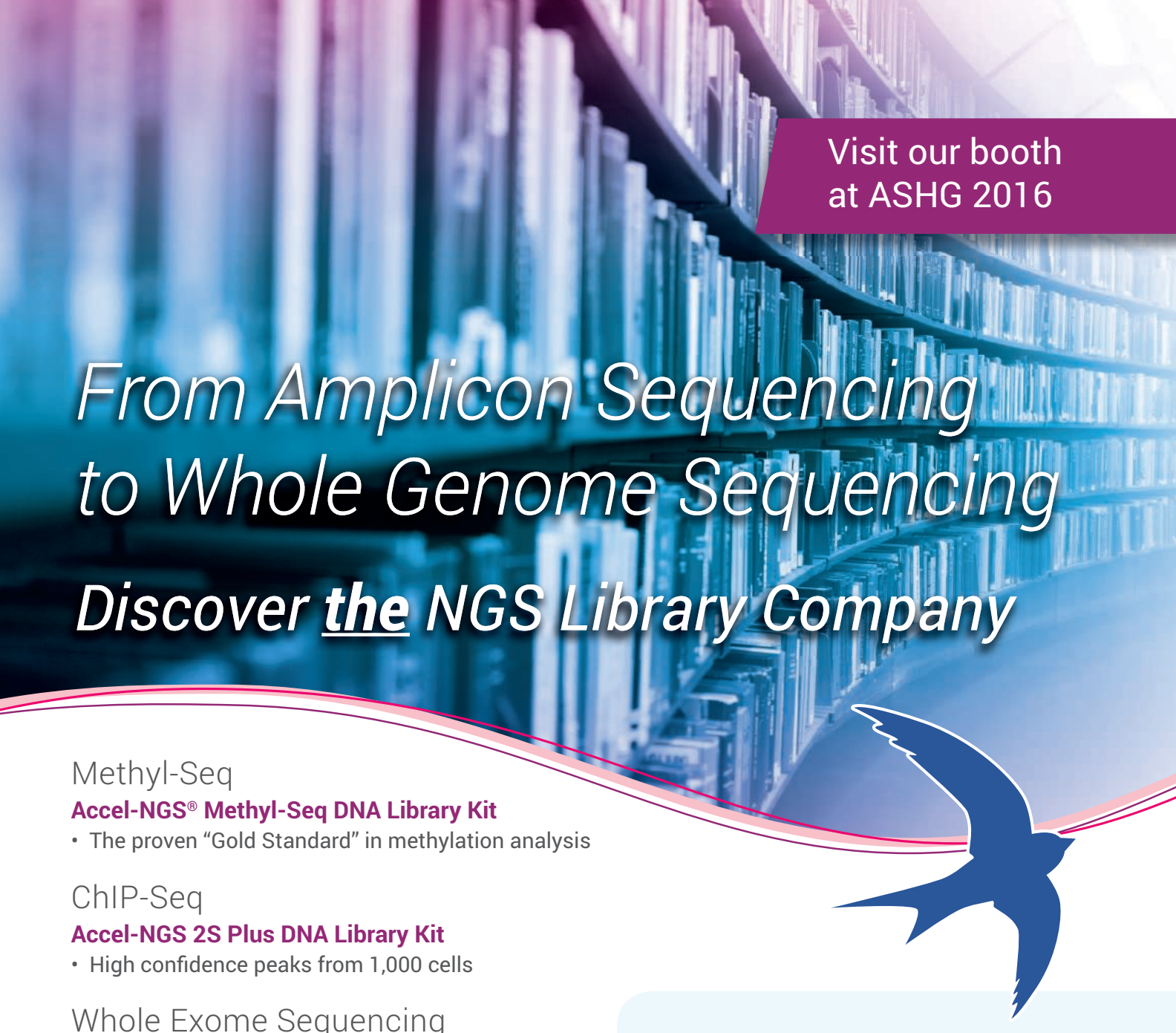

Visit our booth
at ASHG 2016

From Amplicon Sequencing to Whole Genome Sequencing

*Discover **the** NGS Library Company*

Methyl-Seq
Accel-NGS® Methyl-Seq DNA Library Kit
- The proven "Gold Standard" in methylation analysis

ChIP-Seq
Accel-NGS 2S Plus DNA Library Kit
- High confidence peaks from 1,000 cells

Whole Exome Sequencing
Accel-NGS 2S Hyb DNA Library Kit
- Minimizing duplicates, maximizing sequencing data

Whole Genome Sequencing
Accel-NGS 2S PCR-Free DNA Library Kit
- Enabling PCR-free libraries from as little as 10 ng

Amplicon Sequencing for Oncology
Accel-Amplicon™ Panels
- Delivering 1% mutation detection from 10 ng of DNA in 2-hours

Visit booth #1211 at the
2016 ASHG Annual Meeting

Vancouver, Canada | October 18-22, 2016

Swift BIOSCIENCES™

The NGS Library Company
Visit www.swiftbiosci.com

FOCUS ON CAREERS

FACULTY

Business principles for basic researchers

Leadership, management, and marketing sound like skills for CEOs, not scientists. Running a research group requires MBA-type strengths, though, such as budgeting, mediating, and negotiating. Some universities now offer workshops on business principles for scientists and engineers, lending credence to the idea that mixing business with science is a path to success.

See the full story on page 124.

Upcoming Features
Focus on Wales—October 14
Top Employers Survey—October 28
Regional Focus: China—November 4

Produced by the *Science*/AAAS Custom Publishing Office

Dropsense 96

96well DropPlates
Focus on plate oriented workflows

2µL samples
Native sample read-out, no dilutions

2 UV/VIS methods in one box
A260/A280 + cDrop contamination ID

Software toolbox available
Robot integration, IQ/OQ and CFR21p11

cDrop

Specific DNA, RNA & protein quantification
Alternative for fluo-based assays

Contamination detection
See how pure samples really are

Immediate analysis
No dye, No assay, Save time

Easy cDrop app selection
One app fits many extractions

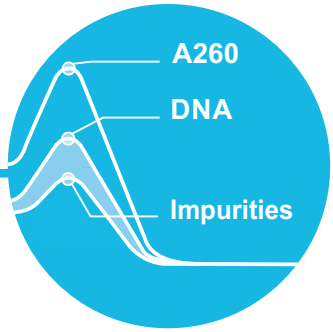

MICROFLUIDICS

Easy sample loading
Capillary intake and storage

No evaporation
Samples stable up to 2 hours

Flexible loading
1 to 96 sample analyses
Range: 1,5 - 10.000 ng/µl DNA
0,02 - 146 mg/ml IgG

trinean

www.trinean.com

Novogene

Leading Edge Genomic Services & Solutions

HiSeq X Ten
4000, 2500

Whole Genome Sequencing
(Human, Plants and Animals),
Exome & RNA-Seq,
Epigenomics...

QUALITY
Guaranteed Q30 > Illumina's

ANALYSIS
Expert bioinformatics
Publication ready reports

TECHNOLOGY
World's largest capacity
HiSeq X Ten (2 sets) & 4000

EXPERTISE
200 publications in top journals
10,000 projects completed

support@novogene.com novogene.com

Any Sample Type, Any Application, FastPrep-24™ 5G has You covered!

Powerful • Intuitive • Flexible

Sample Preparation for Nucleic Acid and Protein Extraction

FastPrep-24™ 5G is the market leader in sample preparation. Complete and thorough grinding of up to 48 samples in 40 seconds or less, guaranteed. The system is intuitive with an interactive user-friendly touchscreen that includes more than 70 recommended protocols.

Interchangeable sample holders give you flexibility in sample tube processing sizes (2 ml, 4.5 ml, 15 ml or 50 ml) at either cryogenic or ambient temperature. Optimized Lysing Matrix and all-inclusive Purification Kits make the FastPrep-24™ 5G truly the most advanced sample preparation system ....Period!

Often Imitated, Never Duplicated!

Visit www.mpbio.com/sampleprep-offer for current special promotions on FastPrep Instruments, purification kits and lysing matrix.

MP Biomedicals - It's What's Inside that Counts!

www.mpbio.com

MP Biomedicals USA: 800.854.0530 • MP Biomedicals Europe: 00800.7777.9999

MP™

There's nothing more personal than genomics

Powerful stories. New possibilities. Francis, and others like him, inspire us to create the genomic solutions that help researchers uncover new biologic insights that advance cancer's identification and treatment. Illumina next-generation sequencing and array-based solutions help researchers achieve deeper and more accurate analysis of a tumor's molecular profile. Our hope is to accelerate discoveries that will improve the entire cancer care continuum from earliest detection to companion diagnostics and personalized treatments.

Together we'll advance precision medicine and improve human health.
www.illumina.com/precisionmedicine

Genomic solutions to transform possibility into progress.
Oncology | Reproductive Health | Inherited Conditions | HLA

illumina®

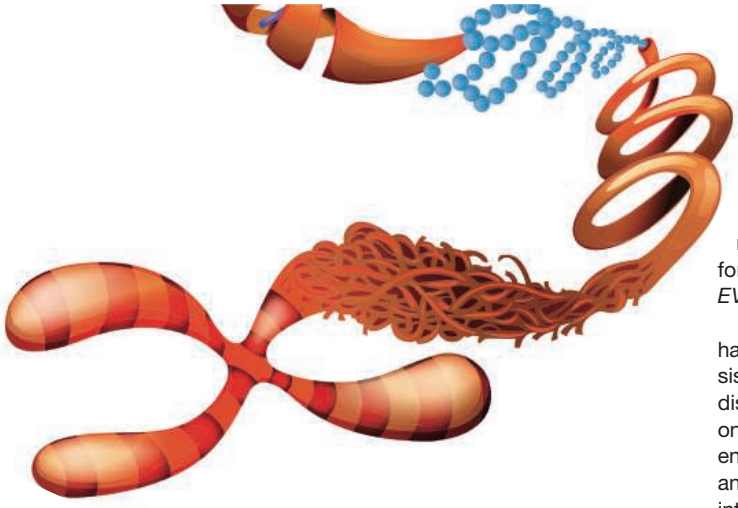

Chromatin untangled: New methods map genomic structure

With some 2 meters of DNA squished into the micron-sized nucleus of every mammalian cell, to call that space "cozy" is an understatement. Yet for cells, the genome poses issues not only of compaction but of functionality: The DNA must be packaged such that it remains accessible to gene regulatory factors. Indeed, chromatin architecture plays a key role in gene regulation, but until recently, researchers had few tools with which to study that relationship. **By Jeffrey M. Perkel**

For decades, researchers have recognized that cancer cells often carry a raft of chromosomal abnormalities. A translocation joining pieces of human chromosomes 9 and 22 produces the so-called "Philadelphia chromosome," a structural abnormality associated with chronic myeloid leukemia. And certain forms of prostate cancer are associated with gene fusions that place ETS-family transcription factors under the control of androgen-responsive promoters. In both of those events, no genetic material is lost; it simply moves from one location to another. But genes are fused in the process, and proteins that normally are tightly regulated become constitutively active, leading inexorably to disease.

Some forms of acute myelogenous leukemia (AML) also harbor specific genetic aberrations—in this case, on the long arm of chromosome 3. That region, called "3q26," contains *EVI1,* a gene that is normally expressed only in early hematopoietic progenitors but is turned off at differentiation. But in certain cases of AML, *EVI1* is turned on permanently.

To find out why, H. Ruud Delwel, professor of molecular leukemogenesis at **Erasmus University Medical Center** in Rotterdam, the Netherlands, and his team sequenced the translocation breakpoints for 3q26. It turns out that 3q26 could break either upstream or downstream of *EVI1*—it didn't seem to matter, says Delwel. But the other breakpoint was tightly restricted to another piece of chromosome 3 located some 40 megabases away: an 18,000-base-pair segment of 3q21, sandwiched between *GATA2* and *RPN1*. There's no gene or promoter there, so no gene fusion per se occurs. But there is a regulatory element present, a 1,000-base pair sequence that normally drives the *GATA2* promoter in hematopoietic stem cells. The AML translocation forces that enhancer to switch genetic allegiances, activating *EVI1* while concurrently shutting down *GATA2*.

The net result is a pair of genetic anomalies, both of which have been independently associated with leukemia. Prognosis for these patients is exceptionally poor, Delwel says. But disease does not result simply from changes in linear distance on the chromosome. After all, it's theoretically possible that an enhancer, even one located megabases away, could reach out and activate a distant but otherwise silent promoter. Yet, such interactions are largely precluded by the basic folding architecture of the genome. The translocation associated with AML fundamentally alters that architecture on chromosome 3, making such interactions far more likely.

Today, armed with an increasingly sophisticated, high-resolution toolset, researchers are decoding the architectural secrets of chromatin with unprecedented clarity. Some are using population-based sequencing approaches, while others are exploiting the power of microscopy to study chromatin architecture on a cell-by-cell basis. Still others are developing methods to probe the genome at the single-cell level and in living cells. There's much left to do. But according to Job Dekker, a Howard Hughes Medical Institute investigator at the **University of Massachusetts Medical School,** a corner has been turned: Researchers have advanced from simply cataloging chromatin structure to actually manipulating it. "We are now at the stage where we can do classical structure–function studies," he says.

Chromatin in the key of C

Researchers have long known that the eukaryotic nucleus must be ordered, thanks to "chromosome painting" studies suggesting each chromosome exists in its own domain. Yet the structure within those domains remained mysterious for several years. Then, in 2012, researchers proposed that eukaryotic chromosomes fold into relatively predictable structures called "topologically associating domains" (TADs), and that these structures prevent enhancers from activating genes all over the genome by effectively restricting their actions to within a few hundred thousand bases. "TADs gave us a physical understanding of where the boundaries of such elements could act," explains Bing Ren, professor of cellular and molecular medicine at the **Ludwig Institute for Cancer Research** in La Jolla, California, whose lab was one of three to first describe these domains.

To define TADs, researchers use a variety of techniques, collectively called the "C methods." In 2002, Dekker developed the first such approach, chromosome conformation capture (3C), as a postdoc in Nancy Kleckner's laboratory—a strategy he dreamed up as a way to study chromatid pairing during meiosis.

Though they differ in the particulars, C methods all rely on proximity ligation, using DNA ligase to suture together two

Upcoming Features
Neurotechniques—November 4 ■ *Cell Analysis—November 25* ■ *Genomics—January 13*

"Even in phenotypically identical cells, the way chromosomes fold is highly variable from cell to cell."
—Peter Fraser, Babraham Institute, UK

linearly distant DNA fragments that happen to be close together in 3D space. In 3C, linked fragments are isolated and identified by PCR, using primers to both candidate regions; subsequent variants of 3C have multiplexed the method, improved its resolution, and broadened its reach to identify interactions over broad chromosomal regions or even genome-wide. Today, they represent the foundational technology of chromatin architecture analysis.

Alternative strategies include ChIA-PET (chromatin interaction analysis using paired-end tag sequencing), which effectively blends a genome-scale variant of 3C with chromatin immunoprecipitation (ChIP) to isolate those interactions associated with specific proteins; and DamID (DNA adenine methyltransferase identification), which identifies lamina-associating domains—chromatin regions associated with the inner face of the nuclear membrane, which tend to be transcriptionally silent—by fusing lamin proteins with a bacterial methyltransferase and monitoring the location of methylated sequences.

Epigenetics product vendor **Active Motif** offers a commercial tool that it says may also be used to map chromatin loops. The enChIP (engineered DNA-binding molecule-mediated ChIP) assay kit uses an antigen-tagged, enzymatically inactive ("dead") Cas9 protein to map the specificity of the nuclease for genome editing applications via ChIP. But according to product manager Kyle Hondorp, the assay can also capture chromatin-looping events.

Perhaps the most widely used approach these days, however, is Hi-C. Erez Lieberman Aiden, assistant professor of genetics at **Baylor College of Medicine,** developed that approach in collaboration with Dekker while a graduate student with Eric Lander at the Broad Institute of MIT and Harvard. As he recalls, "There was a seminar or something, and Eric commented that the Illumina sequencers generated so much data that it was often in one's interest to figure out how to translate a [genetic] problem into a sequencing problem, and then it would just be this game-changer."

Aiden recognized that coupling nuclear ligation with an unbiased, high-throughput sequencing-based approach—essentially updating a gel-based method published in 1993 by Vanderbilt University researcher Katherine Cullen—could represent just such a game-changer. But his original protocol, published in 2009, was "a bit of a letdown," says Aiden. Hi-C data generally take the form of heat maps of contact frequencies. Contact domains stand out in such data as a sequence of dark squares along the diagonal. But with Hi-C resolutions in the tens of thousands of bases, loops between enhancers and promoters were simply too small to be detected.

Aiden's team identified two problems with the original method, he says. One was sequencing throughput. A "back-of-the-envelope" calculation suggested he might need 10 billion reads in order to actually capture promoter–enhancer interactions—this in 2007, when 10 billion sequencing reads was more "than had ever been generated in the history of the world." But the method was also laborious and clunky, and produced inherently blurry maps. So, his team, led by Suhas Rao and Miriam Huntley, spent five years honing the method and waiting for sequencing throughput to catch up. One of the most important changes, he says, was restoring the ligation step to the intact nucleus, as in Cullen's original work (in 3C, the nucleus is disrupted first). Eventually, in 2014, they published an updated method called "in situ Hi-C" that featured kilobase resolution sharp enough to capture chromosomal looping events, which appear as dark, off-axis dots on Hi-C heat maps.

Going single-cell

Today, researchers are using C methods to address a number of vexing biological questions. Amy Kenter of the **University of Illinois College of Medicine at Chicago** used them to identify three "subdomains" within the mouse immunoglobulin heavy-chain locus—data that may explain the nuances of antibody gene recombination. Edith Heard, head of the Genetics and Developmental Biology Department at the **Institut Curie** in France, worked with Dekker and applied allele-specific Hi-C (a method in which each sequencing read can be assigned to either the paternal or maternal chromosome) to inactivation of one of the X chromosomes in female mammals, and found that the inactive X assembles not into TADs (as the active X does) but into two massive "megadomains" separated by a "hinge" at the DXZ4 macrosatellite region. Disruption of that region, or loss of the X-inactivation-associated noncoding RNA *Xist* (X-inactive specific transcript), alters this partitioning as well as the expression of the few genes that normally manage to "escape" inactivation. (Aiden independently published similar findings a week later.) And Danny Reinberg, a Howard Hughes Medical Institute investigator at **New York University (NYU) Langone Medical Center**, has used C methods to probe and disrupt the exquisite temporal regulation of the *Hox* body-plan-regulating gene cluster.

Yet for all that researchers can learn from such methods, these techniques describe populations, not individual cells, each of which may display a different chromosomal conformation, or be at a different stage of the cell cycle, says Peter Fraser, head of the Nuclear Dynamics Programme at the **Babraham Institute** in Cambridge, United Kingdom. As a consequence, the resulting contact maps may not actually represent any cell in the population at all—they are the equivalent, he explains, of trying to capture the dynamics of soccer by photoaveraging hundreds of snapshots of a game. "It would just give you sort of a lump," he says.

Fraser's solution to that problem is single-cell Hi-C, a method he first described in 2013. The key to the method, Fraser says, is keeping the nuclei intact prior to ligation. "It makes it cleaner and less noisy," he explains, than disrupting the nuclei first (as in Aiden's original Hi-C protocol). But initially, his team cont.>

Featured Participants

Active Motif
www.activemotif.com

Albert Einstein College of Medicine
www.einstein.yu.edu

Babraham Institute
www.babraham.ac.uk

Baylor College of Medicine
www.bcm.edu

Center for Integrative Biology
cbi-toulouse.fr/eng

Department of Genome Sciences, University of Washington
www.gs.washington.edu

Erasmus University Medical Center
www.erasmusmc.nl/?lang=en

Harvard University
www.harvard.edu

Insititut Curie
www.institut-curie.org

Janelia Research Campus, Howard Hughes Medical Institute
www.janelia.org

Ludwig Institute for Cancer Research
www.ludwigcancerresearch.org

New York University Langone Medical Center
nyulangone.org

University of Illinois College of Medicine at Chicago
www.chicago.medicine.uic.edu

University of Massachusetts Medical School
www.umassmed.edu

could probe only about 2.5% of the contacts in any given cell, in perhaps a dozen cells at a time—today, improvements have boosted coverage about 10- to 20-fold, and upped throughput to some 400 cells a week. "We can do experiments with thousands of single-cell Hi-C datasets, which allow us to see how a population behaves, but from the single-cell level," he explains. The data suggest that TADs are less stable than researchers believed. "Even in phenotypically identical cells, the way chromosomes fold is highly variable from cell to cell," he says.

More recently, Jay Shendure of the **University of Washington's Department of Genome Sciences** and his colleagues reported in *Science* on a highly multiplexed approach that uses DNA barcoding (rather than physical cell isolation) to extend single-cell Hi-C to thousands of cells at once.

Still other researchers probe chromatin architecture at the single-cell level using fluorescence in situ hybridization (FISH), an inherently single-cell technique that uses fluorescent probes and statistical analysis to infer the relative positioning of chromosomal domains in the nucleus. Heard, for instance, used FISH probes positioned on either side of DXZ4 to visually demonstrate that chromosome folding differs on the active and inactive X chromosomes in mice, thus validating her Hi-C findings.

But unlike C methods, FISH is low throughput (in terms of the number of genomic loci that can be analyzed at once) and low resolution. Xiaowei Zhuang, a Howard Hughes Medical Institute investigator at **Harvard University**, and her colleagues recently provided a solution to the former problem, at least, with the development of a method to multiplex FISH by using Oligopaint probes and sequential hybridization to image tens of thousands of genomic loci and possibly more. Using this approach, the team mapped the position of each TAD on a chromosome one by one. By connecting the dots defined by the resulting signals, the team effectively traced the 3D topology of a given chromosome in individual fixed cells—a strategy they applied to human chromosomes 20, 21, 22, and X.

According to Zhuang, the resulting data are consistent with population-based Hi-C datasets—for instance, they also catch a glimpse of the DXZ4 "hinge" in the inactive X chromosome—but also reveal spatial features that were not previously known. "The compartment assignments of TADs in our approach, which is an entirely different approach compared to Hi-C … are essentially identical," she says. "It's really remarkable."

And we're live

Ultimately, of course, what matters is not chromatin structure in fixed cells, but how that structure changes as the cells grow, divide, and respond to stimuli. "That requires a live-cell technique, and there isn't a good one actually developed yet," says Robert Singer, chair of anatomy and structural biology at the **Albert Einstein College of Medicine** in New York.

Many groups are addressing that problem, however, including several funded by the National Institutes of Health Common Fund's 4D Nucleome program, says Jane Skok, professor of pathology at NYU, who sits on the project's advisory board. Skok, for instance, has used dead Cas9 nuclease and modified guide RNAs to visually tag specific (albeit repetitive) chromosomal regions, including the immunoglobulin heavy-chain gene, in live cells. Others have published similar approaches. For example, Singer and Wulan Deng, a project scientist at the **Howard Hughes Medical Institute's Janelia Research Campus,** dubbed their approach "CASFISH," and Hanhui Ma of the University of Massachusetts Medical School developed a six-color strategy called "CRISPRainbow."

Another option is ANCHOR, developed by Kerstin Bystricky, head of the Chromatin and Gene Expression group at the **Center for Integrative Biology** and professor at the University of Toulouse, France. ANCHOR involves inserting a handful of binding sites for the bacterial ParB protein near the locus to be imaged, and expressing a ParB-fluorescent protein fusion in the same cells. Unlike Cas9-based approaches, which require one DNA target site for every binding event, ParB has the useful property of tending to accumulate, explains Bystricky. Thus, binding of a single protein dimer quickly nucleates more molecules. As each protein molecule is fluorescently tagged, the net effect is a highly amplified fluorescent signal.

By combining that approach with live-cell RNA visualization, Bystricky's team has found that actively transcribing genes tend to be less mobile than silent genes—a counterintuitive observation, she says. "There was this belief that transcription activation would increase mobility," she explains.

According to Dekker, the pieces are falling into place for researchers to begin transitioning from structural characterization to manipulation. But there remains the challenge of data integration, he says. Often, data produced by one method only partially matches that of another. "I'm an optimist," he says. "I like to think [that FISH and Hi-C methods] are both true. But we don't understand how they both can be true at the same time." Given the rapid advancement in chromatin conformation methods, the explanation may not be long in coming.

Jeffrey M. Perkel is a freelance science writer based in Pocatello, Idaho.

DOI: 10.1126/science.opms.p1600108

FISH Probes

A new range of nonhuman fluorescence in situ hybridization (FISH) probes has been developed for visualizing pig, chicken, and mouse chromosomes. The Cytocell Chromoprobe Multiprobe Porcine, Chicken, and Mouse products add to the extensive catalog of human Cytocell FISH probes already available. These probes are set to benefit animal husbandry and research. It is now possible to detect a wide range of chromosomal aberrations in these species with specific, clear, high-intensity signals and minimal background, delivering quality, reproducible results. The probes were developed using Oxford Gene Technology's rapid probe development capability and proprietary Chromoprobe technology, which effectively simplifies the FISH procedure and makes it safe and quick to use. Enabling multiple FISH probes to be hybridized on the same slide, the Chromoprobe Multiprobe System also allows rapid screening for a number of DNA sequences in a single analysis, and can be customized according to requirements.

Oxford Gene Technology
For info: +44-(0)-1865-856800
www.ogt.com

Nucleic Acid Extraction Kits

Analytik Jena introduces a global innovation in nucleic acid extraction to the market. The innovative SmartExtraction technology does not require the use of phenol/chloroform, ion exchangers, filter columns, or filter plates, nor does it need suspensions from magnetic or paramagnetic particles for binding nucleic acids. Innovatively modified surfaces for nucleic acid binding (Smart Modified Surfaces) form the basis of the patent-pending technology. SmartExtraction can be operated manually, automated, or used under field conditions. Because of the extremely high binding capacities of the modified surfaces, the achieved yield of nucleic acids is practically unlimited, unlike that obtained through magnetic particle-based extraction, for example. In addition, the new technology also allows isolation of nucleic acids that are present only in very low concentrations in a biological sample. Because of its universality, this process can be implemented with all standard automated pipetting systems.

Analytik Jena AG
For info: +49-(0)-36-41-77-70
www.analytik-jena.com

FISH Slide Hybridizer

The RapidFISH slide hybridizer is designed to simplify fluorescence in-situ hybridization (FISH) procedures for FFPE tissue samples, cell suspensions, and other tissue preparation procedures. FISH testing is used worldwide to identify biological markers in the form of DNA/RNA. Temperature control and humidity are essential for FISH probes to bind to RNA and DNA. RapidFISH has a self-clamping slide tray design that maintains the required humidity; microscope slides in RapidFISH do not require coverslips to be glued, because the removable tray of the slide incubator traps moisture in the system. Elimination of this step decreases processing time and ensures that the specimens stay hydrated during processing. RapidFISH features an easy-to-use control system for regulating temperature and time. It has a small footprint yet still maintains excellent temperature stability and uniformity because of its dual-heater convection system.

Boekel Scientific
For info: 215-396-8200
www.boekelsci.com

Gene Editing System

The PluriQ G9 Gene Editing System is a complete system for culturing and transfecting human pluripotent stem cells for gene editing. The system includes the G9 Maintenance Medium and G9 VTN Human Recombinant (vitronectin) plate coating for culturing human induced pluripotent or embryonic stem cells in a manner that maximizes transfection by using the EditPro Stem Transfection Reagent (included) to transfect genome-editing constructs. EditPro Stem is optimized for delivery of CRISPR/Cas9 editing via DNA Cas9 vectors, Cas9 messenger RNA (mRNA) with double-stranded DNA (g-block), Cas9 mRNA with trans-activating CRISPR (tracr)/guide RNA, or Cas9 protein with tracr/guide RNA. It is also effective for delivery of transcription activator-like effector nuclease (TALEN) and zinc finger nuclease (ZFN) editing tools, giving the researcher total flexibility in experimental design. With such high-efficiency delivery—up to 90%—antibiotic selection in the editing design is not needed. Additionally, the reagents have low cell toxicities, do not affect pluripotency, and are effective in small amounts, resulting in a low cost per well.

MTI-GlobalStem
For info: 888-545-0238
www.mti-globalstem.com

Genomics Sample Preparation Microplate

Designed with thickened walls and strengthened ribs underneath to stop cracking or leaking when used in Geno/Grinder or Tissulyser machines, the robust 96-well, 2-mL deep-well Genomics Sample Preparation Plate sets a new standard for high-throughput genomics sample preparation. It has been proven to withstand demanding applications—steel ball bearings in the wells shaken at up to 1,500 rpm—used to homogenize seeds, leaves, or tissue ready for DNA extraction. Manufactured from superior grade, ultraclean, polypropylene samples, the Genomics Sample Preparation Plate has been tested at the National Centre for Mass Spectroscopy Excellence at Swansea University (United Kingdom) and has been found to be free of measurable leachates/extractables, as determined on their most sensitive time-of-flight MS instruments. The plates are sold individually or as part of a package including a matching silicone impact support mat and exome variation analyzer cap mat.

Porvair Sciences
For info: +44-(0)-1978-666222
www.porvair-sciences.com

Electronically submit your new product description or product literature information! Go to www.sciencemag.org/products/newproducts.dtl for more information.

Newly offered instrumentation, apparatus, and laboratory materials of interest to researchers in all disciplines in academic, industrial, and governmental organizations are featured in this space. Emphasis is given to purpose, chief characteristics, and availability of products and materials. Endorsement by *Science* or AAAS of any products or materials mentioned is not implied. Additional information may be obtained from the manufacturer or supplier.

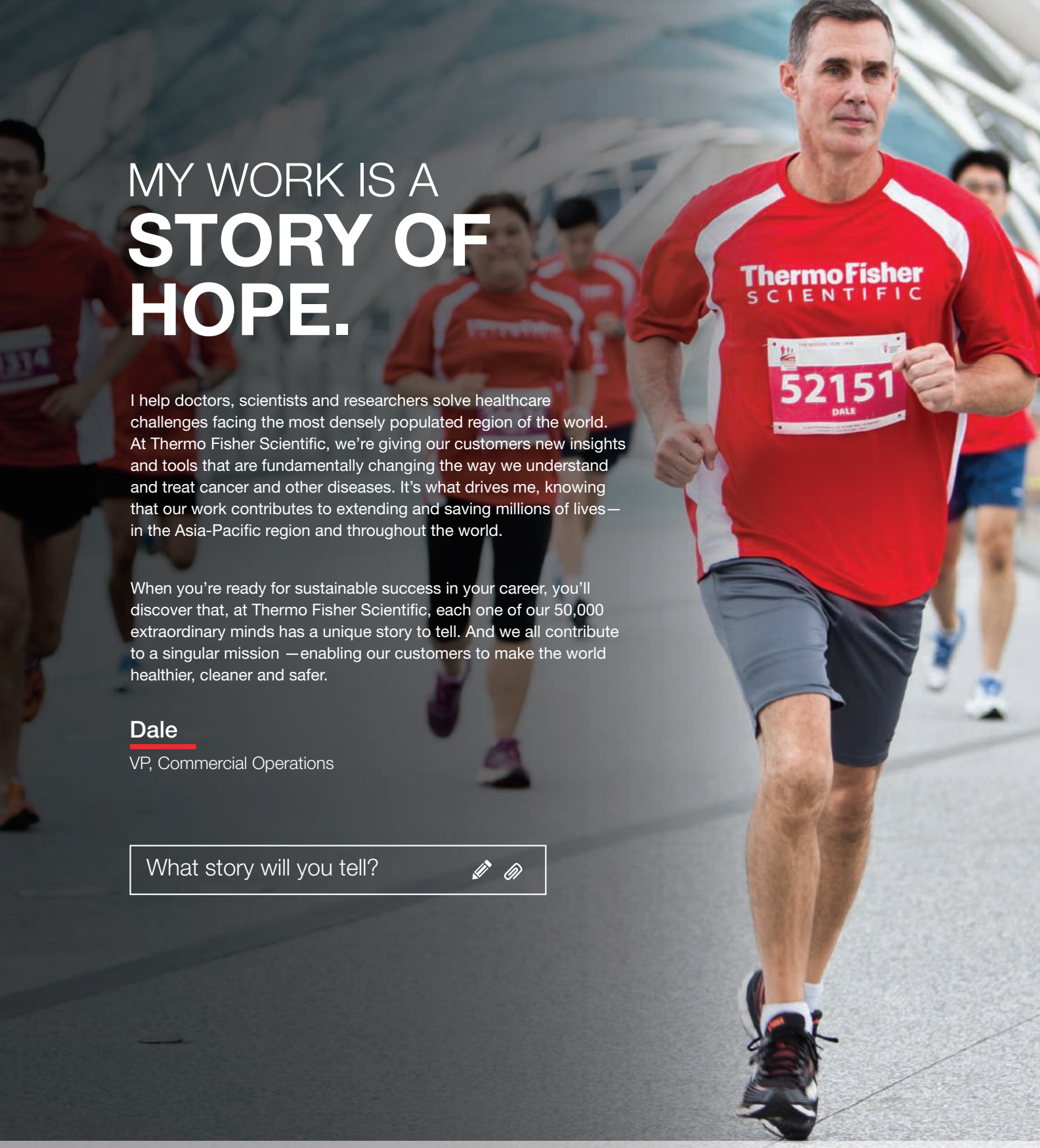

MY WORK IS A **STORY OF HOPE.**

I help doctors, scientists and researchers solve healthcare challenges facing the most densely populated region of the world. At Thermo Fisher Scientific, we're giving our customers new insights and tools that are fundamentally changing the way we understand and treat cancer and other diseases. It's what drives me, knowing that our work contributes to extending and saving millions of lives—in the Asia-Pacific region and throughout the world.

When you're ready for sustainable success in your career, you'll discover that, at Thermo Fisher Scientific, each one of our 50,000 extraordinary minds has a unique story to tell. And we all contribute to a singular mission —enabling our customers to make the world healthier, cleaner and safer.

Dale

VP, Commercial Operations

What story will you tell?

Explore our opportunities at **jobs.thermofisher.com** and join our team.

ThermoFisher SCIENTIFIC

Thermo Fisher Scientific is an Equal Employment Opportunity/ Affirmative Action employer and a VEVRAA Federal Contractor.

R&D Systems is Your New Trusted Source for Luminex® Instrumentation!

Direct access to Luminex staff for world-class on-site and 24x7x365 remote support

Unlimited emergency equipment repair

Discounts and special acquisition programs tailored to any lab's budget

Learn more about Luminex® instruments | rndystems.com/luminexinstruments

bio-techne®

Global info@bio-techne.com bio-techne.com/find-us/distributors TEL +1 612 379 2956
North America TEL 800 343 7475 **Europe | Middle East | Africa** TEL +44 (0)1235 529449
China info.cn@bio-techne.com TEL +86 (21) 52380373

bio-techne.com

Science Careers Advertising

For full advertising details, go to ScienceCareers.org and click For Employers, or call one of our representatives.

Tracy Holmes
Worldwide Associate Director
Science Careers
Phone: +44 (0) 1223 326525

THE AMERICAS

E-mail: advertise@sciencecareers.org
Fax: +1 (202) 289 6742

Tina Burks
Phone: +1 (202) 326 6577

Nancy Toema
Phone: +1 (202) 326 6578

Online Job Posting Questions
Phone: +1 (202) 312 6375

EUROPE / INDIA / AUSTRALIA / NEW ZEALAND / REST OF WORLD

E-mail: ads@science-int.co.uk
Fax: +44 (0) 1223 326532

Sarah Lelarge
Phone: +44 (0) 1223 326527

Kelly Grace
Phone: +44 (0) 1223 326528

Online Job Posting Questions
Phone: +44 (0) 1223 326528

JAPAN

Katsuyoshi Fukamizu (Tokyo)
E-mail: kfukamizu@aaas.org
Phone: +81 3 3219 5777

Hiroyuki Mashiki (Kyoto)
E-mail: hmashiki@aaas.org
Phone: +81 75 823 1109

CHINA / KOREA / SINGAPORE / TAIWAN / THAILAND

Danny Zhao
E-mail: dzhao@aaas.org
Phone: +86 131 4114 0012

ScienceCareers
FROM THE JOURNAL SCIENCE AAAS

ScienceCcareers.org

Institut Pasteur

Creation of new junior research groups at Institut Pasteur

The Institut Pasteur has launched an international call for junior candidates wishing to establish new independent research groups in the cutting edge interdisciplinary environment of its campus in Paris, France.

The Institut Pasteur is a non-profit private foundation dedicated to fundamental, interdisciplinary research and to the translation of the knowledge to medicine and public health. Topics of interest include microbiology (bacteria, viruses, parasites and fungi) and infectious diseases, immunology, cell biology, developmental biology and stem cells, neuroscience, genomics, structural biology, genetics and cancer.

Successful **junior candidates*** will be appointed with a permanent position, and as head of a group of 6 people. These groups will be created for a period of 5 years and may thereafter compete for a full research group.

Highly attractive packages to match the experience of the candidate will be provided, including institutional salaries (Principal investigator, technician, secretary, post-doctoral fellows), a substantial contribution to running costs and equipment, access to on campus state-of-the-art technology core facilities, as well as support for relocation expenses and administrative issues.

Applications shall be submitted online at: **https://aap4.voozanoo.net/register** and shall include:

1. A web form summarizing the application.
2. A complete application file using the template which can be downloaded from the submission website. The template should be filled and uploaded as a single PDF file.

The deadline for submission of the applications is **December 2, 2016**, by 5:00 pm CET.
Shortlisted applicants will be notified by mid-January 2017, and will be invited for interview to take place mid-February 2017. The final ranking will be established by the Pasteur Scientific Council during its March 2017 session.

Further information on the institute can be found at **http://www.pasteur.fr/en**

Contact: aap4@pasteur.fr

* Institut Pasteur is an equal opportunity employer. Junior group leaders should be less than 8 years after PhD at the time of submission. Women are eligible up to 11 years after their PhD if they have one child and up to 14 years after their PhD if they have two or more children.

Institut Pasteur

Junior Research Group
Institut Pasteur – Danone Research

DANONE RESEARCH DANONE

Call for candidates to head a junior research group on microbiome and western life style at Institut Pasteur in Paris, France

The Institut Pasteur and Danone Nutricia Research have launched an international call for a **junior* research** group studying the gut host and microbiome homeostasis on the Institut Pasteur campus in Paris. The position is open for an outstanding candidate who wishes to develop a cutting-edge research program on the short and long term effects of western stressors on gut microbial ecology, genetics and immunity throughout the lifespan. Another aim of this group will be to identify dietary solutions that improve gut microbiome resilience and attenuate the impact of western stressors.

The Institut Pasteur is a non-profit private foundation dedicated to fundamental, interdisciplinary research and to the translation of the knowledge to medicine and public health. Topics of interest include microbiology (bacteria, viruses, parasites and fungi) and infectious diseases, immunology, cell biology, developmental biology and stem cells, neuroscience, genomics, structural biology, genetics and cancer.
Danone is an international company present in 5 continents with one unique mission: "bringing health through food to as many people as possible". Danone Nutricia Research, the research entity of the group, has been collaborating for decades with key outstanding academic partners to develop breakthrough scientific concepts that support the development of nutritional products to maintain human health.

The applicant will benefit from an attractive package, including institutional salaries (Principal investigator, technician, post-doctoral fellows), a substantial contribution to running costs and equipment, access to on campus state-of-the-art technology core facilities, as well as support for relocation expenses and administrative issues.

Candidates should send their formal applications by E-mail to the following address:
IPDanone@pasteur.fr

The application shall comprise the following (in order) in a SINGLE pdf file:

1. A brief introductory letter.
2. A project summary (one page).
3. A Curriculum Vitae (including list of past and current funding) and a full publication list, highlighting the 5 major publications.
4. A description of past and present research activities (up to 5 pages, Arial font size 11 with 1.5 spacing).
5. The proposed research project (up to 6 pages, Arial font size 11 with 1.5 spacing) and how it would fit in the defined topic.

The deadline for applications is December 2, 2016 5:00 pm CET.
Shortlisted applicants will be notified by mid-January 2017, and will be invited for interview to take place mid-February 2017. The final ranking will be established by the Pasteur Scientific Council during its March 2017 session.
Further information on the institute can be found at **http://www.pasteur.fr/en**
Contact: **IPDanone@pasteur.fr**

* Institut Pasteur is an equal opportunity employer. Junior group leaders should be less than 8 years after PhD at the time of submission. Women are eligible up to 11 years after their PhD if they have one child and up to 14 years after their PhD if they have two or more children.

Faculty Positions in Cancer Research
Huntsman Cancer Institute, University of Utah
An NCI-designated Comprehensive Cancer Center

Huntsman Cancer Institute (HCI) at the **University of Utah Health Sciences Center (UUHSC)** is an NCI-designated Comprehensive Cancer Center and member of the National Comprehensive Cancer Network (NCCN), supporting and fostering a vibrant research enterprise in a highly collegial environment. HCI has a strong history of academic achievement and impact, as well as a commitment to excellence in patient care, research, teaching, and service. HCI is undergoing a major expansion, including a new research building, and is seeking outstanding candidates for **faculty** positions at all levels and ranks in basic, translational, and population sciences cancer research.

HCI leadership is committed to developing disease-oriented research teams (DOTs) as a mechanism to enhance translational research. DOTs specialize in adult and pediatric cancer research in the following areas: colon cancer, genitourinary and hematologic malignancies, hepatobiliary cancer, melanoma, neuro-oncology, pancreatic cancer, sarcoma, upper aero digestive tract (with existing strengths in lung cancer) and women's cancers. Candidates whose cancer research interests align with the HCI DOTs are strongly encouraged to apply.

Basic Cancer Research: We seek junior and senior investigators with innovative basic cancer biology programs that emphasize mechanistic approaches. Areas of interest include signal transduction, stem cells, gene regulation/transcription, chromatin/epigenetics, genome stability/DNA repair, cancer metabolism, cancer genetics, metastasis, epithelial cancers, tumor immunology, hematologic malignancies, pediatric/youth cancers, and mechanisms of therapy resistance. Applicants will align with and benefit from our cancer DOTs, which facilitate translation of basic science discoveries through collaborative team science approaches.

Translational Cancer Research: This broad-based recruitment seeks outstanding scientists in a number of areas, including animal models, signal transduction, cancer genetics, target validation, drug discovery/validation, epigenetics and gene expression, DNA damage and repair, tumor immunology, cancer initiating cells, and clinical cancer research. Candidates whose scientific interests dovetail with the clinical strengths of the HCI DOTs are particularly encouraged to apply.

Cancer Control and Population Sciences: We seek outstanding scientists in a number of areas, including cancer prevention (including behavioral interventions), cancer epidemiology, with emphasis on molecular/clinical epidemiology or genetic epidemiology, cancer survivorship, exercise and cancer, health outcomes, risk communication, rural health, implementation science, and biostatistics. We are looking for collaborative and engaged colleagues interested in advancing their career through interdisciplinary team science.

HCI and the UUHSC provide access to state-of-the-art equipment and services through exceptional Core Facilities (www.cores.utah.edu) that enhance both discovery and translational science. HCI also offers state-of-the-art laboratories, including a new 220,000 sq. ft. research building which doubles its research space, opening in summer 2017. The U of U offers robust graduate programs for training PhD and MD/PhD students. Visit www.huntsmancancer.org for more information.

Applicants for Assistant Professor should hold a PhD or MD/PhD (or equivalent), have received appropriate postdoctoral training and have a record of impact and research productivity. Requirements for senior positions include a proven record of independent funding and innovative research. HCI particularly encourages and welcomes applications from physician-scientists across the continuum of cancer research. Highly competitive recruitment packages are available with appointment and rank in an academic department at the U of U determined by the applicants' qualifications.

Submit a curriculum vitae; cover letter with professional experience, including scientific accomplishments and leadership responsibilities; a three-page research plan; and three letters of recommendation. Applications accepted continuously, with evaluations beginning November 15, 2016, until positions are filled or closed.

Apply online: http://utah.peopleadmin.com/postings/57123 • E-mail: hci.recruitment@hci.utah.edu
OR
Huntsman Cancer Institute, University of Utah
Attn: Recruitment Office, Room 5160
2000 Circle of Hope, Salt Lake City, UT 84112-5550

The University of Utah Health Sciences Center (UUHSC) is a patient focused center distinguished by collaboration, excellence, leadership, and respect. The UUHSC values candidates who are committed to fostering and furthering the culture of compassion,collaboration, innovation, accountability, diversity, integrity, quality, and trust that is integral to our mission.

The University of Utah is an Affirmative Action/Equal Opportunity employer and does not discriminate based upon race, national origin, color, religion, sex, age, sexual orientation, gender identity/expression, disability, or status as a Protected Veteran. Upon request, reasonable accommodations in the application process will be provided to individuals with disabilities. To inquire about the University's nondiscrimination policy or to request disability accommodation, please contact: Director, Office of Equal Opportunity and Affirmative Action, 201 South Presidents Circle, Room 135, Salt Lake City, UT 84112 801-581-8365.

The University of Utah values candidates who have experience working in settings with students from diverse backgrounds, and possess a demonstrated commitment to improving access to higher education for historically underrepresented students.

Business principles for basic researchers

Leadership, management, and marketing sound like skills for CEOs, not scientists. Running a research group requires MBA-type strengths, though, such as budgeting, mediating, and negotiating. Some universities now offer workshops on business principles for scientists and engineers, lending credence to the idea that mixing business with science is a path to success. **By Chris Tachibana**

Imagine meeting the director of your research institute on the way to the lab. She asks about your work. Do you give her a vague description, overwhelm her with details, or intrigue her with a brief, compelling science story? **Rainer Mauersberger,** coordinator of the International Max Planck Research School for Astronomy and Astrophysics in Bonn, Germany, uses this scenario to show how a business-school device—an "elevator speech"—benefits researchers. Although Mauersberger and many other scientists apply business principles to their work, some doubt that a field associated with sales and profits has anything to offer them. This article presents the case for business training for science faculty.

Business skills, says **Lucila Ohno-Machado,** are essential for academic scientists who want to advance their careers. She speaks from experience, as chair of the Department of Biomedical Informatics at the University of California, San Diego. Although Ohno-Machado holds a Master of Business Administration (MBA) degree from the University of São Paulo, Brazil, she has never worked in business. "I wanted to do health informatics," she explains, "and my university had an MBA track in informatics systems." Ohno-Machado says her business training helped her expand her research group. Specifically, she says, it taught her the basics of "hiring people, assembling a good team, measuring our performance, and planning for expenses." It was also useful for the next step in her career.

"Scientists are selected to be a chair or division leader based on accomplishments in their field," says Ohno-Machado, "but these are management positions. Scientists in these roles need to know about things like accounting, resource management, and organizational development." Ohno-Machado urges experienced researchers to learn management skills and to take on executive academic positions; she particularly encourages women and minorities to do so. "That is the only way to have more diverse people in leadership," she says.

Role playing: Not just for actors and businesspeople

Even faculty who aren't planning administrative careers want to be effective leaders and lab managers (see *Science* Careers: bit.ly/297HXXx). Anyone who has witnessed a dispute or personality clash at work understands how training in mediation, negotiation, and conflict resolution can save time and energy. Increasingly, opportunities to learn these skills are available right on campus. One example is a leadership workshop for faculty that originated at the Massachusetts Institute of Technology (MIT) in Boston, Massachusetts. Developed in 2002 by **Charles Leiserson,** professor of computer science and engineering, and Chuck McVinney, management consultant, the workshop has trained nearly 1,000 people at MIT and elsewhere.

During a sabbatical at an information technology firm in 1999, Leiserson saw how a brief, intense workshop turned what he calls a dysfunctional group of engineers into a well-oiled machine. Back at MIT, Leiserson proposed similar training for professors, saying to administrators, "I've seen how training can prevent human-level mistakes that cause untoward fallout. Let me see if I can adapt these business management materials for academic settings." MIT supported his time to develop the workshop. Rather than project management, though, Leiserson says the focus of the training is on "conspicuous weaknesses for many scientists— cont.>

Lucila Ohno-Machado

PHOTOS (FROM TOP): © SISACORN/SHUTTERSTOCK.COM; COURTESY OF UC SAN DIEGO HEALTH

Upcoming Features

Focus on Wales—October 14 ■ *Top Employers Survey—October 28* ■ *Regional Focus: China—November 4*

Memorial Sloan Kettering Cancer Center

Faculty positions at the Sloan Kettering Institute Memorial Sloan Kettering Cancer Center

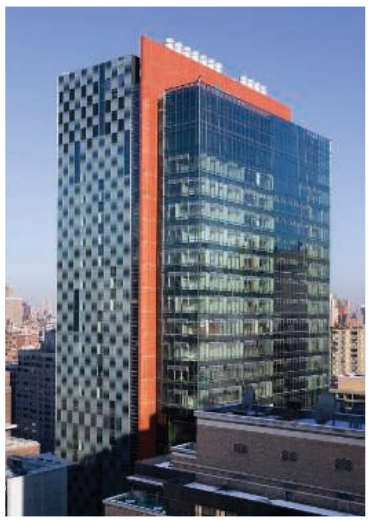

OPPORTUNITIES IN BIOMEDICAL RESEARCH

- **Cancer Genetics**
- **Cell Signaling & Regulation**
- **Chemistry & Chemical Biology**
- **Computational Biology**
- **Experimental Therapeutics**
- **Genome Integrity, Gene expression, and Epigenetics**
- **Immunology**
- **Stem Cell Biology & Regenerative Medicine**
- **Structural Biology**

JOIN OUR FACULTY

Successful candidates will hold an appointment in one of SKI's research programs.
Candidates may apply to up to two programs:

Cancer Biology & Genetics
Chair: Scott Lowe, PhD

Cell Biology
Interim Chair: Marilyn Resh, PhD

Chemical Biology
Chair: Derek Tan, PhD

Computational Biology
Chair: Dana Pe'er, PhD

Developmental Biology
Chair: Kathryn Anderson, PhD

Immunology
Chair: Alexander Rudensky, PhD

Molecular Biology
Chair: John Petrini, PhD

Molecular Pharmacology
Chair: David Scheinberg, MD, PhD

Structural Biology
Chair: Nikola Pavletich, PhD

Research and Training

- 130 research laboratories housed in state-of-the-art buildings
- Core facilities offering cutting-edge scientific services
- Over 800 pre- and post-doctoral trainees
- Appointments in the Gerstner Sloan Kettering Graduate School of Biomedical Sciences and the Weill Cornell Graduate School of Medical Sciences

Visit **www.ski.edu** to learn more.

Application deadline: **November 1, 2016**
Apply at: **https://facultysearch.ski.edu**

MSK is an equal opportunity and affirmative action employer committed to diversity and inclusion in all aspects of recruiting and employment. All qualified individuals are encouraged to apply and will receive consideration without regard to race, color, gender, gender identity or expression, sexual orientation, national origin, age, religion, creed, disability, veteran status or any other factor which cannot lawfully be used as a basis for an employment decision.

communication, relationships, and building a work culture." The course builds skills in these areas using a method that seems ill-suited to engineers and scientists: role-playing.

The technique works because it is tailored for scientists. The role-playing situations address real-life issues such as disputes over first authorship or students with low motivation. Participants get comfortable with their roles using method-acting activities in which they talk about the emotions that people in those situations might experience. This approach resembles courses from the Alan Alda Center for Communicating Science, located at Stony Brook University. The center's workshops use improvisational theater exercises to help scientists be genuine, clear, and responsive when talking about their work. Leiserson says that effective communication is an important overall goal of his workshop, and is not just for resolving disagreements. The practical benefits of good communication are enormous, he says: "If you can persuasively convey the mission statement of your research, you can convince administrators, colleagues, the public, and granting agencies about the impact of your work."

From left: "Business and Management Principles for Scientists" Course Director Dr. Rob Carnahan, Team members Bethany Carboneau, David Sprinzen, Roxana Loperena, Aaron Ehlinger, and Office of Career Development leaders Dr. Kathleen Gould and Dr. Kim Petrie.

Faculty naturally worry about spending time on this type of training. But workshop participants tell Leiserson that minimizing misunderstandings in their research groups actually saves time. The MIT course also works because of its academic roots. Rather than impose a management system on participants, the workshops give faculty autonomy in finding their own effective leadership style. Leiserson and McVinney use the engineering principle of iterative improvement—which involves repeated testing, analysis, and refinement—to continually develop the course.

Marketing? Really?

Effective leadership, team management, and communication have clear applications in basic research. But some areas, like marketing, seem outside the realm of academic science. Nonetheless, a few years ago, Mauersberger took a two-day workshop from Marc Kuchner, astrophysicist at NASA's Goddard Space Flight Center and author of *Marketing for Scientists: How to Shine in Tough Times.* At the time, Mauersberger was working at the European Southern Observatory in Santiago, Chile. He says, "My colleagues and I thought, 'We're nerds, we don't need to learn marketing. We do good science and it sells itself.'" But he had been thinking about why so many scientists with amazing results give lackluster presentations. "People make slides with bullet points," he says. "The audience reads the points faster than the speaker talks, then turn to their smartphones and read their email." Kuchner's workshop, it turned out, included a section on using marketing ideas to create inspiring scientific presentations.

The main lesson Mauersberger got from the workshop, he says, was to structure a talk like a movie: Create a line of tension from the beginning to the end. Describe the state of the field, then build drama by revealing unsolved questions. Provide methods and data—the meat of your story—but move briskly, and consider peoples' attention spans. End by presenting the resolution to the foreshadowed drama and showing how you've changed the field. And don't pack too much into your talk. Most presentations, especially at a long conference, are forgotten. If attendees remember two or three main messages, Mauersberger says, it's a success.

Structuring a research talk as a film might sound glib, but presenters should do so out of courtesy to their audience, Mauersberger advises. "If I give a boring talk," he explains, "I've been impolite to my colleagues, taking their time and energy." Although no scientist wants to be considered a salesperson, he says, it's noticeable that brilliant scientists who can also convince people about their ideas are the ones who attain influential positions and excel in them.

Hit the (virtual) business books

For researchers at institutions that don't offer workshops, self-study is an option. **Jeffrey Engler** was a virology researcher for 22 years before becoming associate dean of the University of Alabama at Birmingham Graduate School. He learned business principles that apply to academic settings by taking massive open online courses (MOOCs). "I started taking MOOCs," he says, "because my grad-school duties include overseeing professional development—helping students gain skills for careers in academics, industry, business, or policy. I took MOOCs to find out if they provide useful, specific training for students." Engler chose topics helpful for students and postdocs, such as education, decision-making, and innovation, but found himself applying the content, sometimes in unanticipated ways. "A course on emotional intelligence helped me think through what good mentors do," he says. "It's helped me talk with students about their goals, aspirations, and values as they choose career paths."

Although Engler says MOOCs vary in their usefulness, he recommends that faculty try them. They can take as little time as one evening a week, he adds. He also encourages open-mindedness about how the lessons apply to academic environments. "Go to Coursera or edX and try a course you think will be fun," he says. "Try to finish it, too."

Faculty members might worry that their institution won't recognize the value of training outside their discipline. Engler understands and would like to see academic culture change to reward more diverse training. "Skills in finance, management, and teaching especially benefit team-based interdisciplinary science," he says. Cultural changes could come with the next generation of scientists. Engler says that students and postdocs he talks with are excited about combining research with teaching, mentoring, and business.

A little savvy goes a long way

Young biomedical researchers were the target audience for a pilot training module at Vanderbilt University titled "Business and Management Principles for Scientists." The module was supported by the Burroughs Wellcome Fund with cont.>

PHOTO: VANDERBILT UNIVERSITY

"I liked learning about hiring people and thinking about what kind of team member they will be."

—Sarah Baum

Featured Participants

International Max Planck Research School for Astronomy and Astrophysics
www.mpifr-bonn.mpg.de/en/imprs

Massachusetts Institute of Technology
web.mit.edu

University of Alabama Birmingham Graduate School
www.uab.edu/graduate

University of California, San Diego
www.ucsd.edu

Additional Resources

Vanderbilt University
www.vanderbilt.edu

Alan Alda Center for Communicating Science
www.centerforcommunicatingscience.org/alan-alda

Burroughs Wellcome Fund
www.bwfund.org

Coursera
www.coursera.org

edX
www.edx.org

Marketing for Scientists: How to Shine in Tough Times
http://marketingforscientists.com

Kathy Gould, professor of cell and developmental biology at Vanderbilt School of Medicine, as principal investigator. Development, oversight, and teaching were coordinated by **Kim Petrie,** assistant professor of medical education and administration, **Rob Carnahan,** director of the Antibody and Protein Resource core facility and associate professor of cancer biology, and **Joe Rando,** associate professor of managerial studies.

One-quarter of the students and postdocs who participated in the training were planning academic careers. For these scientists, the module offered valuable tools, particularly for their first startup year. "Faculty are generally given lab space and possibly a million-dollar budget, but no background in how to manage it," Carnahan says. "Most people get up to speed on their own but if they don't, the lab suffers."

Gaining the know-how to launch a basic research program is exactly why **Sarah Baum,** postdoctoral fellow at the Vanderbilt Brain Institute, took the training module. "I have friends who just got academic jobs, and they're making budgets for startup packages," she says. "The training helped me think about the financial aspects of a lab and how to balance spending between purchases and people." Baum has been thinking about the management style she wants for her own lab, so she appreciated learning about building and leading a team. "The way your team works and the people you attract to it are vital to your research productivity," she says, "so I liked learning about hiring people and thinking about what kind of team member they will be. I want a group that's not just smart people but smart people who work well together."

Reid Bolus, Vanderbilt University molecular physiology and biophysics graduate student, was interested in the financial sections of the module. Conversations with his advisor made him realize the amount of budgeting and planning required to run a lab. Like Baum, Bolus says the sessions on management were valuable. "We learned what it takes to be a good leader and motivator," he says, "and that your job is to set the framework and culture of the lab. You have to know how to communicate, listen, accept criticism, and manage people with different personalities."

Baum says that friends at other institutions who are also going into academia are eager to hear what she learned. Based on her experience and their interest, she recommends that universities offer business training to early career scientists. Exposure to business ideas gives trainees specific skills for starting and running a lab, says Gould, but also gives them more confidence and a greater sense of purpose about their work. "One of my students took the module," she said, "and at two hours a week, it didn't affect her lab work. It kept her motivated, and she enjoyed it and got a lot out of it."

Time Management 101

To be successful, a business training course for scientists must directly demonstrate its value to research. Like Leiserson and McVinney's MIT workshop, the Vanderbilt module was tailored for scientists. The sessions on business principles came first, but the rest of the course was practical, an approach enthusiastically recommended by both Baum and Bolus. In the practical sessions, teams of participants developed business-based solutions to real-world challenges from the university's core facilities. Carnahan offers an example: "Faculty members often have to decide about investing in new technology," he says. "To do that, it would help to have data-driven decision-making processes, like decision trees about buying new equipment."

Finally, to promote the module among the faculty, Gould and Petrie applied marketing methods adapted for their audience of academic scientists. They built relationships and communicated a specific message about how the module could help early career scientists. "Faculty are data-driven," says Gould, "so I went to 19 faculty meetings last year to talk about the data on jobs for our trainees and how this module could help them."

Even with endorsements from established and early career researchers, science faculty might be reluctant to commit their own or their trainees' time to a business workshop. These researchers can start small. The university's technology transfer office or business and management school might have seminars or networking opportunities for an initial exposure to business ideas. For those who still hesitate about getting business skills to improve research productivity, Leiserson offers advice he learned from his father: "If you hate doing something, get good at it," he says. "Then you don't have to spend so much time at it. Engineering professors love the technical part of their job, so we tell them, 'Get good at management and work relationships and you'll have more time for being a nerd.'"

Chris Tachibana is a science writer based in Seattle, USA, and Copenhagen, Denmark.

DOI: 10.1126/science.opms.r1600168

PHOTO: COURTESY OF SARAH BAUM

DO YOUR RESEARCH **HERE.**

JOIN US.

THE JACKSON LABORATORY

Join The Jackson Laboratory (JAX) as an assistant, associate or full professor in Bioinformatics and Computational Biology Research in Bar Harbor, ME and Farmington, CT.

JAX is a nonprofit biomedical research institution which offers a collaborative environment that fosters multidisciplinary approaches to investigate complex biological questions. Faculty use genetic and genomic approaches to conduct basic and translational research on fundamental biological processes in disease using mouse models and human studies. JAX is home to the internationally recognized Mouse Genome Informatics (MGI) databases and the Gene Ontology and Human Phenotype Ontology projects.

Join our faculty to pursue computational approaches in:

- Systems genetics
  Systems approaches to complex trait analysis, including genetic analysis of transcript expression, histone modifications, and protein abundance
- Cancer computational biology
  Focus areas include models of cancer biology, tumor evolution, tumor-immune system interactions, and mechanisms of therapy response and resistance
- Cross-organism bioinformatics
  Create and align animal models of human disease with clinical genetics, including algorithms to translate results for both the genome and phenome

Successful candidates must hold a Ph.D. and/or M.D. degree; have two to five years of postdoctoral training; a record of significant research accomplishments; and present long-term research goals for establishing and/or maintaining a successful research program.

Apply now by submitting a curriculum vitae and a concise statement of research interests and plans as one document to *www.jax.org/careers/faculty.html*. In addition, please arrange to have three letters of reference sent to: *facultyjobs@jax.org*.

The Jackson Laboratory is an EEO/AA employer. All qualified applicants will receive consideration for employment without regard to race, color, religion, sex, national origin, disability or protected veteran status.

The Jackson Laboratory

Leading the search for tomorrow's cures

ASSISTANT PROFESSOR POSITIONS

Plant Systematics, Ecohydrology, Pharmacology and/or Natural Products Discovery

The Department of Biological Sciences at The University of Alabama invites applications for three full-time (9-month) tenure-track faculty positions at the rank of Assistant Professor in Plant Systematics, Assistant Professor in Ecohydrology and Assistant Professor of Pharmacology and/or Natural Products Discovery to begin August 16, 2017.

For the **Plant Systematics position**, all taxonomic groups of vascular plants will be considered. Applicants whose research integrates field and museum-based studies with modern genomic approaches to address fundamental questions in taxonomy, systematics, biogeography, and evolution of vascular plants are encouraged to apply. The successful applicant is expected to curate The University of Alabama Herbarium (UNA) maintained by the Department of Biological Sciences and must provide evidence of curatorial experience and/or other relevant abilities. The Herbarium at the University of Alabama contains significant holdings of vascular plants from the USA and the neotropics, and particularly from SE USA freshwater habitats. Individuals interested in diversifying this actively growing collection are encouraged to apply. The successful candidate also would serve as the Department's liaison with the University of Alabama Arboretum. Teaching responsibilities will include undergraduate courses in plant systematics, dendrology or field botany, and one or more graduate courses in the successful candidate's area of expertise.

For the **Ecohydrology position** we seek applicants to establish an extramurally funded and internationally recognized research program centered on the interactions and feedbacks between ecological systems and water fluxes through any component of the hydrologic cycle. Applicants should employ integrative, multi-scale approaches that combine field-based work and modeling to characterize relationships between the water cycle, regional climate, and the dynamics of terrestrial and/or aquatic systems, and must be committed to excellence in teaching and mentoring undergraduate and graduate students. We are particularly interested in applications from individuals with a demonstrated record of research in improving our understanding of coupled processes at scales ranging from watersheds to regions and in the context of global environmental change. The successful candidate will be encouraged to leverage Alabama's unique and diverse water resources to support an innovative research program, and to forge collaborations with the new NOAA National Water Center, which opened on the UA campus in 2014, and the diverse faculty at UA and Dauphin Island Sea Lab with interests in water-related research.

For the **Pharmacologist position** we seek applicants with research interests that fall within the broad area of Pharmacology and/or Natural Products Discovery. Applicants must have completed a Ph.D. and post-doctoral or equivalent experience. The successful candidate will be expected to establish a productive and extramurally funded research program involving biochemical, molecular, ecological and/or computational approaches toward the identification and analysis of bioactive compounds with either health and/or environmental impacts. Evidence of significant intellectual contributions to the field and a commitment to teaching at both the graduate and undergraduate level are required. The individual hired should be able to teach courses in pharmacology and/or biochemistry, participate in the interdisciplinary UA Biological Sciences graduate program, and contribute to the service activities of the department. In addition to fostering opportunities to collaborate with diverse faculty conducting drug discovery and ecological research in this department, the successful candidate will enhance existing scientific ties and opportunities with colleagues in the UA Departments of Chemistry and Chemical and Biological Engineering, as well as the University of Alabama School of Medicine and the HudsonAlpha Institute for Biotechnology.

A complete application includes (1) an application letter; (2) CV; (3) statement of research interests and goals; (4) statement of teaching interests and philosophy; and (5) a list of at least four references (including contact information). Letters of reference will be requested by the search committee as appropriate. To apply, complete the online application at **https://facultyjobs.ua.edu/postings/39634** for the Plant Systematics position; **https://facultyjobs.ua.edu/postings/39635** for the Ecohydrology position; or **https://facultyjobs.ua.edu/postings/39611** for the Pharmacology position), and upload all requested documents. Questions about the Plant Systematics position may be addressed to Dr. Juan Lopez-Bautista (**jlopez@ua.edu**; 205-348-1791). Questions about the Ecohydrology position may be addressed to Dr. Julia Cherry (**julia.cherry@ua.edu**). Questions about the Pharmacology position may be addressed to Dr. Guy Caldwell (**gcaldwel@ua.edu**). Consideration of applications will begin immediately and will continue until the positions are filled. Prior to hiring, the final candidates will be required to pass a pre-employment background investigation. The anticipated start date is August 16, 2017 for all positions. Additional information about the Department of Biological Sciences and this available position can be found on our website at **http://bsc.ua.edu**. Applications from women and members of traditionally under-represented groups in Biology are especially encouraged. The University of Alabama is an Equal Opportunity/Equal Access Employer and actively seeks diversity among its employees. Minority and women candidates are especially encouraged to apply.

THE UNIVERSITY OF ALABAMA®
THE CAPSTONE OF HIGHER EDUCATION

PURDUE
UNIVERSITY

Tenure Track Assistant Professor Position in Cryo-EM
Markey Center for Structural Biology
Department of Biological Sciences

The Department of Biological Sciences, Purdue University, is initiating a major effort to expand its investment in cryo- electron microscopy with a new tenure-track assistant professor position in this exciting area of science. The Structural Biology Group at Purdue is recognized worldwide for its leadership in structural biology of viruses, membrane proteins, and technical approaches to crystallographic and electron microscopy challenges. Creative investigators trained in single particle cryo-EM or whole cell electron tomography are sought to enhance these current structural investigations. Areas of research interest include studies of macromolecular complexes, viruses and other pathogens, membrane proteins, signaling in cancer biology, target molecules for structure-based drug discovery and methods development in structural biology by cryo-EM. This position is aligned with other major campus-wide investments in the life sciences including the Center for Drug Discovery (http://www.purdue.edu/research/pcdd/), the Center for Integrative Neurosciences (http://www.purdue.edu/discoverypark/pillars/integrative-neuroscience-center/), the Institute for Inflammation, Immunology and Infectious Disease (http://www.purdue.edu/discoverypark/pillars/pi4d/) and the Purdue Center for Cancer Research (http://www.cancerresearch.purdue.edu).

Applicants must have a Ph.D. or equivalent in Biology or an appropriate discipline and at least 2 years of relevant postdoctoral experience. A successful applicant for this position is expected to direct a dynamic and collaborative research program in structural biology using cryo-electron microscopy to address fundamental biological questions, to excel at teaching at the undergraduate and/or graduate level and participate in ongoing programs at Purdue.

Extensive opportunities for collaboration exist across the Purdue campus. Our department alone has over 50 faculty members conducting research in structural biology, neurobiology, virology, microbiology, molecular and cell biology, bioinformatics, evolutionary biology and ecology and biology education (http://www.bio.purdue.edu/). These opportunities are enhanced by a highly interactive community of scientists within the Colleges of Science, Agriculture, Pharmacy, Veterinary Medicine and Engineering and existing and emerging interdisciplinary centers in the life sciences. Cutting edge equipment for cryo-electron microscopy is available, including an FEI Titan Krios cryo-EM with K2 direct electron detector and Volta phase plate system in the Hockmeyer Hall Cryo-EM Facility (http://cryoem.bio.purdue.edu). We have strong, well-established infrastructure for structural biology in Hockmeyer Hall, including state-of-the-art robotics, as well as advanced imaging analysis and biophysical instrumentation available in modern core facilities at the Bindley Bioscience Center and the Birck Nanotechnology Center in Discovery Park (http://www.purdue.edu/discoverypark/), and advanced super-computing resources for data storage, processing and analysis (http://www.rcac.purdue.edu).

Applications should be submitted electronically to **https://hiring.science.purdue.edu/** as a single PDF file containing a letter of interest, a detailed curriculum vitae, contact information for three references, a two to three page summary of research interests, and a one-page teaching statement. Purdue University's Department of Biological Sciences is committed to advancing diversity in all areas of faculty effort, including scholarship, instruction and engagement. Candidates should address at least one of these areas in their cover letter, indicating past experiences, current interests or activities, and/or future goals to promote a climate that values diversity and inclusion. As an ADVANCE institution, Purdue University is dedicated to the recruitment, retention and advancement of women STEM faculty. Inquiries should be directed to **Cynthia Stauffacher, Chair, Structural Biology Search Committee at StructureSearch@bio.purdue.edu or Structural Biology Search Committee, Department of Biological Sciences, Purdue University, 915 W. State St., West Lafayette, IN 47907-2054**. Review of applications will begin **October 1, 2016** and continue until the position is filled. A background check is required for employment in this position.

Purdue University is an EOE/Affirmative Action Employer. All qualified applicants, including minorities, women, individuals with disabilities and veterans are encouraged to apply.

AAAS

American Association for the Advancement of Science

Science & Technology Policy Fellowships

Enhancing Policy, Transforming Careers

Where science and policy change the world. And you.

The Roger Revelle Fellowship in Global Stewardship is designed to provide midcareer professors the opportunity to address global stewardship issues by applying a multidisciplinary background toward solutions to societal problems including ecosystems, population, sustainable development, and climate change.

"The Revelle Fellowship is an excellent opportunity to re-invent, re-launch, or re-energize a career."

Franklin Carrero-Martínez, Ph.D., Biology, Roger Revelle Fellow in Global Stewardship, U.S. Department of State

Current: Program Director, Office of International Science and Engineering/Office of the Director, National Science Foundation

Applications accepted May 1 — November 1.

To learn more and apply visit **go.stpf-aaas.org/Science4.html**

OPEN FACULTY POSITIONS
INSTITUTE OF MOLECULAR BIOLOGY
ACADEMIA SINICA, TAIWAN, ROC

One tenure-track faculty position is open for a highly qualified individual to establish independent research programs **in all disciplines of molecular and cellular biology**. Applicants should hold a Ph.D. degree or its equivalent, with appropriate postdoctoral research experience. The successful recruit will be appointed at the levels of **Assistant, Associate,** or **Full Research Fellows** (equivalent to academic ranks of Assistant, Associate and Full Professors at universities), and receive a generous multi-year start-up package, followed by annual intramural support.

The Institute of Molecular Biology at Academia Sinica (**http://www.imb.sinica.edu.tw/en**) provides an active and stimulating research environment, is well supported by both extramural and long-term intramural funding, and features several core facilities (cell imaging, microarray, Next Generation Sequencing, RNAi, electrophysiology, FACS, bioinformatics and mouse facilities) that provide state-of-the-art resources and key technical expertise to the Institute's research community. Recent research works were published in top journals such as Science, Nature, and Cell. Currently two Ph.D. programs, with one recruiting international students, are formally affiliated with the Institute. English is the official language for seminars and lectures at the Institute, and proficiency in Chinese language is not a prerequisite for application.

Applicants should send their Curriculum Vitae, a description of past research accomplishments and future research plans, and arrange for three letters of recommendation to be sent directly to:

Dr. Soo-Chen Cheng, Director
c/o Ms. Vivi Chiang
Institute of Molecular Biology,
Academia Sinica
Taipei, Taiwan 11529, ROC

The selection process will start on **December 15, 2016** until the positions are filled. Further information can be obtained from **Ms. Vivi Chiang** at **vivi@imb.sinica.edu.tw**

UNIVERSITY OF MARYLAND

University of Maryland, College Park
Director: Earth System Science Interdisciplinary Center (ESSIC)

Leading a significantly expanded vision for ESSIC, the Director will leverage excellence across the campus relevant to the Earth system to build co-operative partnerships with the natural sciences and departments in a wide range of colleges, including but not limited to Agriculture and Natural Resources, Engineering, Public Health, and Public Policy. S/he will be a scientist of the highest quality in any of the disciplines essential to understanding the Earth system and must be a recognized player in the Earth system community, with a strong record of strategic leadership and a demonstrated ability to work collaboratively and successfully, nationally and internationally, inside and beyond academia. ESSIC has 11 academic faculty and 150 research scientists, with an annual research income of approximately $35M, and the Director must have a strong commitment to faculty and staff development. Appointed for a five year (renewable) term reporting to the Dean of the College of Computer, Mathematical and Natural Sciences s/he will also hold a tenured Full Professorship in an appropriate department on the campus. Ph.D. or equivalent required.

Applicants should submit as a SINGLE document a Curriculum Vitae including publications, a description of how their research and their experience qualify them for this position and the names and contact information for five referees. For more detail see **http://essic.umd.edu** Please apply at: **http://go.umd.edu/essicdir**.

The position will remain open until filled, but for best consideration applications should be received by **December 31, 2016**. Inquiries may be sent to: Professor Steve Halperin at **shalper@umd.edu**.

The University of Maryland, College Park, is an Equal Opportunity/ Affirmative Action Employer.

KU THE UNIVERSITY OF KANSAS

Computational Biology

The Center for Computational Biology (Computational Biology Program) and the Department of Molecular Biosciences invite applications for an assistant professor, tenure-track faculty position to begin as early as August 18, 2017. The interdisciplinary Center for Computational Biology (www.compbio.ku.edu) complements existing strengths in the Department of Molecular Biosciences (www.molecularbiosciences.ku.edu), including structural biology, computational chemistry, proteomics, systems biology, and developmental/molecular genetics, as well as strengths in drug design and information technology in the Schools of Pharmacy and Engineering. The Center fosters international activities in Computational Biology and combines outstanding research and a Ph.D. program.

Required Qualifications: Ph.D. and postdoctoral experience in a discipline related to Computational Biology is expected by the start date of the appointment; potential for excellence in research in Computational Biology; demonstrated commitment to teaching life sciences courses; and strong record of research accomplishments in at least one of the following areas: modeling of macromolecular structure and dynamics, biomolecular design, modeling of protein networks, systems biology, genomics, chemical biology, and computer-aided drug discovery. For a complete announcement and to apply online, go to **https://employment.ku.edu/academic/7136BR**. A complete online application includes the following materials: curriculum vitae; letter of application, statement of teaching interests, research plan, and the names, e-mail, and contact information for three professional references. Initial review of applications will begin **November 14, 2016** and will continue as long as needed to identify a qualified pool. Direct inquiries to Dr. Ilya Vakser (vakser@ku.edu). The successful candidate for the position must be eligible to work in the U.S. prior to the start of the position.

The University of Kansas is especially interested in hiring faculty members who can contribute to the climate of diversity in the College of Liberal Arts and Sciences and four key campus-wide strategic initiatives: (1) Sustaining the Planet, Powering the World; (2) Promoting Well-Being, Finding Cures; (3) Building Communities, Expanding Opportunities; and (4) Harnessing Information, Multiplying Knowledge. For more information, see www.provost.ku.edu/planning/themes.

KU is an EO/AAE, full policy http://policy.ku.edu/IOA/nondiscrimination.

WASHINGTON STATE UNIVERSITY

School of the Environment
Quantities Forest Ecology
Assistant Professor

The School of the Environment (SoE) at Washington State University (WSU) is seeking a dynamic, motivated colleague with expertise in forest ecology to join a productive and innovative team of biological and physical science faculty. Expertise sought in quantitative approaches to forest ecology. This is a 9-month, tenure-track, full-time faculty position that begins August 16, 2017 on the campus in Pullman, Washington.

Job Duties: The successful applicant will contribute to the continued development of a forestry degree by developing and teaching undergraduate and graduate courses involving statistical, geospatial and computational tools, and traditional and modern field-based forest measurement techniques. The successful applicant is expected to develop an internationally-recognized research program, including the training of M.S. and Ph.D. students. **Required:** Ph.D. at the time of application in a discipline related to forest ecology and management with an emphasis on quantitative ecology.

Screening of application materials begins **November 15, 2016**, and will continue until position is filled. Applications must include: a detailed letter of application describing how your experience and training meet the qualifications, a current curriculum vitae, a research statement (four pages maximum), a teaching philosophy statement (three pages maximum), and contact information for three professional references from whom the applicant will request letters of recommendation. Please contact **Dr. Mark E. Swanson, Search Committee Chair**, at **markswanson@wsu.edu**, **509-335-1349** for questions about this position. Visit **www.wsujobs.com** (Search **#122149**). For additional information on Washington State University, CAHNRS or SoE, visit cahnrs.wsu.edu and cahnrs.wsu.edu/soe.

EEO/AA/ADA.

Faculty Position in Gene Regulation, Genomics, and Reproduction

The **Cecil H. and Ida Green Center for Reproductive Biology Sciences**, an endowed basic science research center within the University of Texas Southwestern Medical Center Department of Obstetrics and Gynecology, is recruiting to fill a newly-created Tenure-track Assistant Professor Position. We invite applications from outstanding candidates studying aspects of signaling, gene regulation, and genome function, especially in the areas of chromatin and transcription, epigenetics, nuclear endpoints of cellular signaling pathways, nuclear receptors, RNA biology, genome organization, and genome evolution. We are interested in a wide variety of model systems and experimental approaches, including biochemistry, molecular biology, structural biology, animal models, genetics, genomics, proteomics, bioinformatics, and computational biology. The Green Center's research programs focus on, but are not limited to, reproduction and development in a broad sense, as well as aspects of endocrinology, stem cells, cancer, metabolism, inflammation, immunity, and neurobiology.

For this search, we are particularly interested in recruiting a candidate who represents one or more of these areas of biology:

• ***Signaling, chromatin, and gene regulation***, using a wide array of experimental approaches to address fundamental questions in nuclear signaling, chromatin, transcription, epigenetics, and RNA biology.

• ***Molecular biology of female reproductive systems***, from stems cells, oogenesis, and fertilization, to implantation, placental function, pregnancy, and parturition, using cell-based or physiological models in combination with molecular or genomic approaches.

• ***Genomic, bioinformatic, computational, and evolutionary approaches to understanding gene regulation***, using state-of-the-art genomic and computational tools.

The Green Center promotes and supports cutting-edge, integrative, and collaborative basic research in reproduction, development, and related areas of biology, as well as strong connections between basic and clinical research. This recruitment is part of a major university and department-supported renovation and rejuvenation of The Green Center over the past 6 years. Successful candidates will be housed in a newly renovated state-of-the-art research facility and provided a generous start-up package, and are expected to establish scientifically rigorous and externally funded research programs and participate in center, department, and university teaching and training programs. To learn more about The Green Center, visit: http://www.utsouthwestern.edu/education/medical-school/departments/green-center/index.html

Candidates must have a Ph.D. or M.D. or equivalent in a relevant field of study, postdoctoral or comparable experience, and a demonstrated record of research excellence. Applicants should send a letter of application, curriculum vitae, and a statement of planned research projects as pdf files to **GreenCenter@UTSouthwestern.edu**. Please indicate one of the three research areas listed above (Molecular biology of female reproduction; Gene regulation; Genomics) in the subject line of the email. Applicants should also arrange for three letters of reference to be sent directly to the above e-mail address. Review of applications will begin on **October 15, 2016**, and will continue during the 2016–2017 academic year or until the position is filled, although applicants are encouraged to submit their materials as soon as possible.

UT Southwestern is an Affirmative Action/Equal Opportunity Employer. Women, minorities, veterans, and individuals with disabilities are encouraged to apply.

COLLEGE OF PHARMACY
MEDICINAL CHEMISTRY
UNIVERSITY OF MICHIGAN

Faculty Member in Medicinal Chemistry (rank open)

As part of the College of Pharmacy's continuing emphasis on research at the interface of Chemistry and Biology, **the Department of Medicinal Chemistry** at the **University of Michigan**, (Ann Arbor, MI Campus) invites applications for a tenure-track faculty position, academic rank commensurate with qualifications. The Department of Medicinal Chemistry has long been recognized as one of the leading programs in the country in the application of modern chemical, biochemical and computational approaches aimed at the discovery and development of valuable chemical probes and drug molecules. This program involves faculty and students from not only the Department of Medicinal Chemistry in the College of Pharmacy but also departments in the Medical School, the College of Literature, Science, and the Arts, and the Life Sciences Institute. A successful applicant will be expected to develop and sustain an independent research program in physical, chemical, biological and/or computational aspects of drug discovery and should complement existing research programs in the department. Potential areas of research may include, but are not limited to: bioorganic chemistry, computational chemistry, structural biochemistry and/or synthetic organic chemistry. A distinguished academic record, the potential for independent, fundable research and a commitment to quality teaching at the undergraduate, graduate and graduate professional levels are essential. Applicants at the Associate/Full Professor level will need to demonstrate success in attracting extramural research funding and teaching experience. Collaboration is a core value of the faculty and administration of the University of Michigan and the opportunities for collaboration are extensive. Applications will be reviewed commencing **November 1, 2016** and will continue until the position is filled. Applications including a letter of interest, curriculum vitae, a research prospective and the names and contact information for five (5) professional references should be submitted via email to Sarah Lloyd (**COP-MedChemDept@med.umich.edu**). Department URL: **https://pharmacy.umich.edu/medchem**

The University of Michigan is an Equal Opportunity/Affirmative Action Employer and is responsive to the needs of dual career couples.

ARE YOU A CREATIVE MICROBIOLOGIST WHO EXCELS AT WORKING COLLABORATIVELY AND PUSHING DISCIPLINARY BOUNDARIES?

Then we want to hear from you. The College of Biological Sciences at the University of Minnesota announces a cluster hire in microbial biology that will recruit **three tenure-track assistant professors** in the Department of Plant and Microbial Biology. We seek outstanding microbiologists who utilize various approaches to understand microorganisms in fundamental, environmental and/or applied contexts. We encourage applicants working in: **Archaeal Biology, Environmental Metagenomics, Eukaryotic Microbiology, Industrial Microbiology and Microbial Cellular Biology.** Successful candidates will have a Ph.D. in microbiology or a related field with appropriate postdoctoral experience, a strong publication record and be committed to graduate and undergraduate education.

Learn more about research themes and specific positions at the college's faculty hiring website.
z.umn.edu/cbsfacultyhiring

College of Biological Sciences
University of Minnesota

INDIANA UNIVERSITY
SCHOOL OF MEDICINE
Office of the Dean

The Indiana University School of Medicine (IUSM) is pleased to announce the launch of the Precision Health initiative, created with the bold goal of addressing major and large-scale health problems facing humanity through multidisciplinary teams of outstanding, innovative researchers. Precision Health was selected as the first recipient of funding from the Indiana University Grand Challenges Program that is a $300 million research expansion across the entire University. The $120 million investment to IUSM in precision medicine is focused on hiring approximately 40 new, full-time faculty members. Precision Health will also support the creation of new facilities, centers, and user platforms, including new gene editing and sequencing cores at the IUSM, and a GMP facility to produce cellular therapeutics. This investment will be leveraged with other IUSM resources to significantly expand the scope of this initiative.

As part of the Precision Health Initiative, the IUSM will be recruiting visionary leaders for the below leadership positions, supported with substantial institutional resources including generous endowed chairs to support personal research and startup, funds to recruit a cadre of faculty to implement this vision, and an opportunity to leverage/expand state of the art facilities.

1. **Director of Cell Therapy and Human Immunology**
2. **Director of Chemical Biology and Biotherapeutics**
3. **Director of Data Sciences and Informatics**
4. **Director of Genomic Medicine**

Candidates interested in these leadership opportunities, or other Precision Health jobs, should visit **http://faculty.medicine.iu.edu/phijobs** to learn more and to apply.

The successful candidates will possess MD and/or PhD degrees, extramurally funded research programs, academic credentials appropriate for an appointment with tenure, and eligibility for licensure in Indiana if applicable. It is preferred that candidates have clinical and research interests in cancer and neurological diseases in adults, children, and minority populations. The administrative expectations include strategic alignment with Precision Health goals, scientific leadership, recruiting, and fiscal responsibilities.

Indiana University is a multi-campus public research institution, and a world leader in professional, medical, and technological education with an annual operating budget of $2.1 billion. The IUSM has over $320 million in grants awarded for fiscal year 2015-2016, the majority of which come from the NIH. Additionally, IUSM provides an interdisciplinary and interactive scientific environment with many multidisciplinary centers and state-of-the-art core facilities. IUSM's clinical partner, IU Health, operates an organized system of care across 18 hospitals that offers unmatched potential for clinical, educational, and research collaborations.

Indiana University is an Equal Opportunity and Affirmative Action Employer. All qualified applicants will receive consideration for employment without regard to race, color, ethnicity, religion, age, sex, sexual orientation or identity, national origin, disability status, or protected veteran status. This institution is also a provider of ADA services.

Perelman School of Medicine University of Pennsylvania | CEET
CENTER OF EXCELLENCE IN ENVIRONMENTAL TOXICOLOGY

Center of Excellence In Environmental Toxicology (CEET) Translational Research Program in Asthma - Faculty Positions

The Center of Excellence in Environmental Toxicology at the **Perelman School of Medicine** at the **University of Pennsylvania** seeks candidates for several Associate, Full, and/or Assistant Professor positions in the tenure track. Applicants must have an M.D. /Ph.D degree.

Individuals with a clinical research program in adult or pediatric asthma; or a translational research program working on airway hyper-responsiveness, aberrant lung injury or repair, drug resistance, inhalation toxicology, allergy and immunology, gene-environment interactions or epigenetic therapies are sought.

Individuals at the senior level have the opportunity to lead this program and significant resources can be made available. Senior applicants (Associate and Full Professor) are expected to have a nationally recognized extramurally funded research program in asthma. Junior Applicants (Assistant Professor) are expected to have a MD/PhD; several years of postdoctoral or clinical research experience and the potential to generate their own grant support.

The faculty appointment will be in an appropriate department in the Perelman School of Medicine. Depending on the applicant's credentials, academic appointments are available in the Department of Medicine (within the Divisions of Pulmonary and Critical Care Medicine or Translational Medicine and Human Genetics) in the Department of Systems Pharmacology and Translational Therapeutics or in the Department of Pediatrics, based in the Children's Hospital of Philadelphia.

Applicants should submit their CV, names of three references, and a description of their current or future research program online.

We seek candidates who embrace and reflect diversity in the broadest sense. The University of Pennsylvania is an EOE. Minorities/Women/Individuals with disabilities/Protected Veterans are encouraged to apply.

Apply online at: **https://www.med.upenn.edu/apps/faculty_ad/index.php/g/d4437**

Research Assistant Professor
Systems Pharmacology and Translational Therapeutics

Perelman School of Medicine
University of Pennsylvania

The Department of Pharmacology at the **Perelman School of Medicine** at the **University of Pennsylvania** seeks candidates for an Assistant Professor position in the non-tenure research track. The successful applicant will have experience in the field of (i) enzymology of xenobiotic metabolism and disposition; (ii) genetic and epigenetic regulation of xenobiotic metabolizing enzymes; and (iii) molecular/cellular mechanisms of hormonal or chemical carcinogenesis. Application of analytical chemistry (e.g. mass spectrometry); biophysical techniques (e.g. structural biology, transient kinetics); and or systems approaches is preferred with a focus on problems in human health and disease. Applicants must have a Ph.D. degree.

Successful applicants will work closely with the Director of the Center of Excellence in Environmental Toxicology (CEET) in these areas and will be expected to generate their own independent grant funding. Applicants should hold a Ph.D. degree in a biomedical science and have three or more years of postdoctoral experience and a strong publication record. To learn more about the CEET visit: http://ceet.upenn.edu/.

We seek candidates who embrace and reflect diversity in the broadest sense.
The University of Pennsylvania is an EOE. Minorities/Women/Individuals with disabilities/Protected Veterans are encouraged to apply.

Apply for this position online at:
https://www.med.upenn.edu/apps/faculty_ad/dex.php/g/d4431

Memorial Sloan-Kettering Cancer Center
The Best Cancer Care, Anywhere

Head Genetically Engineered Mouse Models Core Facility

Sloan-Kettering Institute

The Sloan Kettering Institute (SKI) is seeking a leader for the Genetically Engineered Mouse Models Core Facility (GEMMCF), formerly known as the Transgenic Core Facility. This position is a non-tenure laboratory track faculty position and is partially supported by funds from the Memorial Sloan Kettering Cancer Center (MSKCC) Cancer Center Support Grant from the National Cancer Institute.

The overarching goals of the GEMMCF are to support the production of genetically engineered mouse models and support efficient colony management of existing strains. We are looking for a leader capable of building a world-class facility by applying and developing cutting edge transgenic and genome editing techniques, as well as colony management via cryopreservation and in vitro fertilization services. To support ongoing implementation of new technologies, the GEMMCF will receive substantial support from the Geoffrey Beene Cancer Research Center and from the MSKCC Center for Precision Disease Modeling funded by an NIH U54 grant (https://www.mskcc.org/research-areas/programs-centers/geoffrey-beene-research/pilot-center-precision-disease-modeling).

The GEMMCF Core Head will oversee all Core operations including supervision of staff providing services for gene targeting and genome editing. The Core Head will be the point of contact with academic users both internal and external to the institution, providing consultation for experimental design and data analysis and supporting publications and grant applications.

To qualify, candidates must have a Ph.D. in developmental biology, genetics, embryology or a related field as well as at least 5 years of relevant post degree experience that includes proven skills in all aspects of transgenic and gene targeted mouse production. Previous experience in managing a transgenic unit in a multi-user environment and experience in generating mouse strains using genome editing are preferred. The successful applicant should demonstrate ability to maintain the core on the cutting edge. Strong communication and interpersonal skills are also required.

The deadline for this application is **December 15, 2016.** Interested candidates should send a cover letter, CV and a list of three references to Diane Tabarini. **tabarind@mskcc.org**

www.ski.edu

MSKCC is an equal opportunity and affirmative action employer committed to diversity and inclusion in all aspects of recruiting and employment. All qualified individuals are encouraged to apply and will receive consideration without regard to race, color, gender, gender identity or expression, sexual orientation, national origin, age, religion, creed, disability, veteran status or any other factor which cannot lawfully be used as a basis for an employment decision.

UT Southwestern Medical Center

TENURE-TRACK POSITIONS

The Department of Physiology invites outstanding scientists with Ph.D., M.D., or equivalent degrees to apply for tenure-track faculty positions at the level of Assistant or Associate Professor. Candidates who use innovative optical, mechanical, electrical, molecular biological or computational methods with important applications to physiological systems, ranging from individual genes and proteins to cells and organs are encouraged to apply. The scientific excellence of the candidates is more important than the specific area of research.

These positions are part of the continuing growth of the Department at one of the country's leading academic medical centers. They will be supported by significant laboratory space, competitive salaries, state-of-the-art core facilities and exceptional start up packages. The University of Texas Southwestern Medical Center is the scientific home to six Nobel Prize laureates and many members of the National Academy of Sciences and Institute of Medicine. UT Southwestern conducts more than 3,500 research projects annually totaling more than $417 million. Additional information about the Department of Physiology can be found at **http://www.utsouthwestern.edu/education/medical-school/departments/physiology/index.html**.

Applicants should submit a CV, a brief statement of current and proposed research, and summary of your two most significant publications describing the importance of the work (100-150 words each). Please arrange to have three letters of recommendation sent on his/her behalf. All items should be submitted to **http://academicjobsonline.org/ajo/jobs/7612**. Completed applications will be reviewed starting **November 1, 2016**. You may email questions to **ron.doris@utsouthwestern.edu**.

UT Southwestern Medical Center is an Equal Opportunity/Affirmative Action Employer. Women, minorities, veterans and individuals with disabilities are encouraged to apply.

Department of Biology

The Department of Biology at Drexel University (www.drexel.edu/biology) is accepting applications for a tenure-track faculty position at the assistant or associate professor level. We are seeking an outstanding scientist who will enhance existing strengths within the department and catalyze additional areas of scientific growth. We are particularly interested in individuals utilizing cellular, molecular biological, biochemical and/or genomic based strategies to answer fundamental questions in cellular and molecular biology. Successful candidates at the assistant professor level are expected to establish extramurally funded research programs while those at the associate professor level are expected to have an ongoing extramurally funded research program. Competitive compensation and start-up packages are available. The Department of Biology is a dynamic research intensive department that is in the initial stages of an exciting growth phase where we plan to add 10-12 new tenure-track/tenured faculty positions over the next 5-6 years.

Drexel's vibrant Biology faculty pursues research in the areas of neuroscience, microbiology, epigenetics, cell and developmental biology, molecular evolution and cancer biology using model and non- model organisms. Drexel Biology is housed in the exceptional research and educational facilities of the Papadakis Integrated Sciences Building which include a state-of-the-art Cell Imaging Center with super-resolution, two-photon and confocal microscopes. With recent HHMI funding, the department is also committed to biology education research and seeks to advance STEM education through pedagogical change and faculty development. The department is centered in the University City area of Philadelphia with several academic and research institutions concentrated in a rich urban atmosphere.

The anticipated start date for this position will be September 2017. Applicants should have a PhD, MD, or DPhil as well as appropriate postdoctoral experience. Please submit a CV, two-page statement of research interests & goals, and statement on teaching philosophy and experience to Drexel Jobs, (Requisition **7845**) to the link listed: **www.drexeljobs.com/applicants/Central?quickFind=81555**.

Three letters of reference should be emailed to **bioapply@drexel.edu** with the applicant's name as a subject line. Review of applications will begin **November 15, 2016**, and continue until the position is filled. Please address all correspondence to **Dr. Katy Gonder, Chair of the Biology Search Committee, Dept. of Biology, Drexel University, 3245 Chestnut St., Philadelphia, PA 19104 (bioapply@drexel.edu)**.

Drexel University is an Equal Opportunity/Affirmative Action Employer and encourages applications from women, members of minority groups, disabled individuals, and veterans.

Scientific Director, Centre for Neuroinformatics
Centre for Addiction and Mental Health (CAMH)
Toronto, Ontario

Big things are happening at CAMH: A paradigm shift driven by computation, algorithms and analytics.

This is an unprecedented, scientific leadership opportunity to shape a new centre and lead the next set of fundamental discoveries in brain research. Supported by a multi-million dollar philanthropic gift and fully-affiliated with the University of Toronto, CAMH's Centre for Neuroinformatics will leverage the largest mental health patient database in Canada, and combine world-leading talent specializing in computational approaches to brain science, a robust data integration platform, and analytical tools to accelerate and revolutionize the world's understanding of the brain and brain- based illnesses.

In the coming years, under your leadership as the inaugural Scientific Director, the Centre will be at the forefront of breakthroughs in brain science through the development and application of novel algorithms, computational models, integrative methods, and data visualization techniques. Scientist development, a key focus for the Centre, will help to address the scarcity of talent and propel sustainable, productive collaborations between local, national and international research teams.

As Scientific Director, you will create a bold, global vision for the Centre that leverages the computational and analytical assets and strengths of CAMH, the University of Toronto, and the Canadian and international neuroscience community. You will lead and inspire a team of scientists and operational support staff, and champion excellence through local, national and international collaborations.

As the ideal candidate, you are an internationally respected leader in neuroinformatics, bioinformatics, computational biology, computational modelling, statistical genetics, or a related field who has had great success in forming multi-centre collaborations and significant experience working with biological (molecular, genetic and epigenetics) and clinical data in the context of brain- based disorders.

If you are interested in applying or learning more, please contact Brian Bachand, **bbachand@boyden.com** or Michael Naufal, **mnaufal@boyden.com**. For more about CAMH, Canada's largest mental health and addiction teaching hospital, as well as one of the world's leading research centres in the area of brain science, addiction and mental health, visit **www.camh.ca**

As an employment equity employer, CAMH actively seeks Aboriginal peoples, visible minorities, women, people with disabilities, (including people with who have experienced mental health and substance use challenges), and additional diverse identities for our workforce.

We thank all applicants for their interest, however only those under consideration for the role will be contacted.

POSITIONS OPEN

ASSISTANT PROFESSOR

The Department of Earth, Atmospheric, and Planetary Sciences at the Massachusetts Institute of Technology invites qualified candidates to apply for a tenure track position at the assistant professor level beginning July 2017 or thereafter. Applicants with research interests in Planetary Science are encouraged to apply. We seek an outstanding scientist with interest in and potential for innovation and leadership in teaching at the undergraduate and graduate levels and research. The search is in the broad area of Planetary Science encompassing our Solar System as well as exoplanets, including theory, observation, and instrumentation. However, we are especially interested in individuals whose research complements existing MIT expertise.

Applicants must hold a Ph.D. in Planetary Science or related field by the start of employment and must demonstrate ability to excel in teaching. A complete application must include curriculum vitae, two-page description of research and teaching plans and three letters of recommendations.

Applications are being accepted at Academic Jobs Online: **https://academicjobsonline.org/ajo/jobs/7724** To receive full consideration, complete applications must be received by: **December 1, 2016**.

Search Contact: **Ms. Karen Fosher, HR Administrator, EAPS, Massachusetts Institute of Technology, 54-924, 77 Massachusetts Avenue, Cambridge, MA 02139-4307; email: kfosher@mit.edu**

MIT is an Equal Employment Opportunity Employer. All qualified applicants will receive consideration for employment and will not be discriminated against on the basis of race, color, sex, sexual orientation, gender identity, religion, disability, age, genetic information, veteran status, ancestry, or national or ethnic origin.

ASSISTANT/ASSOCIATE PROFESSOR
Department of Biochemistry and Biophysics
Texas A&M University

The Department of Biochemistry and Biophysics invites applications for a **TENURE-TRACK ASSOCIATE PROFESSOR** position. We seek an exceptional scientist committed to establishing a nationally competitive research program in area of biophotonics. This position is part of a new initiative in biophotonics at Texas A&M University and AgriLife Research that builds on expertise in the Center for Biophotonics and the Institute for Quantum Science and Engineering. Individuals who have expertise in Raman spectroscopy, fluorescence, or other optical approaches and technologies useful for imaging biological systems and for the analysis of biomolecules are encouraged to apply. The successful candidate will have a doctoral degree in a relevant field and be expected to teach courses in relevant disciplines. Please send a PDF file that contains a cover letter, curriculum vitae, research summary (past, present, and planned), a teaching statement and contact information for three professional references to email: **daisy@tamu.edu.** Applications received by **November 30** will be guaranteed full consideration by the Search Committee, although review of applications will continue until the position is filled. *Equal Opportunity Employer*

ECOLOGY FACULTY POSITION
AT DUKE UNIVERSITY

Duke University's Department of Biology is seeking to fill a tenure-track **ASSISTANT PROFESSOR** faculty position in Ecology to begin in August 2018. We are searching for candidates who use empirical or theoretical approaches to study species interactions of any kind and how they are shaped by or modulate ecological responses to environmental changes, broadly defined. We welcome candidates with research interests in any taxon and at any level of organization. Application materials include a curriculum vitae, a research statement, a statement of teaching interests and philosophy, and names of three references. Applications should be submitted through Academic Jobs Online at website: **https://academicjobsonline.org/ajo/jobs/8134**. Applications received by **November 1, 2016** will be guaranteed full consideration. *Duke University, located in Durham, North Carolina, is an Affirmative Action/Equal Opportunity Employer committed to providing employment opportunity without regard to an individual's age, color, disability, genetic information, gender, gender identity, national origin, race, religion, sexual orientation, or veteran status.*

Assistant Professor Positions (Tenure-Track, Three Positions) Cell Biology, Comparative/Integrative Physiology, and Developmental Biology Department of Biological Sciences College of Science Louisiana State University

The Department of Biological Sciences seeks applicants for three tenure-track faculty positions at the level of Assistant Professor in the following areas: **Cell Biology** (Requisition **#R00000076**), **Comparative/Integrative Physiology** (Requisition **#R00001551**), and **Developmental Biology** (Requisition **#R00000086**). Biological Sciences is a large and dynamic department housed within LSU's College of Science with research ranging across all levels of biological organization from molecules to ecosystems. Information about the department is available at http://www.lsu.edu/science/biosci

Successful candidates are expected to establish and maintain a vigorous, extramurally funded research program in one of the following areas: (1) eukaryotic cell biology, (2) comparative or integrative physiology at any level from cells to organ systems, or (3) eukaryotic developmental biology. Other responsibilities include supervising graduate students, contributing to undergraduate/graduate teaching, directing/supervising student research and participating in service activities pertaining to the mission of the Department and advancement of the profession. Preference will be given to individuals with a record of achievement in research that complements the departmental strengths.

Required Qualifications: Ph.D. or equivalent in Biology or related field; and post-doctoral research experience are required. Applicants must have a successful track record of independent research.

A competitive salary and start-up package will be offered. An offer of employment is contingent on a satisfactory pre-employment background check. Application review will begin on **November 15, 2016** and will continue until a candidate is selected.

Apply online and view a more detailed ad at:
https://lsu.wd1.myworkdayjobs.com/en-US/LSU/job/LSU---Baton-Rouge/Assistant-Professor-of-Developmental-Biology_R00000086 (Developmental Biology)

https://lsu.wd1.myworkdayjobs.com/en-US/LSU/job/LSU---Baton-Rouge/Assistant-Professor-of-Cell-Biology_R00000076 (Cell Biology)

https://lsu.wd1.myworkdayjobs.com/en-US/LSU/job/LSU---Baton-Rouge/Assistant-Professor-of-Biological-Sciences_R00001551 (Comparative or Integrative Physiology)

LSU is committed to diversity and is an Equal Opportunity/Equal Access Employer.

UCL Division of Biosciences
Research Department of Cell and Developmental Biology

Head of Research Department and Professor

The Division of Biosciences at UCL seeks to appoint a Professor to serve as Head of the Research Department of Cell and Developmental Biology from the 1st August 2017. CDB is one of four Research Departments in the Division, which comprises the basic biological sciences at UCL, and is the largest Division within the Faculty of Life Sciences. The current Research Department of CDB has major strengths in developmental biology, neuroscience and the use of model systems to study fundamental problems in this area. The Department also houses outstanding research in basic cell biology (mitochondrial biology and cell signalling) and in the evolution of vertebrate development. The successful candidate will have a world-class record of research in a complementary area. We particularly encourage applications from investigators interested in stem cell and tissue biology or mammalian neurodevelopment, as well as from investigators who use genetics of model systems to address CDB areas of research.

As Head of the Research Department, the post-holder will be responsible for oversight of all academic enterprise related to research and teaching in the Department and for promotions and mentoring. The post-holder will work closely with the Divisional Director to set the budget for the Department and organise the Department's space within the Division.

The post-holder will be expected to have a PhD or equivalent degree and a record of successful external funding to support a cutting-edge research programme, as well as considerable experience of undergraduate and post-graduate teaching in the areas of CDB. Administrative experience is desirable.

The appointment will be full time on the UCL Professorial Grade. The salary range will be negotiable on the professorial scale, but not less than £67,885 per annum, inclusive of London Allowance.

Please ensure you read the further particulars carefully before applying for the post as candidates must meet all essential criteria to be considered.

For further details about the vacancy and how to apply online please go to http://www.ucl.ac.uk/hr/jobs/ and search on Reference Number: 1585622.

Applications should include a cover letter, curriculum vitae and an account of current research activities, teaching and administrative experience, and a plan of future research intentions. Please also include the names of three referees to be contacted following a successful interview.

If you would like to discuss the post informally please contact the Director of Biosciences, Professor Frances Brodsky on email: f.brodsky@ucl.ac.uk. For any queries regarding the application process, please contact Biosciences Staffing on email: biosciences.staffing@ucl.ac.uk and quote the reference 1585622.

Closing Date: 23rd October 2016
Latest time for the submission of applications: 23:59
Interview Date: 21st-22nd November 2016

We particularly welcome female applicants and those from an ethnic minority, as they are under-represented within UCL at this level.

Yale Cancer Biology Institute

Assistant, Associate, or Full Professors

The Cancer Biology Institute (YCBI) and the Yale Cancer Center (YCC) are pleased to invite applications from basic and physician scientists for a faculty position in the area of genitourinary medical oncology. Appointments at Yale at the Assistant, Associate, or Full Professor level in the tenure track are available in a number of departments depending on the candidate's focus, and rank will be commensurate with experience and accomplishments. Applicants must have an M.D. and/or Ph.D. or equivalent degree and have demonstrated excellent qualifications in research and education.

We are seeking outstanding and highly motivated individuals with demonstrated potential for vibrant and creative research excellence, and who are working on central problems in cancer biology and translational research, with a specific emphasis on genitourinary cancers. The successful applicant will be located at Yale's state-of-the-art West Campus YCBI facility, which was established to unearth molecular and cellular biological underpinnings common to cancers of all types, identify new molecular targets, and develop new drug treatments to contain or eradicate these cancers. In concert with YCC, the Institute aims to become a driver of basic science through connections with clinical and translational research already at Yale. The Institute also fosters close collaboration with the Systems Biology, Chemical Biology, Nanobiology, and Microbial Sciences Institutes on Yale's West Campus, and will work directly with the Yale Centers for Genome Analysis and Molecular Discovery.

Ideal candidates are expected to have in place a foundational scientific vision for building a robust and competitive program to unearth new and fundamental cancer cellular or molecular biology that can be translated to human clinical benefit. Candidates will also be expected to contribute to graduate and undergraduate education. Special preference for this position will be given for candidates with a capability and interest in developing bladder, prostate, or renal cancer projects. Successful candidates for a mid- or senior-level appointment should be nationally and internationally recognized experts in the field of cancer biology, an extensive publication record, and a robust funding portfolio.

Applicants should submit a letter describing qualifications, along with a CV, a two-page summary of current and proposed research, and three letters of reference to the following Interfolio website: **https://apply.interfolio.com/37392**.

Informal inquiries may be submitted by email to the leadership of the Yale Cancer Biology Institute or Genitourinary Medical Oncology, at **cancerbiologyinstitute@yale.edu**. Consideration of applications will begin **December 1st, 2016**.

Yale University is an Equal Opportunity/Affirmative Action Employer. We seek candidates who embrace and reflect diversity in the broadest sense. Yale values diversity among its students, staff, and faculty and strongly welcomes applications from women, persons with disabilities, protected veterans, and underrepresented minorities.

NYU School of Medicine
NYU LANGONE MEDICAL CENTER

Director of the Stewart and Judith Colton Center for Autoimmunity

The NYU School of Medicine is accepting applications for the position of Professor and Director of the Judith and Stewart Colton Center for Autoimmunity. The mission of the Colton Center is to elucidate the initiating immunological events and to develop new diagnostics and treatments for autoimmune diseases (http://www.med.nyu.edu/colton-center-for-autoimmunity). The director will lead an extensive research effort among leading physicians and scientists with diverse expertise across the Medical Center's scientific community in order to to advance translational science in the field of autoimmune diseases.

To qualify, the director must have scientific expertise in the area of immunology, significant publications in high impact journals and a record of success in obtaining NIH funding. Candidates must be an associate or full professor, be able to provide leadership and a strategic vision for the Colton Center.

Applications are electronic only at **https://apply.interfolio.com/36764**, where you will be asked to upload the following documents:

1. Cover Letter
2. Curriculum Vitae

Equal Opportunity Employer: disability/veteran. VEVRAA Federal Contractor

---

Kansas City, MO

UMKC

Assistant/Associate Professor

The School of Biological Sciences at the University of Missouri – Kansas City invites applications for two full-time tenure track faculty positions at the rank of Assistant or Associate Professor. We encourage applications from individuals who employ molecular, cellular, or in silico approaches to address fundamental biological questions. The primary attributes we seek in candidates are (1) demonstrated excellence in research, as the faculty member would be expected to initiate or continue an independent, extramurally funded research program, and (2) potential or demonstrated excellence in teaching and mentoring.

UMKC is an equal access, equal opportunity, affirmative action employer that is fully committed to achieving a diverse faculty and staff.

To apply visit **http://apptrkr.com/885270**

POSITIONS OPEN

TENURE-TRACK ASSISTANT PROFESSOR IN MICROBIOME RESEARCH

The Department of Biological Sciences (http://www.albany.edu/biology), University at Albany, State University of New York, invites applications for a tenure-track position at the **ASSISTANT PROFESSOR** level in the broad area of host-microbe interactions. The applicant should have a research interest in the interactions of microorganisms with their hosts, taking advantage of contemporary genome-wide high-throughput methods, advanced bioinformatics, and systems approaches.

The successful candidate will contribute to the Department's graduate program in Ecology and Evolutionary Biology and/or in Molecular, Cellular, Developmental, and Neural Biology and will be expected to teach at the undergraduate and graduate levels in courses appropriate to their expertise. Initial salary and startup funds are competitive. The successful candidate is expected to establish a sustained, externally funded research program that may include collaborative research. Applicants should have the ability to interact with a diverse faculty working across many research areas. Local opportunities for collaboration include faculty in the Life Sciences (http://www.albany.edu/lifesciences), the School of Public Health (http://www.albany.edu/sph) as well as the New York State Department of Health (www.wadsworth.org) and the RNA Institute (https://www.rna.albany.edu).

Application materials will be accepted on-line at website: **https://albany.interviewexchange.com/jobofferdetails.jsp?JOBID=76740&CNTRNO=1&TSTMP=1475243576601**

TWO ASSISTANT PROFESSOR POSITIONS IN CHEMISTRY ANALYTICAL/PHYSICAL AND ENVIRONMENTAL CHEMISTRY UTAH STATE UNIVERSITY

The Department of Chemistry and Biochemistry at Utah State University (USU) invites applications for up to two tenure-track positions at the **ASSISTANT PROFESSOR** level beginning Fall 2017. Candidates must have a PhD in chemistry or a related field and postdoctoral or equivalent experience. The position requires the development of an externally funded research program and teaching at the undergraduate and graduate levels. Investigators with interests in analytical chemistry or the interface of analytical and physical chemistry, especially in the areas of environmental and water chemistry, are encouraged to apply. Application information can be found on-line at website: **http://jobs.usu.edu** (REQ ID: F1600189); letters of reference will be requested automatically via a system email from USU requesting your references to upload a letter on your behalf. Evaluation of applications will begin **October 30, 2016** and will continue until the position is filled. For further information please visit our website at http://www.chem.usu.edu. *Utah State University is an Equal Opportunity/Affirmative Action Employer committed to assembling a diverse faculty. Women and members of minority groups are strongly encouraged to apply.*

PRINCETON UNIVERSITY DEPARTMENT OF CHEMISTRY ASSISTANT PROFESSOR

The Department of Chemistry at Princeton University invites applications for a tenure-track assistant professor position in all areas of chemistry. We seek a faculty member who will create a climate that embraces excellence and diversity with a strong commitment to research and teaching that will enhance the work of the department and attract and retain a diverse student body. We strongly encourage applications from members of all underrepresented groups.Candidates are expected to have completed the Ph.D. in chemistry or a related field at the time of appointment. Applicants should submit a description of research interests, curriculum vitae, a list of publications, and contact information for three referees online at website **jobs.princeton.edu/applicants/Central?quickFind=67134**. The deadline for applications is October 15, 2015. *Princeton University is an Equal Opportunity Employer. All qualified applicants will receive consideration for employment without regard to race, color, religion, sex, national origin, disability status, protected veteran status, or any other characteristic protected by law. This position is subject to the University's background check policy.*

Yale *Cancer Biology Institute*

Assistant, Associate, or Full Professors

The Cancer Biology Institute, part of the Yale Comprehensive Cancer Center (YCC) at Yale University School of Medicine, invites applications from basic and physician scientists for Assistant, Associate, or Full Professor positions in the tenure track. Appointment at Yale is available in a number of departments, and rank will be commensurate with experience and accomplishments. Applicants must have an M.D. and/or Ph.D. or equivalent degree and have demonstrated excellent qualifications in research and education. The successful candidates will have experience in the field of cancer biology, with specific target areas for these recruitments being cancer proteomics, metabolomics/metabolism, bioinformatics, cancer genetics and genomics, chemical biology, RNA/transcriptomics, tumor microenvironment, and tumor immunology. Responsibilities include establishing a vigorous and independently funded research program in cancer biology while supervising and mentoring students with diverse backgrounds plus contributing to the graduate and medical school educational missions. We seek individuals with strong records of independent creative accomplishments, who will interact productively with colleagues within the Cancer Biology Institute, across the Yale West Campus, and across the Yale Comprehensive Cancer Center – taking advantage of the unique opportunities to translate basic findings from the Institute into clinical practice.

The Cancer Biology Institute is one of 6 newly-formed multi-disciplinary research institutes on Yale's burgeoning West Campus, which is self-contained but conveniently linked to Yale's nearby New Haven campuses and the Yale Cancer Center. Additional West Campus assets include the Systems Biology, Chemical Biology, Nanobiology, and Microbial Sciences Institutes, as well as state-of-the-art core facilities in high throughput cell biology, imaging, small molecule discovery, genomic analysis and other technologies. Linkage to these Institutes provides unique opportunities for interdisciplinary research in the Cancer Biology Institute that is simultaneously poised for translation through close involvement with the YCC and Smilow Cancer Hospital at Yale-New Haven.

Please submit a letter describing qualifications, along with a CV, a two-page summary of current and proposed research, and three letters of reference to the following Interfolio website: **https://apply.interfolio.com/37394**.

Informal inquiries may be submitted to Drs. Mark Lemmon and Joseph Schlessinger, Co-Directors, Yale Cancer Biology Institute, at **cancerbiologyinstitute@yale.edu**. Consideration of applications will begin **November 14th, 2016**.

Yale University is an Equal Opportunity/Affirmative Action Employer. We seek candidates who embrace and reflect diversity in the broadest sense. Yale values diversity among its students, staff, and faculty and strongly welcomes applications from women, persons with disabilities, protected veterans, and underrepresented minorities.

Department of Pharmacology Yale University

Assistant or Associate Professor of Pharmacology

The Department of Pharmacology at Yale University School of Medicine invites applications for Assistant or Associate Professor positions in the tenure track. Applicants must have an M.D. and/or Ph.D. or equivalent degree and have demonstrated excellent qualifications in research and education. Areas of interest may encompass any aspect of modern drug discovery, including studies of molecular function such as proteomics, chemical biology, structural biology (including electron microscopy) and computational biology in different areas of cell signaling, metabolism, genetic diseases and epigenetic mechanisms.

Responsibilities include establishing a vigorous and independently funded research program in cancer biology while supervising and mentoring students with diverse backgrounds plus contributing to the graduate and medical school educational missions. We seek individuals with strong records of independent creative accomplishments, who will interact productively with colleagues within the Department and across Yale School of Medicine.

Pharmacology at Yale University has a rich history of pre-eminence in drug discovery, indeed the first cancer chemotherapy clinical trials were conducted here. Today, the research in our Department encompasses a broad range of fields, with researchers aiming to both understand and treat human disease, with particular strengths in drug discovery, integrative cell signaling, structural biology, and neuroscience. For more details, see https://medicine.yale.edu/pharm/.

Please submit a letter describing qualifications, along with a CV, a two-page summary of current and proposed research, and three letters of reference to the following Interfolio website: https://etc

Informal inquiries may be submitted electronically to Prof. Joseph Schlessinger, Chair of Pharmacology, c/o Nathan Kucera (**nathan.kucera@yale.edu**).

Consideration of applications will begin **December 1st, 2016**.

Yale University is an Equal Opportunity/Affirmative Action Employer. We seek candidates who embrace and reflect diversity in the broadest sense. Yale values diversity among its students, staff, and faculty and strongly welcomes applications from women, persons with disabilities, protected veterans, and underrepresented minorities.

Caltech

CALIFORNIA INSTITUTE OF TECHNOLOGY invites applications for a tenure-track faculty position at the assistant professor level in the Division of Chemistry and Chemical Engineering. Candidates with strong commitments to research and teaching excellence are encouraged to apply.

BIOCHEMISTRY

Assistant professor level in biochemistry and related areas. The term of the initial appointment is four years and is contingent upon completion of all requirements for a Ph.D. in biochemistry or closely related fields. Interested candidates should apply electronically at **https://applications.caltech.edu/job/bmb**. Candidates unable to apply electronically may submit curriculum vitae, publication list, teaching statement, description of proposed research, and three letters of recommendation to: **Chair of the Biochemistry Search Committee, Division of Chemistry and Chemical Engineering, M/C 164-30, California Institute of Technology, Pasadena, CA 91125**. Applications should be received by **November 1, 2016**.

CHEMICAL ENGINEERING

Exceptionally well-qualified applicants at the associate or full professor level may also be considered. The term of the initial untenured appointment is four years and is contingent upon completion of all requirements for a Ph.D. in chemical engineering or in a related field. Interested candidates should apply electronically **https://applications.caltech.edu/job/chemeng**. Candidates unable to apply electronically may submit curriculum vitae, publication list, teaching statement, a description of proposed research, and three letters of recommendation to: **Chair of the Chemical Engineering Search Committee, M/C 210-41, California Institute of Technology, Pasadena, CA 91125**. Applications should be received by **December 15, 2016**.

CHEMISTRY

Exceptionally well-qualified applicants at the tenured level may also be considered. Areas of particular interest includes experimental physical chemistry, inorganic chemistry, and biochemistry, although applications in any area of chemistry broadly defined are welcome. The term of the initial appointment is four years, and the appointment is contingent upon completion of all requirements for a Ph.D. in chemistry or in a related field. Interested candidates should apply electronically at **https://applications.caltech.edu/job/chemistry**. Candidates unable to apply electronically may submit a curriculum vitae, publication list, teaching statement, description of proposed research, and three letters of recommendation to: **Chair of the Chemistry Search Committee, M/C 164-30, California Institute of Technology, Pasadena, CA 91125**. Applications should be received by **October 15, 2016**.

EOE of Minorities/Females/Protected Vets/ Disability.

Massachusetts Institute of Technology

Come work with us!

Department of Biological Engineering

Faculty positions in Biological Engineering

The MIT Department of Biological Engineering invites applications for tenure-track faculty positions at the assistant professor level, to begin July 2017 or on a mutually agreed date thereafter. Applicants should hold a Ph.D. in a science or engineering discipline related to biological engineering. A more senior faculty appointment may be considered in special cases. Candidates should aspire to direct a leading research program that fuses molecular/cellular bioscience with quantitative engineering analysis/synthesis approaches. Areas of high priority include microbial systems and infectious disease. Faculty duties include teaching at the graduate and undergraduate levels as well as oversight of research, and candidates should be capable of instructing in our core biological engineering educational curricula.

Candidates must register with the BE search website at http://be-fac-search.mit.edu, and must submit application materials electronically to this website. Candidate applications should include a description of professional interests and goals in both teaching and research. Each application should include a curriculum vitae and the names and addresses of three or more references who will provide recommendation letters. References should submit their letters directly at the http://be-fac-search.mit.edu website.

Applications received by 1st December 2016 will be given priority.

Questions may be directed to: Prof. Douglas Lauffenburger, Head, Department of Biological Engineering, MIT 16-343, Cambridge, MA 02139-4307, lauffen@mit.edu

MIT is an Affirmative Action/Equal Opportunity employer committed to diversity and inclusion.

http://web.mit.edu

University of Massachusetts Medical School
UMASS

RNA Therapeutics Institute

Tenure-Track Positions

The RNA Therapeutics Institute (RTI) at the University of Massachusetts Medical School, actively seeks M.D. and M.D./Ph.D. applicants for tenure-track, physician-scientist faculty positions. Successful candidates will conduct innovative research to understand normal physiology and development, disease mechanisms and/or to develop novel diagnostics or therapies. Candidates need not necessarily conduct research directly focused on RNA biology or development of RNA therapeutics, but should indicate how their research will synergize with ongoing research within the RTI and the greater UMass Medical School community.

Physician scientists and researchers with significant industrial experience who wish to return to academia are particularly encouraged to apply. Other specialties of interest include synthetic chemists, materials scientists, computational researchers, bioengineers, geneticists, cell and molecular biologists, and biochemists.

The RTI is housed in a new state-of-the-art research building, and is central to a campus-wide interdisciplinary initiative in RNA therapeutics, stem cell biology and gene therapy designed to facilitate collaboration among basic scientists, preclinical investigators and clinicians. As a recipient of a Clinical and Translational Science Award (CTSA) from the NIH, UMass Medical School seeks to build an environment in which basic, applied and clinical researchers collaborate to inform our understanding of human disease and accelerate development of novel diagnostics and therapies. To further encourage collaboration, all RTI investigators hold joint appointments within other departments on campus.

Applicants should submit a cover letter, curriculum vitae, a two-page statement of research interests, and contact information for three references to **https://academicjobsonline.org/ajo/jobs/7506**. Applications will be reviewed expeditiously, with interviews commencing in November. Inquiries (but not application materials) may be directed to Tiffanie Gardner at **Tiffanie.Gardner@umassmed.edu**. Applications at the Assistant, Associate and Full Professor levels will be considered. The position will remain open until filled.

As an Equal Opportunity and Affirmative Action Employer, UMW recognizes the power of a diverse community and encourages applications from individuals with varied experiences, perspectives and backgrounds.

Professor (Open Rank)

DEPARTMENT OF BIOENGINEERING

College of Engineering

University of Illinois at Urbana-Champaign

The Department of Bioengineering at the University of Illinois at Urbana-Champaign (UIUC) seeks full-time Bioengineering faculty for tenured or tenure-track positions in the areas of translational bioengineering, computational biology at the cell and molecular levels, neuro-engineering, and cancer bioengineering.

Please visit the website **http://my.bioen.illinois.edu/join** to view the complete position announcement and application instructions. Applications received prior to **January 15, 2017** will receive full consideration.

The University of Illinois conducts criminal background checks on all job candidates upon acceptance of a contingent offer.

*Illinois is an equal opportunity employer and all qualified applicants will receive consideration for employment without regard to race, religion, color, national origin, sex, sexual orientation, gender identity, age, status as a protected veteran, or status as a qualified individual with a disability. Illinois welcomes individuals with diverse backgrounds, experiences, and ideas who embrace and value diversity and inclusivity. (**www.inclusiveillinois.illinois.edu**)*

ILLINOIS
UNIVERSITY OF ILLINOIS AT URBANA-CHAMPAIGN

Faculty Positions (All Ranks)

DEPARTMENT OF MECHANICAL SCIENCE AND ENGINEERING

College of Engineering

University of Illinois at Urbana-Champaign

The Department of Mechanical Science and Engineering at the University of Illinois at Urbana-Champaign invites applications for multiple faculty positions in all ranks. Emphasis is on the areas of (i) manufacturing and (ii) energy and sustainability; however, excellent candidates will be considered in all areas related to mechanical science and engineering.

A doctoral degree is required, and salary is commensurate with qualifications and experience. Applications received by **December 4, 2016**, will receive full consideration. Early applications are encouraged. Interviews may take place before the given date; applications received after that date may be considered until positions are filled. The expected start date of a position offered/accepted through this search is August 16, 2017, but other start dates will be considered.

A full position description and information on how to apply can be found on the University of Illinois Urbana-Champaign online jobsite **http://jobs.illinois.edu**. For further information regarding application procedures, please address questions to: **mechse-facultyrecruiting@illinois.edu.**

The University of Illinois conducts criminal background checks on all job candidates upon acceptance of a contingent offer.

ILLINOIS
UNIVERSITY OF ILLINOIS AT URBANA-CHAMPAIGN

www.inclusiveillinois.illinois.edu

Illinois is an EOE employer/Vet/Disabled

POSITIONS OPEN

TENURE-TRACK FACULTY POSITION in BIOCHEMISTRY & MOLECULAR BIOPHYSICS at KANSAS STATE UNIVERSITY

The Department of Biochemistry and Molecular Biophysics at Kansas State University (http://www.k-state.edu/bmb/) in Manhattan, KS, invites applications for a tenure-track position at the **ASSISTANT or ASSOCIATE PROFESSOR** level, to begin in August, 2017. Applicants must have a Ph.D. or equivalent degree and postdoctoral experience. Candidates at the associate level must have an established, extramurally-funded research program. The position includes competitive salary and start-up funding, as well as health and retirement benefits. We desire applicants with research interests that complement existing programs, including, but not limited to: physical/structural biochemistry, computational biology, membrane transport or biochemistry, molecular bases of diseases, insect biochemistry, especially in the context of agriculture or human and animal disease. We seek individuals who will develop a strong research program and excel in teaching a diverse population of undergraduate and graduate students (website: **http://www.k-state.edu/bchem/department/employment/index.html** for additional information). Applicants should submit a single PDF file with their curriculum vitae, a statement of research and teaching, and selected reprints at website: **http://careers.k-state.edu/cw/enus/job/497648**. Please also obtain three letters of reference, sent to Professor John Tomich, Search Committee Chair (email: jtomich@ksu.edu). Review of applications will begin on **November 20, 2016** and continue until the position is filled. A background check is required for all new employees. *Kansas State University is an Equal Opportunity Employer and actively seeks diversity among its employees.*

UNM HEALTH SCIENCES CENTER

Junior Faculty Position

The Clinical and Translational Science Center at the University of New Mexico invites applicants for a junior faculty member for our Mentored Career Development (KL2) Scholar Program at the Assistant Professor level in the tenure or flex track beginning in the Spring of 2017. Individuals with a MD, PhD, MD/PhD or equivalent degree engaged in all types of clinical and translational research relevant to the Departments of Internal Medicine, Molecular Genetics and Microbiology or Psychiatry and Behavioral Science are encouraged to apply. The successful Scholar candidate will have 75% of their effort committed to their research and 25% committed to other duties and will be able to become a faculty member in one of the following departments in the School of Medicine: Internal Medicine, Molecular Genetics and Microbiology, or Psychiatry and Behavioral Science.

For complete details or to apply, visit **https://unmjobs.unm.edu**. Reference posting #: 0836236. For best consideration, apply by: **November 11, 2016**. This position will remain open until filled.

UNM is an EEO/AA Employer.

LIFE SCIENCES INSTITUTE
UNIVERSITY OF MICHIGAN

Tenure Track Faculty Position

The Life Sciences Institute (LSI) at the University of Michigan invites applications for a position at the rank of Assistant or Associate Professor in any research area. Additional consideration may be given to scientists using electron cryo-microscopy to address important biological questions.

Faculty will hold research professor appointments in the LSI and a tenure-track or tenured instructional appointment in one of the University's schools and colleges. Joint appointments are likely in the Medical School, the College of Literature, Sciences and the Arts, the College of Engineering, the School of Public Health, the Dental School, and the College of Pharmacy. All faculty are expected to participate in the University of Michigan's teaching mission and to demonstrate commitment to service in the larger community.

The LSI is a scientific enterprise at the University of Michigan dedicated to fundamental discovery in the biological, biomedical and biochemical sciences in a state-of-the-art collaborative physical space (www.lsi.umich.edu). Through basic discovery, the institute seeks to advance knowledge in critical areas of biology with an ultimate goal of contributing to human health including cancer, metabolic disorders, brain disorders, and infectious disease.

The LSI is currently home to 22 faculty members in the disciplines of cell biology, genetics, physiology, structural biology, stem cell biology, and chemistry, including three Howard Hughes Medical Institute investigators and four members of the National Academies of Medicine or Science. Our culture centers on upholding scientific excellence, embracing risk, and collaborating across disciplines to achieve an impact greater than the sum of our individual parts.

In addition to faculty labs, the institute houses state-of-the-art instrumentation and computing, including the following transmission electron microscopes: 300kV Titan Krios, 200kV Talos Artica, 120kV Tecnai G2 Spirit, and 100vK Morgagni. Additional institute resources include high-throughput screening center with extensive chemical collections and a unique library of natural product extracts, and a comprehensive protein production and X-ray crystallography facility. The LSI is also home to the U-M Program in Chemical Biology — which offers a Ph.D. in chemical biology and an M.S. in cancer chemical biology.

Candidates are expected to develop an internationally recognized program of scholarly research and to excel in teaching and mentoring at the graduate level. The position will remain open until filled but preference will be given to applicants who have submitted all requested materials prior to **November 15, 2016**. Applicants should send a single PDF containing a cover letter, curriculum vitae, copies of up to three reprints, and a one- to two-page summary of research plans and arrange to have three confidential letters of reference (in PDF format) sent directly to: **lsisearch@umich.edu**. The LSI is a participant in the Michigan Biological Sciences Scholars Program (http://bssp.med.umich.edu/) which recruits top researchers to the University of Michigan Medical School. Individuals from groups under-represented in the sciences are encouraged to apply.

The University of Michigan is supportive of the needs of dual career couples and is a non-discriminatory, affirmative action employer.

University of New Hampshire

Faculty Positions
Department of Molecular, Cellular and Biomedical Sciences

The Department of Molecular, Cellular and Biomedical Sciences in the College of Life Sciences and Agriculture at the University of New Hampshire invites applications for two tenure-track faculty. These positions are at the Assistant Professor level and require demonstrated interests and expertise in 1) **Cell Biology** and 2) **Immunology**. Candidates must have a Ph.D. and demonstrated potential to develop and lead productive research programs.

We seek individuals who can integrate their areas of strength with existing academic and research programs. Successful candidates will be expected to compete successfully in national funding initiatives and to achieve national and international recognition in their field. They will also be expected to train graduate students and teach courses at the undergraduate and graduate levels.

Complete application information is available at: **https://jobs.usnh.edu/**. Review of applications will begin on Dec. 2, 2016 and will continue until positions are filled.

All applicants will be required to apply online at **http://jobs.usnh.edu**. Please direct all inquiries to W. Kelley Thomas, Search Committee Chair, **Kelley.Thomas@unh.edu**.

The University seeks excellence through diversity among its administrators, faculty, staff, and students. The university prohibits discrimination on the basis of race, color, religion, sex, age, national origin, sexual orientation, gender identity or expression, disability, veteran status, or marital status. As a NSF ADVANCE grant recipient, the University of New Hampshire strives to enhance the recruitment, retention and advancement of women faculty and other underrepresented groups in STEM disciplines. Application by members of all underrepresented groups is encouraged.

POSITIONS OPEN

Marine Biological Laboratory | THE UNIVERSITY OF CHICAGO

Hibbitt Early Career Fellows Program

The Marine Biological Laboratory in Woods Hole, Massachusetts announces the **Hibbitt Early Career Fellows Program**, designed to allow exceptional scientists early in their careers to establish their own research programs as an alternative to traditional postdoctoral positions. Recent Ph.D. (or equivalent degree) graduates with proven research excellence will be given space, resources, and support needed to run independent labs under the mentorship of a network of sponsors. Fellows will not have formal teaching or administrative responsibilities, but will be eligible to teach in MBL courses and workshops.

Fellows will take advantage of MBL's unique research environment and resources, in the context of a collegial, collaborative, and interdisciplinary network of investigators, and will be able to apply for external funding as P.I. or co-P.I. to add strength to their research programs.

Applications are encouraged in research areas that can benefit from and contribute to MBL's strategic strengths, in particular those relevant to **marine and aquatic organismal biology** and/or **marine microbial diversity and ecology**.

MBL is especially committed to consideration of candidates from historically underrepresented talent pools, including women and minority candidates.

Applications will be accepted starting
November 1, 2016
Appointment of the initial cohort of Hibbitt Fellows is expected to be announced in Spring 2017.

For information and application:
www.mbl.edu/HibbittFellows

By **Lorena A. Barba**

The hard road to reproducibility

Early in my Ph.D. studies, my supervisor assigned me the task of running computer code written by a previous student who was graduated and gone. It was hell. I had to sort through many different versions of the code, saved in folders with a mysterious numbering scheme. There was no documentation and scarcely an explanatory comment in the code itself. It took me at least a year to run the code reliably, and more to get results that reproduced those in my predecessor's thesis. Now that I run my own lab, I make sure that my students don't have to go through that.

In 2012, I wrote a manifesto in which I committed to best practices for reproducibility. Today, a new student arriving in my group finds all of our research code in tidy repositories, where every change is recorded automatically. Version control is our essential technology for record keeping and collaboration. Whenever we publish a paper, we create a "reproducibility package," deposited online, which includes the data sets and all the code that is needed to recreate the analyses and figures. These are the practices that work for us as computational scientists, but the principles behind them apply regardless of discipline.

It takes new students some time to learn how to work to these standards, but we have documentation and training materials to make it as painless as possible. My students don't resent investing their time in this. They know that practices like ours are crucial for the integrity of the scientific endeavor. They also appreciate that our approach will help them show potential future employers that they are careful, conscientious researchers.

I am pleased when our group is recognized for our high standards in other people's writings, and when we are invited to speak about these practices at meetings. But we've found we still have a lot to learn about what it takes for research, even when done to high standards of reproducibility, to be replicated. A couple years ago, we published a paper applying computational fluid dynamics to the aerodynamics of flying snakes. More recently, I asked a new student to replicate the findings of that paper, both as a training opportunity and to help us choose which code to use in future research. Replicating a published study is always difficult—there are just so many conditions that need to be matched and details that can't be overlooked—but I thought this case was relatively straightforward. The data were available. The whole analysis was open for inspection. The additional details were documented in the supplementary materials. It was the very definition of reproducible research.

"My students and I continuously discuss and perfect our standards."

Three years of work and hundreds of runs with four different codes taught us just how many ways there are to go wrong! Failing to record the version of any piece of software or hardware, overlooking a single parameter, or glossing over a restriction on how to use another researcher's code can lead you astray.

We've found that we can only achieve the necessary level of reliability and transparency by automating every step. Manual actions are replaced by scripts or logged into files. Plots are made only via code, not with a graphical user interface. Every result, including those from failed experiments, is documented. Every step of the way, we want to anticipate what another researcher might need to either reproduce our results (run our code with our data) or replicate them (independently arrive at the same findings).

About 150 years ago, Louis Pasteur demonstrated how experiments can be conducted reproducibly—and the value of doing so. His research had many skeptics at first, but they were persuaded by his claims after they reproduced his results, using the methods he had recorded in keen detail. In computational science, we are still learning to be in his league. My students and I continuously discuss and perfect our standards, and we share our reproducibility practices with our community in the hopes that others will adopt similar ideals. Yes, conducting our research to these standards takes time and effort—and maybe our papers are slower to be published. But they're less likely to be wrong. ■

Lorena A. Barba is an associate professor at The George Washington University in Washington, D.C. Send your story to SciCareerEditor@aaas.org.

ILLUSTRATION: ROBERT NEUBECKER